frontiers | Research Topics

Personalized medicine in neuroscience: Molecular to system approach

Edited by
Ali Yadollahpour, Ti-Fei Yuan and Sergio Machado

Published in
Frontiers in Medicine
Frontiers in Integrative Neuroscience

ISSN 1664-8714
ISBN 978-2-8325-4127-2
DOI 10.3389/978-2-8325-4127-2

About Frontiers

Frontiers is more than just an open access publisher of scholarly articles: it is a pioneering approach to the world of academia, radically improving the way scholarly research is managed. The grand vision of Frontiers is a world where all people have an equal opportunity to seek, share and generate knowledge. Frontiers provides immediate and permanent online open access to all its publications, but this alone is not enough to realize our grand goals.

Frontiers journal series

The Frontiers journal series is a multi-tier and interdisciplinary set of open-access, online journals, promising a paradigm shift from the current review, selection and dissemination processes in academic publishing. All Frontiers journals are driven by researchers for researchers; therefore, they constitute a service to the scholarly community. At the same time, the *Frontiers journal series* operates on a revolutionary invention, the tiered publishing system, initially addressing specific communities of scholars, and gradually climbing up to broader public understanding, thus serving the interests of the lay society, too.

Dedication to quality

Each Frontiers article is a landmark of the highest quality, thanks to genuinely collaborative interactions between authors and review editors, who include some of the world's best academicians. Research must be certified by peers before entering a stream of knowledge that may eventually reach the public - and shape society; therefore, Frontiers only applies the most rigorous and unbiased reviews. Frontiers revolutionizes research publishing by freely delivering the most outstanding research, evaluated with no bias from both the academic and social point of view. By applying the most advanced information technologies, Frontiers is catapulting scholarly publishing into a new generation.

What are Frontiers Research Topics?

Frontiers Research Topics are very popular trademarks of the *Frontiers journals series*: they are collections of at least ten articles, all centered on a particular subject. With their unique mix of varied contributions from Original Research to Review Articles, Frontiers Research Topics unify the most influential researchers, the latest key findings and historical advances in a hot research area.

Find out more on how to host your own Frontiers Research Topic or contribute to one as an author by contacting the Frontiers editorial office: frontiersin.org/about/contact

Personalized medicine in neuroscience: Molecular to system approach

Topic editors

Ali Yadollahpour — The University of Sheffield, United Kingdom
Ti-Fei Yuan — Shanghai Jiao Tong University, China
Sergio Machado — Federal University of Santa Maria, Brazil

Citation

Yadollahpour, A., Yuan, T.-F., Machado, S., eds. (2024). *Personalized medicine in neuroscience: Molecular to system approach*. Lausanne: Frontiers Media SA.
doi: 10.3389/978-2-8325-4127-2

Table of contents

frontiers in Medicine

ORIGINAL RESEARCH
published: 27 November 2020
doi: 10.3389/fmed.2020.598055

Neutrophil to Lymphocyte Ratio Predicts Outcome of Stroke by Cervicocranial Arterial Dissection

Guangbi Sun[1†], Yi Yang[1†], Zhiguo Chen[1†], Le Yang[2], Shanshan Diao[1], Shicun Huang[1], Yiqing Wang[1], Yiting Wang[1], Baoliang Sun[3], Xia Yuan[1] and Xingshun Xu[1,4*]*

[1] Department of Neurology, The First Affiliated Hospital of Soochow University, Suzhou, China, [2] School of Public Health, Fujian Medical University, Fuzhou, China, [3] Department of Neurology, The Second Affiliated Hospital, Shandong Academy of Medical Sciences, Shandong First Medical University, Taian, China, [4] The Institute of Neuroscience, Soochow University, Suzhou, China

OPEN ACCESS

Edited by:
Ti-Fei Yuan,
Shanghai Jiao Tong University, China

Reviewed by:
Qing Liu,
Peking Union Medical College Hospital (CAMS), China
Fang Zhang,
Mass General Research Institute, United States
Yujiao Lu,
Augusta University, United States

***Correspondence:**
Xia Yuan
yx2077@sina.com
Xingshun Xu
xingshunxu@suda.edu.cn

[†]These authors have contributed equally to this work

Specialty section:
This article was submitted to Precision Medicine, a section of the journal Frontiers in Medicine

Received: 23 August 2020
Accepted: 03 November 2020
Published: 27 November 2020

Citation:
Sun G, Yang Y, Chen Z, Yang L, Diao S, Huang S, Wang Y, Wang Y, Sun B, Yuan X and Xu X (2020) Neutrophil to Lymphocyte Ratio Predicts Outcome of Stroke by Cervicocranial Arterial Dissection. Front. Med. 7:598055. doi: 10.3389/fmed.2020.598055

Background and Purpose: Neutrophil to lymphocyte ratio (NLR) is positively associated with poor prognosis in patients with cerebral infarction. The goal of this prospective study is to explore the predictive value of NLR in patients with acute ischemic stroke (AIS) caused by cervicocranial arterial dissection (CCAD).

Methods: Ninety-nine patients with AIS caused by CCAD met criteria for inclusion and exclusion were selected for this study. We collected baseline data on the admission including NLR. The primary poor outcome was major disability (modified Rankin Scale score $\geq$ 3) or death at 3 months after AIS.

Results: A total of 20 (20.2%) patients had a poor outcome at 3 months after AIS. According to the 3-month outcome, the patients were divided into two groups and univariate and multivariable analyses were conducted. Among the risk factors, elevated NLR levels were independently associated with 3-month poor outcomes. Further, we made the ROC curve to evaluate the predictive value of NLR level on prognosis. The area under the curve was 0.79 and a cut-off value of NLR was 2.97 for differentiating the poor outcome. We divided patients into groups according to the cut-off value. Patients with high NLR have a higher risk of poor outcome than those with low NLR ($P < 0.05$).

Conclusion: As an inflammatory marker, elevated NLR levels were associated with 3-month poor outcome in AIS caused by CCAD.

Keywords: cervicocranial arterial dissection, acute ischemic stroke, inflammation, neutrophil to lymphocyte ratio, 3-month outcome

INTRODUCTION

Arterial dissection is the angiopathy that blood flow enters the artery wall and causes vascular wall tissue dissect. Arterial dissection leads to various pathological changes, such as the stenosis or occlusion of the lumen and dissecting aneurysm of the artery (1). With the development of imaging techniques and clinical knowledge, incidence of cervicocranial arterial dissection (CCAD) is increasing. It has become a common cause of stroke in young patients, in whom it accounts for 10–25% (2). The etiology of CCAD is still unclear.

Trauma and connective tissue diseases can only explain partial dissection (3). Inflammation is known to be involved in the development of a variety of vascular diseases (4–7). Recently, infections have been reported to be associated with the occurrence and pathogenesis of CCAD (8). In previous studies on AIS, inflammation and immune response are also important parts of pathophysiology of stroke (9–11). Therefore, we speculated inflammatory response is important in AIS by CCAD.

The neutrophil to lymphocyte ratio (NLR), as a simple parameter of innate (neutrophil), and adaptive (lymphocyte) immune response, is easy to obtain from peripheral blood (12). Recent studies show NLR can predict the prognosis and mortality of patients with aortic dissection or cerebral infarction (5, 13, 14). Qun et al. (15) demonstrated that high NLR was highly correlated with the 3-month poor outcome of AIS. Clinical values of NLR in prognoses of patients with AIS caused by CCAD have not been fully explored. Therefore, we conducted a comprehensive analysis of those patients to explore the prognostic value of NLR on the 3-month outcome.

MATERIALS AND METHODS

Study Population

Patients with AIS by CCAD in the First Affiliated Hospital of Soochow University from April 2014 to October 2019 were selected as the research subjects. Data were collected from electronic patient records and administrative databases used for quality improvement.

CCAD was initially diagnosed by computed tomography angiography (CTA), and was further confirmed by digital subtraction angiography (DSA) or high-resolution magnetic resonance imaging (HR-MRI); in addition, thickened vascular intima and atherosclerotic plaque formation were excluded (16). All cases of AIS were confirmed by MRI. The diagnosis of CCAD was made according the previous description (17). The diagnostic criteria included the following factors: clinical symptoms such as neck pain, edema, and signs of Horner's syndrome; the disruption of normal arterial wall on CTA or DSA imaging including stenosis, intimal flap, false lumen, mural thrombus, and pseudoaneurysm; the exclusion of vessel hypoplasia, pseudodissection, and the signs of atherosclerosis such as vessel calcification (17). We confirmed the relationship between CCAD and AIS that the dissected artery was the only responsible vessel and the only cause of AIS by HR-MRI or CTA imaging. In addition, cardiogenic stroke was excluded in all patients by cardiac examination.

Exclusion criteria were as follows: (1) Patients with AIS admitted more than 48 h; (2) Patients had a history of infection within 2 weeks before admission that was defined as fever ($T \geq 38^{\circ}C$) and at least one other typical symptoms (cough, rhinitis, hoarseness, sneezing, or vomiting); (3) Patients had a history of cancer, chronic inflammation, hematological diseases, autoimmune diseases, or treatment with immunosuppressive agents; (4) Patients had a stroke history within 6 months or the modified Rankin scale (mRS) > 0 before the onset; (5) Patients did not complete a blood count within 24 h of admission; (6) There was no evidence of AIS at this admission; (7) patients with iatrogenic and traumatic dissections. The diagnosis of CCAD was made by two senior imaging doctors.

Clinical Information Collection

We collected baseline data including gender, age, history of trauma, history of head and neck pain, cerebral vascular risk factors such as hypertension, and diabetes. Peripheral venous blood samples were collected on the morning of the second day after admission with an overnight fasting.

Evaluation of 3-Month Outcome

Modified Rankin Scale (mRS) was used to evaluate the 3-month outcome after the onset of AIS. The primary outcome was death or major disability at 3 months after AIS. other outcomes were stroke recurrence and hemodynamics of the diseased vessels. The poor outcome was defined as the mRS ≥ 3.

Statistical Analysis

Continuous variables were analyzed as mean and standard deviation or the median and interquartile range while categorical variables were analyzed as frequency and percentage, properly. The differences among continuous variables were analyzed by the Student's *t*-test or the Mann-Whitney *U*-test while differences among categorical variables were assessed by the Chi-square test. Logistic regression analysis was used to find risk factors associated with poor prognosis in patients with AIS caused by CCAD after adjusting for other variables selected from univariate analyses. Receiver operating curves (ROC) were used to evaluate the predictive value of NLR level and to establish optimal cut-off values of NLR correlated with poor outcome. Statistical analysis was performed in SPSS 25.0. A value of $P < 0.05$ was considered statistically significant.

RESULTS

Study Population and Baseline Characteristics

A total of 168 patients with CCAD were admitted between April 2014 and October 2019 in the First Affiliated Hospital of Soochow University (Suzhou city, China). The CCAD mainly showed dual-chamber sign, line-like sign, endometrial flap sign, bead sign, or rat tail sign in CTA or DSA examination. HR-MRI revealed signs of hematoma, aneurysm-like dilatation, or double cavity with true cavity stenosis in the dissection. Among these patients, 69 patients were excluded according to the exclusion criteria, and 99 patients met the study criteria. Patient baseline characteristics were shown in **Table 1**. The average age of all patients was 47.72 ± 11.94; 79 (79.8%) were male and the ratio of male to female was about 4:1. 17 (17.2%) patients had a smoking history; 43 (43.4%) had a hypertension history; 11 (11.1%) had type 2 diabetes; 11 (11.1%) had a stroke history or TIA; and 18 (18.2%) had a history of trauma. White blood cell (WBC) was 8.91 ± 2.88 × 10^9 /L; neutrophil count was 5.54 (4.08, 7.88) × 10^9/L, and lymphocyte count was 1.64 (1.27, 2.09) × 10^9 /L; NLR was 3.21 (2.44, 4.91). All of our patients received anticoagulant or antiplatelet therapy and five patients

TABLE 1 | The clinical characteristics of patients with AIS caused by CCAD.

Characteristics	Patients ($n = 99$)
Demographics	
Age in years, mean ± SD	47.72 ± 11.94
Male, *n* (%)	79 (79.80)
Smoking, *n* (%)	17 (17.20)
Drinking, *n* (%)	7 (7.10)
Medical history	
History of trauma, *n* (%)	18 (18.20)
History of head and neck pain, *n* (%)	16 (16.20)
Hypertension, *n* (%)	43 (43.40)
Diabetes, *n* (%)	11 (11.10)
CHD, *n* (%)	1 (1.00)
History of stoke or TIA, *n* (%)	11 (11.10)
Clinical features	
Patients with vascular occlusion, *n* (%)	59 (59.60)
SBP in mmHg, mean ± SD	132.03 ± 16.80
DBP in mmHg, mean ± SD	80.60 ± 12.69
FGB in mmol/l, median (IQR)	5.01 (4.49, 6.01)
TC in mmol/l, median (IQR)	3.83 (3.23, 4.57)
TG in mmol/l, median (IQR)	1.23 (0.95, 1.73)
HDL in mmol/l, median (IQR)	1.01 (0.87, 1.23)
LDL in mmol/l, median (IQR)	2.23 (1.68, 2.85)
WBC in $\times 10^9$/l, mean ± SD	8.91 ± 2.88
NLR, median (IQR)	3.21 (2.44, 4.91)
N in $\times 10^9$/l, median (IQR)	5.54 (4.08, 7.88)
L in $\times 10^9$/l, median (IQR)	1.64 (1.27, 2.09)
CRP, median (IQR)	2.72 (0.73, 9.22)
NIHSS at admission, median (IQR)	4.00 (2.00, 10.00)
NIHSS at discharge, median (IQR)	2.00 (1.00, 6.00)
Primary outcome: major disability (mRS score 3-6)	
3-month mRS, median (IQR)	1.00 (0.00, 2.00)
3-month poor outcome, *n* (%)	20 (20.20)
Other outcomes	
Hemorrhage, *n* (%)	5 (5.05)
Recurrent ischemic stroke, *n* (%)	3 (3.00)
Improved hemodynamics of diseased vessels, *n* (%)	58 (58.60)

(5.05%) stopped medication after intracranial/gastrointestinal hemorrhage during treatment. Among them, 20 (20.2%) patients had a poor outcome at 3 months after AIS; 3 (3%) patients had recurrent ischemic stroke, and 58 (58.6%) patients of ultrasound showed improved hemodynamics of diseased vessels.

Risk Factors Associated With Poor Outcome in Patients With AIS Caused CCAD

According to the outcome after a 3-month follow-up, the patients were divided into two groups: the good outcome group with 79 patients (mRS < 3) and the poor outcome group with 20 patients (mRS ≥ 3). Statistical analysis indicated that there were significant differences on FGB, WBC, NLR, neutrophil count, C-reactive protein, NIHSS at admission and NIHSS score at discharge, 3-month mRS between two groups ($P < 0.05$); However, there was no difference on age, gender, history of trauma, hypertension, diabetes, CHD, smoking, or drinking, TC, TG, HDL, LDL, neutrophil count, recurrent ischemic stroke, improved hemodynamics of diseased vessels, hemorrhage, and other factors between two groups ($P > 0.05$, **Table 2**).

Binary logistic regression analysis was used to determine factors that were significantly associated with poor outcome at 3 months after AIS. After the factors that might potentially affect the outcome were adjusted, our results indicated that NLR (adjusted OR, 2.457; 95%CI, 1.096–5.508; $P = 0.03$), TG (adjusted OR, 10.015; 95%CI, 1.143–87.736; $P = 0.04$), WBC (adjusted OR, 1.794; 95%CI, 1.056–3.049; $P = 0.03$), age (adjusted OR, 1.258; 95%CI, 1.015–1.559; $P = 0.04$), ANC (adjusted OR, 2.919; 95%CI, 1.198–7.111; $P = 0.02$), and NIHSS (adjusted OR, 1.767; 95%CI, 1.234–2.529; $P = 0.002$) at admission were associated with 3-month poor outcome in the study. However, history of trauma, history of head and neck pain, smoking, type 2 diabetes, SBP, FGB, LDL, history of stroke or TIA and ALC showed no association with poor outcome ($P > 0.05$, **Table 3**).

NLR Was Associated With 3-Month Poor Outcome

Since NLR is a simple and convenient biomarker to obtain and was validated in patients with AIS, we examined whether NLR was a more specific biomarker for 3-month outcome in patients with AIS caused by CCAD. According to the NLR value, the study population was divided into three tertiles, each containing 33 people. In the first tertile (NLR 2.05, 1.24–2.86), the poor outcome rate was 3%; in the second tertile (NLR 3.21, 2.42–4.00), the poor outcome rate was 15.2%; in the third tertile (NLR 6.15, 2.96–9.34), the poor outcome rate was 42.4% (**Figure 1**). We used the Jonckheere-Terpstra test to evaluate the relationship of the poor outcome rate and NLR and found that the difference on the poor outcome rate between each tertile was statistically significant ($P < 0.001$), indicating that high NLR level was associated with 3-month poor outcome.

Further, we made the ROC curve to evaluate the predictive value of NLR level on prognosis. An NLR value of 2.97 was calculated as an optimal cut-off value to discriminate between good and poor outcome of patients with AIS caused by CCAD. The area under the curve was 0.79 (95%CI, 0.69–0.89). An NLR value of 2.97 as a cut-off value for differentiating the poor outcome with a sensitivity of 95% and a specificity of 53% (**Figure 2**).

Patients With High NLR Have an Increased Risk of Poor Outcome

According to the cut-off point, the patients were divided into a high NLR group with 56 patients (≥ 3) and a low NLR group with 43 patients (<3). We found statistically significant differences on drinking, history of stroke or TIA, WBC, neutrophil count, lymphocyte count, C-reactive protein levels, NIHSS at admission, NIHSS score at discharge, and 3-month mRS between the two

TABLE 2 | Clinical and laboratory findings in patients with poor and good outcome.

Characteristics	mRS ≥ 3 (*N* = 20)	mRS < 3 (*N* = 79)	*P*-value
Demographics			
Age in years, mean ± SD	51.35 ± 9.58	46.80 ± 12.35	0.13
Male, *n* (%)	17 (85.00)	62 (78.50)	0.76
Smoking, *n* (%)	2 (10.00)	15 (19.0)	0.51
Drinking, *n* (%)	1 (5.00)	6 (7.60)	1.00
Medical history			
History of trauma, *n* (%)	3 (15.00)	15 (19.00)	1.00
History of head and neck pain, *n* (%)	1 (5.00)	15 (19.00)	0.18
Diabetes, *n* (%)	4 (20.00)	7 (8.90)	0.23
Hypertension, *n* (%)	10 (50.00)	33 (41.80)	0.62
CHD, *n* (%)	0 (0.00)	1 (1.30)	1.00
History of stroke or TIA, *n* (%)	1 (5.00)	10 (12.70)	0.45
Clinical features			
Patients with vascular occlusion, *n* (%)	15 (75.00)	44 (55.70)	0.13
SBP in mmHg, median (IQR)	138.50 (119.25, 150.00)	130.00 (121.00, 139.00)	0.32
DBP in mmHg, median (IQR)	80.50 (67.75, 90.00)	80.00 (72.00, 90.00)	0.96
FGB in mmol/l, median (IQR)	6.02 (5.13, 7.87)	4.88 (4.46, 5.50)	0.01
TC in mmol/l, median (IQR)	4.04 (3.36, 4.72)	3.77 (3.20, 4.50)	0.20
TG in mmol/l, median (IQR)	1.36 (1.02, 1.75)	1.19 (0.94, 1.68)	0.44
HDL in mmol/l, median (IQR)	1.05 (0.91, 1.32)	0.99 (0.87, 1.18)	0.43
LDL in mmol/l, median (IQR)	2.48 (1.90, 2.83)	2.13 (1.65, 2.91)	0.22
WBC in $\times 10^9$/l, mean ± SD	11.12 ± 3.21	8.35 ± 2.51	<0.001
NLR, median (IQR)	5.26 (3.25, 7.81)	2.90 (2.16, 4.23)	<0.001
N in $\times 10^9$/l, median (IQR)	8.62 (5.91, 10.87)	5.08 (3.83, 6.66)	<0.001
L in $\times 10^9$/l, median (IQR)	1.56 (1.05, 1.88)	1.64 (1.28, 2.20)	0.20
CRP, median (IQR)	11.27 (4.10, 14.04)	2.07 (0.68, 6.05)	0.002
NIHSS at admission, median (IQR)	16.00 (12.00, 17.50)	3.00 (2.00, 7.00)	<0.001
NIHSS at discharge, median (IQR)	10.00 (8.00, 11.75)	2.00 (1.00, 4.00)	<0.001
Outcome			
3-month mRS, median (IQR)	3.50 (3.00, 4.00)	1.00 (0.00, 1.00)	<0.001
Hemorrhage, *n* (%)	2 (10.00)	3 (3.80)	0.06
Recurrent ischemic stroke, *n* (%)	1 (5.00)	2 (2.50)	0.50
Improved hemodynamics of diseased vessels, *n* (%)	10 (50.00)	48 (60.80)	0.45

groups ($P < 0.05$). However, there was no statistically significant difference in other factors between the two groups ($P > 0.05$, **Table 4**). In the high NLR group, 19 patients (33.9%) had 3-month poor outcome, whereas in the low NLR group, 1 patient (2.3%) had 3-month poor outcome (**Table 4**). Compared with patients in the low NLR group, patients in the high NLR group had higher poor outcome rate ($P < 0.01$).

DISCUSSION

NLR is a composite marker of absolute peripheral neutrophil and lymphocyte counts and reflects the burden of inflammation (12). Previous studies showed that inflammation played an important role in the pathogenesis of arterial dissection and stroke (7, 18–20). In this study, we showed that high NLR was an independent predictor of 3-month poor outcome for AIS caused by CCAD. It was a convenient and simple indicator of inflammatory response after CCAD-induced AIS. To our knowledge, this study was the first time to analyze the relationship between NLR and 3-month outcome in CCAD-induced AIS patients.

Previous study showed that inflammation played an important role in the initiation and progression of ischemic cerebrovascular diseases (20). Therefore, NLR, the marker of inflammation, may also reflect the progress and prognosis of ischemic cerebrovascular diseases. Oz et al. (7) found that NLR at the time of admission was a predictor of the short-term outcome of patients with Stanford type aortic dissection. Kocaturk et al. (21) and Qun et al. (15) also confirmed that NLR can predict the 3-month prognosis of AIS. Considering that AIS caused by CCAD may have different inflammatory changes from AIS, we expanded the previous study by screening AIS patients with CCAD. We recruited 99 patients with AIS by CCAD as the research objects; however, we still found that NLR is a good

TABLE 3 | Binary logistic regression analysis predicting the poor outcome in patients with AIS caused by CCAD.

Model	Independent variable	Adjusted OR	95% CI	*P*-value
Model 1	Age	1.092	0.951–1.255	0.212
(with NLR)	History of trauma	0.225	0.016–3.237	0.273
	History of head and neck pain	0.013	0.000–5.504	0.159
	Smoking	5.190	0.217–123.918	0.309
	Diabetes	0.605	0.011–32.534	0.805
	NIHSS at admission	1.712	1.268–2.310	<0.001
	SBP	0.997	0.942–1.054	0.912
	FGB	1.444	0.746–2.798	0.276
	LDL	0.431	0.144–1.291	0.133
	TG	10.015	1.143–87.736	0.037
	History of stroke or TIA	0.318	0.001–164.345	0.719
	NLR	2.457	1.096–5.508	0.029
	CRP	0.937	0.786–1.117	0.470
Model 2	Age	1.160	0.999–1.347	0.052
(with WBC)	History of trauma	0.065	0.002–2.124	0.124
	History of head and neck pain	0.094	0.002–5.167	0.247
	Smoking	2.518	0.163–39.006	0.509
	Diabetes	0.445	0.013–14.924	0.651
	NIHSS at admission	1.586	1.222–2.058	0.001
	SBP	1.000	0.946–1.058	0.991
	FGB	1.380	0.749–2.542	0.301
	LDL	0.532	0.177–1.602	0.262
	TG	4.383	0.861–22.310	0.075
	History of stroke or TIA	0.447	0.003–71.029	0.756
	WBC	1.794	1.056–3.049	0.031
	CRP	1.018	0.868–1.193	0.829
Model 3	Age	1.258	1.015–1.559	0.036
(with ANC)	History of trauma	0.025	0.000–1.382	0.072
	History of head and neck pain	0.039	0.000–6.445	0.213
	Smoking	5.620	0.229–137.640	0.290
	Diabetes	0.125	0.001–24.015	0.439
	NIHSS at admission	1.767	1.234–2.529	0.002
	SBP	1.014	0.952–1.079	0.672
	FGB	1.695	0.668–4.304	0.267
	LDL	0.274	0.061–1.224	0.090
	TG	13.744	1.093–172.838	0.042
	History of stroke or TIA	0.040	0.000–533.520	0.507
	ANC	2.919	1.198–7.111	0.018
	CRP	1.038	0.866–1.244	0.688
Model 4	Age	1.037	0.934–1.152	0.495
(with ALC)	History of trauma	0.646	0.052–7.961	0.733
	History of head and neck pain	0.119	0.002–7.372	0.312
	Smoking	1.171	0.101–13.603	0.899
	Diabetes	1.326	0.053–33.282	0.864
	NIHSS at admission	1.637	1.289–2.078	0.000
	SBP	0.997	0.947–1.049	0.902
	FGB	1.254	0.800–1.968	0.324
	LDL	0.602	0.237–1.527	0.285
	TG	3.649	0.656–20.295	0.139
	History of stroke or TIA	1.363	0.047–39.716	0.857
	ALC	0.350	0.071–1.739	0.199
	CRP	1.005	0.881–1.147	0.942

ANC, absolute neutrophil count; ALC, absolute lymphocyte count; OR, odds ratio; CI, confidence interval.

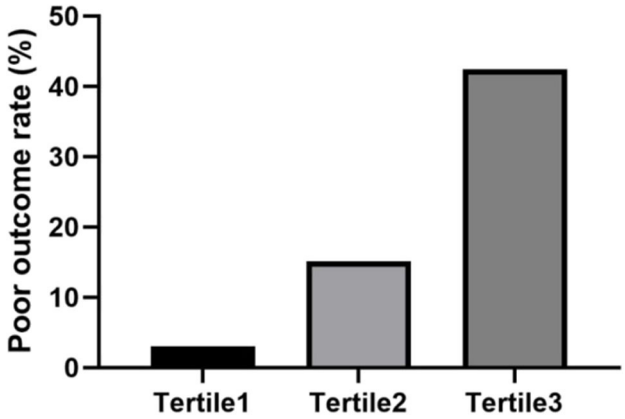

FIGURE 1 | The percentage of patients with poor outcome was stratified by the tertile of NLR. Patients were divided into three groups according to the tertiles of NLR (NLR $\leq$ 2.59, 2.59 $<$ NLR $\leq$ 4.23, NLR $>$ 4.23). The poor outcome rate was calculated. The difference between each tertile was assessed by Jonckheere-Terpstra test ($P < 0.001$).

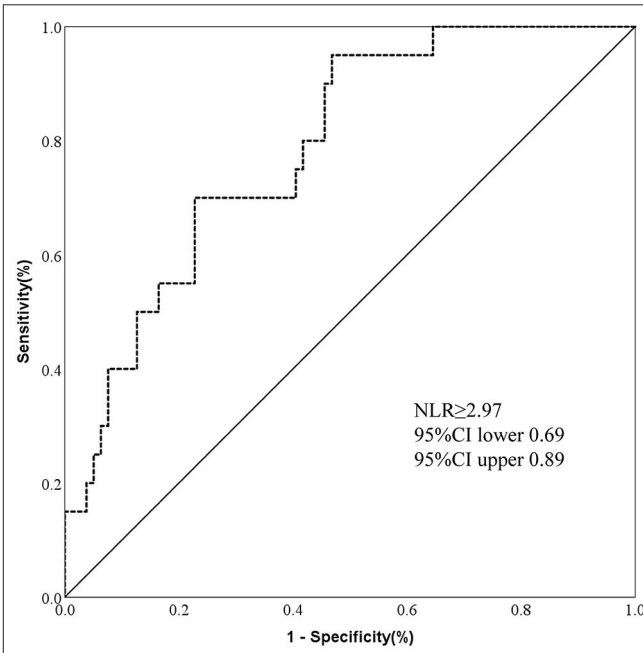

FIGURE 2 | ROC showed predictive value of NLR for 3-month poor outcome in AIS by CCAD. [$n = 99$; sensitivity = 0.95; specificity = 0.53; NLR = 2.97; area under curve (AUC) = 0.79].

predictor of poor outcome at 3 months. Interestingly, 79.8% of patients were male, showing a strong gender predisposition. In addition, for our total CCAD patients ($n = 168$ with or without AIS), male patients accounted for about 66.0%. In previous CCAD population-based studies, it seemed a slight gender predisposition favoring males (53–57%) (22). This may be due to the selection bias caused by small sample size in our study.

TABLE 4 | Clinical and laboratory findings in patients with low and high NLR.

Characteristics	NLR ≥ 2.97 (*N* = 56)	NLR < 2.97 (*N* = 43)	*P*-value
Demographics			
Age in years, mean ± SD	47.41 ± 10.88	48.12 ± 13.31	0.77
Male, *n* (%)	43.00 (76.80)	36.00 (83.70)	0.39
Smoking, *n* (%)	7.00 (12.50)	10.00 (23.30)	0.16
Drinking, *n* (%)	1.00 (1.80)	6.00 (14.00)	0.02
Medical history			
History of trauma, *n* (%)	10.00 (17.90)	8.00 (18.60)	0.92
History of head and neck pain, *n* (%)	10.00 (17.90)	6.00 (14.00)	0.60
Hypertension, *n* (%)	25.00 (44.60)	18.00 (41.90)	0.78
Diabetes, *n* (%)	7.00 (12.50)	4.00 (9.30)	0.62
CHD, *n* (%)	1.00 (1.80)	0.00 (0.00)	0.38
History of stroke or TIA, *n* (%)	3.00 (5.40)	8.00 (18.60)	0.04
Clinical features			
Patients with vascular occlusion, *n* (%)	32.00 (57.10)	27.00 (62.80)	0.57
SBP in mmHg, mean ± SD	134.34 ± 16.66	129.02 ± 16.69	0.12
DBP in mmHg, mean ± SD	81.84 ± 13.25	78.98 ±11.89	0.27
FGB in mmol/l, median (IQR)	5.32 (4.44, 6.66)	4.84 (4.61, 5.32)	0.41
TC in mmol/l, median (IQR)	3.88 (3.34, 4.71)	3.76 (3.16, 4.44)	0.33
TG in mmol/l, median (IQR)	1.31 (0.97, 1.67)	1.17 (0.95, 1.81)	0.42
HDL in mmol/l, median (IQR)	1.05 (0.90, 1.24)	0.95 (0.87, 1.18)	0.61
LDL in mmol/l, median (IQR)	2.26 (1.75, 2.97)	2.10 (1.56, 2.78)	0.14
WBC in $\times 10^9$/l, mean ± SD	10.06 ± 2.85	7.42 ± 2.15	<0.001
NLR, median (IQR)	4.73 (3.57, 6.68)	2.26 (1.71, 2.59)	<0.001
N in $\times 10^9$/l, median (IQR)	7.11 (5.55, 9.22)	4.08 (3.52, 4.96)	<0.001
L in $\times 10^9$/l, median (IQR)	1.49 (1.12, 1.84)	1.89 (1.52, 2.61)	<0.001
CRP, median (IQR)	5.61 (1.42, 13.26)	1.42 (0.49, 4.07)	0.01
NIHSS at admission, median (IQR)	8.00 (2.00, 14.00)	3.00 (2.00, 5.00)	<0.001
NIHSS at discharge, median (IQR)	5.00 (1.25, 8.75)	1.00 (1.00, 3.00)	<0.001
Primary outcome: mRS score			
3-month mRS, median (IQR)	1.00 (0.00, 3.00)	0.00 (0.00, 1.00)	<0.001
3-month Poor outcome, *n* (%)	19.00 (33.90)	1.00 (2.30)	<0.001
Other outcomes			
Recurrent ischemic stroke, *n* (%)	1.00 (1.80)	2.00 (4.70)	0.41
Improved hemodynamics of diseased vessels, *n* (%)	35.00 (62.50)	23.00 (53.50)	0.37
Hemorrhage, *n* (%)	4 (7.14)	1 (2.32)	0.384

However, male gender predisposition may be further examined in CCAD patients in future studies.

The increase in NLR indicates the suppression of lymphocytes or the excessive activation of neutrophils (12). After the occurrence of acute aortic dissection and AIS, systemic immune suppression may occur due to the brain's immune response (23–25), especially for T cells and natural killer cells in lymphocytes (26). The function of lymphocyte in ischemic brain injury and ischemic vascular endothelial is still controversial at present, but certain specific subtypes have been shown to play a protective role in the pathophysiology of cerebral ischemia (24, 26). Some studies suggested that lymphopenia was an early feature of stroke, which is a sign of persistent brain damage, stress response, and the greater possibility of infection (26). Acute stroke can trigger the reduction of regulatory T cells that suppress the inflammatory response to increase tissue damage (23, 24, 26, 27). We didn't find a correlation between low lymphocyte and 3-month poor outcome.

Considerable studies have demonstrated the damaging effects of neutrophils on vascular endothelial cells in arterial dissection and ischemic brain tissues (20, 28–32). Due to the similar pathogenesis, we speculate that neutrophils play an important role in the occurrence and development of AIS caused by CCAD. Infiltration of inflammatory cells can usually be found in the ischemic arterial walls of patients with CCAD and AIS (18, 28, 33). Peripheral neutrophils penetrate into the blood vessel walls and release vasoactive or cytotoxic media, including reactive oxygen species, proteases, matrix metalloproteinase (MMP), and cytokines, which may lead to the destruction of the extracellular matrix and the collapse of the vessel walls (32, 34). Our study

found higher neutrophil count and higher leukocyte count baselines both correlate with 3-month poor outcome in the binary logistic regression analysis.

However, NLR reflects the balance of neutrophil and lymphocyte levels, which can comprehensively reflect the immune status, and the ratio may be more stable than a single parameter. In this study, we also used NIHSS at admission to analyze CCAD patients and found that the scale may not adequately capture all forms of functional change. The NIHSS has many advantages; however, it may miss some functional changes when used in place of neurological examination or blood parameters to measure improvement stroke (35, 36). Therefore, we collected both NIHSS score at admission and blood biochemical parameters to analyze their correlation with the prognosis of patients. Although statistical analysis showed that many factors, including NIHSS, were associated with prognosis, NLR was still independently associated with 3-month prognosis in binary regression analysis after adjusting for confounding factors. We took NLR = 2.97 as the cutoff value. The proportion of 3-month poor outcome in patients with high NLR was significantly higher than that in patients with low NLR, which was consistent with previous studies of a single ischemic stroke with a larger size of samples. In addition, we also found that the age and triglyceride level were associated with 3-month outcome. This may be related to the pathogenesis of CCAD. However, there was no significant difference between two groups in the improvement of the hemodynamics of the diseased vessels and the risk of recurrent ischemic stroke at 3 months.

A higher NLR level may indicate devascularization, early neurological deterioration and systemic immune dysfunction. These events increase the risk of death and poor outcome in AIS caused by CCAD. Generally, as an available clinical indicator, NLR has strong practicability for acute clinical decision-making and prognosis judgment.

There are also some limitations in our research. First, the number of cases of AIS caused by CCAD is relatively small. The insufficient sample size leads to weakened statistical strength of conclusions. Second, the study is observational in nature. We can't prove the causal relationship between NLR and 3-month adverse outcome. Third, our study included patients with anterior and posterior circulation dissections and did not explore the relationship between cerebral infarct volume and poor prognosis.

SUMMARY

The NLR level is related to the 3-month poor outcome of patients with AIS caused by CCAD. When NLR $\geq$ 2.97, the risk of poor outcome increases. This reliable and easy-to-use predictor could contribute to clinical treatment strategy design in patients with CCAD. Further studies should be performed to expand the sample size and investigate the relevant inflammation and immune pathways.

DATA AVAILABILITY STATEMENT

The original contributions generated for the study are included in the article/supplementary materials, further inquiries can be directed to the corresponding author/s.

ETHICS STATEMENT

This study involving human participants were reviewed and approved by the Institutional Review Board of the First Affiliated Hospital of Soochow University. All patients provided their written informed consent.

CONSENT FOR PUBLICATION

All the authors approved the manuscript and are consent for the submission.

AUTHOR CONTRIBUTIONS

GS, YY, ZC, and XX designed the study. GS, YY, ZC, SD, SH, YiqW, and YitW evaluated the subjects and collected the data. LY, BS, and YY analyzed the data. GS, YY, XY, and XX wrote the manuscript. All authors contributed to the article and approved the submitted version.

FUNDING

This work was supported by the grants from National Key R&D Program of China (2017YFE0103700), the National Natural Science Foundation of China (81120108011 and 81771454), Shandong Provincial Natural Science Foundation (ZR2019ZD32), and the Priority Academic Program Development of Jiangsu Higher Education Institutions.

REFERENCES

1. Thanvi B, Munshi SK, Dawson SL, Robinson TG. Carotid and vertebral artery dissection syndromes. *Postgrad Med J.* (2005) 81:383–8. doi: 10.1136/pgmj.2003.016774
2. Debette S, Leys D. Cervical-artery dissections: predisposing factors, diagnosis, and outcome. *Lancet Neurol.* (2009) 8:668–78. doi: 10.1016/S1474-4422(09)70084-5
3. Park KW, Park JS, Hwang SC, Im SB, Shin WH, Kim BT. Vertebral artery dissection: natural history, clinical features and therapeutic considerations. *J Korean Neurosurg Soc.* (2008) 44:109–15. doi: 10.3340/jkns.2008.44.3.109
4. Sullivan GW, Sarembock IJ, Linden J. The role of inflammation in vascular diseases. *J Leukocyte Biol.* (2000) 67:591–602. doi: 10.1002/jlb.67.5.591
5. Kalkan ME, Kalkan AK, Gündeş A, Yanartaş M, Oztürk S, Gurbuz AS, et al. Neutrophil to lymphocyte ratio: a novel marker for predicting hospital mortality of patients with acute type A aortic dissection. *Perfusion.* (2017) 32:321–7. doi: 10.1177/0267659115590625
6. Li C, Zhang F, Shen Y, Xu R, Chen Z, Dai Y, et al. Impact of neutrophil to lymphocyte ratio (NLR) index and its periprocedural change (NLR_{Δ}) for percutaneous coronary intervention in patients with chronic total occlusion. *Angiology.* (2017) 68:640–6. doi: 10.1177/0003319716649112
7. Oz K, Iyigun T, Karaman Z, Çelik Ö, Akbay E, Akinc O, et al. Prognostic value of neutrophil to lymphocyte ratio and risk factors for mortality in patients with stanford type a aortic dissection. *Heart Surg Forum.* (2017) 20:E119–23. doi: 10.1532/hsf.1736

8. Grau AJ, Brandt T, Buggle F, Orberk E, Mytilineos J, Werle E, et al. Association of cervical artery dissection with recent infection. *Arch Neurol.* (1999) 56:851–6. doi: 10.1001/archneur.56.7.851
9. Brait VH, Jackman KA, Walduck AK, Selemidis S, Diep H, Mast AE, et al. Mechanisms contributing to cerebral infarct size after stroke: gender, reperfusion, T lymphocytes, and Nox2-derived superoxide. *J Cereb Blood Flow Metab.* (2010) 30:1306–17. doi: 10.1038/jcbfm.2010.14
10. Klehmet J, Harms H, Richter M, Prass K, Volk HD, Dirnagl U, et al. Stroke-induced immunodepression and post-stroke infections: lessons from the preventive antibacterial therapy in stroke trial. *Neuroscience.* (2009) 158:1184–93. doi: 10.1016/j.neuroscience.2008.07.044
11. Zhou J, Wu J, Zhang J, Xu T, Zhang H, Zhang Y, et al. Association of stroke clinical outcomes with coexistence of hyperglycemia and biomarkers of inflammation. *J Stroke Cereb Dis.* (2015) 24:1250–5. doi: 10.1016/j.jstrokecerebrovasdis.2015.01.028
12. Song SY, Zhao XX, Rajah G, Hua C, Kang RJ, Han YP, et al. Clinical significance of baseline neutrophil-to-lymphocyte ratio in patients with ischemic stroke or hemorrhagic stroke: an updated meta-analysis. *Front Neurol.* (2019) 10:1032. doi: 10.3389/fneur.2019.01032
13. Brooks SD, Spears C, Cummings C, VanGilder RL, Stinehart KR, Gutmann L, et al. Admission neutrophil-lymphocyte ratio predicts 90 day outcome after endovascular stroke therapy. *J Neurointerv Surg.* (2014) 6:578–83. doi: 10.1136/neurintsurg-2013-010780
14. Yang Y, Sun G, Diao S, Yang L, Dong W. Diagnostic performances of neutrophil to lymphocyte ratio and lymphocyte to monocyte ratio in acute ischemic stroke caused by cervicocranial arterial dissection. *J Clin Lab Anal.* (2020) e23515. doi: 10.1002/jcla.23515
15. Qun S, Tang Y, Sun J, Liu Z, Wu J, Zhang J, et al. Neutrophil-to-lymphocyte ratio predicts 3-month outcome of acute ischemic stroke. *Neurotox Res.* (2017) 31:444–52. doi: 10.1007/s12640-017-9707-z
16. Markus HS, Levi C, King A, Madigan J, Norris J. Antiplatelet therapy vs anticoagulation therapy in cervical artery dissection: the cervical artery dissection in stroke study (CADISS) randomized clinical trial final results. *JAMA Neurol.* (2019) 76:657–64. doi: 10.1001/jamaneurol.2019.0072
17. Hassan AE, Jadhav V, Zacharatos H, Chaudhry SA, Rodriguez GJ, Mohammad YM, et al. Determinants of neurologic deterioration and stroke-free survival after spontaneous cervicocranial dissections: a multicenter study. *J Stroke Cereb Dis.* (2013) 22:389–96. doi: 10.1016/j.jstrokecerebrovasdis.2011.09.017
18. Chen WT, Chang FC, Huang HC, Tsai JY, Chung CP. Total and differential leukocyte counts in ischemic stroke caused by vertebrobasilar artery dissection. *J Neurol Sci.* (2019) 404:101–5. doi: 10.1016/j.jns.2019.07.022
19. Yan J, Read SJ, Henderson RD, Hull R, O'Sullivan JD, McCombe PA, et al. Frequency and function of regulatory T cells after ischaemic stroke in humans. *J Neuroimmunol.* (2012) 243:89–94. doi: 10.1016/j.jneuroim.2011.12.019
20. Chamorro Á, Dirnagl U, Urra X, Planas AM. Neuroprotection in acute stroke: targeting excitotoxicity, oxidative and nitrosative stress, and inflammation. *Lancet Neurol.* (2016) 15:869–81. doi: 10.1016/S1474-4422(16)00114-9
21. Kocaturk O, Besli F, Gungoren F, Kocaturk M, Tanriverdi Z. The relationship among neutrophil to lymphocyte ratio, stroke territory, and 3-month mortality in patients with acute ischemic stroke. *Neurol Sci.* (2019) 40:139–46. doi: 10.1007/s10072-018-3604-y
22. Blum CA, Yaghi S. Cervical artery dissection: a review of the epidemiology, pathophysiology, treatment, and outcome. *Arch Neurosci.* (2015) 2:26670. doi: 10.5812/archneurosci.26670
23. Papp V, Molnár T, Bánáti M, Illés Z. [Immune responses and neuroimmune modulation in the pathogenesis of acute ischemic stroke and poststroke infections]. *Ideggyogy Sz.* (2010) 63:232–46.
24. Macrez R, Ali C, Toutirais O, Le Mauff B, Defer G, Dirnagl U, et al. Stroke and the immune system: from pathophysiology to new therapeutic strategies. *Lancet Neurol.* (2011) 10:471–80. doi: 10.1016/S1474-4422(11)70066-7
25. del Porto F, Proietta M, Tritapepe L, Miraldi F, Koverech A, Cardelli P, et al. Inflammation and immune response in acute aortic dissection. *Ann Med.* (2010) 42:622–9. doi: 10.3109/07853890.2010.518156
26. Urra X, Cervera A, Villamor N, Planas AM, Chamorro A. Harms and benefits of lymphocyte subpopulations in patients with acute stroke. *Neuroscience.* (2009) 158:1174–83. doi: 10.1016/j.neuroscience.2008.06.014
27. Meisel C, Schwab JM, Prass K, Meisel A, Dirnagl U. Central nervous system injury-induced immune deficiency syndrome. *Nat Rev Neurosci.* (2005) 6:775–86. doi: 10.1038/nrn1765
28. Justicia C, Panés J, Solé S, Cervera A, Deulofeu R, Chamorro A, et al. Neutrophil infiltration increases matrix metalloproteinase-9 in the ischemic brain after occlusion/reperfusion of the middle cerebral artery in rats. *J Cereb Blood Flow Metab.* (2003) 23:1430–40. doi: 10.1097/01.WCB.0000090680.07515.C8
29. Soubhye J, Aldib I, Delporte C, Prévost M, Dufrasne F, Antwerpen PV. Myeloperoxidase as a target for the treatment of inflammatory syndromes: mechanisms and structure activity relationships of inhibitors. *Curr Med Chem.* (2016) 23:3975–4008. doi: 10.2174/0929867323666160607111806
30. Trentini A, Rosta V, Spadaro S, Bellini T, Rizzo P, Vieceli Dalla Sega F, et al. Development, optimization and validation of an absolute specific assay for active myeloperoxidase (MPO) and its application in a clinical context: role of MPO specific activity in coronary artery disease. *Clin Chem Lab Med.* (2020) 58:1749–58. doi: 10.1515/cclm-2019-0817
31. Siegel RJ, Koponen M. Spontaneous coronary artery dissection causing sudden death. Mechanical arterial failure or primary vasculitis? *Arch Pathol Lab Med.* (1994) 118:196–8.
32. Li D, Liu S, Teng F, Yang W, Zhang L, Deng Y, et al. Temporal change of leukocytes and chemokines in aortic dissection patient: relationship to regional lesion on aorta. *Int J Cardiol.* (2013) 168:3065–6. doi: 10.1016/j.ijcard.2013.04.094
33. Eskenasy-Cottier AC, Leu HJ, Bassetti C, Bogousslavsky J, Regli F, Janzer RC. A case of dissection of intracranial cerebral arteries with segmental mediolytic "arteritis". *Clin Neuropathol.* (1994) 13:329–37.
34. Gautier S, Ouk T, Tagzirt M, Lefebvre C, Laprais M, Pétrault O, et al. Impact of the neutrophil response to granulocyte colony-stimulating factor on the risk of hemorrhage when used in combination with tissue plasminogen activator during the acute phase of experimental stroke. *J Neuroinflamm.* (2014) 11:96. doi: 10.1186/1742-2094-11-96
35. Marsh EB, Lawrence E, Gottesman RF, Llinas RH. The NIH stroke scale has limited utility in accurate daily monitoring of neurologic status. *Neurohospitalist.* (2016) 6:97–101. doi: 10.1177/1941874415619964
36. Peters HT, White SE, Page SJ. The national institutes of health stroke scale lacks validity in chronic hemiparetic stroke. *J Stroke Cereb Dis.* (2015) 24:2207–12. doi: 10.1016/j.jstrokecerebrovasdis.2015.05.011

Conflict of Interest: The authors declare that the research was conducted in the absence of any commercial or financial relationships that could be construed as a potential conflict of interest.

frontiers in Medicine

ORIGINAL RESEARCH
published: 04 December 2020
doi: 10.3389/fmed.2020.608441

FAM83A as a Potential Biological Marker Is Regulated by miR-206 to Promote Cervical Cancer Progression Through PI3K/AKT/mTOR Pathway

Li Rong[1], Haiyu Li[1], Zhaodong Li[1], Jing Ouyang[2], Yongping Ma[1], Fangzhou Song[1] and Yaokai Chen[2]**

[1] Chongqing Public Health Medical Center, Chongqing, China, [2] Chongqing Medical University, Chongqing, China

OPEN ACCESS

Edited by:
Ali Yadollahpour, The University of Sheffield, United Kingdom

Reviewed by:
Samaneh Rashidi, Ahvaz Jundishapur University of Medical Sciences, Iran
Shengye Wang, Zhejiang Cancer Hospital, China

***Correspondence:**
Yaokai Chen
yaokaichen@hotmail.com
Fangzhou Song
fzsongcq@163.com

Specialty section:
This article was submitted to Precision Medicine, a section of the journal Frontiers in Medicine

Received: 20 September 2020
Accepted: 26 October 2020
Published: 04 December 2020

Citation:
Rong L, Li H, Li Z, Ouyang J, Ma Y, Song F and Chen Y (2020) FAM83A as a Potential Biological Marker Is Regulated by miR-206 to Promote Cervical Cancer Progression Through PI3K/AKT/mTOR Pathway. Front. Med. 7:608441. doi: 10.3389/fmed.2020.608441

Background and Objective: Chemotherapy and radiotherapy are effective treatment options for cervical cancer (CC), but their efficacy is limited by short survival rate of about 5 years particularly for advance stage CC. Bioinformatics analysis combined with experimental *in vivo* and *in vitro* data can identify potential markers of tumorigenesis and cancer progression to improve CC prognosis and survival rate of the patients. This study aims to investigate the prognostic value of family with sequence similarity 83, member A (FAM83A) gene and miR-206 in promoting CC progression and the involved genetic signaling pathways.

Method: This was a bioinformatic analysis study based on RNA sequencing data of The Cancer Genome Atlas (TCGA) and Gene Expression Omnibus (GEO) databases and verification by *in vivo* and *in vitro* experimental data. It was designed to evaluate whether the aberrantly expressed gene signatures could serve as new potential biomarker to improve prognosis prediction in CC. The TCGA RNA sequencing data [306 cervical squamous cell carcinoma (SCC) and endocervical adenocarcinoma samples and 13 adjacent samples] and GEO data (GSE9750 and GSE52903 datasets) were integrated and performed a bioinformatics analysis.

Results: The results showed that CC-associated FAM83A gene serves as a key regulator of CC development and progression. Functionally, we observed that FAM83A is significantly overexpressed in CC, which is linked to poor overall survival as well as disease-free survival in CC patients. The *in-vitro* and *in-vivo* assessments performed after silencing FAM83A revealed that cell proliferation was significantly inhibited and the S-phase cell cycle arrest was induced. Mechanistically, FAM83A plays a role in PI3K/AKT signaling, and its downstream molecules could

promote CC cell proliferation. Furthermore, functionality assessments by *in-vitro* luciferase reporter system and immunoblot analysis showed that miR-206 was the upstream of FAM83A and negatively correlated with FAM83A.

Conclusion: The miR-206/FAM83A/PI3K/AKT signaling pathway possibly serves as a critical effector in CC progression indicating the potential prognostic value of FAM83A gene as a novel biomarker for CC progression.

Keywords: cervical cancer, FAM83A, prognosis, biomarker, miR-206, survival

BACKGROUND

Cervical cancer (CC) is the fourth most common female cancer and the second most prevalent cancer among young women (age group: 15–44 years old) worldwide accounting for approximately 570,000 new cases each year (1–5). Although great efforts on human papilloma virus (HPV) vaccines have been made to protect women from CC, it is still the second leading cause of tumors specific to women, next only to breast cancer (6–8). Developing countries account for 80% of the world's breast cancer cases. Squamous cell carcinoma (SCC) is the most prevalent histological type of CC accounts for approximately 80% of all CCs. Despite the relatively high mortality of CCs, little is known on definitive diagnosis and prognosis markers of these cancers (9).

Prognostic and diagnostic biomarkers play crucial roles in predicting the treatment response, prognosis and disease progression in cancer, developing new therapies, and elucidating tumorigenesis mechanisms (10, 11). High throughput profiling methods including next-generation sequencing and gene microarray have shown great potentials for identifying reliable prognostic biomarkers for different cancers (12, 13). The use of bioinformatics for analysis of gene sequencing and expression data can help developing prognostic and diagnostic biomarkers for cancers including CCs. Genotype-Tissue Expression (GTEx) and The Cancer Genome Atlas (TCGA) projects consisting of excellent databases of a very large RNA sequence data of cancerous and normal samples, provide good opportunities for high throughput modeling and bioinformatics analysis to determine diagnostic and prognostic biomarkers of cancer (9, 14, 15). TCGA database covers changes in 33 key cancer genomes and contains more than two petabytes of genomic data that are publicly available to help improve cancer prevention, diagnosis, and treatment (16–21). Different bioinformatics studies using the datasets of TCGA and Gene Expression Omnibus (GEO) gene microarrays have analyzed the gene sequencing and expression profiles of different tumors and demonstrated that abnormal overexpression or genes are key factors involved in the cancer progression (22, 23).

Family with sequence similarity 83, member A (FAM83A) that was first identified as a potential tumor-specific gene a bioinformatics approach is located on chromosome 8q24 (24). Previous studies have shown that FAM83A is aberrantly expressed in several human cancers including pancreatic, lung, breast, testis and bladder cancers (23, 25–29) indicating that FAM83A could possibly play an oncogenic role during the development and progression cancer. It has been shown that FAM83A is significantly overexpressed and associated with poorer overall survival (OS) and disease-free survival (DFS) in specific cancers including lung, breast, and pancreatic cancer. For instance, overexpression of FAM83A markedly facilitated, whereas inhibition of FAM83A decreased, cancer stem cell (CSC)-like features and chemoresistance both *in vitro* and in an *in vivo* mouse model of pancreatic cancer (23).

Different high-throughput modeling studies have analyzed the gene sequencing and expression profiles of CC and reported that aberrantly expressed genes are key factors involved in the cancer progression (22, 23). However, reviewing the literature shows that the differentially expressed genes (DEGs) associated with CC were rarely reported. In this regard, TCGA sequencing and GEO gene microarrays along with bioinformatics analysis can be employed to identify the DEGs affecting the biological functions of CC at the genetic level.

In the present study, we integrated the TCGA RNA sequencing data (306 cervical SCC and endocervical adenocarcinoma samples and 13 adjacent samples) and GEO data comprising the GSE9750 and GSE52903 datasets and performed a bioinformatics analysis. We identified the FAM83A gene is closely related to CC and further studied its biological function on CC and potential molecular regulatory mechanism.

MATERIALS AND METHODS

RNA Sequencing and Microarray Data Analysis

The cervical SCC data and GTEx RNA sequencing data and a CC gene expression microarray comprising the GSE9750 and GSE52903 datasets were downloaded from the TCGA (https://cancergenome.nih.gov/abouttcga) and GEO (https://www.ncbi.nlm.nih. gov/geo/) datasets, respectively. The Limma package of R/bioconductor (bioconductor, USA) was used to screen the DEGs (settings: $q < 0.05$, $|\log2(\text{fold change})| \geq 4$). Hierarchical clustering and visualization were performed by the heatmap package of R.

Immunohistochemistry Analysis

The surgical specimens examined in this study included 31 cervical SCC tissues and 31 corresponding para-carcinoma tissues obtained from the First Affiliated Hospital of Changde Vocational and Technical College between July 2013 and June 2015. Immunohistochemistry (IHC) analysis was carried out by initially dewaxing and rehydrating slides. This was followed by

subjection to heat-induced epitope retrieval in citrate buffer. Incubation of slides with a rabbit anti-FAM83A polyclonal antibody (bs-16014R, BIOSS) at 4°C overnight was then carried out. This was followed by staining of sections with DAB (Maixin Bio, China) for 5 min. The specific FAM83A *in situ* hybridization (ISH) signal was judged as brown spots, and Image-Pro Plus 6.0 software was used to evaluate the expression level (30, 31).

Cell Culture

Human cervical epithelial cells (CerEpiC), Human CC cell lines HeLa, SiHa, and CaSki (purchased from the Shanghai cell bank, Chinese Academy of Sciences) were cultured in Dulbecco's Modified Eagle Medium (HyClone, USA) containing 10% fetal bovine serum (HyClone, USA), 100 U/mL penicillin, 100 mg/mL streptomycin at 37°C in an environment containing 5% CO_2.

RNA Interference

The sequences of the small interfering RNAs of FAM83A (GenePharma, China), control siRNA sequences (GenePharma, China), short hairpin RNA (GenePharma, China) were listed, respectively as follows:

Sense: 5′-GGGCUGACUUUAGUGACAA-3′

Antisense: 5′-UUGUCACUAAAGUCAGCCC-3′

Sense: 5′-UUCUCCGAACGUGUCACGUTT-3′

Antisense: 5′-ACGUGACACGUUCGGAGAATT-3′

Sense: 5′-CACCGGGCTGACTTTAGTGACAACGAATTGTCACTAAAGTCAGCCC-3′

Antisense: 5′-AAAAGGGCTGACTTTAGTGACAATTCGTTGTCACTAAAGTCAGCCC-3′

The siRNA underwent transfection using Lipofectamine RNAiMAX Reagent (Invitrogen) according to the instructions. The Lentviral3-GFP-shRNA was used for infection of CaSki cells for 24 h, then culturing of cells in DMEN medium containing puromycin (3 μg/mL) was carried out, in order to form a stable cell line knocking down FAM83A.

In vitro Cell Proliferation and Cell Cycle Assays

Cell activity was examined by CCK-8 Kits (Dojindo Laboratories, Japan) following transient transfection of siRNA for 24, 48, and 72 h. Treated cells were collected and underwent washing with phosphate-buffered saline. This was followed by fixation with 70% ethanol for 30 min. Next, it was incubated with 100 μL of RNase A for 30 min, followed by staining with propidium iodide (PI) for a duration of 30 min in the dark. Then, cycle distribution was analyzed by flow cytometry (FCM; BD, Influx).

In vivo Tumor Growth Assay

All procedures of this study were approved by local ethics committee "Animal Care and Use Committee" of Chongqing Medical University, Chongqing, China which were in complete accordance with the regulations of "Guide for the Care and Use of Laboratory Animals." The BALB/c female nude mice ($n = 6$), 4–6 weeks of age, were obtained from the "Experimental Animal Center" of Chongqing Medical University, Chongqing, China. The nude mice were randomized into control and experimental groups. In total, subcutaneous injection of 1×10^6 shCtrl and shFAM83A CaSki cells were administered into the back of nude mice. Tumor growth was observed weekly for 5 weeks. This was followed by measurement and calculation of the tumor volume. After 5 weeks, mice were sacrificed, then tumors were excised and weighed. All of the data were represented as mean ± standard deviation (SD).

Luciferase Reporter Assay

With reference to our previous experimental methods (32), synthesis of the wild-type and mutant fragment sequences of the 3'-untranslated region (UTR) of FAM83A were carried out followed by cloning into the pmirGLO vector (Promega, Madison). Cells inoculation in 24-well plates was carried out followed by co-transfection with pmirGLO-FAM83A-wild-type (WT), pmirGLO-FAM83A-mut, and miR-206 mimics or a control by Lipofectamine 2000. After a period of 48 h, luciferase assays were done with a Dual Luciferase Reporter Assay System (Promega). Examination of Luciferase activity was then determined with the Dual Luciferase Assay Kit (Promega) as per protocol.

Statistical Analysis

The data were presented as Mean ± SD for all statistical analyses and data presentation unless otherwise is expressed. Student's *t*-test was used to investigate the differences between the two groups; the association between FAM83A expression and clinicopathological factors was investigated by Chi-square test. $P < 0.05$ was taken as statistically significant difference.

RESULTS

Identification of FAM83A as a Cervical Cancer-Specific Gene

To determine critical genes involved in the development of CC, the TCGA cervical SCC and GTEx RNA sequencing data and a CC gene expression microarray comprising the GSE9750 and GSE52903 datasets were analyzed. As seen in **Figure 1A**, we identified 252 misregulated genes in the TCGA database, 144 in the GSE9750 dataset, and 170 in the GSE52903 dataset (fold change > 4.0, $q < 0.05$). It was then discovered that, in all datasets, five genes were consistently overexpressed and three genes consistently under-expressed (**Figure 1B**). In the preliminary experiments, we detected the expression of these five up-regulated genes in CC tissues and cells by PCR, and found that FAM83A was most consistent and significant both in tissues and cells. Therefore, FAM83A was selected for further experimental validation and analyzed its biological behaviors in CC.

FAM83A Is Overexpressed in Cervical Cancer and Correlates With Patient Survival

We explored the potential role of FAM83A in CC tumorigenesis using different analyses. We analyzed the expression of FAM83A in six cancers (cervical SCC and endocervical adenocarcinoma, cholangiocarcinoma, kidney chromophore, kidney renal clear cell carcinoma, rectal adenocarcinoma, and liver hepatocellular

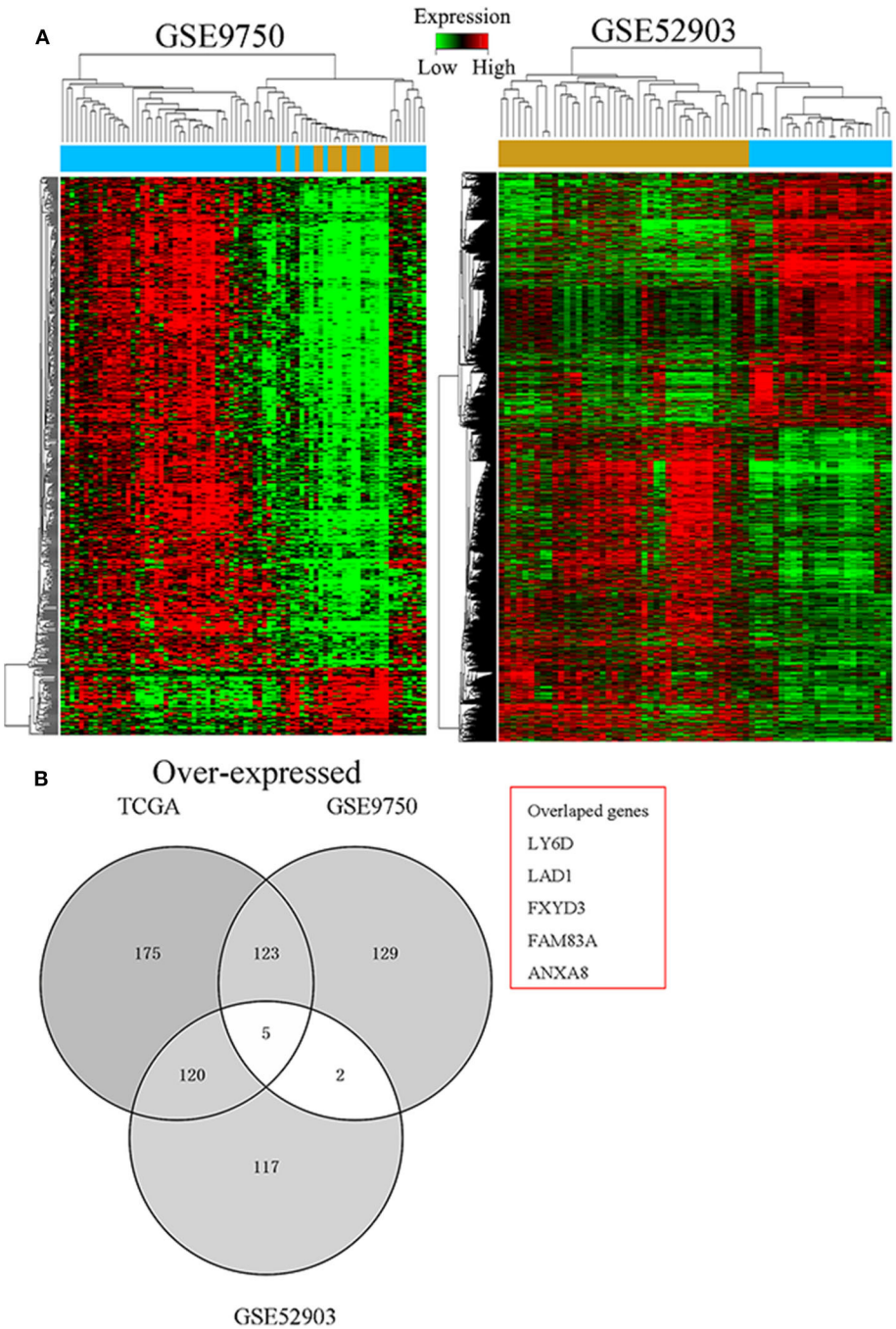

FIGURE 1 | Identification of FAM83A as a cervical cancer-specific gene. **(A)** Hierarchical clustering analysis of genes that were differentially expressed (fold change > 4; $q < 0.05$) in cervical cancer and normal tissues. **(B)** Overlap of aberrantly expressed genes in the TCGA CESC data and GEO datasets.

carcinoma) using TCGA sequencing datasets. The result showed that FAM83A is upregulated in CC tissues (**Figure 2A**). Low FAM83A expression was predictive of better OS (log-rank $P = 0.05$) and better DFS (log-rank $P = 0.0004$) (**Figure 2B**). To further verify the expression of FAM83A in CC, then we used qRT-PCR and IHC assays for examination of the level of FAM83A in CC tissues and adjacent ones. It was found that FAM83A was highly upregulated in 80.6% (25/31) of CC tissues compared to adjacent tissues (**Figures 2C,D**). To study the relation between FAM83A and CC clinical characteristics, the patients were split in two groups based on FAM83A levels. To do so, immunohistochemical staining was used to statistically score the expression level of FAM83A in CC tissues, which was higher than the mean as the high expression group and lower than

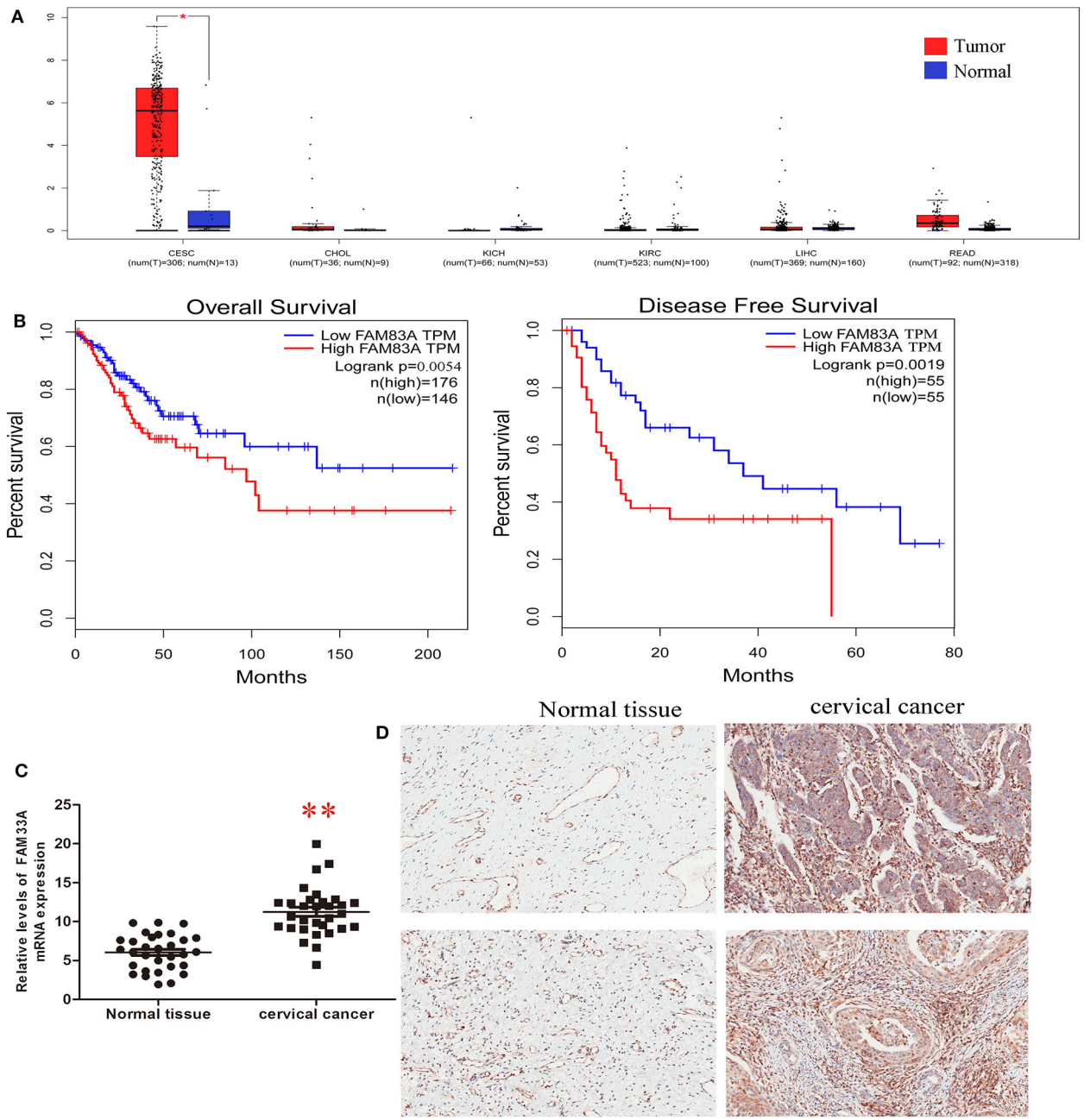

FIGURE 2 | FAM83A is overexpressed in cervical cancer. **(A)** Analyses of FAM83A expression levels in cervical SCC and endocervical adenocarcinoma (CESC), cholangiocarcinoma (CHOL), kidney chromophobe (KICH), kidney renal clear cell carcinoma (KIRC), liver hepatocellular carcinoma (LIHC), and rectal adenocarcinoma (READ) samples using TCGA sequencing data. **(B)** Kaplan–Meier analysis of overall survival and disease-free survival in patients with cervical cancer ($P < 0.001$ for both overall survival and disease-free survival) based on FAM83A expression. **(C)** qRT-PCR was performed to detect FAM83A expression in cervical cancer and matched normal tissues ($n = 31$). **(D)** IHC was performed to detect FAM83A expression in cervical cancer and matched normal tissues ($n = 31$).

the mean as the low expression group. Statistical results showed no correlation between FAM83A expression and age, number of lymph nodes, size of tumors or clinical stage ($P > 0.05$). On the other hand, FAM83A expression was significantly correlated with the histopathological type ($P < 0.05$) as well as lymph node status ($P < 0.05$) (**Table 1**).

FAM83A Inhibits Cell Viability and Induces Cell Cycle Arrest

We used qRT-PCR and immunoblot analysis to detect the expression of FAM83A in HCerEpiC, highly metastatic cells (CaSki), as well as low metastatic cells (HeLa and SiHa). It was found that FAM83A expression was more in CC cell lines

TABLE 1 | Relationship between FAM83A expression and clinicopathological factors.

Characteristic	FAM83A		*P*-value
	High expression	Low expression	
Age (year)			0.235
≥50	10	4	
<50	15	2	
Lymph node number			0.219
≥25	6	3	
<25	19	3	
Lymph node status			0.007
N0	20	1	
N1	5	5	
Histological type			0.0001
Malignant	25	6	
Normal	7	24	
Tumor size (cm)			0.646
<3	9	2	
≥3	16	4	
Clinical stage			0.146
I	4	2	
II	15	3	
III	6	1	

when compared to cervical epithelial cells. The CaSKi cells (high metastatic) the expression was the highest (**Figure 3A**). To further understand the biological role of FAM83A in regulation of CC cells, FAM83A was knocked down in CaSki cells (with high FAM83A expression) by siRNA/shRNA-mediated silencing. The qRT-PCR and immunoblot analysis confirmed that FAM83A expression levels were markedly reduced in CaSki cells (**Figure 3B**). As shown in **Figure 3C**, FCM was performed to determine whether FAM83A plays a role in regulating the cell cycle. FCM showed that the knockdown of FAM83A in CaSki cells resulted in a remarkable rise in the percentage of cells in G1 phase while reduced the proportion of cells in S-phase. These above results indicated that silence of FAM83A blocked the cell cycle from progressing and inhibited CC cells activity. Moreover, CCK-8 assays demonstrated that silencing FAM83A markedly inhibited the proliferation of CC cells *in vitro* (**Figure 3D**). For further confirmation of FAM83A role in the tumorigenesis of CC, nude mice were injected with FAM83A stable knockdown CaSki cells as well as control cells. FAM83A knockdown significantly restrained tumor growth in nude mice (**Figure 3E**). The IHC analysis showed that the FAM83A knockdown group had less Ki67-positive cells when compared with those from the control group (**Figure 3F**).

PI3K/Akt Signaling Is Essential for FAM83A-Promoted CC Proliferation

For further elucidation of molecular mechanisms of proliferation inhibition as well as cell cycle arrest by FAM83A depletion in CC, a gene set enrichment analysis (GSEA) of publicly available TCGA cervical SCC data was performed. We were excited to find that FAM83A expression was correlated with the activation of phosphatidylinositol 3 kinase (PI3K)/protein kinase B (AKT) signaling (**Figure 4A**). Therefore, we hypothesized that FAM83A affects the activity of PI3K/Akt/mTOR signal path in CC cells. Subsequently, our western blot analysis demonstrated that FAM83A knockdown lead to significant dephosphorylation of PI3K, Akt, and mTOR in CaSki cells (**Figure 4B**).

Loss of miR-206 Expression Induces FAM83A Overexpression in CC

To identify whether microRNAs (miRNAs) are involved in regulation of FAM83A in CC cells, we performed a bioinformatics analysis using the PicTar, miRanda (miRBase), and TargetScan in order to predict the potential microRNA regulating FAM83A. The miR-206 was selected to target FAM83A utilizing these above programs. Correlation analysis of FAM83A expression and miR-206 revealed that FAM83A has a significant negative correlation with miR-206 in the TCGA dataset (**Figure 4C**). Immunoblot analysis indicated that the overexpression of miR-206 dramatically decreased FAM83A protein expression in CaSki cells (**Figure 4D**). Subsequently, we constructed luciferase reporters including the putative miR-206 binding sites, which contain WT or mutated miR-206 binding sites. Experimental data indicated that overexpression of miR-206 weakened the luciferase activity of the WT reporter vector without effecting the mutant reporter vector (**Figure 4E**). In a word, these above experiments consistently indicated that loss of miR-206 expression increases the expression of FAM83A, which promotes cell proliferation *via* the PI3K/AKT/mTOR pathway and imposes an additional posttranscriptional modulation (**Figure 4F**).

DISCUSSION

In this present study, TCGA RNA sequencing data including cervical SCC and endocervical adenocarcinoma samples and paracancer samples and GEO data comprising the GSE9750 and GSE52903 datasets were analyzed using bioinformatics analysis. Five genes (KRT17, FXYD3, KRT5, FAM83A, and CLDN4) were consistently overexpressed and three genes (CDKN2A, MCM5, and RFC4) were under-expressed in these above three datasets.

We found that FAM83A is specifically overexpressed in CC tissue but not in cholangiocarcinoma, kidney chromophobe, kidney renal clear cell carcinoma, rectal adenocarcinoma, or liver hepatocellular carcinoma. From TCGA database, we predicted that FAM83A expression in cancerous tissue and paracancer tissue in cervical SCC and endometrial adenocarcinoma (CESC) was significantly different. We did not mention the difference of FAM83A expression between cervical SCC and endometrial adenocarcinoma. At this time, we aimed to explore the role of FAM83A in CC cancer and its prognostic value.

Some studies have investigated the roles of FAM83A in PI3K/AKT signaling pathways in cancer. Lee et al. reported that in the breast cancer FAM83A possibly contributes in

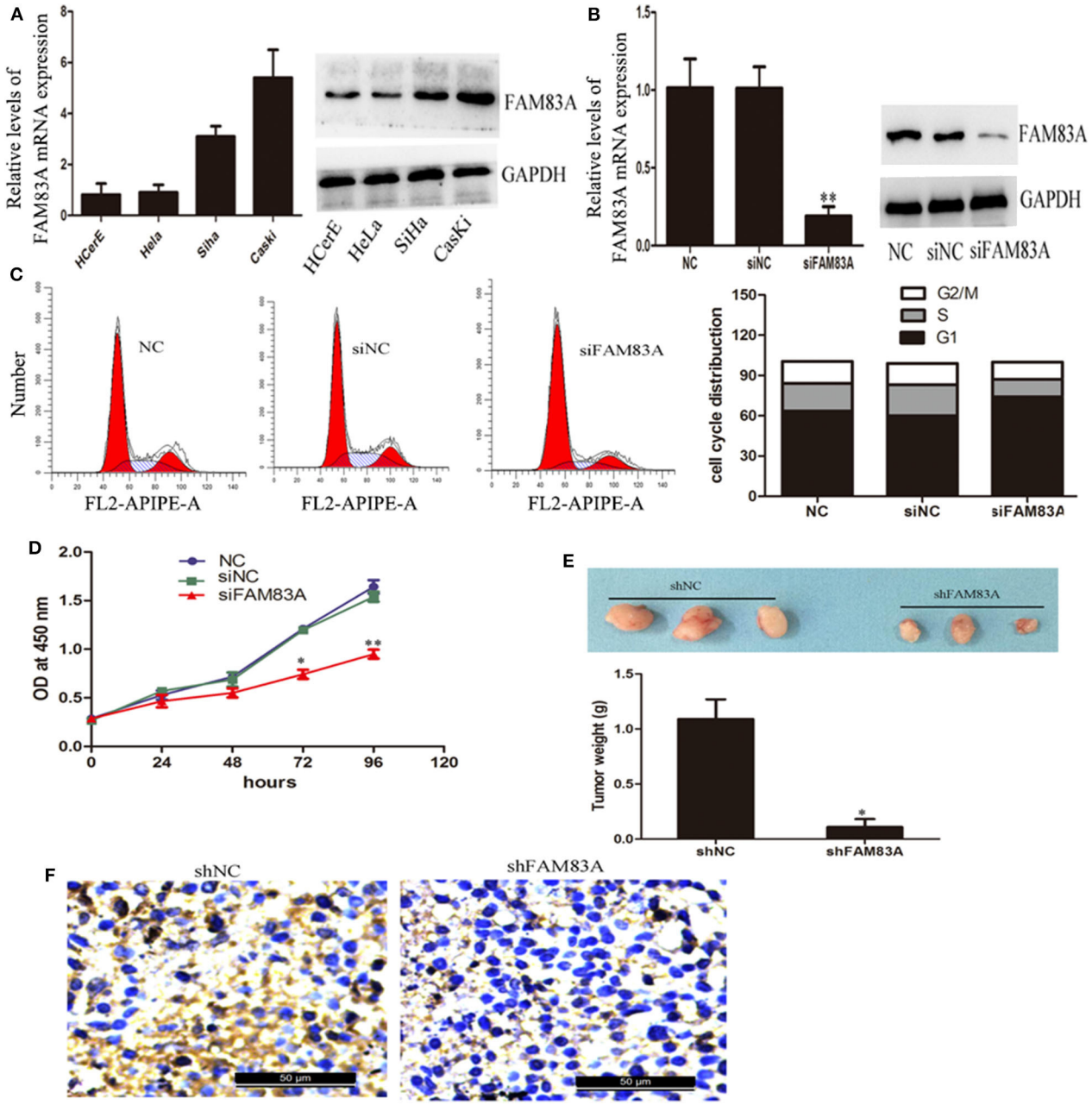

FIGURE 3 | Knockdown of FAM83A expression inhibits cervical cancer cell proliferation *in vitro* and *in vivo*. **(A)** qRT-PCR and western blot analysis were performed to detect the expression of FAM83A in cervical cancer cell lines, normal human cervical epithelial cells (HCerEpiC), two low metastatic cervical cancer cell lines (HeLa and SiHa) and one highly metastatic cell line (CaSki). **(B)** qRT-PCR and immunoblot analysis confirmed that the FAM83A expression levels were significantly knocked down in CaSki cells. **(C)** FCM analysis of the effect of FAM83A knockdown on cell cycle distribution. **(D)** A CCK-8 assay was performed to detect cell proliferation of the control or siFAM83A-transfected CaSki cells. **(E)** Knockdown of FAM83A inhibits CaSki cell tumor growth *in vivo*. **(F)** Ki67 immunostaining of tumor samples from the FAM83A knockdown and control CaSki groups. Error bars represent the means of three independent experiments. $^{*}P < 0.05$, $^{**}P < 0.01$.

exerting resistance to tyrosine kinase inhibitors *via* activating epidermal growth factor receptor (EGFR)/PI3K/AKT signaling pathway *via* interacting with c-RAF and phosphatidylinositol 3 kinase p85. These findings indicate that FAM83A overexpression might result in chemoresistance (33, 34). Similarly, both *in vitro* and *in vivo* models silencing FAM83A significantly reduces proliferation, anchorage-independent growth and metastatic capacities of breast cancer cells.

PI3K/AKT signaling pathway is an intracellular signal transduction pathway that plays roles in proliferation, metabolism, cell survival and growth, and angiogenesis in

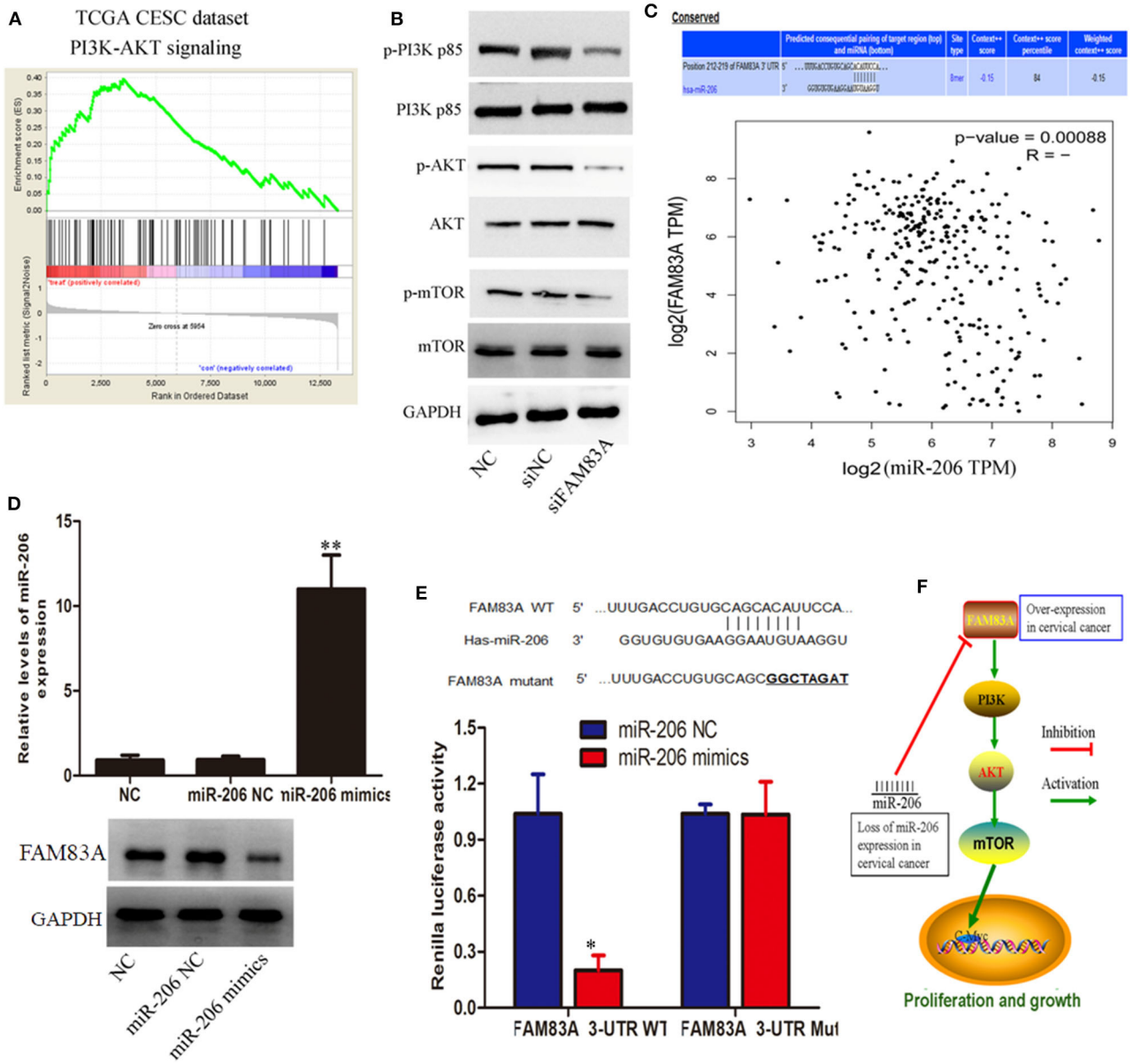

FIGURE 4 | miR-206/FAM83A/PI3K/AKT signaling pathway molecules serve as critical effectors in cervical cancer progression. **(A)** GSEA plot showing that FAM83A expression was correlated with PI3K/AKT signaling-related gene signatures. **(B)** Protein levels of PI3K, p-PI3K, AKT, p-AKT, mTOR, and p-mTOR in CaSki cells are shown, and glyceraldehyde 3-phosphate dehydrogenase (GAPDH) was used as a loading control. **(C)** Schematic of binding sites in the FAM83A 3'-UTR complementary to the "seed region" of miR-206. Correlation analysis of FAM83A expression and miR-206. **(D)** The overexpression of miR-206 dramatically decreased the protein expression of FAM83A in CaSki cells. **(E)** The complementary sequences or the mutant (underlined) binding site of FAM83A or the miR-206 binding site in the 3'-UTR of FAM83A from different mammalian species. **(F)** Summary of the mechanism of FAM83A in cervical cancer. Error bars represent the means of three independent experiments. $^{*}P < 0.05$, $^{**}P < 0.01$.

response to extracellular signals. This signaling pathway is mediated through serine and/or threonine phosphorylation of different types of downstream compounds, of them PI3K and AKT are the main proteins. The effects of FAM83A on PI3K/AKT pathway have been investigated in few cancers (22, 35–37). Liu et al. analyzed TCGA database and reported that FAM83A is overexpressed in hepatocellular carcinoma (HCC) cells and plays a cancer-promoting and treatment-resistance role. Their functional bioinformatics analyses indicated that FAM83A promoted the PI3K/AKT signaling pathway, its downstream c-JUN protein, and epithelial-to-mesenchymal transition (EMT)-related protein levels, including downregulation of E-cadherin and upregulation of Vimentin and N-cadherin. They reported that c-JUN induced FAM83A

expression through direct binding to its promoter region, which forms a positive-feedback loop for FAM83A/PI3K/AKT/c-JUN. Liu et al. concluded that FAM83A serves as a tumorigenesis of HCC and promotes migration, invasion and metastasis through triggering a FAM83A/PI3K/AKT/c-JUN positive-feedback loop (38).

Hu et al. examined the roles and possible mechanism of FAM83A in non-small cell lung cancer (NSCLC) progression through bioinformatics analysis of GEO and TCGA databases and RT-PCR and reported high FAM83A expression in NSCLC that was associated with the poor prognosis (35). *In vitro* model showed that silencing FAM83A by siRNA/shRNA markedly reduced cell proliferation, induced cell apoptosis, and inhibited cell motility. *In vivo* experiments showed that silencing FAM83A in A549 cells reduced subcutaneous tumor growth and lung metastasis as well as phosphorylation of ERK and PI3K/AKT/mTOR (35). Contrary, FAM83A overexpression promoted cell proliferation and metastasis invasion *in vitro* that was suppressed by PI3K inhibitor and ERK inhibitor respectively. Their findings demonstrated that FAM83A promotes oncogenesis of NSCLC partly through ERK and PI3K/AKT/mTOR pathways (35).

Based on the expression level of FAM83A, we divided the patients into high and low-risk groups based on the median risk score in the TCGA dataset as a cut-off value, and the median OS and DFS in the low-risk group was pronounced higher of the one in the high-risk group. PCR and IHC results confirmed the expression characteristic of FAM83A in CC clinical samples. It was seen that the expression quantity of FAM83A was markedly correlated with histopathological type and lymph node status. Furthermore, our results demonstrated that silencing FAM83A markedly inhibited CC cell proliferation both in *in-vitro* as well as *in-vivo* experiments, meanwhile induced cell cycle arrest *in vitro*. FAM83A is a probable protooncogene that regulates the EGF/EGFR signaling pathway (39, 40) and seems vital for activating RAS/MAPK signaling cascade under the stimulation of EGFR. This gene also activates signaling cascades independent of EGFR regulation.

We performed a GSEA analysis on the cervical SCC samples of the TCGA database and found a regulatory relationship between FAM83A and PI3K/AKT pathway. The experiments demonstrated that FAM83A alters the activity of PI3K/Akt/mTOR signaling in CC.

MiRNAs have attracted considerable and wide attention in the regulation of gene expression because of their important status in cellular differentiation and embryonic stem cell growth. We performed a bioinformatics analysis using three different types of prediction software including PicTar, TargetScan, and miRanda (miRBase). We found that miR-206 directly suppresses FAM83A expression in CC. Subsequently, our western blot analysis and luciferase reporter assay consistently indicated that loss of miR-206 expression upregulated the expression of FAM83A. One interesting question is that overexpression of FAM83A or inhibition of miR-206 in cell lines such as HCerEpiC is enough to drive the cancer progression? And how do PI3K or AKT inhibitors influence such effects? We hypothesized that overexpression of FAM83A or miR206 in normal HCerEpiC might affect normal cell physiological function, which may be a driver for malignant transformation of normal cells. If extrapolated from our results, the addition of PI3K or AKT inhibitors may partially reverse the previously assumed effect. However, conducting further well-designed studies investigating such hypotheses is recommended.

CONCLUSION

In conclusion, our current experimental research reveal that molecules involved in the miR-206/FAM83A/PI3K/AKT signaling pathway serve as critical effectors in CC progression, meanwhile, FAM83A, as a potential protooncogene is closely related to the survival and prognosis of CC, may serve as potential therapeutic targets in CC.

DATA AVAILABILITY STATEMENT

The datasets presented in this study can be found in online repositories. The names of the repository/repositories and accession number(s) can be found in the article/ **Supplementary Material**.

ETHICS STATEMENT

All procedures were in agreement with the Guide for the Care and Use of Laboratory Animals and approval was obtained by the Animal Care and Use Committee of Chongqing Medical University. All procedures performed in our research were in accordance with the related ethical standards.

AUTHOR'S NOTE

LR and HL are postdoctoral researchers jointly trained by Chongqing Public Health Medical Center and Chongqing Medical University.

AUTHOR CONTRIBUTIONS

LR, HL, and FS: conceptualization. LR, YM, and ZL: methodology. YM and HL: software. LR, YC, and FS: validation, resources, and project administration. LR, HL, and YM: formal analysis. LR and HL: investigation. LR, HL, and ZL: data curation. LR: writing-original draft preparation. YM, YC, and FS: writing-review and editing. HL and JO: visualization. JO and YC: supervision. LR and YC: funding acquisition. All authors contributed to the article and approved the submitted version.

FUNDING

This research was supported in part by Chongqing Natural Science Foundation Project (Grant Number: cstc2019jcyj-msxmX0428; project leader: LR), Chongqing Natural Science Foundation Project (Grant number: cstc2018jscx-mszd0075; project leader: FS), and The National Science and Technology Major Project of China during the 13th Five-year Plan Period (Grant Number: 2018ZX10302104; project leader: YC).

ACKNOWLEDGMENTS

We thank the Basic Medicine College of Chongqing Medical University for providing the study data and related help.

SUPPLEMENTARY MATERIAL

The Supplementary Material for this article can be found online at: https://www.frontiersin.org/articles/10.3389/fmed.2020.608441/full#supplementary-material

REFERENCES

1. Fitzmaurice C, Abate D, Abbasi N, Abbastabar H, Abd-Allah F, Abdel-Rahman O, et al. Global, regional, and national cancer incidence, mortality, years of life lost, years lived with disability, and disability-adjusted life-years for 29 cancer groups, 1990 to 2017: a systematic analysis for the global burden of disease study. *JAMA Oncol*. (2019) 5:1749–68. doi: 10.1001/jamaoncol.2019.2996
2. Chen D, Juko-Pecirep I, Hammer J, Ivansson E, Enroth S, Gustavsson I, Feuk L, Magnusson PK, McKay JD WE and GU. Genome-wide association study of susceptibility loci for cervical cancer. *J Natl Cancer Inst*. (2013) 105:624–33. doi: 10.1093/jnci/djt051
3. Wilbur DC. Practical issues related to uterine pathology: *in situ* and invasive cervical glandular lesions and their benign mimics: emphasis on cytology–histology correlation and interpretive pitfalls. *Mod Pathol*. (2016) 29(Suppl. 1):S1–11. doi: 10.1038/modpathol.2015.138
4. Berti FCB, Pereira APL, Cebinelli GCM, Trugilo KP, Brajão de Oliveira K. The role of interleukin 10 in human papilloma virus infection and progression to cervical carcinoma. *Cytokine Growth Factor Rev*. (2017) 34:1–13. doi: 10.1016/j.cytogfr.2017.03.002
5. Wieringa HW, van der Zee AGJ, de Vries EGE, van Vugt MATM. Breaking the DNA damage response to improve cervical cancer treatment. *Cancer Treat Rev*. (2016) 42:30–40. doi: 10.1016/j.ctrv.2015.11.008
6. Fetcko K, Gondim DD, Bonnin JM, Dey M. Cervical cancer metastasis to the brain: a case report and review of literature. *Surg Neurol Int*. (2017) 8:181. doi: 10.4103/sni.sni_111_17
7. Thomas M, Narayan N, Pim D, Tomaić V, Massimi P, Nagasaka K, et al. Human papillomaviruses, cervical cancer and cell polarity. *Oncogene*. (2008) 27:7018–30. doi: 10.1038/onc.2008.351
8. Gadducci A, Guerrieri ME, Greco C. Tissue biomarkers as prognostic variables of cervical cancer. *Crit Rev Oncol/Hematol*. (2013) 86:104–29. doi: 10.1016/j.critrevonc.2012.09.003
9. Tomczak K, Czerwińska P, Wiznerowicz M. The Cancer Genome Atlas (TCGA): an immeasurable source of knowledge. *Contemp Oncol*. (2015) 19:A68–77. doi: 10.5114/wo.2014.47136
10. Zheng H, Zhang G, Zhang L, Wang Q, Li H, Han Y, et al. Comprehensive review of web servers and bioinformatics tools for cancer prognosis analysis. *Front Oncol*. (2020) 10:68. doi: 10.3389/fonc.2020.00068
11. Lu C, Yang M, Luo F, Wu FX, Li M, Pan Y, et al. Prediction of lncRNA-disease associations based on inductive matrix completion. *Bioinformatics*. (2018) 34:3357–64. doi: 10.1093/bioinformatics/bty327
12. Falzone L, Candido S, Salemi R, Basile MS, Scalisi A, McCubrey JA, et al. Computational identification of microRNAs associated to both epithelial to mesenchymal transition and NGAL/MMP-9 pathways in bladder cancer. *Oncotarget*. (2016) 7:72758–66. doi: 10.18632/oncotarget.11805
13. Lánczky A, Nagy Á, Bottai G, Munkácsy G, Szabó A, Santarpia L, et al. miRpower: a web-tool to validate survival-associated miRNAs utilizing expression data from 2178 breast cancer patients. *Breast Cancer Res Treat*. (2016) 160:439–46. doi: 10.1007/s10549-016-4013-7
14. Anaya J. OncoLnc: linking TCGA survival data to mRNAs, miRNAs, and lncRNAs. *Peer J Comput Sci*. (2016) 4:e1780v1. doi: 10.7287/peerj.preprints.1780v1
15. Barrett T, Wilhite SE, Ledoux P, Evangelista C, Kim IF, Tomashevsky M, et al. NCBI GEO: archive for functional genomics data sets—update. *Nucleic Acids Res*. (2013) 41(D1):D991–5. doi: 10.1093/nar/gks1193
16. Neapolitan R, Jiang X. Inferring aberrant signal transduction pathways in ovarian cancer from TCGA Data. *Cancer Inform*. (2014) 13s1(Suppl. 1):CIN.S13881. doi: 10.4137/CIN.S13881
17. Koehorst JJ, van Dam J, Saccenti E, Martins dos Santos VAP, Suarez-Diez M, Schaap PJ. SAPP: functional genome annotation and analysis through a semantic framework using FAIR principles *Bioinformatics*. (2017) 34:1401–3. doi: 10.1093/bioinformatics/btx767
18. Mamatjan Y, Agnihotri S, Goldenberg A, Tonge P, Mansouri S, Zadeh G, et al. Molecular signatures for tumor classification: an analysis of The Cancer Genome Atlas data. *J Mol Diagn*. (2017) 19:881–91. doi: 10.1016/j.jmoldx.2017.07.008
19. Weisenberger DJ. Characterizing DNA methylation alterations from the cancer genome atlas. *J Clin Invest*. (2014) 124:17–23. doi: 10.1172/JCI69740
20. Mei Y, Tang Z, Li Z, Yang X. Repeatability and reproducibility of quantitative corneal shape analysis after orthokeratology treatment using image-pro plus software. *J Ophthalmol*. (2016) 2016:1732476. doi: 10.1155/2016/1732476
21. Li S, Xu F, Li H, Zhang J, Zhong A, Huang B, et al. S100A8^{+} stroma cells predict a good prognosis and inhibit aggressiveness in colorectal carcinoma. *Oncoimmunology*. (2017) 6:e1260213. doi: 10.1080/2162402X.2016.1260213
22. Bartel CA, Jackson MW. HER2-positive breast cancer cells expressing elevated FAM83A are sensitive to FAM83A loss. *PLoS ONE*. (2017) 12(5). doi: 10.1371/journal.pone.0176778
23. Chen S, Huang J, Liu Z, Liang Q, Zhang N, Jin Y. FAM83A is amplified and promotes cancer stem cell-like traits and chemoresistance in pancreatic cancer. *Oncogenesis*. (2017) 6:e300. doi: 10.1038/oncsis.2017.3
24. Li Y, Dong X, Yin Y, Su Y, Xu Q, Zhang Y, et al. BJ-TSA-9, a novel human tumor-specific gene, has potential as a biomarker of lung cancer. *Neoplasia*. (2005) 7:1073–80. doi: 10.1593/neo.05406
25. Cipriano R, Miskimen KLS, Bryson BL, Foy CR, Bartel CA, Jackson MW. Conserved oncogenic behavior of the FAM83 family regulates MAPK signaling in human cancer. *Mol Cancer Res*. (2014) 12:1156–65. doi: 10.1158/1541-7786.MCR-13-0289
26. Zhang J, Sun G, Mei X. Elevated FAM83A expression predicts poorer clinical outcome in lung adenocarcinoma. *Cancer Biomark*. (2019) 26:367–73. doi: 10.3233/CBM-190520
27. Liu L, Ma C, Xu Q, Cheng L, Xiao L, Xu D, et al. A rapid nested polymerase chain reaction method to detect circulating cancer cells in breast cancer patients using multiple marker genes. *Oncol Lett*. (2014) 7:2192–8. doi: 10.3892/ol.2014.2048
28. Richtmann S, Wilkens D, Warth A, Lasitschka F, Winter H, Christopoulos P, et al. FAM83A and FAM83B as prognostic biomarkers and potential new therapeutic targets in NSCLC. *Cancers (Basel)*. (2019) 11:652. doi: 10.3390/cancers11050652
29. Snijders AM, Lee SY, Hang B, Hao W, Bissell MJ, Mao JH. FAM83 family oncogenes are broadly involved in human cancers: an integrative multi-omics approach. *Mol Oncol*. (2017) 11:167–79. doi: 10.1002/1878-0261.12016
30. Khenkhar M, Uhlig PC, David KA, Bigley AL, Sherry L. Digital image analysis of automated mRNA in situ hybridization and immunohistochemistry to quantify HER3 expression in cancer tissues. *J Clin Oncol*. (2016) 34(Suppl. 15):e23172.

31. Ahmad N, Haider S, Jagannathan S, Anaissie E, Driscoll JJ. MicroRNA theragnostics for the clinical management of multiple myeloma. *Leukemia*. (2014) 28:732–8. doi: 10.1038/leu.2013.262
32. Li H, Jia Y, Cheng J, Liu G, Song F. LncRNA NCK1-AS1 promotes proliferation and induces cell cycle progression by crosstalk NCK1-AS1/MIR-6857/CDK1 pathway. *Cell Death Dis*. (2018) 9:198. doi: 10.1038/s41419-017-0249-3
33. Lee SY, Meier R, Furuta S, Lenburg ME, Kenny PA, Xu R, et al. FAM83A confers EGFR-TKI resistance in breast cancer cells and in mice. *J Clin Invest*. (2012) 122:3211–20. doi: 10.1172/JCI60498
34. Grant S. FAM83A and FAM83B: Candidate oncogenes and TKI resistance mediators. *J Clin Invest*. (2012) 122:3048–51. doi: 10.1172/JCI64412
35. Hu H, Wang F, Wang M, Liu Y, Wu H, Chen X, et al. FAM83A is amplified and promotes tumorigenicity in non-small cell lung cancer *via* ERK and PI3K/Akt/mTOR pathways. *Int J Med Sci*. (2020) 17:807–14. doi: 10.7150/ijms.33992
36. Xu J, Lu W. FAM83A exerts tumor-suppressive roles in cervical cancer by regulating integrins. *Int J Oncol*. (2020) 57:509–21. doi: 10.3892/ijo.2020.5078
37. Zhou F, Geng J, Xu S, Meng Q, Chen K, Liu F, et al. FAM83A signaling induces epithelial-mesenchymal transition by the PI3K/AKT/Snail pathway in NSCLC. *Aging (Albany NY)*. (2019) 11:6069–88. doi: 10.18632/aging.102163
38. Liu C, Peng X, Li Y, Liu S, Hou R, Zhang Y, et al. Positive feedback loop of FAM83A/PI3K/AKT/c-Jun induces migration, invasion and metastasis in hepatocellular carcinoma. *Biomed Pharmacother*. (2020) 123:109780. doi: 10.1016/j.biopha.2019.109780
39. Rhyasen GW, Starczynowski DT. Deregulation of microRNAs in myelodysplastic syndrome. *Leukemia*. (2012) 26:13–22. doi: 10.1038/leu.2011.221
40. Contreras J, Rao DS. MicroRNAs in inflammation and immune responses. *Leukemia*. (2012) 26:404–13. doi: 10.103-8/leu.2011.356

Conflict of Interest: The authors declare that the research was conducted in the absence of any commercial or financial relationships that could be construed as a potential conflict of interest.

frontiers in Medicine

ORIGINAL RESEARCH
published: 17 December 2020
doi: 10.3389/fmed.2020.617321

Ozone Exposure Induces Metabolic Disorders and NAD+ Depletion Through PARP1 Activation in Spinal Cord Neurons

Shulin Ma[1], *Xu Zhao*[1], *Cong Zhang*[1], *Panpan Sun*[1], *Yun Li*[1], *Xiaowen Lin*[1], *Tao Sun*[1] *and Zhijian Fu*[1,2]*

[1] *Department of Pain Management, Shandong Provincial Hospital, Cheeloo College of Medicine, Shandong University, Jinan, China,* [2] *Department of Pain Management, Shandong Provincial Hospital Affiliated to Shandong First Medical University, Jinan, China*

Background and Objective: Ozone therapy has shown therapeutic efficacy in different disorders particularly low back pain (LBP). However, ozone therapy has been associated with toxic effects on the respiratory, endocrine, cardiovascular systems as well as nervous system because of its strong oxidizing capacity. Recent studies have reported possible associations between ozone exposure and metabolic disorders, but the findings are controversial and little is known on the mechanisms of action. This study aims to investigate the cytotoxic effects of ozone exposure and possible mechanism of action in the animal model.

Methods: Wistar neonate rats with the age of 24 h after birth were sacrificed by cervical dislocation under general anesthesia, then immersed in 75% alcohol and iodophor for 5 min, respectively. The spinal cord was isolated and cut to samples of ∼1 mm^3 and prepared for further experiments. The spinal cord neurons (SCNs) were exposed to ozone at different concentrations and then cultured in 96-well plates with glass bottom for 7 days. The cell viability, ATP levels and the NAD+ concentration were determined and compared between the different experimental groups and the control group.

Results: Analyses of the data by non-targeted liquid chromatography-mass spectrometry (LC-MS) analysis determined the metabolic disorder in SCNs following the ozone exposure. Moreover, our assessments showed that ozone exposure resulted in DNA damage, poly (ADP)-ribose polymerase-1 (PARP1) excessive activation, nicotinamide adenine dinucleotide (NAD+) depletion and decrease of ATP level in SCNs. The PARP1 inhibitor can inhibit the cytotoxic effect of ozone to SCNs without inhibiting the activation of AMP-activated protein kinase (AMPK). Our findings revealed that the cytotoxic effects of ozone to SCNs might be mediated by excessive PARP1 activation and subsequent NAD+ depletion. Moreover, using PARP1 inhibitor can protect SCNs from cytotoxic effects of ozone by preventing NAD+ depletion during ozone exposure.

Conclusion: Ozone exposure seems to induce metabolic disorders and NAD+ depletion through excessive PARP1 activation in SCNs.

Keywords: ozone, metabolomics, nicotinamide adenine dinucleotide, ATP level, spinal cord neurons

OPEN ACCESS

Edited by:
Ali Yadollahpour,
The University of Sheffield,
United Kingdom

Reviewed by:
Shengye Wang,
Zhejiang Cancer Hospital, China
Samaneh Rashidi,
Ahvaz Jundishapur University of Medical Sciences, Iran

***Correspondence:**
Zhijian Fu
zhijian_fu@163.com

Specialty section:
This article was submitted to Precision Medicine, a section of the journal Frontiers in Medicine

Received: *14 October 2020*
Accepted: *23 November 2020*
Published: *17 December 2020*

Citation:
Ma S, Zhao X, Zhang C, Sun P, Li Y, Lin X, Sun T and Fu Z (2020) Ozone Exposure Induces Metabolic Disorders and NAD+ Depletion Through PARP1 Activation in Spinal Cord Neurons. Front. Med. 7:617321. doi: 10.3389/fmed.2020.617321

INTRODUCTION

Ozone is an inorganic molecule and allotrope of oxygen with strong oxidizing capacity. It is a highly reactive agent consisting of three oxygen atoms bonded in a V-like shape (1). It occurs both naturally in the atmosphere and as a man-made product by industrial activities (1, 2). Ozone is the major photochemical constitute of polluted air, which induces a dose-dependent oxidative stress in tissues due to its strong capacity to produce free radicals from different interactions including protein oxidation, enzymatic inactivation, lipoperoxidation of cell membranes, DNA destruction, and cell apoptosis (1, 3, 4). Despite of these interactions, ozone has been widely used for different musculoskeletal disorders (5–7). During the last decade, ozone therapy alone or in combination with other modalities, has been extensively used in clinical practice for treatment of herniated discs, low back pain (LBP) and other chronic pains (4–8). Further translational and clinical trials have shown the therapeutic efficacy and safety of ozone for other disorders including degenerative disorders, vascular and immune diseases (4, 9–12). The main administrations routes of ozone in the ozone therapy are percutaneous, intradiscal, and intramuscular routes. Current evidence shows the potential therapeutic efficacy of ozone therapy in herniated discs and for pain management in LBP (4, 6, 13, 14). However, ozone therapy has been associated with toxic effects on the respiratory, endocrine, cardiovascular systems as well as nervous system because of its strong oxidizing property and inducing systemic inflammation (12, 15–19). Ginanneschi et al. reported that transcutaneous intradiscal injection of ozone for L4–L5 disk herniation resulted in ventral and dorsal root injury (20). In this regard, some studies have investigated the effects and mechanisms of action of ozone exposure on metabolic disorders and reported the associations between ozone exposure and metabolic disorders (11, 18). Although many studies have been conducted on the cytotoxic effects of ozone, the underlying signaling pathways and molecular mechanisms of susceptibility and the disorder are not fully understood. However, evidence from human and animal studies suggests that ozone-induced neuroinflammation, oxidative stress, microglial activation, cerebrovascular dysfunction, and alterations in the blood-brain barrier are the main mechanisms of ozone induced cytotoxicity in central nervous system (11). Defining the cytotoxicity and mechanisms of action of ozone exposure particularly in spinal cord neurons (SCNs) is necessary to develop efficient ozone therapy as well as new protective strategies for individuals at risk. In this regard, a better understanding of the mediators and involved signaling pathways is of prime importance.

The nuclear enzyme poly(ADP)-ribose polymerase-1 (PARP1) is the primary subtype of a protein family, which contains polyadenosine diphosphate ribose and polymerase activity (21). PARP1 is a key moderator for cell death in oxidative stress, ischemia, and excitotoxicity (21, 22). PARP1 utilizes oxidized nicotinamide adenine dinucleotide (NAD+) as a substrate to catalyze the covalent attachment of ADP-ribose units onto various target proteins, such as aspartate, glutamate, lysine, tyrosine, and serine. Moreover, PARP1 catalyzes the addition of NAD+ of poly (ADP)-ribose (PAR) onto itself in response to oxidative DNA damage (21).

Recently, researchers have employed metabolomics analysis to investigate the roles and molecular pathways involved in cellular metabolism disorders under oxidative stress (23, 24). Oxidized NAD (NAD+) and reduced NAD (NADH) as metabolic cofactors play vital role in cellular energy metabolism and are also involved in calcium homeostasis, mitochondrial function, oxidative stress, gene expression, aging and apoptosis (25–27). DNA damage-induced PARP activation leads to depletion of NAD+ which subsequently impedes cellular energy metabolism. Moreover, PARP1 activation could hinder hexokinase (HK), which is a crucial enzyme in the glycolysis pathway through PARylation process and subsequently leading to ATP deprivation and cell death called id parthanatos (28–31).

The signaling pathways involved in the neuronal death induced by PARP1 activation are not yet fully determined. Different studies have been conducted on this regard (29, 32–34).

Enrichment analysis revealed NAD+-related metabolic disorders induced by excessive activation of PARP1 after DNA damage (35). Activating PARP1 would lead to cytosolic NAD+ depletion and mitochondrial release of apoptosis-inducing factor (AIF), and different studies have investigated the causal relationships between PARP1 activation and NAD+ depletion. Strong evidence shows that NAD+ depletion is a causal process in PARP1-mediated cell death so that NAD+ depletion and glycolytic failure result in mitochondrial AIF release (36).

Conrad et al. showed that NAD+ depletion is necessary and sufficient for PARP1-mediated neuronal death (36). They used extracellular NAD+ to restore neuronal NAD+ levels after PARP1 activation. Exogenous NAD+ used P2X (6) -gated channels to enter neurons to restore cytosolic NAD+ that subsequently inhibited excess PARP1 activation and prevented the AIF translocation, glycolytic inhibition, mitochondrial failure, and neuron death. They used metabolic substrates, such as pyruvate, hydroxybutyrate, or acetoacetate to circumvent the glycolytic inhibition and then prevented mitochondrial failure and neuron death. Other finding of this group was that using NAD+ glycohydrolase to deplete intracellular cytosolic NAD+ lead to blockage of the glycolysis inhibition, AIF translocation, mitochondrial depolarization, and neuron death, and the process was independent of PARP1 activation (36).

NAD+ is an important coenzyme in redox reaction of cells and plays significant roles in the process of cell tricarboxylic acid cycle (TCA), fat β oxidation, glucose metabolism, and amino acid metabolism (37). Recent studies have confirmed that excessive PARP1 activation could promote NAD+ depletion, which could affect cell energy metabolism and reduce ATP levels leading to cell necrosis (22). Some studies have investigated the causal relationship of PARP activation and subsequent NAD+

Abbreviations: LBP, Low back pain; SCNs, spinal cord neurons; LC-MS, liquid chromatography-mass spectrometry; PARP1, poly (ADP)-ribose polymerase-1; NAD+, nicotinamide adenine dinucleotide; AMPK, AMP-activated protein kinase; TCA, tricarboxylic acid cycle; PMSF, phenylmethylsulfonyl fluoride; DAPI, 4′,6-diamidino-2-phenylindole; RT, retention time; LKB1, liver kinase B1.

depletion and cell death and demonstrated direct evidence on causal relationship between PARP activation, NAD+ depletion, and cell death (38–41). However, later studies have demonstrated that excessive PARP activation and NAD+ depletion is not the only pathway to cell death. Heller et al. used islet cells from mice with a disrupted and inactivated PARP gene ($PARP^{-/-}$ mice) to investigate the effects of DNA-damaging radicals and relationship between PARP activation, NAD+ depletion, and cell death. They reported that mutant islet cells showed more resistant to the toxicity of DNA-damaging radicals and did not show NAD+ depletion after exposure to the DNA-damaging radicals (41). This finding indicates that most of NAD+ depletion following the exposure to oxidative factors is due to PARP activation. They also reported that 3-aminobenzamide, an ADP-ribosylation inhibitor, partially protected islet cells with intact PARP gene but not $PARP^{-/-}$ cells from lysis following nitride oxide or ROI treatment. This finding confirms that the protective action of 3-aminobenzamide is only due to PARP inhibition. They also observed that the mutant cells underwent an alternative pathway of cell death that did not require PARP activation and NAD+ depletion. They confirmed the causal relationship of PARP activation and subsequent islet cell death and concluded there is an alternative pathway of cell death independent of PARP activation and NAD+ depletion (41). Few studies have reported that pulmonary fibroblasts from the $PARP^{-/-}$ mice are protected against peroxynitrite-induced cell injury, in comparison to the fibroblasts of the corresponding wild-type animals (42). Furthermore, Eliasson et al. demonstrated that neural cells of $PARP^{-/-}$ mice show significant protection against different oxidants inducing glutamate-mediated ischemic injuries indicating the involvement of PARP activation in neuronal damage following focal cerebral ischemia (43). The resistance of inactivated PARP gene to different oxidative factors has been reported in different diseases including diabetes. For instance, Burkart et al. showed $PARP^{-/-}$ mice are completely resistant to the development of diabetes induced by the beta-cell toxin streptozocin (44). The findings of the previous studies have suggested that PARP1 inhibitors might have protective effects against oxidative stress-induced cell necrosis.

This study aimed to investigate the effects and possible mechanisms of action of ozone on SCNs metabolism using metabolomics analysis. The findings show that NAD+ depletion is caused by excessive activation of PARP1. Moreover, we found that ozone-induced DNA damage could be one of the main causes of ozone-induced metabolic disorders of SCNs. Using PARP1 inhibitors can prevent NAD+ depletion and promote cell viability during ozone exposure.

MATERIALS AND METHODS

Animals and Reagents

The Wistar neonate rats used in this experiment were obtained from the Experimental Animal Center of Shandong University, Shandong, China. The 24-h born Wistar neonate rats were selected for the experiments and treated according to regulations of the National Institutes of Health and all the experimental procedures of this study were approved by the Animal Protection and Use Committee of School of Medicine of Shandong University, Jinan, Shandong, China. During the experiment, efforts were made to reduce the pain caused by the operation.

The cultivating materials including neurobasal medium, DMEM/F12, medium B27 supplement, fetal bovine serum, and trypsin were purchased from Gibco BRL, Life Technologies (Scotland, UK). The agents for laboratory assessments including Poly-L-lysine, L-glutamine, penicillin, streptomycin, ABT-888, cytarabine, protease inhibitors, phenylmethylsulfonyl fluoride (PMSF) were purchased from Beyotime, Beyotime Biotechnology (China).

Isolation and Cultivation of SCNs

The extraction and isolation and cultivation of SCNs from neonatal rats were performed as per the method described previously with slight modifications (45). Briefly, the 24-h newborn rats were obtained and sacrificed by cervical dislocation under general anesthesia, then immersed in 75% alcohol and iodophor for 5 min, respectively. The spinal cord tissue was isolated and cut into small pieces of $\sim 1 \times 1$ mm^3. The micro-slices were then blocked for digestion through moving into digestion medium containing 1 ml 0.25% trypsin in 37°C for 10–30 min. Fifty microliter of fetal bovine serum was used to terminate digestion. The cells were separated from tissues carefully and then centrifuged at 1,000 rpm for 5 min. The supernatant was taken and the sediment was re-suspended in DMEM/F12 medium containing 10% fetal bovine serum and penicillin and streptomycin with the final concentration of 100 U/ml and 0.1 mg/ml, respectively. Then, the cell density was adjusted to 5×105 /ml. The cells were inoculated into a 6-well culture plate coated with 0.1 g/L of Poly-L-lysine and cultured in an incubator containing 5% carbon dioxide at 37°C. Six hours later, the whole amount of medium was replaced with neuron-specific culture medium (containing 2 mmol/L L-glutamine, 2% B27 additive, final concentration of 100 U/ml and 0.1 mg/ml penicillin and streptomycin, respectively). After the medium was changed for 24 h, the solution was changed in half once every 2 days, and cytarabine with the final concentration of 0.05 mg/ml was added on the third day to inhibit the growth of glial cells. The cells could be used for subsequent experiment 6–8 days after plating.

Immunofluorescence Identification

The isolated SCNs were cultured in 96-well plates with glass bottom for 7 days. The medium was absorbed completely. The cells were fixed with paraformaldehyde for 15 min, permeabilized for 5 min at the room temperature with 0.5% Triton X-100, and blocked with goat serum at room temperature for 1 h. The cells were incubated with anti-NF200 (Boster, BM0100, 1:100) overnight at 4°C. On the second day, the cells were incubated with the secondary antibody (Beyotime, A0216, 1:400) at room temperature for 1 h. The 4′,6-diamidino-2-phenylindole (DAPI) counterstain was used to show the chondrocyte nuclei. The stained SCNs were observed under a fluorescence microscope.

Ozone Exposure and Drug Treatment

The SCNs were exposed to ozone with different concentrations in a computer-controlled external exposure chamber, and the ozone concentration was monitored with an ozone analyzer (model 400 A, Advanced Pollution Instrumentation, San Diego, CA), implemented in the exposed chamber, and connected to a computer for monitoring and adjustment. After ozone treatment, subsequent experiments were performed after washing the samples with PBS for three times. The final concentration of ABT-888 was 10 um. The SCNs were treated with diluted ABT-888 2 h before ozone exposure.

Cell Viability Assessment

Cell viability was detected by using a Cell Counting Kit-8 (CCK-8) (Beyotime Biotechnology, China). The assessment was performed according to the instructions of the manufacturer. Briefly, the cell density was adjusted to 2×10^5 and the cell suspension was inoculated in a 96-well plate (100 μl/well). The plate was pre-incubated in a humidified incubator (at 37°C, 5% CO_2) and ABT-888 was added to the wells, then the plate was exposed to ozone after 2 h. Then, 1 h later, 10 μl of the CCK-8 solution was added to each well of the plate slowly. The plate was incubated for 4 h in the incubator. Finally, the absorbance of the sample was measured at 450 nm using a microplate reader. The cell survival rate was normalized to the untreated control group.

Measurement of ATP Level

ATP levels were detected by using an ATP assay kit (Beyotime Biotechnology, China). According to the instructions provided by the manufacturer, the cells were first lysed by lysis buffer, which was then centrifuged at 12,000 rpm for 5 min at 4°C, and the supernatant was then collected for further assessments. The protein concentration was determined using a BCA kit (Beyotime Biotechnology, China), and then 100 μl of ATP detection working solution was added to the 96-well plate, which was placed at room temperature for 5 min. Then, 100 μl sample or standard solution was added to each well. The RLU value was determined by a chemiluminometer, and the ATP concentration was determined to refer to the RLU standard curve determined by the standard in the kit. Finally, the ATP level was calculated as per the following Equation (1):

$$\text{ATP level} = \text{ATP concentration} / \text{total protein concentration} \quad (1)$$

LC-MS Analysis

LC-MS is the most widely used metabolomics analysis thanks to its adaptable components including the ionization technique, stationary, and mobile phases (46, 47). The SCNs were collected into a centrifuge tube and centrifuged at 3,500 rpm for 10 min. The cells were re-suspended by adding 0.5 ml ultrapure water. Then 0.5 ml of low-temperature methanol (−20°C pre-cooled for 6 h) was added and centrifuged at 3,500 rpm for 10 min at 4°C. The supernatant was absorbed and the sample was placed into a 1.5 ml EP tube to be stored at −80°C. Before the test, the sample was carefully thawed on ice. Then, 10 μL of internal standard (2.8 mg/mL, chlorophenylalanine) was added to the sample, which was ultrasonically extracted at 4°C for 30 min, silenced at −20°C for 1 h, centrifuged at 12,000 rpm for 15 min at 4°C, and transferred into the injection vial for testing after 200 μL of the supernatant was removed. Analysis platform was as follows: LC-MS (Thermo, Ultimate 3000LC, Q Exactive). Column: Hyper gold C18 (100 × 2.1 mm 1.9 μm). The chromatographic separation condition was as follows: Column temperature: 40°C; Flow rate: 0.3 mL/min; Mobile phase A: water + 5% acetonitrile + 0.1% formic acid; Mobile phase B: acetonitrile + 0.1% formic acid; Injection volume: 10 μL; Automatic injector temperature: 4°C. ESI+: Heater Temp 300°C; Sheath Gas Flow rate, 45 arb; Aux Gas Flow Rate, 15 arb; Sweep Gas Flow Rate, 1 arb; spray voltage, 3.0 KV; Capillary Temp, 350°C; S-Lens RF Level, 30%. ESI−: Heater Temp 300°C, Sheath Gas Flow rate, 45 arb; Aux Gas Flow Rate, 15 arb; Sweep Gas Flow Rate, 1 arb; spray voltage, 3.2 KV; Capillary Temp,350°C; S-Lens RF.

Western Blot Assessment

The SCNs were lysed with a cell lysate containing PMSF and phosphatase inhibitors. The cell lysates were collected and centrifuged at 14,000 rpm for 5 min. The supernatants were taken and the protein concentration was determined using a BCA kit (Beyotime Biotechnology, China). The protein sample was boiled for 10 min before loading, and then electrophoresed using 10% SDS gel, transferred to a PVDF membrane, blocked with 5% skim milk at room temperature for 1 h, and then the membranes were incubated overnight at 4°C with anti-PARP1(Abcam, ab151794, 1:1,000 dilution), anti-PAR(CST, #83732, 1:1,000 dilution), anti-γH2AX(CST, #2577, 1:1,000 dilution), anti-GAPDH(CST, #5174, 1:1,000 dilution), anti-p-AMPK (CST, #2535, 1:1,000 dilution), and anti-AMPK (CST, #2532, 1:1000 dilution) primary antibodies in dilution buffer. The cells were incubated with the horseradish peroxidase (HRP)-conjugated anti-rabbit IgG (Beyotime Biotechnology, A0216, 1:1,000 dilution). The membranes were developed using the enhanced chemiluminescence substrate LumiGLO (Millipore, Bedford, MA, USA).

NAD Assay

The NAD+ concentration was determined by using the NAD/NADH Assay Kit (Abcam, ab65348) according to the instructions of the manufacturer. This assessment was performed as follows. The cells were collected by cell scraping, washed with pre-cooled PBS three times, lysed with the extracted buffer solution and centrifuged with the centrifugal machine at 12,000 rpm for 5 min at 4°C. The supernatant was collected. First, the protein concentration was determined using a BCA kit (Beyotime Biotechnology, China), and then samples were heated at 60°C for 30 min so that NAD+ in the sample could decompose completely. Then, 50 μl of both samples were taken and mixed with 100 μl Reaction Mix and placed at room temperature for 5 min. Then, 10 μl of NADH Developer was added to each well and placed at room temperature for 2 h. The OD450 was measured with a multi-functional microplate reader.

Statistical Analysis

All data were expressed as Mean ± Standard Deviation (SD). The data were sorted and checked and then the data matrix was imported into SIMCA-P 13.0 (Umetrics AB, Umea, Sweden) software for multivariate statistical analysis. Statistical package for social sciences (SPSS) (Version 20, Windows, IBM Statistics, Chicago, IL, USA) was used for data analyses. Differences among the groups were compared by one-way analysis of variance (ANOVA), then followed by Tukey multiple comparison test or Bonferroni test for pairwise comparison. Differences were considered to be significant at $p < 0.05$. In all experiments, the assessments were repeated at least three times in an independent protocol and the average values were calculated and considered for further analysis. The LC-MS test data were extracted and preprocessed using the Compound Discoverer software (ThermoFisher Scientific, USA), which was finally compiled into two-dimensional data matrix format, including Retention time (RT), molecular weight (CompMW), observation volume, number of substances to be extracted, and peak intensity.

RESULTS

Morphological Observation and Identification of Cultured SCNs

Cells were observed by inverted phase-contrast microscopy 4 h after seeding in 6-well culture plates. It was observed that most of the cells were attached to the wall of the culture plate. The cells were round and transparent, with good refractive index and stereoscopic effect. A part of the nuclei can be clearly observed. Moreover, 24 h after the seeding, a large number of cells were found to have protrusions, the length of which accounted for about 1/2 of the cell. Forty eight hours after the seeding, the number of protruding cells increased, accounting for about 1/3 of the total number of cells, and the length of the protrusion increased. Ninety six hours after the seeding, more cell debris was observed under the microscope, which was caused by the addition of cytarabine inhibiting the glial cells on the third day of culture. On the 7th day of culture, the cells were aggregated slightly, and the cell protrusions grew obviously. The neurons and their protrusions were connected and formed a network. On the 7th day of culture, immunofluorescence staining with an anti-NF200 monoclonal antibody was performed. The results showed that more than 90% of cells show positive expression of NF-200 (**Figures 1A,B**).

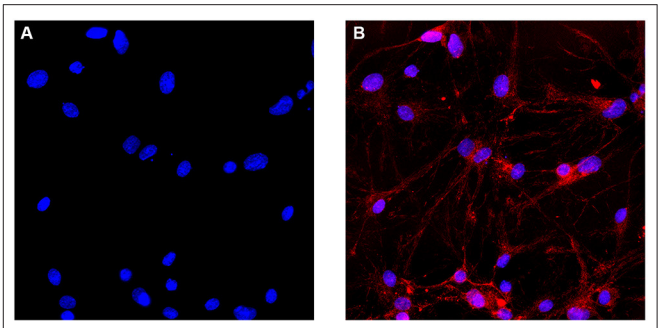

FIGURE 1 | Immunofluorescence identification of SCNs. **(A)** Cell nuclei are identified with DAPI. **(B)** SCNs are stained with the anti-NF200 monoclonal antibody. More than 90% of the cultured cells show positive expression of NF200 on the day 7 of *ex vivo* culture. The number of NF200-positive neurons are counted per area and expressed as percentage of total number of cells (Scale bar: 40 μm).

Ozone Exposure and SCNs Viability

In the majority of the ozone therapy for LBP, the common concentration of the ozone is 30 μg/ml, and some studies have tried to use a concentration of 40 μg/ml or even higher (4, 6, 7, 14, 48, 49). Therefore, when observing the influence of ozone on the viability of SCNs, 10, 20, 30, 40, 50, and 60 μg/ml ozone were applied. The results showed that the cell viability of the SCNs decreased with the increase in ozone concentration. The cell viability of 10, 20, 30 μg/ml ozone treatment groups were not significantly different from the control group, while the viability of SCNs in the 40, 50, 60 μg/ml ozone treatment groups were significantly lower than the control group. The viability of SCNs in the 40 μg/ml ozone treatment group was 71.91%, and the cell viability in 50 and 60 μg/ml ozone treatment groups was 49.97 and 30.43%, respectively (**Figure 2A**). Since 50 and 60 μg/ml concentrations are not recommended in the most clinical applications, 30 and 40 μg/ml concentrations were used for further subsequent experiments.

Ozone Exposure and ATP Level of SCNs

Previous studies have found that ozone exposure can reduce intracellular ATP level (50–52). Therefore, the influences of 30 and 40 μg/ml concentrations on the energy metabolism index (ATP level) of SCNs were studied first. Our results showed that the groups received 30 and 40 μg/ml doses of ozone, 15 min after the exposure the intracellular ATP level significantly decreased compared with the control group. After that, the ATP level of 30 μg/ml ozone exposure group recovered gradually, whereas the 40 μg/ml ozone exposure group showed further rapid decline in the ATP level. After 60 min, the 40 μg/ml ozone exposure decreased the ATP level of SCNs compared with the control and 30 μg/ml ozone exposure groups (**Figure 2B**).

Ozone Exposure and Metabolic Disorder of SCNs

To explore specific influences of ozone on the metabolism of SCNs, non-targeted LC-MS metabolomics technique was employed in this study. The SCNs of 40 μg/ml ozone exposure group and the control group were analyzed by non-targeted LC-MS technique to obtain ion chromatogram in Electrospray ionization (ESI) (±) mode, and the LC-MS data were extracted and pre-processed with Compound Discoverer software to obtain a data matrix consisting of information, such as retention time, accurate molecular weight and peak intensity, including a total of 2,268 (ESI+) and 2,210 (ESI–) features. Unsupervised PCA analysis results showed that PC1 in positive mode contained 46.0% cumulative variance, followed by PC2 13.9%, while PC1 in negative mode, contained 43.6% cumulative variance, followed by PC2 15.3% (**Figures 3A,B**). Abundance metabolites with significant differences between the 40 μg/ml

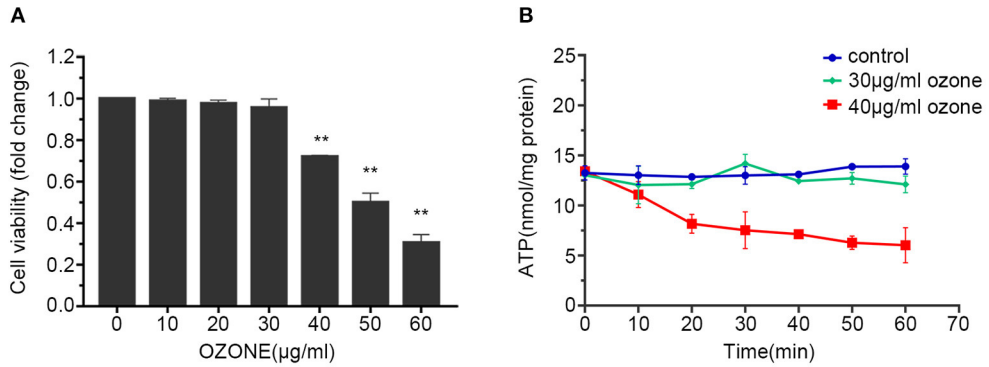

FIGURE 2 | Ozone decreases the viability and ATP levels of SCNs. **(A)** SCNs are exposed by ozone at 10, 20, 30, 40, 50, 60 μg/ml concentrations for 1 h, and cell viability was measured by CCK-8 assay. **(B)** The ATP levels of SCNs are determined by ATP assay kit after 30 and 40 μg/ml ozone exposure for 10–60 min. Data are presented as Mean ± SD of three independent experiments. $^{**}P < 0.01$, compared with the control.

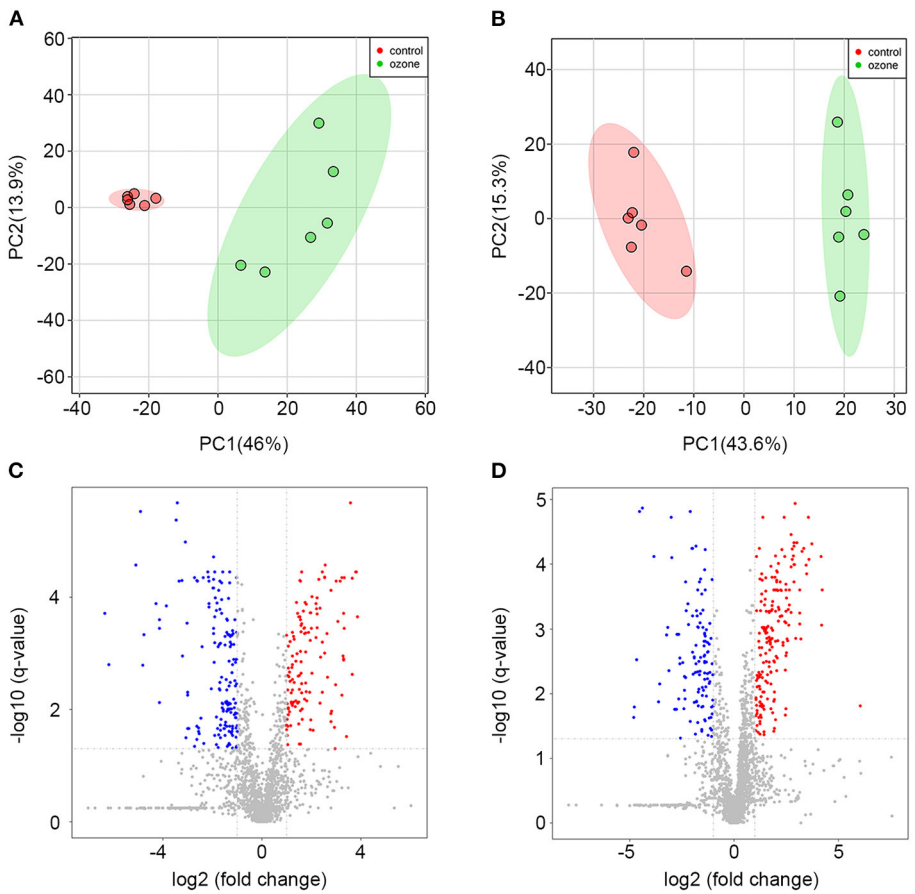

FIGURE 3 | Metabolomics profiling analyses for 40 μg/ml ozone group vs. control group. **(A)** Score plots of the principal component (PC) distinguishing 40 μg/ml ozone group ($n = 6$) from control group ($n = 6$) based on their metabolomics pattern with PC-1 (46.0%) and PC-2 (13.9%) in ESI+ mode. **(B)** Score plots of the PC distinguishing 40 μg/ml ozone group from control group based on their metabolomics pattern with PC-1 (43.6%) and PC-2 (15.3%) in ESI- mode. **(C,D)** Volcano plot demonstrates metabolite changes in ESI (±) mode. Fold change (FC) on the x-axis and FDR-adjusted *P*-values on the y-axis. Black vertical and horizontal lines show the filtering criteria (FC = 1.0 and FDR corrected *P*-value <0.05).

ozone exposure group and the control group were determined through the volcano plot (**Figures 3C,D**). Then, different substances between different groups were clustered and analyzed and the thermograms were used to reflect relative changes of 23 important metabolic molecules. The most affected pathways were related to fatty acid, tricarboxylic acid cycle, purine

metabolism, niacin and nicotinamide metabolism, amino acid, lipid metabolism, and riboflavin metabolism pathway (**Figure 4**). In these differentially expressed metabolites, it was observed that after exposure to 40 μg/ml ozone for 1 h, the levels of ADP and AMP in the SCNs increased (**Figure 4**). Moreover, our study showed that the level of ATP in the SCN cells decreased after ozone exposure. Generally, the ratio of ATP/ADP and ATP/AMP in cells could reflect the energy metabolism of cells. Decrease in the ratio indicated the abnormal energy metabolism of SCNs after ozone exposure (53). The intracellular synthesis pathway of NAD+ mainly includes *de novo* production and salvage pathways (54). Niacinamide is a precursor molecule of NAD+ salvage synthesis, whose level decreased after ozone exposure, which indicated that the intracellular NAD+ salvage synthesis pathway was activated (**Figure 4**). Moreover, levels of aconitine and UDP-glucose were elevated, indicating the utilization of cellular glucose and TCA circulatory disorders (**Figure 4**). Meanwhile, a series of abnormal changes of pathways including fatty acid metabolism, amino acid metabolism, and lipid metabolism reflected the abnormal metabolism of SCNs under 40 μg/ml ozone exposure (**Figure 4**). It is worth noting that the decrease of NAM levels and ATP/AMP, ATP/ADP ratios suggests that intracellular NAD+ is consumed excessively, resulting in metabolic disorder.

Ozone and DNA Damage, PAPR1 Excessive Activation, and NAD+ Depletion

Studies have reported that excessive activation of PARP1 by cellular DNA damage under oxidative stress can lead to NAD+ depletion and a decrease in ATP levels. Strong evidence confirms that ozone can cause DNA damage (51, 55–57). Therefore, γH2AX, PARP1, PAR, NAD+, and ATP levels are measured to evaluate the toxic effects of 30 and 40 μg/ml ozone on SCNs. The results demonstrated that the levels of DNA damage marker protein in the 30 μg/ml ozone group showed no significant difference with the control group and similarly there was no significant difference between PARP1 levels and PAR levels, compared with the control group (**Figures 5A–D**). However, the levels of γH2AX in the 40 μg/ml ozone group increased significantly compared with the control group, indicating the presence of a DNA damage in the SCNs (**Figures 5A,D**). There was no significant difference between PARP1 and the control group, and the PAR levels increased significantly compared with the control group, indicating that PARP1 was excessively activated (**Figures 5A–C**). As it was expected, the intracellular NAD+ and ATP levels in 40 μg/ml ozone group decreased significantly compared with the control group (**Figures 5E,F**). These results demonstrate that 40 μg/ml ozone could deplete the NAD+ in SCNs, accompanying PARP1 excessive activation and DNA damage.

PARP1 Inhibitors and SCNs Protection Against Ozone Exposure and NAD+ Depletion

Many studies have revealed that PARP1 inhibitors could protect cells by preventing NAD+ excessive consumption (22, 58). In this study, we observed the mechanism of ABT-888 alleviating the toxicity of ozone to SCNs. The results showed that after application of ABT-888, the PAR levels of SCNs under 30 and 40μg/ml ozone exposure conditions showed no significant difference with the control group (**Figures 5A–C**). Moreover, there was no significant decrease in NAD+ and ATP levels of 30 and 40 μg/ml ozone groups, compared with the control group (**Figures 5E,F**). The viability of SCNs was significantly higher than that of the non-inhibitor intervention groups after 40 and 50 μg/ml ozone exposure, indicating that PARP1 inhibitors could avoid NAD+ depletion by preventing PARP1 excessive activation and exert neuron-protective effects under the ozone exposure conditions (**Figure 6C**).

DISCUSSION

This study investigated the cytotoxic effects of ozone exposure on SCNs through determining the induction of the metabolic disorder and the possible involved signaling pathways in these neurons. The metabolic disorder in SCNs induced by ozone exposure was demonstrated by non-targeted LC-MS analysis. Moreover, our findings showed that NAD+ depletion caused by excessive PARP1 activation could serve as the main cause of abnormal cellular metabolism. We also found that PARP1 inhibitors could protect SCNs from ozone exposure through avoiding energy metabolism disorders caused by NAD+ depletion.

Currently, ozone therapy is widely used to treat lumbar disc herniation, soft tissue pain and arthritis in different countries including Germany, Italy, Spain, and China (3). In 2004, Muto et al. conducted a clinical retrospective study on 2,200 patients treated with intervertebral ozone injection. The results showed that the positive rate of treatment of patients with single-segment disc herniation, extensive disc degeneration, and the calcified intervertebral disc was 64, 40, and 25%, respectively (59). In 2012, Francisco et al. conducted a statistical analysis of four previous clinical random cohort studies and eight clinical retrospective observations on ozone treatment of LBP, among which evidence levels for the study of the intervertebral disc and paravertebral ozone injection were II-1 and II-3. The grading of recommendation was 1C for intradiscal ozone therapy and 1B for paravertebral ozone therapy (13). The findings showed that ozone is effective in treating LBP. However, due to the powerful oxidative property of ozone, irregular treatment may injure the nerves and the surrounding tissues. Some cases have reported that ozone treatment of lumbar disc herniation can cause injury to the ventral and dorsal root ganglia (20). However, there are still fewer studies on the effects of ozone on SCNs. Therefore, it is necessary to study thoroughly the influences of ozone exposure on SCNs.

Previous studies have found that ozone exposure can reduce intracellular ATP levels (51). Therefore, in this study, the influences of ozone on the ATP level of SCNs at concentrations of 30 and 40 μg/ml were measured first, and it was found that the intracellular ATP concentration recovered rapidly after a short decline at the concentration of 30 μg/ml.

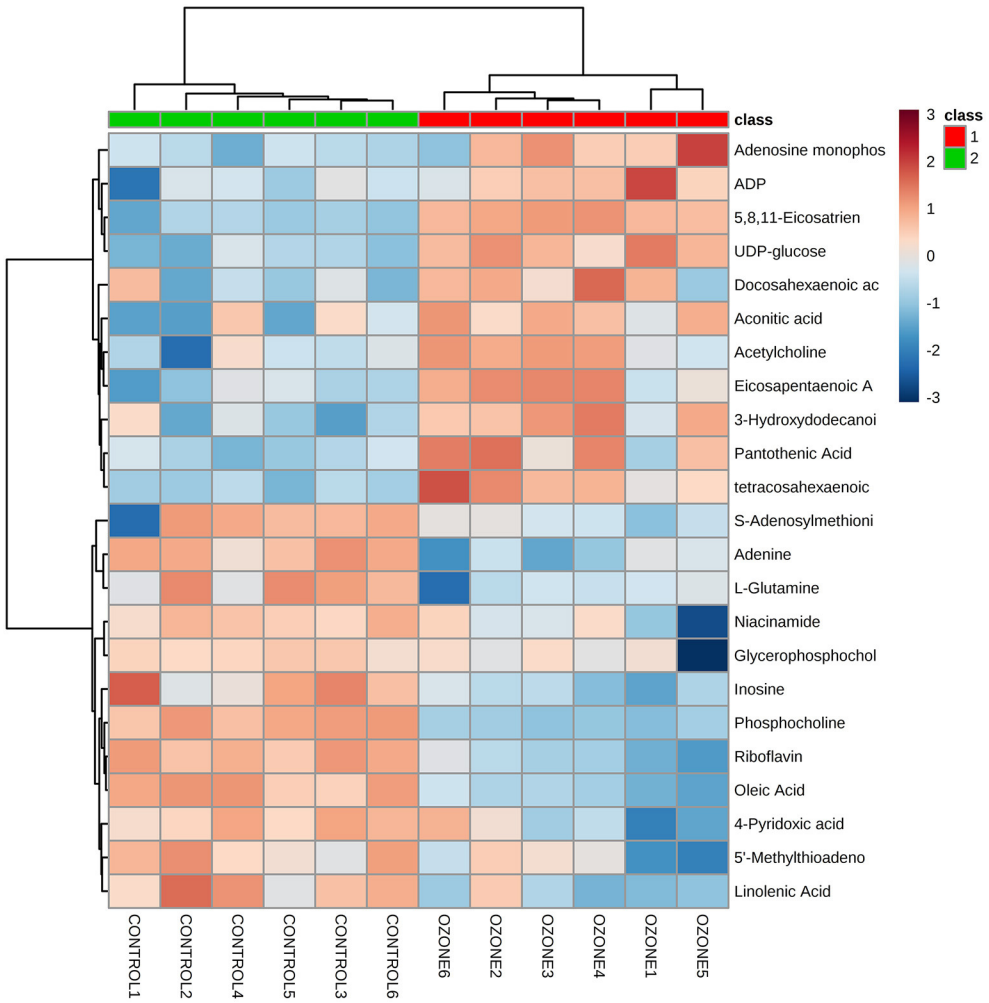

FIGURE 4 | Heat maps shows a comparison between 40 μg/ml ozone group and control group using normalized intensities of 23 significant metabolites. Two distinct clusters are identified. Orange and blue, respectively indicate increased and decreased expression compared with control groups.

Nevertheless, the intracellular ATP levels in 40 μg/ml ozone group declined continuously.

Subsequently, non-targeted LC-MS analysis was employed to analyze further specific changes of intracellular metabolism of SCNs after 40 μg/ml ozone exposure. The results showed that the expressions of metabolic molecules, such as ADP, AMP, aconitic acid, and UDP-glucose increased, while the molecular expressions of NAM, L-glutamine, and riboflavin were down-regulated. Furthermore, all differentially expressed metabolic molecules included mainly fatty acid, tricarboxylic acid cycle, purine metabolism, niacin and nicotinamide metabolism, amino acid, lipid metabolism, and riboflavin metabolism pathways. First, it can be clarified that the intracellular ATP/ADP and ATP/AMP ratios can reflect the energy metabolism conditions, because as the most basic energy metabolism-related molecule in cells, decrease of its ratio indicates the energy metabolism of SCNs after ozone exposure is disordered (60, 61). NAD+ is an essential coenzyme for redox reaction in cells which actively participates in many physiological reactions, such as TCA, fat beta-oxidation. Therefore, it is of great significance in the metabolic utilization of nutrients, such as sugar, fat and amino acids. As the most important hydrogen donor in the electron transport chain, NAD+ participates in the production of ATP (62). Furthermore, NAD+-related metabolites, such as coenzyme II [NADP (H)], NAM, and ADP ribose played important roles in human cell energy metabolism, oxidative stress regulation and signaling pathway transmission (37). The synthesis pathways of NAD+ in cells mainly include the salvage synthesis pathway using NAM and the *de novo* synthesis pathway using tryptophan. The results of metabolomics analysis demonstrated that NAM levels reduced significantly after ozone exposure, indicating the over-consumption of NAM by salvage pathways of NAD+. Moreover, elevated levels of aconitine and UDP-glucose suggested disorders of cellular TCA cycle and glucose utilization (63). Our study has validated further that ozone could cause a series of differential expressions of metabolic

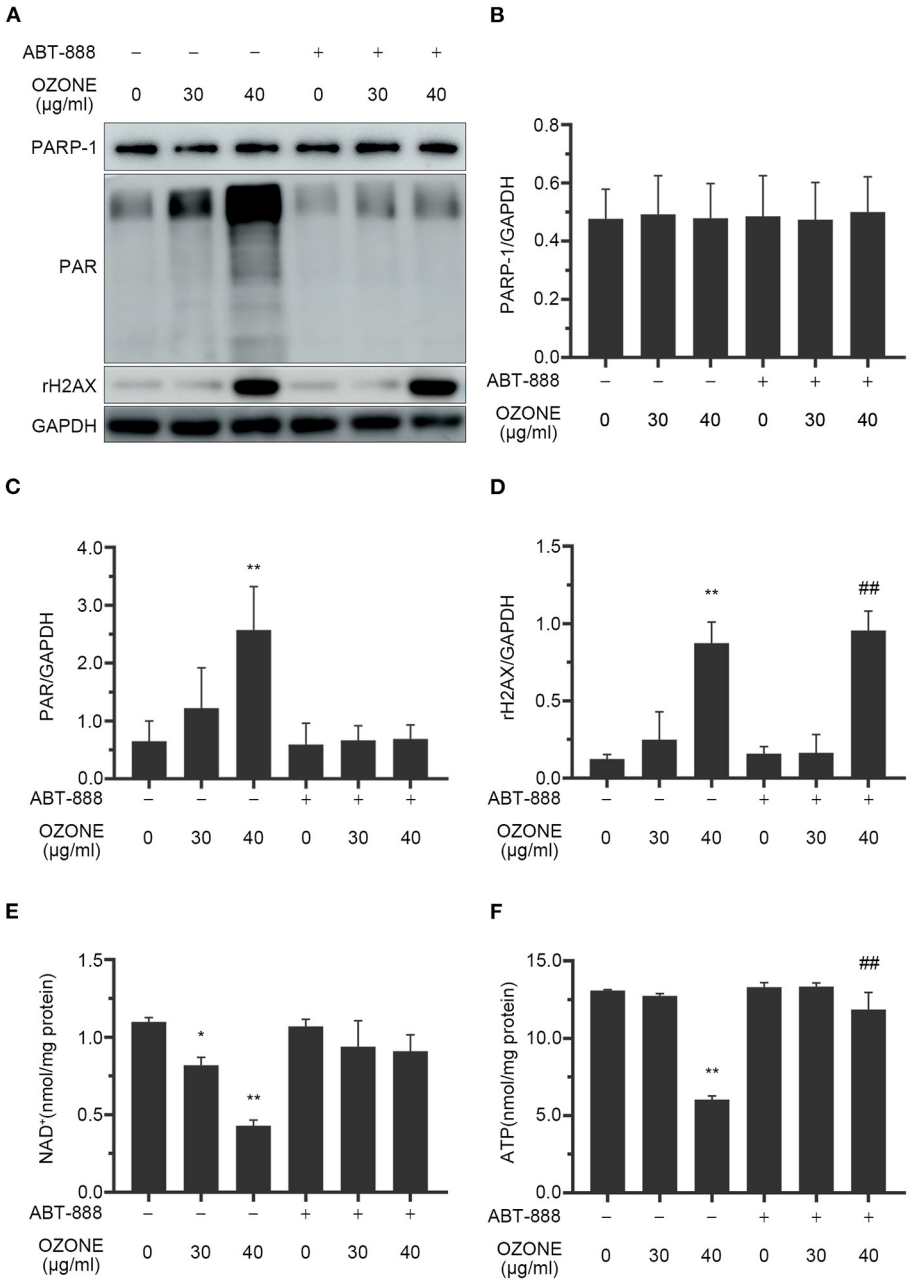

FIGURE 5 | Ozone causes DNA damage, PAPR-1 excessive activation, NAD+ depletion and decline of ATP levels of SCNs. ABT-888 inhibits the NAD+ and ATP declines by inhibiting PARP1 excessive activation. **(A–D)** SCNs are treated with ozone (30 and 40 μg/ml for 60 min) in the absence or presence of ABT-888. The levels of PARP1, PAR, and γH2AX are measured and quantified by western blot. **(E,F)** Ozone exposure decreases the levels of NAD+ and ATP, which are prevented by ABT-888 pretreatment. Data are expressed as Mean ± SD of three independent experiments. $^{*}P < 0.05$, $^{**}P < 0.01$, compared with the control without ABT-888 pretreatment; $^{\#\#}P < 0.01$, compared with control with 40 μg/ml ozone without ABT-888.

molecules in SCNs, and suggested that the metabolic disorders were associated with excessive consumption of NAD+.

Studies have found that ozone exposure can cause DNA damage in cells and a significant decrease in ATP levels and lead to a reduced Sirtuin3 expression (51). Cheng et al. found that single-cell gel electrophoresis and elevated levels of 8-oxoguanine suggested that ozone exposure induced an increase in DNA single-strand breaks in A549 cells (55). NAD+ is an energy-sensitive metabolic molecule, and the only substrate for the coenzyme I depleting enzymes (PARP, CD38, CD157, SIRT1-SIRT7) and its excessive depletion leads to impaired intracellular energy metabolism (64). However, under oxidative stress, DNA single-strand break in the cells activates PARP1, which leads to depletion of a large amount of NAD+ to repair the damaged

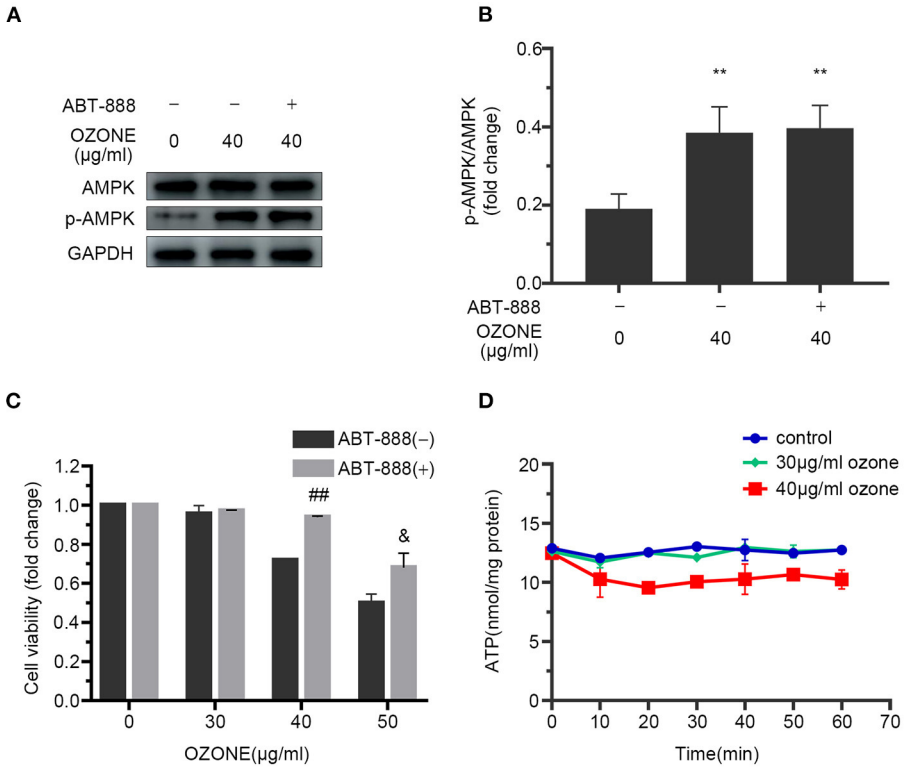

FIGURE 6 | ABT-888 prevents the declines in viability and ATP level of SCNs after 40 μg/ml ozone exposure. **(A,B)** 40 μg/ml ozone exposure activates AMPK of SCNs in the absence or presence of ABT-888. **(C)** ABT-888 improves the viability of SCNs with 40 and 50 μg/ml ozone exposure. **(D)** ATP level is measured after 10–60 min ozone exposure with 30 and 40 μg/ml doses. The data are presented as Mean ± SD of three independent experiments. $^{**}P < 0.01$, compared with the control; $^{\#\#}P < 0.01$, compared with 40 μg/ml ozone groups without ABT-888 pretreatment; $^{\&}P < 0.05$, compared with 50 μg/ml ozone groups without AB.

DNA. Several studies have shown that the NAD+ depletion caused by excessive activation of PARP1 is an important cause of disorder of cell energy metabolism and cell death (34). In this study, γH2AX, PARP1, PAR, NAD+, and ATP levels are measured to evaluate the DNA damage of cells at 30 and 40 μg/ml ozone concentrations and the influences of the accompanying PARP1 activation on cellular NAD+ and ATP levels. DNA damage marker protein γH2AX increased after ozone exposure, suggesting that ozone exposure could induce DNA damage in SCNs, which is consistent with the findings of the previous similar studies. Further studies have revealed that 40 μg/ml ozone exposure can cause excessive activation of PARP1 in SCNs and cause a decrease of intracellular NAD+ and ATP levels, thereby leading to cell death.

The signaling pathways of DNA damage are vital for the maintenance of genome integrity and dictating DNA repair pathway choice or cell fate decision. PARP1 serves as a rapid sensor for a DNA damage that plays vital roles in driving the early chromatin organization and DNA repair pathway choice at the damage sites. After a DNA damage, PARP1 is rapidly triggered in a damage dose-dependent manner. However, little is known on the influences of PARP1 activation on the damaged cells at the cellular level. Murata et al. used a new combined phasor approach to investigate the effects of PARP1 activation in response to DNA damage on the cellular level (65). They employed fluorescence-based biosensors and fluorescence lifetime imaging microscopy combined with laser micro-irradiation to assess metabolic changes at high spatiotemporal resolution in a living cell (65). They observed that nuclear DNA damage activated PARP-dependent NAD+ depletion, which in turn triggered a rapid cell-wide accumulation of the bound NADH fraction. Their findings showed that PARP activation induces a change in the cellular metabolism that leads to activation of a pro-survival response (65). The NAD+ depletion and NADH accumulation on the cell-wide dimension was accompanied by a metabolic balance shift to oxidative phosphorylation (oxphos) over glycolysis. This study along with the other similar findings discussed that the oxphos inhibition leads to parthanatos due to rapid PARP-dependent ATP deprivation demonstrating that oxphos is a vital factor for recovery and survival of the damaged cell (34, 35, 65).

Several studies have confirmed that PARP1 inhibitors could protect cells from excitotoxicity and DNA damages (57, 65). Zhang et al. reported that PAPR1 inhibitors can counteract the NAD+ depletion caused by atrial fibrillation and alleviate oxidative stress and DNA damage in cardiomyocytes (57). Other studies have demonstrated that PARP1 inhibitors can

improve the survival rate of HepG2 cells under oxidative stress, and metabolomics analysis technology has confirmed that its protective effect is related to NAD+ depletion caused by excessive activation of PARP1 (35). However, so far there is no report on the use of PARP1 inhibitors to protect SCNs under ozone exposure conditions. In this study, ABT-888 was employed to inhibit PARP1 activation 2 h before ozone exposure and the results showed that PARP1 activation was inhibited under ozone exposure, while intracellular NAD+ and ATP levels were elevated significantly compared with the control group received no ABT-888 inhibition (**Figures 5E,F**). Under the exposure conditions of 40 and 50 μg/ml ozone, PARP1 inhibitor increased the viability of SCNs.

Mammalian target of rapamycin (mTOR) signaling pathway incorporates both intracellular and extracellular signals into an integrated central regulator for cell metabolism, growth, proliferation and survival. Some studies have demonstrated that ozone in the dose range used for therapeutic applications exerts different therapeutic effects through AMPK phosphorylation and AMPK/mTOR signaling pathways (11, 66). Evidence shows that reduced autophagy in chondrocytes is the main etiology for articular cartilage degradation and thus development of OA (67–69). Zhao et al. investigated the role of autophagy induction in the therapeutic effects of ozone on osteoarthritis (OA) chondrocytes (11). They reported that ozone improved the decreased level of autophagy in chondrocytes exposed with cytokine interleukin-1β (IL-1β) through activation of the AMPK/mTOR signaling pathway. Moreover, ozone treatment decreased inflammation and restored metabolic balance in the chondrocytes.

Ozone exposure significantly decreased mTOR and P62, whereas increased LC3 II, Beclin-1, and ULK1 proteins in the OA prone chondrocytes. Furthermore, ozone significantly upregulated the levels of p-AMPK, and the improved autophagy in chondrocytes stimulated with IL-1β was suppressed by com C. In addition, ozone treatment significantly suppressed inflammation and regulated metabolism in IL-1β-stimulated chondrocytes. AMPK activation plays a vital role in facilitating autophagy after ozone exposure in chondrocytes stimulated with IL-1β.

However, the specific mechanisms and signaling pathways involved in the activation of AMPK by ozone are not yet fully understood. AMPK serves crucial role in regulating cell energy metabolism and the main factors responsible for AMPK activation are ATP/AMP and ATP/ADP ratios as well as intracellular AMP levels AMPK (70). Our study showed that 30 and 40 μg/ml doses of ozone decreased the ATP levels within 20 min after the exposure (**Figure 2B**). Moreover, 40 μg/mL ozone significantly increased the levels of ADP and AMP in the SCNs. Previous *in vitro* dose-response studies have shown that ozone in low concentrations (20–40 g/ml of oxygen-ozone) is not toxic to astroglial cells, whereas in higher concentrations (60 μg/mL) significantly decreases cell viability (71). Our findings showed that ozone exposure increased the levels of AMPK phosphorylation in SCNs (**Figures 6A,B**). However, intracellular ATP levels decreased gradually under 40 μg/ml ozone exposure. Our results in support of previous studies, showed that excessive activation of PARP1 could result in DNA damage and NAD+ depletion, and subsequently reduce cell viability. The use of PARP1 inhibitor improved the viability of SCNs under ozone exposures with dosages of 40 and 50 μg/ml (**Figure 6C**). Meanwhile, after the application of PARP1 inhibitor, intracellular ATP levels in SCNs still decreased 15 min after ozone exposure. After that, unlike the ABT-888(−) groups, intracellular ATP levels of ABT-888(+) groups recovered gradually and maintained a relatively stable level (**Figure 6D**). The levels of AMPK phosphorylation showed no significant difference with the ABT-888(−) groups, which might be because the intracellular ATP level was still lower than that of the normal group after the application of PARP1 inhibitor (**Figures 6A,B,D**). Furthermore, previous studies have shown that ROS could activate AMPK directly by oxidizing its cysteine residues (72, 73). Moreover, liver kinase B1 (LKB1) was the upstream kinase of AMPK, which can also activate AMPK by phosphorylating the 172th threonine on the activation loop of AMPK α subunit (74). Nevertheless, the mechanisms by which ozone activates AMPK in SCNs are still unclear and need further studies.

PARP plays important roles in choosing proper DNA repair pathway and improving its efficiency and cell survival. Moreover, excessive PARP activation regulates metabolism and senescence and also influences DNA repair and both apoptosis and necrosis cell death (21). NAD+ depletion by damage-induced PARP activation could lead to inhibition of cellular energy metabolism, because both NAD+ and NADH are actively involved in metabolic process of cellular energy production (27). Moreover, PARP1 activation inhibits hexokinase (HK), which results in ATP deprivation and subsequent cell death parthanatos (28, 31, 75). Parthanatos cell death needs PAR-dependent nuclear translocation of AIF from mitochondria, however, parthanatos cell death has also been reported independent of AIF. In addition, PARP activation induces intracellular acidification that increases the risk of necrosis cell death (76). Therefore, the downstream effects of PARP activation are complex so that the casual association and exact relationships between the levels of DNA damage and the impact of PARP signaling on energy metabolism and/or triggering cell death is not well-understood.

CONCLUSION

This study investigated the cytotoxic effects of ozone exposure at different doses on cell viability, ATP levels and the NAD+ concentration in SCNs in animal model. The findings showed that 40 μg/ml ozone exposure could cause DNA damage and metabolic disorders of SCNs. PARP1 inhibitors could prevent NAD+ depletion caused by excessive activation of PARP1 during ozone exposure and thus alleviate the toxicity of ozone to SCNs without inhibiting the activation of AMPK.

DATA AVAILABILITY STATEMENT

The raw data supporting the conclusions of this article will be made available by the authors, without undue reservation.

ETHICS STATEMENT

The animals used in this experiment are selected strictly according to relevant regulations of the National Institutes of Health and approved by the Animal Protection and Use Committee of School of Medicine of Shandong University.

AUTHOR CONTRIBUTIONS

SM and XZ: conceptualization. SM: methodology, software, formal analysis, resources, writing—original draft preparation, and visualization. ZF, TS, and XL: validation. YL: investigation. CZ and PS: data curation. ZF: writing—review and editing, supervision, project administration, and funding acquisition. All authors contributed to the article and approved the submitted version.

FUNDING

This work was supported by grants from the National Natural Science Foundation of China (No. 81271346 and No. 81771199).

ACKNOWLEDGMENTS

The authors would like to thank Shandong provincial hospital affiliated to Shandong University and Experimental Animal Center of Shandong University.

REFERENCES

1. Mauro R Di, Cantarella G, Bernardini R, Rosa M Di, Barbagallo I, Distefano A, et al. The biochemical and pharmacological properties of ozone: the smell of protection in acute and chronic diseases. *Int J Mol Sci.* (2019) 20:634. doi: 10.3390/ijms20030634
2. Bocci V, Di Paolo N. Oxygen-ozone therapy in medicine: an update. *Blood Purif.* (2009) 28:373–6. doi: 10.1159/000236365
3. Bocci V, Borrelli E, Zanardi I, Travagli V. The usefulness of ozone treatment in spinal pain. *Drug Des Dev Ther.* (2015) 9:2677–85. doi: 10.2147/DDDT.S74518
4. Braidy N, Izadi M, Sureda A, Jonaidi-Jafari N, Banki A, Nabavi SF, et al. Therapeutic relevance of ozone therapy in degenerative diseases: focus on diabetes and spinal pain. *J Cell Physiol.* (2018) 233:2705–14. doi: 10.1002/jcp.26044
5. Seyam O, Smith NL, Reid I, Gandhi J, Jiang W, Khan SA. Clinical utility of ozone therapy for musculoskeletal disorders. *Med Gas Res.* (2018) 8:103–10. doi: 10.4103/2045-9912.241075
6. Zhang Y, Ma Y, Jiang J, Ding T, Wang J. Treatment of the lumbar disc herniation with intradiscal and intraforaminal injection of oxygen-ozone. *J Back Musculoskelet Rehabil.* (2013) 26:317–22. doi: 10.3233/BMR-130386
7. Andreula CF, Simonetti L, De Santis F, Agati R, Ricci R, Leonardi M. Minimally invasive oxygen-ozone therapy for lumbar disk herniation. *Am J Neuroradiol.* (2003) 24:996–1000.
8. Kiliç M, Erçalik T. The effect of lumbar spinal surgery history on intradiscal O_2-O_3 treatment results in patients with lumbar disk herniation. *Sisli Etfal Hastan Tip Bul.* (2019) 53:148–53. doi: 10.14744/SEMB.2018.50480
9. Elawamy A, Kamel EZ, Hassanien M, Wahba OM, Amin SE. Implication of two different doses of intradiscal ozone-oxygen injection upon the pain alleviation in patients with low back pain: a randomized, single-blind study. *Pain Phys.* (2018) 21:E25–31. doi: 10.36076/ppj.2018.1.E25
10. Smith N, Wilson A, Gandhi J, Vatsia S, Khan S. Ozone therapy: An overview of pharmacodynamics, current research, and clinical utility. *Med Gas Res.* (2017) 7:212–9. doi: 10.4103/2045-9912.215752
11. Zhao X, Li Y, Lin X, Wang J, Zhao X, Xie J, et al. Ozone induces autophagy in rat chondrocytes stimulated with IL-1β through the AMPK/mTOR signaling pathway. *J Pain Res.* (2018) 11:3003–17. doi: 10.2147/JPR.S183594
12. Rivas-Arancibia S, Zimbrón LFH, Rodríguez-Martínez E, Maldonado PD, Borgonio Pérez G, Sepúlveda-Parada M. Oxidative stress-dependent changes in immune responses and cell death in the substantia nigra after ozone exposure in rat. *Front Aging Neurosci.* (2015) 7:65. doi: 10.3389/fnagi.2015.00065
13. De Oliveira Magalhaes FN, Dotta L, Sasse A, Teixeira MJ, Fonoff ET. Ozone therapy as a treatment for low back pain secondary to herniated disc: a systematic review and meta-analysis of randomized controlled trials. *Int J Ozone Ther.* (2012) 11:15–30.
14. Steppan J, Meaders T, Muto M, Murphy KJ. A metaanalysis of the effectiveness and safety of ozone treatments for herniated lumbar discs. *J Vasc Interv Radiol.* (2010) 21:534–48. doi: 10.1016/j.jvir.2009.12.393
15. Oberdörster G, Finkelstein JN, Johnston C, Gelein R, Cox C, Baggs R, et al. Acute pulmonary effects of ultrafine particles in rats and mice. *Res Rep Health Eff Inst.* (2000) 5–74; disc. 75–86.
16. Wu AH, Wu J, Tseng C, Yang J, Shariff-Marco S, Fruin S, et al. Association between outdoor air pollution and risk of malignant and benign brain tumors: the multiethnic cohort study. *JNCI Cancer Spectr.* (2020) 4:pkz107. doi: 10.1093/jncics/pkz107
17. Henriquez A, House J, Miller DB, Snow SJ, Fisher A, Ren H, et al. Adrenal-derived stress hormones modulate ozone-induced lung injury and inflammation. *Toxicol Appl Pharmacol.* (2017) 329:249–58. doi: 10.1016/j.taap.2017.06.009
18. Miller DB, Karoly ED, Jones JC, Ward WO, Vallanat BD, Andrews DL, et al. Inhaled ozone (O_3)-induces changes in serum metabolomic and liver transcriptomic profiles in rats. *Toxicol Appl Pharmacol.* (2015) 286:65–79. doi: 10.1016/j.taap.2015.03.025
19. Tham A, Lullo D, Dalton S, Zeng S, van Koeverden I, Arjomandi M. Modeling vascular inflammation and atherogenicity after inhalation of ambient levels of ozone: exploratory lessons from transcriptomics. *Inhal Toxicol.* (2017) 29:96–105. doi: 10.1080/08958378.2017.1310333
20. Ginanneschi F, Cervelli C, Milani P, Rossi A. Ventral and dorsal root injury after oxygen-ozone therapy for lumbar disk herniation. *Surg Neurol.* (2006) 66:619–20. doi: 10.1016/j.surneu.2006.01.025
21. Gupte R, Liu Z, Kraus WL. PARPs and ADP-ribosylation: recent advances linking molecular functions to biological outcomes. *Genes Dev.* (2017) 31:101–26. doi: 10.1101/gad.291518.116
22. Graziani G, Szabó C. Clinical perspectives of PARP inhibitors. *Pharmacol Res.* (2005) 52:109–18. doi: 10.1016/j.phrs.2005.02.013
23. Andrisic L, Dudzik D, Barbas C, Milkovic L, Grune T, Zarkovic N. Short overview on metabolomics approach to study pathophysiology of oxidative stress in cancer. *Redox Biol.* (2018) 14:47–58. doi: 10.1016/j.redox.2017.08.009
24. González-Domínguez R, García-Barrera T, Gómez-Ariza JL. Metabolite profiling for the identification of altered metabolic pathways in Alzheimer's disease. *J Pharm Biomed Anal.* (2015) 107:75–81. doi: 10.1016/j.jpba.2014.10.010
25. Stringari C, Edwards RA, Pate KT, Waterman ML, Donovan PJ, Gratton E. Metabolic trajectory of cellular differentiation in small intestine by phasor fluorescence lifetime microscopy of NADH. *Sci Rep.* (2012) 2:568. doi: 10.1038/srep00568
26. Poljsak B, Kovac V, Dahmane R, Levec T, Starc A. Cancer etiology: a metabolic disease originating from life's major evolutionary transition? *Oxidat Med Cell Longev.* (2019) 2019:7831952. doi: 10.1155/2019/7831952
27. Heikal AA. Intracellular coenzymes as natural biomarkers for metabolic activities and mitochondrial anomalies. *Biomark Med.* (2010) 4:241–63. doi: 10.2217/bmm.10.1
28. Andrabi SA, Umanah GKE, Chang C, Stevens DA, Karuppagounder SS, Gagné JP, et al. Poly(ADP-ribose) polymerase-dependent energy depletion occurs through inhibition of glycolysis. *Proc Natl Acad Sci USA.* (2014) 111:10209–14. doi: 10.1073/pnas.1405158111

29. Fouquerel E, Goellner EM, Yu Z, Gagné JP, de Moura MB, Feinstein T, et al. ARTD1/PARP1 negatively regulates glycolysis by inhibiting hexokinase 1 independent of NAD+ depletion. *Cell Rep.* (2014) 8:1819–31. doi: 10.1016/j.celrep.2014.08.036
30. Feng FY, de Bono JS, Rubin MA, Knudsen KE. Chromatin to clinic: the molecular rationale for PARP1 inhibitor function. *Mol Cell.* (2015) 58:925–34. doi: 10.1016/j.molcel.2015.04.016
31. Andrabi SA, Dawson TM, Dawson VL. Mitochondrial and nuclear cross talk in cell death: parthanatos. *Ann N Y Acad Sci.* (2008) 1147:233–41. doi: 10.1196/annals.1427.014
32. Fouquerel E, Sobol RW. ARTD1 (PARP1) activation and NAD+ in DNA repair and cell death. *DNA Repair (Amst).* (2014) 23:27–32. doi: 10.1016/j.dnarep.2014.09.004
33. Alano CC, Ying W, Swanson RA. Poly(ADP-ribose) polymerase-1-mediated cell death in astrocytes requires NAD+ depletion and mitochondrial permeability transition. *J Biol Chem.* (2004) 279:18895–902. doi: 10.1074/jbc.M313329200
34. Islam BU, Habib S, Ali SA, Moinuddin, Ali A. Role of peroxynitrite-induced activation of poly(ADP-Ribose) polymerase (PARP) in circulatory shock and related pathological conditions. *Cardiovasc Toxicol.* (2017) 17:373–83. doi: 10.1007/s12012-016-9394-7
35. Cheng M-L, Lin J-F, Huang C-Y, Li G-J, Shih L-M, Chiu DT-Y, et al. Sedoheptulose-1,7-bisphospate accumulation and metabolic anomalies in hepatoma cells exposed to oxidative stress. *Oxid Med Cell Longev.* (2019) 2019:5913635. doi: 10.1155/2019/5913635
36. Alano CC, Garnier P, Ying W, Higashi Y, Kauppinen TM, Swanson RA. NAD+ depletion is necessary and sufficient for poly(ADP-ribose) polymerase-1-mediated neuronal death. *J Neurosci.* (2010) 30:2967–78. doi: 10.1523/JNEUROSCI.5552-09.2010
37. Sasaki Y. Metabolic aspects of neuronal degeneration: from a NAD+ point of view. *Neurosci Res.* (2019) 139:9–20. doi: 10.1016/j.neures.2018.07.001
38. Tafani M, Karpinich NO, Hurster KA, Pastorino JG, Schneider T, Russo MA, et al. Cytochrome c release upon Fas receptor activation depends on translocation of full-length Bid and the induction of the mitochondrial permeability transition. *J Biol Chem.* (2002) 277:10073–82. doi: 10.1074/jbc.M111350200
39. Tang KS, Suh SW, Alano CC, Shao Z, Hunt WT, Swanson RA, et al. Astrocytic poly(ADP-ribose) polymerase-1 activation leads to bioenergetic depletion and inhibition of glutamate uptake capacity. *Glia.* (2010) 58:446–57. doi: 10.1002/glia.20936
40. Ying W, Alano CC, Garnier P, Swanson RA. NAD+ as a metabolic link between DNA damage and cell death. *J Neurosci Res.* (2005) 79:216–23. doi: 10.1002/jnr.20289
41. Heller B, Wang Z, Wagner E, Radons J, Burkle A, Fehsel K, et al. Inactivation of the poly(ADP-ribose) polymerase gene affects oxygen radical and nitric oxide toxicity in islet cells. *J Biol Chem.* (1995) 270:11176–80. doi: 10.1074/jbc.270.19.11176
42. Szabó C, Virág L, Cuzzocrea S, Scott GS, Hake P, O'Connor MP, et al. Protection against peroxynitrite-induced fibroblast injury and arthritis development by inhibition of poly(ADP-ribose) synthase. *Proc Natl Acad Sci USA.* (1998) 95:3867–72. doi: 10.1073/pnas.95.7.3867
43. Eliasson MJL, Sampei K, Mandir AS, Hurn PD, Traystman RJ, Bao J, et al. Poly(ADP-ribose) polymerase gene disruption renders mice resistant to cerebral ischemia. *Nat Med.* (1997) 3:1089–95. doi: 10.1038/nm1097-1089
44. Burkart V, Wang ZQ, Radons J, Heller B, Herceg Z, Stingl L, et al. Mice lacking the poly(ADP-ribose) polymerase gene are resistant to pancreatic beta-cell destruction and diabetes development induced by streptozocin. *Nat Med.* (1999) 5:314–9. doi: 10.1038/6535
45. Eldeiry M, Yamanaka K, Reece TB, Aftab M. Spinal cord neurons isolation and culture from neonatal mice. *J Vis Exp.* (2017) 2017:55856. doi: 10.3791/55856
46. Zang X, Monge ME, Fernández FM. Mass spectrometry-based non-targeted metabolic profiling for disease detection: recent developments. *Trends Anal Chem.* (2019) 118:158–69. doi: 10.1016/j.trac.2019.05.030
47. Zheng SJ, Liu SJ, Zhu QF, Guo N, Wang YL, Yuan BF, et al. Establishment of liquid chromatography retention index based on chemical labeling for metabolomic analysis. *Anal Chem.* (2018) 90:8412–20. doi: 10.1021/acs.analchem.8b00901
48. Bonetti M, Fontana A, Cotticelli B, Volta GD, Guindani M, Leonardi M. Intraforaminal O_2-O_3 versus periradicular steroidal infiltrations in lower back pain: randomized controlled study. *Riv Ital di Ossigeno-Ozonoterapia.* (2006) 5:55.
49. Splendiani A, Perri M, Conchiglia A, Fasano F, Di Egidio G, Masciocchi C, et al. MR assessment of lumbar disk herniation treated with oxygen-ozone diskolysis: the role of DWI and related ADC versus intervertebral disk volumetric analysis for detecting treatment response. *Neuroradiol J.* (2013) 26:347–56. doi: 10.1177/197140091302600316
50. Puckette M, Iyer NJ, Tang Y, Dai X, Zhao P, Mahalingam R. Differential mRNA translation in medicago truncatula accessions with contrasting responses to ozone-induced oxidative stress. *Mol Plant.* (2012) 5:187–204. doi: 10.1093/mp/ssr069
51. McCarthy JT, Pelle E, Dong K, Brahmbhatt K, Yarosh D, Pernodet N. Effects of ozone in normal human epidermal keratinocytes. *Exp Dermatol.* (2013) 22:360–1. doi: 10.1111/exd.12125
52. Zhang YQ, Wu QP, Zhang JM, Yang XH. Effects of ozone on membrane permeability and ultrastructure in *Pseudomonas aeruginosa*. *J Appl Microbiol.* (2011) 111:1006–15. doi: 10.1111/j.1365-2672.2011.05113.x
53. Ke R, Xu Q, Li C, Luo L, Huang D. Mechanisms of AMPK in the maintenance of ATP balance during energy metabolism. *Cell Biol Int.* (2018) 42:384–92. doi: 10.1002/cbin.10915
54. Rajman L, Chwalek K, Sinclair DA. Therapeutic potential of NAD-boosting molecules: the *in vivo* evidence. *Cell Metab.* (2018) 27:529–47. doi: 10.1016/j.cmet.2018.02.011
55. Cheng T-J, Kao H-P, Chan C-C, Chang WP. Effects of ozone on DNA single-strand breaks and 8-oxoguanine formation in A549 cells. *Environ Res.* (2003) 93:279–84. doi: 10.1016/S0013-9351(03)00041-0
56. Rodríguez-Vargas JM, Ruiz-Magãa MJ, Ruiz-Ruiz C, Majuelos-Melguizo J, Peralta-Leal A, Rodríguez MI, et al. ROS-induced DNA damage and PARP-1 are required for optimal induction of starvation-induced autophagy. *Cell Res.* (2012) 22:1181–98. doi: 10.1038/cr.2012.70
57. Zhang D, Hu X, Li J, Liu J, Baks-te Bulte L, Wiersma M, et al. DNA damage-induced PARP1 activation confers cardiomyocyte dysfunction through NAD+ depletion in experimental atrial fibrillation. *Nat Commun.* (2019) 10:1307. doi: 10.1038/s41467-019-09014-2
58. Hyo Chol Ha, Snyder SH. Poly(ADP-ribose) polymerase is a mediator of necrotic cell death by ATP depletion. *Proc Natl Acad Sci USA.* (1999) 96:13978–82. doi: 10.1073/pnas.96.24.13978
59. Muto M, Andreula C, Leonardi M. Treatment of herniated lumbar disc by intradiscal and intraforaminal oxygen-ozone (O_2-O_3) injection. *J Neuroradiol.* (2004) 31:183–9. doi: 10.1016/S0150-9861(04)96989-1
60. Lee SJ, Kwon CH, Kim YK. Alterations in membrane transport function and cell viability induced by ATP depletion in primary cultured rabbit renal proximal tubular cells. *Korean J Physiol Pharmacol.* (2009) 13:15–22. doi: 10.4196/kjpp.2009.13.1.15
61. Wang YM, Pu P, Le WD. ATP depletion is the major cause of MPP+ induced dopamine neuronal death and worm lethality in α-synuclein transgenic *C. elegans*. *Neurosci Bull.* (2007) 23:329–35. doi: 10.1007/s12264-007-0049-3
62. Porter RK, Brand MD. Mitochondrial proton conductance and H+/O ratio are independent of electron transport rate in isolated hepatocytes. *Biochem J.* (1995) 310:379–82. doi: 10.1042/bj3100379
63. Chen J, Yu Y, Gao J, Yang S. UDP-glucose dehydrogenase: the first-step oxidation is an NAD+ -dependent bimolecular nucleophilic substitution reaction (Sn_2). *Int J Biol Sci.* (2019) 15:341–50. doi: 10.7150/ijbs.28904
64. Komirishetty P, Areti A, Sistla R, Kumar A. Morin mitigates chronic constriction injury (CCI)-induced peripheral neuropathy by inhibiting oxidative stress induced PARP over-activation and neuroinflammation. *Neurochem Res.* (2016) 41:2029–42. doi: 10.1007/s11064-016-1914-0
65. Murata MM, Kong X, Moncada E, Chen Y, Imamura H, Wang P, et al. NAD+ consumption by PARP1 in response to DNA damage triggers metabolic shift critical for damaged cell survival. *Mol Biol Cell.* (2019) 30:2584–97. doi: 10.1091/mbc.E18-10-0650
66. Lu L, Pan C, Chen L, Hu L, Wang C, Han Y, et al. AMPK activation by peri-sciatic nerve administration of ozone attenuates CCI-induced neuropathic pain in rats. *J Mol Cell Biol.* (2017) 9:132–43. doi: 10.1093/jmcb/mjw043

67. Sasaki H, Takayama K, Matsushita T, Ishida K, Kubo S, Matsumoto T, et al. Autophagy modulates osteoarthritis-related gene expression in human chondrocytes. *Arthritis Rheum.* (2012) 64:1920–8. doi: 10.1002/art.34323
68. Li YS, Zhang FJ, Zeng C, Luo W, Xiao WF, Gao SG, et al. Autophagy in osteoarthritis. *Joint Bone Spine.* (2016) 83:143–8. doi: 10.1016/j.jbspin.2015.06.009
69. Chou HC, Chen CH, Chou LY, Cheng TL, Kang L, Chuang SC, et al. Discoidin domain receptors 1 inhibition alleviates osteoarthritis via enhancing autophagy. *Int J Mol Sci.* (2020) 21:1–13. doi: 10.3390/ijms21196991
70. Zmijewski JW, Banerjee S, Bae H, Friggeri A, Lazarowski ER, Abraham E. Exposure to hydrogen peroxide induces oxidation and activation of AMP-activated protein kinase. *J Biol Chem.* (2010) 285:33154–64. doi: 10.1074/jbc.M110.143685
71. Zhou N, Fu Z, Sun T. Effects of different concentrations of oxygen–ozone on rats' astrocytes *in vitro*. *Neurosci Lett.* (2008) 441:178–82. doi: 10.1016/j.neulet.2008.06.036
72. Cardaci S, Filomeni G, Ciriolo MR. Redox implications of AMPK-mediated signal transduction beyond energetic clues. *J Cell Sci.* (2012) 125:2115–25. doi: 10.1242/jcs.095216
73. Jeon SM, Hay N. The double-edged sword of AMPK signaling in cancer and its therapeutic implications. *Archiv Pharma Res.* (2015) 38:346–57. doi: 10.1007/s12272-015-0549-z
74. Jeon SM. Regulation and function of AMPK in physiology and diseases. *Exp Mol Med.* (2016) 48:e245. doi: 10.1038/emm.2016.81
75. Wang Y, Kim NS, Haince JF, Kang HC, David KK, Andrabi SA, et al. Poly(ADP-ribose) (PAR) binding to apoptosis-inducing factor is critical for PAR polymerase-1-dependent cell death (parthanatos). *Sci Signal.* (2011) 4:ra20. doi: 10.1126/scisignal.2000902
76. Ruffell B, Affara NI, Coussens LM. Differential macrophage programming in the tumor microenvironment. *Trends Immunol.* (2012) 33:119–26. doi: 10.1016/j.it.2011.12.001

Conflict of Interest: The authors declare that the research was conducted in the absence of any commercial or financial relationships that could be construed as a potential conflict of interest.

frontiers in Medicine

ORIGINAL RESEARCH
published: 19 February 2021
doi: 10.3389/fmed.2021.630962

Liraglutide Protects Nucleus Pulposus Cells Against High-Glucose Induced Apoptosis by Activating PI3K/Akt/ mTOR/Caspase-3 and PI3K/Akt/GSK3β/Caspase-3 Signaling Pathways

Mingyan Yao[1,2†], Jing Zhang[3†], Zhihong Li[2], Xiaoliang Bai[4], Jinhui Ma[5] and Yukun Li[1]*

[1] Department of Endocrinology, The Third Hospital of Hebei Medical University, Shijiazhuang, China, [2] Department of Endocrinology, Baoding No.1 Central Hospital, Baoding, China, [3] Department of Cardiology, Affiliated Hospital of Hebei University, Baoding, China, [4] Department of Orthopedics, Baoding No.1 Central Hospital, Baoding, China, [5] Department of Endocrinology, Affiliated Hospital of Hebei University, Baoding, China

OPEN ACCESS

Edited by:
Ali Yadollahpour,
The University of Sheffield,
United Kingdom

Reviewed by:
Fangzhou Song,
Chongqing Medical University, China
Shengye Wang,
Zhejiang Cancer Hospital, China

***Correspondence:**
Yukun Li
yukunli.hebei@gmail.com

[†]These authors share first authorship

Specialty section:
This article was submitted to Precision Medicine, a section of the journal Frontiers in Medicine

Received: 18 November 2020
Accepted: 25 January 2021
Published: 19 February 2021

Citation:
Yao M, Zhang J, Li Z, Bai X, Ma J and Li Y (2021) Liraglutide Protects Nucleus Pulposus Cells Against High-Glucose Induced Apoptosis by Activating PI3K/Akt/ mTOR/Caspase-3 and PI3K/Akt/GSK3β/Caspase-3 Signaling Pathways. Front. Med. 8:630962. doi: 10.3389/fmed.2021.630962

Background and Objective: Diabetes mellitus (DM) is reportedly a significant risk factor for intervertebral disc degeneration (IDD). Incretin system and particularly glucagon-like peptide 1 (GLP-1) because of its glucose-lowering effects has become an important target in therapeutic strategies of type 2 diabetes (T2D). Liraglutide is a GLP-1 receptor (GLP-1R) agonist with glucoregulatory and insulinotropic functions as well as regulatory functions on cell proliferation, differentiation, and apoptosis. However, little is known on the roles and signaling pathways of apoptosis protecting effects of liraglutide in IDD. This study aimed to investigate the potential protective effects of liraglutide against high glucose-induced apoptosis of nucleus pulposus cells (NPCs) and the possible involved signaling pathways.

Methods: The human NPCs were incubated with 100 nM liraglutide alone or in combination with LY294002 (PI3K inhibitor), rapamycin (mTOR inhibitor), and SB216763 (GSK3β inhibitor) in a high glucose culture for 48 h. The four groups were assessed further for apoptosis and genes expressions. The apoptotic effect was evaluated by flow cytometry and further confirmed by cell death detection enzyme-linked immunoassay plus (ELISAPLUS). The gene and protein expression levels were assessed by quantitative real-time polymerase chain reaction (qRT-PCR) and Western blotting techniques. The results were comparatively assessed between the four groups.

Results: The results confirmed the presence of GLP-1R in the NPCs indicating that liraglutide inhibited the high glucose-induced apoptosis, which was blocked by silencing GLP-1R with siRNA. Moreover, liraglutide stimulated the phosphorylation of Akt, mTOR and GSK3β. Treatment with LY294002 significantly increased the apoptosis of NPCs and reduced the levels of their downstream substrates (p-AKT, p-mTOR, and p-GSK3β). Further assessments revealed that activation of mTOR and GSK3β

was almost completely inhibited by rapamycin and SB216763, respectively, which significantly increased the caspase-3 levels.

Conclusion: Liraglutide could protect NPCs against high glucose-induced apoptosis by activating the PI3K/AKT/mTOR/caspase-3 and PI3K/AKT/GSK3β/caspase-3 signaling pathways.

Keywords: apoptosis, liraglutide, nucleus pulposus cells, signaling pathway, diabetes mellitus

BACKGROUND

Intervertebral disc degeneration (IDD) is a common disease worldwide with significant socioeconomic burden and adverse effects on quality of life in patients. IDD has been reported as a significant contributor to low back and leg pain (1). Diabetes mellitus (DM) has been reportedly a significant risk factor for several disorders including IDD (2–4). Incretin system and particularly glucagon-like peptide 1 (GLP-1) because of its glucose-lowering effects has become an important target in therapeutic strategies of type 2 diabetes (T2D). The intervertebral disc (IVD) is consisted of the three distinct regions including nucleus pulposus, annulus fibrosis and cartilage endplate, providing stability and flexibility to the spinal column (5), and it is mainly caused by the decline in the quantity and activity of nucleus pulposus cells (NPCs) (6). High glucose environment has been previously reported to inhibit cellular proliferation and induce cell apoptosis, which subsequently promote the IDD progression (4, 7). Therefore, suppression of high glucose-induced aberrant apoptosis might be helpful in preventing the development of IDD in diabetic patients.

Incretin system has become an important therapeutic target for T2D treatment, mainly because of "the incretin effect," which explains oral glucose ingestion results in greater insulin secretion, compared to isoglycemic intravenous glucose infusion (8, 9). Incretin hormones are gastrointestinal hormones produced by the intestinal mucosa after oral nutrient intake and are capable of promoting insulin secretory responses and lowering blood glucose levels in a glucose-dependent manner during hyperglycemic conditions (10–12). Incretins decrease insulin release when glucose levels are approximately normal. Two incretin hormones are identified so far including glucose-dependent insulinotropic polypeptide and GLP-1 (13). GLP-1 has drawn significant research interest mainly because of its capacities in lowering glucose, slowing gastric emptying, improving insulin sensitivity, and inhibiting glucagon secretion (14–18). Moreover, GLP-1 is actively involved in regulation of cell proliferation and apoptosis through multiple pathways (19–21). However, the therapeutic applications of native GLP-1 are limited mainly due to its rapid degradation and short half-life. GLP-1 receptor (GLP-1R) agonists with long half-life that are resistant to degradation can overcome this limitation (17, 22, 23). Liraglutide is a human GLP-1R analog that shares a 97% homology with endogenous GLP-1, with a significantly longer half-life of about 13 h. It is a powerful antidiabetic agent and has been reported to inhibit oxidative stress and apoptosis in various cells (24, 25). However, to our knowledge, there is no published study the role and molecular mechanism underlying of liraglutide in IDD.

The phosphatidylinositol 3-kinase (PI3K)/protein kinase B (Akt) signaling pathway is an intracellular signal transduction pathway involved in the regulation of multiple cellular and molecular physiological processes and plays vital roles in metabolism, proliferation, cell survival, growth, migration, angiogenesis, and apoptosis in response to extracellular signals (10, 26–29). The activation form of phosphor-Akt (p-Akt) can promote cell proliferation and inhibit cell apoptosis by regulating downstream proteins. It has been reported that GLP-1 protects insulin-secreting cells from H_2O_2-induced apoptosis through Cyclic adenosine monophosphate (cAMP) and PI3K dependent signaling pathways (30). Moreover, studies on C3H10T1/2 mesenchymal stem cells and MC3T3-E1 cells have demonstrated that the protective effects of GLP-1 are possibly mediated by activation of Akt process and possibly its downstream of mechanistic target of rapamycin kinase (mTOR) and Glycogen synthase kinases-3β (GSK3β) (31, 32).

In the present study we aim to investigate the potential protective effects of liraglutide, GLP-1R agonist, against high glucose-induced apoptosis in the NPCs and the possible involved signaling pathways that mediate the anti-apoptotic action of liraglutide.

MATERIALS AND METHODS

Cell Culture and Experimental Design

All the experiments and assessments in this study were approved by local ethics committee of the Third Hospital of Hebei Medical University, Shijiazhuang, China which were in complete accordance with the ethical standards and regulations of human studies of the Helsinki declaration (2014). Human NPCs were purchased from American Science Cell Research Laboratories and cultured in Nucleus Pulposus Cell Medium (NPCM) according to the manufacturer guidelines and the method previously described (23). The cultivation process was performed under NPCM with standard conditions (37 C, 21% O_2 and 5% CO_2). The cultivation medium contained 500 ml of basal

Abbreviations: IDD, Intervertebral Disc Degeneration; NPCs, Nucleus Pulposus Cells; qRT-PCR, Quantitative real-time Polymerase Chain Reaction; GLP-1R, GLP-1 Receptor; IVD, Intervertebral Disc; GLP-1, Glucagon-like Peptide-1; p-Akt, Phosphor-Akt; NPCM, Nucleus Pulposus Cell Medium; FBS, Fetal Bovine Serum; Ct, Threshold Cycle; RIPA, Radioimmunoprecipitation Assay; SDS-PAGE, Sodium Dodecyl Sulfate Polyacrylamide Gel Electrophoresis; PVDF, Polyvinylidene Difluoride; TBST, Tris Buffered Saline/tween 20; ECL, Enhanced Chemiluminescence; LSD, Least Significant Difference; MAPK, Mitogen-activated Protein Kinase; PI3K, Phosphatidylinositol 3-kinase.

medium, 10 ml of Fetal Bovine Serum (FBS), 5 ml of NPC growth supplement, and 5 ml of penicillin/streptomycin solution (P/S) (Hyclone, Logan, UT, USA). The cells were washed with fresh medium at the next day to remove unattached cells and residual DMSO (Solarbio, Beijing, China), then were washed every 2–3 days. Once the NPCs reached 70% confluency, the medium was changed every other day until reaching approximate 80–90% confluency. Finally, the NPCs were split 1:3 and then subcultured using 0.25% (w/v) trypsin solution (Sigma, St.Louis, MO, USA).

The resultant third-generation of NPCs were randomly divided into six groups as follows: control (CON) group: cultured in NPCM; High-glucose (HG) group: cultured in high glucose concentration (0.2 M) medium; High-glucose plus liraglutide (HG + LIR) group: cultured in high glucose medium containing liraglutide (100 nM); High glucose plus liraglutide plus LY294002 (HG + LIR + LY) group: cultured in high glucose medium containing liraglutide (100 nM) and a phosphatidylinositol 3-kinase inhibitor (LY294002, 20 μM); High glucose plus liraglutide plus rapamycin (HG + LIR + RAPA) group: cultured in high glucose medium containing liraglutide (100 nM) and rapamycin (inhibitor of mTOR); and high glucose plus liraglutide plus SB216763 (HG + LIR + SB) group: cultured in high glucose medium containing liraglutide (100 nM) and SB216763 (an inhibitor of GSK-3β). The concentrations of agents like liraglutide and inhibitors and cultivating conditions of the experimental groups were determined according to the previously similar studies (23, 32). In all the six groups, the cell vitality, apoptosis rate, and the expression of proteins and genes were determined under the same experimental conditions after 48-h incubation interval.

Measurement of Cell Viability

The cell viability in all the experimental groups was measured by Cell Counting Kit-8 assay (CCK-8, Sigma Aldrich, USA). The CCK-8 assay allows sensitive colorimetric assays for the determination of the number of viable cells in the proliferation and cytotoxicity assays. It uses WST-8 (2-(2-methoxy-4-nitrophenyl)-3-(4-nitrophenyl)-5-(2,4-disulfophenyl)-2H-tetrazolium, monosodium salt) that produces a water-soluble formazan dye upon bioreduction in the presence of an electron carrier, 1-Methoxy PMS. We performed the cell viability assay as per the instructions of the manufacturer and the established method described in the previous study (23). Briefly, the NPCs were seeded in 96-well culture plates at a density of 1.0×10^5/ml (3 wells for each group and 100 μl in each well) in a CO_2 incubator. When reached a confluence of ∼90%, different media were replaced according to our experimental design corresponding to the different interventions and control groups. After 48 h incubation, the CCK-8 assay reagent (10 μl) was added directly to the culture medium for an additional 3 h. The WST-8 was bioreduced by cellular dehydrogenases to an orange formazan product that is soluble in the culture medium. The amount of produced formazan was directly proportional to the number of living cells. A microplate reader (Dynatech MR5000, Eggenstein, Germany) was used to measure the absorbance of each well at 450 nm.

Apoptosis Assessment by Flow Cytometric Analysis

Cell apoptosis was quantitatively determined using an Annexin V-FITC apoptosis detection kit (BD Pharmingen, USA) with propidium iodide (PI) as the viability probe. The assay determines the percentage of cells within a population that are actively undergoing apoptosis. The PI probe was used to determine early apoptotic cells (PI negative, FITC Annexin V positive). The assay was performed as per the instructions of the manufacturer. Briefly, the NPCs were collected by centrifugation (1,000 rpm/min, 5 min, 4°C) after trypsinization with 0.25% trypsin (Sigma, St. Louis, MO, USA) and washing twice with phosphate buffer solution (PBS, Solarbio, China). In the next step, the cells were resuspended in 200 μl of binding buffer and then stained with 10 μl of FITC-Annexin V solution under dark condition for 15 min according to the manufacturer's instructions. Then, 300 μl of binding buffer and 10 μl of PI were added for another 5 min. Finally, NPCs were subjected to a flow cytometry machine (BD Biosciences, San Jose, CA, USA) to analyze the apoptotic cell ratio. The determination of cells was based as follows. The cells with both FITC Annexin V and PI negative were considered viable; cells with FITC-Annexin V positive and PI negative were in early apoptosis; and cells with both FITC-Annexin V and PI positive were counted as late apoptosis or already dead populations. Each experiment was repeated three times independently and the averaged values were used for analyses. The data were expressed as a percentage of the total cell count.

Apoptosis Determination by ELISA

The cell death detection enzyme-linked immunoassay (ELISA) plus kit (Roche Molecular Biochemicals, Germany) was used to determine cell apoptosis. This assay qualitatively and quantitatively determined the cytoplasmic histone-associated-DNA-fragments (mono- and oligonucleosomes) after induced cell death. It was based on the quantitative sandwich-enzyme immunoassay-principle using mouse monoclonal antibodies directed against DNA and histones, respectively. The assessment was performed as per the instructions of the manufacturer. Briefly, the NPCs with different treatments were lysed for 30 min at room temperature (25°C), following by centrifugation for 10 min. The amount of the DNA fragments detected in the supernatants showed the extent of apoptosis in the sample.

Quantitative Real-Time Polymerase Chain Reaction (qRT-PCR)

The qRT-PCR technique was used to detect and quantify the expression level of mRNA encoding Bcl-2, Bax, and caspase-3, respectively. The total RNA of NPCs was extracted using the TRIzol reagent (Invitrogen, USA) and quantified fluorometrically using a CyQuant-Cell Proliferation Assay Kit (Molecular Probes, Eugene, OR, USA), and then reverse-transcribed into cDNA using a ThermoScript RT KIT (Invitrogen, Shanghai, China) according to the manufacturer's instructions. The DNA sequence alignments and primer design for each gene were conducted using Primer Premier 5.0 software (Premier Biosoft

TABLE 1 | Real-time PCR primers [Sequences of forward (F) and reverse (R) primers] used in this study.

Gene	Primer sequences
Caspase-3	F: 5′-TGTTTCCCTGAGGTTTGCTG-3′
	R: 5′-TGCTATTGTGAGGCGGTTGT-3′
Bcl-2	F: 5′-TTCTTTGAGTTCGGTGGGGTC-3′
	R: 5′-TGCATATTTGTTTGGGGCAGG-3′
Bax	F: 5′-TCCACCAAGAAGCTGAGCGAG-3′
	R: 5′-GTCCAGCCCATGATGGTTCT-3′
β-actin	F: 5′-CAGGGCGTGATGGTGGGCA-3′
	R: 5′-CAAACATCATCTGGGTCATCTTCTC-3′

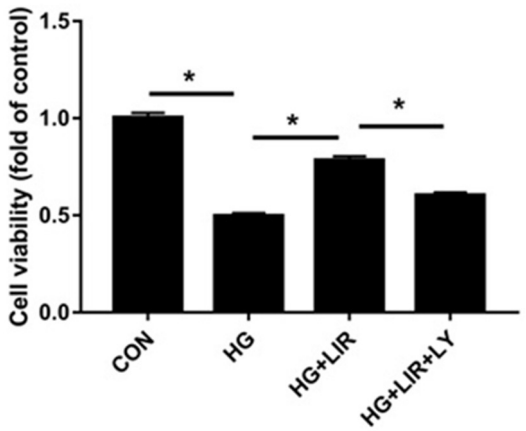

FIGURE 1 | NPCs proliferation activity under different treatments. Cell Counting Kit 8 (CCK-8) assay was used to assess cell proliferation activity. NPCs were treated in four groups as presented in the figure. CON, control; HG, high glucose; LIR, liraglutide; LY, LY294002. Data are expressed as Mean ± SD ($n = 3$). *$P < 0.05$.

International, Palo Alto, California, USA). The sequences of forward/ reverse primers used in this study are presented in **Table 1**.

The cDNA synthesis and amplification approach was employed to determine the expression level of mRNA as per the instructions of the manufacture. A GoScript™ Reverse Transcription System (Promega, USA) was used in a standard volume of 20 μl consisting 10 μl Master Mix, 0.2 μl forward primer, 0.2 μl reverse primer, 2 μl cDNA, and 7.6 μl nuclease-free water. The PCR amplification was performed with the following protocols: 95°C for 3 min, then 40 cycles of 95°C for 10 s, and finally 60°C for 30 s. Standard curves were run in each assay, which produced a linear plot of threshold cycle (Ct) against log (dilution). The expressions of the target gene were quantified based on the concentration of the standard curve and then were presented as relative Ct values. The transcription levels of β-actin were served as a loading control and the transcription levels for all six experimental groups were compared.

Small Interfering RNA (siRNA) Silencing

Small interfering RNA (siRNA) was used to silence the GLP-1R in the NPCs. Transfection of human NPCs with siRNA of the GLP-1R was performed according to the previously described method (33, 34). Briefly, the siRNA was specific and negative siRNAs were purchased from GenePharma Biotechnology, Shanghai, China. After isolation of the NPCs, cells were incubated for 1 h in NPCM medium. The Entranster TM-R4000 (Engreen Biosystem Co, Ltd., New Zealand) was used according to the protocol of the manufacturer employing 200 nM GLP-1R siRNA. Cells were treated with negative control siRNA (SiCON) or GLP-1R siRNA (SiGLP-1R) before liraglutide (LIR) treatment in a high-glucose culture. After transfection, cells were incubated in 12-well plates with NPCM medium for 48 h. Untreated cells as well as the cells treated with negative siRNA were used as negative controls. The siRNA silencing efficiency was determined 48 h post transfection by protein analysis for further experiments.

Western Blotting Analysis

In this study, the protein levels were detected by Western blotting technique, with β-actin as internal reference protein. For Western blotting assay, following appropriate treatment where applicable, the NPCs were homogenized using a radioimmunoprecipitation assay (RIPA) lysis buffer (Beyotime, China) on the ice for 20 min. A Protein BCA Kit (Beyotime, China) was employed to quantify the protein concentration. Then, equal amounts of protein samples were separated by 10% sodium dodecyl sulfate polyacrylamide gel electrophoresis (SDS-PAGE) and then transferred to the polyvinylidene difluoride (PVDF) membranes (Merck Millipore, Billerica, MA, USA). In the final step, the transferred PVDF membranes were blocked against tissue digestion using 5% non-fat milk in Tris Buffered Saline with Tween® 20 (TBST) solution (50 mmol/l Tris, pH: 7.6, 150 mmol/l NaCl, 0.1%) for 1 h at the room temperature (25°C) and then incubated with the appropriate concentration of primary antibodies (Proteintech, Wuhan, China) at 4°C overnight. On the second day, PVDF membranes were washed out three times in the TBST solution and then incubated with the secondary antibodies (Proteintech, Wuhan, China) for 2 h at 37°C. The immunoreactivity bands were interacted with an enhanced chemiluminescence (ECL) kit (Thermo, USA), and the gray values were analyzed using ImageJ software (National Institutes of Health, USA).

Statistical Analysis

Statistical analyses were conducted by Statistical Package for the Social Sciences (SPSS) (Windows, version 22.0). All data were presented as Mean ± Standard Deviation (SD) from the results of at least three independent experiments. Statistical analysis among multiple groups was analyzed by the one way analysis of variance (ANOVA), and the *post-hoc* test was performed using the SNK-q test or the least significant difference (LSD) test. $P < 0.05$ was considered statistically significant.

RESULTS

Liraglutide Inhibits High-Glucose Induced Apoptosis in NPCs

The cell proliferation activities in all experimental groups were measured using the CCK-8 assay. The results showed that the cell proliferation activity in the high-glucose group significantly decreased, compared to the control group ($P < 0.05$). The addition of liraglutide increased the proliferation activity, which was then reversed by adding the inhibitor LY294002 (**Figure 1**) ($P < 0.05$).

The apoptotic effect on the NPCs was evaluated and confirmed by FITC-Annexin V-PI staining and Cell Death ELISAPLUS assessments, respectively. The results showed that high-glucose treatment (0.2 M) significantly increased the percentage of apoptosis, compared with the control group ($P < 0.05$). Moreover, addition of liraglutide suppressed the NPC apoptosis, whereas inhibition of the PI3K/Akt pathway by LY294002 counteracted the inhibiting effects of liraglutide in the high-glucose group ($P < 0.05$) (**Figure 2**).

Liraglutide Regulates the Apoptosis Related Gene Expressions in NPCs

Our results showed that the high-glucose treatment significantly upregulated the expression of pro-apoptotic molecules (Bax and caspase-3), whereas down-regulated the anti-apoptotic molecule (Bcl-2) ($P < 0.05$). Liraglutide partly decreased expression of the pro-apoptotic molecules (Bax and caspase-3), whereas increased expression of the anti-apoptotic molecule (Bcl-2) in a high glucose medium, and the LY294002, a PI3K inhibitor, partly reversed the liraglutide-induced effects of in the high glucose group ($P < 0.05$) (**Figure 3**).

PI3K/Akt/mTOR/Caspase-3 and PI3K/Akt/GSK3β/Caspase-3 Pathways Mediate Liraglutide Anti-apoptosis Effects in NPCs

The activation status and the triggering factors of the intracellular signaling pathways were investigated to determine the molecular mechanisms involved in exerting the anti-apoptosis effects of liraglutide in NPCs. Our results showed that high-glucose treatment of NPCs significantly reduced the expression of anti-apoptotic proteins p-Akt, p-mTOR, and p-GSK3β in the cell apoptosis. Contrary, the liraglutide treatment significantly promoted the phosphorylation of Akt, mTOR and GSK3β, compared with the high-glucose group ($P < 0.05$) (**Figures 4A–D**). The high-glucose treatment significantly upregulated the level of pro-apoptotic caspase-3 protein, whereas liraglutide addition to the medium markedly reduced the expression level of this protein (**Figures 3A,D**). As it was expected, the inhibitor LY294002 significantly decreased the levels of p-Akt, p-mTOR, and p-GSK3β expressions, which liraglutide addition significantly increased the levels of caspase-3 in a high glucose culture ($P < 0.05$) (**Figures 4A–D**).

To further evaluate the apoptosis-inhibiting effect of liraglutide and the role of mTOR and GSK3β as the downstream substrates of Akt process in the NPCs under high-glucose medium, additional Western blot assessments were performed. The cells were incubated with rapamycin (inhibitor of mTOR) and SB216763 (inhibitor of GSK3β) in the high glucose medium combined with liraglutide group. The rapamycin and SB216763 completely prevented the activation of mTOR and GSK3β, respectively ($P < 0.05$). Moreover, rapamycin and SB216763 treatments significantly increased the caspase-3 expression levels in the NPCs ($P < 0.05$) (**Figures 4E–J**). These findings demonstrated that liraglutide could stimulate the PI3K/Akt/mTOR/caspase-3 and PI3K/Akt/GSK3β/caspase-3 signal transduction pathways in the NPCs under high-glucose environment.

Role of GLP-1R in Liraglutide Induced NPCs Apoptosis

The Western blot assessments demonstrated the presence of GLP-1R protein in the NPCs (**Figure 5A**). Cell death ELISAPLUS was performed to determine the apoptosis of NPCs. Our data revealed that silencing GLP-1R with siRNA partly blocked the anti-apoptotic effect of liraglutide (**Figure 5B**), demonstrating that liraglutide prevented apoptosis of NPCs via GLP-1R.

DISCUSSION

This study investigated the anti-apoptotic effects of liraglutide and possible underlying molecular mechanisms in NPCs in high glucose environment. Our findings showed that the inhibition of apoptosis by liraglutide is mediated, at least in part, through PI3K/Akt/mTOR/caspase-3 and PI3K/Akt/GSK3β/caspase-3 signaling pathways. The results also revealed that GLP-1R is involved in NPCs apoptosis and liraglutide mediated inhibition of apoptosis is GLP-1R dependent.

IDD is reportedly a major risk factor for low back pain as well as chronic pain in lower extremities (1). Research is ongoing to understand the pathogenesis of disc degeneration and develop effective therapies for this disorder (35–37). In the recent years, some basic and epidemiological studies have demonstrated that DM is a potential etiological factor of IDD (38, 39). High glucose environment can significantly affect disc biology from disc cell viability to disc matrix metabolism, resulting disc NPCs apoptosis (7, 40). Therefore, inhibiting high glucose-induced NPCs apoptosis has important significance in retarding disc degeneration.

Apoptosis or programmed death is a complicated process that contributes to the structural and functional development of various multicellular organisms. This process contributes to the pathogenesis of several diseases including neurodegenerative diseases, cancer, and immune system dysfunctions. Many factors, majority of them proteins, are actively involved in the apoptosis, the most important of them are caspases, amyloid-B peptide, Bcl-2 family of proteins, p53 gene, and the heat shock proteins (41–44). Apoptotic mechanism consists of three main parts of initiation, execution, and termination. Apoptosis could be triggered by several factors such as alkylating agents, chemotherapeutic agents, oxidative stress, and ionizing radiation

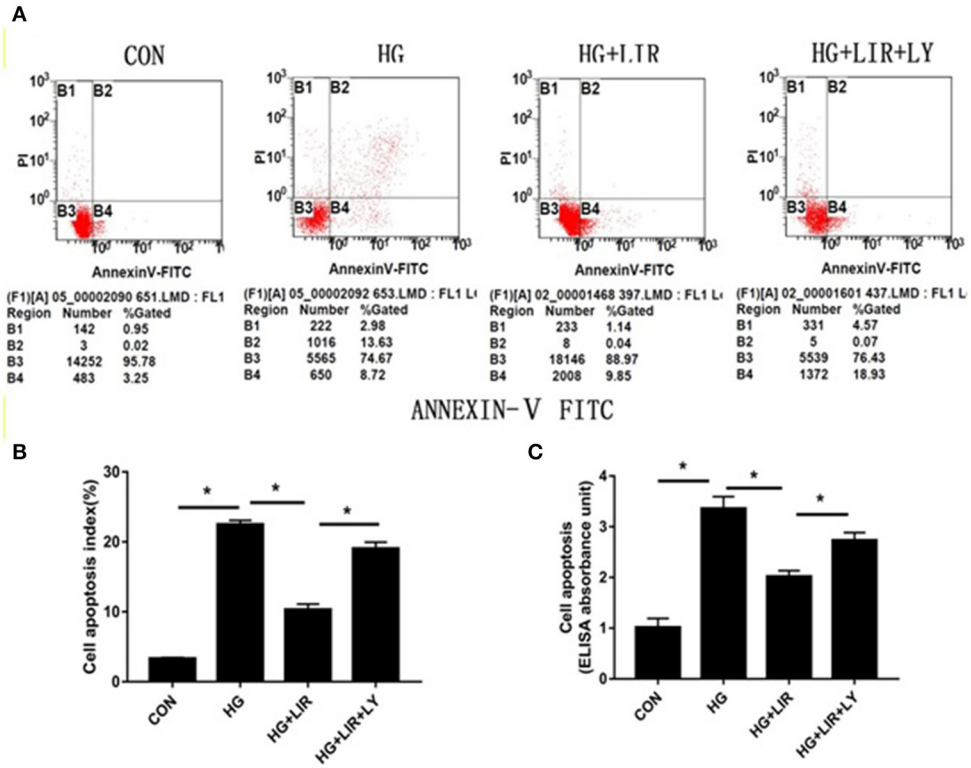

FIGURE 2 | NPCs apoptosis ratio for different treatments. Apoptotic NPCs were detected and confirmed by FITC-Annexin V-PI staining **(A,B)** and Cell Death ELISAPLUS **(C)**, respectively. CON, control; HG, high glucose; LIR, liraglutide; LY, LY294002. Data are expressed as Mean ± SD ($n = 3$). *$P < 0.05$.

or by external factors such as tumor necrosis factor (TNF), cytokines, Fas ligand (FasL) and the TNF-related apoptosis inducing ligand (TRAIL) (45).

Apoptosis is activated by two distinct pathways including intrinsic and external signaling pathways. The intrinsic pathway is activated by internal signals such as DNA damage or growth factor deprivation and is regulated by protein Bcl-2. The external signal of apoptosis induction such as death activators usually bind to receptors at the cell surface.

Liraglutide, a GLP-1 agonist with long half-life, is currently employed as an interesting therapeutic agent for DM. Liraglutide, through binding to GLP-1R, exerts glucoregulatory and insulinotropic functions as well as regulatory functions on cell proliferation, differentiation, and apoptosis (46, 47). However, little is known on the functions of liraglutide in NPCs apoptosis and involved signaling pathways.

A considerable research attention has been devoted on the use of GLP-1 for treatment of T2D (8, 12, 15, 23, 48, 49). This gut incretin hormone has been reported to exert various beneficial effects on different cells including neuronal cells, pancreatic β-cells, gut and hypothalamus. These effects include lowering glucose, slowing gastric emptying, improving insulin sensitivity, enhancing glucose-dependent insulin secretory response, inhibiting glucagon secretion, inhibiting β-cell apoptosis and promoting β-cell proliferation (9, 30, 50–53). Liraglutide is a human incretin-GLP-1 agonist with 97% sequence identity identical to the native human GLP-1 but with a very longer half-life. Recent studies have reported that liraglutide could significantly prevent (by 50%) both the cytokine- and free fatty acid-induced apoptosis in primary rat islet cells in a dose-dependent manner (54).

Ming-yan et al. investigated the effects and possible mechanism of liraglutide on apoptosis of human NPCs (23). They observed that NPCs contained GLP-1R indicating that liraglutide inhibited the high glucose-induced apoptosis of NPCs. Moreover, liraglutide reduced the expression of caspase-3 activity and inhibited reactive oxygen species (ROS) generation and triggered the phosphorylation of Akt under high glucose condition. They showed that pretreatment of NPCs with a PI3K inhibitor (LY294002) prevented the anti-apoptotic effect of liraglutide on NPCs. They concluded that GLP-1R prevented the liraglutide-induced activation of Akt (23). Their findings demonstrated that liraglutide could directly protect NPCs against high glucose-induced apoptosis through impeding oxidative stress and activating the PI3K/Akt/caspase-3 signaling pathway by GLP-1R (23). In light of these findings, we designed this study to investigate the downstream substrates of Akt process in inducing protective effects against high glucose induced apoptosis deaths in NPCs through assessing the roles of mTOR and GSK3β deaths.

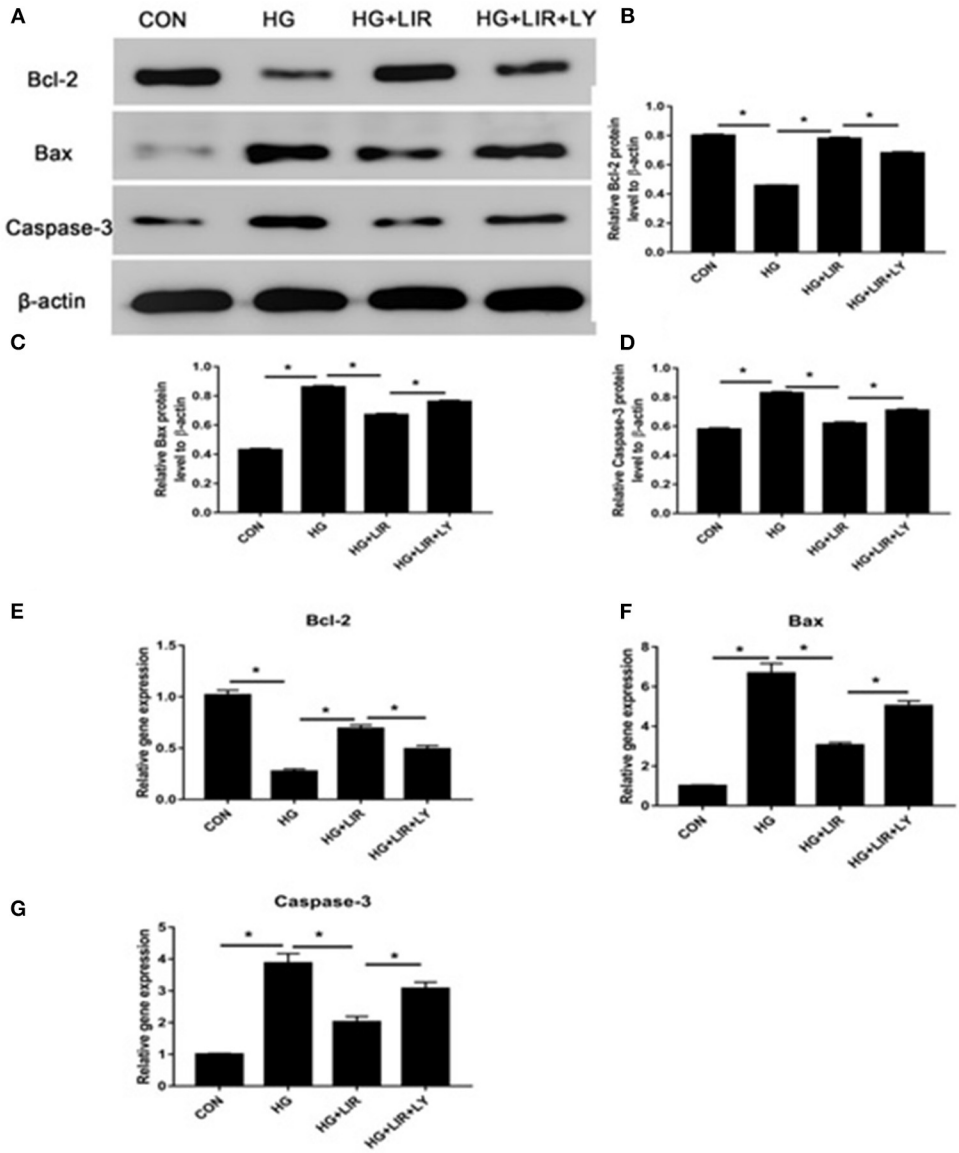

FIGURE 3 | The expressions of pro- and anti-apoptosis molecules in the different treatment groups using Western blot and RT-PCR techniques. The expressions of Bcl-2, Bax, and caspase-3 by Western blot **(A–D)** and RT-PCR **(E–G)**. Liraglutide partly decreased the expressions of Bax and caspase-3, whereas increased the Bcl-2 expression in a high glucose culture and the inhibitor LY294002 partly reversed the liraglutide-induced effects. CON, control; HG, high glucose; LIR, liraglutide; LY, LY294002. Data are presented as Mean ± SD ($n = 3$). *$P < 0.05$.

In our study, we chose the concentration of liraglutide at 100 nM as an optimum concentration (35, 46). Results showed that high glucose markedly increased the percentage of apoptosis and regulated the gene and protein expression related to apoptosis that down-regulated levels of anti-apoptosis molecules (Bcl-2) and up-regulated levels of pro-apoptosis molecules (Bax, caspase-3). The addition of liraglutide significantly decreased the cell apoptosis ratio, up-regulated expression of Bcl-2, and down-regulated Bax and caspase-3 in a high glucose culture.

We further explored the signaling transduction pathway in the protective effects of liraglutide against high glucose-induced NPCs apoptosis. GLP-1 has been reported to be involved in inhibition apoptosis in various cells. GLP-1 binding to GLP-1R leads to the activation of specific signaling pathways including mitogen-activated protein kinase (MAPK, phospholipase C, cAMP/PKA, and PI3K)/Akt (55). Among them, PI3K/Akt pathway plays an important role in regulating the biology of disc cells, and has been reported to interfere with the process for NPCs apoptosis (56–58). The mTOR and GSK3β are downstream effectors of the PI3K/Akt signaling, which can be activated via PI3K/Akt signaling and has been reported to inhibit apoptosis (58–61). To our knowledge, as a GLP-1

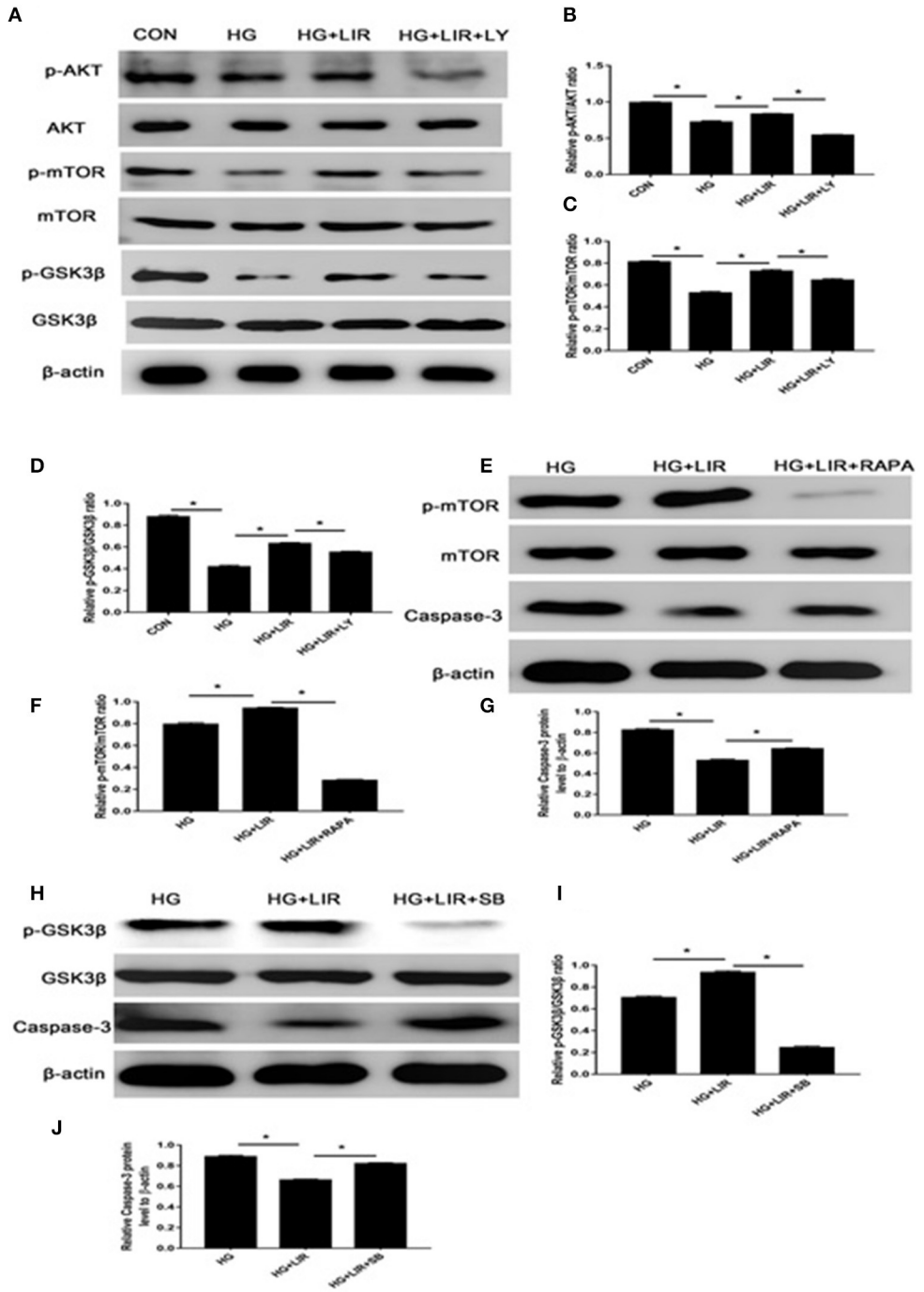

FIGURE 4 | The Western blot assessments of the activations of PI3K/Akt/mTOR/caspase-3 and PI3K/Akt/GSK3β/caspase-3 signaling pathways in anti-apoptotic effects of liraglutide. Cells were exposed to liraglutide (100 nM) and LY294002 (20 μM), respectively. The outcomes of Western blotting on the expressions of Akt **(A,B)**, mTOR **(A,C)**, and GSK3β **(A,D)**. In further assessments, cells were incubated with 100 nM liraglutide and rapamycin or SB216763, respectively. Results of Western blot assessments on expressions of mTOR **(E,F)**, GSK3β **(H,I)**, and caspase-3 **(G,J)**. CON, control; HG, high glucose; LIR, liraglutide; LY, LY294002. Data are expressed as Mean ± SD ($n = 3$). *$P < 0.05$.

agonist, liraglutide exerts its physiological functions through binding to GLP-1R and can activate PI3K/Akt signaling cascade (35, 62). Our data show that liraglutide (100 nM) largely rescued the phosphorylation of Akt, mTOR, and GSK3β (which was inhibited by high glucose) and decreased caspase-3 levels. The LY294002, a PI3K inhibitor, blocks

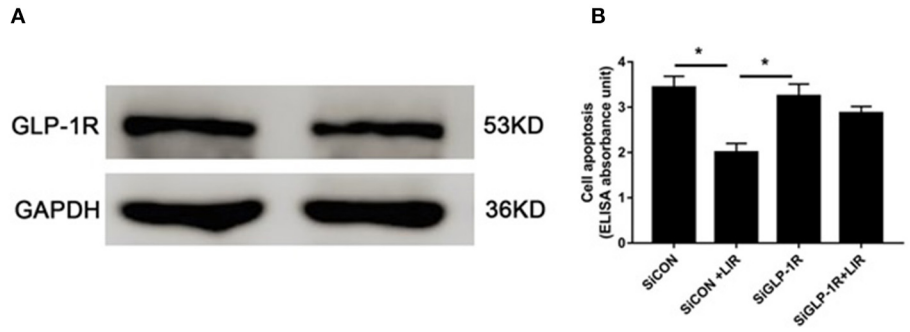

FIGURE 5 | Role of GLP-1R in NPCs apoptosis under high-glucose treatment. **(A)** Western blot analysis showed GLP-1R protein was expressed in the NPCs. **(B)** Silencing GLP-1R with siRNA transfection lead to the liraglutide anti-apoptotic effect inhibition. Before liraglutide (LIR) treatment, cells were treated with GLP-1R siRNA (SiGLP-1R) or negative control siRNA (SiCON), then assessed for apoptosis using cell death detection ELISAPLUS assay. Data are presented as Mean ± SD ($n = 3$). $^*P < 0.05$.

PI3K/Akt signaling pathway in mammalian cells. Treatment with LY294002 significantly increased the apoptosis of NPCs and reduced the levels of their downstream substrates (p-AKT, p-mTOR, and p-GSK3β). To further investigate this issue, rapamycin and SB216763 were used to inhibit activation of mTOR and GSK3β, respectively. Treatment of NPCs with rapamycin and SB216763 induced a significantly increase in caspase-3 levels, which is a critical enzyme for cell survival and apoptosis (63). Therefore, we speculated that the PI3K/Akt/mTOR/caspase-3 and PI3K/Akt/GSK3β/ caspase-3 signaling pathways are involved in the protective effects of liraglutide against high glucose-induced NPCs apoptosis. Furthermore, we ascertained that GLP-1R was expressed in the NPCs. The anti-apoptosis effect of liraglutide was blocked by the inhibition of GLP-1R with siRNA, indicating that the protective effect against high glucose-induced NPCs apoptosis is mediated by GLP-1R.

CONCLUSION

This study investigated the protective effects of liraglutide against high glucose-induced apoptosis in NPCs and also the involved molecular signaling pathways. In conclusion, the present study suggested that liraglutide could attenuate high glucose induced NPCs apoptosis and the activation of PI3K/Akt/mTOR/caspase-3 and PI3K/Akt/GSK3β/caspase-3 signaling pathways may be responsible for its protective effects by binding to GLR-1R. This study provides some theoretical basis for the application of liraglutide in retarding disc degeneration, which still requires further clarification. Future studies should be conducted to determine the precise mechanisms underlying the differential effects of liraglutide on apoptosis and the related processes such as autophagy to optimize the anti-apoptotic and cytoprotective effects of liraglutide.

DATA AVAILABILITY STATEMENT

The datasets presented in this study can be found in online repositories. The names of the repository/repositories and accession number(s) can be found in the article/supplementary material.

ETHICS STATEMENT

The studies involving human participants were reviewed and approved by local ethics committee of the Third Hospital of Hebei Medical University, Shijiazhuang, China (2018-015-1). Written informed consent for participation was not required for this study in accordance with the national legislation and the institutional requirements.

AUTHOR CONTRIBUTIONS

YL and MY: conceptualization. XB: methodology. JZ: software and data curation. ZL and MY: validation, writing—original draft preparation, and supervision. JM: formal analysis and resources. ZL: investigation and visualization. YL: writing—review and editing, project administration, and funding acquisition. All authors contributed to the article and approved the submitted version.

ACKNOWLEDGMENTS

Authors gratefully express their gratitude to all those who have helped authors during the experiments. Moreover, authors thank the staffs of the Hebei Medical University who have assisted the conducting of this study.

REFERENCES

1. Steffens D, Maher CG, Pereira LSM, Stevens ML, Oliveira VC, Chapple M, et al. Prevention of lowback pain a systematic review and meta-analysis. *JAMA Intern Med*. (2016) 176:199–208. doi: 10.1001/jamainternmed.2015.7431
2. Jiang Z, Lu W, Zeng Q, Li D, Ding L, Wu J. High glucose-induced excessive reactive oxygen species promote apoptosis through mitochondrial damage in rat cartilage endplate cells. *J Orthop Res*. (2018) 36:2476–83. doi: 10.1002/jor.24016
3. Park JS, Park JB, Park IJ, Park EY. Accelerated premature stress-induced senescence of young annulus fibrosus cells of rats by high glucose-induced oxidative stress. *Int Orthop*. (2014) 38:1311–20. doi: 10.1007/s00264-014-2296-z
4. Kong CG, Park JB, Kim MS, Park EY. High glucose accelerates autophagy in adult rat intervertebral disc cells. *Asian Spine J*. (2014) 8:543–8. doi: 10.4184/asj.2014.8.5.543
5. Oh CD, Im HJ, Suh J, Chee A, An H, Chen D. Rho-associated kinase inhibitor immortalizes rat nucleus pulposus and annulus fibrosus cells. *Spine*. (2016) 41:E255–61. doi: 10.1097/BRS.0000000000001235
6. Gu T, Shi Z, Wang C, Chen C, Wu J, Wang D, et al. Human bone morphogenetic protein 7 transfected nucleus pulposus cells delay the degeneration of intervertebral disc in dogs. *J Orthop Res*. (2017) 35:1311–22. doi: 10.1002/jor.22995
7. Cheng X, Ni B, Zhang F, Hu Y, Zhao J. High glucose-induced oxidative stress mediates apoptosis and extracellular matrix metabolic imbalances possibly via p38 MAPK activation in rat nucleus pulposus cells. *J Diabetes Res*. (2016) 2016:3765173. doi: 10.1155/2016/3765173
8. Jalewa J, Sharma MK, Hölscher C. Novel incretin analogues improve autophagy and protect from mitochondrial stress induced by rotenone in SH-SY5Y cells. *J Neurochem*. (2016) 139:55–67. doi: 10.1111/jnc.13736
9. Korbut AI, Klimontov VV. Incretin-based therapy: renal effects. *Diabetes Mellit*. (2016) 19:53–63. doi: 10.14341/DM7727
10. Chen J, Xie JJ, Shi KS, Gu YT, Wu CC, Xuan J, et al. Glucagon-like peptide-1 receptor regulates endoplasmic reticulum stress-induced apoptosis and the associated inflammatory response in chondrocytes and the progression of osteoarthritis in rat. *Cell Death Dis*. (2018) 9:212. doi: 10.1038/s41419-017-0217-y
11. Marlet IR, Ölmestig JNE, Vilsbøll T, Rungby J, Kruuse C. Neuroprotective mechanisms of glucagon-like peptide-1-based therapies in ischaemic stroke: a systematic review based on pre-clinical studies. *Basic Clin Pharmacol Toxicol*. (2018) 122:559–69. doi: 10.1111/bcpt.12974
12. Nauck MA, Quast DR, Wefers J, Meier JJ. GLP-1 receptor agonists in the treatment of type 2 diabetes – state-of-the-art. *Mol Metab*. (2020) 14:101102-28. doi: 10.1016/j.molmet.2020.101102
13. Suzuki S, Kawai K, Ohashi S, Mukai H, Murayama Y, Yamashita K. Reduced insulinotropic effects of glucagonlike peptide I-(7-36)-amide and gastric inhibitory polypeptide in isolated perfused diabetic rat pancreas. *Diabetes*. (1990) 39:1320–5. doi: 10.2337/diabetes.39.11.1320
14. Hayes MR, Kanoski SE, Alhadeff AL, Grill HJ. Comparative effects of the long-acting GLP-1 receptor ligands, liraglutide and exendin-4, on food intake and body weight suppression in rats. *Obesity*. (2011) 19:1342–9. doi: 10.1038/oby.2011.50
15. Hinnen D. Glucagon-like peptide 1 receptor agonists for type 2 diabetes. *Diabetes Spectr*. (2017) 30:202–10. doi: 10.2337/ds16-0026
16. Guo XH. The value of short- and long-acting glucagon-like peptide-1 agonists in the management of type 2 diabetes mellitus: experience with exenatide. *Curr Med Res Opin*. (2016) 32:61–76. doi: 10.1185/03007995.2015.1103214
17. Gupta V. Glucagon-like peptide-1 analogues: an overview. *Indian J Endocrinol Metab*. (2013) 17:413. doi: 10.4103/2230-8210.111625
18. Htike ZZ, Zaccardi F, Papamargaritis D, Webb DR, Khunti K, Davies MJ. Efficacy and safety of glucagon-like peptide-1 receptor agonists in type 2 diabetes: a systematic review and mixed-treatment comparison analysis. *Diabetes Obes Metab*. (2017) 19:524–36. doi: 10.1111/dom.12849
19. Ying Y, Zhu H, Liang Z, Ma X, Li S. GLP1 protects cardiomyocytes from palmitate-induced apoptosis via Akt/GSK3b/b-catenin pathway. *J Mol Endocrinol*. (2015) 55:245–62. doi: 10.1530/JME-15-0155
20. De Nigris VD, Prattichizzo F, Mancuso E, Spiga R, Pujadas G, Ceriello A. Teneligliptin enhances the beneficial effects of GLP-1 in endothelial cells exposed to hyperglycemic conditions. *Oncotarget*. (2018) 9:8898–910. doi: 10.18632/oncotarget.22849
21. Tudurí E, López M, Diéguez C, Nadal A, Nogueiras R. Glucagon-like peptide 1 analogs and their effects on pancreatic islets. *Trends Endocrinol Metab*. (2016) 27:304–18. doi: 10.1016/j.tem.2016.03.004
22. Madsbad S, Kielgast U, Asmar M, Deacon CF, Torekov SS, Holst JJ. An overview of once-weekly glucagon-like peptide-1 receptor agonists-available efficacy and safety data and perspectives for the future. *Diabetes Obes Metab*. (2011) 27:394–407. doi: 10.1111/j.1463-1326.2011.01357.x
23. Yao MY, Jing Z, Guo SQ, Bai XL, Li ZH, Xue Z. Liraglutide inhibits the apoptosis of human nucleus pulposus cells induced by high glucose through PI3K/Akt/caspase-3 signaling pathway. *Biosci Rep*. (2019) 39:1–11. doi: 10.1042/BSR20190109
24. Kapodistria K, Tsilibary EP, Kotsopoulou E, Moustardas P, Kitsiou P. Liraglutide, a human glucagon-like peptide-1 analogue, stimulates AKT-dependent survival signalling and inhibits pancreatic β-cell apoptosis. *J Cell Mol Med*. (2018) 22:2970–80. doi: 10.1111/jcmm.13259
25. Hendarto H, Inoguchi T, Maeda Y, Ikeda N, Zheng J, Takei R, et al. GLP-1 analog liraglutide protects against oxidative stress and albuminuria in streptozotocin-induced diabetic rats via protein kinase A-mediated inhibition of renal NAD(P)H oxidases. *Metabolism*. (2012) 61:1422–34. doi: 10.1016/j.metabol.2012.03.002
26. Cheng S, Zhang X, Xu Y, Dai X, Li J, Zhang T, et al. Krüppel-like factor 8 regulates VEGFA expression and angiogenesis in hepatocellular carcinoma. *Sci Rep*. (2018) 8:17415. doi: 10.1038/s41598-018-35786-6
27. Li D, Qu X, Hou K, Zhang Y, Dong Q, Teng Y, et al. PI3K/Akt is involved in bufalin-induced apoptosis in gastric cancer cells. *Anticancer Drugs*. (2009) 20:59–64. doi: 10.1097/CAD.0b013e3283160fd6
28. Zhou, Muxiang, Lubing Gu, Harry W. Findley, Rong Jiang WGW. PTEN reverses MDM2-mediated Chemotherapy resistance by interacting with p53 in acute lymphoblastic leukemia cells | cancer research. *Cancer Res*. (2003) 63:6357–62. Available online at: https://cancerres.aacrjournals.org/content/canres/63/19/6357.full.pdf
29. Martini M, De Santis MC, Braccini L, Gulluni F, Hirsch E. PI3K/AKT signaling pathway and cancer: an updated review. *Ann Med. Inform Healthc*. (2014) 46:372–83. doi: 10.3109/07853890.2014.912836
30. Hui H, Nourparvar A, Zhao X, Perfetti R. Glucagon-like peptide-1 inhibits apoptosis of insulin-secreting cells via a cyclic 5′-adenosine monophosphate-dependent protein kinase A- and a phosphatidylinositol 3-kinase-dependent pathway. *Endocrinology*. (2003) 44:1444–55. doi: 10.1210/en.2002-220897
31. Wang X, Chen J, Rong C, Pan F, Zhao X, Hu Y. GLP-1RA promotes brown adipogenesis of C3H10T1/2 mesenchymal stem cells via the PI3K-AKT-mTOR signaling pathway. *Biochem Biophys Res Commun*. (2018) 506(4):976–82. doi: 10.1016/j.bbrc.2018.10.197
32. Wu X, Li S, Xue P, Li Y. Liraglutide inhibits the apoptosis of MC3T3-E1 cells induced by serum deprivation through cAMP/PKA/β-catenin and PI3K/AKT/GSK3β signaling pathways. *Mol Cells*. (2018) 41:234–43. doi: 10.14348/molcells.2018.2340
33. Suzuki T, Nishida K, Kakutani K, Maeno K, Yurube T, Takada T, et al. Sustained long-term RNA interference in nucleus pulposus cells *in vivo* mediated by unmodified small interfering RNA. *Eur Spine J*. (2009) 18:263–70. doi: 10.1007/s00586-008-0873-9
34. Kakutani K, Nishida K, Uno K, Takada T, Shimomura T, Maeno K, et al. Prolonged down regulation of specific gene expression in nucleus pulposus cell mediated by RNA interference *in vitro*. *J Orthop Res*. (2006) 24:1271–8. doi: 10.1002/jor.20171
35. Huang YC, Hu Y, Li Z, Luk KDK. Biomaterials for intervertebral disc regeneration: current status and looming challenges. *J Tissue Eng Regen Med*. (2018) 12:2188–202. doi: 10.1002/term.2750
36. Park TSW, Kuo A, Smith MT. Chronic low back pain: a mini-review on pharmacological management and pathophysiological insights from clinical and pre-clinical data. *Inflammopharmacology*. (2018) 26:881–98. doi: 10.1007/s10787-018-0493-x
37. Yang Y, Wang X, Liu Z, Xiao X, Hu W, Sun Z. Osteogenic protein-1 attenuates nucleus pulposus cell apoptosis through activating the PI3K/Akt/mTOR pathway in a hyperosmotic culture. *Biosci Rep*. (2018) 38:BSR20181708. doi: 10.1042/BSR20181708

38. Mobbs RJ, Newcombe RL, Chandran KN. Lumbar discectomy and the diabetic patient: incidence and outcome. *J Clin Neurosci*. (2001) 8:10–3. doi: 10.1054/jocn.2000.0682
39. Park EY, Park JB. Dose- and time-dependent effect of high glucose concentration on viability of notochordal cells and expression of matrix degrading and fibrotic enzymes. *Int Orthop*. (2013) 37:1179–86. doi: 10.1007/s00264-013-1836-2
40. Hou G, Zhao H, Teng H, Li P, Xu W, Zhang J, et al. N-cadherin attenuates high glucose-induced nucleus pulposus cell senescence through regulation of the ROS/NF-κB pathway. *Cell Physiol Biochem*. (2018) 47:257–65. doi: 10.1159/000489804
41. Papaliagkas V, Anogianaki A, Anogianakis G, Ilonidis G. The proteins and the mechanisms of apoptosis: a mini-review of the fundamentals. *Hippokratia*. (2007) 11:108–13.
42. Mihara M, Erster S, Zaika A, Petrenko O, Chittenden T, Pancoska P, et al. p53 has a direct apoptogenic role at the mitochondria results p53 rapidly accumulates at mitochondria of primary thymocytes undergoing γIR-. *Mol Cell*. (2003) 11:577–90. doi: 10.1016/S1097-2765(03)00050-9
43. Ghavami S, Shojaei S, Yeganeh B, Ande SR, Jangamreddy JR, Mehrpour M, et al. Autophagy and apoptosis dysfunction in neurodegenerative disorders. *Prog Neurobiol*. (2014) 112:24–49. doi: 10.1016/j.pneurobio.2013.10.004
44. Rybak LP, Ramkumar V. Ototoxicity. *Kidney Int*. (2007) 72:931–5. doi: 10.1038/sj.ki.5002434
45. Hock JM, Krishnan V, Onyia JE, Bidwell JP, Milas J, Stanislaus D, et al. Osteoblast apoptosis and bone turnover. *J Bone Miner Res*. (2001) 16:975–84. doi: 10.1359/jbmr.2001.16.6.975
46. Miao XY, Gu ZY, Liu P, Hu Y, Li L, Gong YP, et al. The human glucagon-like peptide-1 analogue liraglutide regulates pancreatic beta-cell proliferation and apoptosis via an AMPK/mTOR/P70S6K signaling pathway. *Peptides*. (2013) 39:71–9. doi: 10.1016/j.peptides.2012.10.006
47. Wu X, Li S, Xue P, Li Y. Liraglutide, a glucagon-like peptide-1 receptor agonist, facilitates osteogenic proliferation and differentiation in MC3T3-E1 cells through phosphoinositide 3-kinase (PI3K)/protein kinase B (AKT), extracellular signal-related kinase (ERK)1/2, and cAMP/pro. *Exp Cell Res*. (2017) 360:281–91. doi: 10.1016/j.yexcr.2017.09.018
48. Zhou Y, He X, Chen Y, Huang Y, Wu L, He J. Exendin-4 attenuates cardiac hypertrophy via AMPK/mTOR signaling pathway activation. *Biochem Biophys Res Commun*. (2015) 468:394–9. doi: 10.1016/j.bbrc.2015.09.179
49. Kim W, Egan JM. The role of incretins in glucose homeostasis and diabetes treatment. *Pharmacol Rev*. (2008). 60:470–512. doi: 10.1124/pr.108.000604
50. Arden C. A role for Glucagon-Like Peptide-1 in the regulation of β-cell autophagy. *Peptides*. (2018) 100:85–93. doi: 10.1016/j.peptides.2017.12.002
51. Freeman JS. Role of the incretin pathway in the pathogenesis of type 2 diabetes mellitus. *Cleve Clin J Med*. (2009) 76(Suppl. 5):S12–9. doi: 10.3949/ccjm.76.s5.03
52. Farilla L, Hongxiang H, Bertolotto C, Kang E, Bulotta A, Mario UDI, et al. Glucagon-like peptide-1 promotes islet cell growth and inhibits apoptosis in Zucker diabetic rats. *Endocrinology*. (2002) 143:4397–408. doi: 10.1210/en.2002-220405
53. Baggio LL, Drucker DJ. Biology of incretins: GLP-1 and GIP. *Gastroenterology*. (2007) 132:2131–57. doi: 10.1053/j.gastro.2007.03.054
54. Wajcberg E, Amarah A. Liraglutide in the management of type 2 diabetes. *Drug Design Dev Ther*. (2010) 4:279–90. doi: 10.2147/DDDT.S10180
55. Liu Z, Habener JF. Glucagon-like peptide-1 activation of TCF7L2-dependent Wnt signaling enhances pancreatic beta cell proliferation. *J Biol Chem*. (2008) 283:8723–35. doi: 10.1074/jbc.M706105200
56. Gao J, Zhang Q, Song L. Resveratrol enhances matrix biosynthesis of nucleus pulposus cells through activating autophagy via the PI3K/Akt pathway under oxidative damage. *Biosci Rep*. (2018) 38:20180544. doi: 10.1042/BSR20180544
57. Wang T, Yang SD, Liu S, Wang H, Liu H, Ding WY. 17β-estradiol inhibites tumor necrosis factor-α induced apoptosis of human nucleus pulposus cells via the PI3K/Akt pathway. *Med Sci Monit*. (2016) 22:4312–22. doi: 10.12659/MSM.900310
58. Li P, Liang Z, Hou G, Song L, Zhang R, Gan Y, et al. N-cadherin-mediated activation of PI3K/Akt-GSK-3β signaling attenuates nucleus pulposus cell apoptosis under high-magnitude compression. *Cell Physiol Biochem*. (2017) 44:229–39. doi: 10.1159/000484649
59. Liu Z, Wang F, Zhou ZW, Xia HC, Wang XY, Yang YX, et al. Alisertib induces G2/M arrest, apoptosis, and autophagy via PI3K/Akt/mTOR-and p38 MAPK-mediated pathways in human glioblastoma cells. *Am J Transl Res*. (2017) 9:845–73.
60. Liu F, Gao S, Yang Y, Zhao X, Fan Y, Ma W, et al. Antitumor activity of curcumin by modulation of apoptosis and autophagy in human lung cancer A549 cells through inhibiting PI3K/Akt/mTOR pathway. *Oncol Rep*. (2018) 39:1523–31. doi: 10.3892/or.2018.6188
61. Kim DE, Kim B, Shin HS, Kwon HJ, Park ES. The protective effect of hispidin against hydrogen peroxide-induced apoptosis in H9c2 cardiomyoblast cells through Akt/GSK-3β and ERK1/2 signaling pathway. *Exp Cell Res*. (2014) 327:264–75. doi: 10.1016/j.yexcr.2014.07.037
62. Kimura R, Okouchi M, Fujioka H, Ichiyanagi A, Ryuge F, Mizuno T, et al. Glucagon-like peptide-1 (GLP-1) protects against methylglyoxal-induced PC12 cell apoptosis through the PI3K/Akt/mTOR/GCLc/redox signaling pathway. *Neuroscience*. (2009) 162:1212–9. doi: 10.1016/j.neuroscience.2009.05.025
63. Miura M, Chen XD, Allen MR, Bi Y, Gronthos S, Seo BM, et al. A crucial role of caspase-3 in osteogenic differentiation of bone marrow stromal stem cells. *J Clin Invest*. (2004) 114:1704–13. doi: 10.1172/JCI20427

Conflict of Interest: The authors declare that the research was conducted in the absence of any commercial or financial relationships that could be construed as a potential conflict of interest.

frontiers in Medicine

REVIEW
published: 03 March 2021
doi: 10.3389/fmed.2021.649896

CRISPR/Cas: Advances, Limitations, and Applications for Precision Cancer Research

Yue Yang[1†], *Jin Xu*[2†], *Shuyu Ge*[3] *and Liqin Lai*[1*]

[1] Department of Pathology, Tongde Hospital of Zhejiang Province, Hangzhou, China, [2] Department of Otolaryngology, Tongde Hospital of Zhejiang Province, Hangzhou, China, [3] Department of Pharmacy, Tongde Hospital of Zhejiang Province, Hangzhou, China

Cancer is one of the most leading causes of mortalities worldwide. It is caused by the accumulation of genetic and epigenetic alterations in 2 types of genes: tumor suppressor genes (TSGs) and proto-oncogenes. In recent years, development of the clustered regularly interspaced short palindromic repeats (CRISPR) technology has revolutionized genome engineering for different cancer research ranging for research ranging from fundamental science to translational medicine and precise cancer treatment. The CRISPR/CRISPR associated proteins (CRISPR/Cas) are prokaryote-derived genome editing systems that have enabled researchers to detect, image, manipulate and annotate specific DNA and RNA sequences in various types of living cells. The CRISPR/Cas systems have significant contributions to discovery of proto-oncogenes and TSGs, tumor cell epigenome normalization, targeted delivery, identification of drug resistance mechanisms, development of high-throughput genetic screening, tumor models establishment, and cancer immunotherapy and gene therapy in clinics. Robust technical improvements in CRISPR/Cas systems have shown a considerable degree of efficacy, specificity, and flexibility to target the specific locus in the genome for the desired applications. Recent developments in CRISPRs technology offers a significant hope of medical cure against cancer and other deadly diseases. Despite significant improvements in this field, several technical challenges need to be addressed, such as off-target activity, insufficient indel or low homology-directed repair (HDR) efficiency, *in vivo* delivery of the Cas system components, and immune responses. This study aims to overview the recent technological advancements, preclinical and perspectives on clinical applications of CRISPR along with their advantages and limitations. Moreover, the potential applications of CRISPR/Cas in precise cancer tumor research, genetic, and other precise cancer treatments discussed.

Keywords: clustered regularly interspaced short palindromic repeats, CRiSPR/Cas, cancer, precise cancer treatment, genetic editing, diagnosis, precision medicine

OPEN ACCESS

Edited by:
Ali Yadollahpour,
The University of Sheffield,
United Kingdom

Reviewed by:
Shengye Wang,
Zhejiang Cancer Hospital, China
Fangzhou Song,
Chongqing Medical University, China

***Correspondence:**
Liqin Lai
Lailiqin2020@126.com
orcid.org/0000-0001-9972-7346

[†]These authors have contributed equally to this work

Specialty section:
This article was submitted to Precision Medicine, a section of the journal Frontiers in Medicine

Received: *05 January 2021*
Accepted: *25 January 2021*
Published: *03 March 2021*

Citation:
Yang Y, Xu J, Ge S and Lai L (2021) CRISPR/Cas: Advances, Limitations, and Applications for Precision Cancer Research. Front. Med. 8:649896. doi: 10.3389/fmed.2021.649896

INTRODUCTION

Cancer is one of the main causes of disease-associated mortalities worldwide with ever-increasing incidence worldwide (1). Comprehensive and large-scale sequencing databases have shown that genetic alterations, either specific to a certain type or common to several types, play crucial roles in tumorigenesis (2). Determining the structural and functional features of mutated genes,

particularly long-tail molecular alterations, in genetic variations of cancer genomes play pivotal role in advancing cancer research (3, 4). However, systematic functional analysis of genes and mutations are time-consuming, expensive and laborious (5). Discovery of mutations that cause phenotypes relied either on random mutagenesis or indirectly on perturbation of transcripts by RNAi. The development of engineered nucleases such as zinc finger nucleases or transcription activator-like effector nucleases (TALENs) have made it possible to directly target and modify the genomic sequence (6, 7). Recently, genome engineering was greatly accelerated by the development of clustered regularly interspaced short palindromic repeats (CRISPR) technologies. Since the first use of CRISPR/CRISPR associated proteins (CRISPR/Cas) as a genome editing tool in 2013 in mammalian cells (8, 9), this toolbox has been extensively and continuously expanded. CRISPR/Cas systems are currently capable of not only manipulating the genomic sequence of cells and organisms, but also the introducing and site-specific targeting of epigenetic and transcriptional modifications (10–12).

In the past decade, the emergence of the CRISPR technology has brought revolutionary advances into genome engineering and made it powerful tool in different cancer researches including fundamental sciences to translational medicine and precise cancer treatment. The CRISPR/Cas are prokaryote-derived genome editing systems that have shown promising contributions to detect, image, manipulate and annotate specific DNA and RNA sequences in various types of living cells. CRISPR/Cas, capable of specific genome modifications in living eukaryotic cells, making this technology one of the key scientific discoveries of the twenty-first century. The genomic modifications include; sequence deletions, insertions, substitutions, integrations, and epigenetic genes regulation. In the last few years, advancements in this technology make an ability to drive into both basic and clinical research applications. CRISPR/Cas system is an RNA-guided targeted genome engineering platform, attaining a considerable attention in experimental research, and revolutionize different fields of life sciences. Functionally, the CRISPR-Cas system is divided into 2 classes according to the structural composition of the effector genes. The class 1 CRISPR system consists of multi-subunits of effector nuclease complexes and includes the type I, III, and IV CRISPR systems. The class 2 consists of a single effector nuclease, and routine practice of genome editing has been achieved by the development of the Class 2 CRISPR-Cas system, which includes the type II, V, and VI CRISPR-Cas systems. Types II and V are utilized for DNA editing, and type VI for RNA editing. CRISPR techniques can induce both quantitative and qualitative changes in gene expression through the DSB repair pathway, transposase-dependent DNA integration, base editing, and gene regulation using the CRISPR-dCas or type VI CRISPR system.

The CRISPR systems were first observed in *E. coli* in 1987 (13) and then in several other bacteria species (14). The exact functions and roles of these short repeat sequences remained unclear until in 2005, when strong evidences have hypothesized that these repeated sequences function as a part of an adaptive immune system in bacteria. Several studies have reported the similarities between the phage DNA and these repeated sequences (15–17). Further preclinical and animal model studies have demonstrated that CRISPR and CRISPR/Cas are associated to the adaptive immunity targeting foreign viral DNA (18). Mechanistically, two distinct RNAs including the CRISPR RNA (crRNA) and the trans-activating crRNA (tracrRNA) activate and guide Cas proteins to bind viral DNA sequences, which are subsequently cleaved together. The tracrRNA is a distinct type of RNA that interacts with the crRNA to produce the dual guide (g) RNA in CRISPR-Cas systems. The tracrRNA-crRNA interaction is pivotal for pre-crRNA processing, target recognition, and also cleavage.

CRISPR/Cas systems are adaptive (acquired) immune systems of prokaryotic and archaeal microorganisms and rely on ribonucleoprotein effector complexes. They eliminate invading phages, conjugative plasmids, and mobile genetic elements via reserving the memory of the encounters with foreign DNA in unique spacer sequences into CRISPR arrays (17–19). Naturally, CRISPR systems integrate foreign DNA molecule into CRISPR arrays, which subsequently produce crRNAs, and containing protospacer regions that are complementary to antigenic invading DNA molecules, followed by hybridizing each crRNA with other non-coding tracrRNA. A crucial event, which forms a hybrid of crRNA-tracrRNA, and makes a complex with Cas nucleases that cleave target-DNA sequences nearby to short sequences called protospacer adjacent motifs (PAMs) (20, 21). Genetic engineers can manipulate the CRISPR/Cas system efficiently and can target genes of interest to regulate their functions effectively in any eukaryotic organism, particularly in mammalian. The molecular biology of the CRISPR/Cas reveals how it can be operated while using synthetic guide RNAs (gRNAs) and other components to the target region of interest in DNA molecule for the desired application and finds the disease-causing genetic variations (22). Typically, the most widely used CRISPR system i.e., CRISPR/Cas9 targets 5′ of a PAM sequence. They induce double-stranded breaks (DSBs), which can be repaired by 2 DNA repair pathways called, homology directed repair (HDR) and non-homologous end joining (NHEJ) (22). HDR pathway facilitates precise gene modifications in the presence of a repair template (23). However, in the absence of a repair template, DSBs repaired by the NHEJ pathway that introduces insertion or deletions by editing DNA region, resulting in target genes disruption by shifting the reading frame (23, 24).

CRISPR/Cas nucleases-induced DSBs are mostly repaired by efficient eukaryotic cellular NHEJ pathway rather than by the HDR (25). Meanwhile, utilizing the Cas9 nickases can optimize the yields of indel at the genes loci, and enhance the HDR efficiency (26). The efficacy of the HDR pathway can be improved by enhancing the HDR pathway via gene silencing or suppressing non-homologous end-joining proteins activity (23), using small-molecule reagents (23, 27), or expressed proteins (26–28). Currently, DNA repair proteins have shown promising capacities in this regard, but *in vivo* implementation of these strategies are challenging. Moreover, DSBs in cells via DNA repair pathways are described that lead to many undesired genomic alterations, such as large deletions and translocations (29, 30). Various efforts have been made to improve HDR, such

as DNA donor template designing, system delivery, and cell cycle synchronization (26, 31–33).

PROS AND CONS OF CRISPR/CAS TECHNOLOGIES

In the last few years, advances in CRISPR/Cas technologies are spectacular and have shown considerable potential in several fields of life sciences research. CRISPR technologies are now considered more accurate, target-specific, easy to use, and multi-potential. Despite the remarkable advances in CRISPR, several limitations and concerns still exist, which need to be addressed and solved for the optimized Cas systems development. The current attempts at addressing all those concerns have been made to overcome these technical hurdles. In the following sections, the main limitations of the CRISPR technologies and recent advances to address them are discussed.

The off-target effects are still a major concern in complex eukaryotic organisms, most often *in vivo* for therapeutic applications (34, 35). The targeting specificity depends upon the gRNA of Cas9 and PAM sequences, and off-target cleavage in the genome (36). Different online editing programs have been developed and successfully utilized to identify and predict off-target cleavages *in silico*. However, these tools are limited to examining homologous genes and face shortcomings to predict, for example, epigenetic modifications. Technical advances like high throughput genome-wide next-generation sequencing, play an important role in reducing off-target effects (35, 37). Developing a well-optimized and engineered CRISPR system can significantly reduce the off-target effects. For instance, off-target effects can be reduced via increasing the nucleases cleavage specificity or reducing the time frame of functional activity for their applications. Different Cas proteins that exhibit enhancements in on-target specificity have been engineered that include eSpCas9, HF-Cas9, HypaCas9, and Sniper Cas9 (38–41). Another approach is using Cas9 nickases, where one of the endonuclease domains were catalytically inactivated and as a result, the low off-target effect was analyzed in the genome (42, 43). Off-target effects induced by CRISPR can be reduced by limiting the duration of Cas9 activity. For example, the Cas9 system delivered via electroporation had shown a shorter half-life than delivered by other vector systems such as lentiviral or plasmid vector system-based cargo delivery methods. Dosage affects several parameters and the target specificity of cleavage can play an important role in their applications. Alternatively, the target specificity of Cas9 systems can be enhanced by direct modulation of the activity of the genome-editing proteins, Cas9 proteins, by reducing their activity following the target locus alteration (44). The Cas9 nucleases were activated by inserting a modified 4-hydroxytamoxifen-responsive intein, a cell-permeable small molecule, at specific positions in Cas9 (44). These conditionally active Cas9 systems could alter the target genomic sites and were reported to enhance the target specificity human cells, up to 25-folds higher than the wild-type Cas9 (44–47).

Recent evidences have demonstrated that CRISPR system could be a highly efficient approach for the gene editing and manipulation applications in a variety of eukaryotic cells. However, HDR and indel mutation in some genome sites have shown low efficiency. To address the insufficient indel of Cas-system in the target sites, some efforts have been made to increase efficacy by either Cas engineering or gRNA (48, 49). The CRISPR/Cas proteins preceded DSB after the recognition of a PAM sequence (50, 51). Each type of Cas proteins contain their PAM sequence in the genome. Broadly speaking, type II CRISPR/Cas recognizes 3′ G-rich DNA sequences, while another type V, preferred 5′ T-rich sequences for their application.

The main issue in genome editing approaches is the unavailability of PAM in the desired gene loci. However, a range of Cas-nucleases variances such as SpCas9 and Cas12a are now available that are decreasing PAM restriction (52, 53). These kinds of advancements will provide flexibility in genome editing for the desired specific targets. In other ways, artificial intelligence plays a critical role and has been adopted for experimental designing to predict target sequences with high indel efficiency (54). The desired HDR efficiency to make genes functionally correct remains low, though different chemical and engineering tools have been used, i.e., chemical reagents, such as SCR7, NU7441, and KU0060648 (55, 56). The use of a donor template in the form of ssDNA led to increased HDR efficiency in cells (57). CRISPR/Cas often triggers cell apoptosis due to DSBs, rather than the desired genome editing (58). The safety issue raises when this genome editing system is utilized in human pluripotent stem cells (hPSCs). In response to DSBs by CRISPR, the activation of p53 occurred that triggers cellular apoptosis (59).

Recently, genome editing with base editors makes it possible to precisely fix desired targeted point mutations without requiring donor DNA templates, DSBs, or independence on HDR. In recent decades, these editing systems have been catalytically impaired nucleases, as a result, DSBs have not occurred. Importantly, 2 classes of base editors have been established; namely, cytosine base editors (CBEs) and adenine base editors (ABEs); they enable to catalyze the C•G base pairs (bp) conversion to T•A bp, and A•T bp to G•C bp, respectively (60–62). Besides these, catalytically inactivated CRISPR-dCas9 (dCas9) was applied for epigenome modifications instead of a genome that can alter gene regulation. CRISPRa and CRISPRi system has been developed to activate and silence genes, respectively (63). For example, dCas9 in combination with histone deacetylase (HDAC), improved CRISPR system efficacy and optimal positioning and developed an organized system to study epigenome (64). The evaluation of off-target effects can be analyzed through several online bioinformatics tools to predict potential off-targets with similar sequences, such as CCTop (https://crispr.cos.uniheidelberg.de), and Cas-OFFinder.

In addition, technical limitations and advances in the field of CRISPR technologies raise concerns for immunogenic toxicity. Recently, a study has shown that human subjects included, possessed pre-existing antibodies against Cas9. The obtained results showed that more than 50% of their subjects included in the study had immunity against the commonly used bacterial nucleases (65). In their study, the two extensively studied

nucleases for gene therapy of Cas orthologs i.e., SaCas9 and SpCas9, were prevalent in human blood, and the human immune system has shown an immunogenic response against these nucleases. In this regard, extensive studies should be conducted particularly, for *in vivo* gene therapy applications. Furthermore, the gRNA triggers an innate immune response in human cells due to the presence of the phosphate group at the 5′ terminal (66). In addition, CRISPR has been extensively applied in clinical trials to modify somatic cells *ex vivo*, with the aim of reducing risk, and subsequently, transferring for *in vivo* gene therapy applications. However, the germ-line gene editing studies for therapeutic purposes still face ethical challenges. In this regard, the ongoing and near-future clinical trials on somatic CRISPR therapy need to be evaluated for the long-term to check the system efficacy and safety.

CRISPR DELIVERY APPROACHES AND CHALLENGES

An efficient delivery of both Cas9 and the single guide RNA (sgRNA) to the target cell is required for a successful *in vivo* administration of CRISPR/Cas9. The delivery approach should have high editing efficiency, induce low immunogenicity and deliver the Cas9/sgRNA specifically to the target organ or cell type. The first generation genome editing strategies in mammalian cells have been utilized the plasmid based expression of Cas9 and sgRNA (8, 9). Moreover, this approach is efficient for *in vivo* applications in model organisms such as mice because the plasmid can be delivered to the tissue by hydrodynamic injection (67) or electroporation (68–70). However, in these applications the targeting delivery and editing efficiency are limited and control over the Cas9 activity is poor. Therefore, different viral and non-viral delivery strategies have been developed to enhance the performance of *in vivo* delivery of Cas9/sgRNA (71–73).

Adeno-associated virus (AAV) vectors are effective and among the most common used viral vectors for gene therapy because of their unique features including non-integrating nature, high transduction efficiency and serologically compatible with most of human population (74–77). Furthermore, the rich diversity of serotypes with distinct tissue tropisms enables AAVs to selectively target different organs (78, 79). However, the main limiting issue of AAVs for delivery of CRISPR and Cas9 is the limited cargo size of AAVs, so that the Cas systems and sgRNA should be encoded on additional separate vectors (74). AAVs can be administrated systemically or directly applied to the target organ for genome editing applications (75, 80–82). Using lipid nanoparticles (LNPs) is an alternative approach to viral delivery, which offer availability, low cost and high compatibility (83–85). LNPs have been employed for successful delivery of siRNA and mRNA in clinical trials (83, 86). Moreover, recent studies have demonstrated that LNPs can encapsulate and deliver the sgRNA and Cas9 mRNA to murine liver with high delivery efficiency and targeting performance (87–90). Furthermore, multifunction and modified nanoparticles can be additionally loaded with a donor template and thereby allow homology directed repair (91). However, the nanoparticles based carriers with a donor template suffer low editing efficiency (91). The main focus of the current research is on improving and establishing CRISRP/Cas9 as a gene repair tool. However, it is expected that CRISPR/Cas9 would be translated into a therapeutic agent for cancer treatment in clinical setting. To achieve this goal, the main step is developing effective carriers for tissue-specific delivery of Cas9/sgRNA (92–94).

Low editing efficiency in tumors and potential toxicity of the currently available delivery systems are the main limiting factors against translation of CRISPR/Cas9 technology into cancer therapeutics. The presence of an appropriate and effective alternative of delivery strategy is critical for CRISPR/Cas9 delivery, particularly where genome editing systems should be effectively conducted in the targeted organisms or cells. Until now, *in vivo* delivery of the Cas9 system remains challenging. Both physical techniques and viral vectors have been utilized for the delivery of the Cas9-based gene editing platform. The physical approaches are more feasible for *in vitro* delivery, but the viral vectors based techniques usually suffer limited packing capacities and poor safety profile. Recent preclinical and animal studies have demonstrated promising delivery performance and targeting efficacy of non-viral drug delivery systems such as polymeric and lipid nanocarriers for the delivery of CRISPR/Cas9 systems. These non-viral vectors are expected to be candidate carriers for the genome editing platform in the near future. The efforts in optimizing cationic nanocarriers with structural modification are described and promising non-viral vectors under clinical investigations are highlighted.

Different studies have recently developed a safe and effective strategy for antibody-targeted cell-specific delivery of mRNAs and siRNAs through systemically administration of LNPs (95–97). In this regard, few studies have reported promising outcomes in using LNPs for the delivery of Cas9 mRNA and sgRNAs. The initial findings showed that aminoionizable LNPs could serve as a safe and efficient carrier for Cas9 components (87). Rosenblum et al. reported a single intracerebral injection of CRISPR-LNPs against *PLK1* (sgPLK1-cLNPs) into metastatic orthotopic glioblastoma enhanced the *in vivo* gene editing specificity up to ∼70%, which inhibited tumor growth by 50%, induced tumor cell apoptosis, and enhanced survival by 30% (87). The cLNPs were engineered for antibody-targeted cell specific delivery to reach the distributed tumors (87, 88, 97, 98). Intraperitoneal injections of sgPLK1-cLNPs targeting EGFR improved the site specificity of gene editing *in vivo* by 80% for distributed ovarian tumors, and inhibited tumor growth, and increased survival by 80% (87). The capacity of disrupting gene expression *in vivo* in tumors is a promising feature for translating CRISPR tools into clinical applications and paves the way for developing gene editing techniques for cancer research and treatment and potential applications for targeted gene editing of non-malignant tissues.

Methods of Delivery

CRISPR technology has been reported one of the most promising therapeutic tool that could efficiently correct a variety of disease-associated mutations. In this view, it must be transported directly to their target site.

Multiple techniques have been developed for CRISPR delivery such as physical, viral, and non-viral delivery systems (99).

Physical methods include microinjection, transfection, and electroporation that are most suitable for research purposes in cell culture. However, these strategies can be used for *ex-vivo* cell manipulation for adoptive transfer (100). Multiple studies revealed the delivery of Cas9 protein/gRNA ribonucleoprotein complexes into many cells of mammals by electroporation or transfection mediated by liposomes (101, 102). The findings of the studies have reported that the rate of insertion/deletion (InDel), induced by nuclease was 87% in induced pluripotent stem cells (iPSC). Furthermore, off-target cleavage was decreased, as compared with the transfection in plasmid DNA (102). Cas9/gRNAs delivered by lentiviral transduction or plasmid transfection have a longer half-life relative to Cas9–RNP complexes delivered through electroporation. Furthermore, Cas9-RNPs are active immediately post-delivery due to no lag, however, protein synthesis occurs. A reported study has been revealed that LNPs can efficiently deliver Cas9-RNP (71). Viral vectors, such as adenovirus, lentivirus, and adeno-associated virus (AAV) vectors have been used for delivery in clinical trials. Lentiviral vectors have been derived from HIV that provide stable and efficient delivery and can infect dividing as well as non-dividing cells, including the brain cells. Viral genes, such as vpr, vif, and nef are not needed for packaging. Therefore, the underlined genes are deleted while the expression of packaging genes are provided on separate plasmids to decrease the probabilities of reconstruction of wild-type virus (103). Moreover, lentiviral vectors are not suitable for therapeutic uses due to integration but this risk can be lowered via IDLV (104). Adenoviruses are viruses containing a linear double-stranded DNA genome of around 36 Kbp in length with four early and five late transcription units. The majority of the vectors are based upon adenovirus type 5 (Ad5). A recombinant virus has been constructed by removal of the early gene E1 or E1 plus E3 and grown in a packaging cell line that shows the expression of E1 to form infectious recombinant virus. Adenovirus can infect dividing as well as non-dividing cells and not show integration into the host genome (104).

Despite these applications, lentivirus and adenovirus vectors having some drawbacks, particularly safety problems associated with their immunogenicity (105). AAV vectors have significantly lower immunogenicity. AAV is a 4.7 Kb single-stranded DNA virus that needs E1 for the packaging of infectious viruses and can transduce dividing as well as non-dividing cells. In infected cells, the AAV genome can persist in an episomal form, but infrequently shows integration in the host genome. The most commonly used vectors for delivery of Cas9 are AAV because these vectors are very efficient and low immunogenic (106). However, the large size of the Cas9 endonuclease is a complication in its effective delivery with the gene for Streptococcus pyogenes Cas9 being about 4.2 Kb, while the size limit for AAV is between ∼4.5 to 4.9Kb (**Figure 1**). Ran et al. (108) described Cas9 orthologs and revealed that Streptococcus aureus (SaCas9) shows similar potency of editing to SpCas9, but is over 1 Kb shorter and can specifically and efficiently perform gene editing. In recent years, the isolation of another Cas9 ortholog has been carried out from Campylobacter jejuni, which is shorter with a size of 2.95 Kb (109). It has been revealed that the packaging of the CjCas9 gene could be performed in an AAV vector along with gRNA and a marker gene for the generation of high viral titers that may deliver more specific CjCas9, and was revealed to be a targeted endonuclease.

CRISPR APPLICATIONS IN CANCER RESEARCH

Cancer is a disease of aberrant cell signaling that occurs due to a variety of genetic and epigenetic alterations in DNA. These alterations include the oncogenes, which enhance cell proliferation, and the tumor suppressors, which regulate cell growth and metabolism. The underline alterations lead to cancer progression. Nowadays, the ability of CRISPR to correct such cancer-associated alterations is an important objective for cancer diagnosis, cancer therapy, and other related applications. Hence, CRISPR is a promising tool that has been widely adopted in oncology research (**Figure 2**) with focusing on; animal tumor model construction, the discovery of new drug targets; cancer gene therapy, genetic screening related to drug resistance, and many others. In the below section, some of the promising applications of CRISPR in cancer research are summarized.

CRISPR for Tumor Research Modeling

Understanding complex mechanisms at the molecular level that drive tumor progression is a crucial step to advance therapeutics development. Usually, tumors arise due to multiple gene mutations, and this complexity makes it difficult for the development of full-pledge cancer models. In this view, the CRISPR system was considerably used to establish rapid tumor models, both *in vitro* and *in vivo*. These models allow identifying the genetic determinants and a comprehensive detail of the mechanisms that underlying tumor occurrence, progression, and development.

The generation of *in vitro* cancer model, while using CRISPR/Cas in mammalian cell lines with single or multiple gene(s) deletions is now easy and feasible (110), such as CRISPR-based mediated silencing of MELK, a cancer drug (OTS167) target in several clinical trials. The inactivation of MELK via CRISPR remains sensitive to OTS167 and does not affect the potency of cancer-derived cell lines. The underlined study explores the use of CRISPR that accelerate targeted cancer therapy research (111). Furthermore, CRISPR is applied to knock in or knock out functional alleles to develop drug resistance *in vitro*. CRISPR makes it possible to quickly evaluate candidate genes or specific mutations, associated with drug resistance (112). In this regard, a study was performed using CRISPR to identify mutations in crucial genes involved in therapeutic resistance that might be used for drug developmental strategies. For instance, NAMPT has been identified as the main drug target for the anti-cancer agent i.e., KPT-9274 (113). CRISPR, a versatile tool can be utilized to explore the genetic complexity of human cancer malignancies, such as myeloid malignancies, a malignancy that is driven by mutations in several genes, including Dnmt3a, Trp53, Tet2, Runx1, Ezh2, Smc3, Nf1, and Asxl1. By using the CRISPR system in single mouse hematopoietic stem cells, up

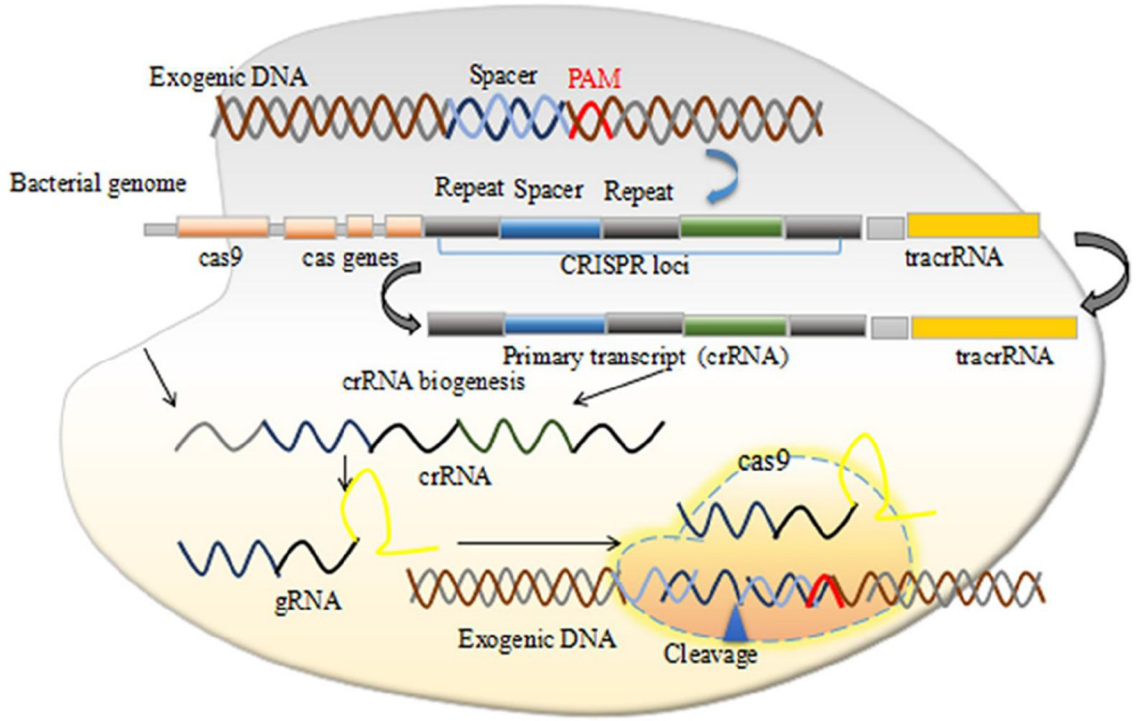

FIGURE 1 | The CRISPR/Cas9 mechanism of action. Permission from (107).

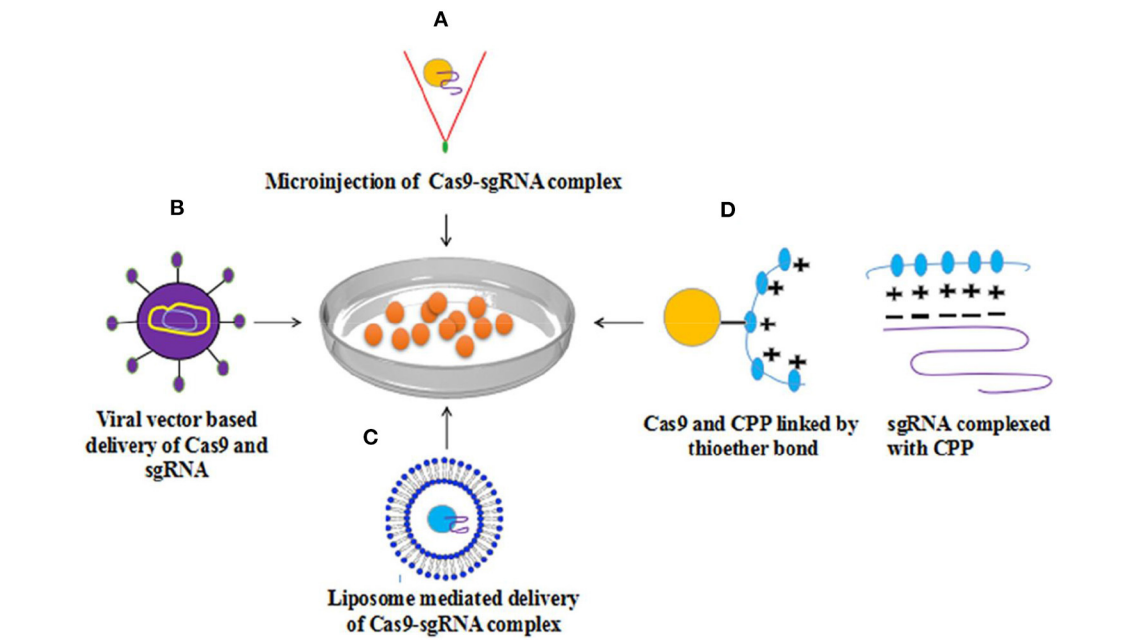

FIGURE 2 | Methods for delivery of Cas9-sgRNA complex to cell **(A)** Microinjection based delivery of Cas9-sgRNA **(B)** viral vector (AAV) based delivery **(C)** Lipofection **(D)** Cas9-sgRNA complex delivery into mammalian cells via Cell-penetrating peptides (CPP) revealed considerable genome editing with elevated level efficiency. With permission (107).

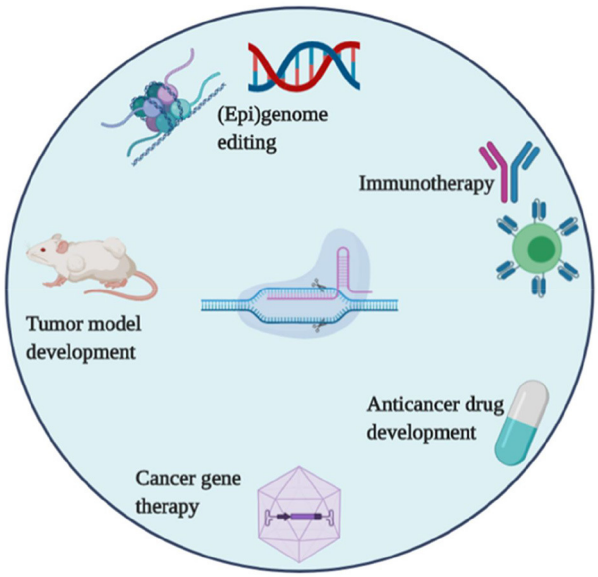

FIGURE 3 | CRISPR/Cas systems applications in tumor research, drug development, and cancer therapies.

to 5 genes were modified that induce the myeloid malignancies in mice (114). This study highlights the role of multiple gene mutations in cancer. CRISPR/Cas systems can be used to establish an *in vivo* tumor model. In exploring a complex mechanism of tumorigenesis, the *in vivo* cancer models play a critical role in the finding of key events i.e., pathogenesis and drug resistance. For example, the CRISPR system was used to attain mutations in important genes; P53, Kras, and Lkb1 in mice. These modifications/mutations in mice led to pathological changes in lung adenocarcinoma (115). The delivery of CRISPR cargoes into the living system plays an important role in model generation. For example, a lentiviral vector system used to deliver CRISPR into the desired target organs *in vivo* that create specific malignancy models (**Figure 3**) (116, 117).

CRISPR-Based Screening Approaches in Cancer

CRISPR is effectively utilized to facilitate the discovery of next-generation targets or candidate genes that are sensitive or resistant to cancer therapy. Using the CRISPR system, several genetic screening studies were performed *in vitro*. It has been reported that in melanoma, the CRISPR library was applied to find the drug resistance mechanism of vemurafenib (PLX), an inhibitor of the BRAF protein kinase. In this study, new PLX-resistant candidates namely; TADA1, TADA2B, CUL3, and NF2 have been revealed (118). Moreover, using cell lines, the CRISPR screening has been utilized to identify oncogenes, and tumor suppressors *in vivo* (119, 120). The study showed the loss-of-function genetic screens and *in vivo* tumor mice models using CRISPR, and confirmed candidates gene and the pathways that are connected in the sensitivity and development of resistance to cancer immunotherapy (121). Strong evidences have highlighted the role of the Cas9 system in combination with RNA scaffolds that can be applied to induce site-specific epigenetic and transcriptional modifications while targeting a crucial region of the OCT4 promoters (122, 123). The OCT4 gene is recognized as one of the key players, which plays a critical role in tumorigenesis and therapy resistance.

Targeting Gene Regulation in Cancer

In cancer, gene regulation has affected both post-transcriptional and translational modifications that evolve cancer cells to survive and adapt within the microenvironment. For example; the Knockdown of micro RNAs (miRNAs) that enhance tumor initiation and development can prevent tumor occurrence, development, and anti-cancer therapy resistance. In this view, a study found a knocked-out miR-17 in colorectal cell line and injected into nude mice (124). The obtained results showed a stable gene-phenotype even after 2 weeks in tumor tissue which indicated that CRISPR can play a critical role in targeting miRNAs and can effectively target tumorigenic miRNAs. In cancers, abnormal expression of epigenetic regulatory genes plays an important role in tumorigenesis processes. Targeting acetyltransferase p300 (associated with a catalytic histone H3 lysine acetylation) using CRISPR system can activate gene promoters and co-regulatory components, which in turn facilitate the expression of the target gene and the associated genes (125).

Tumor Immuno-Regulation and Immunotherapy Approaches

Tumor immune escape is one of the key mechanisms of the cancer cell to survive and adapted in the tumor microenvironment, while the immune system unable to recognize it. Subsequently, tumor cells leash the immune cells through multiple pathways and thereby tumor cell progression and metastasis occur. Cancer immunotherapy is considered as an attractive strategy to target cancers and emerged as a potential therapeutic modality for the treatment of cancers. However, issues are existing to make it more precise for cancer patients (126, 127). In recent years, genetically engineered T cells against tumors have shown remarkable therapeutic effectiveness and performance. In human immune system, T cells play crucial roles in protecting the human body from infection by pathogens and eliminating mutant cells through specific recognition by T cell receptors (TCRs). Cancer immunotherapy utilizes the TCRs based recognition strategy to enhance the antitumor efficacy of T cells through releasing the inhibition of immune checkpoints and expanding adaptive immunity by promoting the adoptive transfer of genetically engineered T cells. T cells genetically equipped with chimeric antigen receptors (CARs) or TCRs have demonstrated significant effectiveness in treating different hematological disorders. However, the main issue of this approach is limited efficacy of engineered T cells in treating solid tumors. CRISPR system provides a new way to make engineered T-cells more efficient for the clinical treatment of different types of cancers (128). Moreover, the production of chimeric antigen receptor T (CAR-T) cells are significantly associated with the cancer therapy. Using CRISPR/Cas9, T-cells are genetically

engineered *in vitro*, where the genes have been inserted and CAR protein have been expressed on the cell-surface that activated and recognized antigen on malignant cells very efficiently (129). Currently, several clinical trials are underway, using CRISPR for cancer immunotherapy applications (clinicaltrials.gov). However, several efficacy and safety challenges still exist on using CRISPR/Cas for clinical applications.

CONCLUSION AND PERSPECTIVES

The precipitous development in CRISPR technologies to their versatile and precise genome engineering in the last few years has been spectacular. These versatile tools now consider as an umbrella term, which revolutionized the life sciences and enabling advances in basic research for a variety of applications. It is believed that CRISPR can be established in clinics that can offer many therapeutic opportunities for treating human diseases, including cancer. Continued progress to improve and revolutionize new ways to deliver genome engineering tools into cells, and advance their capabilities to edit can implement these technologies for many therapeutic applications. CRISPR/Cas systems are widely utilized in tumor research for many applications both *in vitro* and *in vivo* models. Several clinical trials are currently underway, using the CRISPR/Cas system to accelerate or making the therapies more reliable to treat cancer effectively. However, extensive research work is still required to develop and applied these technologies in clinics. These technologies can provide wide-ranging opportunities for specific and desired genome engineering and can become a potent asset for the modern era of medicine. Continuous efforts to understand all their pitfalls, improving editing capabilities, and advances in the delivery systems will ensure the CRISPR system for the full potential to benefit society in near future.

AUTHOR CONTRIBUTIONS

YY and LL: conceptualization, methodology, and writing—review and editing. YY, JX, SG, and LL: resources, data curation, and writing—original draft preparation. YY: supervision, project administration. YY and JX: funding acquisition. All authors contributed to the article and approved the submitted version.

FUNDING

This work was supported by the Chinese Medical and Health Research Project of Zhejiang Province, China (Grant No. 2021ZB052 granted to YY and 2018ZT002 granted to JX).

REFERENCES

1. Fitzmaurice C, Abate D, Abbasi N, Abbastabar H, Abd-Allah F, Abdel-Rahman O, et al. Global, regional, and national cancer incidence, mortality, years of life lost, years lived with disability, and disability-Adjusted life-years for 29 cancer groups, 1990 to 2017: a systematic analysis for the global burden of disease study. *JAMA Oncol.* (2019) 5:1749–68. doi: 10.1001/jamaoncol.2019.2996
2. Tomczak K, Czerwińska P, Wiznerowicz M. The cancer genome atlas (TCGA): an immeasurable source of knowledge. *Contemp Oncol.* (2015) 19:A68–77. doi: 10.5114/wo.2014.47136
3. Lee JK, Choi YL, Kwon M, Park PJ. Mechanisms and consequences of cancer genome instability: lessons from genome sequencing studies. *Annu Rev Pathol Mech Dis.* (2016) 11:283–312. doi: 10.1146/annurev-pathol-012615-044446
4. Garraway LA, Lander ES. Lessons from the cancer genome. *Cell.* (2013) 153:17–37. doi: 10.1016/j.cell.2013.03.002
5. Chmielecki J, Meyerson M. DNA sequencing of cancer: what have we learned? *Annu Rev Med.* (2014) 65:63–79. doi: 10.1146/annurev-med-060712-200152
6. Joung JK, Sander JD. TALENs: a widely applicable technology for targeted genome editing. *Nat Rev Mol Cell Biol.* (2013) 14:49–55. doi: 10.1038/nrm3486
7. Urnov FD, Rebar EJ, Holmes MC, Zhang HS, Gregory PD. Genome editing with engineered zinc finger nucleases. *Nat Rev Genet.* (2010) 11:636–46. doi: 10.1038/nrg2842
8. Cong L, Ran FA, Cox D, Lin S, Barretto R, Habib N, et al. Multiplex genome engineering using CRISPR/Cas systems. *Science.* (2013) 339:819–23. doi: 10.1126/science.1231143
9. Mali P, Yang L, Esvelt KM, Aach J, Guell M, DiCarlo JE, et al. RNA-guided human genome engineering via Cas9. *Science.* (2013) 339:823–6. doi: 10.1126/science.1232033
10. Nelson CE, Gersbach CA. Engineering delivery vehicles for genome editing. *Annu Rev Chem Biomol Eng.* (2016) 7:637–62. doi: 10.1146/annurev-chembioeng-080615-034711
11. Chen Y, Zhang Y. Application of the CRISPR/Cas9 system to drug resistance in breast cancer. *Adv Sci.* (2018) 5:1700964. doi: 10.1002/advs.201700964
12. Nishida K, Arazoe T, Yachie N, Banno S, Kakimoto M, Tabata M, et al. Targeted nucleotide editing using hybrid prokaryotic and vertebrate adaptive immune systems. *Science.* (2016) 353:aaf8729. doi: 10.1126/science.aaf8729
13. Ishino Y, Shinagawa H, Makino K, Amemura M, Nakatura A. Nucleotide sequence of the iap gene, responsible for alkaline phosphatase isoenzyme conversion in Escherichia coli, and identification of the gene product. *J Bacteriol.* (1987) 169:5429–33. doi: 10.1128/JB.169.12.5429-5433.1987
14. Kampmann M. CRISPRi and CRISPRa screens in mammalian cells for precision biology and medicine. *ACS Chem Biol.* (2018) 13:406–16. doi: 10.1021/acschembio.7b00657
15. Bolotin A, Quinquis B, Sorokin A, Dusko Ehrlich S. Clustered regularly interspaced short palindrome repeats (CRISPRs) have spacers of extrachromosomal origin. *Microbiology.* (2005) 151:2551–61. doi: 10.1099/mic.0.28048-0
16. Pourcel C, Salvignol G, Vergnaud G. CRISPR elements in Yersinia pestis acquire new repeats by preferential uptake of bacteriophage DNA, and provide additional tools for evolutionary studies. *Microbiology.* (2005) 151:653–63. doi: 10.1099/mic.0.27437-0
17. Mojica FJ, Díez-Villaseñor C, García-Martínez J, Soria E. Intervening sequences of regularly spaced prokaryotic repeats derive from foreign genetic elements. *J Mol Evol.* (2005) 60:174–82. doi: 10.1007/s00239-004-0046-3
18. Barrangou R, Fremaux C, Deveau H, Richards M, Boyaval P, Moineau S, et al. CRISPR provides acquired resistance against viruses in prokaryotes. *Science.* (2007) 315:1709–12. doi: 10.1126/science.1138140
19. Godde JS, Bickerton A. The repetitive DNA elements called CRISPRs and their associated genes: evidence of horizontal transfer among prokaryotes. *J Mol Evol.* (2006) 62:718–29. doi: 10.1007/s00239-005-0223-z
20. Deltcheva E, Chylinski K, Sharma CM, Gonzales K, Chao Y, Pirzada ZA, et al. CRISPR RNA maturation by trans-encoded small RNA and host factor RNase III. *Nature.* (2011) 471:602–5. doi: 10.1038/nature09886
21. Jinek M, Chylinski K, Fonfara I, Hauer M, Doudna JA, Charpentier E. A programmable dual-RNA-guided DNA endonuclease in adaptive bacterial immunity. *Science.* (2012) 337:816–21. doi: 10.1126/science.1225829

22. Sander JD, Joung JK. CRISPR-Cas systems for editing, regulating and targeting genomes. *Nat Biotechnol.* (2014) 32:347–55. doi: 10.1038/nbt.2842
23. Yeh CD, Richardson CD, Corn JE. Advances in genome editing through control of DNA repair pathways. *Nat Cell Biol.* (2019) 21:1468–78. doi: 10.1038/s41556-019-0425-z
24. Lieber MR, Ma Y, Pannicke U, Schwarz K. Mechanism and regulation of human non-homologous DNA end-joining. *Nat Rev Mol Cell Biol.* (2003) 4:712–20. doi: 10.1038/nrm1202
25. Lieber M. The mechanism of double-strand DNA break repair by the nonhomologous DNA end-joining pathway. *Annu Rev Biochem.* (2010) 79:181–211. doi: 10.1146/annurev.biochem.052308.093131
26. Richardson CD, Ray GJ, DeWitt MA, Curie GL, Corn JE. Enhancing homology-directed genome editing by catalytically active inactive CRISPR-Cas9 using asymmetric donor DNA. *Nat Biotechnol.* (2016) 34:339–44. doi: 10.1038/nbt.3481
27. Chu VT, Weber T, Wefers B, Wurst W, Sander S, Rajewsky K, et al. Increasing the efficiency of homology-directed repair for CRISPR-Cas9-induced precise gene editing in mammalian cells. *Nat Biotechnol.* (2015) 33:543–8. doi: 10.1038/nbt.3198
28. Canny MD, Moatti N, Wan LCK, Fradet-Turcotte A, Krasner D, Mateos-Gomez PA, et al. Inhibition of 53BP1 favors homology-dependent DNA repair and increases CRISPR-Cas9 genome-editing efficiency. *Nat Biotechnol.* (2018) 36:95–102. doi: 10.1038/nbt.4021
29. Kosicki M, Tomberg K, Bradley A. Repair of double-strand breaks induced by CRISPR-Cas9 leads to large deletions and complex rearrangements. *Nat Biotechnol.* (2018) 36:765–71. doi: 10.1038/nbt.4192
30. Cullot G, Boutin J, Toutain J, Prat F, Pennamen P, Rooryck C, et al. CRISPR-Cas9 genome editing induces megabase-scale chromosomal truncations. *Nat Commun.* (2019) 10:1136–55. doi: 10.1038/s41467-019-09006-2
31. Renaud JB, Boix C, Charpentier M, De Cian A, Cochennec J, Duvernois-Berthet E, et al. Improved genome editing efficiency and flexibility using modified oligonucleotides with TALEN and CRISPR-Cas9 nucleases. *Cell Rep.* (2016) 14:2263–72. doi: 10.1016/j.celrep.2016.02.018
32. Nishiyama J, Mikuni T, Yasuda R. Virus-mediated genome editing via homology-directed repair in mitotic and postmitotic cells in mammalian brain. *Neuron.* (2017) 96:755–68. doi: 10.1016/j.neuron.2017.10.004
33. Lin S, Staahl BT, Alla RK, Doudna JA. Enhanced homology-directed human genome engineering by controlled timing of CRISPR/Cas9 delivery. *Elife.* (2014) 3:e04766. doi: 10.7554/eLife.04766
34. Yang HC, Chen PJ. The potential and challenges of CRISPR-Cas in eradication of hepatitis B virus covalently closed circular DNA. *Virus Res.* (2018) 244:304–10. doi: 10.1016/j.virusres.2017.06.010
35. Zischewski J, Fischer R, Bortesi L. Detection of on-target and off-target mutations generated by CRISPR/Cas9 and other sequence-specific nucleases. *Biotechnol Adv.* (2017) 35:95–104. doi: 10.1016/j.biotechadv.2016.12.003
36. Suleiman AAJ, Saedi WY, Muhaidi MJ. Widely used gene editing strategies in cancer treatment a systematic review. *Gene Rep.* (2020) 1:100983–99. doi: 10.1016/j.genrep.2020.100983
37. Yee J. Off-target effects of engineered nucleases. *FEBS J.* (2016) 283:3239–48. doi: 10.1111/febs.13760
38. Lee JK, Jeong E, Lee J, Jung M, Shin E, Kim Y, et al. Directed evolution of CRISPR-Cas9 to increase its specificity. *Nat Commun.* (2018) 9:3048. doi: 10.1038/s41467-018-05477-x
39. Lee J, Jung MH, Jeong E, Lee JK. Using sniper-Cas9 to minimize off-target effects of CRISPR-Cas9 without the loss of on-target activity via directed evolution. *J Vis Exp.* (2019) 144:e59202-10. doi: 10.3791/59202
40. Chen JS, Dagdas YS, Kleinstiver BP, Welch MM, Sousa AA, Harrington LB, et al. Enhanced proofreading governs CRISPR-Cas9 targeting accuracy. *Nature.* (2017) 550:407–10. doi: 10.1038/nature24268
41. Hu JH, Miller SM, Geurts MH, Tang W, Chen L, Sun N, et al. Evolved Cas9 variants with broad PAM compatibility and high DNA specificity. *Nature.* (2018) 556:57–63. doi: 10.1038/nature26155
42. Tsai SQ JKJ. Defining and improving the genome-wide specificities of CRISPR–Cas9 nucleases. *Nat Rev Genet.* (2016) 17:300–12. doi: 10.1038/nrg.2016.28
43. Tycko J, Myer VE, Hsu PD. Methods for optimizing CRISPR-Cas9 genome editing specificity. *Mol Cell.* (2016) 63:355–70. doi: 10.1016/j.molcel.2016.07.004
44. Davis KM, Pattanayak V, Thompson DB, Zuris JA, Liu DR. Small molecule–triggered Cas9 protein with improved genome-editing specificity. *Nat Chem Biol.* (2015) 11:316–8. doi: 10.1038/nchembio.1793
45. Carlson-Stevermer J, Das A, Abdeen AA, Fiflis D, Grindel BI, Saxena S, et al. Design of efficacious somatic cell genome editing strategies for recessive and polygenic diseases. *Nat Commun.* (2020) 11:6277. doi: 10.1038/s41467-020-20065-8
46. Li L, Hu S, Chen X. Non-viral delivery systems for CRISPR/Cas9-based genome editing: challenges and opportunities. *Biomaterials.* (2018) 177:207–18. doi: 10.1016/j.biomaterials.2018.04.031
47. Ghosh D, Venkataramani P, Nandi S, Bhattacharjee S. CRISPR-Cas9 a boon or bane: the bumpy road ahead to cancer therapeutics. *Cancer Cell Int.* (2019) 19:12. doi: 10.1186/s12935-019-0726-0
48. Strecker J, Jones S, Koopal B, Schmid-Burgk J, Zetsche B, Gao L, et al. Engineering of CRISPR-Cas12b for human genome editing. *Nat Commun.* (2019) 10:212. doi: 10.1038/s41467-018-08224-4
49. Moon SB, Kim DY, Ko JH, Kim JS, Kim YS. Improving CRISPR genome editing by engineering guide RNAs. *Trends Biotechnol.* (2019) 37:870–81. doi: 10.1016/j.tibtech.2019.01.009
50. Nishimasu H, Shi X, Ishiguro S, Gao L, Hirano S, Okazaki S, et al. Engineered CRISPR-Cas9 nuclease with expanded targeting space. *Science.* (2018) 361:1259–62. doi: 10.1126/science.aas9129
51. Adli M. The CRISPR tool kit for genome editing and beyond. *Nat Commun.* (2018) 9:1911. doi: 10.1038/s41467-018-04252-2
52. Kleinstiver BP, Prew MS, Tsai SQ, Topkar VV, Nguyen NT, Zheng Z, et al. Engineered CRISPR-Cas9 nucleases with altered PAM specificities. *Nature.* (2015) 523:481–5. doi: 10.1038/nature14592
53. Gao L, Cox DBT, Yan WX, Manteiga JC, Schneider MW, Yamano T, et al. Engineered Cpf1 variants with altered PAM specificities. *Nat Biotechnol.* (2017) 35:789–92. doi: 10.1038/nbt.3900
54. Kim HK, Min S, Song M, Jung S, Choi JW, Kim Y, et al. Deep learning improves prediction of CRISPR–Cpf1 guide RNA activity. *Nat Biotechnol.* (2018) 36:239–48. doi: 10.1038/nbt.4061
55. Maruyama T, Dougan SK, Truttmann MC, Bilate AM, Ingram JR, Ploegh HL. Increasing the efficiency of precise genome editing with CRISPR-Cas9 by inhibition of nonhomologous end joining. *Nat Biotechnol.* (2015) 33:538–42. doi: 10.1038/nbt.3190
56. Robert F, Barbeau M, Éthier S, Dostie J, Pelletier J. Pharmacological inhibition of DNA-PK stimulates Cas9-mediated genome editing. *Genome Med.* (2015) 7:93–101. doi: 10.1186/s13073-015-0215-6
57. Lee K, Mackley VA, Rao A, Chong AT, Dewitt MA, Corn JE, et al. Synthetically modified guide RNA and donor DNA are a versatile platform for CRISPR-Cas9 engineering. *Elife.* (2016) 6:e25312–25325. doi: 10.7554/eLife.25312
58. Hu Z, Yu L, Zhu D, Ding W, Wang X, Zhang C, et al. Disruption of HPV16-E7 by CRISPR/Cas system induces apoptosis and growth inhibition in HPV16 positive human cervical cancer cells. *Biomed Res Int.* (2014) 2014:612823–37. doi: 10.1155/2014/612823
59. Ihry RJ, Worringer KA, Salick MR, Frias E, Ho D, Theriault K, et al. p53 inhibits CRISPR–Cas9 engineering in human pluripotent stem cells. *Nat Med.* (2018) 24:939–46. doi: 10.1038/s41591-018-0050-6
60. Komor AC, Kim YB, Packer MS, Zuris JA, Liu DR, et al. Programmable editing of a target base in genomic DNA without double-stranded DNA cleavage. *Nature.* (2016) 533:420–4. doi: 10.1038/nature17946
61. Gaudelli NM, Komor AC, Rees HA, Packer MS, Badran AH, Bryson DI, et al. Programmable base editing of A● T to G● C in genomic DNA without DNA cleavage. *Nature.* (2017) 551:464–71. doi: 10.1038/nature24644
62. Rees HA DRL. Base editing: precision chemistry on the genome and transcriptome of living cells. *Nat Rev Genet.* (2018) 19:770–88. doi: 10.1038/s41576-018-0059-1
63. Gilbert LA, Horlbeck MA, Adamson B, Villalta JE, Chen Y, Whitehead EH, et al. Genome-scale CRISPR-mediated control of gene repression and activation. *Cell.* (2014) 159:647–61. doi: 10.1016/j.cell.2014.09.029
64. Kwon DY, Zhao YT, Lamonica JM, Zhou Z. Locus-specific histone deacetylation using a synthetic CRISPR-Cas9-based HDAC. *Nat Commun.* (2017) 8:15315. doi: 10.1038/ncomms15315
65. Charlesworth CT, Deshpande PS, Dever DP, Camarena J, Lemgart VT, Cromer MK, et al. Identification of preexisting adaptive

immunity to Cas9 proteins in humans. *Nat Med.* (2019) 25:249–54. doi: 10.1038/s41591-018-0326-x
66. Kim S, Koo T, Jee HG, Cho HY, Lee G, Lim DG, et al. CRISPR RNAs trigger innate immune responses in human cells. *Genome Res.* (2018) 28:367–73. doi: 10.1101/gr.231936.117
67. Xue W, Chen S, Yin H, Tammela T, Papagiannakopoulos T, Joshi NS, et al. CRISPR-mediated direct mutation of cancer genes in the mouse liver. *Nature.* (2014) 514:380–4. doi: 10.1038/nature13589
68. Yadollahpour A, Rezaee Z. Electroporation as a new cancer treatment technique: a review on the mechanisms of action. *Biomed Pharmacol J.* (2014) 7:53–62. Available online at: https://www.scopus.com/inward/record.uri?eid=2-s2.0-84908121242&doi=10.13005%2Fbpj%2F452&partnerID=40&md5=c6a7d7239b624985f4116e34a6fe5a29
69. Zuckermann M, Hovestadt V, Knobbe-Thomsen CB, Zapatka M, Northcott PA, Schramm K, et al. Somatic CRISPR/Cas9-mediated tumour suppressor disruption enables versatile brain tumour modelling. *Nat Commun.* (2015) 6:7391. doi: 10.1038/ncomms8391
70. Maresch R, Mueller S, Veltkamp C, Öllinger R, Friedrich M, Heid I, et al. Multiplexed pancreatic genome engineering and cancer induction by transfection-based CRISPR/Cas9 delivery in mice. *Nat Commun.* (2016) 7:10770. doi: 10.1038/ncomms10770
71. Chen F, Alphonse M, Liu Q. Strategies for nonviral nanoparticle-based delivery of CRISPR/Cas9 therapeutics. *Wiley Interdiscip Rev Nanomed Nanobiotechnol.* (2020) 12:e1609–17. doi: 10.1002/wnan.1609
72. Lv P, Liu X, Chen X, Liu C, Zhang Y, Chu C, et al. Genetically engineered cell membrane nanovesicles for oncolytic adenovirus delivery: a versatile platform for cancer virotherapy. *Nano Lett.* (2019) 19:2993–3001. doi: 10.1021/acs.nanolett.9b00145
73. Yadollahpour A, Rashidi S. Magnetic nanoparticles: a review of chemical and physical characteristics important in medical applications. *Orient J Chem.* (2015) 31:25–30. doi: 10.13005/ojc/31.Special-Issue1.03
74. Senís E, Fatouros C, Große S, Wiedtke E, Niopek D, Mueller AK, et al. CRISPR/Cas9-mediated genome engineering: an adeno-associated viral (AAV) vector toolbox. *Biotechnol J.* (2014) 9:1402–12. doi: 10.1002/biot.201400046
75. Yang Y, Wang L, Bell P, McMenamin D, He Z, White J, et al. A dual AAV system enables the Cas9-mediated correction of a metabolic liver disease in newborn mice. *Nat Biotechnol.* (2016) 34:334–8. doi: 10.1038/nbt.3469
76. Luo J, Luo Y, Sun J, Zhou Y, Zhang Y, Yang X. Adeno-associated virus-mediated cancer gene therapy: current status. *Cancer Lett.* (2015) 356:347–56. doi: 10.1016/j.canlet.2014.10.045
77. Yadollahpour A, Hosseini SAA, Jalilifar M, Rashidi S, Rai BMM. Magnetic nanoparticle-based drug and gene delivery: a review of recent advances and clinical applications. *Int J Pharm Technol.* (2016) 8:11451–66. Available online at: https://www.scopus.com/inward/record.uri?eid=2-s2.0-84975275516&partnerID=40&md5=733b63c2cadfcb469915e0c8561f60af
78. Zincarelli C, Soltys S, Rengo G, Rabinowitz JE. Analysis of AAV serotypes 1-9 mediated gene expression and tropism in mice after systemic injection. *Mol Ther.* (2008) 16:1073–80. doi: 10.1038/mt.2008.76
79. Nieto K, Stahl-Hennig C, Leuchs B, Müller M, Gissmann L, Kleinschmidt JA. Intranasal vaccination with AAV5 and 9 vectors against human papillomavirus type 16 in rhesus macaques. *Hum Gene Ther.* (2012) 23:733–41. doi: 10.1089/hum.2011.202
80. Yu W, Mookherjee S, Chaitankar V, Hiriyanna S, Kim JW, Brooks M, et al. Nrl knockdown by AAV-delivered CRISPR/Cas9 prevents retinal degeneration in mice. *Nat Commun.* (2017) 8:14716. doi: 10.1038/ncomms14716
81. Yang S, Chang R, Yang H, Zhao T, Hong Y, Kong HE, et al. CRISPR/Cas9-mediated gene editing ameliorates neurotoxicity in mouse model of Huntington's disease. *J Clin Invest.* (2017) 127:2719–24. doi: 10.1172/JCI92087
82. Bengtsson NE, Hall JK, Odom GL, Phelps MP, Andrus CR, Hawkins RD, et al. Muscle-specific CRISPR/Cas9 dystrophin gene editing ameliorates pathophysiology in a mouse model for duchenne muscular dystrophy. *Nat Commun.* (2017) 8:16007. doi: 10.1038/ncomms16007
83. Mehnert W, Mäder K. Solid lipid nanoparticles: production, characterization and applications. *Adv Drug Deliv Rev.* (2001) 47:165–96. doi: 10.1016/S0169-409X(01)00105-3
84. Yadollahpour A. Magnetic nanoparticles in medicine: a review of synthesis methods and important characteristics. *Orient J Chem.* (2015) 31:271–7. Available online at: https://www.scopus.com/inward/record.uri?eid=2-s2.0-84983071862&doi=10.13005%2Fojc%2F31.Special-Issue1.33&partnerID=40&md5=bdb96f69ed4c5140be8cff16f4edded4
85. Yadollahpour A, Rashidi S. Magnetic nanoparticles: a review of chemical and physical characteristics important in medical applications. *Orient J Chem.* (2015) 31:25–30. Available online at: https://www.scopus.com/inward/record.uri?eid=2-s2.0-84983233410&doi=10.13005%2Fojc%2F31.Special-Issue1.03&partnerID=40&md5=5a631cd2f5948d5aa5cdce8f6a6a4c5f
86. Pardi N, Hogan MJ, Pelc RS, Muramatsu H, Andersen H, DeMaso CR, et al. Zika virus protection by a single low-dose nucleoside-modified mRNA vaccination. *Nature.* (2017) 543:248–51. doi: 10.1038/nature21428
87. Rosenblum D, Gutkin A, Kedmi R, Ramishetti S, Veiga N, Jacobi AM, et al. CRISPR-Cas9 genome editing using targeted lipid nanoparticles for cancer therapy. *Sci Adv.* (2020) 6:eabc9450. doi: 10.1126/sciadv.abc9450
88. Finn JD, Smith AR, Patel MC, Shaw L, Youniss MR, van Heteren J, et al. A single administration of CRISPR/Cas9 lipid nanoparticles achieves robust and persistent *in vivo* genome editing. *Cell Rep.* (2018) 22:2227–35. doi: 10.1016/j.celrep.2018.02.014
89. Miller JB, Zhang S, Kos P, Xiong H, Zhou K, Perelman SS, et al. Non-Viral CRISPR/Cas gene editing *in vitro* and *in vivo* enabled by synthetic nanoparticle co-delivery of Cas9 mRNA and sgRNA. *Angew Chem Int Ed.* (2017) 56:1059–63. doi: 10.1002/anie.201610209
90. Jiang C, Mei M, Li B, Zhu X, Zu W, Tian Y, et al. A non-viral CRISPR/Cas9 delivery system for therapeutically targeting HBV DNA and pcsk9 *in vivo*. *Cell Res.* (2017) 27:440–3. doi: 10.1038/cr.2017.16
91. Lee K, Conboy M, Park HM, Jiang F, Kim HJ, Dewitt MA, et al. Nanoparticle delivery of Cas9 ribonucleoprotein and donor DNA *in vivo* induces homology-directed DNA repair. *Nat Biomed Eng.* (2017) 1:889–901. doi: 10.1038/s41551-017-0137-2
92. Barata P, Sood AK, Hong DS. RNA-targeted therapeutics in cancer clinical trials: Current status and future directions. *Cancer Treat Rev.* (2016) 50:35–47. doi: 10.1016/j.ctrv.2016.08.004
93. Fougerolles A De, Manoharan M, Meyers R, Vornlocher HP. RNA interference *in vivo*: toward synthetic small inhibitory RNA-based therapeutics. *Methods Enzymol.* (2005) 392:278–96. doi: 10.1016/S0076-6879(04)92016-2
94. O'Loughlin AJ, Mäger I, de Jong OG, Varela MA, Schiffelers RM, El Andaloussi S, et al. Functional delivery of lipid-conjugated siRNA by extracellular vesicles. *Mol Ther.* (2017) 25:1580–7. doi: 10.1016/j.ymthe.2017.03.021
95. Kedmi R, Veiga N, Ramishetti S, Goldsmith M, Rosenblum D, Dammes N, et al. A modular platform for targeted RNAi therapeutics. *Nat Nanotechnol.* (2018) 13:214–9. doi: 10.1038/s41565-017-0043-5
96. Veiga N, Goldsmith M, Granot Y, Rosenblum D, Dammes N, Kedmi R, et al. Cell specific delivery of modified mRNA expressing therapeutic proteins to leukocytes. *Nat Commun.* (2018) 9:4493. doi: 10.1038/s41467-018-06936-1
97. Aksoy YA, Yang B, Chen W, Hung T, Kuchel RP, Zammit NW, et al. Spatial and Temporal control of CRISPR-Cas9-mediated gene editing delivered via a light-triggered liposome system. *ACS Appl Mater Interfaces.* (2020) 12:52433–44. doi: 10.1021/acsami.0c16380
98. Liu J, Chang J, Jiang Y, Meng X, Sun T, Mao L, et al. Fast and efficient CRISPR/Cas9 genome editing *in vivo* enabled by bioreducible lipid and messenger RNA nanoparticles. *Adv Mater.* (2019) 31:e1902575. doi: 10.1002/adma.201902575
99. Rahimi H, Salehiabar M, Charmi J, Barsbay M, Ghaffarlou M, Razlighi MR, et al. Harnessing nanoparticles for the efficient delivery of the CRISPR/Cas9 system. *Nano Today.* (2020) 34:100895–9. doi: 10.1016/j.nantod.2020.100895
100. Li Y, Glass Z, Huang M, Chen ZY, Xu Q. *Ex vivo* cell-based CRISPR/Cas9 genome editing for therapeutic applications. *Biomaterials.* (2020) 234:119711. doi: 10.1016/j.biomaterials.2019.119711
101. Liu W, Rudis MR, Cheplick MH, Millwood RJ, Yang JP, Ondzighi-Assoume CA, et al. Lipofection-mediated genome editing using DNA-free delivery of the Cas9/gRNA ribonucleoprotein into plant cells. *Plant Cell Rep.* (2020) 39:245–57. doi: 10.1007/s00299-019-02488-w
102. Liang X, Potter J, Kumar S, Zou Y, Quintanilla R, Sridharan M, et al. Rapid and highly efficient mammalian cell engineering

via Cas9 protein transfection. *J Biotechnol.* (2015) 208:44–53. doi: 10.1016/j.jbiotec.2015.04.024
103. Hayashi H, Kubo Y, Izumida M, Matsuyama T. Efficient viral delivery of Cas9 into human safe harbor. *Sci Rep.* (2020) 10:1–14. doi: 10.1038/s41598-020-78450-8
104. White MK, Hu W, Khalili K. Gene editing approaches against viral infections and strategy to prevent occurrence of viral escape. *PLoS Pathog.* (2016) 12:e1005953. doi: 10.1371/journal.ppat.1005953
105. Xu CL, Ruan MZ, Mahajan VB, Tsang SH. Viral delivery systems for CRISPR. *Viruses.* (2019) 11:28–35. doi: 10.3390/v11010028
106. Yilmaz BS, Gurung S, Perocheau D, Counsell J, Baruteau J. Gene therapy for inherited metabolic diseases. *J Mother Child.* (2020) 24:53–64. doi: 10.34763/jmotherandchild.20202402si.2004.000009
107. Khan FA, Pandupuspitasari NS, Chun-Jie H, Ao Z, Jamal M, Zohaib A, et al. CRISPR/Cas9 therapeutics: a cure for cancer and other genetic diseases. *Oncotarget.* (2016) 7:52541–52. doi: 10.18632/oncotarget.9646
108. Ran FA, Cong L, Yan WX, Scott DA, Gootenberg JS, Kriz AJ, et al. *In vivo* genome editing using *Staphylococcus aureus* Cas9. *Nature.* (2015) 520:186–91. doi: 10.1038/nature14299
109. Yoo KH, Hennighausen L, Shin HY. Dissecting tissue-specific super-enhancers by integrating genome-wide analyses and CRISPR/Cas9 genome editing. *J Mammary Gland Biol Neoplasia.* (2019) 24:47–59. doi: 10.1007/s10911-018-9417-z
110. Fellmann C, Gowen BG, Lin PC, Doudna JA, Corn JE. Cornerstones of CRISPR–Cas in drug discovery and therapy. *Nat Rev Drug Discov.* (2017) 16:89–100. doi: 10.1038/nrd.2016.238
111. Lin A, Giuliano CJ, Sayles NM, Sheltzer JM. CRISPR/Cas9 mutagenesis invalidates a putative cancer dependency targeted in on-going clinical trials. *Elife.* (2017) 6:e24179. doi: 10.7554/eLife.24179
112. Smurnyy Y, Cai M, Wu H, McWhinnie E, Tallarico JA, Yang Y, et al. DNA sequencing and CRISPR-Cas9 gene editing for target validation in mammalian cells. *Nat Chem Biol.* (2014) 10:623–5. doi: 10.1038/nchembio.1550
113. Neggers JE, Kwanten B, Dierckx T, Noguchi H, Voet A, Bral L, et al. Target identification of small molecules using large-scale CRISPR-Cas mutagenesis scanning of essential genes. *Nat Commun.* (2018) 9:502. doi: 10.1038/s41467-017-02349-8
114. Heckl D, Kowalczyk MS, Yudovich D, Belizaire R, Puram RV, McConkey ME, et al. Generation of mouse models of myeloid malignancy with combinatorial genetic lesions using CRISPR-Cas9 genome editing. *Nat Biotechnol.* (2014) 32:941–6. doi: 10.1038/nbt.2951
115. Platt RJ, Chen S, Zhou Y, Yim MJ, Swiech L, Kempton HR, et al. CRISPR-Cas9 knockin mice for genome editing and cancer modeling. *Cell.* (2014) 159:440–55. doi: 10.1016/j.cell.2014.09.014
116. Annunziato S, Kas SM, Nethe M, Yücel H, Del Bravo J, Pritchard C, et al. Modeling invasive lobular breast carcinoma by CRISPR/Cas9-mediated somatic genome editing of the mammary gland. *Genes Dev.* (2016) 30:1470–80. doi: 10.1101/gad.279190.116
117. Rogers ZN, McFarland CD, Winters IP, Seoane JA, Brady JJ, Yoon S, et al. Mapping the *in vivo* fitness landscape of lung adenocarcinoma tumor suppression in mice. *Nat Genet.* (2018) 50:483–6. doi: 10.1038/s41588-018-0083-2
118. Shalem O, Sanjana NE, Hartenian E, Shi X, Scott DA, Mikkelsen TS, et al. Genome-scale CRISPR-Cas9 knockout screening in human cells. *Science.* (2014) 343:84–7. doi: 10.1126/science.1247005
119. Braun CJ, Bruno PM, Horlbeck MA, Gilbert LA, Weissman JS, Hemann MT. Versatile *in vivo* regulation of tumor phenotypes by dCas9-mediated transcriptional perturbation. *Proc Natl Acad Sic USA.* (2016) 113:E3892–900. doi: 10.1073/pnas.1600582113
120. Song CQ, Li Y, Mou H, Moore J, Park A, Pomyen Y, et al. Genome-wide CRISPR screen identifies regulators of mitogen-activated protein kinase as suppressors of liver tumors in mice. *Gastroenterology.* (2017) 152:1161–73. doi: 10.1053/j.gastro.2016.12.002
121. Manguso RT, Pope HW, Zimmer MD, Brown FD, Yates KB, Miller BC, et al. *In vivo* CRISPR screening identifies Ptpn2 as a cancer immunotherapy target. *Nature.* (2017) 547:413–8. doi: 10.1038/nature23270
122. Fogarty NM, McCarthy A, Snijders KE, Powell BE, Kubikova N, Blakeley P, et al. Genome editing reveals a role for OCT4 in human embryogenesis. *Nature.* (2017) 550:67–73. doi: 10.1038/nature24033
123. Zalatan JG, Lee ME, Almeida R, Gilbert LA, Whitehead EH, La Russa M, et al. Engineering complex synthetic transcriptional programs with CRISPR RNA scaffolds. *Cell.* (2015) 160:339–50. doi: 10.1016/j.cell.2014.11.052
124. Chang H, Yi B, Ma R, Zhang X, Zhao H, Xi Y. CRISPR/cas9, a novel genomic tool to knock down microRNA *in vitro* and *in vivo*. *Sci Rep.* (2016) 6:22312. doi: 10.1038/srep22312
125. Hilton IB, D'ippolito AM, Vockley CM, Thakore PI, Crawford GE, Reddy TE, et al. Epigenome editing by a CRISPR-Cas9-based acetyltransferase activates genes from promoters and enhancers. *Nat Biotechnol.* (2015) 33:510–7. doi: 10.1038/nbt.3199
126. Khalil DN, Smith EL, Brentjens RJ, Wolchok JD. The future of cancer treatment: immunomodulation, CARs and combination immunotherapy. *Nat Rev Clin Oncol.* (2016) 13:273–90. doi: 10.1038/nrclinonc.2016.25
127. Morris EC, Stauss HJ. Optimizing T-cell receptor gene therapy for hematologic malignancies. *Blood, J Am Soc Hematol.* (2016) 127:3305–11. doi: 10.1182/blood-2015-11-629071
128. Kick L, Kirchner M, Schneider S. CRISPR-Cas9: from a bacterial immune system to genome-edited human cells in clinical trials. *Bioengineered.* (2017) 8:280–6. doi: 10.1080/21655979.2017.1299834
129. Benmebarek MR, Karches CH, Cadilha BL, Lesch S, Endres S, Kobold S. Killing mechanisms of chimeric antigen receptor (CAR) T cells. *Int J Mol Sci.* (2019) 20:1283–91. doi: 10.3390/ijms20061283

Conflict of Interest: The authors declare that the research was conducted in the absence of any commercial or financial relationships that could be construed as a potential conflict of interest.

frontiers in Medicine

ORIGINAL RESEARCH
published: 18 March 2021
doi: 10.3389/fmed.2021.650996

Correlation Between Pulmonary Sclerosing Pneumocytoma Features and MSCT Imaging Manifestations in 34 Patients: Implications for Precision Medicine

Gen Xu [1], Zhaoyu Wang [2], Zeng Xiong [3], Manqiu Li [4], Weijun Luo [3], Yong Xu [1] and Tang Min [1]*

[1] Department of Radiology, First People's Hospital of Pingjiang County, Yueyang, China, [2] Shanghai Hengdao Medical Pathology Diagnostic Center, Shanghai, China, [3] Department of Radiology, Xiangya Hospital, Central South University, Changsha, China, [4] Department of Pathology, First People's Hospital of Pingjiang County, Yueyang, China

OPEN ACCESS

Edited by:
Ali Yadollahpour, The University of Sheffield, United Kingdom

Reviewed by:
Fangzhou Song, Chongqing Medical University, China
Zhijian Fu, Shandong Provincial Hospital, China

***Correspondence:**
Zeng Xiong
drxiongzeng@hotmail.com

Specialty section:
This article was submitted to Precision Medicine, a section of the journal Frontiers in Medicine

Received: *08 January 2021*
Accepted: *18 February 2021*
Published: *18 March 2021*

Citation:
Xu G, Wang Z, Xiong Z, Li M, Luo W, Xu Y and Min T (2021) Correlation Between Pulmonary Sclerosing Pneumocytoma Features and MSCT Imaging Manifestations in 34 Patients: Implications for Precision Medicine. Front. Med. 8:650996. doi: 10.3389/fmed.2021.650996

Objective: To identify and analyze the multi-slice computed tomography (MSCT) imaging manifestations and clinicopathological features of PSP to improve the preoperative and intraoperative diagnosis of the disease.

Method: This was a retrospective study conducted on the imaging and clinicopathological data of the PSP patients treated in two major hospitals in China from October 2001 to December 2019. The locations of lung lesions, clinical symptoms, surgical complications, MSCT imaging features, and the corresponding relationship with clinicopathological features were assessed. Then, a new diagnostic approach was defined and used to train imaging and pathological doctors (experimental group). Then, the diagnostic accuracy of the experimental group was evaluated in preoperative and intraoperative diagnosis of PSP.

Results: Thirty-four PSP cases were analyzed (mean: 51.42; range: 39–69 years old). The peripheral type was more common, while 92% of the lesions located in the middle lobe of the right lung and the lower lobe of bilateral lungs. The shortest lesion edge-pleura distance ranged 0 to 30 mm and 46% of the lesions (16/34) were attached to the pleura, 62% (21/34) located at 0–5 mm, 92% (31/34) within 20 mm from the pleura. Diameters of the lesions ranged 8.58 to 68.41 mm, while most of them were 20-40 mm. All lesions showed enhancement, and 97% (33/34) were unevenly enhanced. PSP volume was negatively correlated with the total degree of enhancement ($r = -0.587$, $p < 0.01$), and the volume difference between the obvious enhancement zone and the slight enhancement zone ($r = -0.795$, $p < 0.01$). Welt vessel sign was observed in 61.7% (21/34) of cases, and none of welt vessels entered into the lesions. Vascular-like enhancement area inside the lesion showed no significant correlation with the welt vessels outside the lesion, and no case showed entrance of bronchus into the lesion. The trained experimental group showed significantly greater diagnostic accuracy than the

control group. In particular, the accuracy rate of intraoperative frozen section diagnosis was 60% higher in the experimental group than the control group.

Conclusion: PSP has characteristic imaging manifestations, which can be utilized to improve the preoperative and intraoperative diagnostic coincidence rate of PSP.

Keywords: pulmonary sclerosing pneumocytoma, pathology, multi-slice computed tomography, image pathological control, diagnosis

INTRODUCTION

Pulmonary sclerosing pneumocytoma (PSP), formerly known as pulmonary sclerosing hemangioma (PSH), was first reported by Liehow and Huhell in 1956 as an uncommon lesion with an uncertain origin (1). PSP manifests a pulmonary neoplasm with a complicated and an undefined histogenesis. It was later found to be a tumor in the lung parenchyma that originated from type II alveolar epithelial cells and had a successful clinical process (2, 3). World Health Organization (WHO) (2015) has histologically classified lung tumors and renamed it as pulmonary sclerosing pneumocytoma and identified as a lung adenoma (4). PSP has been reported as the most common benign tumor in the lung, while the incidence rate was relatively high in East Asia. More than 80% of cases occurred in middle-aged women $>$ 50 years of age (5, 6). Since most PSPs were discovered by accident, there were no typical reliable clinical manifestations, and the accuracy rate of the intraoperative frozen section (FSS) was 44.1%, while the delay rate was 15.3% (4). Despite of benign nature, PSP represents a diagnostic challenge due to its controversial etiology and biologic behavior, as well as the diversity of pathohistological findings. The main diagnostic challenge of PSP is that it represents a diversity of pathohistological findings (7). Therefore, the diagnostic accuracy of the preoperative imaging is particularly important. Moreover, definitive diagnosis of PSP currently relies mainly on surgical pathology because the preoperative imaging modalities show poor specificity.

Computed tomography (CT) imaging modalities have shown significant diagnostic and differential diagnostic values for different lung disorders (8–12). PSPs comprise of 4 major histologic patterns with different proportions including hemangiomatous, papillary, sclerotic, and solid. These patterns manifest demonstrate various CT features depending on the composition of PSP (13–18). Studies have demonstrated that CT imaging particularly multi-slice CT (MSCT) imaging offer promising diagnostic values for early or differential diagnosis of different pulmonary lesions and disorders including tuberculosis and diffuse peritoneal lesions (12, 16, 18–20). Meng et al. retrospectively analyzed CT imaging manifestations of three common diffuse peritoneal lesions to evaluate the diagnostic and differential diagnostic value of CT in diffuse peritoneal lesions (19). They analyzed features of CT imaging in patients with diffuse peritoneal lesions (72), including 16 cases with tuberculous peritonitis ($n = 16$), peritoneal metastasis (21), and peritoneal mesothelioma (22). They reported that specific features of CT images have significant diagnostic values for the differential diagnosis of peritoneal diffused lesions. These features are the location of peritoneal lesions, morphology, ascitic fluid and lymph nodes. He et al. retrospectively analyzed the CT features of PSP in 33 patients (confirmed by pathology) to improve the correct rate of CT in diagnosis of PSP. They scanned all patients with plain CT scan and in 29 patients they performed simultaneous CT enhanced scan in addition (18). They reported that PSP is often manifested as a single round soft tissue density nodule. Enhanced scan is characterized by obvious enhancement and continuous enhancement of delayed scan, with some characteristic concomitant signs. They concluded that by considering the variations in CT images associated by age and sex, the diagnostic accuracy of CT images could be improved (18). Reviewing the findings of CT imaging studies in PSP cases it can be clarified that PSP usually manifests as a well-defined, juxta-pleural nodule with strong and homogeneous enhancement on CT (13–16, 23).

Few studies have so far evaluated CT findings of PSP and analyzed the imaging features to determine its pathologic correlation (14, 22, 23). However, the main issue with the previous studies is that the sample size was very small and more importantly the clinical practice still suffers limitations in diagnosis of PSD. These limitations are mainly because the currently used preoperative imaging modalities based on these studies suffer poor specificity and slow process.

The present study was aimed to summarize and evaluate the corresponding relationships between the clinical-pathological features and the MSCT imaging manifestations of PSP in order to improve the preoperative and intraoperative diagnosis of the disease.

MATERIALS AND METHODS

Study Design and Population

All experimental procedures of this study were approved by the local ethics committee of Xiangya Hospital, Central South University, Changsha, China (Code: 202006082) that are in complete accordance with the ethical standards and regulations of human studies of the Helsinki declaration (2014). A total of 34 cases of PSP, who were diagnosed with surgical resection, pathology, and immunohistochemistry, were selected from Xiangya Hospital of Central South University and the First People's Hospital of Pingjiang County, Hunan Province, China from October 2001 to December 2019. The MSCT and pathological data of patients were reviewed. The related information, including gender, age, tumor size, tumor location, pathological features, and imaging manifestations, were

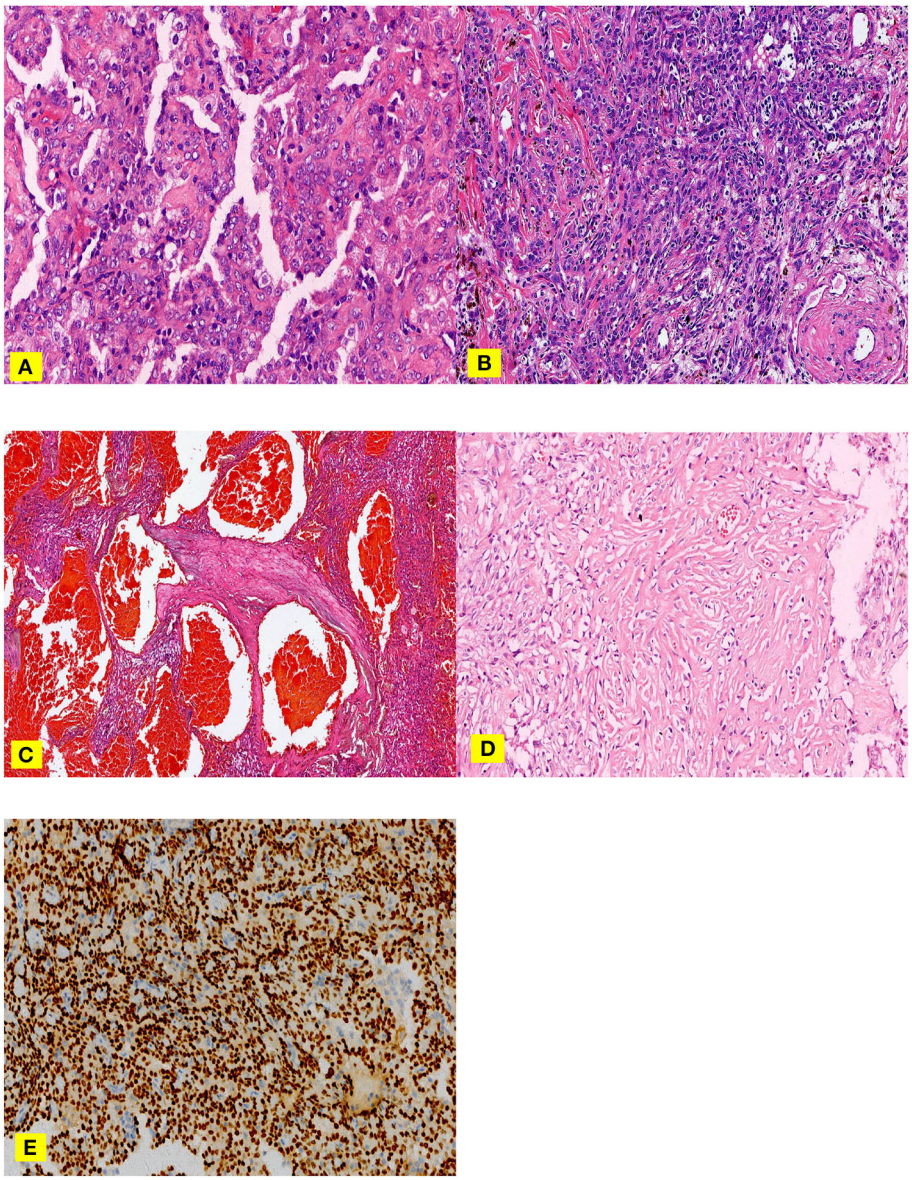

FIGURE 1 | (A–E). H &E staining **(A–C)**, nipple area: surface cubic cells covered on the nipple surface and polygonal cells in the nipple interstitium can be observed **(A)** Solid area: cells were dense, the size was the same, and it was in the shape of a sheet **(B)** Hemangioma-like area: the vasculature-like space dilation, which filled with a large amount of fresh red blood cells. **(C)** Sclerosing area: a large amount of collagen fibers was observed, in which various inflammatory cells and adenoid-like structures lining with a small amount of surface cubic cells. TTF-1 **(E)** Surface cubic cells and polygonal cells were positive.

recorded. None of the selected cases were combined with malignant changes, and the cases of intra-lung metastasis of lung cancer or metastatic lung cancer were excluded. The basis and classification of the pathological diagnosis were referred to WHO (2015) for the histological classification of lung tumors.

Preparation of Tissue Samples

All specimens were fixed with 3.7% neutral formaldehyde, dehydrated routinely, and embedded in paraffin to make wax blocks. A paraffin block with tumor tissues was selected, and each paraffin block was cut into a 4 μm thick section for Hematoxylin and eosin (H&E) staining procedure (**Figure 1**). The slice was then observed under a light microscope. They were read by two attending physicians with relevant experience in the pathology department. If any inconsistencies found, then a third deputy chief physician in the pathology department was jointly discussed and decided.

MSCT Scanning Technology and Parameters

For the MSCT imaging we used the most recommended imaging protocol for focal and diffuse lung diseases recommended in literature and according to the instructions of the manufacturer

(24, 25). pulmonary lung The GE LightSpeed 64-slice Volume Computed Tomography (VCT) (GE Healthcare) with Nemoto high-pressure injector were used for image acquisition with the scan parameters of 120 kV and 10–400 mA. Automatic tube current modulation (ATCM) technology was used in which the noise index (NI) value was 15, the screw pitch 0.984: 1, speed 0.5 s, collimation width 64 × 0.625 mm, scanning layer thickness/layer interval 5 mm, reconstruction layer thickness 1.25 mm, and reconstruction interval was 0.5 mm. The subject was taken a supine position with feet entered first, the hands were straight up and raised with support. The scanning range was from the entrance of the rib cage to the bottom of the lungs. The scan was completed under a state of deep breath inhalation. Non-ionic contrast agent ioversol (concentration was 320 mg I/ml) was used, 60–75 ml contrast agent was injected through the right median cubital vein using a 20 G indwelling needle at an injection rate of 3.0 ml/s, followed by an injection of 30 ml normal saline at the same flow rate. Two-phase scanning was performed, while the arterial phase delay time was 25 s, and the parenchyma phase delay time was 60–70 s. After the scanning was completed, the reconstructed cross-section thin slice images were transferred to the AW4.5 workstation for post-processing, including multi-planar reconstruction (MPR), planar reconstruction (CPR) and volume rendering (VR). In the imaging protocol, the window settings (window-width and window-level values) were defined as follows. For mediastinal imaging (window width: 350 Hounsfield unit (HU); window-level: 40 HU) and for lung imaging (window width: 1200 HU; window level: −600 HU).

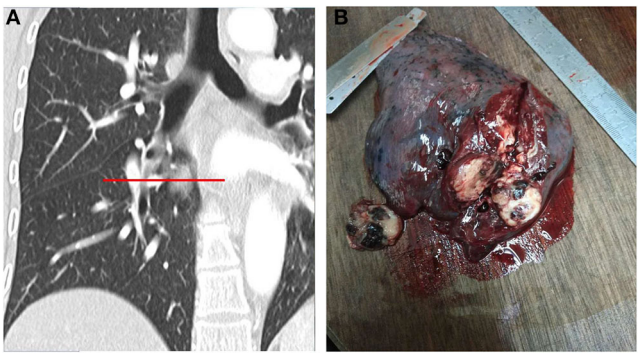

FIGURE 2 | (A,B). MSCT multiplanar reformation and simulation of gross specimen cut **(A)**. The gross specimen of PSP had a clear boundary and was easy to disassociate from the surrounding lung tissues. The cut surface was apricot-white-gray to yellow-brown, with a medium texture, and dark red bleeding areas can be observed **(B)**.

Evaluation and Measurement of MSCT Imaging Manifestations

Evaluation Methods

The MSCT image data of 34 patients were reviewed by two attending physicians with specific expertise in the radiology department. If any discrepancies found, then a third Deputy

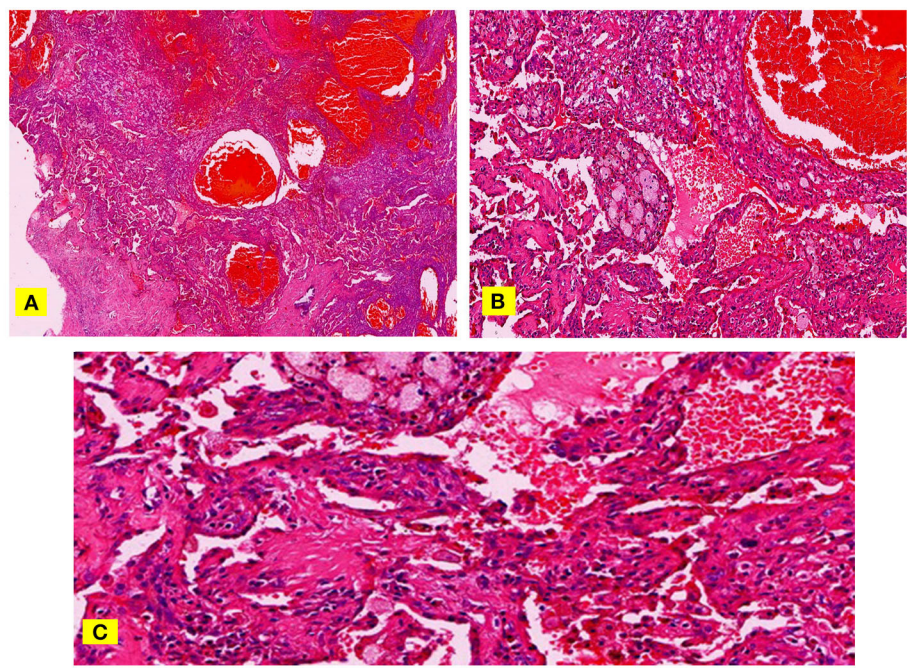

FIGURE 3 | (A–C) H & E staining, papillary stromal and hemangioma-like area filled with a lot of fresh red blood cells **(A)**. At high magnification, some nipples are immature and migrate to the hemangioma-like areas **(B)**. The space between these immature nipples is more obvious and communicates with the hemangioma-like area **(C)**.

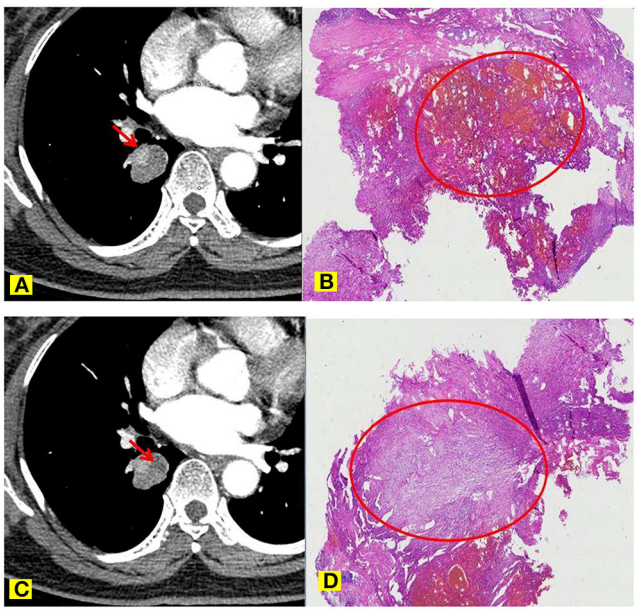

FIGURE 4 | (A–D). Comparison of MSCT imaging manifestations **(A)** and pathological features **(B)** of PSP nipple areas and hemangioma-like areas. Comparison of MSCT imaging manifestations **(C)** and pathological features **(D)** of PSP solid areas and sclerosing areas.

Chief Physician in the radiology department was jointly discussed and decided.

Similarly, the pathological section data of 34 patients were reviewed by two attending doctors in the pathology department with relevant experience and followed the same protocol as above.

Contents and Standards of Image Evaluation

The collected MSCT images were evaluated as per the following procedures.

1. The tumors were examined by their site and location, the shortest distance between the edge of the lesion and the pleura, morphology, size, density, etc.
2. External signs of tumors on MSCT have been identified by welt vessel sign, halo sign, air crescent sign, calcification, necrosis, cystic changes, lobulation sign, atelectasis, pleural traction and thickening, enlargement of hilar and mediastinal lymph nodes, etc.
3. Internal features of tumors on MSCT were evaluated using the image analyses. According to the net increased CT value, that was, the absolute value of the difference between the CT values of enhanced scan and the plan scan, referring to the Swensen standard (26), it was divided into a non-enhanced area (increased CT value <15 Hu), a marginally enhanced area (CT value increased by 15–25 Hu), a moderately enhanced area (CT value increased by 25–45 Hu), and a significantly enhanced area (CT value increased by> 45 Hu).

Contents and Standards of Pathological Evaluation

The pathological evaluations of the samples were conducted using conducted as follows:

1. Basic information on the size, location, central or peripheral type, and overall morphology of the tumors were examined and recorded by an expert oncologist.
2. Microscopic histopathological observations were done on H&E stained transverse section of the samples included two types of cells (surface cubic cells and polygonal cells) and four structures (nipple area, sclerosing area, solid area, and hemangioma-like area) while atypia cell was not visible, but foam cells were often present.
3. Immunohistochemical characteristics were achieved by diffuse TTF-1 positive expression when CK7 was expressed only on the surface of the epithelium.

Measurements

The measurements were performed as per the following steps:

1. When the long diameter of the lesion was higher than 10 mm, three consecutive levels were measured. If the CT value was >10 HU, the median value was considered. If the CT value of the three levels was equal or <10 Hu, then, the average value was considered.
2. If the long diameter of the lesion was <10 mm, the CT values of only 1–2 layers were measured, and the average value was taken.
3. When the range-of-interest (ROI) was >70% of the lesion, the selected measurement area avoided the necrosis, cystic, and calcification regions as much as possible.

Considering the above terms and criteria, the collected MSCT images were evaluated and the imaging features were recorded and sorted in the specific tables for further analyses (**Figure 2**). For each variable, three independent measurements were performed, and the averaged value was considered along with the standard deviation (SD).

Performance of a New Diagnostic Method in Clinical Setting

The performance and accuracy of the new diagnostic method were evaluated as per the following scenario:

5.1. Five radiologists were selected as an experimental group (one Deputy Chief Physician, two attending physicians, and two physicians), and the new diagnostic approach summarized above was used for teaching. Another five radiologists were selected as the control group (1 Deputy Chief Physician, two attending physicians, and two physicians), and the traditional diagnostic method was used for teaching. Both groups of physicians had a double-blind model, qualifications, years of experience, degrees, and proportions were the same. There was no statistically significant difference in composition ratios of age and gender. After the lecture, the two groups of doctors read the same set of PSP (pathologically confirmed) image data respectively and diagnosed the images. The coincidence rate of image-pathological diagnosis has been statistically

analyzed. There were 10 cases in each group, 1 point was awarded for each correct diagnosis.

5.2. Three radiologists were selected as an experimental group (1 Deputy Chief Physician and two attending physicians), and the new diagnostic method, summarized earlier was taught to them. The main features of the images, important to reach a diagnosis along with the samples were used to train the experimental group as the new diagnostic imaging. Another three radiologists were selected as the control group (1 Deputy Chief Physician and two attending physicians), and the standard diagnostic approach was used for teaching. Both groups of doctors used a double-blind model, qualifications, years of practice, degrees, and proportions were the same, and there was no statistically significant difference in composition ratios of age and gender. After the training course, the two groups of doctors read the same set of PSP (pathologically confirmed) image data respectively and then diagnosed the images. The coincidence rate of image-pathological diagnosis has been statistically analyzed. There were 10 cases in each group, 1 point was awarded for each correct diagnosis.

STATISTICAL ANALYSIS

6.1. Chi-square test and Fisher's exact probability method were used to evaluate the relationship between the type and extent of the MSCT enhancement, pathological characteristics, and various pathological tissue structures of the PSP. A multivariate regression model (Logistic model) was used to analyze the correlation between clinicopathological features and MSCT imaging of PSP and age, gender, location, the shortest distance between lesion margin and pleura, and histological types. All tests were two-sided, while $P < 0.05$ was considered as statistically significant. Statistical package for social sciences (SPSS) (version 21) package was used for statistical analysis.

RESULTS

Clinical Characteristics

A total of 34 patients with PSP were selected. There were 1 male (3%) and 33 females (97%), with a minimum age of 39 years, maximum age of 69 years, the average age of 51.42 years, and a median age of 52 years. The age was normally distributed. Among them, 14 cases (41.17%) were <50 years of age, and 20 cases (58.83%) were more than or equal to 50 years of age. Except for two cases of long-term cough and one evidence of blood in sputum, the remaining 31 cases were all identified by physical examinations. The median age of this group of cases was older than that reported in some literature at home and abroad, which may be because the recommended age of physical examination for LDCT was > 40 years old in Hunan Province, China. Since most PSPs were discovered by chance and did not have traditional and reliable clinical manifestations, the present study did not consider the impact of clinical signs and symptoms of PSP on the results of the research.

MSCT Plain Scanning Manifestations

Distribution

The results of the examination showed that all the 34 cases were single isolated lesions. They were located in the middle lobe of the right lung in 10 cases, the inferior lobe of the right lung in 10 cases, superior lobe of the left lung in 2 cases, inferior lobe of the left lung in 11 cases, and hilus pulmonis in 1 case.

Size

The long diameter of the lesion ranged from 8.58 to 68.41 mm, the small one was 8.58 mm, and the largest was about 68.41 mm. Most of the lesions ranged from 20 to 40 mm.

Lesion Margin-Pleura Shortest Distance

The shortest distance between the lesion margin and the pleura was between 0.00 and 29.16 mm. Among them, the lesion was grown attached to the pleura in 16 cases that was, the distance was 0.00 mm, the distance was 0–5 mm in 21 cases, 0–10 mm in 25 cases, 0–20 mm in 31 cases, and > 20 mm in three cases (**Figure 3**).

The Relationship Between the Lesion Size and the Distance From the Pleura

Through the Logistic model analysis, there was no significant correlation between the lesion size and the shortest distance from the pleura ($R^2 = 0.066$).

MSCT Enhancement Manifestations

Enhancement Form, Degree, and Characteristics

Among the 34 cases in this group, except for one PSP nodule with a long diameter of 8.58 mm, which was almost uniformly enhanced, the remaining cases showed uneven enhancement. The CT value of the apparent enhancement area in the lesion increased by an average of 67.06 HU, while the CT value of most lesions increased by 40–70 HU (**Figure 4**). The CT value of the slight enhancement area increased by an average of 16.22 HU, and the CT value of most lesions increased by 10–20 HU. The lesion was negatively correlated with the total degree of enhancement ($r = -0.587, p < 0.01$), and negatively correlated with the difference in volume between the obvious enhancement area and the slight enhancement area ($r = -0.795$, $p < 0.01$), that is, the smaller the lesion volume, the larger the obvious enhancement area, the smaller the slight enhancement area, the larger the lesion volume, the smaller the obvious enhancement area and the larger the slight enhancement area.

The Relationship Between Blood Vessels, Bronchus, and Lesions

Of the 34 cases in this group, 21 cases showed signs of welt vessel (61.7%), but none of these welt vessels entered the lesion, and there was no obvious correlation between the vascular-like enhancement area inside the lesion and the welt vessels outside the lesions. All the 24 cases had no bronchial entry into the lesions.

Pathological Manifestations

Gross Specimen

The 34 cases of PSP in this group had clear boundaries and were easily dissociated from the surrounding lung tissues. The colors of the cut surface were apricot-white-gray to yellow-brown, with a medium texture. In some cases, dark red bleeding areas, hemosiderin deposition areas, and calcification have been observed. In all cases, no mediastinum, hilus pulmonis, parabronchial, or interlobar lymph node metastasis were observed.

Microstructures

One case showed that the sclerosing area was not obvious, and the remaining 33 cases showed all four growth patterns (nipple area, sclerosing area, solid area, and hemangioma-like area). None of the cases showed one growth pattern. Among 34 cases, the solid area was dominated in 11 cases (32.3%), the sclerosing area was dominated in 9 cases (26.4%), the hemangioma-like area was dominated in 10 cases (29.4%), and nipple area was dominated in four cases (11.7%).

Immunohistochemistry

In all the 34 cases, immunohistochemical analysis showed positive expression of TTF-1 in polygonal cells and surface cubic cells.

EVALUATION OF IMAGING AND PATHOLOGICAL DIAGNOSTICIANS

The assessment results of the experimental group (nine points for imaging diagnosticians and eight points for pathological diagnosticians) were significantly higher than those for the control group (six points for imaging diagnosticians and five points for pathological diagnosticians). In particular, the accuracy of intraoperative frozen section diagnosis was 60% higher in the experimental group than that in the control group.

DISCUSSION

There were 33 females in this group of patients with PSP. Devouassoux-shishebonar et al. (27) investigated the immunohistochemistry of 100 cases of PSP and found that sex hormone receptors, especially progesterone receptors, were expressed in most of the PSP ring cells, suggesting that the high incidence in women was related to female hormones.

Statistics analysis revealed that all 34 cases of lesions in this group occurred in the lungs, with a peripheral type of 97%, in which 92% of the lesions (31/34) were within 20 mm from the pleura, and 46% of the lesions (16/34) were grown with attachment to the pleura (including mediastinal pleura and interlobular pleura). We believe that this sign can be used as one of the reliable features of preoperative imaging diagnosis for PSP. The histological reasons for this feature are currently unclear and may be related to the fact that PSP originates from type II alveolar epithelial cells, but further research is still needed.

Interestingly, lung adenocarcinoma, which also originates from type II alveolar epithelial cells, also occurs primarily in the extrapulmonary area. Of course, PSP and lung adenocarcinoma have obvious histological and imaging differences that will not be repeated here.

PSP originates from type II alveolar epithelial cells and is an intraparenchymal tumor with well clinical processes (2, 3). The growth pattern is the real expansive growth. It originates from a primary structure bud and can be continuously replicated based on that structure, pushing outwards. Since it is not invasive, theoretically, it is impossible to pass through natural pulmonary arteriovenous and bronchial tubes. Pathological data have confirmed that the hemangioma-like PSP components are not a real vascular structure, and there are no normal pulmonary blood vessels and bronchial structures in PSP. While reviewing the MSCT imaging findings of this group of patients, 15 cases showed welt vessel signs, but none of them entered the lesion. In all 24 cases, no bronchus came the lesion, and the results obtained from imaging analysis were fully consistent with the pathological features. Therefore, we believe that this sign can be used as the second reliable feature of PSP for preoperative imaging diagnosis.

Among the 34 cases in this group, except for one case of PSP nodule with a long diameter of 8.58 mm, that was almost uniformly enhanced, the remaining cases showed uneven enhancement. Besides, the smaller the volume of PSP lesions, the greater the proportion of obvious areas of enhancement, and the smaller the proportion of slight enhancement areas. In contrast, the larger the lesion volume, the smaller the proportion of obvious enhancement areas, and the higher the proportion of slight enhancement areas. Pathological specimens showed that the smaller the lesion volume, the higher the proportions of both hemangioma-like and nipple areas on the tissue configuration, and the lower the proportions of solid and sclerosing areas. In contrast, the larger the lesion, the higher the proportions of solid and the sclerosing regions, the lower the proportions of both hemangioma-like and nipple areas. By combining high magnification observations, fresh red blood cells with complete morphology can be seen in the interstitial space of the hemangioma-like regions and the nipple areas, suggesting that these gaps can be connected to the hemangioma-like areas through specific channels. In addition, the nipple areas are mostly migrating with the hemangioma-like areas, which can better explain the connectivity between the two. The essence of the hemangioma-like area is that a cavity is filled with a large volume of fresh blood, which includes many normal and intact red blood cells, indicating its fluidity feature. Moreover, there are tiny blood vessels in the interstitial space of the nipple areas, but the cross-section of the lumen is far less than the interstitial space. Combined with the MSCT imaging manifestation, the obvious contrast-enhanced area corresponded to the nipple and the hemangioma-like regions, and the slightly enhanced regions corresponded to the solid area and the sclerosing area.

This characteristic of PSP is due to the clear expression of CK, EMA, SP-B, and TTF-1 on the surface cubic cells, suggesting that they originate from alveolar type II cells or have a tendency to differentiate into alveolar type II cells (28). The polygonal cells in the interstitium have clear expressions of Vimentin, Syn, and weak EMA expression, indicating that the polygonal cells in the interstitium have the potential for multi-directional differentiation (29, 30). Nakatani et al. (31) and Wang Yan et al. (32) concluded through immunohistochemical staining

of PSP that polygonal cells and surface cubic cells are tumor parenchymal cells in PSP tissues in different differentiation directions, and both have the characteristics of mutual migration in histology. As a result, PSP formation has undergone a process of evolution from hemangioma type to the nipple type, the solid type, and then to the sclerosing type. Combining the pathological specimens and MSCT imaging manifestations, the smaller lesions are mainly hemangioma-like and/or nipple types, so the enhancement is obvious. With the extension of the course of the disease and the increase of the lesion volume, the solid and sclerosing structures of the lesion gradually increase and are unevenly distributed, so that the degree of enhancement on MSCT in this area is lower, making the entire lesion appear unevenly enhanced. All 34 cases in this group have the abovementioned features. Therefore, we believe that this pathological feature of PSP and the derived MSCT imaging manifestations can be used as the third reliable feature of preoperative imaging diagnosis. There are several reports, which described other external and surrounding traditional MSCT manifestations of PSP tumors (such as welt vessel signs, halo sign, false capsule signs, air crescent signs, etc.), and this study did not repeat them here.

CONCLUSION

As a common benign tumor of the lung parenchyma, PSP is frequently detected in middle-aged women. The right lung is more common than the left lung, while the inferior lobe is more common than the superior lobe. By studying the correlation between clinicopathological features and MSCT imaging manifestations, we believe that the following features are reliable imaging signs for the preoperative and intraoperative diagnosis of PSP. These imaging characteristics can be summarized as follows:

1. It appears as close to the pleura.
2. There is no correlation between the lesion and its surrounding blood vessels and bronchi.
3. After dynamic enhancement scanning, the lesion volume is negatively correlated with the range of obvious enhancement areas. With the extension of the disease and the increase of the lesion volume, the area of the obvious enhancement decreases, and the range of the slight enhancement area increases, making the whole lesion appear unevenly enhanced.
4. While analyzing pathological frozen sections, it is important to combine MSCT images, including enhanced scanning, round non-lobulated, and surrounding halo bleeding, which are found to be very intuitive features of the PSP.
5. There is no pulmonary artery and bronchus passing through in frozen sections.
6. The center of the PSP nipple structure is the polygonal cells rather than the fibrous blood vessel axis.

At the same time, the experimental group mastering the new diagnostic approach scored nine points (imaging diagnostician) and eight points (pathological diagnostician), respectively, while the control group using traditional knowledge scored six points (imaging diagnostician) and five points (pathological diagnostician). Therefore, while grasping the knowledge of traditional PSP imaging and pathological diagnosis, if we can further apply the new knowledge we have summarized to the clinic, the accuracy of preoperative and intraoperative diagnosis will be significantly improved. Of course, our assessment subjects are very limited, and there will be some errors in the statistical results, but it cannot cover up the fact that the new diagnostic method can significantly improve the accuracy of preoperative and intraoperative diagnosis of PSP.

While PSP is a benign tumor, there are few reports of case studies related to other malignant tumors or with hilar, mediastinum, peribronchial, and interlobular lymph node metastases. Dacic et al. (33) reported that the p53 gene on the 17q arm of the PSP chromosome showed a high frequency of loss of heterozygosity, which known to be a possible malignant tumor. Wang Yan (34) investigated 19 cases of PSP and found that the mutation rate of p53 genes in tissues was up to 15.8%, which was similar to that of other malignant tumors, suggesting that PSP may have possible malignant biological behaviors.

The malignant behaviors of PSP are expressed through lymph node metastasis (7), but these features have been reported to have no significant effect on the prognosis of patients (21, 35). Since the mechanisms of lymph node metastasis of PSP are still not clear, it is recommended that patients diagnosed with PSP and treated with surgery should be followed up for a long period of time. Although there is no reliable evidence of recurrence or metastasis in the remaining cases except four in which loss of follow-up occurred in this group, the outcome of this group still requires long-term follow-up.

DATA AVAILABILITY STATEMENT

The original contributions presented in the study are included in the article/supplementary material, further inquiries can be directed to the corresponding author/s.

ETHICS STATEMENT

All experimental procedures of this study were approved by the local ethics committee of Xiangya Hospital, Central South University, Changsha, China (Code: 202006082) and were in accordance with the ethical standards and regulations of human studies of the Helsinki declaration (2014). The patients/participants provided their written informed consent to participate in this study.

AUTHOR CONTRIBUTIONS

GX and ZX conceived and designed research. GX, ZW, ZX, ML, WL, YX, and TM conducted experiments. ML and WL analyzed data. GX and ZX edited and wrote the final version of manuscript. All authors were involved in drafting the manuscript as well as revising it critically for relevant intellectual content. All authors read and approved the manuscript.

REFERENCES

1. Liebow AA, Hubbell DS. Sclerosing hemangioma (histiocytoma, xanthoma) of the lung. *Cancer.* (1956) 9:53–75.
2. Devouassoux-Shisheboran M, Hayashi T, Linnoila RI, Koss MN, Travis WD. A clinicopathologic study of 100 cases of pulmonary sclerosing hemangioma with immunohistochemical studies: TTF-1 is expressed in both round and surface cells, suggesting an origin from primitive respiratory epithelium. *Am J Surg Pathol.* (2000) 24:906–16.
3. William D. *WHO Classification of Tumors of The Lung, Pleura,Thymus and Heart*. Lyon: lARC (2015).
4. Yang CH, Lee LY. Pulmonary sclerosing pneumocytoma remains a diagnostic challenge using frozen sections: a clinicopathological analysis of 59 cases. *Histopathology.* (2018) 72:500–8. doi: 10.1111/his.13391
5. Illei PB, Rosai, J KD. Expression of thyroid transcription factor-1 and other markers in sclerosing hemangioma of the lung. *Arch Pathol Lab Med.* (2001) 125:1335–9. doi: 10.5858/2001-125-1335-EOTTFA
6. Wang EH, Dai SD, Qi FJ, Hong-Tao X, Wei Q. Gene expression and clonality analysis of the androgen receptor and phosphoglycerate kinase genes in polygonal cells and cuboidal cells in so-called pulmonary sclerosing hemangioma. *Mod Pathol.* (2007) 20:1208–15. doi: 10.1038/modpathol.3800964
7. Lovrenski A, Vasilijević M, Panjković M, Tegeltija D, Vučković D, Baroš I, et al. Sclerosing pneumocytoma: a ten-year experience at a Western Balkan University hospital. *Med.* (2019) 55:1–9. doi: 10.3390/medicina55020027
8. Kazerooni EA. High-Resolution CT of the lungs. *Am J Roentgenol.* (2001) 177:501–19. doi: 10.2214/ajr.177.3.1770501
9. Bonelli FS, Hartman TE, Swensen SJ, Sherrick A. Accuracy of high-resolution CT in diagnosing lung diseases. *Am J Roentgenol.* (1998) 170:1507–12. doi: 10.2214/ajr.170.6.9609163
10. Arakawa H, Niimi H, Kurihara Y, Nakajima Y, Webb WR. Expiratory high-resolution CT: diagnostic value in diffuse lung diseases. *Am J Roentgenol.* (2000) 175:1537–43. doi: 10.2214/ajr.175.6.1751537
11. Ostridge K, Wilkinson TMA. Present and future utility of computed tomography scanning in the assessment and management of COPD. *Eur Respir J.* (2016) 48:216–28. doi: 10.1183/13993003.00041-2016
12. Rui-yun L, Wei-jun F, Hui-li R, Hui-ru L, Hui Z. Study on CT manifestations of non-tuberculous mycobacterium pulmonary disease patients with and without diabetes mellitus. *Chin J Antituberc.* (2020) 42:962. doi: 10.3969/j.issn.1000-6621.2020.09.014
13. Wang QB, Chen YQ, Shen JJ, Zhang C, Song B, Zhu XJ, et al. Sixteen cases of pulmonary sclerosing haemangioma: CT findings are not definitive for preoperative diagnosis. *Clin Radiol.* (2011) 66:708–14. doi: 10.1016/j.crad.2011.03.002
14. Chung MJ, Lee KS, Han J, Sung YM, Chong S, Kwon OJ. Pulmonary sclerosing hemangioma presenting as solitary pulmonary nodule: Dynamic CT findings and histopathologic comparisons. *Am J Roentgenol.* (2006) 187:430–7. doi: 10.2214/AJR.05.0460
15. Shin SY, Kim MY, Lee HJ, Oh SY, Jang SJ. Clustered pulmonary sclerosing pneumocytoma in a young man: a case report. *Clin Imaging.* (2014) 38:532–5. doi: 10.1016/j.clinimag.2014.01.016
16. Shin SY, Kim MY, Oh SY, Lee HJ, Hong SA, Jang SJ, et al. Pulmonary sclerosing pneumocytoma of the lung: CT characteristics in a large series of a tertiary referral center. *Med.* (2015) 94. doi: 10.1097/MD.0000000000000498
17. Suzuki H, Saitoh Y, Koh E, Hoshino H, Kase D, Kasei Y, et al. Pulmonary sclerosing hemangioma with pleural dissemination: Report of a case. *Surg Today.* (2011) 41:258–61. doi: 10.1007/s00595-009-4220-5
18. He W, Zhou X, Li F, Lyu Y, Zhou Z, Li C, et al. Analysis of CT features of pulmonary sclerosing pneumocytoma. *Chin J Antituberc.* (2018) 40:724. doi: 10.3969/j.issn.1000-6621.2018.07.011
19. Meng H, Li-fang G, Jian-mei Z, Meng-jun W, Ren-gui W. Value of CT scan for diagnosis and differential diagnosis of diffuse peritoneal lesions. *Chin J Antituberc.* (2020) 42:227. doi: 10.3969/j.issn.1000-6621.2020.03.009
20. Makimoto Y, Yamamoto S, Takano H, Motoori K, Ueda T, Kazama T, et al. Imaging findings of radiation-induced sarcoma of the head and neck. *Br J Radiol.* (2007) 80:790–7. doi: 10.1259/bjr/20938070
21. Wang X, Zhang L, Wang Y, Jia X, Wang J, Zhang H. Sclerosing pneumocytoma with metastasis to the mediastinal and regional lymph nodes. *Indian J Pathol Microbiol.* (2018) 61:407–9. doi: 10.4103/IJPM.IJPM_98_17
22. Cheung YC, Ng SH, Chang JWC, Tan CF, Huang SF, Yu CT. Histopathological and CT features of pulmonary sclerosing haemangiomas. *Clin Radiol.* (2003) 58:630–5. doi: 10.1016/S0009-9260(03)00177-6
23. Liu W, Tian XY, Li Y, Zhao Y, Li B, Li Z. Coexistence of pulmonary sclerosing hemangioma and primary adenocarcinoma in the same nodule of lung. *Diagn Pathol.* (2011) 6:41. doi: 10.1186/1746-1596-6-41
24. Aziz ZA, Padley SP, Hansell DM. CT techniques for imaging the lung: recommendations for multislice and single slice computed tomography. *Eur J Radiol.* (2004) 52:119–36. doi: 10.1016/j.ejrad.2004.01.005
25. Schoepf UJ, Bruening RD, Hong C, Eibel R, Aydemir S, Crispin A, et al. Multislice helical CT of focal and diffuse lung disease: Comprehensive diagnosis with reconstruction of contiguous and high-resolution CT sections from a single thin-collimation scan. *Am J Roentgenol.* (2001) 177:179–84. doi: 10.2214/ajr.177.1.1770179
26. Low SY, Teo F, Eng P, Tan PH. Pulmonary sclerosing hemangioma: Pitfalls in management. *Asian Cardiovasc Thorac Ann.* (2011) 19:139–42. doi: 10.1177/0218492311399177
27. Devouassoux-Shisheboran M'Hayashi T LR. Aclinicopathologic study of 100 cases of pulmonary sclerosing hemangioma with immunohistochemical studies:TTF-1 is express in bothround and surface cells, suggesting an origin from primitive respiratory epithelium. *Am J Surg Pathol.* (2000) 24:906–16. doi: 10.1097/00000478-200007000-00002
28. Wang E, Lin D, Wang Y, Wu G, Yuan X. Immunohistochemical and ultrastructural markers suggest different origins for cuboidal and polygonal cells in pulmonary sclerosing hemangioma. *Hum Patho1.* (2004) 35:503–8. doi: 10.1016/j.humpath.2003.10.015
29. Wang EH ZJ. *Clinical and Pathological Diagnosis and Differential Diagnosis—Trachea, Lungs, Pleura, and Mediastinal Disorders*. Beijing: People's Health Publishing House (2018).
30. Hissong E, Rao R. Pneumocytoma (sclerosing hemangioma), a potential pitfall. *Diagn Cytopathol.* (2017) 45:744–9. doi: 10.1002/dc.23720
31. Nakatani Y, Inayama Y, Kamijo S, Ogawa N. Sclerosing lung hemagioma. *Am J Surg Pathol.* (1999) 23:240–1. doi: 10.1097/00000478-199902000-00019
32. Wang Y, Wang EH, Wu GP, Zhang Z, Lin D. Immunohistochemical and ultrastructual study of so-called sclerosing hemangioma of the lung suggests different origins of cells. *Chinese J Lung Cancer.* (2003) 6:92–3. doi: 10.3779/j.issn.1009-3419.2003.02.02
33. Dacic S, Sasatomi E, Swalsky PA, Kim DW, Finkelstein SD, Yousem SA. Loss of heterozygosity patterns of sclerosing angioma of the lung and bronchioloalveolar carcinoma indicate a similar molecular pathogenesis. *Arch Pathol Lab Med.* (2004) 128:880–4. doi: 10.5858/2004-128-880-LOHPOS
34. Wang Y, Dai SD, Qi FJ, Xu HT, Wang EH. p53 protein expression and genetic mutation in two primary cell types in pulmonary sclerosing haemangioma. *J Clin Pathol.* (2008) 61:192–6. doi: 10.1136/jcp.2007.050401
35. Pokharel S, Dhillon SS, Ylagan L, George S, Yendamuri S. Sclerosing pneumocytoma with lymph node metastasis. *J Thorac Oncol.* (2016) 11:1802–4. doi: 10.1016/j.jtho.2016.06.005

Conflict of Interest: The authors declare that the research was conducted in the absence of any commercial or financial relationships that could be construed as a potential conflict of interest.

frontiers in Medicine

REVIEW
published: 30 September 2021
doi: 10.3389/fmed.2021.735590

Optimization of BCG Therapy Targeting Neutrophil Extracellular Traps, Autophagy, and miRNAs in Bladder Cancer: Implications for Personalized Medicine

*Chenyu Mao, Xin Xu, Yongfeng Ding and Nong Xu**

Department of Medical Oncology Cancer Center, The First Affiliated Hospital, College of Medicine, Zhejiang University, Hangzhou, China

Bladder cancer (BC) is the ninth most common cancer and the thirteenth most common cause of mortality worldwide. Bacillus Calmette Guerin (BCG) instillation is a common treatment option for BC. BCG therapy is associated with the less adversary effects, compared to chemotherapy, radiotherapy, and other conventional treatments. BCG could inhibit the progression and recurrence of BC by triggering apoptosis pathways, arrest cell cycle, autophagy, and neutrophil extracellular traps (NETs) formation. However, BCG therapy is not efficient for metastatic cancer. NETs and autophagy were induced by BCG and help to suppress the growth of tumor cells especially in the primary stages of BC. Activated neutrophils can stimulate autophagy pathway and release NETs in the presence of microbial pathogenesis, inflammatory agents, and tumor cells. Autophagy can also regulate NETs formation and induce production of reactive oxygen species (ROS) and NETs. Moreover, miRNAs are important regulator of gene expression. These small non-coding RNAs are also considered as an essential factor to control the levels of tumor development. However, the interaction between BCG and miRNAs has not been well-understood yet. Therefore, the present study discusses the roles of miRNAs in regulations of autophagy and NETs formation in BCG therapy in the treatment of BC. The roles of autophagy and NETs formation in BC treatment and efficiency of BCG are also discussed.

Keywords: bladder cancer, Bacillus Calmette Guerin, autophagy, neutrophil extracellular traps, miRNAs, biomarkers

OPEN ACCESS

Edited by:
Ali Yadollahpour, The University of Sheffield, United Kingdom

Reviewed by:
Fangzhou Song, Chongqing Medical University, China
Yukun Li, Hebei Medical University, China

****Correspondence:***
Nong Xu
nongxu@zju.edu.cn

Specialty section:
This article was submitted to Precision Medicine, a section of the journal Frontiers in Medicine

Received: *02 July 2021*
Accepted: *05 August 2021*
Published: *30 September 2021*

Citation:
Mao C, Xu X, Ding Y and Xu N (2021) Optimization of BCG Therapy Targeting Neutrophil Extracellular Traps, Autophagy, and miRNAs in Bladder Cancer: Implications for Personalized Medicine. Front. Med. 8:735590. doi: 10.3389/fmed.2021.735590

INTRODUCTION

Bladder cancer (BC) is one of the several types of cancers arising from the tissues of the urinary bladder and is the thirteenth most common cause of mortality and the ninth most common cancer worldwide (1). Conventional factors such as tumor grade, stage, and lymphatic and vascular extension, are utilized as prognostic markers and indicators for BC. However, the currently used prognostic markers have a limited ability to predict progression, recurrence, metastasis, and response to therapy (2). After the initial treatment of BC, a long-term follow-up is essential to prevent BC recurrence. Generally, constant surveillance includes performing a cystoscopy every

3 months for 2 years, then every 6 months for 2 years, and eventually annually, supposing no recurrence (3, 4). Bacillus Calmette Guerin (BCG), as live-attenuated strain of *Mycobacterium bovis*, is considerably similar to *Mycobacterium tuberculosis* in antigenic composition and has been used for treating BC (5). In this respect, immune responses has important role to combat with tumors. Neutrophils are the first leukocytes that counteract against tumor and are able to produce some special compositions that are neutrophil extracellular traps (NETs) (6). Autophagy (autophagocytosis) is defined as the general term for degradation of cytoplasmic components within lysosomes, which is completely different from endocytosis-mediated lysosomal degradation of extracellular and plasma membrane proteins (7–11). Autophagy is classified into three main types including macroautophagy, microautophagy, and chaperone-mediated autophagy and in the medical literature the term "autophagy" is usually referred to macroautophagy unless otherwise specified. A highly specialized organelle called the autophagosome mediates the whole autophagy process through which damaged organelles and cytosolic components are degraded into autophagolysosome, which is created by the fusing autophagosomes with lysosomes (in metazoan cells) or vacuoles (in yeast and plant cells) (12). Autophagy consists of several successive stages mainly including sequestration, transport to lysosomes, degradation, and utilization of degradation products and each of these stages might exert different function. Several studies have shown that BCG therapy can lead to activation of NETs and autophagy, which both prevent tumor growth or metastasis (13, 14). Another effective factor is the epigenetic agents. MicroRNAs (miRNAs) are the non-coding small RNAs that were identified to regulate expression of genes involved in the control of proliferation, development, and apoptosis (15). Additionally, findings of several animal model and human studies have indicated that miRNAs might contribute in suppressing the growth of tumor cells in a manner that imbalance of miRNAs gene expression could result in excessive proliferation of cancerous cells. In this regard, miRNAs play a crucial role in prognosis of the BC especially initial phase (16). Furthermore, miRNAs have also capacity to stimulate autophagy and NETs formation in neutrophils and inhibit tumor metastasis (17). BCG therapy could prevent recurrence and progression of tumor in BC. However, dysregulation of some cellular and molecular processes such as autophagy pathway and NETs formation could result in metastasis stimulation in BC (18). Dysregulation of miRNAs expression facilitates the growth and proliferation of tumor cells and tumor invasiveness can be promoted by autophagy process and NETs formation (19). Interestingly, therapeutic options may serve as regulatory agents to inhibit cancer progression and improve BCG therapy efficacy through complex network of miRNAs, autophagy and NETs, which can have significant effects on the efficacy of BCG therapy in BC treatment (20–22). Although BCG therapy has been administrated for BC treatment for decades, its therapeutic efficacy should be more evaluated to elucidate the roles of miRNAs in autophagy regulation and NETs formation and their mutual interactions. Moreover, miRNAs are important regulator of gene expression. These small non-coding RNAs have been reportedly considered as pivotal factors controlling and regulating the levels of tumor development. However, the interactions between BCG and miRNAs have not been well-understood yet. Therefore, the present study discusses the roles of miRNAs in regulations of autophagy and NETs formation in BCG therapy in the treatment of BC. The roles of autophagy and NETs formation in BC treatment and efficiency of BCG are also discussed.

BCG THERAPY IN BLADDER CANCER

Morales et al. was the first group reported the treatment efficacy of BCG therapy for BC (23). After several clinical trials and strong evidence on the efficacy of this technique, intravesical BCG has been established as a standard treatment for high-risk, non-muscle-invasive BC in different stages including lamina propria-invasive tumors (stage T1), carcinoma *in situ* (CIS) (stage Tis), and high-grade papillary tumors (stage Ta) (24, 25).

In these situations, BCG therapy could be correlated with a decreased risk of recurrence compared with transurethral resection alone, and the risk of progression to invasive disease would also be reduced by using BCG therapeutic approach (26–28). In addition, findings of the recent studies have demonstrated that the effectiveness and therapeutic outcome of BCG therapy in BC are comparable with intravesical chemotherapy, meanwhile BCG therapy is more effective in decreasing the risk of tumor recurrence, but the its toxicity can be more severe (29–31).

NEUTROPHILS AND CANCER

Neutrophils as a crucial element of innate immunity in any organisms play important roles in responding to different inflammatory and invading pathogens such as microbes, bacteria and fungi (32). These predominant leukocytes are among the first blood cells recruited to an inflammatory site (33). NETs are a network of chromatin structure with related enzyme including elastase, myeloperoxidase, and cathepsin G which were released by stimulation with phorbol myristate acetate (PMA), carcinogenesis substance. NETs can trap, neutralize, and kill the extracellular bacteria, viruses, fungi, and parasites. Moreover, NET release occurs initially through a cell death process termed NETosis (34). This process begins with interrupt of the nuclear envelope and continue with chromatin decondensation into the cytoplasm of intact cells. Moreover, NETiosis can occur following the secreted nuclear chromatin that is accompanied by the release of granule proteins through degranulation (35).

Neutrophils have been reportedly to involve in different biological functions including phagocytosis, secretion of chemo-attractant and degranulation, and respiratory burst. Recent evidence has demonstrated a new biological function for neutrophils that is releasing of NETs (34, 36). NETs are specialized network structures composing mainly of histones, de-condensed chromatin, and effector cytokines, that is, myeloperoxidase (MPO). The main strategy of neutrophils for triggering immune defense response to prevent the invading pathogenic microorganisms from escaping the immune system

and expanding the infection, neutrophils first locate and capture the pathogens through releasing NETs and subsequently trigger other immune cells and initiate systemic immune defense.

NETosis AND CANCER

The role of NETs in tumor progression remains poorly understood. The findings of the both animal and human studies suggest a potential association between tumor progression and intra-tumoral NET deposition in both experimental models and in human cancer patients (36–38). Zychlinsky et al. evaluated the presence of tumor-associated neutrophils (TANs) and NETs in surgical resection specimens from eight patients with sarcoma as determined by positive staining for extracellular myeloperoxidase (MPO) 25% of these patients (2 patients), demonstrated intra-tumor NET deposition (36). These two patients developed early relapse after performing post-neoadjuvant chemotherapy and surgery, although the site was not specified in the study (36). Therefore, it seems that Ewing sarcoma cells can stimulate TANs to release NETs. The ability of tumor cells to involve neutrophils to produce NETs has been displayed in a number of tumor types. This phenomenon indicates the possibility that NETs play a fundamental role in tumor biology (39). In this regard, Demers et al. demonstrated that several tumor types including lung neoplasms and mammary, hematologic are able to involve circulating neutrophils to produce NETs (39). The evidence presented in the literature thus far suggest that NETs my promote tumor progression within the primary tumor (40).

As previously stated, NETs have usually strong adhesive characteristics, which enable them to bind pathogens and platelets. It, thereby, seems to hypothesis that NETs also provide intravascular networks facilitating tumor cell adhesion and extravasation in hematogenous metastasis. Actually, neutrophils is able to promote the arrest of circulating tumor cells, especially under inflammatory conditions, which remarks at a role of NETs in this process (41–43). Additional direct evidence arises from a recent *in vitro* study demonstrating that lung carcinoma cells display 4–5 fold increased adhesion to NETs as compared with unstimulated neutrophil monolayers (37, 44).

Another important aspect which should be paid attention is the role of neutrophil in the cancer microenvironment. In this regard, some studies which has been recently performed in the field of neutrophil roles in tumor microenvironment suggest that neutrophil exhibit substantial plasticity which could be polarized to an N1 antitumoral or N2 protumoral phenotype in response to the microenvironment, the same of the M1/M2 macrophages polarization (45, 46). Tumor-associated N2 neutrophils are identified by high expression of VEGF, CXCR4, gelatinase B, and MMP9 and can be induced on exposure to high TGF-β levels. Vice versa, N1 neutrophils express immunopotentiating cytokines and chemokines such as IFN-γ, CXCR3, and low levels of arginase and also are induced on TGF- β blockade and are able to eliminate cancer cells (45, 47).

In this regard, a performed study by Berger-Achituv et al. showed that NETs have either pro– or anti-tumor function, depending on factors such as tumor microenvironment and type of cancer. For instance, within the microenvironment of the tumor, TGF-β can induce TANs with pro-tumorigenic features. However, TANs produce pro-inflammatory cytokines and have tumoricidal activity without TGF-β (45).

In addition, neutrophils can enhance tumor growth through production of matrix metalloproteinase (MMP)-9 that inhibits tumor cell apoptosis in the respiratory tract and can increase tumor angiogenesis and neovascularization (48, 49). Nevertheless, neutrophils can also have cytotoxic effects on tumor cells by generating many types of reactive oxygen species (ROS) (50, 51). Notably, in a study was demonstrated that neutrophils inhibited metastatic seeding by secreting hydrogen peroxide in a mouse model of breast cancer (52). Neutrophils also secret defensins, which have anti-angiogenetic characteristics and can lyse cancer cells, recruit dendritic cells (DCs) as antigen presenting cell (53). NETs are thought to have anti-tumorigenic effects, for example through activating immune responses and killing of tumor cells. On the other hand, NETs could have a pro-tumorigenic function by promoting metastases. In fact, NETs may act to physically take tumor cells and inhibit their dissemination to adjacent tissues. Various components of NETs have been indicated to be cytotoxic to tumor cells. MPO was demonstrated to destroy B-16 melanoma cells and prevent their growth in mice after implantation (54). Interestingly, patients with MPO deficiency probably have a high incidence of cancer (7/14 patients, 50%) (55). NETs can eradicate activated endothelial cell, may by histones, damaging tumor-feeding blood vessels (56). NE produced by TANs cleaves Cyclin E to other isoforms with lower molecular weight and therefore facilitates their presentation to cytotoxic T cells (CTLs) (57). Indeed, NETs have a modulatory role to establish the bridge between innate and adaptive immunity by activating plasmacytoid DCs through toll-like receptor 9 (TLR9), an intracellular receptor that preferentially binds DNA. NETs have capability to prime T cells by TCR signaling that implicates direct contact (58). Alternatively, NETs, which contain different proteases, could represent a pro-tumorigenic activity by degradation of the extracellular matrix and increase metastasis. NETs may also create a hurdle between cancer cells and the immune system, thereby collaborating with cancer cells to evade from immune recognition. Consequently, it has been reported that patients with metastatic disease showed NETs formation relapsed that may refer to the pro-tumorigenic mechanism of NETs (36). Moreover, there is a recent evidence indicating that neutrophils from certain donors have capable to kill cancer cells in a cell-specific manner and that neutrophil killing of cancer cells may be improved by β-glucan treatment, making neutrophil a persuadable candidate for cancer immunotherapy (59). Various studies that induce neutrophilia through prolonged G-CSF treatment in tumors show a shift form a chronic to an acute inflammatory environment and an anticancer effect (60). Notably, mammary tumor cell lines stimulate NETosis *in vitro*, but there is no strong evidence for NET formation in these tumors *in vivo* (61). On the other hand, some studies have been demonstrated that NETiosis is able to counteract against cancer metastasis (47). One underlying mechanism for metastasis suppression seems to be the NET-mediated capture of migrating

tumor cells, particularly at places of inflammation, which can be blocked with neutrophil elastase (NE) and protein-arginine deiminase type 4 (PAD4) inhibitors (62). Therefore, targeting NETs through these pathways could be a promising therapeutic option to treat cancer. In the next section we will discuss about the role of BCG therapy in BC and the interaction between NETs and BCG for treatment of BC (62).

Collectively, neutrophil-induced NETs act as an inhibitor for development of tumor metastasis through elastase, MPO, and other enzymes. In contrast, a few evidence demonstrated that produced NETs from the TANs in microenvironment of tumor could lead to progress of tumor cells.

NEUTROPHILS IN BCG THERAPY

BCG instillation into bladder provides a localized infection that involves both attachment and then internalization into normal and malignancy urothelial cells through fibronectin process mediated by integrin adhesion molecules (63–65). Recent studies have demonstrated that neutrophils are able to migrate to the bladder after BCG stimulates bladder epithelial cells to secrete chemokines. Also, another study showed that neutrophils have important role in anticancer outcome of BCG therapy. In this regard, Suttman et al. reported that neutrophils could be reason of positive outcome to BCG therapy in a mouse bladder tumor model (66). They found that BCG therapy has no effect after depletion of neutrophil that result in a reduction in survival compared with non-depleted controls. Neutrophils release IL-8, MIF, MIP-1α, and GRO-α when are stimulated with BCG *in vitro*. Therefore, BCG-induced chemokine secretion by neutrophils is sufficient to recruit macrophages, which eventually recruit T cells. According to these findings, Suttman and their colleagues, suggest that BCG administration can result in the influx of neutrophils that coordinate the subsequent macrophages and T cell recruitment via the release of chemokines (66). Interestingly, in consideration of Suttman et al.'s results, it is proposed that the BCG-induced antitumor responses are mediated by activated T cells, whereas neutrophils recruit other immune cells with indirectly mechanism (65, 66). Additionally, neutrophils have a direct antitumor immunity through the production of soluble TRAIL, tumor necrosis factor related apoptosis inducing ligand, into the bladder environment (65).

In another study, Liu et al. evaluated the formation of NETs by induction of BCG instillation. They have shown that tumor cell proliferation was inhibited by treatment with NETs as well as cytotoxicity of NETs on tumor cells. Their results demonstrated that BCG-induced NETs promote dose- and time-dependent apoptosis of tumor cells and G0/G1 phase arrest. Obtained findings from the Liu et al.'s study demonstrated BCG-activated tumors stimulated more NETs than non-activated ones. Also, neutrophil adhesion and NETs release were increased by stimulation with supernatant of activated cells which representing a significant role for cytokines. Their results also suggest that BC cells induce NETs via TNF-α and IL-8 secretion following BCG stimulation. Eventually, they concluded that BCG-induced NETs suppressed tumors through multiple mechanisms including cytotoxicity effects, induction of apoptosis and cell cycle arrest. Some studies have been shown that NETs could suppress migration and invasion of tumor cells by induction of apoptosis and exert cytotoxicity mechanism on tumor cells (13). Besides, role of Neutrophils has been proven for T cells trafficking to the bladder after BCG perfusion (66). Actually, CD4+ T cells are the main contributors in BCG therapy, according to IFN-γ cytokine production or activation of CD8+ T and NK cells (66, 67). Furthermore, NETs could prime T cells and activate dendritic cells (DCs). NETs treatment upregulate CD4 expression *in vitro*, and CD3+ and CD14+ cells in tumors that could be an important index for potentiating of immunity. Generally, the presence of monocyte, Th1 cells, and CTLs in environment of tumor could result in tumor regression and also this cellular population can coincide with a favorable prognosis (13). It has been demonstrated that NETs have either tumor pro- or anti-tumor activity. Therefore, some agents such as cytokine profile in the microenvironment and cancer type are the determinative subject for progression or suppression of tumor cells (68, 69). At high concentrations, release of MPO and NE as important components of NETs have cytotoxicity effect on tumor cells, but reducing the release may result in the conversion of anti-tumor to pro-tumor function (70, 71). Therefore, NETs have different roles based on variation in multiple stimuli, neutrophil action site, and induction with BCG or others (13).

Collectively, neutrophils are induced by BCG activation to form NETs. In other words, the direct role of BCG-induced NETs has been indicated by cytotoxicity effect, apoptosis induction, cell cycle arrest, and inhibition of tumor cells migration into bladder environment. Besides, NETs have also indirect role through stimulation immunity and recruitment of T cells and macrophages to prevent tumor growth. In the next section, it will be discussed about the effect of autophagy pathways and its relation with NETs and BCG therapy in BC.

AUTOPHAGY AND NETs

The autophagy functions can be classified into two categories including generation of essential metabolic degradation products and clearance of intracellular defective organelles and macromolecules (72).

One of the best conserved-function of autophagy is associated with adaptation to starvation among many various organisms. When growth requirements increase or nutrients are scarce, metabolic intermediates were produced by autophagy contribution which mainly happened for sustaining cell survival (73). The mTOR as a serine/threonine protein kinase can form two different protein complexes that known as mTORC1 and mTORC2. Evidence shows that mTOR is a main control way for autophagy pathway, which mTORC1 could control catabolic activity via the process of autophagy. This mechanism is proceed by integrates signals from multiple pathways, sensing the levels of nutrients and growth factors (74). Along with, AMP-dependent protein kinase (AMPK) is the key sensor of cellular energy status which activate autophagy pathway (20–25). Substantial regulators of autophagy are the class I and class III

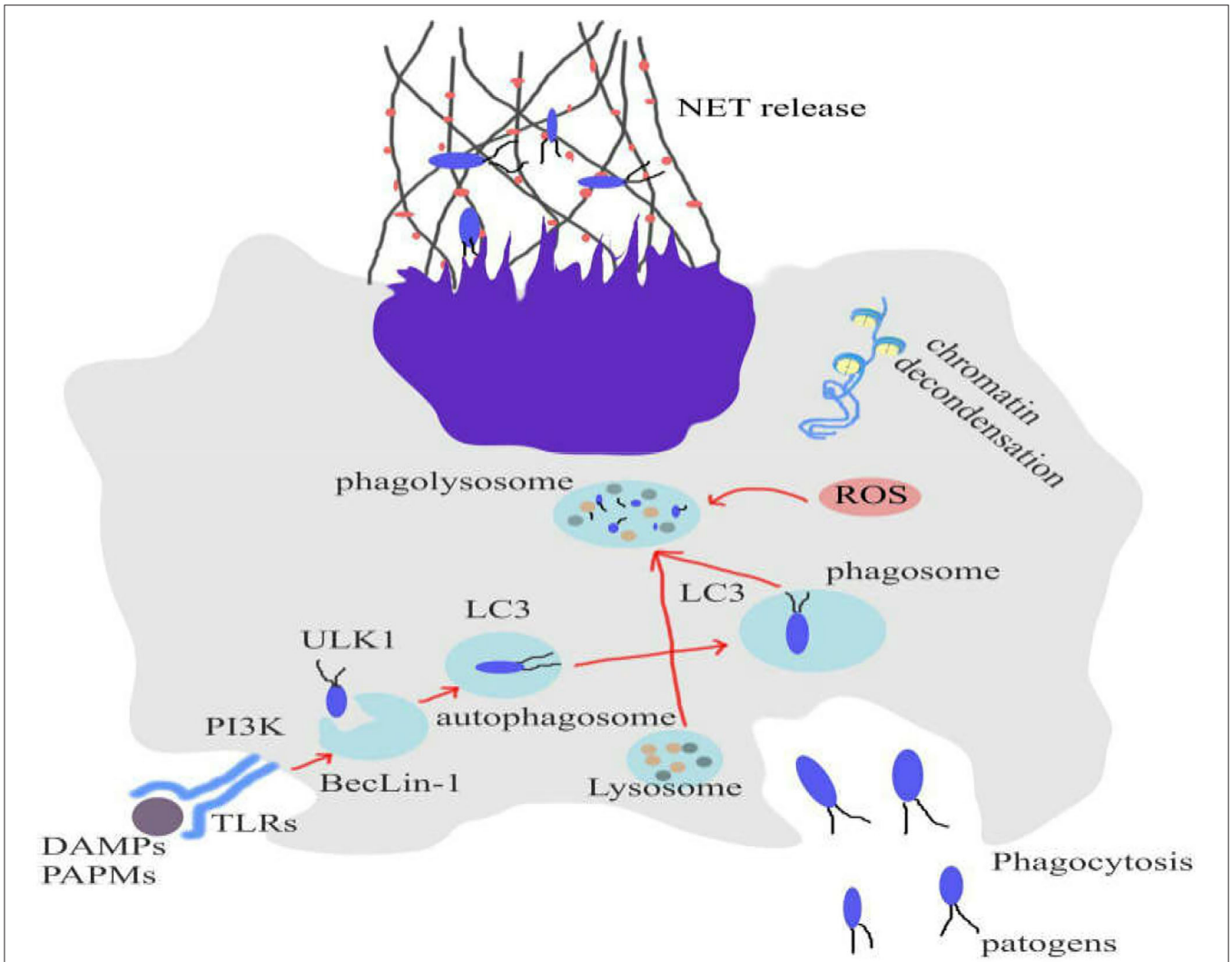

FIGURE 1 | Role of autophagy and ROS production to form NETosis. Inhibition of either NADPH oxidase or autophagy could prevent the chromatin decondensation that is crucial for NETosis, resulting in apoptotic cell death. NETosis can eliminate infections and tumors.

phosphatidylinositol 3-kinase (PI3K) pathways. Class I PI3K activates mTORC1 and inhibits the beginning of autophagy. In contrary, class III PI3K can induce autophagy directly (75).

Initiation, elongation, autophagosome completion, fusion with the lysosome, and degradation are five steps of autophagy process (76). When nutrients and energy in cells are empty, mTORC1 is inactivated, it can no longer prevent the autophagy initiation complex which are involving the protein kinases unc-51-like kinases 1 and 2 (ULK1/2), ATG13, ATG101, and FIP200. These protein kinases are able to form a newly phagophore membrane carrying ATG14, endoplasmic reticulum-associated protein. Recruitment of Beclin 1, Vps34, and Vps15, was performed through the nascent phagophore membrane which in turn results in the formation of an activated class III PI3K complex that also produces phosphatidylinositol 3-phosphate (PI3P) (77). The elongation step initiates the enlargement and final closure of and extending membrane, leading a completed autophagosome. Double-membrane organelle would be formed by two ubiquitin-like protein-conjugation systems, essential for the elongation phase. Dissociation of ATG12-ATG5 conjugation occur from the outer autophagosomal membrane after that vesicle formation is complete. Microtubule-associated proteins 1A/1B light chains (LC3) is another conjugation system which are cleaved by ATG4 upon autophagy induction, causing cytoplasmic LC3-I. In addition, LC3II conjugation complex was created through more lipidation with phosphatidylethanolamine (PE), which is then combined into both inner and outer autophagosomal membranes. The presence of LC3-II in the autophagosomal membranes is commonly considered as a marker for detection of double-membrane autophagic organelles. On the other hand, p62 is necessary for aggregating and binding polyubiquitinated protein to LC3-II to provide a situation that phagophore could engulf cytosolic elements, to grow, and consequently to close the autophagosome.

Generally, accumulation of p62 occurs when autophagy is inhibited, and the decrease of p62 also represents suitable vesicle degradation and autophagic flux (78–80). At the final steps, the autophagolysosome content, which is produced by the fusion of autophagosome with lysosome is degraded via hydrolytic enzymes (18, 76, 81, 82). In this regard, the role of autophagy is important for major neutrophil functions, including phagocytosis, differentiation, degranulation, cytokine production, cell death, and NETs formation. ATG proteins are main members in the neutrophil differentiation pathway. ATG5 is needed in both canonical and non-canonical autophagy. In addition, the role of ATG5 has been demonstrated to differentiate neutrophil (83). Moreover, mTORC1 has a pivotal role in the regulation of autophagy so that differentiation of neutrophilic precursor cells could be ceased by using pharmacological inhibition of mTORC1- induced autophagy – or p38 mitogen-activated protein kinase (MAPK) (77). Therefore, autophagy exhibits a mutual regulating interaction by the p38–mTORC1 axis (83).

Different *in vivo* studies have demonstrated that metabolism and autophagy are programmed for neutrophil differentiation. In this regard, findings of some studies have exhibited that reduced ATG gene expression is correlated with acute myeloid leukemia (AML) samples (84). It has been demonstrated that neutrophils were primed by autophagy for increased NETs formation, which is notable for appropriate neutrophil effector functions during sepsis (85). Actually, neutrophils have a potency to increase autophagy induction in patients who survived sepsis. On the other hand, there is an abnormally autophagy function in neutrophils isolated from patients who could not survive sepsis. However, in murine models of sepsis, the autophagy reinforcement improved survival through a NET-dependent mechanism (86).

Interestingly, autophagy and ROS production as two main regulators of NETosis have a close correlation to each other. Autophagy induction can occur through ROS burst, which in turn is necessary to maintain effective ROS production (87).

Remijsen et al. have studied the roles of autophagy and ROS production in formation process of NETosis (88). Their findings demonstrated that a combination of ROS production and autophagy is required for PMA-induced-NET formation in human neutrophils. Inhibition of either NADPH oxidase or autophagy could prevent the chromatin decondensation that is crucial for NETosis, resulting in apoptotic cell death. Additionally, they reported that there was not any NADPH oxidase activity in neutrophils, isolated from patients with chronic granulomatous disease (CGD). The evidences showed that these neutrophils are incapable of producing NETs (88) (**Figure 1**).

Similarly, other studies have demonstrated that neutrophils from patients with acute gouty arthritis (AGH) display autophagy-mediated spontaneous NET release (89). Currently, it has also been demonstrated that reduced expression levels of Atg5 interplayed to decreased capacity of neutrophils to form NETs when TLR2 ligand stimulation has occurred in aged mice. This suggests that it may represents a major role of autophagy in maintaining the mechanism of NETs (90).

On the other hand, some studies have reported contradictory findings on the contribution of autophagy in NET release. Particularly, *Atg5*-knockout mouse neutrophils, that display decreased autophagic activity, kept the capacity to release extracellular DNA. Moreover, PI3K is able to prevent NET formation inhibition by human neutrophils (91). Consequently, it maybe exists an autophagy-independent NETosis pathway (91, 92).

Collectively, activated neutrophil may promote autophagic activity and NET formation. Also, autophagy induces NET formation. But in relation to cancers specially BC, whether autophagy is able to induce NETs formation has yet to be determined and now there are no papers which discussed clearly in the literature. However, according to similar studies which have been conducted, it seems that autophagy-induced NETs formation would happen in tumor microenvironment through tumor-associated neutrophils (N2). However, further investigations certainly should be performed to clarify the matter.

In the next section, the role of autophagy in cancer and angiogenesis will be discussed.

AUTOPHAGY AND CANCER

Findings of the studies on the role of autophagy process as a driver of cell death or a pro-survival process in response to specific stressors are controversial. Autophagy has been initially described as a cytoprotective process under nutrient deprivation, whereas recent findings of several studies have demonstrated that autophagy process is a cell death driver in which it is involved in promoting cell death.

Recently, the paradoxical role of autophagy in cancer progression or suppression has been widely evaluated. Actually, cancer type, genetic context, and stage were affected by autophagy which can determine tumor cell destiny (93). Some studies demonstrated that autophagy is established as a tumor suppressive mechanism and the autophagy defective could be related to genomic instability, malignant transformation, and tumorigenesis (94, 95). Also, Beclin-1 acts as a tumor suppressive that allelic loss of this gene can results in incidence of some types of cancer including prostate, ovarian, and breast cancer (41, 94, 96). Moreover, the tumor suppressor function of Beclin-1 is exerted through binding and activating Vps34 which lead to induce autophagy (97). In this regard, Autophagy is able to maintain genome integrity and inhibit tumor initiation. Deletion of tumor suppressor PTEN and elevation of the PI3K/Akt/mTOR pathway, which is prevalent in many cancers, could be the cause for reduced cytoprotective autophagy and uncontrolled proliferation (98). Evidence shows that mTOR signaling suppresses the pro-autophagic protein AMBRA1, which can regulate cell proliferation by dephosphorylating c-myc (99). These Interpretations imply that impairment of autophagy can increase the risk of tumors (96, 100). Meanwhile, the case of established tumors is completely wrapped and the modulating role of autophagy in cell proliferation is highly context-dependent. High levels of autophagy are often occurred in cancers with BRAF and KRAS driver mutations. This increased

autophagy is crucial for PDAC tumor growth and sustenance, and halting it results in tumor regression (101). Similarly, Atg7 deletion in BRAF-driven lung cancer model cause to inhibit autophagy pathway that indicating tumor regression and reversal of malignancy (102). There are various opposite interpretations that challenge the proliferative roles of increase autophagy in tumor cells. For example, Results of studies suggest autophagy inducers including rapamycin and its derivatives which are known inhibitors of mTOR, can also prevent mTOR-dependent cell proliferation via induction of cell cycle arrest in MDA-MB-231 breast cancer cells and cell lymphoma (103, 104).

In conclusion, the evidence demonstrates that autophagy can regulate proliferation in a context-dependent manner. These studies express coordination of autophagy with proliferation that support a dual function of autophagy in one of the essential indexes of cancer.

AUTOPHAGY AND ANGIOGENESIS

Tumor angiogenesis occur with formation new blood vessels from the existing vasculature. To angiogenesis, tumor needs to some growth factors such as vascular endothelial growth factor (VEGF) and tumor growth factor-β (TGF-β). Angiogenesis supports tumor growth by providing nutrients for cancer cells, consequently aiding in tumor growth, invasion, and metastasis (105, 106). Additionally, when vascular supply of cells is terminated, the hypoxic situation is established and autophagy induced through HIF-α-mediated signaling (107). The increased levels of autophagy can facilitate tumor cells survive to sustain oxygen stress and could become resistant without blood supply. On the other hand, a specific role of autophagy in angiogenesis has been reported in neuroblastoma cells that showed that autophagy is able to suppress angiogenesis through degradation of pro-angiogenesis peptide which is called gastrin-releasing peptide (GRP) (108). Autophagy inhibits tumor cell necrosis and inflammation and mediates nutrients and hypoxia. It therefore diminishes the recruitment of macrophages at the primary tumor site, which is important for metastasis induction. Inhibition of epithelial-mesenchymal transition (EMT) by autophagy could occur through degradation of p62/SQSTM1 and its cargo TWIST, which promotes EMT. TWIST is helix-loop-helix transcription factor that regulates human osteogenic linage (109).

The process of migration and metastasis initiates when the cells lose contact with adjacent cells, detach from extracellular matrix (ECM), undergo EMT, and eventually become motile. Anoikis, as a type of apoptosis, occurs after tumor cells detach from surrounding ECM. However, tumor cells can evade from anoikis via autophagy induction that provides Anoikis resistance (110). When the separated tumor cells reach the favorable site, they may remain latent until they can find new contacts with the ECM. At this stage, autophagy generally helps in their survival through unknown mechanisms. For instance, ARH1, tumor suppressor gene, is able to induce autophagy and increase tumor cell latency in ovarian cancer. Latency tumor is a barrier for cancer treatment (109). Moreover, studies have determined that autophagy induction by starvation results in promoted metastasis and invasion of hepatocellular carcinoma cells. This event regulated by TGFβ/smad3 signaling (111).

Collectively, autophagy can suppress incidence of invasion and metastasis by inhibiting inflammation and tissue necrosis. But if the tumor cells detach from ECM, elevated levels of autophagy help them avoid apoptotic cell death and maintain latency in a distant site (109, 110). Thereby, autophagy acts as a double-edged sword in tumor progression or suppression (112).

AUTOPHAGY AND BCG

In this regard, it has been demonstrated that there is a relationship between BCG therapy and autophagy pathway. Because both BCG and wild-type *Mycobacterium tuberculosis* secrete many antigens including the ag85 complex, we concluded that generated antigens could be targeted into the autophagic pathway. It seems that such an event would promote the production of peptides from ag85 complex and their subsequent loading on to MHC II proteins. A study evaluated the effect of induction autophagy on the efficacy of BCG vaccine containing the immunodominant Ag85B. Their results showed that induction of autophagy increases Ag85B presentation through MHCII pathway and thereby elevates vaccine efficacy. Also, autophagy increases Ag85B presentation by macrophages (113).

In a comparative study evaluated the effect of BCG on gastric cancer cell line MGC-803. They reported that BCG therapy increases protein level of Atg-3 and lymphocyte immunocompetence to induce cell apoptosis and autophagy in gastric cancer cells (114). Collectively, some studies indicated that BCG is tightly associated with induction of autophagy in various cancers. BCG therapy is able to induce autophagy pathway and kill the tumor cells. Therefore, autophagy can be considered as an important agent to reinforce the effect of BCG on inhibition of tumor growth.

Recently, it has been demonstrated that there is an association between protective mechanisms of BCG and epigenetic alternations in innate immune cells (115). In this regard, Buffen et al. have studied the effects of BCG therapy on autophagy and its relation with epigenetic alternation in BC. Their findings demonstrated that BCG-induced autophagy could act as a central event modulating epigenetic alternations on innate immunity. Furthermore, they reported polymorphism in ATG2B gene controls epigenetic alterations in both *in vivo* and *in vitro* models in BC (20). Thereby, epigenetic alterations are the noteworthy topic in BCG therapy. In this respect, epigenetic and miRNAs are regulators of gene expression. The current literature shows that miRNAs play a crucial role in autophagy pathway, BCG therapy and NETs process. We will discuss these roles in next sections in more details.

MiRNAs ROLE IN AUTOPHAGY AND BCG THERAPY

MiRNAs is a group of non-coding small RNAs that can have different effects on oncogenesis by acting as oncogene or tumor suppressor in microenvironment-dependent manner (116).

Various studies conducted on the roles of miRNAs in BC have demonstrated that some miRNAs are overexpressed, whereas some other miRNAs are down-regulated during BC development. Gottardo et al. evaluated expression of miRNAs in 27 bladder specimens. They found that miR-17-5p, miR-23a, miR-23b, miR-26b, miR-103-1, miR-185, miR-203, miR-205, miR-221, and miR-223 were remarkably upregulated in BC. In fact, the function of a specific miRNA depends on its target genes. Thus, upregulated miRNAs that impact oncogenes can be considered as tumor-suppressing miRNAs, and downregulated miRNAs that impact tumor suppressor genes can be considered as onco-miRNAs (117). Another study showed that expression of four miRNAs (miR-199a-3p, miR-195, miR-133a, and miR-30a-3p) was downregulated in tumors, however, these miRNAs usually act as tumor suppressors (37). On the contrary, miR-200c and miR21 are upregulated in BC tissues and could be an agent for the progression of BC (118, 119). The expression of miRNAs are detected using molecular techniques such as microarray or deep sequencing in patients with BC. Many types of samples obtained from clinical tissue specimens, fluids, body, and BC cell lines (120–122). Because autophagy incidence is inside cells, the present study evaluates the expression of miRNAs in BC tissue samples. miRNAs have several roles in the regulation of autophagy processes such as recycling, degradation, fusion, vesicle nucleation, vesicle elongation, and induction (123).

As mentioned in previous section about autophagy process, the ATG13, FIP200, and ULK1/2 and its negative regulator mTORC1 are the components of ULK complex which are required for initiating the autophagy process. It has been reported that the miR106b and miR20a have a repress activity on autophagy by targeting ULK1 (124). Another study demonstrated that the miR25 has a direct effect on ULK1 expression and it was considered as a novel regulator of autophagy (125). Moreover, miR26b can inhibit autophagy by targeting ULK-2 (126). In addition, miR20a has been reported to modulate autophagy through targeting FIP200 (127). MiR15a, miR16, and miR18 exert pro-autophagic effect by inhibiting mTORC expression and have been recognized as onco-miR (128, 129). The Beclin-1-PI3KCIII-Vps15 complex, ATG2-18 complex, and ATG9 are fundamental components for the vesicle nucleation as the second step of autophagy process. Several miRNAs can regulate this step of autophagy. For instance, miR30a AND miR17 were identified to suppress Beclin-1 expression, therefore disrupting vesicle nucleation (130, 131). Also, the results of some studies have been revealed that miR199a and miR152 can directly target ATG14 to negatively regulate the activation of the Beclin-1-PI3KCIII-Vps15 complex (132, 133). Furthermore, studies have reported that activity of ATG2-18 complex and ATG9 are repressed by miR130a and miR34a (134, 135). Several miRNAs contribute in regulating the expression of ATG12-5-16 components such as miR30a, miR23b, and miR106b throughout the process of vesicle elongation and completion (125, 136, 137). Moreover, there are other reports indicating that miR101 can target ATG4 to suppress autophagy (138). In addition, miR199a and miR423 have been reported to regulate the resistance by targeting ATG7 and develop autophagy (116, 139). MiR204 was demonstrated to stop the activation of ILC3-II, applying a similar effect in this process (140).

Eventually, the cargo inside and autolysosome maturation undergo degradation and recycling process. MiR101 was identified to inhibit RAB5, a main regulator of autolysosome fusion (138). In addition, a study reported that miR194 has an essential role in autolysosome fusion through targeting LAMP2 (141). UV Radiation Resistance Associated Gene (UVRAG) which is a main component of the Beclin1-Vps34 complex and plays a central role in autolysosome maturation. miR-183 and miR-125b were discovered to target UVRAG (142, 143) (**Figure 2**). ATG7 is overexpressed in human invasive BC tissues. It has been demonstrated that miR190a facilitates BC invasion and autophagy through stabilizing ATG7 mRNA by binding to its 3′UTR (144).

Collectively, dysregulation of miRNAs serves to progress the cancer through targeting components of autophagy pathway. Thereby, modification of miRNAs expression could help to suppress the invasion of cancer.

As discussed above, the main objective of BCG therapy is preventing occurrence and progression of cancer. Some studies have indicated that MImiR-9-3, miR-124-2, miR-124-3, and miR-137 were frequently methylated in the initiation phase of cancers which can be utilized as potential biomarkers for BC diagnosis (145). Interestingly, to our knowledge there is no published study that had investigated the possible effects of BCG on miRNAs profile expression. However, several studies have been conducted on the roles of BCG and miRNAs in infectious diseases. For examples, a performed study evaluated the alteration of immune-related miR142-3p in macrophage RAW264.7 cells in treatment with BCG infection (146). Their results showed that miR142-3p can negatively regulate the production of pro-inflammatory mediators IL-6, TNF-α, and NF-κB (NF-κB1) in the macrophages by post-transcriptionally down-regulating IRAK-1 protein expression (146). Moreover, another study demonstrated that *M. bovis* BCG induces Toll-like receptor 2 (TLR2)-dependent miR155 expression, which establishes signaling cross talk among mitogen-activated protein kinases (MAPKs), protein kinase Cδ (PKCδ), and phosphatidylinositol 3-kinase (PI3K) and recruitment of c-ETS and NF-κB to miR-155 promoter. Finally, they indicated the cellular reprogramming was organized by miR155 during immune responses to mycobacterial infection (147).

Collectively, BCG is capable of stimulating immune responses and triggering signaling molecular pathway in interaction with miRNAs. It seems that BCG instillation can influence miRNAs expression in BC tissue. However, further studies should be conducted to shed more light on this interaction in BC.

Currently, there is little evidence on how miRNAs can alter NETosis process. However, some studies conducted about the interaction between miRNA expression and neutrophil. In this regard, as study showed that neutrophil-associated miR-99b-5p, miR-191-5p, and miR-197-3p transcript levels were remarkably lower in *mycobacterium tuberculosis* (MT) infections. Differentially expression of miRNAs in neutrophils can predominantly effect the signaling pathways leading to

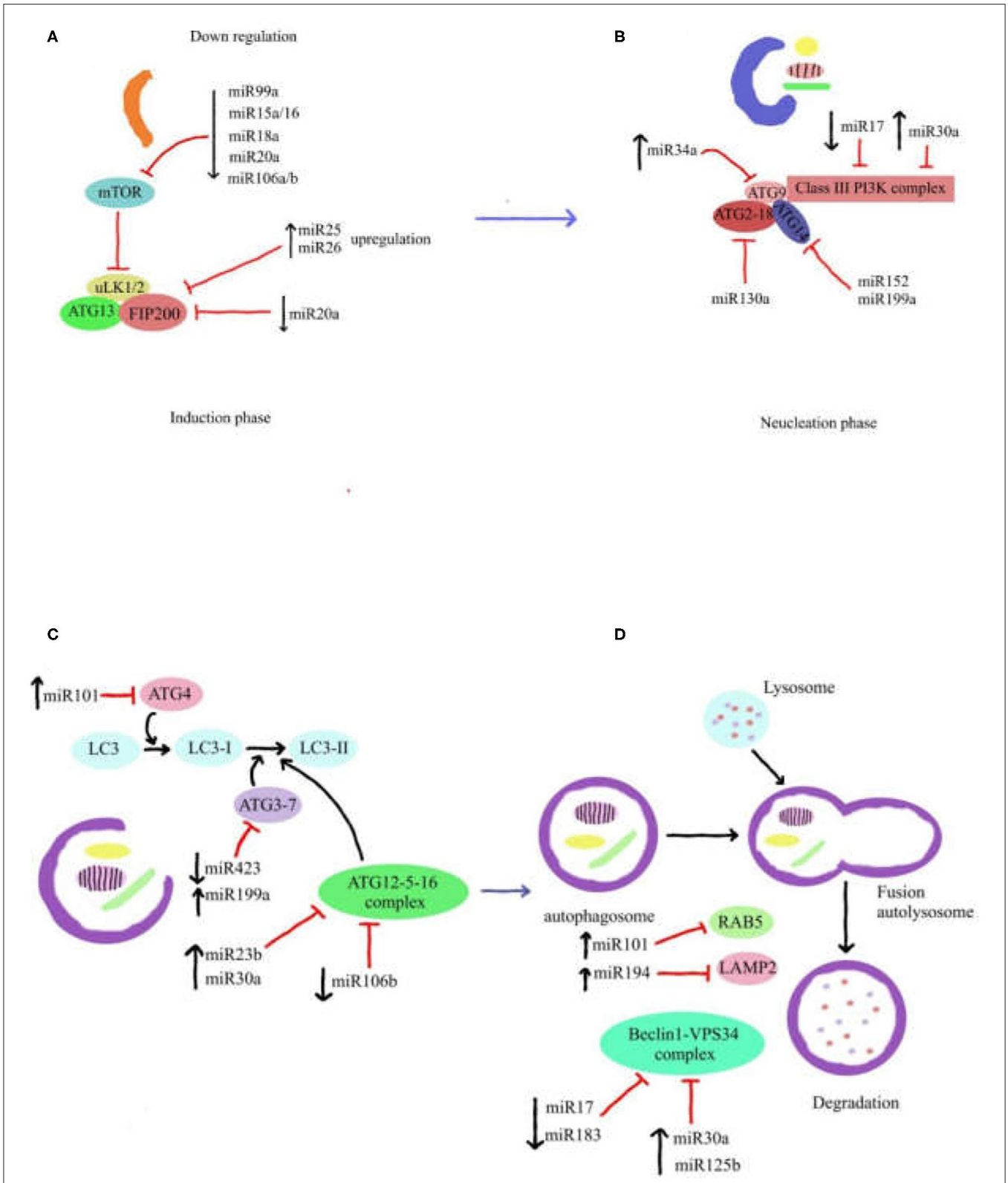

FIGURE 2 | Role of miRNAs in autophagy pathway. Autophagy process is illustrated in four steps **(A–D)**, in which miRNAs affect each of autophagy components. The various roles of miRNAs demonstrate that miRNA gene expression can regulate components of autophagy pathway. Some of these miRNAs have important role in each step of autophagy process. Autophagy pathway can be also inhibited by downregulation and/or upregulation of miRNAs gene expression.

cytokine productions. The reduced expression in MT cases could indicate a lack of inhibition on signaling pathways, which may result in elevated production of pro-inflammatory cytokines such as IFN-γ (148).

As was discussed previously, IFN-γ is a crucial cytokine in immune responses to microbial infections. In this regard, a study demonstrated significance of IFN-γ role in NETs function when lung neutrophils of mice infected by *Streptococcus pneumonia*, *Staphylococcus aureus*, and *Escherichia coli*. Their results revealed that decreased formation of NETs in IFN-γ-deficient mice could result in the increase in S. *pneumonia* bacterial numbers (149, 150).

Gantier comprehensively investigated roles of role of miRNAs in neutrophil's formation, function, and biology and reported a list including 48 miRNAs that are expressed in neutrophils (149). Thus, we found that miRNAs have important role in regulation of neutrophil biology. Among expressed miRNAs in neutrophil, miR1 and miR133 were down-regulated in patients with myeloproliferative disorder. Furthermore, miR223 has been demonstrated to be one of the main miRNAs expressed by human granulocytes (CD15). A study reported an essential role of miR223 in neutrophil differentiation by evaluating miR223-deficient mice (151). Ward et al. indicated that miR-34b, miR-328, miR-483-3p, miR-491-3p, miR-595, and miR-1281 miRNAs were up-regulated when neutrophils treated with GM-CSF. Indeed, GM-CSF treatment led to delay apoptosis and senescence (152). IL-8 as a CXC chemokine ligand has a necessary function in the recruitment of human leukocytes specially neutrophils and also produced by various immune cells such as neutrophils, macrophages, and epithelial cells stimulated with TNF-α. miR17 can directly target IL-8 mRNA, therefore miR17 inhibition could cause a drastically increase in IL-8 production (153). On the contrary, miR155 can increase IL-8 secretion from neutrophils of patients with cystic fibrosis by the suppression of SHIP expression. Elevated miR-155 levels can straightly decrease levels of SHIP-1, which ordinarily destabilize IL-8 mRNA via Akt signaling (154). Hence, therapeutic approaches should focus on decreasing miR155 and increasing miR17 levels which could dampen IL-8 production by neutrophils.

Some studies also determined that neutrophils have capability to polarize and migrate toward center of tumor cells that highly express these chemotactic factors (155, 156). As soon as, the maximum production zone of the chemokine to be reached, the gradient of chemotactic concentration vanishes. Chemotactic stimulus can establish NETs formation when high level of receptor is occupied (89). A study with using intravital microscopy in tumors could observe that neutrophils are able to move to the tumor and form NETs (personal communication). In the tumor microenvironment, these structures have been related often to processes that favor metastasis (37, 157, 158). A study in mice also indicated that NETs facilitate the metastasis capacity of tumor cells favoring their migration (159). However, the extent to which NETs can alter the function of other immune cells in the tumor microenvironment has not been directly demonstrated (160).

There are relatively scarce data about the roles of miRNAs in neutrophil biology in the literature. Different expression of miRNAs in tumor microenvironment could be a useful option to prognosis and detection and treatment various cancers specially BC.

BCG OPTIMIZATION FOR BLADDER CANCER

Todays, molecular targeting as a novel therapeutic approach is considered for improving survival and prognosis in patients with BC (161). Various studies have shown that abnormally expressed miRNAs involvement to BC progression by exerting as oncogenes or tumor suppressors. Recent reports have demonstrated that the non-invasive detection of miRNAs from body fluids, including urine and blood of BC patients, can be used to improve prognosis and diagnosis (162, 163). Thereby, the recognition of dysregulated miRNAs to promote clinical applications in BC is really pivotal. Autophagy is contributed in several steps of cancer development, and the collection of evidence associating the dysregulation of autophagy-related miRNAs in cancer has arisen remarkably (164). As yet, about 400 miRNAs have been accredited as predicted to have interactions associated with autophagy (164). In this respect, a study identified various dysregulated miRNAs in BC (165). For instance, the findings of some studies revealed that miR-99a-5p exhibited a tumor suppressor role via targeting mTOR in BC (166). Additionally, miR-30a-5p was another miRNA that increased drug sensitivity to cisplatin by targeting Beclin-1 and ATG5 in BC (167). Thereby, the performed studies have been demonstrated a promising effect of the miRNAs in BC therapy (161). On the other hand, NETs formation in tumor regulation of autophagy by miRNAs can enhance the NETs formation in patients with BC (13, 113, 168). Generally, NETs formation can facilitate BCG performance in BC treatment. Autophagy and NETs are able to suppress tumor activity through specific mechanisms including mTOR signaling pathway and produced ROS of neutrophils, respectively (13, 65). Thus, promoting NETs performance and modifying autophagy by miRNAs can be utilized to improve BCG therapy in patients with BC. Additional efforts are essential to assess the therapeutic roles of candidate miRNAs and its interaction between NETs formation and autophagy pathway. Eventually, further investigations are necessary to further clarify novel RNA networks in BC cells.

CONCLUSION

BCG therapy is usually prescribed to the patients with non-muscle invasive BC. Review of the current evidence shows that miRNAs play significant roles in triggering and regulating autophagy process and autophagy-induced NETs formation, which subsequently can promote BCG therapy in patients with BC. Moreover, BCG-induced NETs have been reportedly to exert cytotoxic effects, induce apoptosis, cell cycle arrest, and inhibition of tumor cells migration into bladder environment. Moreover,

neutrophils can prim T cells and activate DCs to robust immune responses against tumor growth. Therefore, it could be concluded that utilization of miRNAs network as a therapeutic approach may reinforce BCG function at high efficiency through inducing autophagy which in turn can enhance ROS producing and NETs formation by stimulating neutrophils.

AUTHOR CONTRIBUTIONS

CYM and NX were responsible for the conception and design of the study. XX performed the study retrieval. XX and YD contributed to quality evaluation. CYM and XX contributed to the data collection and statistical analysis. CYM drafted the manuscript. NX and CYM were responsible for the revision of the manuscript. The final manuscript had been read and approved by all authors.

FUNDING

This work was supported by the Zhejiang Provincial Natural Science Foundation of China (No. LQ19H160027 to CYM).

ACKNOWLEDGMENTS

Authors would like to thank all the members of Medical Oncology Cancer Center department, The First Affiliated Hospital, College of Medicine, Zhejiang University, Hangzhou, Zhejiang, China for their thoughtful comments on preparation of this manuscript.

REFERENCES

1. Von Der Maase H, Sengelov L, Roberts JT, Ricci S, Dogliotti L, Oliver T, et al. Long-term survival results of a randomized trial comparing gemcitabine plus cisplatin, with methotrexate, vinblastine, doxorubicin, plus cisplatin in patients with bladder cancer. *J Clin Oncol*. (2005) 23:4602–8. doi: 10.1200/JCO.2005.07.757
2. Bellmunt J, Von Der Maase H, Mead GM, Skoneczna I, De Santis M, Daugaard G, et al. Randomized phase III study comparing paclitaxel/cisplatin/ gemcitabine and gemcitabine/cisplatin in patients with locally advanced or metastatic urothelial cancer without prior systemic therapy: EORTC intergroup study 30987. *J Clin Oncol*. (2012) 30:1107–13. doi: 10.1200/JCO.2011.38.6979
3. Grossman HB, Natale RB, Tangen CM, Speights VO, Vogelzang NJ, Trump DL, et al. Neoadjuvant chemotherapy plus cystectomy compared with cystectomy alone for locally advanced bladder cancer. *N Engl J Med*. (2003) 349:859–66. doi: 10.1056/NEJMoa022148
4. Necchi A, Pond GR, Giannatempo P, Di Lorenzo G, Eigl BJ, Locke J, et al. Cisplatin-based first-line therapy for advanced urothelial carcinoma after previous perioperative cisplatin-based therapy. *Clin Genitourin Cancer*. (2015) 13:178–84. doi: 10.1016/j.clgc.2014.08.010
5. Kaufmann E, Sanz J, Dunn JL, Khan N, Mendonça LE, Pacis A, et al. BCG educates hematopoietic stem cells to generate protective innate immunity against tuberculosis. *Cell*. (2018) 172:176–190.e19. doi: 10.1016/j.cell.2017.12.031
6. Hisada Y, Grover SP, Maqsood A, Houston R, Ay C, Noubouossie DF, et al. Neutrophils and neutrophil extracellular traps enhance venous thrombosis in mice bearing human pancreatic tumors. *Haematologica*. (2020) 105:218–25. doi: 10.3324/haematol.2019.217083
7. Mizushima N, Levine B, Cuervo AM, Klionsky DJ. Autophagy fights disease through cellular self-digestion. *Nature*. (2008) 451:1069–75. doi: 10.1038/nature06639
8. Galluzzi L, Pietrocola F, Levine B, Kroemer G. Metabolic control of autophagy. *Cell*. (2014) 159:1263–76. doi: 10.1016/j.cell.2014.11.006
9. Feng Y, He D, Yao Z, Klionsky DJ. The machinery of macroautophagy. *Cell Res*. (2014) 24:24–41. doi: 10.1038/cr.2013.168
10. Kang R, Xie Y, Zeh HJ, Klionsky DJ, Tang D. Mitochondrial quality control mediated by PINK1 and PRKN: links to iron metabolism and tumor immunity. *Autophagy*. (2019) 15:172–3. doi: 10.1080/15548627.2018.1526611
11. Parzych KR, Klionsky DJ. An overview of autophagy: morphology, mechanism, and regulation. *Antioxidants Redox Signal*. (2014) 20:460–73. doi: 10.1089/ars.2013.5371
12. Mizushima N. Autophagy: process and function. *Genes Dev*. (2007) 21:2861–73. doi: 10.1101/gad.1599207
13. Liu K, Sun E, Lei M, Li L, Gao J, Nian X, et al. BCG-induced formation of neutrophil extracellular traps play an important role in bladder cancer treatment. *Clin Immunol*. (2019) 201:4–14. doi: 10.1016/j.clim.2019.02.005
14. Vita F, Siracusano S, Abbate R, Ciciliato S, Borelli V, Soranzo MR, et al. BCG prophylaxis in bladder cancer produces activation of recruited neutrophils. *Can J Urol*. (2011) 18:5517–23. Available online at: https://www.canjurol.com/abstract.php?ArticleID=&version=1.0&PMID=21333042
15. Baehrecke EH. miRNAs: micro managers of programmed cell death. *Curr Biol*. (2003) 13:R469–72. doi: 10.1016/S0960-9822(03)00405-6
16. Usuba W, Urabe F, Yamamoto Y, Matsuzaki J, Sasaki H, Ichikawa M, et al. Circulating miRNA panels for specific and early detection in bladder cancer. *Cancer Sci*. (2019) 110:408–19. doi: 10.1111/cas.13856
17. Fu LL, Wen X, Bao JK, Liu B. MicroRNA-modulated autophagic signaling networks in cancer. *Int J Biochem Cell Biol*. (2012) 44:733–6. doi: 10.1016/j.biocel.2012.02.004
18. Eskelinen EL. The dual role of autophagy in cancer. *Curr Opin Pharmacol*. (2011) 11:294–300. doi: 10.1016/j.coph.2011.03.009
19. Chen PS, Su JL, Hung MC. Dysregulation of MicroRNAs in cancer. *J Biomed Sci*. (2012) 19:90. doi: 10.1186/1423-0127-19-90
20. Buffen K, Oosting M, Quintin J, Ng A, Kleinnijenhuis J, Kumar V, et al. Autophagy controls BCG-induced trained immunity and the response to intravesical BCG therapy for bladder cancer. *PLoS Pathog*. (2014) 10:1004485. doi: 10.1371/journal.ppat.1004485
21. Heneghan HM, Miller N, Kerin MJ. MiRNAs as biomarkers and therapeutic targets in cancer. *Curr Opin Pharmacol*. (2010) 10:543–50. doi: 10.1016/j.coph.2010.05.010
22. Kiselyov A, Bunimovich-Mendrazitsky S, Startsev V. Treatment of Non-Muscle Invasive Bladder Cancer with Bacillus Calmette-Guerin (BCG): Biological markers and simulation studies. *BBA Clinical*. (2015) 4:27–34. doi: 10.1016/j.bbacli.2015.06.002
23. Morales A, Eidinger D, Bruce AW. Intracavitary Bacillus Calmette Guerin in the treatment of superficial bladder tumors. *J Urol*. (1976) 116:180–2. doi: 10.1016/S0022-5347(17)58737-6
24. Babjuk M, Oosterlinck W, Sylvester R, Kaasinen E, Böhle A, Palou-Redorta J, et al. EAU guidelines on non-muscle-invasive urothelial carcinoma of the bladder, the (2011) Update. *Eur Urol*. (2011) 59:997–1008. doi: 10.1016/j.eururo.2011.03.017
25. Hall MC, Chang SS, Dalbagni G, Pruthi RS, Seigne JD, Skinner EC, et al. Guideline for the management of nonmuscle invasive bladder cancer (Stages Ta, T1, and Tis): (2007). *Update. J Urol*. (2007) 178:2314–30. doi: 10.1016/j.juro.2007.09.003
26. Han RF, Pan JG. Can intravesical bacillus Calmette-Guérin reduce recurrence in patients with superficial bladder cancer? A meta-analysis of randomized trials. *Urology*. (2006) 67:1216–23. doi: 10.1016/j.urology.2005.12.014
27. Shelley MD, Kynaston H, Court J, Wilt TJ, Coles B, Burgon K, et al. A systematic review of intravesical bacillus Calmette-Guérin plus transurethral resection vs transurethral resection alone in Ta and T1 bladder cancer. *BJU Int*. (2001) 88:209–16. doi: 10.1046/j.1464-410x.2001.02306.x

28. Sylvester RJ, van der Meijdendonald APM, Lamm L. Intravesical bacillus calmette-guerin reduces the risk of progression in patients with superficial bladder cancer: a meta-analysis of the published results of randomized clinical trials. *J Urol*. (2002) 168:1964–70. doi: 10.1016/S0022-5347(05)64273-5
29. Redelman-Sidi G, Glickman MS, Bochner BH. The mechanism of action of BCG therapy for bladder cancer-A current perspective. *Nat Rev Urol*. (2014) 11:153–62. doi: 10.1038/nrurol.2014.15
30. Shang PF, Kwong J, Wang ZP, Tian J, Jiang L, Yang K, et al. Intravesical bacillus calmette-guérin versus epirubicin for Ta and T1 bladder cancer. *Cochrane Database Syst Rev*. (2011) 5:CD006885. doi: 10.1002/14651858.CD006885.pub2
31. Shelley MD, Wilt TJ, Court J, Coles B, Kynaston H, Mason MD. Intravesical bacillus Calmette-Guérin is superior to mitomycin C in reducing tumour recurrence in high-risk superficial bladder cancer: a meta-analysis of randomized trials. *BJU Int*. (2004) 93:485–90. doi: 10.1111/j.1464-410X.2003.04655.x
32. Kanaya K, Kondo K, Suzukawa K, Sakamoto T, Kikuta S, Okada K, et al. Innate immune responses and neuroepithelial degeneration and regeneration in the mouse olfactory mucosa induced by intranasal administration of Poly(I:C). *Cell Tissue Res*. (2014) 357:279–99. doi: 10.1007/s00441-014-1848-2
33. Mantovani A, Cassatella MA, Costantini C, Jaillon S. Neutrophils in the activation and regulation of innate and adaptive immunity. *Nat Rev Immunol*. (2011) 11:519–31. doi: 10.1038/nri3024
34. Brinkmann V, Zychlinsky A. Neutrophil extracellular traps: Is immunity the second function of chromatin? *J Cell Biol*. (2012) 198:773–83. doi: 10.1083/jcb.201203170
35. Branzk N, Papayannopoulos V. Molecular mechanisms regulating NETosis in infection and disease. *Semin Immunopathol*. (2013) 35:513–30. doi: 10.1007/s00281-013-0384-6
36. Berger-Achituv S, Brinkmann V, Abed UA, Kühn LI, Ben-Ezra J, Elhasid R, et al. A proposed role for neutrophil extracellular traps in cancer immunoediting. *Front Immunol*. (2013) 4:48. doi: 10.3389/fimmu.2013.00048
37. Cools-Lartigue J, Spicer J, McDonald B, Gowing S, Chow S, Giannias B, et al. Neutrophil extracellular traps sequester circulating tumor cells and promote metastasis. *J Clin Invest*. (2013) 123:3446–58. doi: 10.1172/JCI67484
38. Sangaletti S, Tripodo C, Vitali C, Portararo P, Guarnotta C, Casalini P, et al. Defective stromal remodeling and neutrophil extracellular traps in lymphoid tissues favor the transition from autoimmunity to lymphomas. *Cancer Discov*. (2014) 4:110–29. doi: 10.1158/2159-8290.CD-13-0276
39. Demers M, Krause DS, Schatzberg D, Martinod K, Voorhees JR, Fuchs TA, et al. Cancers predispose neutrophils to release extracellular DNA traps that contribute to cancer-associated thrombosis. *Proc Natl Acad Sci USA*. (2012) 109:13076–81. doi: 10.1073/pnas.1200419109
40. Cools-Lartigue J, Spicer J, Najmeh S, Ferri L. Neutrophil extracellular traps in cancer progression. *Cell Mol Life Sci*. (2014) 71:4179–94. doi: 10.1007/s00018-014-1683-3
41. Liang S, Hoskins M, Khanna P, Kunz RF, Dong C. Effects of the tumor-leukocyte microenvironment on melanoma–neutrophil adhesion to the endothelium in a shear flow. *Cell Mol Bioeng*. (2008) 1:189–200. doi: 10.1007/s12195-008-0016-8
42. McDonald B, Spicer J, Giannais B, Fallavollita L, Brodt P, Ferri LE. Systemic inflammation increases cancer cell adhesion to hepatic sinusoids by neutrophil mediated mechanisms. *Int J Cancer*. (2009) 125:1298–305. doi: 10.1002/ijc.24409
43. Spicer JD, McDonald B, Cools-Lartigue JJ, Chow SC, Giannias B, Kubes P, et al. Neutrophils promote liver metastasis via Mac-1-mediated interactions with circulating tumor cells. *Cancer Res*. (2012) 72:3919–27. doi: 10.1158/0008-5472.CAN-11-2393
44. Erpenbeck L, Schön MP. Neutrophil extracellular traps: protagonists of cancer progression? *Oncogene*. (2017) 36:2483–90. doi: 10.1038/onc.2016.406
45. Fridlender ZG, Sun J, Kim S, Kapoor V, Cheng G, Ling L, et al. Polarization of tumor-associated neutrophil phenotype by TGF-β: "N1" versus "N2" TAN. *Cancer Cell*. (2009) 16:183–94. doi: 10.1016/j.ccr.2009.06.017
46. Piccard H, Muschel RJ, Opdenakker G. On the dual roles and polarized phenotypes of neutrophils in tumor development and progression. *Crit Rev Oncol Hematol*. (2012) 82:296–309. doi: 10.1016/j.critrevonc.2011.06.004
47. Powell DR, Huttenlocher A. Neutrophils in the tumor microenvironment. *Trends Immunol*. (2016) 37:41–52. doi: 10.1016/j.it.2015.11.008
48. Acuff HB, Carter KJ, Fingleton B, Gorden DL, Matrisian LM. Matrix metalloproteinase-9 from bone marrow-derived cells contributes to survival but not growth of tumor cells in the lung microenvironment. *Cancer Res*. (2006) 66:259–66. doi: 10.1158/0008-5472.CAN-05-2502
49. Masson V, De La Ballina LR, Munaut C, Wielockx B, Jost M, Maillard C, et al. Contribution of host MMP-2 and MMP-9 to promote tumor vascularization and invasion of malignant keratinocytes. *FASEB J*. (2005) 19 :1–17. doi: 10.1096/fj.04-2140fje
50. Dallegri F, Ottonello L, Ballestrero A, Dapino P, Ferrando F, Patrone F, et al. Tumor cell lysis by activated human neutrophils: analysis of neutrophil-delivered oxidative attack and role of leukocyte function-associated antigen 1. *Inflammation*. (1991) 15:15–30. doi: 10.1007/BF00917906
51. Lichtenstein A. Stimulation of the respiratory burst of murine peritoneal inflammatory neutrophils by conjugation with tumor cells. *Cancer Res*. (1987) 47: 2211–7.
52. Granot Z, Henke E, Comen EA, King TA, Norton L, Benezra R. Tumor entrained neutrophils inhibit seeding in the premetastatic lung. *Cancer Cell*. (2011) 20:300–14. doi: 10.1016/j.ccr.2011.08.012
53. Al-Benna S, Shai Y, Jacobsen F, Steinstraesser L. Oncolytic activities of host defense peptides. *Int J Mol Sci*. (2011) 12:8027–51. doi: 10.3390/ijms12118027
54. Odajima T, Onishi M. Inactivation of urate oxidase by a system composed of lactoperoxidase, hydrogen peroxide and bromide. *Cell Biochem Funct*. (1998) 16:139–47. doi: 10.1002/(SICI)1099-0844(199806)16:2<139::AID-CBF781>3.0.CO;2-2
55. Lanza F, Giuliani AL, Amelotti F, Spisani S, Traniello S CG. Depressed neutrophil-mediated tumor cell cytotoxicity in subjects affected by hereditary myeloperoxidase deficiency and secondary neoplasia. *Haematologica*. (1988) 73:355.
56. Saffarzadeh M, Juenemann C, Queisser MA, Lochnit G, Barreto G, Galuska SP, et al. Neutrophil extracellular traps directly induce epithelial and endothelial cell death: a predominant role of histones. *PLoS ONE*. (2012) 7:32366. doi: 10.1371/journal.pone.0032366
57. Mittendorf EA, Alatrash G, Qiao N, Wu Y, Sukhumalchandra P, St. John LS, et al. Breast cancer cell uptake of the inflammatory mediator neutrophil elastase triggers an anticancer adaptive immune response. *Cancer Res*. (2012) 72:3153–62. doi: 10.1158/0008-5472.CAN-11-4135
58. Tillack K, Breiden P, Martin R, Sospedra M. T lymphocyte priming by neutrophil extracellular traps links innate and adaptive immune responses. *J Immunol*. (2012) 188:3150–9. doi: 10.4049/jimmunol.1103414
59. Yan J, Kloecker G, Fleming C, Bousamra M, Hansen R, Hu X, et al. Human polymorphonuclear neutrophils specifically recognize and kill cancerous cells. *Oncoimmunology*. (2014) 3:e950163. doi: 10.4161/15384101.2014.950163
60. Souto JC, Vila L, Brú A. Polymorphonuclear neutrophils and cancer: Intense and sustained neutrophilia as a treatment against solid tumors. *Med Res Rev*. (2011) 31:311–63. doi: 10.1002/med.20185
61. Demers M, Wagner DD. NETosis: a new factor in tumor progression and cancer-associated thrombosis. *Semin Thromb Hemost*. (2014) 40:277–83. doi: 10.1055/s-0034-1370765
62. Cedervall J, Olsson AK. NETosis in cancer. *Oncoscience*. (2015) 2:900–1. doi: 10.18632/oncoscience.264
63. Becich MJ, Carroll S, Ratliff TL. Internalization of bacille calmette-guerin by bladder tumor cells. *J Urol*. (1991) 145:1316–24. doi: 10.1016/S0022-5347(17)38622-6
64. Luo YI, Szilvasi A, Chen X, DeWolf WC, O'Donnell MA. A novel method for monitoring Mycobacterium bovis BCG trafficking with recombinant BCG expressing green fluorescent protein. *Clin Diagn Lab Immunol*. (1996) 3:761–8. doi: 10.1128/cdli.3.6.761-768.1996
65. Simons MP, O'Donnell MA, Griffith TS. Role of neutrophils in BCG immunotherapy for bladder cancer. *Urologic Oncol*. (2008) 26:341–5. doi: 10.1016/j.urolonc.2007.11.031

66. Suttmann H, Riemensberger J, Bentien G, Schmaltz D, Stöckle M, Jocham D, et al. Neutrophil granulocytes are required for effective Bacillus Calmette-Guérin immunotherapy of bladder cancer and orchestrate local immune responses. *Cancer Res*. (2006) 66:8250–7. doi: 10.1158/0008-5472.CAN-06-1416
67. Böhle A, Brandau S. Immune mechanisms in bacillus Calmette-Guerin immunotherapy for superficial bladder cancer. *J Urol*. (2003) 170:964–9. doi: 10.1097/01.ju.0000073852.24341.4a
68. Brincks EL, Risk MC, Griffith TS. PMN and anti-tumor immunity-The case of bladder cancer immunotherapy. *Semin Cancer Biol*. (2013) 23:183–9. doi: 10.1016/j.semcancer.2013.02.002
69. Zhou S-L, Zhou Z-J, Hu Z-Q, Huang X-W, Wang Z, Chen E-B, et al. Tumor-associated neutrophils recruit Macrophages and T-regulatory cells to promote progression of hepatocellular carcinoma and resistance to sorafenib. *Gastroenterology*. (2016) 150:1646–58.e17. doi: 10.1053/j.gastro.2016.02.040
70. Di Carlo E, Forni G, Lollini PL, Colombo MP, Modesti A, Musiani P. The intriguing role of polymorphonuclear neutrophils in antitumor reactions. *Blood. Am Soc Hematol*. (2001) 97:339–45. doi: 10.1182/blood.V97.2.339
71. Houghton AMG. The paradox of tumor-associated neutrophils: Fueling tumor growth with cytotoxic substances. *Cell Cycle*. (2010) 9:1732–7. doi: 10.4161/cc.9.9.11297
72. Mizushima N, Komatsu M. Autophagy: renovation of cells and tissues. *Cell*. (2011) 147:728–41. doi: 10.1016/j.cell.2011.10.026
73. Kroemer G, Mariño G, Levine B. Autophagy and the integrated stress response. *Mol Cell*. (2010) 40:280–93. doi: 10.1016/j.molcel.2010.09.023
74. Sancak Y, Bar-Peled L, Zoncu R, Markhard AL, Nada S, Sabatini DM. Ragulator-rag complex targets mTORC1 to the lysosomal surface and is necessary for its activation by amino acids. *Cell*. (2010) 141:290–303. doi: 10.1016/j.cell.2010.02.024
75. Sridharan S, Jain K BA. Regulation of autophagy by kinases. *Cancers*. (2011) 3:2630–54. doi: 10.3390/cancers3022630
76. Yang Z, Klionsky DJ. Mammalian autophagy: Core molecular machinery and signaling regulation. *Curr Opin Cell Biol*. (2010) 22:124–31. doi: 10.1016/j.ceb.2009.11.014
77. Simon HU, Friis R, Tait SWG, Ryan KM. Retrograde signaling from autophagy modulates stress responses. *Science Signaling*. (2017) 10:eaag2791. doi: 10.1126/scisignal.aag2791
78. Bjørkøy G, Lamark T, Pankiv S, Øvervatn A, Brech A, Johansen T. Chapter 12 monitoring autophagic degradation of p62/SQSTM1. *Methods Enzymol*. (2009) 451:181–97. doi: 10.1016/S0076-6879(08)03612-4
79. Bitto A, Lerner CA, Nacarelli T, Crowe E, Torres C, Sell C. p62/SQSTM1 at the interface of aging, autophagy, and disease. *Age*. (2014) 36:1123–37. doi: 10.1007/s11357-014-9626-3
80. Ichimura Y, Komatsu M. Selective degradation of p62 by autophagy. *Semin Immunopathol*. (2010) 32:431–6. doi: 10.1007/s00281-010-0220-1
81. Li WW, Li J, Bao JK. Microautophagy: lesser-known self-eating. *Cell Mol Life Sci*. (2012) 69:1125–36. doi: 10.1007/s00018-011-0865-5
82. Liu H, He Z, Simon HU. Targeting autophagy as a potential therapeutic approach for melanoma therapy. *Semin Cancer Biol*. (2013) 23:352–60. doi: 10.1016/j.semcancer.2013.06.008
83. RoŽman S, Yousefi S, Oberson K, Kaufmann T, Benarafa C, Simon HU. The generation of neutrophils in the bone marrow is controlled by autophagy. *Cell Death Differ*. (2015) 22:445–56. doi: 10.1038/cdd.2014.169
84. Huang Y, Tan P, Wang X, Yi Y, Hu Y, Wang D, et al. Transcriptomic insights into temporal expression pattern of autophagy genes during monocytic and granulocytic differentiation. *Autophagy*. (2018) 14:558–9. doi: 10.1080/15548627.2018.1425060
85. Tan C, Aziz M, Wang P. The vitals of NETs. *J Leukocyte Biol*. (2020) 14:1–12. doi: 10.1002/JLB.3RU0620-375R
86. Park SY, Shrestha S, Youn YJ, Kim JK, Kim SY, Kim HJ, et al. Autophagy primes neutrophils for neutrophil extracellular trap formation during sepsis. *Am J Respir Crit Care Med*. (2017) 196:577–89. doi: 10.1164/rccm.201603-0596OC
87. Filomeni G, De Zio D, Cecconi F. Oxidative stress and autophagy: the clash between damage and metabolic needs. *Cell Death Differ*. (2015) 22:377–88. doi: 10.1038/cdd.2014.150
88. Remijsen Q, Kuijpers TW, Wirawan E, Lippens S, Vandenabeele P, Vanden Berghe T. Dying for a cause: NETosis, mechanisms behind an antimicrobial cell death modality. *Cell Death Different*. (2011) 18:581–8. doi: 10.1038/cdd.2011.1
89. Skendros P, Mitroulis I, Ritis K. Autophagy in neutrophils: from granulopoiesis to neutrophil extracellular traps. *Front Cell Dev Biol*. (2018) 6:109. doi: 10.3389/fcell.2018.00109
90. Xu F, Zhang C, Zou Z, Fan EKY, Chen L, Li Y, et al. Aging-related Atg5 defect impairs neutrophil extracellular traps formation. *Immunology*. (2017) 151:417–32. doi: 10.1111/imm.12740
91. Germic N, Stojkov D, Oberson K, Yousefi S, Simon HU. Neither eosinophils nor neutrophils require ATG5-dependent autophagy for extracellular DNA trap formation. *Immunology*. (2017) 152:517–25. doi: 10.1111/imm.12790
92. Pieterse E, Rother N, Yanginlar C, Hilbrands LB, van der Vlag J. Neutrophils discriminate between lipopolysaccharides of different bacterial sources and selectively release neutrophil extracellular traps. *Front Immunol*. (2016) 7:484. doi: 10.3389/fimmu.2016.00484
93. Eisenberg-Lerner A, Kimchi A. The paradox of autophagy and its implication in cancer etiology and therapy. *Apoptosis*. (2009) 14:376–91. doi: 10.1007/s10495-008-0307-5
94. Kung CP, Budina A, Balaburski G, Bergenstock MK, Murphy ME. Autophagy in tumor suppression and cancer therapy. *Crit Rev Eukaryotic Gene Expression*. (2011) 21:71–100. doi: 10.1615/CritRevEukarGeneExpr.v21.i1.50
95. White E. Deconvoluting the context-dependent role for autophagy in cancer. *Nat Rev Cancer*. (2012) 12:401–10. doi: 10.1038/nrc3262
96. Liang XH, Jackson S, Seaman M, Brown K, Kempkes B, Hibshoosh H, et al. Induction of autophagy and inhibition of tumorigenesis by beclin 1. *Nature*. (1999) 402:672–6. doi: 10.1038/45257
97. Furuya N, Yu J, Byfield M, Pattingre S, Levine B. The evolutionarily conserved domain of Beclin 1 is required for Vps34 binding, autophagy and tumor suppressor function. *Autophagy*. (2005) 1:46–52. doi: 10.4161/auto.1.1.1542
98. Yang ZJ, Chee CE, Huang S, Sinicrope FA. The role of autophagy in cancer: therapeutic implications. *Mol Cancer Therapeut*. (2011) 10:1533–41. doi: 10.1158/1535-7163.MCT-11-0047
99. Cianfanelli V, Fuoco C, Lorente M, Salazar M, Quondamatteo F, Gherardini PF, et al. AMBRA1 links autophagy to cell proliferation and tumorigenesis by promoting c-Myc dephosphorylation and degradation. *Nat Cell Biol*. (2015) 17:20–30. doi: 10.1038/ncb3072
100. Takamura A, Komatsu M, Hara T, Sakamoto A, Kishi C, Waguri S, et al. Autophagy-deficient mice develop multiple liver tumors. *Genes Dev*. (2011) 25:795–800. doi: 10.1101/gad.2016211
101. Yang S, Wang X, Contino G, Liesa M, Sahin E, Ying H, et al. Pancreatic cancers require autophagy for tumor growth. *Genes Dev*. (2011) 25:717–29. doi: 10.1101/gad.2016111
102. Guo JY, Karsli-Uzunbas G, Mathew R, Aisner SC, Kamphorst JJ, Strohecker AM, et al. Autophagy suppresses progression of K-ras-induced lung tumors to oncocytomas and maintains lipid homeostasis. *Genes Dev*. (2013) 27:1447–61. doi: 10.1101/gad.219642.113
103. Yazbeck VY, Buglio D, Georgakis GV, Li Y, Iwado E, Romaguera JE, et al. Temsirolimus downregulates p21 without altering cyclin D1 expression and induces autophagy and synergizes with vorinostat in mantle cell lymphoma. *Exp Hematol*. (2008) 36:443–50. doi: 10.1016/j.exphem.2007.12.008
104. Chatterjee A, Mukhopadhyay S, Tung K, Patel D, Foster DA. Rapamycin-induced G1 cell cycle arrest employs both TGF-β and Rb pathways. *Cancer Lett*. (2015) 360:134–40. doi: 10.1016/j.canlet.2015.01.043
105. Hanahan D, Weinberg RA. The hallmarks of cancer. *Cell*. (2000) 100:57–70. doi: 10.1016/S0092-8674(00)81683-9
106. Cavallaro U, Christofori G. Molecular mechanisms of tumor angiogenesis and tumor progression. *J Neurooncol*. (2000) 50:63–70. doi: 10.1023/A:1006414621286
107. Hu YL, DeLay M, Jahangiri A, Molinaro AM, Rose SD, Carbonell WS, et al. Hypoxia-induced autophagy promotes tumor cell survival and adaptation to antiangiogenic treatment in glioblastoma. *Cancer Res*. (2012) 72:1773–83. doi: 10.1158/0008-5472.CAN-11-3831
108. Kim KW, Paul P, Qiao J, Lee S, Chung DH. Enhanced autophagy blocks angiogenesis via degradation of gastrin-releasing peptide in neuroblastoma cells. *Autophagy*. (2013) 9:1579–90. doi: 10.4161/auto.25987

109. Kenific CM, Thorburn A, Debnath J. Autophagy and metastasis: another double-edged sword. *Curr Opin Cell Biol.* (2010) 22:241–5. doi: 10.1016/j.ceb.2009.10.008
110. Guadamillas MC, Cerezo A, del Pozo MA. Overcoming anoikis - pathways to anchorageindependent growth in cancer. *J Cell Sci.* (2011) 124:3189–97. doi: 10.1242/jcs.072165
111. Li J, Yang B, Zhou Q, Wu Y, Shang D, Guo Y, et al. Autophagy promotes hepatocellular carcinoma cell invasion through activation of epithelial–mesenchymal transition. *Carcinogenesis.* (2013) 34:1343–51. doi: 10.1093/carcin/bgt063
112. Huang T, Song X, Yang Y, Wan X, Alvarez AA, Sastry N, et al. Autophagy and hallmarks of cancer. *Crit Rev Oncog.* (2018) 23:247–67. doi: 10.1615/CritRevOncog.2018027913
113. Jagannath C, Lindsey DR, Dhandayuthapani S, Xu Y, Hunter RL, Eissa NT. Autophagy enhances the efficacy of BCG vaccine by increasing peptide presentation in mouse dendritic cells. *Nat Med.* (2009) 15:267–76. doi: 10.1038/nm.1928
114. Yao K, Wang W, Li H, Lin J, Tan W, Chen Y, et al. Bacillus Calmette Guérin (BCG) activates lymphocyte to promote autophagy and apoptosis of gastric cancer MGC-803 cell. *Cell Mol Biol.* (2018) 64:11–6. doi: 10.14715/cmb/2018.64.6.3
115. Kleinnijenhuis J, Quintin J, Preijers F, Joosten LAB, Ifrim DC, Saeed S, et al. Bacille Calmette-Guérin induces NOD2-dependent nonspecific protection from reinfection via epigenetic reprogramming of monocytes. *Proc Natl Acad Sci USA.* (2012) 109:17537–42. doi: 10.1073/pnas.1202870109
116. Lin JF, Chen PC, Hwang TIS. Autophagy modulation by dysregulated micrornas in human bladder cancer. *Urol Sci.* (2019) 30:46–52. doi: 10.4103/UROS.UROS_97_18
117. Gottardo F, Liu CG, Ferracin M, Calin GA, Fassan M, Bassi P, et al. Micro-RNA profiling in kidney and bladder cancers. *Urol Oncol Semin Orig Investig.* (2007) 25:387–92. doi: 10.1016/j.urolonc.2007.01.019
118. Zhang HH, Qi F, Cao YH, Zu XB, Chen MF. Expression and clinical significance of microRNA-21, maspin and vascular endothelial growth factor-C in bladder cancer. *Oncol Lett.* (2015) 10:2610–6. doi: 10.3892/ol.2015.3540
119. Cheng Y, Zhang X, Li P, Yang C, Tang J, Deng X, et al. MiR-200c promotes bladder cancer cell migration and invasion by directly targeting RECK. *Onco Targets Ther.* (2016) 9:5091–9. doi: 10.2147/OTT.S101067
120. Han Y, Chen J, Zhao X, Liang C, Wang Y, Sun L, et al. MicroRNA expression signatures of bladder cancer revealed by deep sequencing. *PLoS ONE.* (2011) 6:18286. doi: 10.1371/journal.pone.0018286
121. Ichimi T, Enokida H, Okuno Y, Kunimoto R, Chiyomaru T, Kawamoto K, et al. Identification of novel microRNA targets based on microRNA signatures in bladder cancer. *Int J Cancer.* (2009) 125:345–52. doi: 10.1002/ijc.24390
122. Tölle A, Jung M, Rabenhorst S, Kilic E, Jung K, Weikert S. Identification of microRNAs in blood and urine as tumour markers for the detection of urinary bladder cancer. *Oncol Rep.* (2013) 30:1949–56. doi: 10.3892/or.2013.2621
123. Yao D, Jiang Y, Gao S, Shang L, Zhao Y, Huang J, et al. Deconvoluting the complexity of microRNAs in autophagy to improve potential cancer therapy. *Cell Proliferation.* (2016) 49:541–53. doi: 10.1111/cpr.12277
124. Wu H, Wang F, Hu S, Yin C, Li X, Zhao S, et al. MiR-20a and miR-106b negatively regulate autophagy induced by leucine deprivation via suppression of ULK1 expression in C2C12 myoblasts. *Cell Signal.* (2012) 24:2179–86. doi: 10.1016/j.cellsig.2012.07.001
125. Wang Z, Wang N, Liu P, Chen Q, Situ H, Xie T, et al. MicroRNA-25 regulates chemoresistance-associated autophagy in breast cancer cells, a process modulated by the natural autophagy inducer isoliquiritigenin. *Oncotarget.* (2014) 5:7013–26. doi: 10.18632/oncotarget.2192
126. John Clotaire DZ, Zhang B, Wei N, Gao R, Zhao F, Wang Y, et al. MiR-26b inhibits autophagy by targeting ULK2 in prostate cancer cells. *Biochem Biophys Res Commun.* (2016) 472:194–200. doi: 10.1016/j.bbrc.2016.02.093
127. Li S, Qiang Q, Shan H, Shi M, Gan G, Ma F, et al. MiR-20a and miR-20b negatively regulate autophagy by targeting RB1CC1/FIP200 in breast cancer cells. *Life Sci.* (2016) 147:143–52. doi: 10.1016/j.lfs.2016.01.044
128. Huang N, Wu J, Qiu W, Lyu Q, He J, Xie W, et al. MiR-15a and miR-16 induce autophagy and enhance chemosensitivity of Camptothecin. *Cancer Biol Ther.* (2015) 16:941–8. doi: 10.1080/15384047.2015.1040963
129. Qased AB, Yi H, Liang N, Ma S, Qiao S, Liu X. MicroRNA-18a upregulates autophagy and ataxia telangiectasiamutated gene expression in HCT116 colon cancer cells. *Mol Med Rep.* (2013) 7:559–64. doi: 10.3892/mmr.2012.1214
130. Chatterjee A, Chattopadhyay D, Chakrabarti G. miR-17-5p downregulation contributes to paclitaxel resistance of lung cancer cells through altering Beclin1 expression. *PLoS ONE.* (2014) 9:95716. doi: 10.1371/journal.pone.0095716
131. Zhu H, Wu H, Liu X, Li B, Chen Y, Ren X, et al. Regulation of autophagy by a beclin 1-targeted microRNA, miR-30a, in cancer cells. *Autophagy.* (2009) 5:816–23. doi: 10.4161/auto.9064
132. He J, Yu JJ, Xu Q, Wang L, Zheng JZ, Liu LZ, et al. Downregulation of ATG14 by EGR1-MIR152 sensitizes ovarian cancer cells to cisplatin-induced apoptosis by inhibiting cyto-protective autophagy. *Autophagy.* (2015) 11:373–84. doi: 10.1080/15548627.2015.1009781
133. Xu N, Zhang J, Shen C, Luo Y, Xia L, Xue F, et al. Cisplatin-induced downregulation of miR-199a-5p increases drug resistance by activating autophagy in HCC cell. *Biochem Biophys Res Commun.* (2012) 423:826–31. doi: 10.1016/j.bbrc.2012.06.048
134. Kovaleva V, Mora R, Park YJ, Plass C, Chiramel AI, Bartenschlager R, et al. miRNA-130a targets ATG2B and DICER1 to inhibit autophagy and trigger killing of chronic lymphocytic leukemia cells. *Cancer Res.* (2012) 72:1763–72. doi: 10.1158/0008-5472.CAN-11-3671
135. Huang J, Sun W, Huang H, Ye J, Pan W, Zhong Y, et al. MiR-34a modulates angiotensin II-induced myocardial hypertrophy by direct inhibition of ATG9A expression and autophagic activity. *PLoS ONE.* (2014) 9:94382. doi: 10.1371/journal.pone.0094382
136. Yu Y, Cao L, Yang L, Kang R, Lotze M, Tang D. microRNA 30A promotes autophagy in response to cancer therapy. *Autophagy.* (2012) 8:853–5. doi: 10.4161/auto.20053
137. Zhai Z, Wu F, Chuang AY, Kwon JH. MiR-106b fine tunes ATG16L1 expression and autophagic activity in intestinal epithelial HCT116 cells. *Inflamm Bowel Dis.* (2013) 19:2295–301. doi: 10.1097/MIB.0b013e31829e71cf
138. Frankel LB, Wen J, Lees M, Høyer-Hansen M, Farkas T, Krogh A, et al. MicroRNA-101 is a potent inhibitor of autophagy. *EMBO J.* (2011) 30:4628–41. doi: 10.1038/emboj.2011.331
139. Stiuso P, Potenza N, Lombardi A, Ferrandino I, Monaco A, Zappavigna S, et al. MicroRNA-423-5p promotes autophagy in cancer cells and is increased in serum from hepatocarcinoma patients treated with sorafenib. *Mol Ther Nucleic Acids.* (2015) 4:e233. doi: 10.1038/mtna.2015.8
140. Xiao J, Zhu X, He B, Zhang Y, Kang B, Wang Z, et al. MiR-204 regulates cardiomyocyte autophagy induced by ischemia-reperfusion through LC3-II. *J Biomed Sci.* (2011) 18:35. doi: 10.1186/1423-0127-18-35
141. Yumioka T, Osaki M, Sasaki R, Yamaguchi N, Onuma K, Iwamoto H, et al. Lysosome-associated membrane protein 2 (LAMP-2) expression induced by miR-194-5p downregulation contributes to sunitinib resistance in human renal cell carcinoma cells. *Oncol Lett.* (2018) 15:893–900. doi: 10.3892/ol.2017.7423
142. Cao W, Qian G, Luo W, Liu X, Pu Y, Hu G, et al. miR-125b is downregulated in systemic lupus erythematosus patients and inhibits autophagy by targeting UVRAG. *Biomed Pharmacother.* (2018) 99:791–7. doi: 10.1016/j.biopha.2018.01.119
143. Huangfu L, Liang H, Wang G, Su X, Li L, Du Z, et al. miR-183 regulates autophagy and apoptosis in colorectal cancer through targeting of UVRAG. *Oncotarget.* (2016) 7:4735–45. doi: 10.18632/oncotarget.6732
144. Zhu J, Tian Z, Li Y, Hua X, Zhang D, Li J, et al. ATG7 Promotes Bladder Cancer Invasion via Autophagy-Mediated Increased ARHGDIB mRNA Stability. *Adv Sci.* (2019) 6:1801927. doi: 10.1002/advs.201801927
145. Shimizu T, Suzuki H, Nojima M, Kitamura H, Yamamoto E, Maruyama R, et al. Methylation of a panel of microRNA genes is a novel biomarker for detection of bladder cancer. *Eur Urol.* (2013) 63:1091–100. doi: 10.1016/j.eururo.2012.11.030
146. Xu G, Zhang Z, Wei J, Zhang Y, Zhang Y, Guo L, et al. MicroR-142-3p down-regulates IRAK-1 in response to *Mycobacterium bovis* BCG infection in macrophages. *Tuberculosis.* (2013) 93:606–11. doi: 10.1016/j.tube.2013.08.006

147. Ghorpade DS, Leyland R, Kurowska-Stolarska M, Patil SA, Balaji KN. MicroRNA-155 Is Required for *Mycobacterium bovis* BCG-mediated apoptosis of macrophages. *Mol Cell Biol.* (2012) 32:2239–53. doi: 10.1128/MCB.06597-11
148. van Rensburg IC, du Toit L, Walzl G, du Plessis N, Loxton AG. Decreased neutrophil–associated miRNA and increased B-cell associated miRNA expression during tuberculosis. *Gene.* (2018) 655:35–41. doi: 10.1016/j.gene.2018.02.052
149. Gantier MP. The not-so-neutral role of microRNAs in neutrophil biology. *J Leukoc Biol.* (2013) 94:575–83. doi: 10.1189/jlb.1012539
150. Yamada M, Gomez JC, Chugh PE, Lowell CA, Dinauer MC, Dittmer DP, et al. Interferon-γ production by neutrophils during bacterial pneumonia in mice. *Am J Respir Crit Care Med.* (2011) 183:1391–401. doi: 10.1164/rccm.201004-0592OC
151. Liu Q, Li A, Tian Y, Wu JD, Liu Y, Li T, et al. The CXCL8-CXCR1/2 pathways in cancer. *Cytokine Growth Factor Rev.* (2016) 31:61–71. doi: 10.1016/j.cytogfr.2016.08.002
152. Jones SA, Wolf M, Qin S, Mackay CR, Baggiolini M. Different functions for the interleukin 8 receptors (IL-8R) of human neutrophil leukocytes: NADPH oxidase and phospholipase D are activated through IL-8R1 but not IL-8R2. *Proc Natl Acad Sci USA.* (1996) 93:6682–6. doi: 10.1073/pnas.93.13.6682
153. Karin N. Chemokines and cancer: new immune checkpoints for cancer therapy. *Curr Opin Immunol.* (2018) 51:140–5. doi: 10.1016/j.coi.2018.03.004
154. Yousefi S, Stojkov D, Germic N, Simon D, Wang X, Benarafa C, et al. Untangling "NETosis" from NETs. *Eur J Immunol.* (2019) 49:221–7. doi: 10.1002/eji.201747053
155. Azevedo PO, Paiva AE, Santos GSP, Lousado L, Andreotti JP, Sena IFG, et al. Cross-talk between lung cancer and bones results in neutrophils that promote tumor progression. *Cancer Metastasis Revi.* (2018) 37:779–90. doi: 10.1007/s10555-018-9759-4
156. Weiß E, Kretschmer D. Formyl-peptide receptors in infection, inflammation, and cancer. *Trends Immunol.* (2018) 39:815–29. doi: 10.1016/j.it.2018.08.005
157. Park J, Wysocki RW, Amoozgar Z, Maiorino L, Fein MR, Jorns J, et al. Cancer cells induce metastasis-supporting neutrophil extracellular DNA traps. *Sci Transl Med*. (2016) 8:361ra138. doi: 10.1126/scitranslmed.aag1711
158. Pasquier J, Vidal F, Hoarau-Véchot J, Bonneau C, Daraï E, Touboul C, et al. Surgical peritoneal stress creates a pro-metastatic niche promoting resistance to apoptosis via IL-8. *J Transl Med.* (2018) 16:271. doi: 10.1186/s12967-018-1643-z
159. Tohme S, Yazdani HO, Al-Khafaji AB, Chidi AP, Loughran P, Mowen K, et al. Neutrophil extracellular traps promote the development and progression of liver metastases after surgical stress. *Cancer Res*. (2016) 76:1367–80. doi: 10.1158/0008-5472.CAN-15-1591
160. Gonzalez-Aparicio M, Alfaro C. Influence of interleukin-8 and neutrophil extracellular trap (NET) formation in the tumor microenvironment: is there a pathogenic role? *J Immunol Res.* (2019) 2019:6252138. doi: 10.1155/2019/6252138
161. Blanca A, Cheng L, Montironi R, Moch H, Massari F, Fiorentino M, et al. Mirna expression in bladder cancer and their potential role in clinical practice. *Curr Drug Metab.* (2017) 18:712–22. doi: 10.2174/1389200218666170518164507
162. Jin N, Jin X, Gu X, Na W, Zhang M, Zhao R. Screening biomarkers of bladder cancer using combined miRNA and mRNA microarray analysis. *Mol Med Rep.* (2015) 12:3170–6. doi: 10.3892/mmr.2015.3739
163. Zhang Y, Zhang D, Lv J, Wang S, Zhang Q. MiR-125a-5p suppresses bladder cancer progression through targeting FUT4. *Biomed Pharmacother.* (2018) 108:1039–47. doi: 10.1016/j.biopha.2018.09.100
164. Chen L, Zhou Y, Sun Q, Zhou J, Pan H, Sui X. Regulation of autophagy by MiRNAs and their emerging roles in tumorigenesis and cancer treatment. In: Galluzzi L, Vitale I, editors. *International Review of Cell and Molecular Biology*. London: Elsevier Inc. (2017). p. 1–26. doi: 10.1016/bs.ircmb.2017.03.003
165. Chen L, Yuan L, Wang G, Cao R, Peng J, Shu B, et al. Identification and bioinformatics analysis of miRNAs associated with human muscle invasive bladder cancer. *Mol Med Rep.* (2017) 16:8709–20. doi: 10.3892/mmr.2017.7726
166. Lin JF, Tsai TF, Lin YC, Chen HE, Chou KY, Hwang TIS. Benzyl isothiocyanate suppresses IGF1R, FGFR3 and mTOR expression by upregulation of miR-99a-5p in human bladder cancer cells. *Int J Oncol.* (2019) 54:2106–16. doi: 10.3892/ijo.2019.4763
167. Fu XT, Shi YH, Zhou J, Peng YF, Liu WR, Shi GM, et al. MicroRNA-30a suppresses autophagy-mediated anoikis resistance and metastasis in hepatocellular carcinoma. *Cancer Lett.* (2018) 412:108–17. doi: 10.1016/j.canlet.2017.10.012
168. Boone BA, Orlichenko L, Schapiro NE, Loughran P, Gianfrate GC, Ellis JT, et al. The receptor for advanced glycation end products (RAGE) enhances autophagy and neutrophil extracellular traps in pancreatic cancer. *Cancer Gene Ther.* (2015) 22:326–34. doi: 10.1038/cgt.2015.21

Conflict of Interest: The authors declare that the research was conducted in the absence of any commercial or financial relationships that could be construed as a potential conflict of interest.

frontiers in Integrative Neuroscience

ORIGINAL RESEARCH
published: 05 January 2022
doi: 10.3389/fnint.2021.717629

Integrated Analysis to Obtain Potential Prognostic Signature in Glioblastoma

Jia-Qi Chen[1,2†], Nuo Zhang[3†], Zhi-Lin Su[4], Hui-Guo Qiu[4], Xin-Guo Zhuang[4] and Zhi-hua Tao[1]*

[1] Department of Laboratory Medicine, The Second Affiliated Hospital of Zhejiang University, Hangzhou, China, [2] Department of Clinical Laboratory, The People's Hospital of Lishui, Lishui, China, [3] Beijing Rehabilitation Hospital of Capital Medical University, Beijing, China, [4] Department of Laboratory Medicine, The First Affiliated Hospital of Xiamen University, Xiamen, China

Glioblastoma multiforme (GBM) is the most malignant and multiple tumors of the central nervous system. The survival rate for GBM patients is less than 15 months. We aimed to uncover the potential mechanism of GBM in tumor microenvironment and provide several candidate biomarkers for GBM prognosis. In this study, ESTIMATE analysis was used to divide the GBM patients into high and low immune or stromal score groups. Microenvironment associated genes were filtered through differential analysis. Weighted gene co-expression network analysis (WGCNA) was performed to correlate the genes and clinical traits. The candidate genes' functions were annotated by enrichment analyses. The potential prognostic biomarkers were assessed by survival analysis. We obtained 81 immune associated differentially expressed genes (DEGs) for subsequent WGCNA analysis. Ten out of these DEGs were significantly associated with targeted molecular therapy of GBM patients. Three genes (S100A4, FCGR2B, and BIRC3) out of these genes were associated with overall survival and the independent test set testified the result. Here, we obtained three crucial genes that had good prognostic efficacy of GBM and may help to improve the prognostic prediction of GBM.

Keywords: glioblastoma multiforme, microenvironment, WGCNA, prognostic biomarkers, estimate

OPEN ACCESS

Edited by:
Ali Yadollahpour, The University of Sheffield, United Kingdom

Reviewed by:
Jincheng Guo, Beijing University of Chinese Medicine, China
Francesco Fornai, University of Pisa, Italy

***Correspondence:**
Zhi-hua Tao
zrtzh@zju.edu.cn

† These authors have contributed equally to this work

Received: *31 May 2021*
Accepted: *29 November 2021*
Published: *05 January 2022*

Citation:
Chen J-Q, Zhang N, Su Z-L, Qiu H-G, Zhuang X-G and Tao Z-h (2022) Integrated Analysis to Obtain Potential Prognostic Signature in Glioblastoma. Front. Integr. Neurosci. 15:717629. doi: 10.3389/fnint.2021.717629

INTRODUCTION

Glioblastoma multiforme (GBM) is the most malignant and multiple tumors of the central nervous system (CNS), which is classified as grade IV glioma by the World Health Organization (WHO) (Ostrom et al., 2013; Louis et al., 2016; Hanif et al., 2017). GBM is a heterogeneous disease involving multiple subtypes with different clinical and molecular characteristics (Friedmann-Morvinski, 2014; Lee et al., 2018). The diagnosis of GBM is based on grading and histomorphology. However, the classification does not predict clinical outcomes after GBM development (Sasmita et al., 2018). To date, there was almost no biomarker that could translate into a significant survival benefit to GBM patients and the median survival of patients was only 15 months (Zhao et al., 2019).

In GBM, tumor cells interact with resident cells (neurons, glial cells, etc.) entangled in the extracellular matrix (ECM) and vascular system (De Luca et al., 2018). Glial cells play an important role in cancer progression (Friedmann-Morvinski et al., 2012). The peritumor tissue microenvironment is key to current and future research on tumor-sensitive therapies. GBM

can affect the cellular morphology and function of the CNS through intercellular interactions (Martinez-Outschoorn et al., 2014). Glial cells are inextricably linked to the GBM, and their immune role has been well documented. Microglia and macrophages can rapidly respond to alterations in CNS homeostasis, including brain tumors. Microglia and macrophages have also been found to induce GBM cell cycle arrest and differentiation (Sarkar et al., 2014). Therefore, an in-depth study of the tumor microenvironment of GBM could help to reveal its tumorigenic mechanisms. The tumor microenvironment (TME) has attracted more and more attention recently (Yang et al., 2018). TME is composed of a variety of cell types and plays a vital role in tumors (Hanahan and Weinberg, 2000). TME and its function is crucial for understanding the mechanism of tumor development (Duchnowska et al., 2016; Velaei et al., 2016). Estimation of stromal and immune cells in malignant tumor tissues using expression data (ESTIMATE) is an algorithm to help researchers to estimate the proportion of immune cells and stromal cells in tumors based on the gene expression profile (Yoshihara et al., 2013; Li et al., 2016).

Recently, the advances of bioinformatics and high-throughput data have identified potential tumor biomarkers, which could help to develop better prognostic predictions of GBM (Mehta et al., 2010). Weighted gene co-expression network analysis (WGCNA) is a bioinformatics method that could explore the correlation between genes and clinical characteristics and screen crucial genes for further verification (Langfelder and Horvath, 2008; Yuan et al., 2020). In the study, we applied the ESTIMATE algorithm and differential analysis to identify immune-associated genes in GBM for prognosis prediction. We also used the WGCNA to construct a co-expression network and to filter potential gene modules and crucial genes. Our study could provide new opinion to help to find some essential prognostic biomarkers in GBM.

MATERIALS AND METHODS

Description of the Cohort and Sources of Data

The high-throughput RNA-seq data and clinical information of 539 GBM patients were downloaded from the TCGA database. The genes' expression level of raw count data was quantified as fragments per kilobase million (FPKM) and normalized by log2-based transformation. The samples that lacked overall survival traits were eliminated, and only 412 patients were selected to subsequent analysis. Then, we used the ESTIMATE algorithm to calculate the immune and stromal scores of the samples. A test data contains 237 GBM patients' expression levels and clinical data was downloaded from the CGGA database (Bao et al., 2014).

Differential Expression Analysis

We classified the 412 patients into high immune associated and low immune associated groups or high stromal associated and low stromal associated groups by immune score or stromal score based on ESTIMATE analysis. Then, the "limma" R package was used to perform the differential expression analyses between high and low score groups. The DEGs were selected with an absolute log2 fold change $\geq$0.263 and an adjusted *P*-value $<$0.05.

Co-expression Network Construction and Module Identification

The immune associated DEGs were input into the WGCNA to construct co-expression network by WGCNA package. With the help of the function *pickSoftThreshold*, a signed adjacency matrix was calculated to reach approximate scale-free topology of the network ($R^2 > 0.8$). Then, the weighted adjacency matrix was transformed into a topological overlap matrix (TOM) to minimize effects of spurious associations. A dynamic cut-tree algorithm was used to identify stable modules. Next, the correlation between module eigengene (ME) and clinical data was defined as module significance (MS). The correlation between ME and genes was expressed as module membership (MM). In detail, ME means the first principal component of a given model and represents the gene expression profile of the entire model. MS means the average gene significance of all the genes involved in the module. MM means the correlation between a given gene expression profile and a given model eigengene. Genes with both high gene significance (GS $>$0.1) and high module membership (MM $>$0.6) were defined as hub genes.

Enrichment Analysis and Survival Analysis

KEGG, GO, and Hallmark analysis were performed to explore the potential functions and involved pathways of DEGs. We used the "clusterProfile" R package (Yu et al., 2012) and Metascape web tool (Zhou et al., 2019) to do the analysis.

A Kaplan–Meier curve was used for survival analysis and the curves were used to display the impact on the patients' survival of candidate genes. Multivariate cox regression analysis was performed to assess whether the genes were independent prognostic factors for patient survival. The "survival" R package was used to perform the above analysis. Furthermore, the OSgbm tool was used to verify the prognostic biomarkers though a combined dataset contains 684 GBM patients (Dong et al., 2019).

RESULTS

Identification of Differentially Expressed Genes Related to Tumor Microenvironments

A total of 412 eligible patients' expression levels and paired clinical data were obtained from the TCGA database. After the ESTIMATE analysis, we distinguished these patients into two groups based on the median value of immune or stromal score. Then, we performed differential expression analysis to identify differentially expressed genes associated with microenvironments. In the immune group, there were 81 DEGs, 79 DEGs were up-regulated, and 2 DEGs were down-regulated (**Figures 1A,B**). Similarly, 58 genes were differentially expressed according to stromal score, 57 DEGs were up-regulated, and 1 DEG was down-regulated (**Figures 1C,D**). As

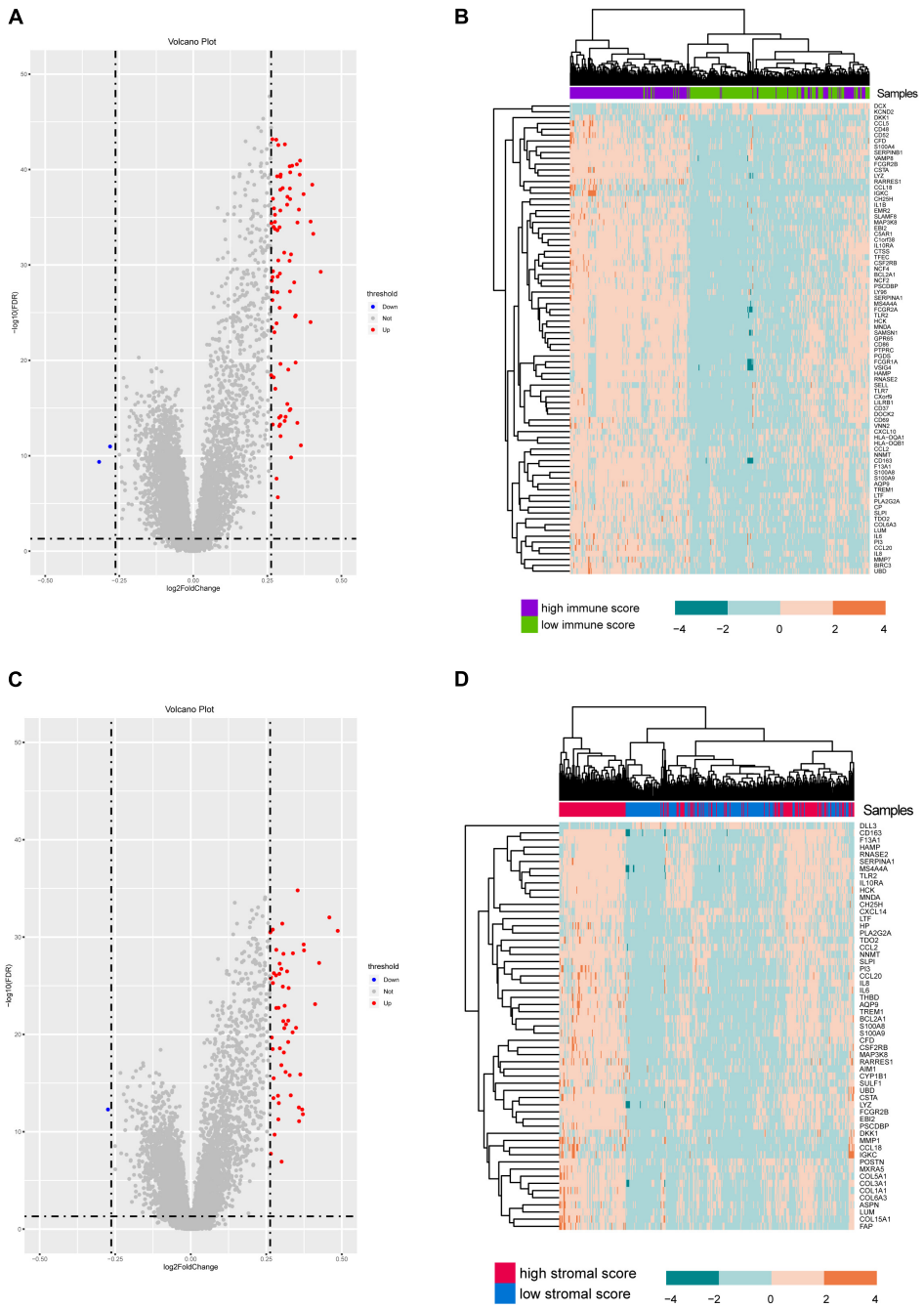

FIGURE 1 | Differential analysis of 412 GBM samples. **(A,C)** Volcano plot shows DEGs between GBM and normal samples. Red represents upregulated DEGs while blue shows the downregulated one ($P < 0.05$). **(B,D)** Heatmap showing the expression level of these differentially expressed genes.

shown in **Supplementary Figure 2**, the immune associated DEGs were mainly enriched in the IL-17 signaling pathway, Toll-like receptor signaling pathway, and phagosome (KEGG pathway) (**Supplementary Figure 2A**), and humoral immune response, neutrophil activation, and neutrophil mediated immunity (GO terms) (**Supplementary Figure 2B**). Also, the stromal DEGs were mainly enriched in cytokine-cytokine receptor interaction, chemokine signaling pathway, IL-17 signaling pathway (KEGG pathway) (**Supplementary Figure 2C**), and acute inflammatory response, leukocyte migration, and response to lipopolysaccharide (GO terms) (**Supplementary Figure 2D**). Interestingly, the clustering analysis showed that immune-related differential genes could classify GBM patients into two categories, whereas stroma-related differential genes did not have such classification efficacy (**Figures 1B,D**). In this study, we selected the immune associated DEGs for further analysis.

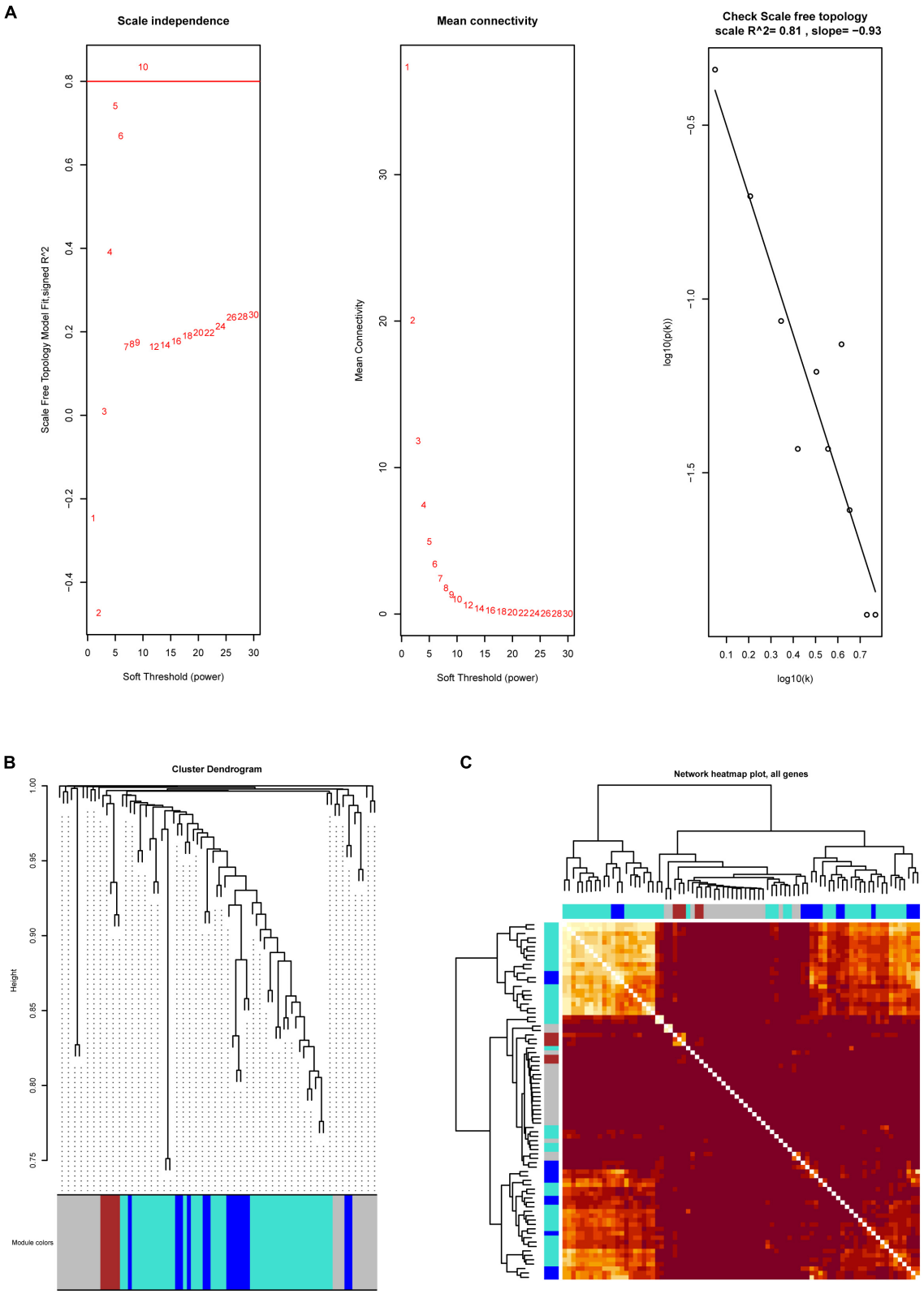

FIGURE 2 | The WGCNA analysis of immune-related DEGs. **(A)** Network topology analysis to select suitable soft-threshold powers. The *x*-axis and *y*-axis reflect the soft-thresholding power and the scale-free topology model fit index, respectively. **(B)** Clustering dendrogram of genes, with dissimilarity based on topological overlap, together with assigned module colors. **(C)** Heatmap showing the expression pattern correlation between these modules.

WGANA to Obtain the Candidate Genes With Co-expression Pattern

Based on the differential analyses, the 81 DEGs that are related to the immune system were selected to construct a co-expression network. To prove that the network we constructed is a scale-free network (a network in which a few nodes have many connections, most nodes have a few connections, and the distribution of node degrees in the network conforms to a power-law distribution) and not a random network, we first performed a topology analysis. After a topology analysis of the network, the soft power was set at 10 which the scale independence could reach to 0.81 to perform the subsequent analysis (**Figure 2A**). Then, we obtained three co-expression modules (MEbrown, MEblue, and MEturquoise) (**Figure 2B**). It indicated that the immune-related DEGs played three different functions in GBM. Subsequently, we calculated the relationships between the identified modules. It showed that the expression pattern was independent between these modules (**Figure 2C**).

A Co-expression Module Was Associated With Targeted Molecular Therapy in Glioblastoma Multiforme

We further explored the three different co-expression modules' function. We correlated the three modules with GBM patients' clinical traits to search for potential key modules (**Figure 3A**). The results illustrated that the gray module was significantly

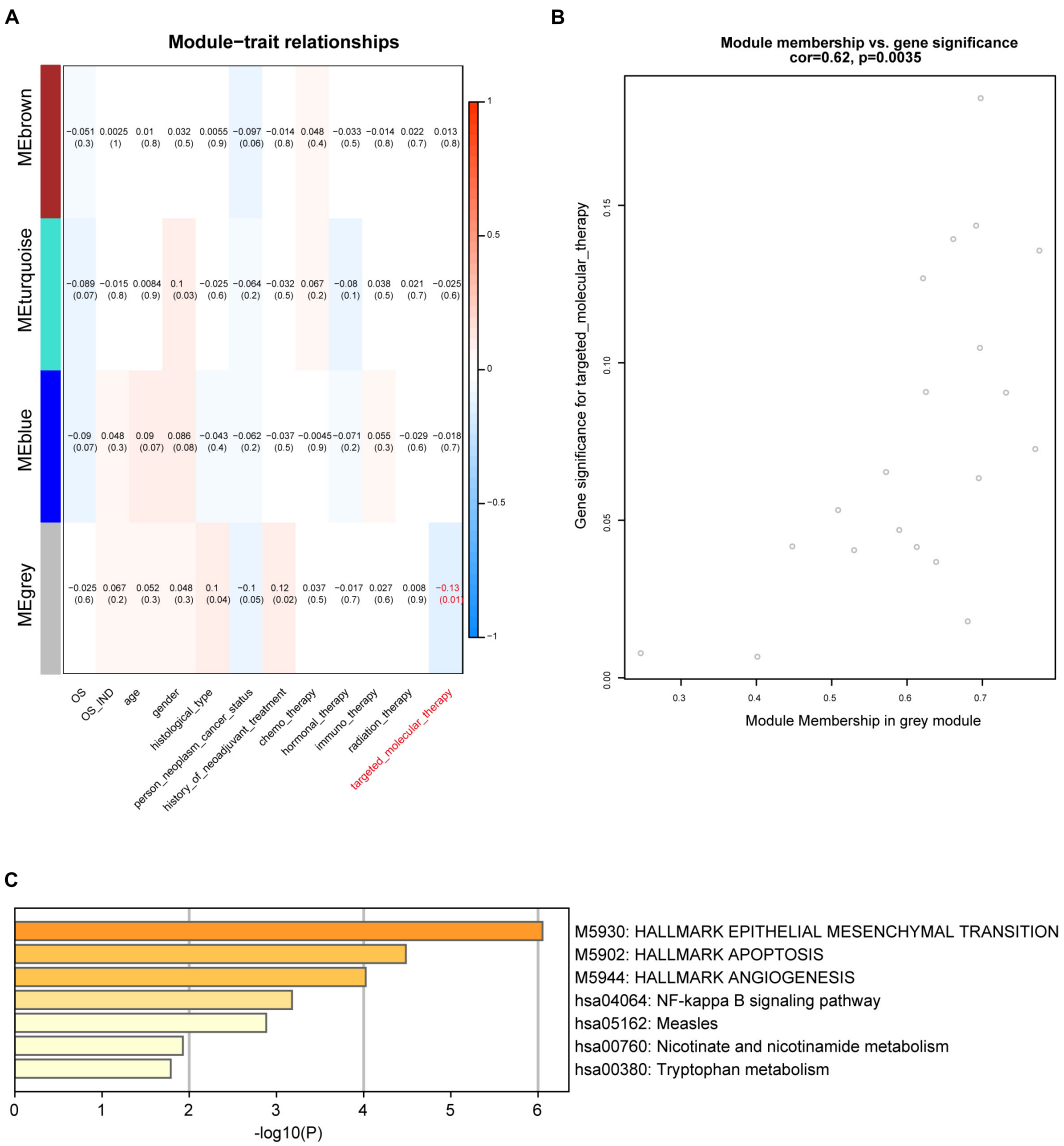

FIGURE 3 | Module-trait associations. **(A)** Module-trait relationships. Each row represents a module when each column indicates a clinical trait. Every cell shows the correlation coefficient and *P*-value. **(B)** Dot plot showing the gray module's genes significance and module membership in targeted molecular therapy. **(C)** Enrichment analysis of differentially expressed genes in the gray module.

related to targeted molecular therapy in GBM patients. There are 20 candidate genes in this module, 10 out of these genes in the gray module were identified as the hub genes which related to targeted molecular therapy (**Figure 3B**). We used enrichment analysis to explore the potential function of the hub genes. The result showed that the hub genes were significantly enriched

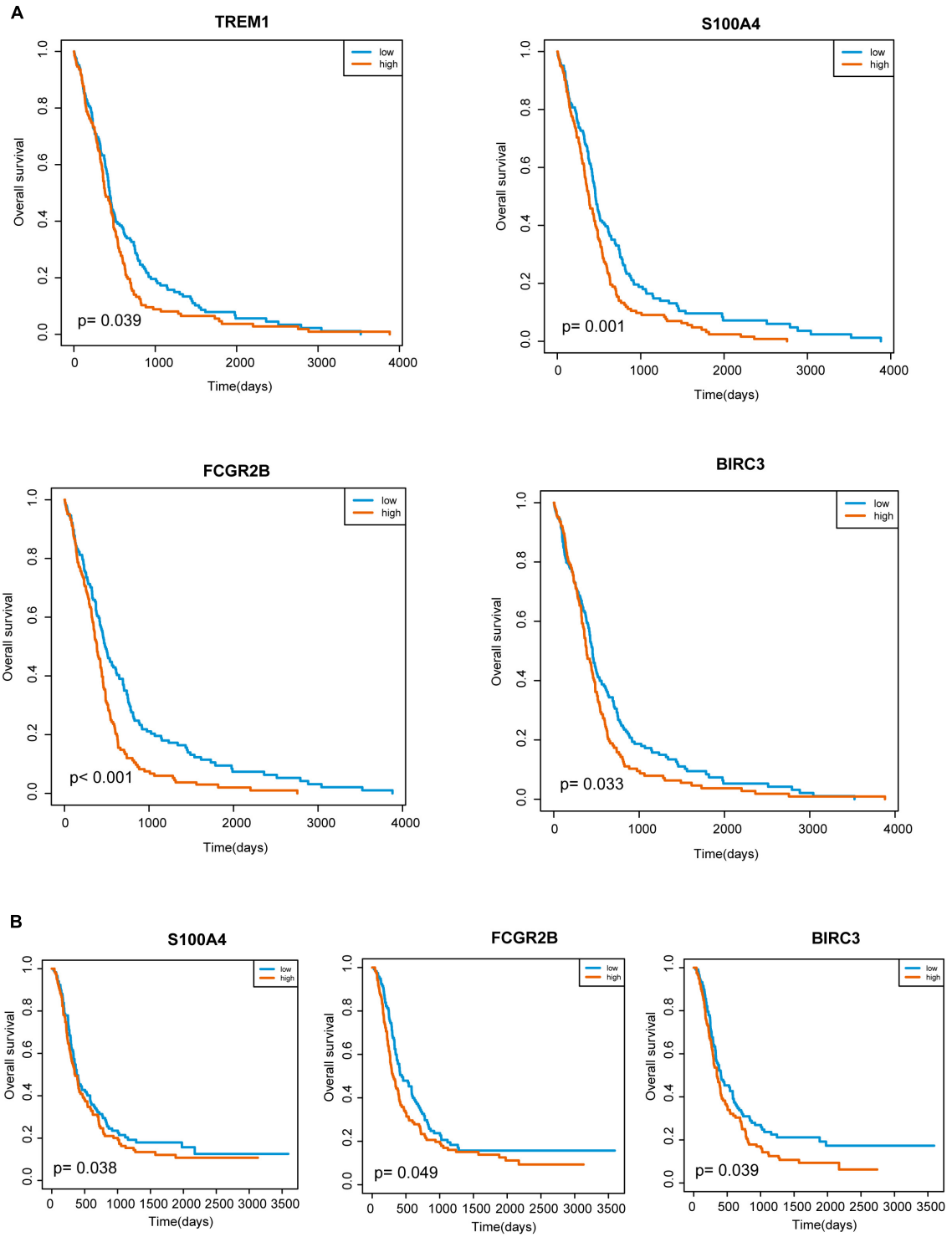

FIGURE 4 | Survival analysis of targeted molecular therapy associated key genes. **(A)** Four genes are potential prognostic biomarkers in TCGA GBM dataset. **(B)** Three out of the four genes are stable survival associated in test data.

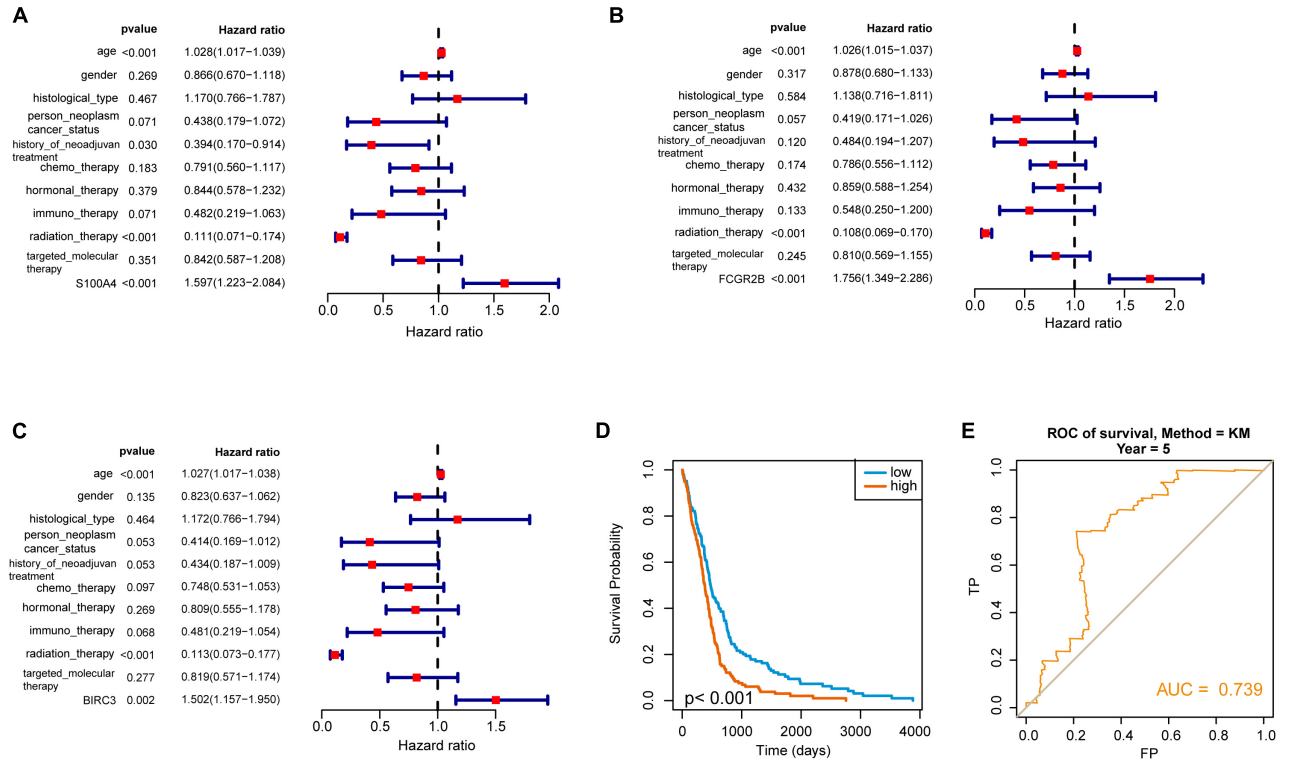

FIGURE 5 | Selection of independent prognostic genes in GBM. **(A–C)** Forest plot showed the hazard ratio of three hub genes (S100A4, FCGR2B, and BIRC3) and suggested that these genes are independent prognostic factors. **(D)** The Kaplan–Meier curve showed that the survival model played an excellent prognostic ability in GBM. **(E)** ROC analysis showed the AUC of the model. It reflected that it is a good prognostic model in GBM.

in Apoptosis, NF-kappa B signaling pathway, and tryptophan metabolism. This indicated that the hub genes may regulate GBM progression through these pathways (**Figure 3C**).

Three Crucial Hub Genes Associated With Targeted Molecular Therapy Were Potential Prognostic Biomarkers

To further determine these hub genes' ability and find out the potential prognostic genes, all the 10 targeted molecular therapy associated crucial genes were tested by Kaplan–Meier analysis. The result showed that 4 genes (TREM1, S100A4, FCGR2B, and BIRC3) out of these hub genes were significantly associated with OS in 412 GBM patients (**Figure 4A**). Then, we selected a dataset that contains 237 GBM samples for the validation. It showed that three crucial genes (S100A4, FCGR2B, and BIRC3) were survival associated (**Figure 4B**). The multivariate cox regression analysis also found the three genes were independent prognostic factors (**Figures 5A–C**). A survival model constructed by the three genes also performed a good prognostic efficacy (**Figure 5D**) and the AUC of the model reached to 0.739 (**Figure 5E**). Finally, another test set which contained 684 GBM patients' survival information was also used to testify as to the crucial genes' prognostic efficacy (**Supplementary Figure 2**). The result showed that all the three genes are stable prognostic biomarkers and may be the prognostic biomarkers of GBM.

DISCUSSION

Glioblastoma multiforme is the most malignant brain tumor and requires powerful biomarkers to perform effective treatment (Szopa et al., 2017). High-throughput sequencing provides insights into understanding the pathogenesis and the development of therapeutic biomarkers (Tsimberidou, 2015). Multiple molecular analysis has been used for tumor biology prediction or risk stratification (Chen et al., 2020). To date, the microenvironment has been investigated in numerous cancer studies (Bi et al., 2020; Du et al., 2020; Mao et al., 2020). However, the comprehensive prognostic value of crucial microenvironment-associated biomarkers has not been exploited in GBM.

Here, we applied bioinformatics analysis to integrate high-throughput data from GBM and obtained three microenvironment-associated biomarkers (**Supplementary Figure 1**). Three potential prognostic biomarkers of GBM were obtained in our study. S100A4 encodes a member of the S100 protein family. This protein family is mainly involved in cell cycle progression and plays a role in microtubule protein polymerization. Aberrant expression of this protein family is associated with tumor metastasis (Sadigh et al., 2019). S100A4 has been reported to be associated with cancer cell migration and metastasis and is important in tumor onset and progression (Atlasi et al., 2016; Liu et al., 2018). In GBM, S100A4 was

reported to be associated with the migration and invasion of cancer cells (Zhou et al., 2020). FCGR2B encodes a receptor for the immunoglobulin gamma complex and is involved in the regulation of immune responses and antibody production by B cells (Danzer et al., 2020). FCGR2B has been reported to be associated with anti-GBM disease in Chinese (Zhou et al., 2010). The gene variants of FCGR2B can influence intravenous immunoglobulin response (Shrestha et al., 2011). BIRC3 encodes an IAP family protein. It could inhibit apoptosis by binding to TRAF1 and TRAF2 (Zheng et al., 2010). BIRC3 is a novel prognostic indicator and a potential therapeutic target for cancer (Fu et al., 2019). The expression of BIRC3 could enhance NF-kB translocation and then influence the sensitivity of treatment (Asslaber et al., 2019). Here, we found the three genes played a novel role in the prognosis of GBM. They may be used for further clinical study.

CONCLUSION

In this study, we use WGCNA to analyze the high-throughput sequencing data of GBM and identified DEGs associated with the immune microenvironment. Then, the key gene modules associated with GBM patients' clinical characteristics were obtained. In addition, we identified a gray module consisting of 20 genes which was significantly relevant to the targeted molecular therapy. Ten genes were identified as hub genes and three of them were survival associated. The independent test set of CGGA verified our result. Our results filtered a module and three crucial genes that acted as crucial roles in the prognostic of GBM. The result may provide novel information to improve the prognosis of the tumor.

DATA AVAILABILITY STATEMENT

The original contributions presented in the study are included in the article/**Supplementary Material**, further inquiries can be directed to the corresponding author.

AUTHOR CONTRIBUTIONS

J-QC and NZ: data collection, data analysis, interpretation, and drafting. Z-HT: study design, study supervision, and final approval of the manuscript. Z-LS, H-GQ, and X-GZ: technical support and critical revision of the manuscript. All authors read and approved the final manuscript.

FUNDING

Financial support for this work was provided by Medical and Health Science and Technology Project of Zhejiang Province (Nos. 2018KY923, 2019KY802, and 2020KY1070) and Talent Project of Lishui Science and Technology Bureau (2018RC07).

SUPPLEMENTARY MATERIAL

The Supplementary Material for this article can be found online at: https://www.frontiersin.org/articles/10.3389/fnint.2021.717629/full#supplementary-material

REFERENCES

Asslaber, D., Wacht, N., Leisch, M., Qi, Y., Maeding, N., Hufnagl, C., et al. (2019). BIRC3 expression predicts CLL progression and defines treatment sensitivity via enhanced NF-kappaB nuclear translocation. *Clin. Cancer Res.* 25, 1901–1912. doi: 10.1158/1078-0432.CCR-18-1548

Atlasi, Y., Noori, R., Marolin, I., Franken, P., Brandao, J., Biermann, K., et al. (2016). The role of S100a4 (Mts1) in Apc- and Smad4-driven tumour onset and progression. *Eur. J. Cancer* 68, 114–124. doi: 10.1016/j.ejca.2016.09.012

Bao, Z. S., Chen, H. M., Yang, M. Y., Zhang, C. B., Yu, K., Ye, W. L., et al. (2014). RNA-seq of 272 gliomas revealed a novel, recurrent PTPRZ1-MET fusion transcript in secondary glioblastomas. *Genome Res.* 24, 1765–1773. doi: 10.1101/gr.165126.113

Bi, K. W., Wei, X. G., Qin, X. X., and Li, B. (2020). BTK has potential to be a prognostic factor for lung adenocarcinoma and an indicator for tumor microenvironment remodeling: a study based on TCGA data mining. *Front. Oncol.* 10:424. doi: 10.3389/fonc.2020.00424

Chen, Y., Liao, L. D., Wu, Z. Y., Yang, Q., Guo, J. C., He, J. Z., et al. (2020). Identification of key genes by integrating DNA methylation and next-generation transcriptome sequencing for esophageal squamous cell carcinoma. *Aging (Albany N. Y.)* 12, 1332–1365. doi: 10.18632/aging.102686

Danzer, H., Glaesner, J., Baerenwaldt, A., Reitinger, C., Lux, A., Heger, L., et al. (2020). Human Fcgamma-receptor IIb modulates pathogen-specific versus self-reactive antibody responses in lyme arthritis. *Elife* 9:55319. doi: 10.7554/eLife.55319

De Luca, C., Colangelo, A. M., Alberghina, L., and Papa, M. (2018). Neuro-immune hemostasis: homeostasis and diseases in the central nervous system. *Front. Cell Neurosci.* 12:459. doi: 10.3389/fncel.2018.00459

Dong, H., Wang, Q., Li, N., Lv, J., Ge, L., Yang, M., et al. (2019). OSgbm: an online consensus survival analysis web server for glioblastoma. *Front. Genet.* 10:1378. doi: 10.3389/fgene.2019.01378

Du, G. W., Yan, X., Chen, Z., Zhang, R. J., Tuoheti, K., Bai, X. J., et al. (2020). Identification of transforming growth factor beta induced (TGFBI) as an immune-related prognostic factor in clear cell renal cell carcinoma (ccRCC). *Aging* 12, 8484–8505. doi: 10.18632/aging.103153

Duchnowska, R., Peksa, R., Radecka, B., Mandat, T., Trojanowski, T., Jarosz, B., et al. (2016). Immune response in breast cancer brain metastases and their microenvironment: the role of the PD-1/PD-L axis. *Breast Cancer Res.* 18:43. doi: 10.1186/s13058-016-0702-8

Friedmann-Morvinski, D. (2014). Glioblastoma heterogeneity and cancer cell plasticity. *Crit. Rev. Oncog.* 19, 327–336. doi: 10.1615/critrevoncog.2014011777

Friedmann-Morvinski, D., Bushong, E. A., Ke, E., Soda, Y., Marumoto, T., Singer, O., et al. (2012). Dedifferentiation of neurons and astrocytes by oncogenes can induce gliomas in mice. *Science* 338, 1080–1084. doi: 10.1126/science.1226929

Fu, P. Y., Hu, B., Ma, X. L., Yang, Z. F., Yu, M. C., Sun, H. X., et al. (2019). New insight into BIRC3: a novel prognostic indicator and a potential therapeutic target for liver cancer. *J. Cell Biochem.* 120, 6035–6045. doi: 10.1002/jcb.27890

Hanahan, D., and Weinberg, R. A. (2000). The hallmarks of cancer. *Cell* 100, 57–70. doi: 10.1016/s0092-8674(00)81683-9

Hanif, F., Muzaffar, K., Perveen, K., Malhi, S. M., and Simjee Sh, U. (2017). Glioblastoma multiforme: a review of its epidemiology and pathogenesis through clinical presentation and treatment. *Asian Pac. J. Cancer Prev.* 18, 3–9. doi: 10.22034/APJCP.2017.18.1.3

Langfelder, P., and Horvath, S. (2008). WGCNA: an R package for weighted correlation network analysis. *BMC Bioinform.* 9:559. doi: 10.1186/1471-2105-9-559

Lee, E., Yong, R. L., Paddison, P., and Zhu, J. (2018). Comparison of glioblastoma (GBM) molecular classification methods. *Semin. Cancer Biol.* 53, 201–211. doi: 10.1016/j.semcancer.2018.07.006

Li, B., Severson, E., Pignon, J. C., Zhao, H., Li, T., Novak, J., et al. (2016). Comprehensive analyses of tumor immunity: implications for cancer immunotherapy. *Genome Biol.* 17:174. doi: 10.1186/s13059-016-1028-7

Liu, Y., Geng, Y. H., Yang, H., Yang, H., Zhou, Y. T., Zhang, H. Q., et al. (2018). Extracellular ATP drives breast cancer cell migration and metastasis via S100A4 production by cancer cells and fibroblasts. *Cancer Lett.* 430, 1–10. doi: 10.1016/j.canlet.2018.04.043

Louis, D. N., Perry, A., Reifenberger, G., von Deimling, A., Figarella-Branger, D., Cavenee, W. K., et al. (2016). The 2016 world health organization classification of tumors of the central nervous system: a summary. *Acta Neuropathol.* 131, 803–820. doi: 10.1007/s00401-016-1545-1

Mao, M., Yu, Q., Huang, R., Lu, Y., Wang, Z., and Liao, L. (2020). Stromal score as a prognostic factor in primary gastric cancer and close association with tumor immune microenvironment. *Cancer Med.* 9, 4980–4990. doi: 10.1002/cam4.2801

Martinez-Outschoorn, U. E., Lisanti, M. P., and Sotgia, F. (2014). Catabolic cancer-associated fibroblasts transfer energy and biomass to anabolic cancer cells, fueling tumor growth. *Semin. Cancer Biol.* 25, 47–60. doi: 10.1016/j.semcancer.2014.01.005

Mehta, S., Shelling, A., Muthukaruppan, A., Lasham, A., Blenkiron, C., Laking, G., et al. (2010). Predictive and prognostic molecular markers for cancer medicine. *Ther. Adv. Med. Oncol.* 2, 125–148. doi: 10.1177/1758834009360519

Ostrom, Q. T., Gittleman, H., Farah, P., Ondracek, A., Chen, Y., Wolinsky, Y., et al. (2013). CBTRUS statistical report: primary brain and central nervous system tumors diagnosed in the United States in 2006-2010. *Neuro Oncol.* 15(Suppl. 2), ii1–ii56. doi: 10.1093/neuonc/not151

Sadigh, A. R., Mihanfar, A., Fattahi, A., Latifi, Z., Akbarzadeh, M., Hajipour, H., et al. (2019). S100 protein family and embryo implantation. *J. Cell Biochem.* 120, 19229–19244. doi: 10.1002/jcb.29261

Sarkar, S., Doring, A., Zemp, F. J., Silva, C., Lun, X., Wang, X., et al. (2014). Therapeutic activation of macrophages and microglia to suppress brain tumor-initiating cells. *Nat. Neurosci.* 17, 46–55. doi: 10.1038/nn.3597

Sasmita, A. O., Wong, Y. P., and Ling, A. P. K. (2018). Biomarkers and therapeutic advances in glioblastoma multiforme. *Asia. Pac. J. Clin. Oncol.* 14, 40–51. doi: 10.1111/ajco.12756

Shrestha, S., Wiener, H. W., Olson, A. K., Edberg, J. C., Bowles, N. E., Patel, H., et al. (2011). Functional FCGR2B gene variants influence intravenous immunoglobulin response in patients with Kawasaki disease. *J. Allergy Clin. Immunol.* 128, 677–680. doi: 10.1016/j.jaci.2011.04.027

Szopa, W., Burley, T. A., Kramer-Marek, G., and Kaspera, W. (2017). Diagnostic and Therapeutic Biomarkers in Glioblastoma: Current Status and Future Perspectives. *Biomed. Res. Int.* 2017:8013575. doi: 10.1155/2017/8013575

Tsimberidou, A. M. (2015). Targeted therapy in cancer. *Cancer Chemother. Pharmacol.* 76, 1113–1132. doi: 10.1007/s00280-015-2861-1

Velaei, K., Samadi, N., Barazvan, B., and Soleimani Rad, J. (2016). Tumor microenvironment-mediated chemoresistance in breast cancer. *Breast* 30, 92–100. doi: 10.1016/j.breast.2016.09.002

Yang, L., Song, X., Gong, T., Jiang, K., Hou, Y., Chen, T., et al. (2018). Development a hyaluronic acid ion-pairing liposomal nanoparticle for enhancing anti-glioma efficacy by modulating glioma microenvironment. *Drug. Delivery* 25, 388–397. doi: 10.1080/10717544.2018.1431979

Yoshihara, K., Shahmoradgoli, M., Martinez, E., Vegesna, R., Kim, H., Torres-Garcia, W., et al. (2013). Inferring tumour purity and stromal and immune cell admixture from expression data. *Nat. Commun.* 4:2612. doi: 10.1038/ncomms3612

Yu, G., Wang, L. G., Han, Y., and He, Q. Y. (2012). clusterProfiler: an R package for comparing biological themes among gene clusters. *Omics J. Integrat. Biol.* 16, 284–287. doi: 10.1089/omi.2011.0118

Yuan, Y., Chen, J., Wang, J., Xu, M., Zhang, Y., Sun, P., et al. (2020). Identification Hub genes in colorectal cancer by integrating weighted gene co-expression network analysis and clinical validation in vivo and vitro. *Front. Oncol.* 10:638. doi: 10.3389/fonc.2020.00638

Zhao, J., Wang, L., Hu, G., and Wei, B. (2019). A 6-gene risk signature predicts survival of glioblastoma multiforme. *Biomed. Res. Int.* 2019:1649423. doi: 10.1155/2019/1649423

Zheng, C., Kabaleeswaran, V., Wang, Y., Cheng, G., and Wu, H. (2010). Crystal structures of the TRAF2: cIAP2 and the TRAF1: TRAF2: cIAP2 complexes: affinity, specificity, and regulation. *Mol. Cell* 38, 101–113. doi: 10.1016/j.molcel.2010.03.009

Zhou, X. J., Lv, J. C., Yu, L., Cui, Z., Zhao, J., Yang, R., et al. (2010). FCGR2B gene polymorphism rather than FCGR2A, FCGR3A and FCGR3B is associated with anti-GBM disease in Chinese. *Nephrol. Dial Transplant* 25, 97–101. doi: 10.1093/ndt/gfp374

Zhou, Y., Wang, Y., Wu, S., Yan, Y., Hu, Y., Zheng, Z., et al. (2020). Sulforaphane-cysteine inhibited migration and invasion via enhancing mitophagosome fusion to lysosome in human glioblastoma cells. *Cell Death Dis.* 11:819. doi: 10.1038/s41419-020-03024-5

Zhou, Y., Zhou, B., Pache, L., Chang, M., Khodabakhshi, A. H., Tanaseichuk, O., et al. (2019). Metascape provides a biologist-oriented resource for the analysis of systems-level datasets. *Nat. Commun.* 10:1523. doi: 10.1038/s41467-019-09234-6

Conflict of Interest: The authors declare that the research was conducted in the absence of any commercial or financial relationships that could be construed as a potential conflict of interest.

Publisher's Note: All claims expressed in this article are solely those of the authors and do not necessarily represent those of their affiliated organizations, or those of the publisher, the editors and the reviewers. Any product that may be evaluated in this article, or claim that may be made by its manufacturer, is not guaranteed or endorsed by the publisher.

frontiers in Medicine

ORIGINAL RESEARCH
published: 21 February 2022
doi: 10.3389/fmed.2022.833829

Identification of the Signature Genes and Network of Reactive Oxygen Species Related Genes and DNA Repair Genes in Lung Adenocarcinoma

Ye Zhao[1†], *Hai-Ming Feng*[2†], *Wei-Jian Yan*[2] *and Yu Qin*[1*]

[1] First Clinical Medical College, Lanzhou University, Lanzhou, China, [2] Department of Thoracic Surgery, The Second Affiliated Hospital of Lanzhou University, Lanzhou, China

OPEN ACCESS

Edited by:
Ali Yadollahpour,
The University of Sheffield,
United Kingdom

Reviewed by:
Shengye Wang,
Zhejiang Cancer Hospital, China
Fangzhou Song,
Chongqing Medical University, China

***Correspondence:**
Yu Qin
yuqin@lzu.edu.cn

[†]*These authors have contributed equally to this work*

Specialty section:
This article was submitted to Precision Medicine, a section of the journal Frontiers in Medicine

Received: *12 December 2021*
Accepted: *10 January 2022*
Published: *21 February 2022*

Citation:
Zhao Y, Feng H-M, Yan W-J and Qin Y (2022) Identification of the Signature Genes and Network of Reactive Oxygen Species Related Genes and DNA Repair Genes in Lung Adenocarcinoma. Front. Med. 9:833829. doi: 10.3389/fmed.2022.833829

Reactive Oxygen Species (ROS) are present in excess amounts in patients with tumors, and these ROS can kill and destroy tumor cells. Therefore, tumor cells upregulate ROS-related genes to protect them and reduce their destructing effects. Cancer cells already damaged by ROS can be repaired by expressing DNA repair genes consequently promoting their proliferation. The present study aimed to identify the signature genes of and regulating network of ROS-related genes and DNA repair genes in lung adenocarcinoma (LUAD) using transcriptomic data of public databases. The LUAD transcriptome data in the TCGA database and gene expressions from Gene Expression Omnibus (GEO) were analyzed and samples were clustered into 5 ROS-related categories and 6 DNA repair categories. Survival analysis revealed a significant difference in patient survival between the two classification methods. In addition, the samples corresponding to the two categories overlap, thus, the gene expression profile of the same sample with different categories and survival prognosis was further explored, and the connection between ROS-related and DNA repair genes was investigated. The interactive sample recombination classification was used, revealing that the patient's prognosis was worse when the ROS-related and DNA repair genes were expressed at the same time. The further research on the potential regulatory network of the two categories of genes and the correlation analysis revealed that ROS-related genes and DNA repair genes have a mutual regulatory relationship. The ROS-related genes namely NQO1, TXNRD1, and PRDX4 could establish links with other DNA repair genes through the DNA repair gene NEIL3, thereby balancing the level of ROS. Therefore, targeting ROS-related genes and DNA repair genes might be a promising

strategy in the treatment of LUAD. Finally, a survival prognostic model of ROS-related genes and DNA repair genes was established (TERT, PRKDC, PTTG1, SMUG1, TXNRD1, CAT, H2AFX, and PFKP). The risk score obtained from our survival prognostic model could be used as an independent prognostic factor in LUAD patients.

Keywords: DNA repair, lung adenocarcinoma, prognostic analysis, reactive oxygen species (ROS), regulatory network

INTRODUCTION

Reactive oxygen species (ROS) are small oxygen-derived active small molecules, including O2·-,·OH, RO2·, and RO·(1). ROS can be produced by exogenous or endogenous sources, and when they are in excess amount, compared with the concentration of antioxidants in the body, the system is out of balance, and the antioxidants are not able anymore to completely remove or reduce ROS. On the one hand, their accumulation damages biological macromolecules, including DNA, leading to different type of tumors. On the other hand, the increase of the level of intracellular ROS can allow the selective killing of tumor cells (2). A high ROS amount is detected in most cancer patients (3). The expression of ROS-related proteins increases in many types of cancer, and they are involved in cell growth, proliferation, differentiation, protein synthesis, glucose metabolism, cell survival and inflammation (4). Oxidative stress and non-small cell lung cancer (NSCLC) have a mutually promoting and dependent relationship (5–9). Indeed, the presence of oxidative stress greatly increases gene damage, and the damage to the mitochondrial DNA of alveolar cells can cause energy supply barriers, promote tumor blood vessel formation, and inhibit tumor immune microenvironment. These multiple effects promote the occurrence of NSCLC. In addition, the abnormal expression of specific transcription factors and downstream cell signaling pathways caused by and related to oxidative stress allow a rapid development and metastasis of NSCLC. Furthermore, NSCLC cells maintain the oxidative stress response at the appropriate level for their proliferation and survival by regulating their antioxidant levels and ROS levels (10, 11).

The internal and external environmental factors including ROS can cause DNA damage. If the damage is not repaired in time and correctly, it causes the instability of the genome, threatening the survival of cells. In order to maintain the stability of the structure and function of DNA in a complex genomic environment, a timely and reasonable response to damaged signals should be provided. Under the condition of DNA damage, coordinated regulation of damage repair mechanisms and dynamic chromatin changes are required for the maintenance of genetic and epigenetic information. Thus, cells should correct the damages before the replication process in order to maintain the integrity of the genetic material. Therefore, the DNA repair system plays a vital role in maintaining the normal physiological functions of cells (12). At present, more than 100 repair enzymes are known that participate in the DNA repair process. The DNA repair system in the cell mainly includes five pathways: direct damage reversal repair, base excision repair, nucleotide excision repair, recombination repair, and mismatch repair (13). If the repair function is defective, or when a key protein in a specific DNA damage repair pathway is mutated, DNA damage may lead to two results: one is cell death; the other is gene mutation, or malignant transformation into tumor cells. It is worth noting that although defects in DNA repair function can cause tumors, the DNA repair function of cancer cells is not reduced; on the contrary, it is significantly increased, and can fully repair the DNA damage caused by chemotherapeutic drugs. This is also one of the reasons why most anti-cancer drugs are not effective (14).

Therefore, in this study the combined action of ROS genes with DNA repair genes on the prognosis of patients diagnosed with lung adenocarcinoma (LUAD) was explored. Since this is a cancer type with a high incidence and high mortality rate, our aim was to find a potential correlation between ROS genes and DNA repair genes, to evaluate whether the inhibition of the repair of damaged tumor cells could increase tumor cell death and ameliorate the prognosis of patients. In this way, a potential combined therapeutic therapy can be also considered.

MATERIALS AND METHODS

Data Source and Pre-processing

The RNA-Seq based transcriptome profiles (FPKM; Fragments Per Kilobase of transcript per Million mapped reads) and corresponding clinical data of LUAD patients were downloaded from the Cancer Genome Atlas (TCGA) portal using the gdc-client software downloading tool. Additionally, the gene expression profiles in LUAD patients (GSE68465, sequenced using Affymetrix, HG-U133A plus 2.0 Array, up to November 2020) were also obtained from the Gene Expression Omnibus (GEO) database (http://www.ncbi.nlm.nih.gov/geo/). All analyses were performed using the R software (R Foundation for Statistical Computing, Vienna, Austria, 3.4.1 Version).

ROS and DNA Repair Gene Acquisition and Sorting

The ROS-related genes and DNA repair genes were downloaded from the Molecular Signatures Database (MSigDB) for use

with the Gene Set Enrichment Analysis (GSEA) database. The intersection of these genes with the genes from TCGA was used to obtain the final ROS-related genes and DNA repair genes. The TCGA samples with incomplete clinical data and survival time <30 days were not taken into consideration and consequently removed.

TABLE 1 | Reclassified samples correspond to samples independently classified based on ROS genes and DNA repair genes.

ROS_cluster	DNA_Repair_cluster	Subtype
ROS_C1	DNA_Repair_C1	ROS_C1_DNA_Repair_C1
ROS_C1	DNA_Repair_C3	ROS_C1_DNA_Repair_C3
ROS_C2	DNA_Repair_C5	ROS_C2_DNA_Repair_C5
ROS_C2	DNA_Repair_C6	ROS_C2_DNA_Repair_C6
ROS_C3	DNA_Repair_C1	ROS_C3_DNA_Repair_C1
ROS_C3	DNA_Repair_C3	ROS_C3_DNA_Repair_C3
ROS_C4	DNA_Repair_C1	ROS_C4_DNA_Repair_C1
ROS_C4	DNA_Repair_C4	ROS_C4_DNA_Repair_C4
ROS_C4	DNA_Repair_C5	ROS_C4_DNA_Repair_C5
ROS_C5	DNA_Repair_C2	ROS_C5_DNA_Repair_C2

Consistent Clustering and Screening of ROS-Related Genes and DNA Repair Related Genes

The ConsensusClusterPlus package of R was used to cluster ROS-related genes and DNA repair genes separately, and the survival analysis was performed to compare the prognostic differences of different categories. Genes showing significant differences in their expression in tumor samples and normal samples were obtained, the screening conditions were set at $p < 0.05$ and $|\text{LogFC}|>1$, and finally the expression of differential genes in different categories were analyzed according to ROS genes and DNA repair genes.

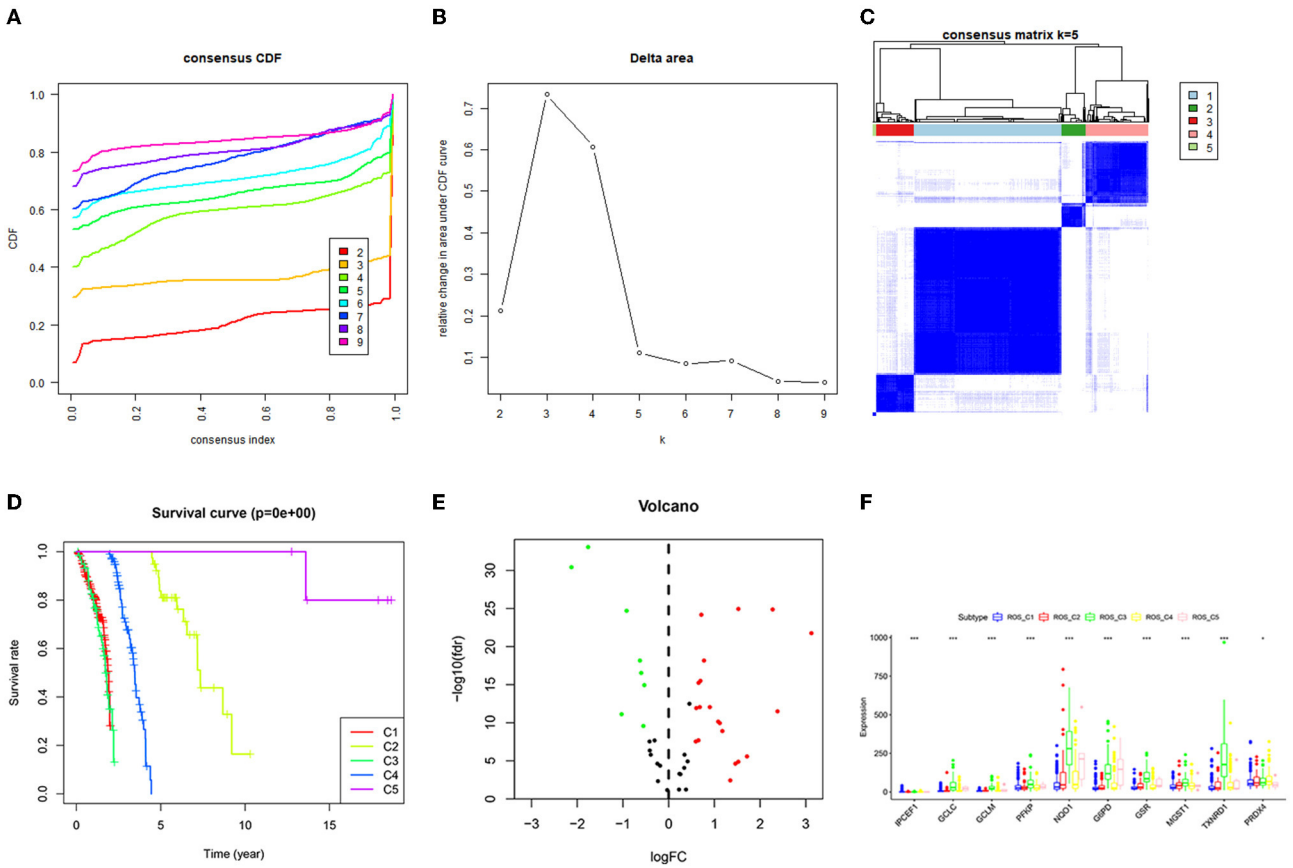

FIGURE 1 | Consistent clustering results of ROS-related genes and screening of differential genes. **(A)** Consistent Cumulative Distribution Function (CDF) diagram: this diagram shows the cumulative distribution function when k takes different values, which is used to determine when k takes the value, CDF reaches an approximate maximum value, and the cluster analysis result is the most reliable at this time. **(B)** Delta Area Plot: this graph shows the relative change of the area under the CDF curve between k and k-1. When k = 6, the area under the curve only increases slightly, so 5 is the appropriate value of k. **(C)** Matrix heat map when k = 5: the rows and columns of the matrix are all samples, and the values of the consistency matrix range from 0 (it is impossible to cluster together) to 1 (always cluster together) from white to dark blue Color indicates that the consistency matrix is arranged according to the consistency classification (the tree diagram above the heat map). The bar between the dendrogram and the heat map is the category. **(D)** Survival prognosis curves of different categories. **(E)** The differential gene volcano map describes the situation of the differential gene. The y-axis of the volcano graph is -log10 (Q-value), that is, qvalue (value after *p*-value correction) is –log10, so the higher the value, the smaller the qvalue is, the more significant it is. The abscissa is Log2 fold change, that is, log2 is taken for fold change, so the closer the points on both sides (each point represents a gene), the greater the increase or decrease in gene expression. **(F)** Genes with significant differences in the C1–C5 categories.

Sample Reclassification and Differential Gene Expression Analysis in Different Prognostic Categories

The categories and prognosis of some samples of the two clustering methods were different. The samples obtained from the two clusters are reclassified in an interactive manner and called ROS_Cn_DNA_Repair_Cm (**Table 1**). Then, differential genes were compared in different categories according to ROS genes and DNA repair genes in the new category.

Regulatory Network and Correlation Analysis Among Target Genes

ROS-related and DNA repair genes significantly different in the new categories were obtained where the samples obtained from the two clusters are reclassified in an interactive manner and called ROS_Cn_DNA_Repair_Cm. A regulatory network was constructed using the STRING database, the correlation coefficient between the two set of genes at the same time was calculated, and then the relationship between ROS-related and DNA repair genes was obtained.

LASSO Regression Analysis for the Construction of the Prognostic Gene Model

Univariate Cox proportional hazards regression analysis was performed to screen target ROS-related genes and DNA repair genes significantly associated with overall survival (OS) in the TCGA LUAD dataset. Then, LASSO Cox regression analysis of the identified OS-related genes was performed using the R-glmnet package. Multivariable Cox proportional hazards regression analysis was performed to establish the prognostic model of the target genes. The LUAD samples were divided into high risk and low risk by the median risk score; the Kaplan–Meier curve was constructed, and the log-rank test was conducted to

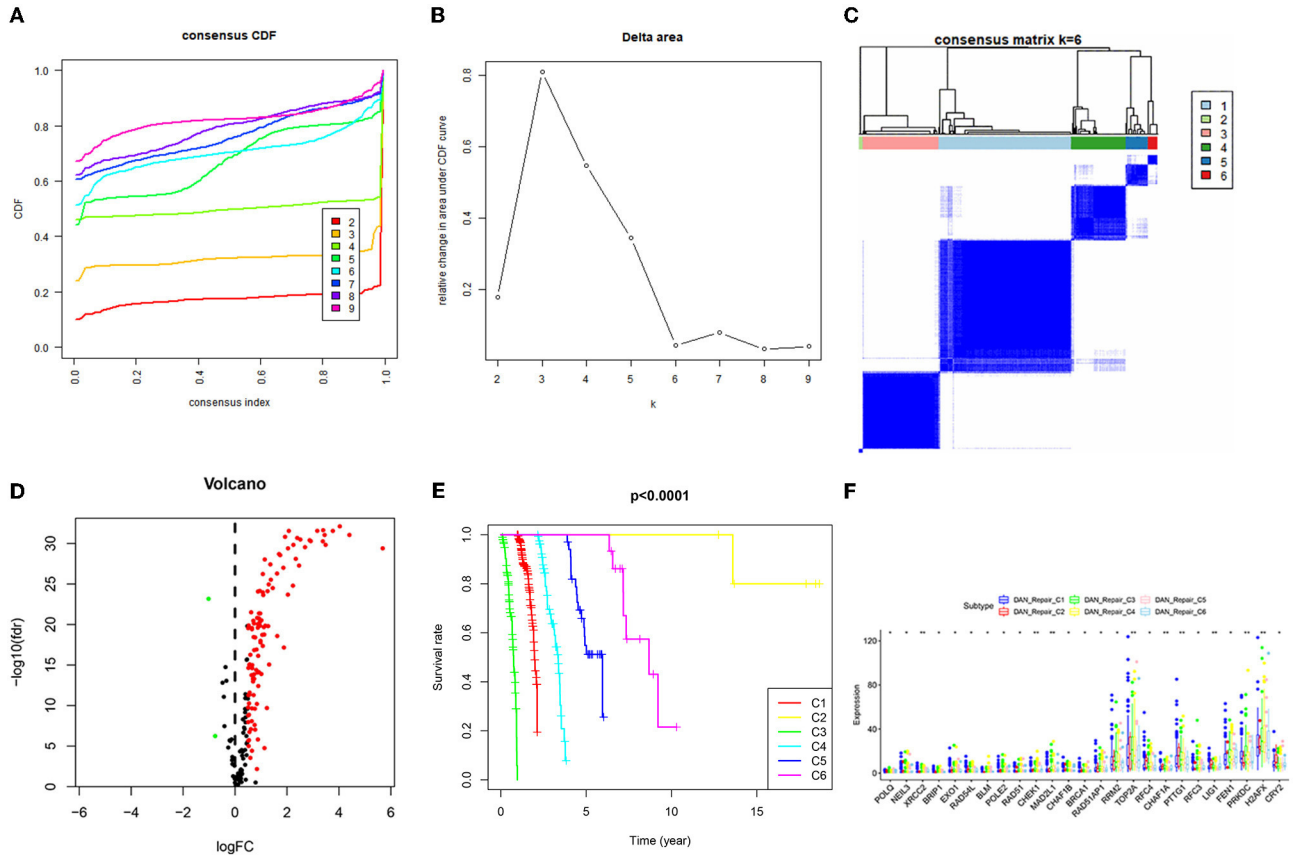

FIGURE 2 | Consistent clustering results of DNA repair related genes and screening of differential genes. **(A)** Consistent Cumulative Distribution Function (CDF) diagram: this diagram shows the cumulative distribution function when k takes different values, which is used to determine when k takes the value, CDF reaches an approximate maximum value, and the cluster analysis result is the most reliable at this time. **(B)** Delta Area Plot: this graph shows the relative change of the area under the CDF curve between k and k-1. When k = 7, the area under the curve only increases slightly, so 6 is the appropriate value of k. **(C)** Matrix heat map when k = 6: the rows and columns of the matrix are all samples, and the values of the consistency matrix range from 0 (it is impossible to cluster together) to 1 (always cluster together) from white to dark blue Color indicates that the consistency matrix is arranged according to the consistency classification (the tree diagram above the heat map). The bar between the dendrogram and the heat map is the category. **(D)** The differential gene volcano map describes the situation of the differential gene. The y-axis of the volcano graph is –log10 (Qvalue), that is, qvalue (value after pvalue correction) is –log10, so the higher the value, the smaller the qvalue is, the more significant it is. The abscissa is Log2 fold change, that is, log2 is taken for fold change, so the closer the points on both sides (each point represents a gene), the greater the increase or decrease in gene expression. **(E)** Survival prognosis curves of different categories. **(F)** Genes with significant differences in the C1–C6 categories.

compare the survival differences between the two groups. The ROC curve was used to evaluate the accuracy of the model. GSE68465 data were used as the validation set to further confirm the model.

RESULTS

Data Processing Results

The ROS-related gene set as the hallmark of ROS-related pathway containing 49 genes, and the DNA repair gene set Kauffmann DNA repair genes (1) containing 230 DNA repair genes were downloaded from the MSigDB and used with the GSEA. The intersection of these genes with the genes from TCGA resulted in a total of 45 ROS-related genes and 194 DNA repair genes. The TCGA samples with incomplete clinical data and survival time <30 days were not taken into consideration and removed, and the data of 465 samples were collected for further analysis.

Consistent Clustering and Screening of ROS-Related Genes and DNA Repair Genes

The consistent clustering of TCGA_ROS data divided the 465 samples into five categories. The survival analysis of the 5 categories revealed a significant difference in survival, with the category C3 having the worst prognosis, while the C5 having the best prognosis. The difference analysis resulted in a total of 14 ROS-related genes (11 up-regulated and 3 down-regulated genes). Then, the expression of differential genes in the 5 categories was compared, and 10 genes were significantly different in C1–C5 (**Figure 1**).

Similar to the above procedure, the consistent clustering of TCGA_DNA repair gene data divided the 465 samples into 6 categories, and survival analysis of these 6 categories revealed that C3 had the worst prognosis, while C2 had the best prognosis. Forty-nine DNA-related differential genes (48 up-regulated genes and 1 down-regulated gene) were obtained, the differences of genes in the 6 categories were compared, and the results revealed that 25 genes were significantly different in C1–C6 (**Figure 2**).

Subsequently, ROS-related and DNA repair genes were visualized in the ROS classification and DNA repair genes and ROS-related genes were visualized in the DNA classification in order to observe the overall expression of genes in the two classifications. Certain differences in the expression of ROS-related and DNA repair genes existed, corresponding to different clustering methods. The most intuitive reaction was that ROS_C3 had the most different prognosis, and the ROS-related and DNA repair genes contained in it were highly expressed. The differences in the expression of the two categories of genes in other categories were not the same, which might be related to the mutual regulation of the two categories of genes (**Figure 3**).

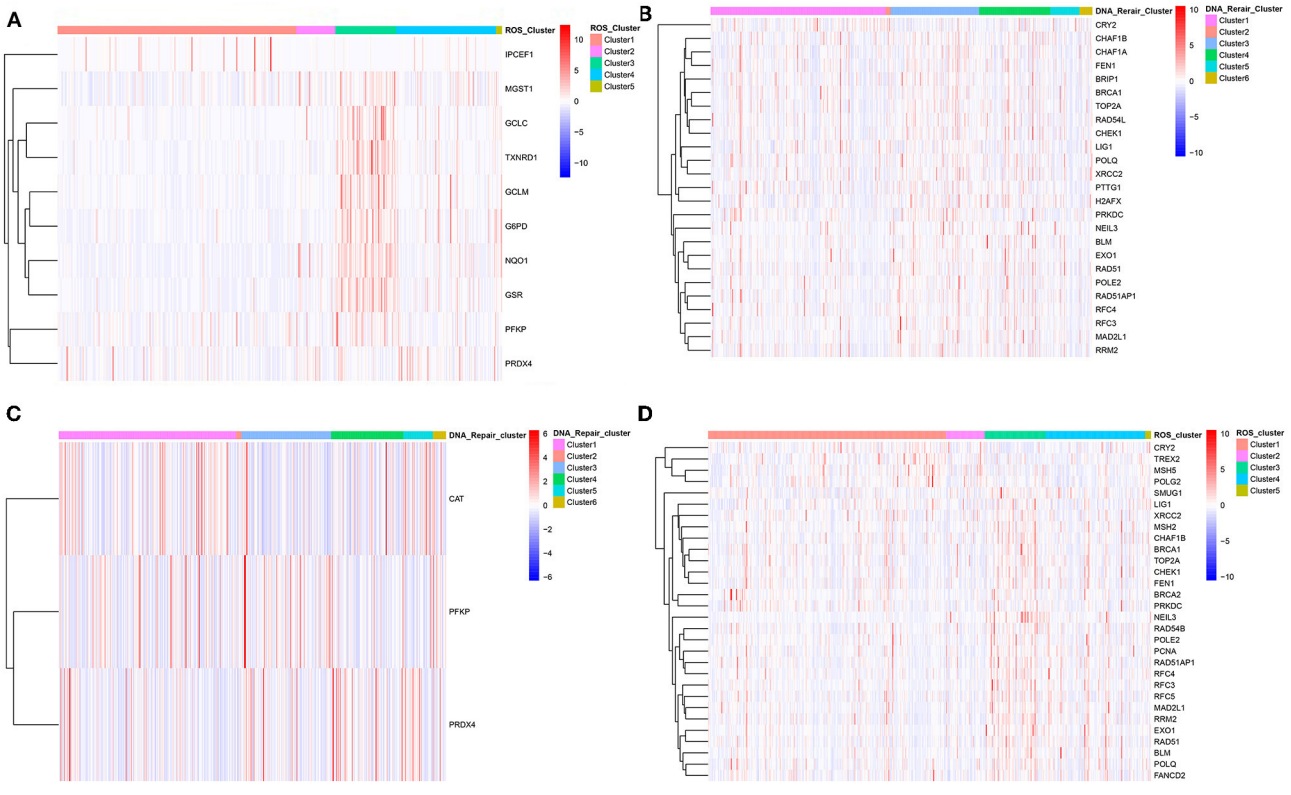

FIGURE 3 | Clustering heat map of ROS-related differential genes and DNA repair-related differential genes in different categories. **(A)** Clustering heat map of differential genes in C1–C5 categories of ROS clustering. **(B)** Clustering heat map of DNA repair-related differential genes in C1–C6 categories of DNA-repair clustering. **(C)** Clustering heat map of ROS-related differential genes in C1–C6 categories of DNA-repair clustering. **(D)** Clustering heat map of DNA-repair-related differential genes in C1–C5 categories of ROS clustering.

Differences in Survival and Gene Expression in the Reclassification Samples

The samples obtained from the two clusters were interactively divided into ten categories, as shown in **Table 1**. The survival analysis revealed that the survival prognosis of the patients whose samples that originally belonged to the ROS category was significantly different after regrouping. The comparison of the expression of the genes between the different new classifications that originally belonged to the ROS category revealed that the higher the expression of up-regulated ROS-related and DNA repair genes, the worse the prognosis, while the down-regulated genes (CYR2, PFKP, CAT) were positively correlated with a longer survival (**Figures 4**, **5**; **Table 2**).

Regulatory Network and Correlation Analysis Among Target Genes

The enrichment of differential ROS-related and DNA repair genes in the ROS_Cn_DNA_Repair_Cm category was visualized by the Venn diagram, and the intersection between the differential genes of the ROS and DNA repair categories was performed to obtain a total of 29 target genes (**Figure 6**). These 29 differentially enriched genes were imported into STRING to

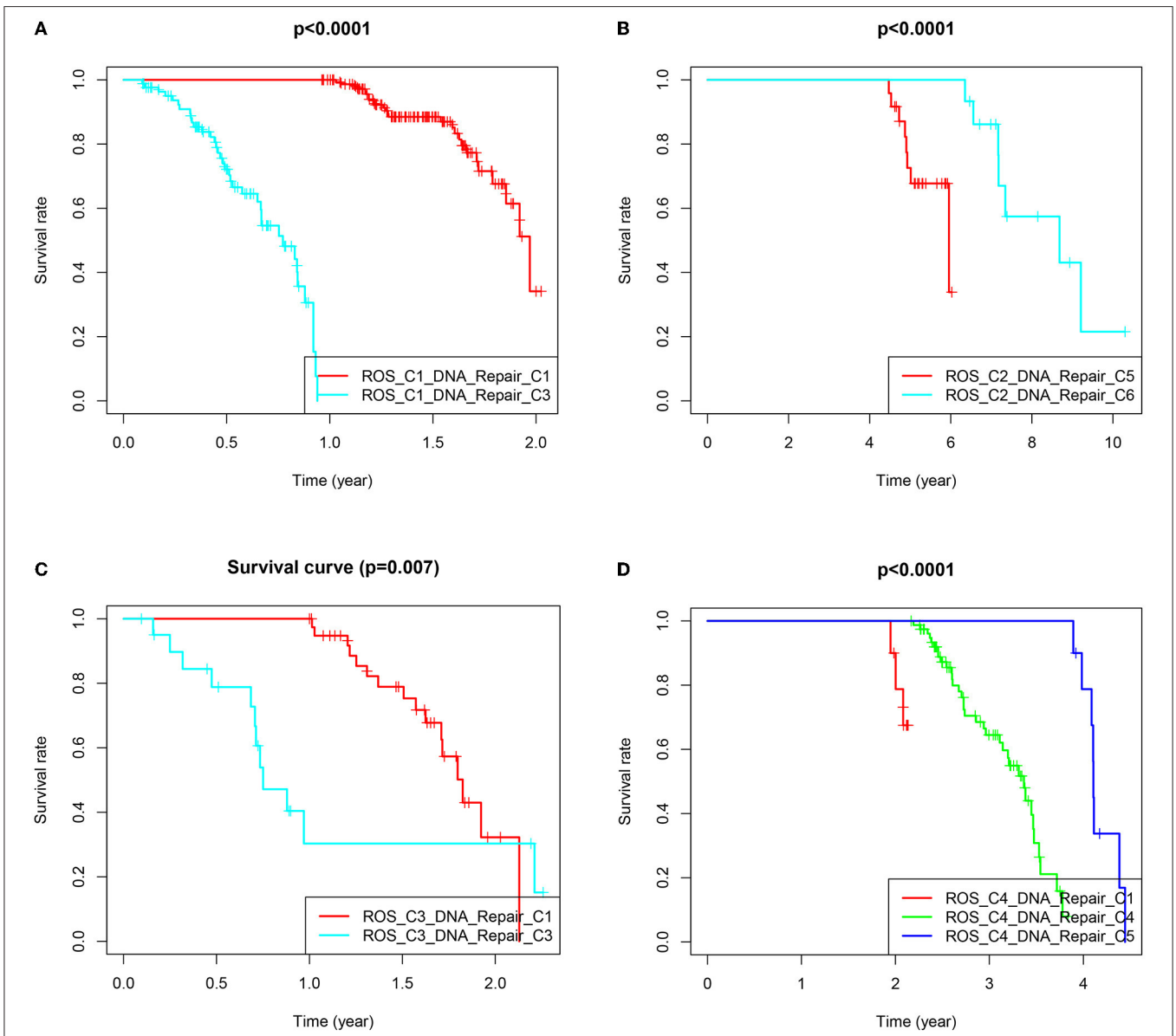

FIGURE 4 | Survival prognostic curves of reclassified samples in different classifications. **(A)** Survival prognostic curves of ROS_C1_DNA_Repair_C1 and ROS_C1_DNA_Repair_C3. **(B)** Survival prognostic curves of ROS_C2_DNA_Repair_C5 and ROS_C2_DNA_Repair_C6. **(C)** Survival prognostic curves of ROS_C3_DNA_Repair_C1 and ROS_C3_DNA_Repair_C3. **(D)** Survival prognostic curves of ROS_C4_DNA_Repair_C1, ROS_C4_DNA_Repair_C4 and ROS_C4_DNA_Repair_C5.

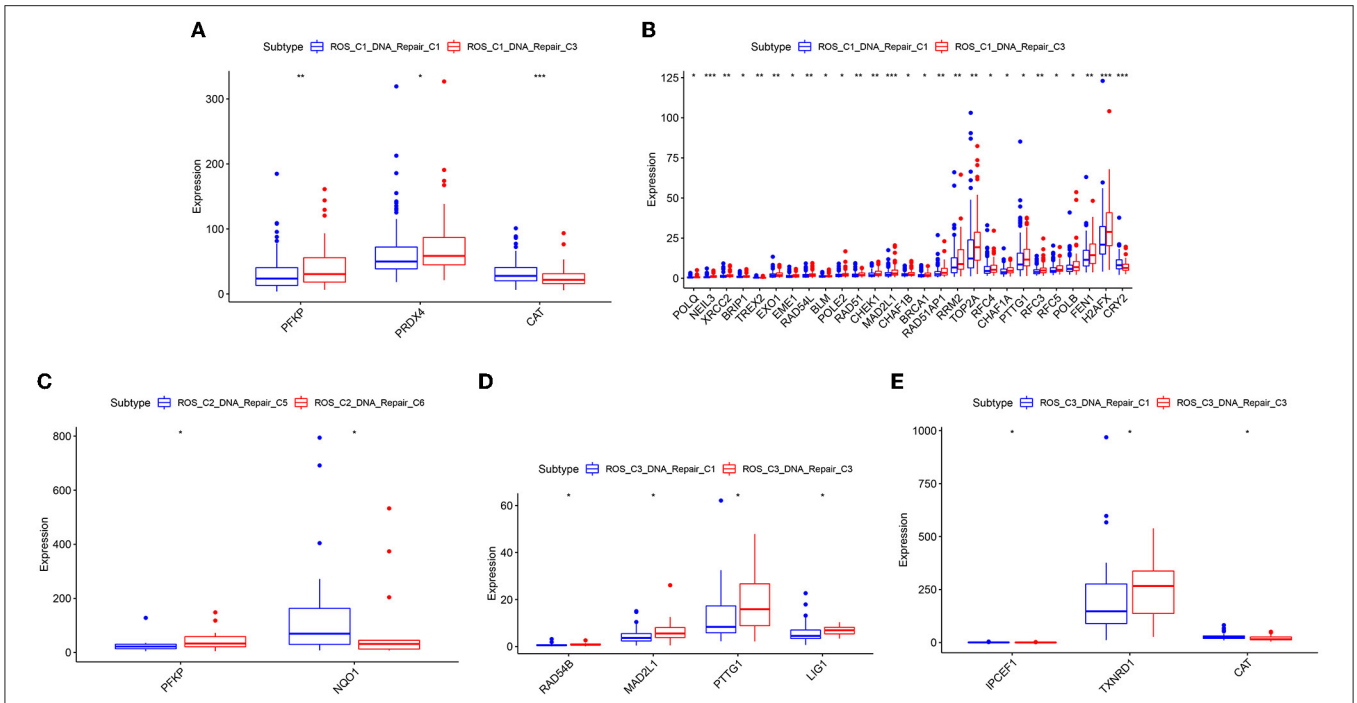

FIGURE 5 | Differentially expressed genes of reclassified samples in different classifications. **(A)** ROS-related differential genes with obvious differences between ROS_C1_DNA_Repair_C1 and ROS_C1_DNA_Repair_C3. **(B)** DNA repair-related differential genes with obvious differences between ROS_C1_DNA_Repair_C1 and ROS_C1_DNA_Repair_C3. **(C)** ROS-related differential genes with obvious differences between ROS_C2_DNA_Repair_C5 and ROS_C2_DNA_Repair_C6. **(D)** DNA repair-related differential genes with obvious differences between ROS_C3_DNA_Repair_C1 and ROS_C3_DNA_Repair_C3. **(E)** ROS-related differential genes with obvious differences between ROS_C3_DNA_Repair_C1 and ROS_C3_DNA_Repair_C3.

TABLE 2 | Up-regulated and down-regulated genes related to the prognosis of reclassified samples.

Subtype	Survival prognosis	
	Bad	**Good**
	Up regulated genes	**Down regulated genes**
ROS_C1_DNA_Repair_C1 ROS_C1_DNA_Repair_C3	PRDX4 POLQ NEIL3 XRCC2 BRIP1 TREX2 EXO1 EME1 RAD54L BLM POLE2 RAD51 CHEK1 MAD2L1 CHAF1B BRCA1 RAD51AP1 RRM2 TOP2A RFC4 CHAF1A PTTG1 RFC3 RFC5 POLB FEN1 H2AFX	PFKP CAT CYR2
ROS_C2_DNA_Repair_C5 ROS_C2_DNA_Repair_C6	NQO1	PFKP
ROS_C3_DNA_Repair_C1 ROS_C3_DNA_Repair_C3	LIG1 MAD2L1 PTTG1 RAD54B IPCEF1 TXNRD1	CAT

construct a gene regulation network and calculate the correlation coefficient among genes. The results showed that the DNA repair genes had a strong internal regulatory relationship. DNA repair and ROS-related genes could be linked through NEIL3-TXNRD1, and the Pearson correlation coefficient between the two was 0.60. In addition, the CYR2 gene showed a negative correlation with other ROS-related and DNA repair genes, while NQO1, PRDX4, and IPCEF1 showed a weak negative correlation with other genes (**Figures 7–9**).

Prognostic Model and Genes Associated With Prognosis

A total of 49 DNA repair and 14 ROS-related genes from the TCGA LUAD data were analyzed by Univariate Cox regression. Twenty-eight genes were associated with a prognosis and were entered into the LASSO regression analysis (**Figure 10**), and a total of eight genes (TERT, PTTG1, SMUG1, PRKDC, H2AFX, PFKP, TXNRD1, and CAT) were identified to build the model. The prognostic value of the risk scores was assessed, which were estimated with the formula: risk score = $\sum$ Xβ* coef β, where coef β was the coefficient and Xβ was the gene relative expression (risk score = TERT*0.102+PTTG1*0.012+SMUG1*0.123+PRKDC* 0.005+ H2AFX*0.002+ PFKP*0.003+TXNRD1*0.0006+CAT*-0.003). As regard the TCGA LUAD data, the risk score in both univariate and multivariate analysis was significantly related to OS (HR = 4.494, 95% CI = 2.563–7.880, $p < 0.001$; HR =4.155, 95% CI = 2.258–6.645, $p < 0.001$, respectively) (**Figures 12A,B**). The patients with low-risk scores showed a significantly better prognosis than those with a high-risk score (**Figures 11A,B**) both in TCGA and GEO LUAD data, as demonstrated by the Kaplan–Meier cumulative curve. The AUC of the risk score

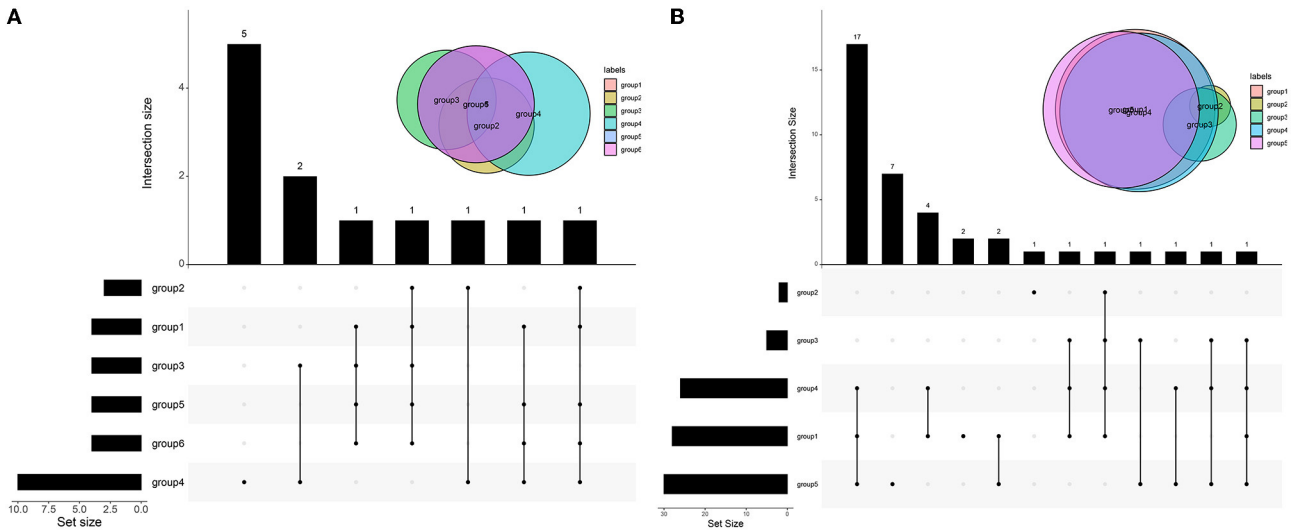

FIGURE 6 | Venn diagram of differential genes in different categories. **(A)** Venn diagrams of ROS-related differential genes in different categories. **(B)** Venn diagrams of DNA repair-related differential genes in different categories. The black in the figure indicates that there is data at that location, and the gray point indicates that there is no data. Connecting different points indicates that there is an intersection. See the bar chart above for specific data. See the bar graph on the left for the total amount of different types of data.

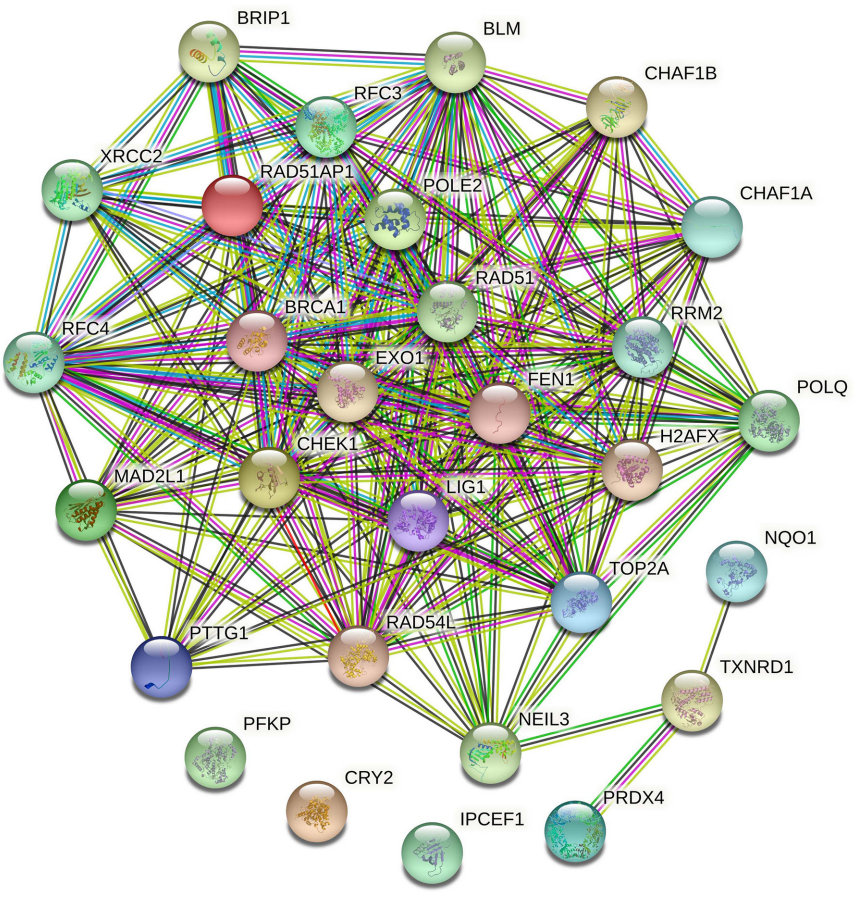

FIGURE 7 | Regulatory network of ROS-related genes and DNA repair genes. The ROS-related genes NQO1, TXNRD1, and PRDX4 could establish links with other DNA repair genes through the DNA repair gene NEIL3.

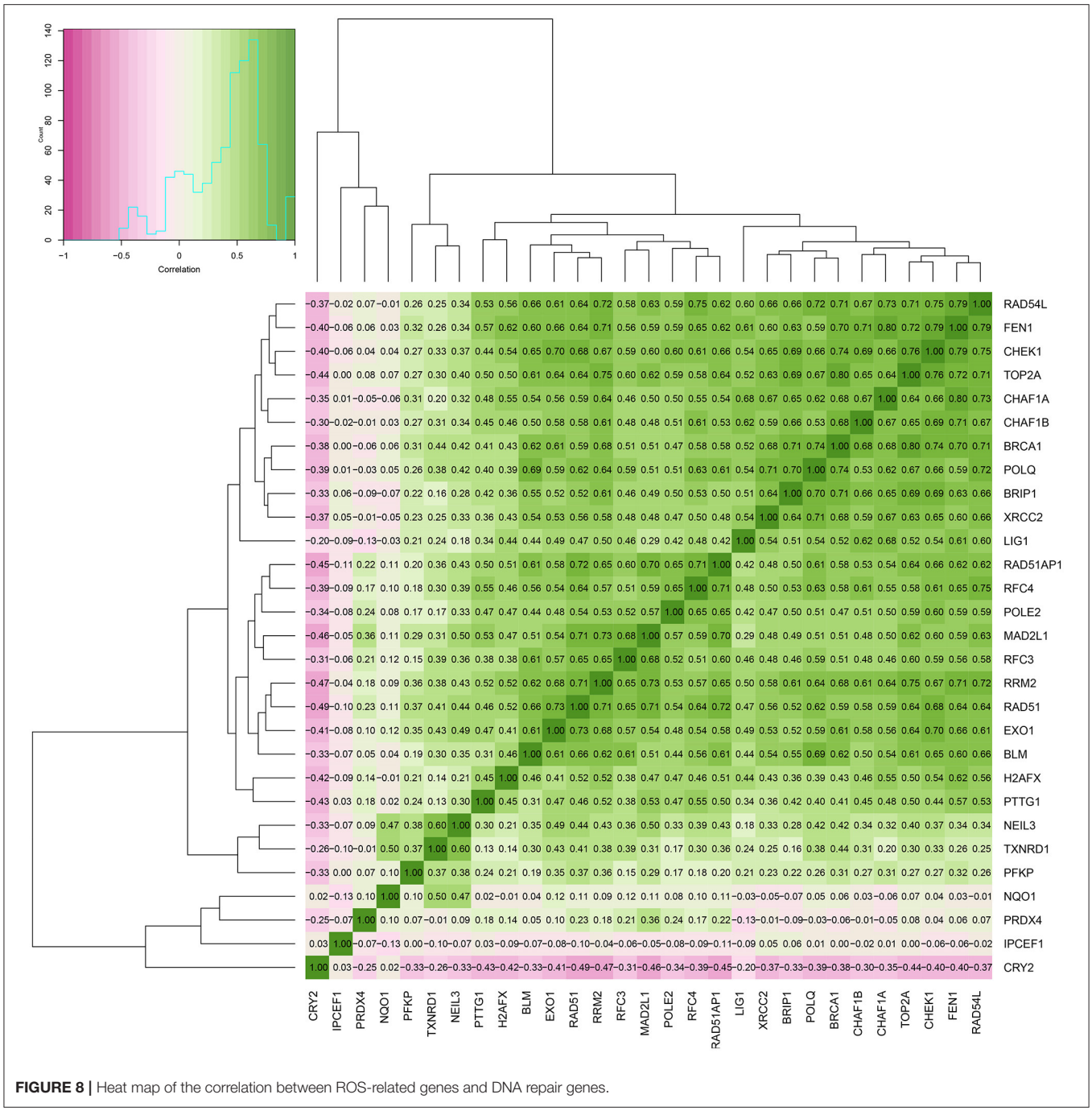

FIGURE 8 | Heat map of the correlation between ROS-related genes and DNA repair genes.

was 0.731, which implied that the Cox model could predict the prognosis quite well (**Figure 12C**).

DISCUSSION

ROS is produced in many cellular compartments including mitochondria, which are the major source of ROS (mROS) (15). Superoxide anion (•O2-), hydrogen peroxide (H2O2) and hydroxyl radical (•OH) belong to a group of highly reactive and heterogeneous molecules derived from oxygen (O2) and are the main forms of ROS in biological systems (16). Many factors in the tumor microenvironment, including the presence of ROS, promote the progress of solid tumors. The increase of ROS level, the imbalance of redox homeostasis and the enhancement of antioxidant capacity are some of the many signs in cancer cells. Therefore, the understanding and elucidating the role of ROS in the tumor microenvironment is essential for developing new methods to combat this disease (17). Various

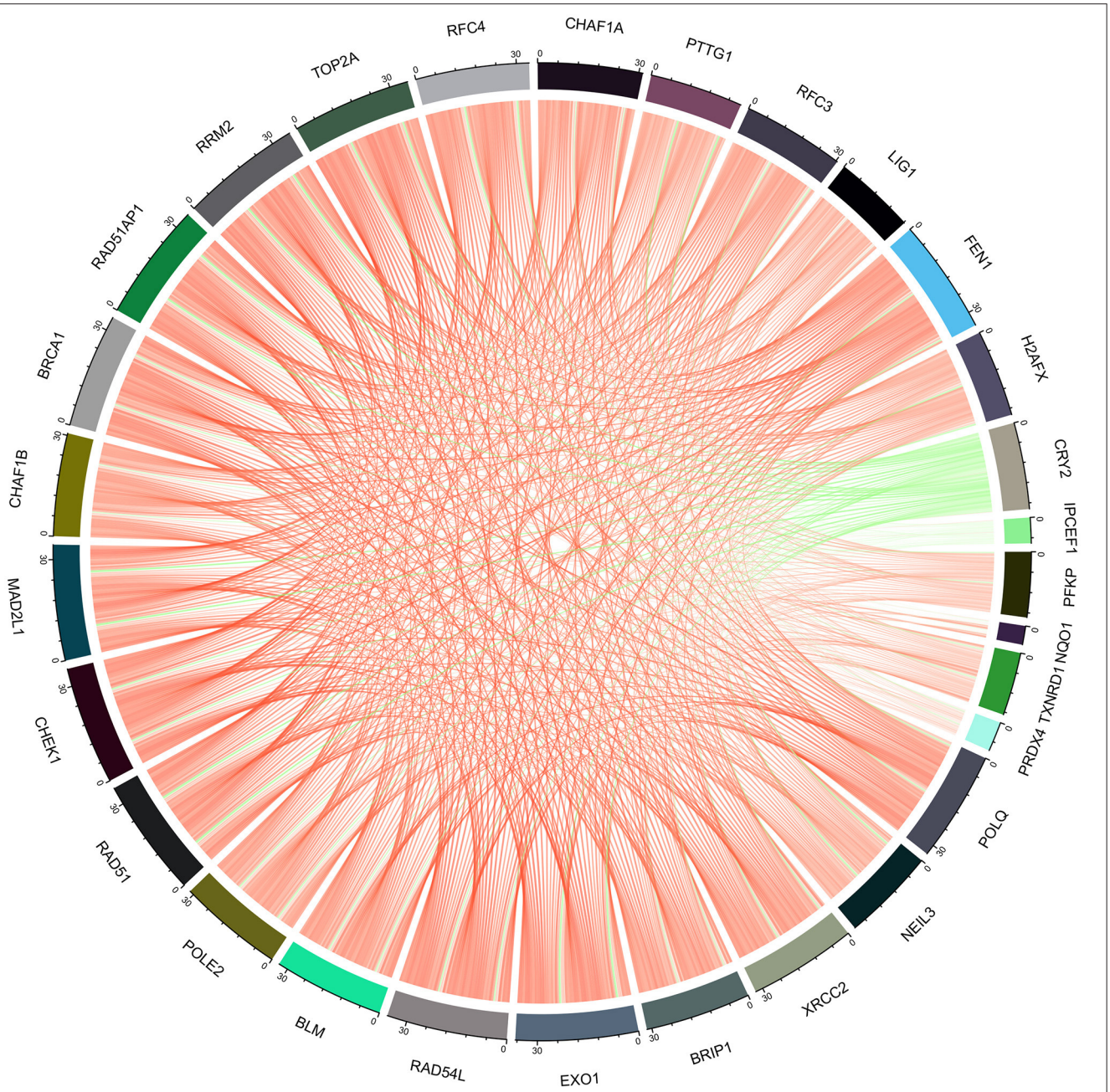

FIGURE 9 | Chord diagram of the correlation between ROS-related genes and DNA repair genes.

tumors, including LUAD, possess high levels of ROS with abnormal metabolism and constitutive carcinogenic signals. ROS are the main effectors of DNA damage associated with cancer and is accompanied by tumor suppression (18, 19). Therefore, tumor cells adapt to the oxidative DNA damage to prevent cell destruction by regulating cell necrosis through the modification in the expression of some genes, thereby inducing the aberrant expression of signaling networks that cause tumorigenesis and metastasis (20). 8-hydroxyguanine is the strongest product of oxidative stress in cells, and is mostly closely related to the occurrence and development of tumors. The DNA repair gene can hydrolyze 8-hydroxyguanine in the base pool to avoid base mismatch and replacement. Once the 8-hydroxyguanine in tumor cells is hydrolyzed by the DNA repair gene, it promotes tumor cell growth. Certain protective effects lead to a malignant phenotype, poor cancer prognosis, or resistance to treatment (21, 22). In some cases, tumors up-regulate the mutagenic repair pathways to survive. Therefore, cancer cells generally rely more

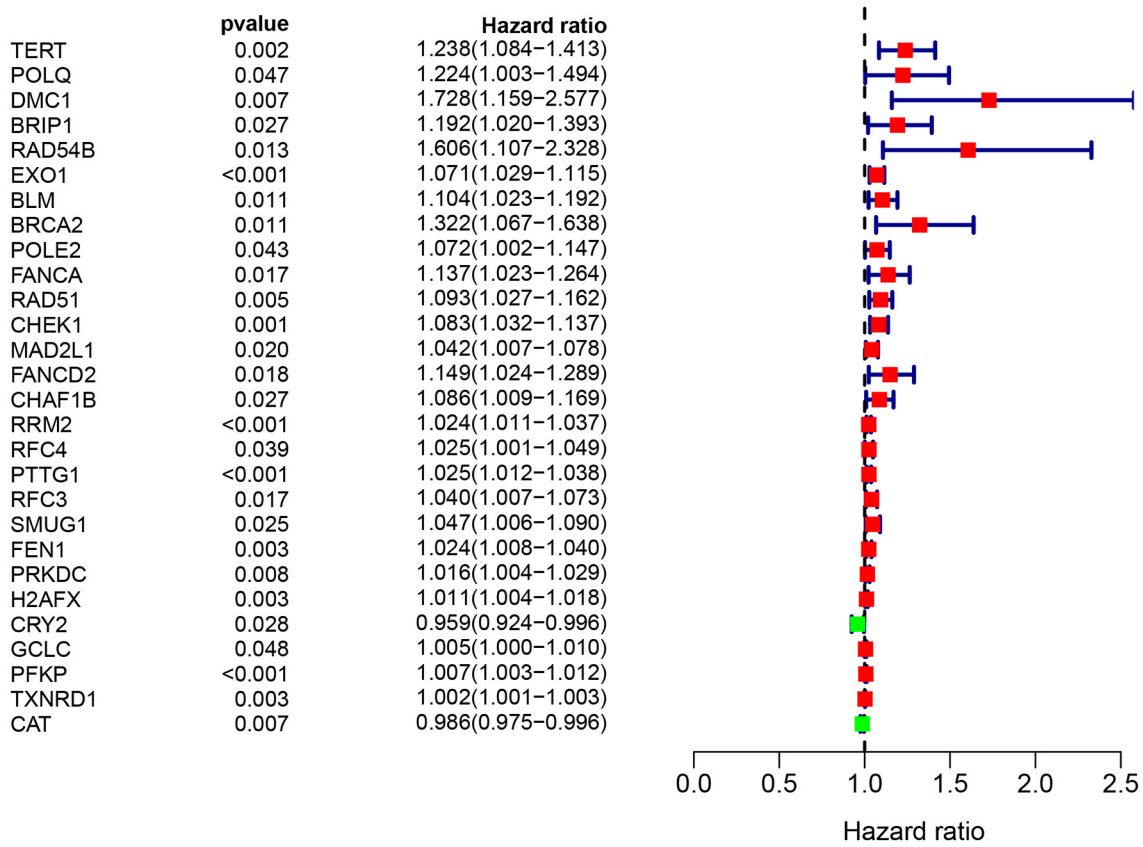

FIGURE 10 | Target genes screened by univariate prognostic analysis.

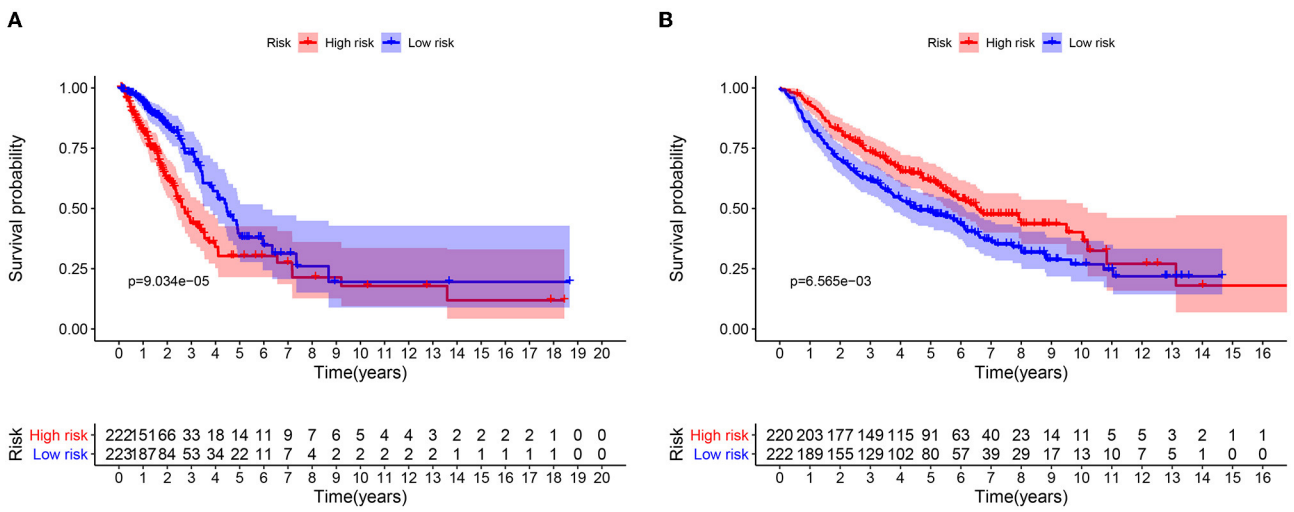

FIGURE 11 | Kaplan-Meier analysis of OS for LUAD patients using TCGA and GEO database. **(A)** Kaplan-Meier survival curves of the relative OS of high- and low-risk groups in TCGA database. **(B)** Kaplan-Meier survival curves of the relative OS of high- and low-risk groups in GEO database.

on repair pathways than normal cells. In addition, cancer cells often have dysfunctional redox homeostasis, and therefore once again, they rely heavily on mechanisms that repair oxidative DNA damage and inhibit enzymes that modify compounds, which can then be incorporated into genomic DNA in their unmodified form. Processes such as replication and oxidative stress provide

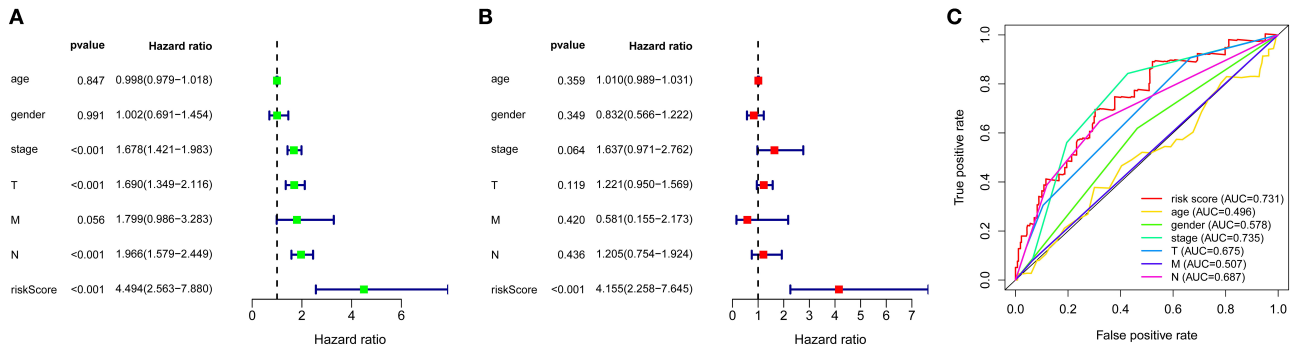

FIGURE 12 | Construction of ROS and DNA-repair-related genes model for patients with LUAD. **(A)** Prognostic values of ROS and DNA-repair -related genes by univariate Cox regression analysis. **(B)** Prognostic values of ROS and DNA-repair -related genes by multivariate Cox regression analysis. **(C)** ROC curve of ROS and DNA-repair -related genes.

a background for ongoing DNA damage in cancer cells and can provide a potential therapeutic window for compounds that exacerbate these processes. Such compounds can accomplish by further emphasizing replication, weakening the ability of cancer cells to handle high levels of replication or oxidative stress, or potentially inhibiting DNA repair and related processes (23–25).

Therefore, in this work, the synergistic tumorigenic effect of ROS-related genes and DNA repair genes was evaluated, and the regulatory relationship between the two groups of genes was further explored. It is important to consider whether it is better to use ROS to kill cancer cells or to inhibit the DNA repair in cancer cells to improve patient prognosis.

The expression of ROS-related genes and DNA repair genes was used to cluster TCGA tumor samples uniformly. ROS-related genes divided tumors into classes, and DNA repair genes divided tumor samples into classes. Significant differences in survival between the internal classifications were obtained by the two clustering methods, and the differentially expressed genes were further screened. Our analysis found that the samples that originally belonged to the ROS classification partial overlapped in the classification of DNA repair genes. After reclassifying the samples according to the two classifications, the prognosis of patients changed when the expression of ROS-related and DNA repair genes in the samples changed. Thus, our hypothesis was that ROS-related and DNA repair genes might have a mutual regulatory relationship, which in turn affected the occurrence and development of tumors. A total of 29 differential genes were finally identified and included 5 ROS-related and 24 DNA repair genes. STRING analysis of the regulatory relationship found that 3 ROS-related genes (NQO1, TXNRD1, and PRDX4) can be repaired by the DNA repair gene NEIL3 and other DNA repair genes.A large amount of evidence showed that NQO1 has a "Janus" effect in cancer biology, playing a role in suppressing cancer and promoting tumors (26). NQO1 is constitutively expressed at a relatively low level in various normal tissues. Under oxidative stress, NF-E2 p45-related factor 2 (Nrf2)/Kelch-like ECH-related protein 1 (Keap1) signaling pathway can cooperate to transcribe a series of defense genes and provide cells with multiple layers of protection against carcinogenesis. These measures include the immediate elimination of ROS (27). The expression of NQO1 is considered as a practical and economical way to control cancer. NQO1 is abnormally up-regulated in solid tumors, and high levels of NQO1 are associated with poor patient prognosis. It is known that cancer cells have a significant increase in ROS production compared to normal cells. In this case, high levels of NQO1 in cancer can help cancer cells to cope with the increased ROS just like normal cells, thus, tumor growth and metastasis is not only not compromised, but promoted (28). Our results showed that NQO1 was correlated with the expression of the DNA repair gene NEIL3 (Pearson correlation coefficient), suggesting its role as a tumor control gene.

The cytoplasmic selenoprotein thioredoxin reductase 1 (TXNRD1) has several different effects related to cancer including the protection of normal cells to evolve into cancer cells or the protection against the promotion of cancer progression. TXNRD1 has a unique connection with Nrf2 signaling and ribonucleotide reductase-dependent deoxyribonucleotide production and it supports a variety of antioxidant systems against oxidative stress. Thus, it is essential that metabolic pathways regulated by TrxR1 are affected in cancer (29). Our regulatory network suggested that TXNRD1 had a significant correlation with the DNA repair gene NEIL3, thus, it might be considered as a potential targeted gene in a combination therapy affecting ROS-related genes and DNA repair genes.

Peroxiredoxin 4 is a typical peroxidase 2-Cys antioxidant in the endoplasmic reticulum, which protect cells against oxidative stress by detoxifying hydrogen peroxide, thus promoting cell survival (30). The role of PRDX4 in cancer received considerable attention. The expression of PRDX4 in NSCLC-derived endothelial cells is higher than that in normal cells (31). Sulfiredoxin is an antioxidant protein induced by H2O2 that acts as a catalyst for reducing the peroxidized PRDXs to reduce their peroxidase activity. Sulfiredoxin is more inclined to combine with PRDX4 than other PRDXs. The up-regulation or down-regulation of the sulfiredoxin-PRDX4 axis can affect the mitogen-activated protein kinase pathway, cAMP response element binding protein and activator protein-1/matrix metalloproteinase axis pathway (32). Furthermore, another study

revealed that the expression of PRDX4 is closely related to the disease-free survival time and short recurrence time of patients with early-stage lung squamous cell carcinoma undergoing early radical surgery (33).

Endonuclease VIII-like 3 (NEIL3) is a DNA glycosylase protein that is involved in oxidative and interstrand crosslink DNA damage repair (34). NEIL3 is highly expressed in various human cancer cells and is associated with metastatic cancer, indicating that it may be necessary to maintain cancer cell growth or malignant progression (21, 35). NEIL3 overexpression is positively correlated with homologous recombination and mismatch repair gene expression. High NEIL3 expression may promote cancer phenotype by increasing genomic instability and/or interfering with other DNA repair (34). Our analysis found that NEIL3 played a pivotal role in the connection between DNA repair genes and ROS-related genes. Therefore, the mutual regulation of ROS-related and DNA repair genes centered on NEIL3 might become an important topic for further studies.

A prognostic model based on all differentially expressed ROS-related genes and DNA repair genes was constructed and combined with the clinical data of the samples, and finally nine genes were selected to calculate the risk score. The results revealed that the prognosis of patients in the high- and low-risk groups was significantly different, and the GEO data verified this result. The multivariate analysis suggested that the risk score could be used as an independent prognostic factor to evaluate patient prognosis. The above mentioned model genes included three ROS-related genes and six DNA repair genes, and TXNRD1 gene played an important role in the regulatory network of the two groups of genes, as revealed by previous studies.

CONCLUSION

This study might highlight the significance of ROS-related and DNA repair genes in LUAD, and the combined target of ROS and DNA repair genes might be a promising strategy in the treatment of LUAD, although further studies should be performed to validate these findings.

DATA AVAILABILITY STATEMENT

The datasets presented in this study can be found in online repositories. The names of the repository/repositories and accession number(s) can be found in the article/supplementary material.

AUTHOR CONTRIBUTIONS

YQ has designed the research. H-MF and YZ analyzed data and wrote the paper. H-MF retrieved and collected data. W-JY were responsible for drawing. All authors have read and approved the final manuscript.

REFERENCES

1. Jayavelu AK, Moloney JN, Böhmer FD, Cotter TG. NOX-driven ROS formation in cell transformation of FLT3-ITD-positive AML. *Exp Hematol.* (2016) 44:1113–22. doi: 10.1016/j.exphem.2016.08.008
2. Mishra A, Aja E, Fletcher HM. Role of superoxide reductase FA796 in oxidative stress resistance in Filifactor alocis. *Sci Rep.* (2020) 10:1–3. doi: 10.1038/s41598-020-65806-3
3. Zorov DB, Juhaszova M, Sollott SJ. Mitochondrial reactive oxygen species (ROS) and ROS-induced ROS release. *Physiol Rev.* (2014) 94:909–50. doi: 10.1152/physrev.00026.2013
4. Storz P. Reactive oxygen species in tumor progression. *Front Biosci.* (2005) 10:1881–96. doi: 10.2741/1667
5. Lawless MW, O'Byrne KJ, Gray SG. Oxidative stress induced lung cancer and COPD: opportunities for epigenetic therapy. *J Cell Mol Med.* (2009) 13:2800–21. doi: 10.1111/j.1582-4934.2009.00845.x
6. Fahmy HM. *In vitro* study of the cytotoxicity of thymoquinone/curcumin fluorescent liposomes. *Naunyn Schmiedebergs Arch Pharmacol.* (2019) 392:1465–76. doi: 10.1007/s00210-019-01688-1
7. Gupta A, Srivastava S, Prasad R, Natu SM, Mittal B, Negi MP, et al. Oxidative stress in non-small cell lung cancer patients after chemotherapy: association with treatment response. *Respirology.* (2010) 15:349–56. doi: 10.1111/j.1440-1843.2009.01703.x
8. Ilonen IK, Räsänen JV, Sihvo EI, Knuuttila A, Salmenkivi KM, Ahotupa MO, et al. Oxidative stress in non-small cell lung cancer: role of nicotinamide adenine dinucleotide phosphate oxidase and glutathione. *Acta Oncologica.* (2009) 48:1054–61. doi: 10.1080/02841860902824909
9. Zhou C, Li S, Liu J, Chu Q, Miao L, Cai L, et al. International consensus on severe lung cancer—the first edition. *Transl Lung Cancer Res.* (2021) 10:2633. doi: 10.21037/tlcr-21-467
10. Liao Z, Chua D, Tan NS. Reactive oxygen species: a volatile driver of field cancerization and metastasis. *Mol Cancer.* (2019) 18:65. doi: 10.1186/s12943-019-0961-y
11. Assi M. The differential role of reactive oxygen species in early and late stages of cancer. *Am J Physiol Regul Integr Comp Physiol.* (2017) 313:R646–53. doi: 10.1152/ajpregu.00247.2017
12. Ouyang KJ, Woo LL, Ellis NA. Homologous recombination and maintenance of genome integrity: cancer and aging through the prism of human RecQ helicases. *Mech Ageing Dev.* (2008) 129:425–40. doi: 10.1016/j.mad.2008.03.003
13. Yousuf A, Bhat MY, Pandith AA, Khan NP, Alam K, Shah P, et al. MGMT gene silencing by promoter hypermethylation in gastric cancer in a high incidence area. *Cell Oncol.* (2014) 37:245–52. doi: 10.1007/s13402-014-0179-3
14. Konstantinopoulos PA, Cheng SC, Hendrickson AE, Penson RT, Schumer ST, Doyle LA, et al. Berzosertib plus gemcitabine versus gemcitabine alone in platinum-resistant high-grade serous ovarian cancer: a multicentre, open-label, randomised, phase 2 trial. *Lancet Oncol.* (2020) 21:957–68. doi: 10.1016/S1470-2045(20)30180-7
15. Idelchik MD, Begley U, Begley TJ, Melendez JA. Mitochondrial ROS control of cancer. *Semin Cancer Biol.* (2017) 47:57–66. doi: 10.1016/j.semcancer.2017.04.005
16. Muller F. The nature and mechanism of superoxide production by the electron transport chain: its relevance to aging. *J Am Aging Assoc.* (2000) 23:227–53. doi: 10.1007/s11357-000-0022-9
17. Panieri E, Santoro MM. ROS homeostasis and metabolism: a dangerous liason in cancer cells. *Cell Death Dis.* (2016)7:e2253. doi: 10.1038/cddis.2016.105
18. Gorrini C, Harris IS, Mak TW. Modulation of oxidative stress as an anticancer strategy. *Nat Rev Drug Discov.* (2013) 12:931–47. doi: 10.1038/nrd4002
19. Rai P, Sobol RW. Mechanisms of MTH1 inhibition-induced DNA strand breaks: the slippery slope from the oxidized nucleotide pool to genotoxic damage. *DNA Repair.* (2019) 77:18–26. doi: 10.1016/j.dnarep.2019.03.001
20. Rai P. Oxidation in the nucleotide pool, the DNA damage response and cellular senescence: Defective bricks build a defective house. *Mutat Res.* (2010) 703:71–81. doi: 10.1016/j.mrgentox.2010.07.010

21. Kauffmann A, Rosselli F, Lazar V, Winnepenninckx V, Mansuet-Lupo A, Dessen P, et al. High expression of DNA repair pathways is associated with metastasis in melanoma patients. *Oncogene.* (2008) 27:565–73. doi: 10.1038/sj.onc.1210700
22. Nakabeppu Y, Ohta E, Abolhassani N. MTH1 as a nucleotide pool sanitizing enzyme: Friend or foe? *Free Radic Biol Med.* (2017) 107:151–8. doi: 10.1016/j.freeradbiomed.2016.11.002
23. Brown JS, O'Carrigan B, Jackson SP, Yap TA. Targeting DNA repair in cancer: beyond PARP inhibitors. *Cancer Discov.* (2017) 7:20–37. doi: 10.1158/2159-8290.CD-16-0860
24. Huber KV, Salah E, Radic B, Gridling M, Elkins JM, Stukalov A, et al. Stereospecific targeting of MTH1 by (S)-crizotinib as an anticancer strategy. *Nature.* (2014) 508:222–7. doi: 10.1038/nature13194
25. Gaillard H, García-Muse T, Aguilera A. Replication stress and cancer. *Nat Rev Cancer.* (2015) 15:276–89. doi: 10.1038/nrc3916
26. Zhang K, Chen D, Ma K, Wu X, Hao H, Jiang S, et al. (P) H: quinone oxidoreductase 1 (NQO1) as a therapeutic and diagnostic target in cancer. *J Med Chem.* (2018) 61:6983–7003. doi: 10.1021/acs.jmedchem.8b00124
27. Nioi P, Hayes JD. Contribution of NAD (P) H: quinone oxidoreductase 1 to protection against carcinogenesis, and regulation of its gene by the Nrf2 basic-region leucine zipper and the arylhydrocarbon receptor basic helix-loop-helix transcription factors. *Mutat Res.* (2004) 555:149–71. doi: 10.1016/j.mrfmmm.2004.05.023
28. Madajewski B, Boatman MA, Chakrabarti G, Boothman DA, Bey EA. Depleting tumor-NQO1 potentiates anoikis and inhibits growth of NSCLC. *Mol Cancer Res.* (2016) 14:14–25. doi: 10.1158/1541-7786.MCR-15-0207-T
29. Arnér ES. Targeting the selenoprotein thioredoxin reductase 1 for anticancer therapy. *Adv Cancer Res.* (2017) 136:139–51. doi: 10.1016/bs.acr.2017.07.005
30. Jia W, Chen P, Cheng Y. PRDX4 and its roles in various cancers. *Technol Cancer Res Treat.* (2019) 18:1533033819864313. doi: 10.1177/1533033819864313
31. Park HJ, Kim BG, Lee SJ, Heo SH, Kim JY, Kwon TH, et al. Proteomic profiling of endothelial cells in human lung cancer. *J Proteome Res.* (2008) 7:1138–50. doi: 10.1021/pr7007237
32. Wei Q, Jiang H, Xiao Z, Baker A, Young MR, Veenstra TD, et al. Sulfiredoxin–peroxiredoxin IV axis promotes human lung cancer progression through modulation of specific phosphokinase signaling. *Proc Nat Acad Sci.* (2011) 108:7004–9. doi: 10.1073/pnas.1013012108
33. Hwang JA, Song JS, Yu DY, Kim HR, Park HJ, Park YS, et al. Peroxiredoxin 4 as an independent prognostic marker for survival in patients with early-stage lung squamous cell carcinoma. *Int J Clin Exp Pathol.* (2015) 8:6627–35.
34. Tran OT, Tadesse S, Chu C, Kidane D. Overexpression of NEIL3 associated with altered genome and poor survival in selected types of human cancer. *Tumor Biology.* (2020) 42:1010428320918404. doi: 10.1177/10104283209 18404
35. Hildrestrand GA, Neurauter CG, Diep DB, Castellanos CG, Krauss S, Bjørås M, et al. Expression patterns of Neil3 during embryonic brain development and neoplasia. *BMC Neurosci.* (2009) 10:1–8. doi: 10.1186/1471-220 2-10-45

Conflict of Interest: The authors declare that the research was conducted in the absence of any commercial or financial relationships that could be construed as a potential conflict of interest.

Publisher's Note: All claims expressed in this article are solely those of the authors and do not necessarily represent those of their affiliated organizations, or those of the publisher, the editors and the reviewers. Any product that may be evaluated in this article, or claim that may be made by its manufacturer, is not guaranteed or endorsed by the publisher.

frontiers in Medicine

ORIGINAL RESEARCH
published: 21 February 2022
doi: 10.3389/fmed.2021.816474

TIGIT Signaling Pathway Regulates Natural Killer Cell Function in Chronic Hepatitis B Virus Infection

Juan Wang[1], *Hongyan Hou*[2]*, *Lie Mao*[2], *Feng Wang*[2], *Jing Yu*[2], *Ying Luo*[2], *Qun Lin*[2] and *Ziyong Sun*[2]*

[1] Department of Blood Transfusion, Tongji Medical College, Tongji Hospital, Huazhong University of Science and Technology, Wuhan, China, [2] Department of Laboratory Medicine, Tongji Medical College, Tongji Hospital, Huazhong University of Science and Technology, Wuhan, China

Background and Objective: Persistent infection of hepatitis B virus (HBV) and liver damage in immune active chronic hepatitis B (CHB) could be partly due to the overreaction of natural killer (NK) cells, including pro-inflammatory cytokine secretion and cytotoxicity. An immunosuppressive receptor, T-cell immunoglobulin and immunoreceptor tyrosine–based inhibitory motif (ITIM) domain (TIGIT) is specifically expressed in NK cells. This study aims to investigate the role of the TIGIT signaling pathway in regulating NK cell functions in patients with CHB.

Method: We comparatively assessed the expression of TIGIT in NK cells of patients with immune active CHB (CHB-IA), carriers of immune control chronic HBV (CHB-IC), and healthy controls (HCs), and then explored mechanisms of the TIGIT signaling pathway in regulating NK cell-mediated liver injury by different molecular assessments.

Result: The expression of TIGIT in NK cells was enhanced in CHB-IC but was reduced in CHB-IA compared with the HC group. In patients with CHB-IA, the expression of TIGIT was inversely correlated with intensity of the liver damage. Moreover, TIGIT-NK cells show higher IFN-γ secretion capability, degranulation activity, and cytotoxicity but lower apoptosis than TIGIT+ NK cells. Blockade of the TIGIT pathway with anti-TIGIT antibody increased NK cell function, while activation of the TIGIT pathway with TIGIT Fc and CD155 Fc chimera protein down-regulated NK cell function.

Conclusion: Our data showed that the TIGIT signaling pathway participates in NK cell impairment, which could be used as a new therapeutic target to protect patients with chronic HBV infection from severe liver injury.

Keywords: hepatitis B virus (HBV), chronic hepatitis B, natural killer (NK) cell, TIGIT, cytokine secretion, cytotoxicity

OPEN ACCESS

Edited by:
Ali Yadollahpour,
The University of Sheffield,
United Kingdom

Reviewed by:
Shengye Wang,
Zhejiang Cancer Hospital, China
Yukun Li,
Hebei Medical University, China

***Correspondence:**
Ziyong Sun
zysun@tjh.tjmu.edu.cn
Hongyan Hou
houhongyan89@163.com

Specialty section:
This article was submitted to Precision Medicine, a section of the journal Frontiers in Medicine

Received: *16 November 2021*
Accepted: *29 December 2021*
Published: *21 February 2022*

Citation:
Wang J, Hou H, Mao L, Wang F, Yu J, Luo Y, Lin Q and Sun Z (2022) TIGIT Signaling Pathway Regulates Natural Killer Cell Function in Chronic Hepatitis B Virus Infection. Front. Med. 8:816474. doi: 10.3389/fmed.2021.816474

INTRODUCTION

Among the primary reasons for liver diseases, chronic hepatitis B virus (HBV) infection has an estimated 350 million carriers globally (1). It has been reported that 14–30% of patients with chronic hepatitis B (CHB) suffer from cirrhosis with end-stage liver disease and hepatocellular carcinoma (HCC) (2), which causes 786,000 deaths per year (3). Normally, chronic infection of HBV involves immune tolerant (IT), immune activated (IA), immune control (IC), and immune escape phases (4). The IA phase is associated with rapid disease progression and

recurrent necroinflammation, while the IC phase (previously called the inactive carrier phase) is often associated with lowered risk of HCC and cirrhosis (1, 4). However, differences in immune mechanisms between patients with CHB-IA and those with CHB-IC are largely unknown, and exploring the mechanisms of why patients with CHB-IA suffer from serious liver injuries and complications might provide a new therapeutic target for early diagnosis and appropriate treatment.

Persistent infection of HBV, death of hepatocytes, and liver injury might be due to the dysfunction of immune system. The liver of patients with CHB with damaged liver cells usually have high levels of non-viral specific lymphocytes. Natural killer (NK) cells make up 30–50% of intrahepatic lymphocytes and play vital roles against HBV infection (5, 6), but uncontrolled NK cell activation in an infected tissues may also lead to chronic immunopathology in these tissues (7). Previous studies have demonstrated that the cytotoxicity and cytokine production of NK cells correlate with the extent of damage to the liver in murine hepatitis models and patients with CHB (8, 9). Some studies have reported that during the CHB-IA stage, liver injury could lead to increased NK cell cytotoxicity (9, 10), which was caused by high levels of interleukins (ILs)-12,−15, and−18 *in situ* and low level of IL-10 (10). Moreover, hepatocyte necrosis (11), mediated by TRAIL, NKG2D/NKG2D ligand, and Fas/Fas-ligand, is another important factor (12). Main findings of the current literature on the activation of NK cells over CHB progression are reduced cytotoxicity, NKp30 and NKG2D expression, and production of IFN-γ (13). However, findings of studies on the activation and functioning of NK cells and their regulating mechanisms are controversial that necessitate conducting further studies to investigate the roles and activating mechanisms of NK cell functions in HBV infection.

T-cell immunoglobulin and immunoreceptor tyrosine–based inhibitory motif (ITIM) domain (TIGIT) is a newly found inhibitory molecule (14), which is expressed in NK cells and T cells at high levels. The TIGIT signaling pathway has been reported to be involved in the progression of various tumors (15–19), autoimmune diseases (20, 21), and chronic infections (15, 22, 23). Previous studies have shown that TIGIT was highly expressed on NK cells from murine acute viral hepatitis and negatively regulated NK-cell activation (24), which reduced liver injury and facilitated liver regeneration (25). Moreover, treatment of HCV infection results in downregulated TIGIT expression in T cells in the case of untreated severe infection (26). In viral hepatitis, TIGIT limits the activity of NK cells *via* the ITIM domain. However, the role of the TIGIT pathway in NK cell activity regulation in patients with CHB is yet to be explored.

Abbreviations: ALT, alanine aminotransferase; IA, immune-active; CHB, chronic hepatitis B; HBV, hepatitis B virus; HCs, healthy controls; IC, immune-control; HCC, hepatocellular carcinoma; HBsAg, hepatitis B surface antigen; HBeAb, hepatitis B e antibody; NK, natural killer; HBeAg, hepatitis B e antigen; IFN-γ, interferon gamma; HBcAg, hepatitis c surface antigen; IL, interleukin; mAbs, monoclonal antibodies; TIGIT, T-cell immunoglobulin and ITIM domain; PBMCs, peripheral blood mononuclear cells; CFSE, carboxyfluorescein-diacetate-succinimidyl-ester; APRI, aspartate aminotransferase-to-platelet ratio index; LPS, lipopolysaccharide.

This study aimed to evaluate the role of TIGIT in regulating NK cell function in patients with CHB. We found that the expression of TIGIT in NK cells decreased in CHB-IA compared with CHB-IC and HCs, and that TIGIT-NK cells show higher IFN-γ secretion capability, degranulation activity, and cytotoxicity but lower apoptosis than TIGIT+ NK cells. Furthermore, TIGIT signaling pathway blockade could restore the activity of NK cells, and activation of this pathway exerted opposite effect on NK cell function. Overall, we discovered a mechanism, for the first time, of TIGIT-mediated regulation of NK cell function, which may act as a novel target for protection of patients with CHB from acute inflammation and liver injury.

MATERIALS AND METHODS

Subjects of This Study

Experimental procedures of this study were approved by the local ethics committee of Tongji Hospital, Tongji Medical College, Huazhong University of Science and Technology, Wuhan, China (ethic code: TJ-IRB20210225), and were in accordance with the ethical standards and regulations of human studies of the Helsinki Declaration (27). Study population included patients with CHB-IA ($n = 74$), CHB-IC ($n = 40$), and healthy controls (HCs) ($n = 40$) who were referred to the Tongji Hospital, Wuhan, China. The age of the participants was between 18 and 60 years old, and they did not undergo immunosuppressive drugs or antiviral therapy within 6 months prior to sampling. Each participant provided written informed consent and was required to fill in a questionnaire regarding his or her medical history and associated treatments.

Each patient fulfilled the amended criteria for CHB (4, 28), patients with CHB-IA were HBsAg+ and HBeAg+ for more than 6 months and ALT > ULN. They were also detected with fluctuating or high levels of HBV replication (>2,000 IU/ml of HBV DNA levels) (4). CHB-IC (previously called inactive carrier) were HBsAg+ more than six-months, anti-HBe+ and HBeAg-, and undetectable serum HBV DNA level with perpetually normal aminotransferases activity. Only patients with compensated liver disease have been selected. HCs were defined as participants with no clinical signs or symptoms of the disease. Criteria for exclusion were tuberculosis, pregnancy, HCV and HIV infection, renal failure, and diabetes mellitus.

Clinical Data Collection

The aspartate aminotransferase-to-platelet ratio index (APRI) score (4) was used to assess cirrhosis and fibrosis in participants with CHB. To do so, aspartate transaminase (AST) and platelet (PLT) levels were measured in the patients. Calculation formula was as follows: APRI score = AST/ULN × 100/PLT (10^9/L). ULN is the upper limit of normal AST in the laboratory during the time of this study (4). When the APRI score is over 2, a patient might suffer from hepatic cirrhosis.

Cell Preparation and Activation

Isolation of peripheral blood mononuclear cells (PBMCs) was conducted on the heparinized blood from patients with CHB-IA, HCs, and patients with CHB-IC using Ficoll-Hypaque

density gradients (Sigma-Aldrich, United States). After isolation, cells were grown in an RPMI-1640 medium from Gibco (NY, United States) containing 10% fetal bovine serum at 37°C in 5% CO_2 atmosphere with appropriate humidity. Monocyte-depleted PBMCs were isolated from the supernatant of PBMCs overnight.

Stimulation of PBMCs and monocyte-depleted PBMCs was performed with LPS (10 μg/ml; Sigma, United States), IL-12 (100 U/ml; BioLegend, United States), HBsAg protein (1.68 mg/ml; Fitzgerald, United States), HBcAg protein (1.8 mg/ml; Fitzgerald), or HBsAg + HBcAg protein mixture (.05 mg/ml) for 24 h. In blocking experiments, IgG control or functional anti-human TIGIT antibody (5 μg/ml) was added and incubated for 24 h. Recombinant Chimera CD155 Fc protein (.5 μg/ml), recombinant human TIGIT Fc Chimera protein (5 μg/ml), or IgG control was included in the culture medium to activate the TIGIT pathway. To detect the intracellular production of IFN-γ, monensin (1 μM) was added to the cultures for the last 6 h of incubation. The cells were collected after stimulation and examined by flow cytometry. The IgG control and monensin were obtained from eBioScience (San Diego, CA, United States), and the recombinant Chimera CD155 Fc protein, recombinant human TIGIT Fc Chimera protein, and IgG control were obtained from R&D Systems, United States.

Flow Cytometry Analysis

Staining of cell surface was conducted on the collected cells, and monoclonal antibodies against TIGIT, CD3, CD56, CD69, CD25, and CD107a (eBioscience Co., San Diego, CA, United States) were added to the cell suspensions. As negative controls, isotype controls having irrelevant specificities were used. Incubation of these suspensions was done on ice for 30 min. To analyze intracellular IFN-γ, fixing and permeabilization of cells were conducted with Fixation and Permeabilization Buffer from BD Biosciences (San Jose, CA, United States). Then, the monoclonal antibody was added against IFN-γ (eBioscience Co., San Diego, CA, United States) and kept in the dark for 30 min. After washing out the samples, pellets were re-suspended in a cold 300-μl staining buffer and analyzed with a FACS Calibur cytometer (Becton Dickinson Co., United States). Analysis of data was performed using FlowJo software version 7.6.1 (Tree Star, Inc., Ashland, OR, United States).

CD107a Degranulation Assay

The expression of CD107a was estimated to investigate the degranulation activity of NK cells (29). PBMCs (2.5 × 105) were stimulated for 24 h with 10 g/ml LPS, and were cultured in the presence or absence of 2.5 × 104 K562 cells with anti-CD107a mAb and 2 M monensin (eBioScience, San Diego, CA, United States) during the last 6 h of incubation. Then, CD3 and CD56 mAbs were used to stain the cells, which were analyzed by flow cytometry.

Cytotoxicity Assay

Cell cytotoxicity assays for the NK cells were carried out according to the methods described in the previous study (30). In brief, purified NK cells from PBMCs of healthy participants and patients with CHB were stimulated in the presence or absence of IL-12 (100 U/ml) for 24 h and accumulated as effector cells. For being used as target cells, labeling of K562 cells was performed with carboxyfluorescein-diacetate-succinimidyl-ester (CFSE) (Sigma-Aldrich, United States). Co-incubation of target cells and effector cells was performed at an effector-to-target (E:T) ratio of 10:1 for 6 h. Only target cells were added to control tubes and used to estimate spontaneous cell death. After washing twice, 5 μl propidium iodide (PI) (eBioscience Co., San Diego, CA, United States) was added into the suspension of cells, and the resulting sample was kept in the dark for 15 min. Then, immediate analysis of cells by flow cytometry was carried out and the target cells that were dead were presented as $CFSE^{high}$ PI + cells.

Apoptosis Analysis

The PBMCs were cultured with LPS (24, 48, and 72 h). After harvesting, percentages of apoptosis cells were determined through Apoptosis Detection Kit from BD Biosciences (San Jose, CA, United States) as per the provided instructions.

Statistical Analysis

Data are presented as the mean ± Standard Error of Mean (SEM). Analysis of statistical differences among groups was done applying the Mann-Whitney U test. The relationship between two factors was assessed by Spearman's rank correlation test for non-parametric data. The statistical analyses were performed using GraphPad Prism software version 5.01 for Windows (GraphPad Software Inc., San Diego, CA, USA). A value was statistically significant at $p < 0.05$ ($^{*}p < 0.05$, $^{**}p < 0.01$, and $^{***}p < 0.001$).

RESULTS

NK Cell Phenotype and TIGIT Levels in Patients With CHB

The basic activation level of NK cells in patients with CHB was estimated by flow cytometry after evaluation of CD69 and CD25 expressions in the NK cells. We observed that CD69 expression on NK cells in CHB-IA Group was significantly higher than that in HC group, but showed no difference between CHB-IA and CHB-IC Group (**Figure 1A**). The expression of CD25 showed no difference among CHB-IA, HCs, and CHB-IC (**Figure 1B**). The baseline production of IFN-γ by NK cells was relatively low without stimulation, and there was no difference among the three groups (**Figure 1C**). CD107a expression in NK cells with K562 as target cells was increased in CHB-IA compared with that in CHB-IC and HCs (**Figure 1D**). Furthermore, we detected TIGIT expression in NK cells of CHB-IA, CHB-IC, and HCs, and found that the percentage of TIGIT+ NK cells decreased in CHB-IA but increased in CHB-IC compared to that in HCs (**Figure 1E**). We also detected the expression of TIGIT in NK cells post-stimulation with LPS or IL-12 and observed no difference (**Supplementary Figure 1**). To assess the relationship between liver injury and TIGIT expression, APRI score was used to assess the level of liver damage. When the APRI score is

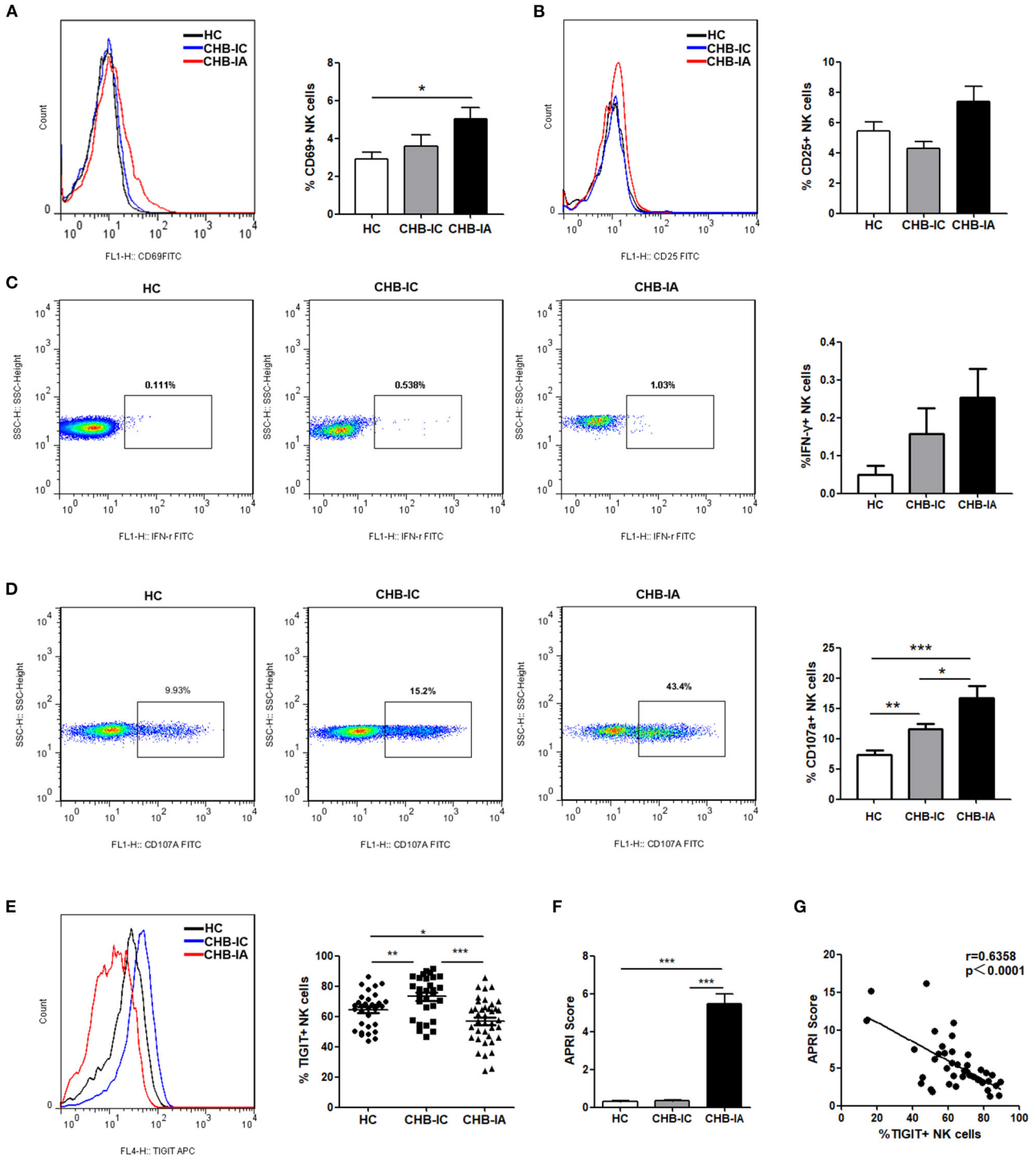

FIGURE 1 | NK cells phenotype and TIGIT levels in the three groups of patients. **(A–C)** PBMCs isolated from CHB-IA, CHB-IC, and healthy individuals were analyzed by flow cytometry without any stimulate. Representative FACS histograms showing the expression of CD69 **(A)** or CD25 **(B)** on peripheral blood NK cells. The mean fluorescence intensity (MFI) of CD69 **(A)** or CD25 **(B)** is shown as mean ± SEM (n = 7∼12). **(C)** Representative FACS plots showing the production of IFN-γ in peripheral blood NK cells without stimulation. The percentages of IFN-γ is also shown as mean ± SEM (n = 10 subjects per group, right). **(D)** The PBMCs isolated from the three groups were stimulated with IL-12 for 24 h with K562 as target cells. Representative FACS plots showing the expression of CD107a on peripheral. The percentages of CD107a + NK cells are shown as mean ± SEM (n = 16–23 subjects per group) (Mann-Whitney U test). **(E)** Representative FACS histograms showing the expression of TIGIT on peripheral blood NK cells. The mean fluorescence intensity (MFI) of TIGIT is also shown as mean ± SEM (n = 10 subjects per group, right). **(F)** APRI score in the three groups is shown as the mean ± SEM (n = 9 subjects per group). Data are from a single experiment representative of three. ***p 0.001 (Student's t-test). **(G)** Correlation between TIGIT and APRI scores expression on NK cells in CHB patients is shown (Spearman's rank correlation test). Each symbol represents an individual donor. Data are from a single experiment representative of three. *$p < 0.05$, **$p < 0.01$, ***$p < 0.001$.

over 2, a patient might suffer from hepatic cirrhosis. The APRI score is correlated with the liver damage level. We found that the APRI score in the CHB-IA group was significantly increased compared with that in CHB-IC and HCs (**Figure 1F**), and that there was an inverse correlation between TIGIT expression and the APRI score in patients with CHB-IA ($r = 0.6358$, $p < 0.0001$) (**Figure 1G**).

Association Between the Expression of TIGIT and NK Cell Phenotype in Patients With CHB-IA

In the next step, we tried to determine the association between the expression of TIGIT and the phenotype of NK cells in the patients with CHB-IA. We found that the percentage of CD69+ and CD25+ cells among the TIGIT-NK cells did not differ significantly from the TIGIT+NK cells in the patients with CHB-IA (**Figures 2A,B**). However, the TIGIT-NK cells had higher baseline IFN-γ production than the TIGIT+NK cells with no stimulation (**Figure 2C**). We also observed that the TIGIT-NK cells possessed significantly higher background CD107a expression than the TIGIT+NK cells (**Figure 2D**).

TIGIT Expression and NK Cell Function Are Inversely Related

We further examined the possible association between expression of TIGIT and NK cell activity. We found lower activation potential of NK cells in CHB-IA, so were degranulation and IFN-γ production ability. After stimulation with LPS, CD69 and CD25 levels in NK cells were lower in the patients with CHB-IA than in the HCs (**Figures 3A,C**). The TIGIT+ NK cells had higher CD69 expression than the TIGIT-NK cells, but no correlation between the expression of TIGIT and CD69 (CD25) was observed (**Figures 3B,D**). Then, we detected the capability of producing IFN-γ by the NK cells by stimulation with IL-12. Our data showed that IFN-γ production by the NK cells in CHB-IA was lower than in HCs and CHB-IC, and that it was inversely correlated with TIGIT expression (**Figures 3E,F**). We also found that the expression of CD107a in NK cells after K562 cell stimulation with LPS as target cells was relatively low in CHB-IA and inversely correlated with TIGIT expression (**Figures 3G,H**). Additionally, we assessed the apoptosis of NK cells and found that the apoptosis level of NK cells in patients with CHB-IA was remarkably less than that in HCs and CHB-IC at different time points by LPS stimulation (**Figure 3I**). The TIGIT+NK cells exhibited higher apoptosis than the TIGIT-NK cells, and the level of TIGIT was associated

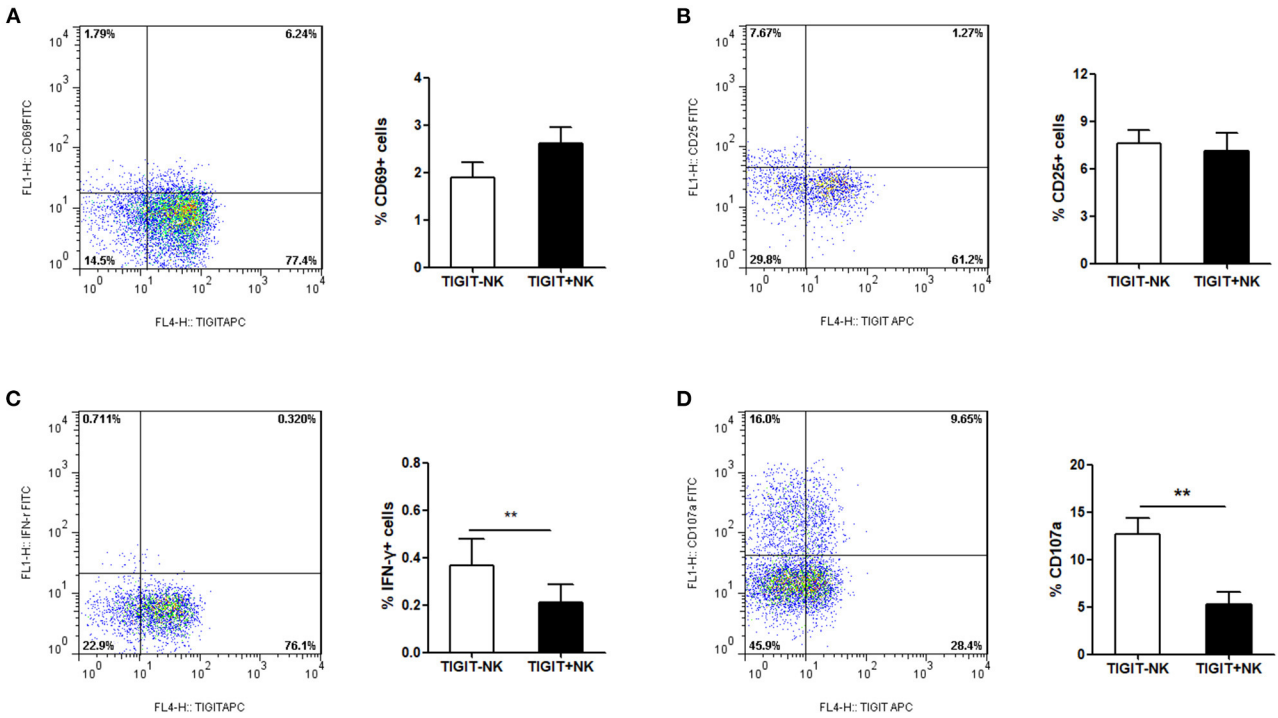

FIGURE 2 | TIGIT expression and NK-cell phenotype in CHB. PBMCs isolated from healthy individuals were analyzed by flow cytometry without any stimulate. FACS plot showing the expressions of CD69 **(A)** or CD25 **(B)** on NK cells from a representative CHB-IA patient. CD69 expression on TIGIT- or TIGIT+ NK cells is shown as the mean ± SEM (n = 12 subjects per group). **(C)** FACS plot showing the expressions of IFN-γ in NK cells from a representative CHB-IA patient. Expression on TIGIT- or TIGIT+ NK cells is shown as the mean ± SEM (n = 8 subjects per group). **(D)** FACS plot showing the expressions of CD107a on NK cells from a representative CHB-IA patient. CD107a expression on TIGIT- or TIGIT+ NK cells is shown as the mean ± SEM (n = 9 subjects per group). Data are from a single experiment representative of three. $^{*}p < 0.05$, $^{**}p < 0.01$, $^{***}p < 0.001$.

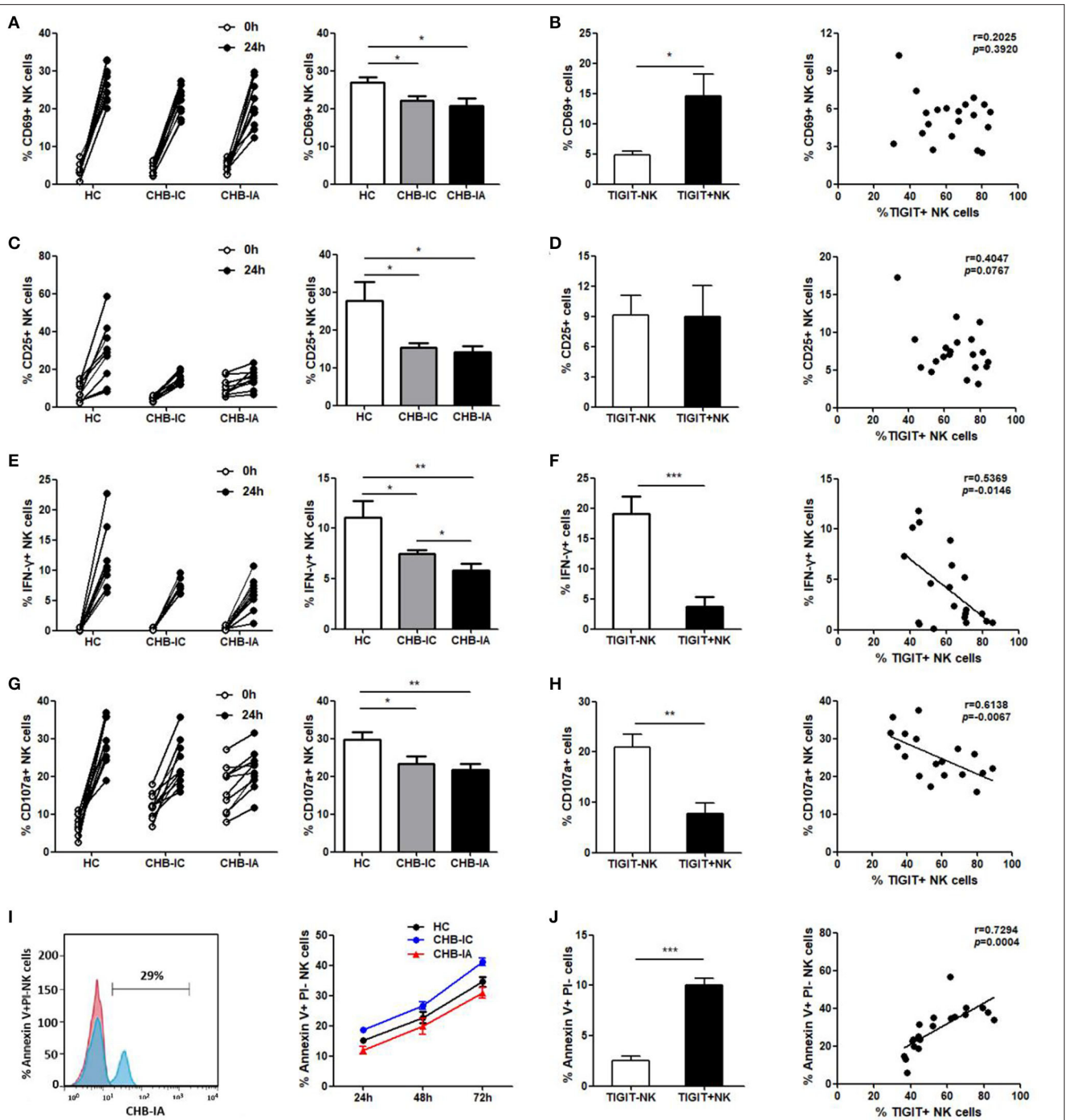

FIGURE 3 | Correlations of TIGIT expression with the function of NK in different groups of the study. PBMCs isolated from CHB-IA, CHB-IC and healthy individuals were stimulated with LPS **(A–D)** or IL-12 **(E, F)** for 24 h. **(A,C)** The percentages of CD69+ **(A)** or CD25+ **(C)** NK cells before and after stimulation with LPS in the three groups were evaluated by flow cytometry. Data are expressed as the mean ± SEM (n = 8–15 subjects per group) and are from a single experiment representative of three. *$p < 0.05$ (Mann-Whitney U test). **(B,D)** The percentages of LPS-stimulated CD69 **(B)** or CD25 **(D)** on TIGIT- or TIGIT+ NK cells was measured by flow cytometry. Correlation between TIGIT expression and percentages of LPS-stimulated CD69 **(B)** or CD25 **(D)** on NK cells is also shown (Spearman's rank). **(E)** The percentages of IFN-γ in NK cells before and after stimulation with IL-12 in the three groups were evaluated by flow cytometry. Data are expressed as the mean ± SEM (n = 10). **(F)** The percentages of IL-12-stimulated IFN-γ in TIGIT- or TIGIT+ NK cells was measured by flow cytometry. Data are shown as the mean ± SEM (n = 10). Correlation between TIGIT expression and percentages of IL-12-stimulated IFN-γ in NK cells is also shown (Spearman's rank). **(G,H)** PBMCs were stimulated with IL-12 in the presence of K562 cells for 24 h. **(G)** The percentages of CD107a+ NK cells before and after stimulation with IL-12 in the three groups were evaluated by flow cytometry. Data are expressed as the mean ± SEM (n = 8–10 subjects per group). **(H)** The percentages of CD107a on TIGIT- or TIGIT+ NK cells was measured

(Continued)

FIGURE 3 | by flow cytometry. Correlation between TIGIT and LPS-stimulated CD107a expression on NK cells (Spearman's rank correlation test). **(I,J)** PBMCs isolated from CHB-IA,CHB-IC and healthy individuals were stimulated with LPS for 24 h, 48h and 72h. **(I)** FACS histograms showing the apoptosis of NK cells from a CHB-IA patient. The apoptosis of (Annexin V+PI-) NK cellsin CHB-IA groups was analyzed at different time points and shown as the mean ± SD (n =5 subjects per group). **(J)** The percentages of Annexin V+PI- on TIGIT- or TIGIT+ NK cells was measured by flow cytometry. Data are shown as the mean ± SEM (n = 5 subjects per group). Data are from a single experiment representative of three. $^{*}p < 0.05$, $^{**}p < 0.01$, $^{***}p < 0.001$.

with the level of NK cell apoptosis in patients with CHB-IA (**Figure 3J**). Therefore, the expression of TIGIT impaired the function but promoted NK cell apoptosis in the patients with CHB-IA.

TIGIT Pathway Blockade Enhances the Function of NK Cells in Patients With CHB-IA

We assessed whether TIGIT pathway blockade would affect the functions of NK cells in patients with CHB-IA. First, we used specific stimulants (HBsAg and HBsAg + HBcAg) and observed high IFN-γ production by the NK cells, as shown in **Figure 4A**. The anti-TIGIT antibody-mediated blockade of the TIGIT signaling pathway significantly enhanced the production of IFN-γ by stimulation of nonspecific and specific stimulants (**Figure 4B**). It has been reported that the ligand of TIGIT, CD155, was expressed in monocyte and dendritic cells. To examine the effect of TIGIT pathway blockade on the NK cells, monocyte-depleted PBMCs were used for assessment. We observed significantly enhanced IFN-γ production in the NK cells tested from PBMCs depleted of monocyte, and the effect was higher than functional blocking antibody (**Figure 4C**). We also observed similar results in the degranulation capacity of NK cells after TIGIT signaling pathway blockade. Specific stimulants could also induce the degranulation of NK cells (**Figure 4D**), and CD107a expression was significantly increased when the TIGIT pathway was blocked (**Figure 4E**). The cytotoxicity of NK cells was also detected, and obvious increase in cytotoxicity was observed after blocking the TIGIT pathway (**Figure 4F**). Moreover, the apoptosis level of NK cells was decreased by blocking the TIGIT pathway (**Figure 4G**). The results confirmed that the TIGIT pathway negatively regulated NK cell function and might act as a protection factor in liver damage during CHB infection.

Activation of TIGIT Pathway Downregulates the Activity of NK Cells in Patients With CHB-IA

In addition, we evaluated the effect of recombinant human chimera TIGIT Fc protein and CD155 Fc protein on the function of NK cells in patients with CHB-IA by activating the TIGIT pathway. Our data reveal that IFN-γ production and CD107a expression in the NK cells following IL-12 stimulation were all significantly decreased when inducted with TIGIT Fc or CD155 Fc protein (**Figures 5A,B**). IL-12 and specific HBsAg + HBcAg mixture were used to activate NK cells, and cytotoxicity was also decreased after activation of the TIGIT pathway (**Figure 5C**). The apoptosis level of NK cells significantly increased when CD155 Fc protein was used to activate the TIGIT pathway (**Figure 5D**). These results indicate that TIGIT pathway activation might downregulate cytokine secretion and cytotoxicity while increasing the apoptosis of NK cells in patients with CHB-IA.

DISCUSSION

This study characterizes the immune activity of TIGIT in NK cells in chronic HBV infection in different stages, demonstrating that the TIGIT negatively regulates NK cells activity in chronic HBV infection, and may protect patients from severe liver injury. Consistent with the findings of earlier studies on NK cells in chronic HBV infection (9, 10), our findings showed that NK cells in patients with CHB-IA are over-activated with increased CD69 expression in NK cells and cytotoxic capacity compared to CHB-IC and HCs, but that the potential abilities of activation, IFN-γ production, and degranulation are much lower, which were the same as the previous study (31). As an active process, chronic HBV infection reflects the interaction between replication of HBV and response of the host immune system. Over-activation of NK cells in patients with CHB-IA can cause severe immunopathology of infected liver, especially increased cytotoxic activity (10). On the other hand, the IFN-γ derived from NK cells exhibits its anti-fibrotic properties by cell cycle arrest, killing activated HSCs, and HSC apoptotic induction (6, 32). In this study, the NK cells derived from the patients with CHB in the IA stage, compared with the individuals in the HC group, showed higher basic cytotoxicity while producing less or normal level of IFN-γ. Increased cytotoxicity of the NK cells can cause liver damage, while the reduced capacity of NK cells for IFN-γ production possibly decreases their antiviral activity and anti-fibrotic ability, which may aggravate liver damage, and the combination of enhanced cytotoxicity and reduced production of IFN-γ may result in liver necro-inflammation and fibrogenesis. Why IFN-γ production was lower than expected? A previous study has shown that NK cells in the liver of patients with CHB produced different amounts of IFN-γ under different stimulations (10), when higher upon PMA/ionomycin and lower upon P815/anti-NCR stimulation in comparison with peripheral NK cells. And in Jang-June Park (33) study, circulating HBeAg was shown to mediated HBV persists with virus-specific and global T-cell dysfunction. Inspired by this, we use HBsAg protein alone or combine with HBcAg protein as specific stimulants, and observed obvious changes in IFN-γ secretion and degranulation

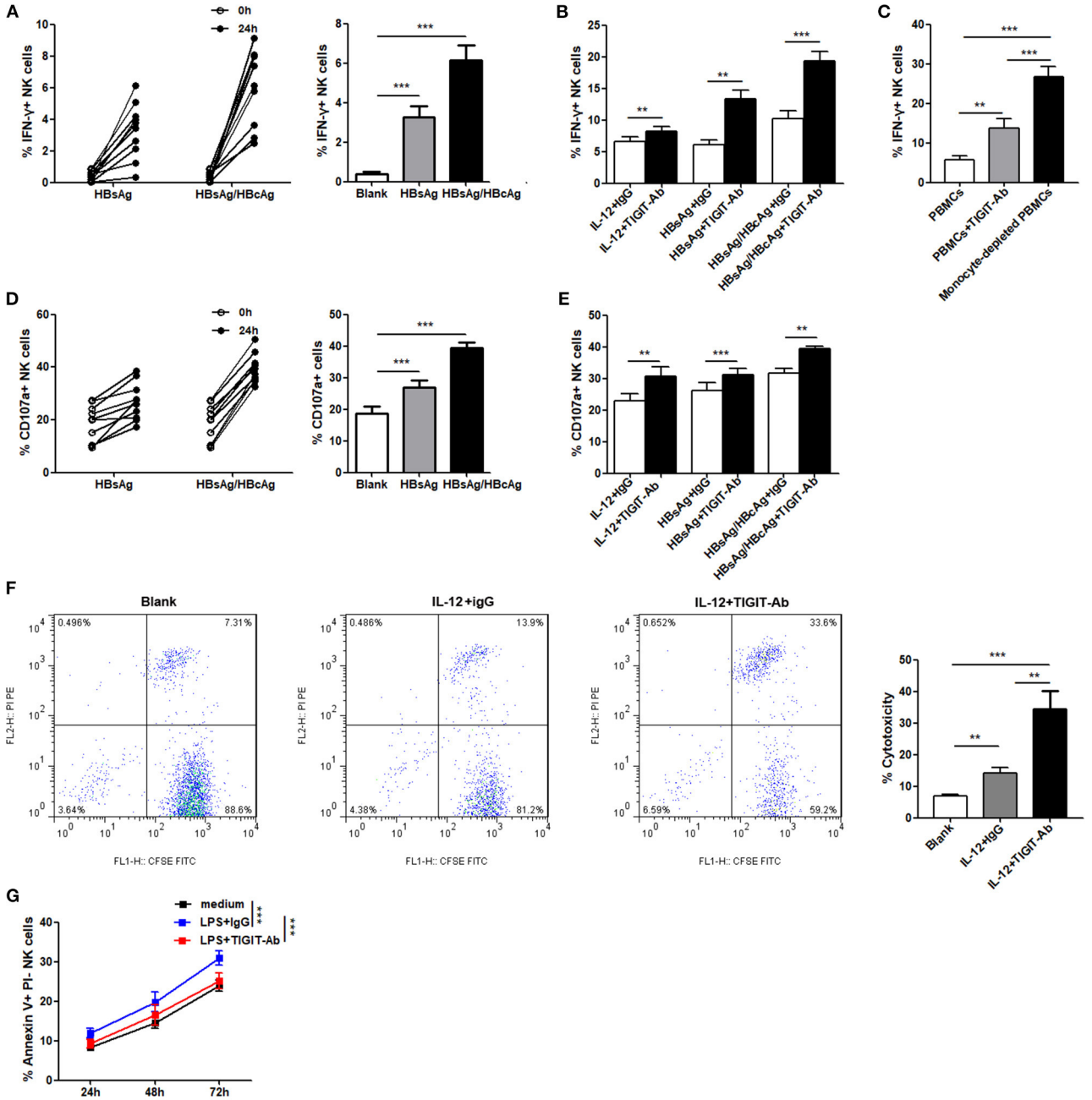

FIGURE 4 | Blockade of the TIGIT pathway affects NK-cell function in CHB-IA. **(A,B,D–F)** PBMCs isolated from CHB-IA were stimulated with IL-12 or specific stimulants (recombinant HBsAg protein or recombinant HBsAg and HBcAg protein mixture) in the **(A,D)** absence or **(B,E)** presence of TIGIT-Ab protein or IgG control for 24 h. The percentages of **(A,B)** IFN-γ and **(D,E)** CD107a in NK cells before and after stimulation were evaluated by flow cytometry (n = 10). **(C)** PBMCs or monocyte-depleted PBMCs were stimulated with IL-12 for 24 h. Representative FACS dot plots showing IFN-γ expression in NK cells from PBMCs or monocyte-depleted PBMCs (n = 10). **(F)** Purified NK cells stimulated with or without IL-12 in the absence or presence of TIGIT-Ab for 24 h were collected as effector cells. K562 cells labeled with CFSE were used as target cells. E:T ratios was 1:10 for 6 h. Representative FACS plots showing cytotoxicity of NK cells. The cytotoxicity of NK cells in CHB-IA was analyzed and shown as the mean ± SD (n = 5 subjects per group). **(G)** PBMCs isolated from CHB-IA were stimulated with LPS in the absence or presence of TIGIT-Ab for 24, 48, and 72h. The percentages of Annexin V+PI- NK cells was measured by flow cytometry. Data are shown as the mean ± SEM (n = 5). Data are from a single experiment representative of three. $^{*}p < 0.05$, $^{**}p < 0.01$, $^{***}p < 0.001$.

than those by using IL12. The results were similar to the previous study in which the plasmid DNA of HBV promoted the activation of NK cells in addition to cytotoxicity and production of IFN-γ in the liver (34). However, the trends did not change. Although we didn't further investigate why NK cells from IA patients produce more CD107a but not IFN-γ, but as showed in a previous study

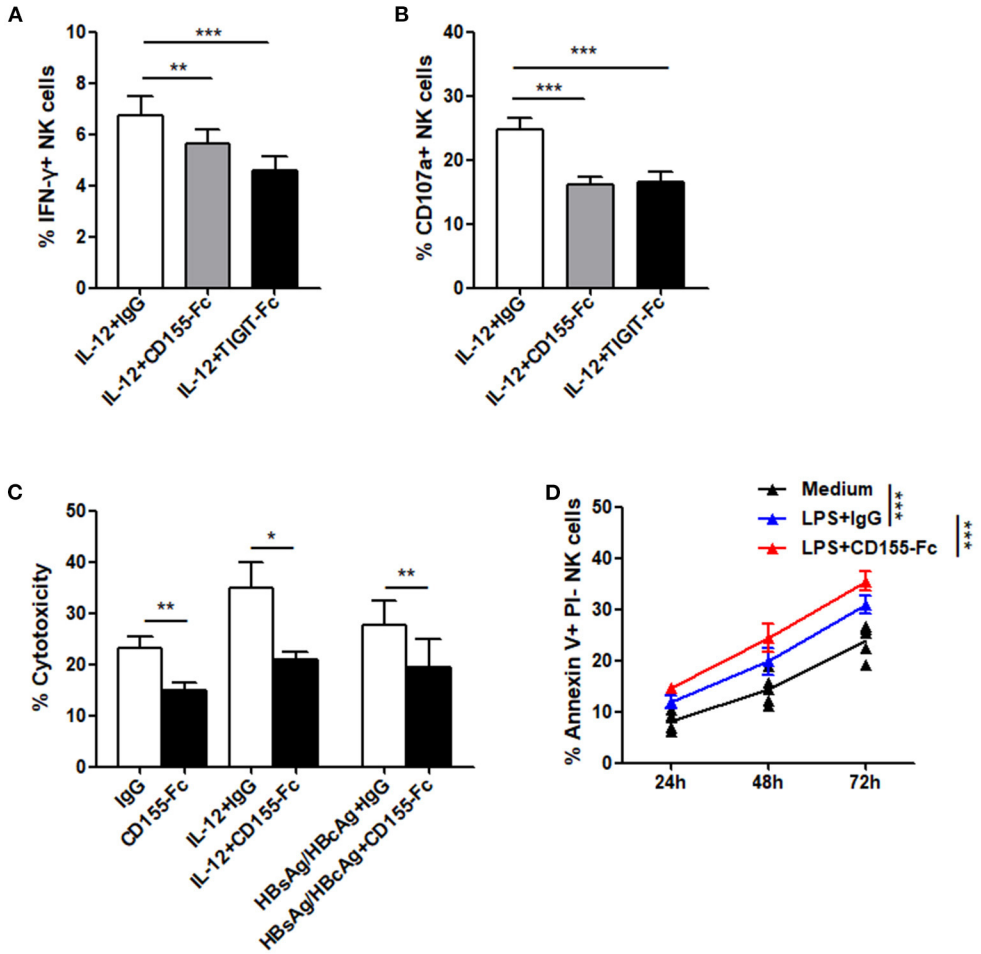

FIGURE 5 | (A–C) PBMCs isolated from CHB-IA were stimulated with IL-12 or specific stimulants (recombinant HBsAg protein or recombinant HBsAg and HBcAg protein mixture) in the **(A,D)** absence or **(B,C)** presence of CD155Fc or TIGIT Fc protein or IgG control for 24 h. The percentages of **(A)** IFN-γ and **(B)** CD107a in NK cells before and after stimulation were evaluated by flow cytometry. **(C)** K562 cells labeled with CFSE were used as target cells. E:T ratios was 1:10 for 6 h. Representative FACS plots showing cytotoxicity of NK cells. The cytotoxicity of NK cells inCHB-IA was analyzed and shown as the mean ± SD (n = 5). **(D)** PBMCs isolated from CHB-IA were stimulated with LPS in the absence or presence of CD155Fc or IgG control or 24, 48, and 72h. The percentages of Annexin V+PI- NK cells was measured by flow cytometry. Data are from a single experiment representative of three. $^{*}p < 0.05$, $^{**}p < 0.01$, $^{***}p < 0.001$.

(15), in which the production of higher levels of IL-12, IL-15 and IL-18 might enhance NK activation and polarization to cytolytic activity *in vitro* in the livers of IA patients. This may be an explanation, but still need further more study. This finding supports the finding of Zhang et al. who reported the hypercytolytic activity of hepatic NK cells is correlated with the level of liver injury in patients with CHB (10). However, further studies should be conducted to shed more light on this effect.

Our group has previously assessed the expression levels of TIGIT in different types of lymphocytes in healthy individuals and found greatest expression levels of TIGIT in NK cells (35), and along with the activity of NK cells in acute infection of HBV, we supposed that TIGIT in NK cells may regulate the function of NK cells. In this study, we observed overexpression of TIGIT in NK cells in the patients with CHB-IC, but TIGIT level was much lower in NK cells of CHB-IA than the healthy individuals. This finding supports the findings of previous studies (32), in which peripheral and hepatic NK cells exhibited enhanced expressions of activation markers and receptors but reduced expression of inhibitory receptors in patients with CHB in comparison to health controls. TIGIT overexpression in IC patients might correlated with less liver damage, while lower expression in IA patients was related with sever liver injury. Liver injury was shown by APRI scores, which can evaluate and stage liver fibrosis with lower cost than FibroScan and biopsy (4). Then, we observed that the expression of TIGIT in NK cells in patients with CHB and HCs shows no change under stimulation, which seems to be stable *in vitro*, according to our previous study, in which TIGIT expression in NK cells did not respond to LPS or IL-12 stimulation (35). These results may suggest that the different clinical outcomes

might be due to the different basic levels. Moreover, TIGIT level was correlated inversely with secretion of IFN-γ and NK cell degranulation, so the TIGIT-negative NK cells have greater ability for IFN-γ secretion and degranulation. These data suggested that TIGIT might be a protected marker expressed by NK cells, which prevented severe liver injury caused by HBV infection.

We examined the association between the TIGIT pathway and NK cell functional changes in patients with chronic HBV. To do so, we used a functional anti-TIGIT antibody and another recombinant TIGIT Fc chimera protein. As a non-agonistic antibody, the anti-TIGIT antibody can be used to block the TIGIT pathway (35). We found that the anti-TIGIT antibody in this study enhanced IFN-γ secretion by NK cells and cytotoxicity function but decreased NK cell apoptosis, which might obstruct liver regeneration (25) and aggravate liver damage (24). However, our study showed an opposite role for the TIGIT Fc chimera protein in a manner that its activation resulted in decreased IFN-γ secretion and cytotoxicity function but increased apoptosis of NK cells. Our finding was consistent with the finding of Chen et al. who reported that TIGIT negatively regulates inflammation by altering a macrophage phenotype (36).

The poliovirus receptor (PVR), a nectin-like family-member, is the TIGIT ligand (PVR, CD155). It is expressed in extremely low amounts in most of adult organs but is expressed in high amounts in dendritic cells (DCs), regenerating liver tissues, some tumor cells, and endothelial cells (37). T cell responses were inversely inhibited by TIGIT by modulation of cytokine profiles of mature DCs through binding with PVR (38). Then, using the CD155 Fc chimera protein, we observed that the production of IFN-γ ability and degranulation role of NK cells in patients with CHB-IA reduced, while the apoptosis level of NK cells increased. On the contrary, we removed monocytes from PBMCs to investigate the influence of PVR, then we observed that the production of IFN-γ in NK cells of patients with CHB-IA increased significantly after IL-12 stimulation, even more than blockade by anti-TIGIT antibodies, which indicates that the inhibition of the TIGIT pathway can only partly be blocked by anti-TIGIT antibodies, and that the ligand PVR (CD155) could play a more important role. TIGTI shares the ligand PVR (CD155) with CD226, which is a costimulatory molecule, but TIGIT attaches to CD155 with greater affinity than with CD226 (39–41). TIGIT pathway was only partly activated by CD155-Fc, which led to lower activation of TIGIT/PVR than by TIGIT Fc chimera protein. This might explain our finding that the suppression of IFN-γ production in NK cells by CD155-Fc was not as severe as that by TIGIT Fc. The TIGIT-PVR interaction creates a bidirectional signaling pathway, which is indicated in negatively regulated immune responses.

Some studies have analyzed hepatic NK cells and demonstrated that higher levels of activation functions and markers are exhibited by hepatic NK cells than in IA patients' peripheral NK cells, and a positive correlation of hyperactivity with liver damage in IA patients (10). In this study, we only used peripheral NK cells, not hepatic NK cells. If we could investigate the hepatic NK cells and relevant cells, including Treg cells, CD4+T cells and CD8+ cells, as well as more detail crosstalk between NK cells and other hepatocytes, it would be more persuasive. In addition, the TIGIT Fc chimera protein plays an activation role in the TIGIT/PVR pathway with enhanced secretion of IL-10 (36). In addition, IL-10 correlated with the status of HBeAg, liver disease progression, and virus replication (42, 43). In patients with positive HBeAg, higher IL-10 and IL-12 serum levels correlate with spontaneous and early seroconversion of HBeAg (44), which may be correlated with TIGIT level. In future study, we can divide patients into more detailed groups according to HBeAg status and different TIGTI levels, and observe outcomes, which may provide a clue to roughly predict the outcome of chronic HBV by TIGIT level.

CONCLUSION

In conclusion, the findings of our study have revealed new evidence that TIGIT plays a protective part in chronic HBV infection. The expression of TIGIT in NK cells of patients with immune active chronic hepatitis B is lower than normal, and the level of TIGIT correlated inversely with NK-cell function in chronic HBV. This mechanism of negative regulation may represent a potential treatment target in the damage to liver by inflammatory diseases induced by acute HBV infection.

DATA AVAILABILITY STATEMENT

The original contributions presented in the study are included in the article/**Supplementary Material**, further inquiries can be directed to the corresponding author/s.

ETHICS STATEMENT

Experimental procedures of this study were approved by the local Ethics Committee of Tongji Hospital, Tongji Medical College, Huazhong University of Science and Technology, Wuhan, China (Ethics code: TJ-IRB20210225) which were in accordance with the ethical standards and regulations of human studies of the Helsinki declaration (2014). Each participant provided written informed consent and was required to fill a questionnaire regarding his or her medical history and associated treatments. The patients/participants provided their written informed consent to participate in this study.

AUTHOR CONTRIBUTIONS

JW is the major contributor to this manuscript and wrote the first version of the manuscript. ZS conducted the analytical part and HH finalized the manuscript. JW, HH, LM, FW, JY, YL, and QL performed the

experiments and analyzed the data. HH and ZS conceived and coordinated the study and critically evaluated the data. All authors read and approved the final version of the manuscript.

FUNDING

This study was supported by the Infectious Diseases Control Project from Ministry of Health of China (2016ZX10004207-004) and National Natural Science Foundation of China (81401639).

SUPPLEMENTARY MATERIAL

The Supplementary Material for this article can be found online at: https://www.frontiersin.org/articles/10.3389/fmed.2021.816474/full#supplementary-material

Supplementary Figure 1 | Expression of TIGIT in NK cells post-stimulation with LPS or IL-12 in the studied groups.

REFERENCES

1. Trépo C, Chan HLY, Lok A. Hepatitis B virus infection. *Lancet*. (2014) 384:2053–63. doi: 10.1016/S0140-6736(14)60220-8
2. Luvisa BK, Hassanein TI. Hepatitis B virus infection and liver decompensation. *Clin Liver Dis*. (2016) 20:681–92. doi: 10.1016/j.cld.2016.07.002
3. Lozano R, Naghavi M, Foreman K, Lim S, Shibuya K, Aboyans V, et al. Global and regional mortality from 235 causes of death for 20 age groups in 1990 and 2010: a systematic analysis for the Global Burden of Disease Study 2010. *Lancet*. (2012) 380:2095–128. doi: 10.1016/S0140-6736(12)61728-0
4. World Health Organization. *Policy Brief: Guidelines for the Prevention, Care and Treatment of Persons With Chronic Hepatitis B Infection* (2015).
5. Racanelli V, Rehermann B. The liver as an immunological organ. *Hepatology*. (2006) 43:S54-62. doi: 10.1002/hep.21060
6. Rehermann B. Pathogenesis of chronic viral hepatitis: differential roles of T cells and NK cells. *Nat Med*. (2013) 19:859–68. doi: 10.1038/nm.3251
7. Wu S, Wang W, Gao Y. Natural killer cells in hepatitis B virus infection. *Brazilian J Infect Dis*. (2015) 19:417–25. doi: 10.1016/j.bjid.2015.05.006
8. Lunemann S, Malone DFG, Hengst J, Port K, Grabowski J, Deterding K, et al. Compromised function of natural killer cells in acute and chronic viral hepatitis. *J Infect Dis*. (2014) 209:1362–73. doi: 10.1093/infdis/jit561
9. Zheng Q, Zhu YY, Chen J, Ye YB, Li JY, Liu YR, et al. Activated natural killer cells accelerate liver damage in patients with chronic hepatitis B virus infection. *Clin Exp Immunol*. (2015) 180:499–508. doi: 10.1111/cei.12597
10. Zhang Z, Zhang S, Zou Z, Shi J, Zhao J, Fan R, et al. Hypercytolytic activity of hepatic natural killer cells correlates with liver injury in chronic hepatitis B patients. *Hepatology*. (2011) 53:73–85. doi: 10.1002/hep.23977
11. Dunn C, Brunetto M, Reynolds G, Christophides T, Kennedy PT, Lampertico P, et al. Cytokines induced during chronic hepatitis B virus infection promote a pathway for NK cell-mediated liver damage. *J Exp Med*. (2007) 204:667–80. doi: 10.1084/jem.20061287
12. Zou Y, Chen T, Han M, Wang H, Yan W, Song G, et al. Increased killing of liver NK cells by Fas/Fas ligand and NKG2D/NKG2D ligand contributes to hepatocyte necrosis in virus-induced liver failure. *J Immunol*. (2010) 184:466–75. doi: 10.4049/jimmunol.0900687
13. Li Y, Wang JJ, Gao S, Liu Q, Bai J, Zhao XQ, et al. Decreased peripheral natural killer cells activity in the immune activated stage of chronic hepatitis B. *PLoS ONE*. (2014) 9:e86927. doi: 10.1371/journal.pone.0086927
14. Yu X, Harden K, Gonzalez LC, Francesco M, Chiang E, Irving B, et al. The surface protein TIGIT suppresses T cell activation by promoting the generation of mature immunoregulatory dendritic cells. *Nat Immunol*. (2009) 10:48–57. doi: 10.1038/ni.1674
15. Johnston RJ, Comps-Agrar L, Hackney J, Yu X, Huseni M, Yang Y, et al. The immunoreceptor TIGIT regulates antitumor and antiviral CD8+ T cell effector function. *Cancer Cell*. (2014) 26:923–37. doi: 10.1016/j.ccell.2014.10.018
16. Dougall WC, Kurtulus S, Smyth MJ, Anderson AC. TIGIT and CD96: new checkpoint receptor targets for cancer immunotherapy. *Immunol Rev*. (2017) 276:112–20. doi: 10.1111/imr.12518
17. Liu X guang, Hou M, Liu Y. TIGIT, a novel therapeutic target for tumor immunotherapy. *Immunol Investig*. (2017) 46:172–82. doi: 10.1080/08820139.2016.1237524
18. Sarhan D, Cichocki F, Zhang B, Yingst A, Spellman SR, Cooley S, et al. Adaptive NK cells with low TIGIT expression are inherently resistant to myeloid-derived suppressor cells. *Cancer Res*. (2016) 76:5696–706. doi: 10.1158/0008-5472.CAN-16-0839
19. Zhang Q, Bi J, Zheng X, Chen Y, Wang H, Wu W, et al. Blockade of the checkpoint receptor TIGIT prevents NK cell exhaustion and elicits potent anti-tumor immunity. *Nat Immunol*. (2018) 19:723–32. doi: 10.1038/s41590-018-0132-0
20. Mao L, Hou H, Wu S, Zhou Y, Wang J, Yu J, et al. TIGIT signalling pathway negatively regulates CD4+ T-cell responses in systemic lupus erythematosus. *Immunology*. (2017) 151:280–90. doi: 10.1111/imm.12715
21. Zhao W, Dong Y, Wu C, Ma Y, Jin Y, Ji Y. TIGIT overexpression diminishes the function of CD4 T cells and ameliorates the severity of rheumatoid arthritis in mouse models. *Exp Cell Res*. (2016) 340:132–8. doi: 10.1016/j.yexcr.2015.12.002
22. Cox MA, Nechanitzky R, Mak TW. Check point inhibitors as therapies for infectious diseases. *Curr Opin Immunol*. (2017) 48:61–7. doi: 10.1016/j.coi.2017.07.016
23. Attanasio J, Wherry EJ. Costimulatory and coinhibitory receptor pathways in infectious disease. *Immunity*. (2016) 44:1052–68. doi: 10.1016/j.immuni.2016.04.022
24. Bi J, Zhang Q, Liang D, Xiong L, Wei H, Sun R, et al. T-cell Ig and ITIM domain regulates natural killer cell activation in murine acute viral hepatitis. *Hepatology*. (2014) 59:1715–25. doi: 10.1002/hep.26968
25. Bi J, Zheng X, Chen Y, Wei H, Sun R, Tian Z. TIGIT safeguards liver regeneration through regulating natural killer cell-hepatocyte crosstalk. *Hepatology*. (2014) 60:1389–98. doi: 10.1002/hep.27245
26. Burchill MA, Golden-Mason L, Wind-Rotolo M, Rosen HR. Memory re-differentiation and reduced lymphocyte activation in chronic HCV-infected patients receiving direct-acting antivirals. *J Viral Hepat*. (2015) 22:983–91. doi: 10.1111/jvh.12465
27. World Medical Association. World medical association declaration of Helsinki: ethical principles for medical research involving human subjects. *JAMA*. (2013) 310:2191–4.
28. Lampertico P, Agarwal K, Berg T, Buti M, Janssen HLA, Papatheodoridis G, et al. EASL (2017). Clinical practice guidelines on the management of hepatitis B virus infection. *J Hepatol*. (2017) 67:370–98. doi: 10.1016/j.jhep.2017.03.021
29. Alter G, Malenfant JM, Altfeld M. CD107a as a functional marker for the identification of natural killer cell activity. *J Immunol Methods*. (2004) 294:15–22. doi: 10.1016/j.jim.2004.08.008
30. Fu X, Liu Y, Li L, Li Q, Qiao D, Wang H, et al. Human natural killer cells expressing the memory-associated marker CD45RO from tuberculous pleurisy respond more strongly and rapidly than CD45RO- natural killer cells following stimulation with interleukin-12. *Immunology*. (2011) 134:41–9. doi: 10.1111/j.1365-2567.2011.03464.x
31. Oliviero B, Varchetta S, Paudice E, Michelone G, Zaramella M, Mavilio D, et al. Natural killer cell functional dichotomy in chronic hepatitis B and chronic hepatitis C virus infections. *Gastroenterology*. (2009) 137:1151–60.e7. doi: 10.1053/j.gastro.2009.05.047

32. Shi J, Zhao J, Zhang X, Cheng Y, Hu J, Li Y, et al. Activated hepatic stellate cells impair NK cell anti-fibrosis capacity through a TGF-β-dependent emperipolesis in HBV cirrhotic patients. *Sci Rep.* (2017) 7:44544. doi: 10.1038/srep44544
33. Park JJ, Wong DK, Wahed AS, Lee WM, Feld JJ, Terrault N, et al. Hepatitis B virus-specific and global T-cell dysfunction in chronic hepatitis B. *Gastroenterology.* (2016) 150:684–95.e5. doi: 10.1053/j.gastro.2015.11.050
34. Yang PL, Althage A, Chung J, Maier H, Wieland S, Isogawa M, et al. Immune effectors required for hepatitis B virus clearance. *Proc Natl Acad Sci USA.* (2010) 107:798–802. doi: 10.1073/pnas.0913498107
35. Wang F, Hou H, Wu S, Tang Q, Liu W, Huang M, et al. TIGIT expression levels on human NK cells correlate with functional heterogeneity among healthy individuals. *Eur J Immunol.* (2015) 45:2886–97. doi: 10.1002/eji.201545480
36. Chen X, Lu PH, Liu L, Fang ZM, Duan W, Liu ZL, et al. TIGIT negatively regulates inflammation by altering macrophage phenotype. *Immunobiology.* (2016) 221:48–55. doi: 10.1016/j.imbio.2015.08.003
37. Li M, Xia P, Du Y, Liu S, Huang G, Chen J, et al. T-cell immunoglobulin and ITIM domain (TIGIT) receptor/poliovirus receptor (PVR) ligand engagement suppresses interferon-γ production of natural killer cells via β-arrestin 2-mediated negative signaling. *J Biol Chem.* (2014) 289:17647–57. doi: 10.1074/jbc.M114.572420
38. Martinet L, Smyth MJ. Balancing natural killer cell activation through paired receptors. *Nat Rev Immunol.* (2015) 15:243–54. doi: 10.1038/nri3799
39. Stanietsky N, Simic H, Arapovic J, Toporik A, Levy O, Novik A, et al. The interaction of TIGIT with PVR and PVRL2 inhibits human NK cell cytotoxicity. *Proc Natl Acad Sci USA.* (2009) 106:17858–63. doi: 10.1073/pnas.0903474106
40. Chan CJ, Martinet L, Gilfillan S, Souza-Fonseca-Guimaraes F, Chow MT, Town L, et al. The receptors CD96 and CD226 oppose each other in the regulation of natural killer cell functions. *Nat Immunol.* (2014) 15:431–8. doi: 10.1038/ni.2850
41. Pauken KE, Wherry EJ. TIGIT and CD226: tipping the balance between costimulatory and coinhibitory molecules to augment the cancer immunotherapy toolkit. *Cancer Cell.* (2014) 26:785–7. doi: 10.1016/j.ccell.2014.11.016
42. Bozkaya H, Bozdayi M, Türkyilmaz R, Sarioglu M, Cetinkaya H, Cinar K, et al. Circulating IL-2, IL-10 and TNF-α in chronic hepatitis B : their relations to HBeAg status and the activity of liver disease. *Hepatogastroenterology.* (2000) 47:1675–9.
43. Poovorawan K, Tangkijvanich P, Chirathaworn C, Wisedopas N, Treeprasertsuk S, Komolmit P, et al. Circulating cytokines and histological liver damage in chronic hepatitis B infection. *Hepat Res Treat.* (2013) 2013:1–7. doi: 10.1155/2013/757246
44. Wu JF, Wu TC, Chen CH, Ni YH, Chen HL, Hsu HY, et al. Serum levels of interleukin-10 and interleukin-12 predict early, spontaneous hepatitis B virus e antigen seroconversion. *Gastroenterology.* (2010) 138:165–172.e3. doi: 10.1053/j.gastro.2009.09.018

Conflict of Interest: The authors declare that the research was conducted in the absence of any commercial or financial relationships that could be construed as a potential conflict of interest.

Publisher's Note: All claims expressed in this article are solely those of the authors and do not necessarily represent those of their affiliated organizations, or those of the publisher, the editors and the reviewers. Any product that may be evaluated in this article, or claim that may be made by its manufacturer, is not guaranteed or endorsed by the publisher.

frontiers in Medicine

REVIEW
published: 22 February 2022
doi: 10.3389/fmed.2022.814986

The Emerging Role of Ultrasonic Nanotechnology for Diagnosing and Treatment of Diseases

*Xinying Liu and Weidong Ge**

Department of Ultrasonography, Zhejiang Provincial People's Hospital, Affiliated People's Hospital, Medical College, Hangzhou, China

Nanotechnology has been commonly used in a variety of applications in recent years. Nanomedicine has also gotten a lot of attention in the medical and treatment fields. Ultrasonic technology is already being used in research as a powerful tool for manufacturing nonmaterial and in the decoration of catalyst supports for energy applications and material processing. For the development of nanoparticles and the decoration of catalytic assisted powders with nanoparticles, low or high-frequency Ultrasonic are used. The Ultrasonic is frequently used in joint venture with the nanotechnology from the past few years and bring tremendous success in various diseases diagnosing and treatment. Numerous kinds of nanoparticles are fabricated with desired capabilities and targeted toward different targets. This review first highlights the Ultrasonic Treatment and processing of Nanoparticles for Pharmaceuticals. Next, we explain various nanoparticles with ultrasonic technology for different diagnosing and treatment of various diseases. Finally, we explain the challenges face by current approaches for their translation in clinics.

Keywords: diagnosis, nanoparticles, nanotechnology, treatment, ultrasonic

OPEN ACCESS

Edited by:
Ali Yadollahpour,
The University of Sheffield,
United Kingdom

Reviewed by:
Zhijian Fu,
Shandong Provincial Hospital, China
Shengye Wang,
Zhejiang Cancer Hospital, China

****Correspondence:***
Weidong Ge
geweidong@hmc.edu.cn

Specialty section:
This article was submitted to Precision Medicine, a section of the journal Frontiers in Medicine

Received: *14 November 2021*
Accepted: *25 January 2022*
Published: *22 February 2022*

Citation:
Liu X and Ge W (2022) The Emerging Role of Ultrasonic Nanotechnology for Diagnosing and Treatment of Diseases. Front. Med. 9:814986. doi: 10.3389/fmed.2022.814986

INTRODUCTION

The production of new compounds and applications has resulted from research into integrated approaches. During the past few decades, ultrasonic-assisted processes have intrigued the imagination of multidisciplinary scientists searching for more effective structures. A special paper on "Ultrasonic Nanotechnology of Ultrasonic Sonochemistry has given an insight into ultrasounds numerous applications. Ultrasound application has become the most imperative technologies to produce different natural amalgams because it is environmentally sustainable, hygienic, prolific, and resourceful. When hydrodynamic bubbles produced by high-octane waves of ultrasound collapse, micro-reactors with temperature and high pressure are created. Efficiency and product yield while speeding up chemical reactions in numerous processes. This question has been extensively discussed to improve the physicochemical properties of nanomaterials when generated by a sonochemical facilitated process. Siadatnasab at el. Reported that sonochemical reaction of methanolic Cu (II) diethyldithiocarbamate with phosphomolybdic acid formed a green precipitate of Cu3 nanohybrid, which was used for sonochemical degradation of Rhodamine B (RhB) (1). Another research group developed a scalable synthesis of tunable titanium nanotubes *via* sonoelectrochemical process (2). They used sonoelectrochemical process to synthesize TiO_2 nanotube arrays on implantable Ti 6–4 structure were generated and tested using a sonoelectrochemical method as a drug delivery system for antibacterial applications (2).

A sonochemical-assisted process was utilized for synthesis and evaluation of nanostructured oil in water emulsions for targeted delivery of protein drugs (3). Protein extracted from a medicinal leech tissue was used to formulate nanoemulsion and sonochemical process was employed to form isotropic and kinetically stable nanoemulsion with least surfactant and optimal solubility and stability for drug delivery of protein drugs. (3). Allami et al. (4) discovered that waves of ultrasound produced biodiesel with lower viscidness, higher oxygen content, and thickness that improved fuel combustion. Ultrasound was used to clean a granulated surface by removing inadequate areas for dissolved substances (5). They utilized an ultrasound-assisted method for photocatalytic dye degradation and adsorbent regeneration to synthesize ZnO nanoparticles. The crystallization process is assisted by hydrodynamic bubbles using ultrasonic irradiation during the process. In this regard, Azarhoosh et al. (6) have used ultrasonic irradiation to complete the representation stage of a aluminophosphate-34 catalyst and evaluated the results of the parameters involved during this process for the adaptation of methanol with light olefins. Synthesis of ZnO nanoparticle was also performed using a sonochemical process, doped with numerous lanthanide cations (7). In a sono-photocatalytic membrane reactor, the produced photocatalysts were able to effectively oxidize the natural contaminant. Panahi et al. (8) used ultrasound waves for the manufacture and synthesis of benzimidazole of a porous zirconium/Aminophylline polymer co-ordination. Increased catalytic synthesis of benzimidazoles was achieved through the electron transfer mechanism below the control of ultrasound waves. Ultrasound waves are one of the most effective extraction methods currently available with safe profile to biological tissues. High-intensity sound waves can cause bioactive compounds to diffuse quickly into the solvent, resulting in a faster extraction time. Bayrami et al. used this technology to create biogenic ZnO nanoparticles for biomedical applications using leaf extracts from medicinally important plants like Nasturtium officinale L. and Vaccinium arctostaphylos L. (9, 10). These bio-synthesized photocatalysts have provided a gateway to several conservational refinement classifications due to improved photocatalytic properties.

ZnO nanoparticles waste was used as sonocatalysis for acetaminophen elimination. The UVC structure degraded acetaminophen to fewer toxic arbitrates (11). The sonocatalytic behavior of ZnTi nano-layered double hydroxide was greatly upgraded when a component of Zn2+ was replaced with Cu2+ (12). A primary reason for this change was the reduced band difference arising from the transition of charge to Cu(II) from Ti(IV) when bridged with oxygen atoms. Another study was carried through a radically mediated process to use znO-loaded nano-cellulose as a tetracycline sonocatalyst (13). The ultrasonically triggered nanocomposite contributed to nearly complete tetracycline dilapidation in combination with peroxymonosulfate. This review first highlights the ultrasonic treatment and processing of Nanoparticles for Pharmaceuticals. Next, we explain various nanoparticles with ultrasonic technology for different diagnosing and treatment of various diseases. Finally, we explain the challenges face by current approaches for their translation in clinics.

ULTRASONIC TREATMENT OF NANOPARTICLES FOR PHARMACEUTICALS

Ultrasound is a pioneering technique used for synthesizing sonochemical, breaking down the agglomeration, blend, and activate particles. Ultrasound is a crucial technique for nanoscale materials, particularly in nanotechnology, to be synthesized and processed. Nano-sized particles are used in a wide variety of scientific and industrial fields as nanotechnology has gained such widespread scientific interest. This versatile and variable material's high potential has also been discovered by the pharmaceutical industry. As a result, nanoparticles are used in several different applications in the pharmaceutical industry. Drug distribution by nanoparticles is a validated process for supplying orally or injected active agents (14). When modern methods open up entirely novel avenues of medical care, nano-formulated medicines can be dosed and distributed even more efficiently. This high-potential technology aids in the delivery of medicines and temperature control to diseased cells. Side effects of drugs don't affect healthy cells because of direct drug delivery. Cancer therapy is one field where nano-formulated drugs have already shown promising results.

NANOMATERIALS PROCESSING

Nanomaterials have a diameter of under 100 nm and are known as particles. Their processing needs to be increased. Agglomerates should be dissolved nanoparticles process, and for bonding forces to shape. Ultrasonic hydrodynamic is a popular process for nanomaterial dispersion and decomposition. Nanomaterials come in a variety of forms and provide opportunities for medicinal research. The inner size of Carbon Nanotubes (CNTs) allows more drug molecules to be condensed and functionalized (14). DNA, active agents, and proteins targeting ligands, and other molecules may be carried into cells by CNTs. CNTs have established themselves as the archetypal nanomaterials, with nanoscience and nanotechnology being one of the most active fields.

SWCNT has a diameter of 1.0–1.4 nm and is much smaller. Cells can absorb nanoparticles and nanotubes (15). Functionalized Carbon Nanotubes (f-CNTs) improved solubility and allowed tumor targeting (**Figure 1**). A sonochemical process can be used to make high-purity single-walled carbon nanotubes (SWCNTs) (16).

The vaccines may be used for the delivery of functional Carbon Nanotubes (f-CNTs). The basic theory is to bind the antigen to the carbon nanotubes while retaining their shape, leading to a certain antibody reaction. Ceramic nanoparticles have a porous surface region that is suitable for the transmission of medicinal items.

Previous studies showed that ULTS of phospholipid-polyethylene glycol (PL-PEGs) fragments of (SWNTs) with the capacity to prevent cellular non-specific absorption. Unfragmented PL-PEG facilitates cellular absorption selective of targeted SWNTs in two different cell receptor groups. The

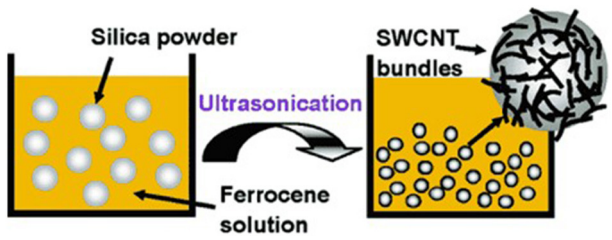

FIGURE 1 | Sonochemical processing of SWCNTs. Shows that silica powder in a solution of the ferrocene-xylene combination was sonicated for 20 min under atmospheric pressure. Sonication produces highly pure SWCNTs on the surface of the silica powder.

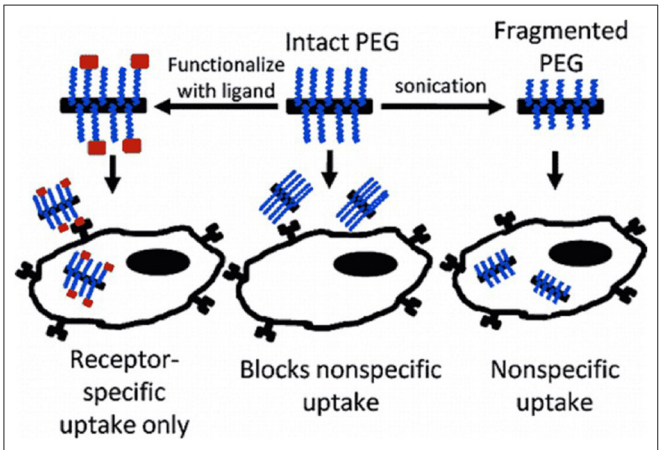

FIGURE 2 | Ultrasonic dispersion of SWCNTs with PL-PEG.

integrity of PEG is crucial to help ligand-functional nanotubes' cellular absorption because fragmentation is a potential side effect of ultrasound for dispersing SWNTs (**Figure 2**) (17, 18).

CONJUGATES OF DRUG POLYMER

Drug-polymers conjugates are manufactured using diverse chemicals on the efficient groups of the pharmaceutical and polymer carrier. The two major types of conjugates are drug conjugates and protein conjugates with adequate polymers (19). The most active polymer of the theragnostic drug-polymer conjugates is N-(2-hydroxypropyl) methacrylamide (HPMA) (19, 20). Yuan et al. (21) recently created theragnostic copolymers based upon poly (HPMA) loaded with Cu-64 and RGD as a target ligand for the target of tumor ontogenesis (**Figure 3**). The drug-polymer conjugate of prostate cancer xerographers was tested by a positron emission tomography (PET) 3 h after intravenous injecting, the tumor Cu-64 radioactivity in rats. The pharmacokinetics of Cu-64 in tumor (21) increased by 1 time with the drug-polymer conjugate.

Polymeric/Magnetic Nanoparticles

To produce polymer nanoparticles, monomer polymerization or polyp dispersion were used (22–26). Magnetite (27) nanoparticles of iron oxide are utilized as magnetic nanoparticles. Iron oxide nanoparticles have been extensively used due to their superparamagnetic properties and biocompatibility. The most practical methods for producing iron oxide nanoparticles are co-precipitation and thermal decomposition (27–31).

Due to their intrinsic theranostic properties, magnetic nanoparticles play a role as a hyperthermia agent with high transverse relaxation time (T2) for MRI and immunotherapeutic platforms for immunological diseases (28, 32–34). Recent evidence reported that autophagy pathway plays significant roles in targeting and degrading polymeric nanoparticles *via* auto-lysosomes (35). Polymeric nanoparticles are affected by cells *via* endocytosis and transferred *via* lysosomes that are an endosome pathway for degradation (**Figure 3**) (35, 36).

In breast cancer cells that overexpress folate receptors and fibroblast cells with a low number of pteroylmonoglutamic Acid receptors, the effect of quantum dots loaded nanoparticles on pteroylmonoglutamic Acid receptor was investigated in this study (37). Results showed that folate-decorated quantum dots loaded synthetic amphiphile nanoparticles were better than fibroblast cells. Synthetic amphiphile copolymers conjugated to targeting ligands may be a successful theragnostic approach for targeted diagnosis and treatment. PLA-TPGS nanoparticles were produced to syndicate their benefits and allow long-term, controlled imaging with a cancer cell. Biocompatibility and cellular absorption were improved because of this novel strategy by lowering their toxicity. The xenograft model was used to examine the biodistribution of the quantum dots and iron oxides loaded synthetic amphiphile nanoparticles among the different structures. *Ex vivo* fluorescent images showed a 51.5% increase in the kidney, 67.1% increase in fluorescent intensity in the liver, and 152.8% increase in the tumor. The blood-brain barrier surface adsorption of nanoparticles revealed that brain samples had more fluorescent signals than other organs.

Inadequate biodistribution of the quantum dots and iron oxides loaded synthetic amphiphile nanoparticles through the selective semipermeable border of endothelial cells (**Figure 4**). The advantages of multimodal imaging system, which results in a probe that is extremely sensitive and has deep infiltration for up to 6 h, confirming the diagnosis made by every individual's imaging. It was also proposed that using this multimodal approach to encapsulate therapeutics and conjugate ligands resulting in the progress of advanced multimodal theragnostic nanomedicine. Medarova et al. (38) developed the use of high resolution *in vivo* optical MRI, NIR and iron oxides for simultaneous imagery and siRNA distribution in tumors. N-succinimidyl-3 propionate was utilized to bind siRNA finished dextran particles to bridge the surface area of iron oxide nanoparticles and later the NIR dye Cy5.5 was also coupled to the surface area. The siRNA dissemination and its silencing capabilities were monitored with MRI and NIR optical imaging for 48 h using dextran coated iron oxide nanoparticles (**Figure 5**) (38).

Solid Lipid Nanoparticles

Nanoparticles of stable lipid are a secure and efficacious substitute for intravascular supply (39). They have a strong

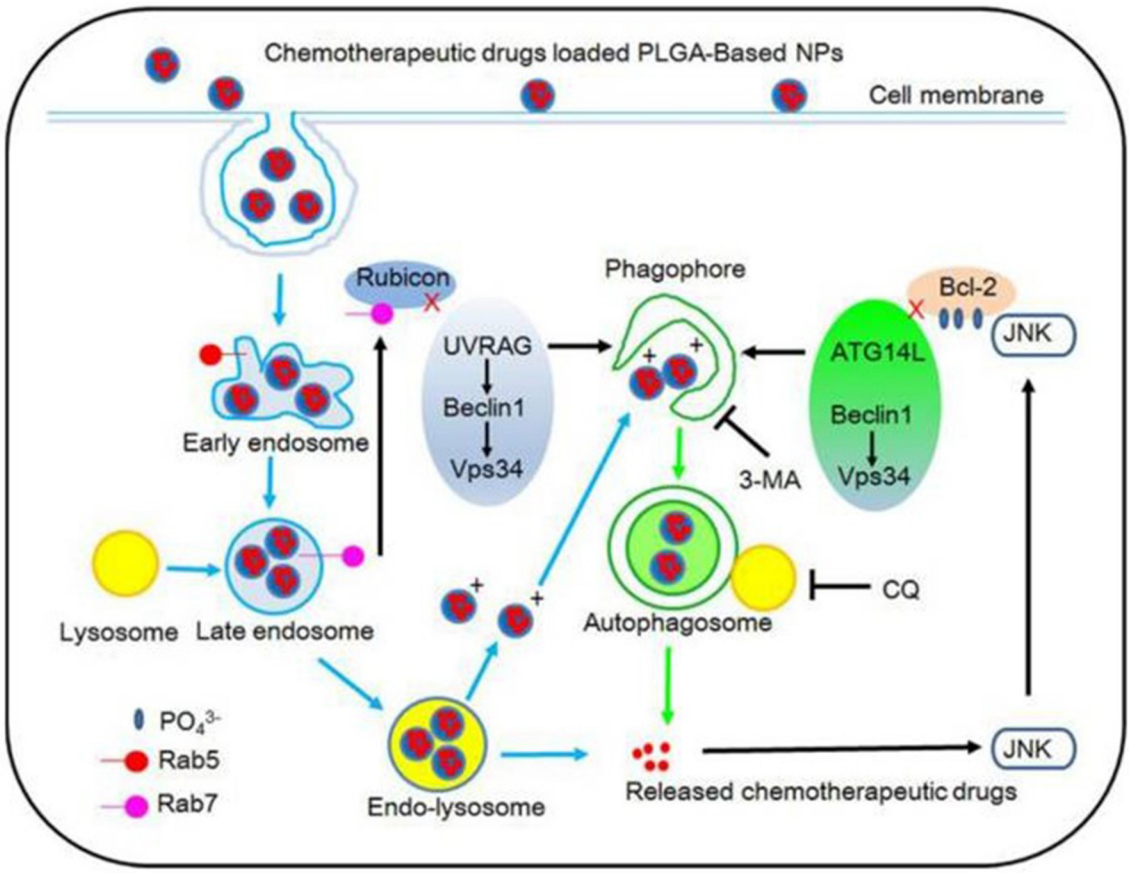

FIGURE 3 | The degradation process of PLGA-based nanoparticles is depicted schematically. Reproduced with permission (35).

hydrophobic heart with medicine inside. Nanomedicine made from biocompatible lipid substances solid at room temperature is Stable lipid nanoparticles. The warm and cold amalgamations are two significant approaches of preparation. Strong lipid nanoparticles enter the blood cell easily because of their compact size and lipotropic surface. The tightened endothelial cell blood-brain barrier is crossed by strong lipid nanoparticles with a range of <100 nm. The high efficiency of medication loads keeps the medication steady in the strong lipid matrix and makes the controlled release (40–42). As for the theranostic platforms for selective co-delivery of diagnostic and therapeutic agents, solid lipid nanoparticles like other nanomedicines are utilized (42, 43). Lymphatic delivery of nanoparticles of solid lipid has been developed as a technique to improve the transfer of beneficial agents into the lymphatic environment, which leads to improved oral bioavailability (44). Bae et al. (45) reported the applications of paclitaxel and siRNA loaded in solid lipid nanoparticles as theranostic anti-cancer agents with beneficial outcomes. The solid lipid nanoparticles were electrically complexed with the exterior surface of solid lipids and were generated with a stable core nanostructure like quantum dots and paclitaxel in the lipid shell, resembling low-density lipoproteins (LDL).

Dendrimers

Dendrimers are a form of synthetic nanomedicine made up of a spherical polymer with a lot of branches. Nanotheranostic systems usually use dendrimers that are 10–100 nm in size (46). Dendrimers can be made in two ways: beginning from the central core and moving outwards (divergent synthesis) or starting from the periphery and working inwards (top–down synthesis) (convergent synthesis). They are made by adding branching units to an amine center over and over again (ethylenediamine or ammonia). Dendrimers are repeatedly rounded by a branching sequence that leads to an early, perfect 3D geometric pattern. Dendrimers were harmful as cell membranes were damaged by their positive surface load. Dendrimers encapsulated drugs are prone to escape fast before hitting the target location in some cases (47, 48). The polymerization degrees are regulated by the synthesis of dendrimers of various sizes, molecular weights, and chemical compositions (49, 50). Theranostic dendrimers have a circular structure that holds both therapeutic and diagnostic agents with several cavities and divisions. The 5th generation of dendrimers with higher hydrophobic value is typically preferred in dendrimers (47–50). Poly (amidoamine) dendrimers generation 5 is coated with a replicant adenovirus serotype 5 carrying the sodium-iodide symporter and tested

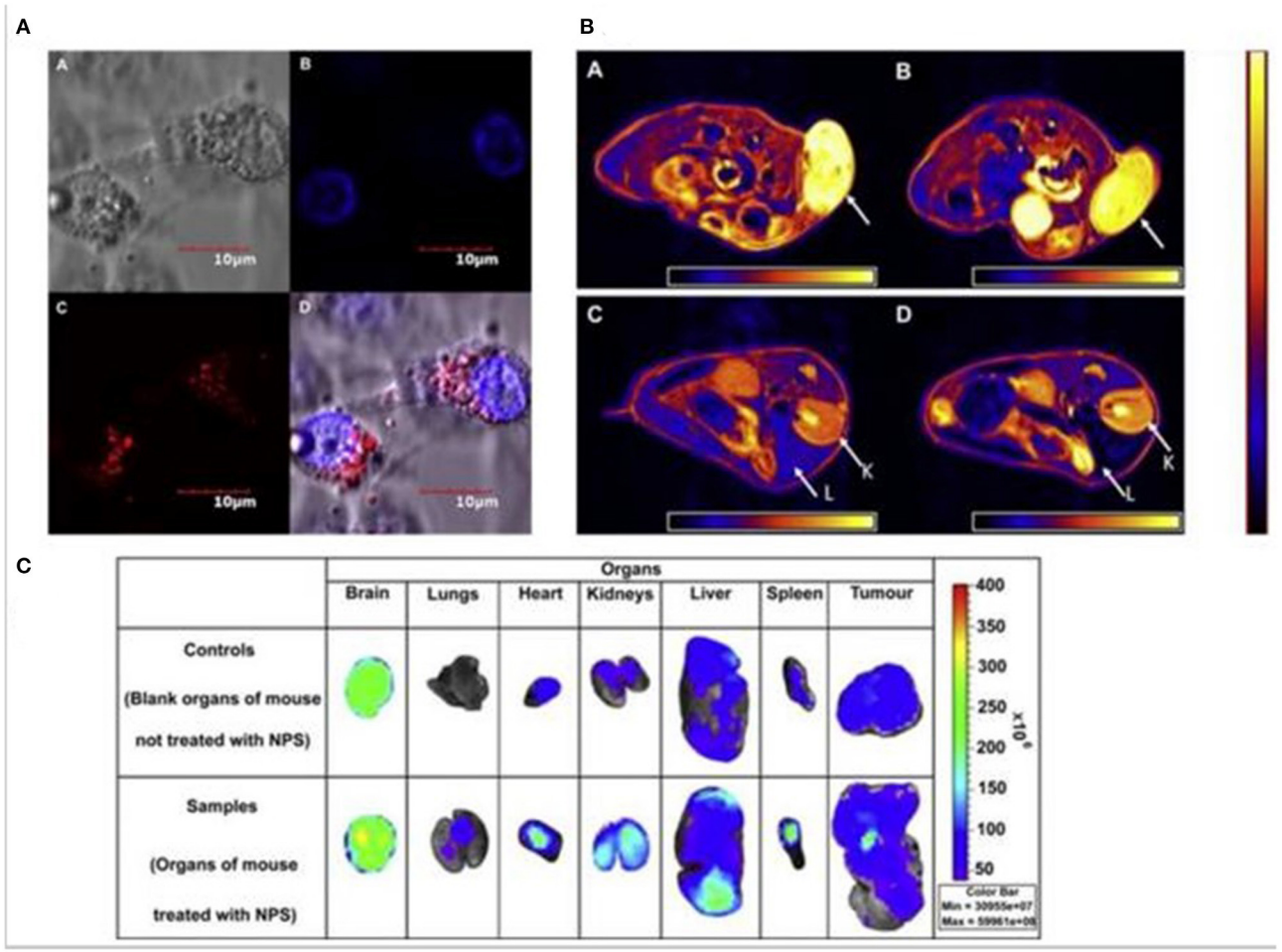

FIGURE 4 | Multi-modal imaging nanoparticles **(A)** Confocal photographs of PLA-TPGS nanoparticles with quantum dots and iron oxides processed *in vitro* with MCF-7. **(B)** MCF 7-graphed tumor-bearing mouse portions of axial MRI photographs. **(C)** Pictures under fluorescent light of various organs. The arrow shows the intensity of the confocol microscopy.

for transudative efficacy in a liver cancer xenograft model using an I-123 scan. *In vitro*, adenovirus serotype showed partial resistance to dendrimer-coating neutralization antibody and increased transduction efficiency in coxsackie adenovirus receptor-negative cells.

The main limitations impeding the clinical applications of adenovirus-mediated gene therapy are excess expression of coxsackie-adenovirus receptor (CAR), excess presence of neutralizing antibodies, and adenovirus sequestration by the liver (51, 52). Recent studies have exhibited the capacities of dendrimers to overcome these limitations through coating of the adenovirus to build adenoviral vectors (52–56). Different studies have reported successful use of this approach in cancer therapy. They used synthetic dendrimers to coat sodium iodide symporter (NIS) as a theranostic gene to develop adenoviral vectors for combination of systemic oncolytic virotherapy and NIS-mediated radiotherapy (54, 55, 57, 58). Taratula et al. (59) designed a new dendrimer-based theranostic system for phthalocyanines (Pc) delivery to tumors for tumor-targeted delivery of phthalocyanines Adding a hydrophobic linker to the Pc molecule during the preparation stage makes physical encapsulation of the hydrophobic compound into a generation 4 polypropylene imine (PPIG4) dendrimer much easier. To boost biocompatibility and tumor-targeted delivery with up to 24 h of photodynamic therapy, PEG and LHRH peptides were applied to the surface of the Pc-PPIG4 complexes. The LHRH-targeted theranostic dendrimer is capable of successful internalization into cancer cells as well as tumor aggregation, according to *in vitro* and *in vivo* imaging studies (59–67).

Liposomes

Liposomes are composed of amphiphilic phospholipids and cholesterol (68). Liposomes are spherical particles with a diameter ranging from 400 to <400 nanometers (62, 69). Liposomes are effective vectors for drug/diagnostic delivery due to their size, hydrophobic and hydrophilic nature, biodegradability, biocompatibility, and immunogenicity. Mechanical dispersion, solvent dispersion, and detergent removal are the three most popular liposome preparation processes. Liposomes have several drawbacks, including poor

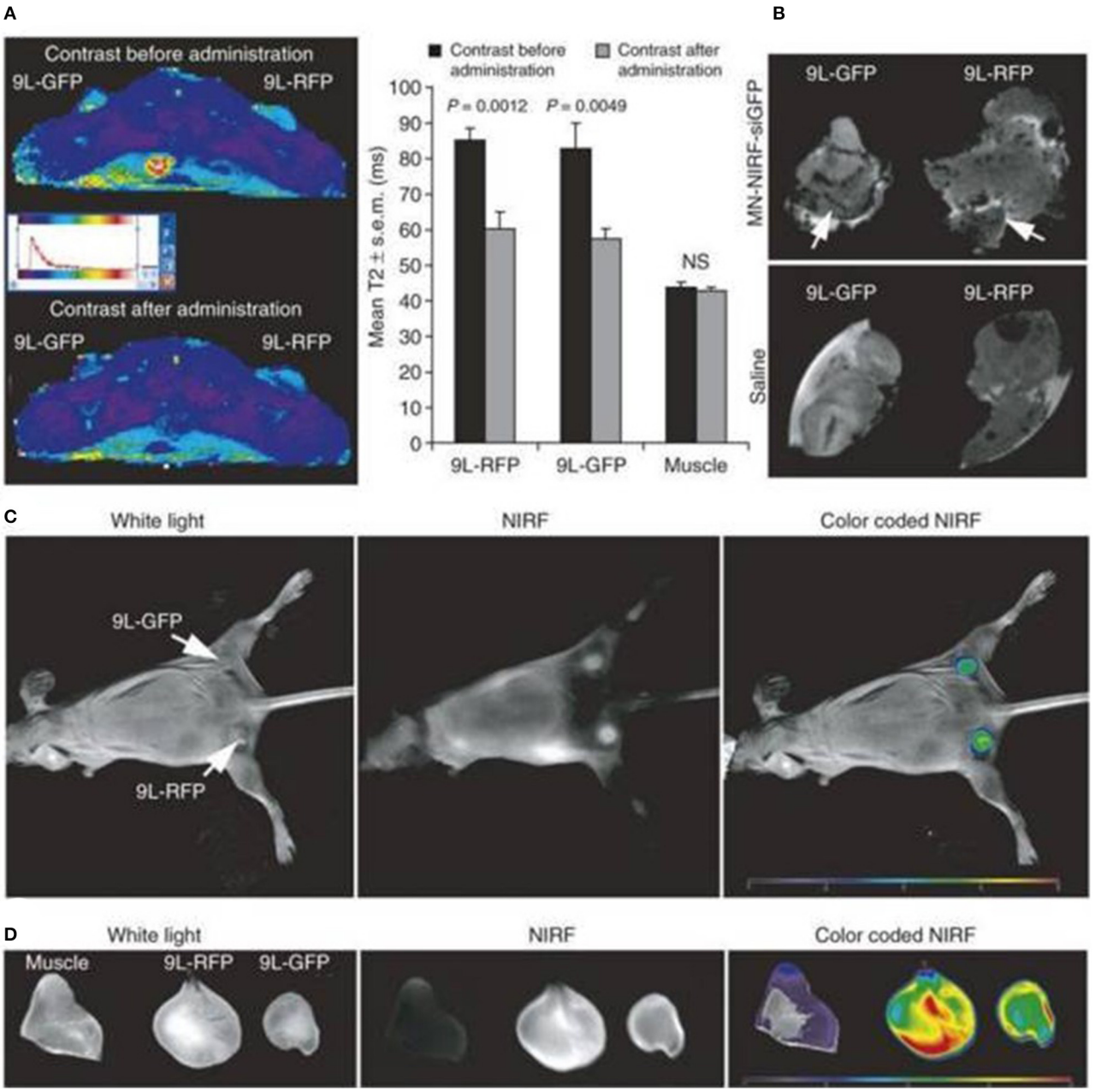

FIGURE 5 | It reveals that *in vivo* MRI was conducted before and after 24 h the administration of nanoparticles (9L-GFP) (9L-RFP) on rats with tumors. **(A)** After the tumor was injected, T2 relaxation reduced dramatically. It should be noted that the T2 muscle tissue relaxation times have not improved. **(B)** *Ex vivo* excised tumor high-resolution RMIs (78 m isotropic). Differentiated signal loss (arrows) indicating the concentration of the probe is quickly recognized in tumors that resulted from muzzle-injected controls. **(C)** The optical *in vivo* NIR imagery of the same rat showed a tumor-based high-intensity NIR signal. This meant that the tissue had been penetrated by the nanoparticle sample. **(D)** *Ex vivo* NIR optic imaging showed a large increase in fluorescence in the polyps substantially more than muscle tissue ($P = 0.0058$). Reproduced with permission from Medarova et al. (38) and Muthu and Singh (39).

drug loading efficiency, batch-to-batch manufacturing volatility, and poor stability (70–72). Beneficial agents may be encapsulated in the middle or integrated into the lipophilic bilayer shell while nanosized diagnostic agents such as iron oxide nanoparticles, quantum dots, and gold nanoparticles may be incorporated in the lipophilic bilayer shell (71, 73–77). Advanced theranostic liposomes are conjugated with molecular biomarkers for a targeted outcome. To resolve immune system opsonization and fast elimination from circulation, stealth liposomes, or PEG-coated liposomes, were established with stability and a longer half-life in blood (74, 75, 78). PEGylated liposomes, standard nude liposomes (without TPGS coating), and TPGS

coated liposomes were tested *in vitro* on cell lines to see whether they could guard against brain tumors and were found to be more effective than those coated with PEGylated liposomes (79). Muthu et al. (80) rendered TPGS-coated theranostic liposomes with and without docetaxel and quantum dots targeting moieties. Targeted theranostic liposomes exhibited higher cellular absorption and cytotoxicity than non-targeted liposomes (**Figure 6**).

Micelles

Micelles are hydrophobic, hydrophilic structures with a self-assembling hydrophilic core for parenteral management of products that are badly water-soluble (81–83). The main synthesis method for micelles in nanoscale is dispersion of surfactants in water which then generates a two-component micelles with a hydrophilic shell and a hydrophobic core (84–86). Polymeric micelles are self-assembled and aggregated nanoscale assemblies with diameter of $\leq$100 nm consisting of amphiphilic copolymers enclosed with an aqueous phase. The hydrophobic and neutral parts of copolymers are bound together due to an attractive force between them, the process which facilitates the micellization. The micellization process depends on the micelle concentration in a manner that when the micelle concentration reaches a threshold level called critical micelle concentration (CMC), the micellization process starts (87, 88). The stability of the micelles is determined by the strong cohesive force between the drug and the center of the polymer and the crosslinking of the core or shell. The mechanism of direct dissolution and the organic solvent system is usually used to produce them (89). The hydrophobic core of micelles, which can be given intravenously in and the outer hydrophilic layer using a targeting agent can be filled with diagnostic agents (90–93). Theranostic micelles with $<$50 nm of renal escape diameter improve the permeability of the endothelial cell and theranostic reticulate system provide solid tumors (94, 95). The paclitaxel-charged micellar formulations of Genexol-PMTM are approved to be an effective standard for the provision of cancer drugs (96–99).

Gold Nanoparticles

Gold nanoparticles with gold nuclei are another versatile medium with desirable values for theranostic systems (100–103). They are made of 1.5% to 10 nm core sizes, offering a powerful drug and ligand conjugation with an expanded surface area 114. Hydrogen tetrachlorocuprate is a common method of preparing gold nanoparticles in the chemical treatment process. Gold nanoparticles can be combined as advanced theranostics with drugs and ligands to precisely identify the target receptor for successfully targeting (104, 105). Therapeutic loading is carried by non-covalent interaction or covalent chemical conjugation. The inherent characteristics of gold nanoparticles are diagnosis characteristics (104–107). Heo et al. (108) defined surface-functionalized Gold nanoparticles of PEG as the theranostic platform associated with beta-cyclodextrin (beta-CD). The inclusion complex Paclitaxel and beta-CD is bound to gold nanoparticles. Gold nanoparticles are more related to cancer cells such as HELA, A549, and MG63 than NIH3T3.

Carbon Nanomaterials

Carbon nanomaterials or nano carbons were analyzed for theranostic purposes because of their peculiar chemical and physical qualities (109). Carbon nanomaterials such as carbon nanotubes (CNT), zero-dimensional (0D), sp2-carbon nanomaterials (sp2-carbon nanomaterials), 2D graphene, and carbon point with the size of nano-clusters smaller than 10 nm (109, 110). Due to its large area, its ability of diagnostic agents, and its aptitude for surface modifications (111–113), CNTs were considered suitable for theranostic applications. CNTs have a cylindrical form due to their various graphene sheet layers. Two kinds of carbon nanotubes are SWCNTs or MWCNNTs. CNTs are common methods for ball-milling, laser therapy, and chemical vapor deposition method (111, 114–118). In recent years, multifunctional CNT-based systems for theranostic applications have resulted from many synthetic methods for CNT functionalization. The theranostic applications for photoluminescent *in vivo* tumor imaging in the 1.0–1.4 m injected intravenously injected SWCNTs and NIR absorbers and heaters at 808 nm for lower doses for photothermal removal were seen by Robinson et al. (119).

Theranostic MWCNTs were first developed by Das et al. (120), *via* mixing acid oxidized MWCNTs with four distinct functional drive elements according to cellular uptake studies.

ULTRASONIC NANOPARTICLES TRANSLATION CHALLENGES IN CLINICS

Biological Challenges

Theranostic nanomedicine has plenty of research into disease diagnosis and treatment to improve human health. Nano theranostics remains a new paradigm for disease detection and care in hospitals. One of the toughest things to bring theranostic nanomedicine to clinics is nano-bio engagement. In interactions with biological materials, nanomedicine can cause problems such as inflammation and other diseases due to its potential toxicity depending on the potential and solubility of different parameters (121–123). A pseudo-allergy linked to complementary activation is an immediate adverse immune response from several nanoplatforms (124, 125). Study about pathophysiology and disease heterogeneity is imperative to the physicochemical characteristics of nanomedicines. Besides, as theranostic nanomedicine is individually distinct, it would be very difficult to have therapeutic clearance for a single-size solution (126). Nanoparticles with high therapeutic properties can not necessarily be good screening instruments, Consequently, the safety profile of human nano theranostics remains a major concern, which needs long-term surveillance of all early and advanced stages of clinical trials (127).

Challenges of Commercialization

The challenge in designing a synthesis technique is also a key concern with the clinical translation of theranostic nanomedicines. Poor reproductivity and low efficient large-scale synthesis, and variable physico-chemical characteristics are common challenges toward clinical applications of nanoparticles. Nanoplatforms with complex manufacturing methods are barely

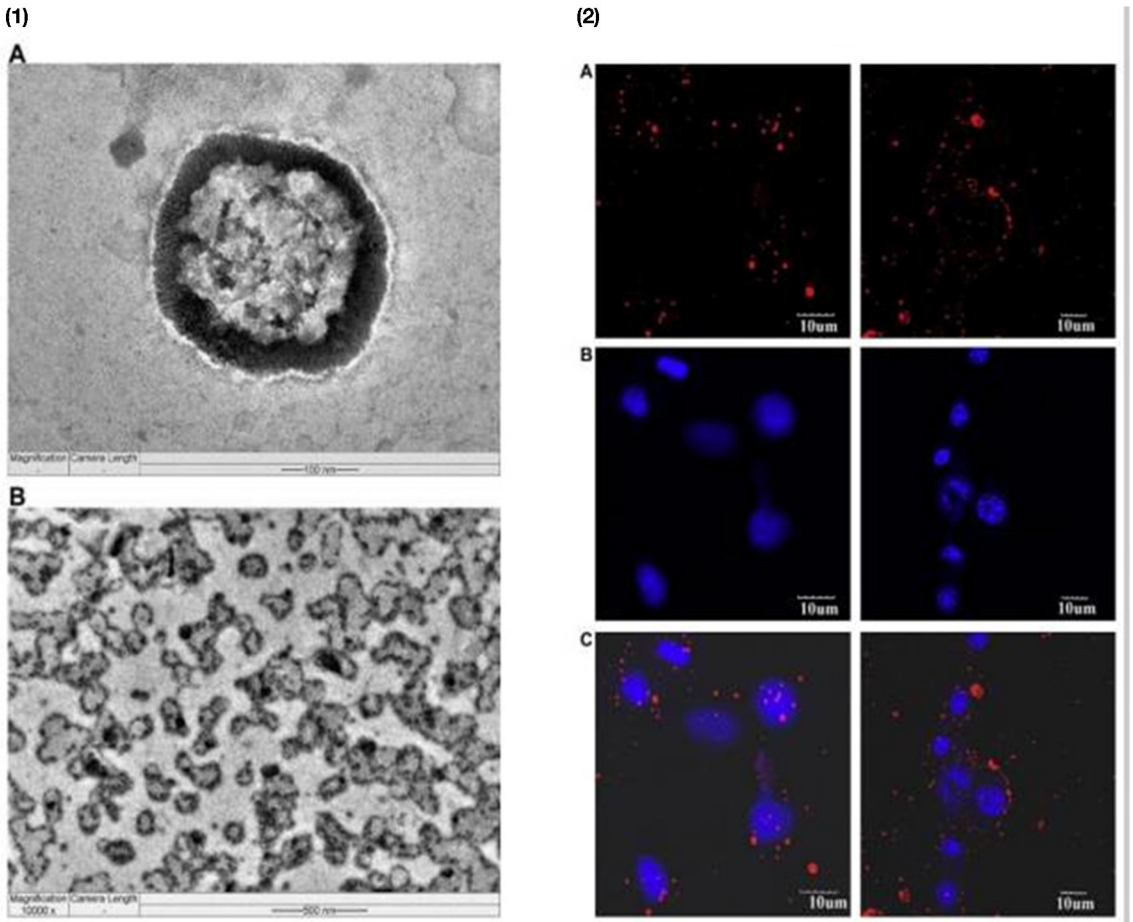

FIGURE 6 | TPGS liposomes were used to transport theranostic drugs *in vitro*. **(1) (A)** A single quantum dots-loaded TPGS coated liposome in a 100 nm scale, and **(B)** multiple quantum dots-loaded TPGS coated liposomes after storage in a 500 nm scale. **(2) (A,B)** Confocal laser scanning microscopy images of MCF-7 cells treated with non-targeted TPGS-based multi-functional liposomes (left column) and targeted TPGS-based multi-functional liposomes (right column) for 2 h (right column). Quantum dots showing red fluorescence from cytoplasmic liposomes, **(B)** channels displaying blue fluorescence from dye-stained nuclei, and **(C)** quantum dots displaying blue fluorescence from dye-stained nuclei, and **(C)** Quantum dots and blue dye merged channels.

incorporated into clinical practice due to disadvantages caused by drug companies (126, 127). Another big issue that needs to be addressed is the broad gap between the research community and regulatory authorities. Many government regulations are used to restrict the commercialization of nanomedicine based on regulatory considerations relevant to quality and manufacturing standards. There is an important effect on a prompt, effective translation of theranostics into the industry (128, 129). However, these criteria may not be satisfactory and need to be updated to validate the performance effectiveness of other human-using nanotheranostics.

Clinical Considerations and Perspectives

The first nanocarrier for drug delivery, approved by the US FDA was Doxil (PEGylated liposomal doxorubicin) and designed for delivery of chemotherapeutic agent doxorubicin (130). The nanoparticles facilitated Doxil, exhibit several advantages over free doxorubicin including selectivity, specificity, and reduced cardiotoxicity (131). The successful clinical outcomes of Doxil in cancer therapy has led to the development of many other nanoscale carriers. Although nanotechnology-assisted theranostic systems are promising inventions in medicine, concerns on the safety of these nanosystems due to unknown characteristics of nanoscale materials have impeded the clinical applications of these systems. To address the concerns on the safety and understand the safety profile conducting animal studies, laboratory experiments and clinical trials is necessary. Stability of nanosystems is other important aspect of nanosystems for successful translation into clinical practice. Exposure to human subjects is inevitable to address these issues. Experiments in human subjects are complementary to *in vitro* and *in vivo* animal studies (132, 133). Failure in human studies can be too expensive and sometimes irrecoverable. Therefore, it is necessary to adopt a novel standardized nano-safety platform to develop reliable systems and avoid potential candidates with adverse outcomes (134).

Considering these risks and the unique characteristics of nanosystems, FDA necessitates conducting preclinical studies involving animals, human cells, or tissues prior to any study on human subjects as clinical trials for any nanoscale medications. Following the evaluation of FDA on the outcomes of the preclinical studies, they allow for Phase I clinical trials which is a dose-response trial with a small group of subjects (sample size: 25–100) to determine the maximum tolerable dose for the target product. These studies are followed by Phase II trials with greater sample size including 100–500 subjects, which evaluate the safety and efficacy of the developed nanomedicine. FDA allows conducting Phase III trials (sample size of 500–3,000 subjects) for those drugs that passed the Phase II clinical trials, and it is determined whether the application will be approved or not based on the findings of the Phase II (133).

To overcome the biological challenges to nanotheranostics, a great deal of research needs to be done about how the interaction between patient biology and nanomedicine is to be understood. In preclinical trials, animal models can be used to assess the appropriateness of theranostic nanomedicine in the treatment and imagery of patient populations of human beings (135). To evaluate future patient risk, nanotoxicology profiles need to be adopted and followed during the early stages of clinical development (124–129, 135–137). Recent advances in nanotheranostics have utilized improved permeability and retention as well as other characteristics of nanoparticles such as surface functionalization, selectivity and sensitivity, and biodegradability.

This would have enormous potential for theranostic applications in developing bio-mimetic nanoparticles, which exploit the normal functioning of the source. The effect of theranostics can be further improved by the use of smart stimuli-based nanoparticles to release therapeutic loads on the site. This method of provision and real-time analysis would help the clinician to adjust a care plan for heterogeneous and adaptive diseases. A mindful awareness needs to spread for the technical problems facing the industry in marketing systems. Good collaboration is required between laboratory and pharmaceutical groups. For large-scale theranostic nanoparticles synthesis and improvements on good manufacturing, practice must be made. Process optimization applications like Aspen is useful in an industrial setting to define key parameters to maximize performance in the early stages of manufacture and cope with batch-to-batch variations. This could be in a supervised and efficient way (138).

Production success depends on the readiness of the employees for product specifications and barriers. Theranostic nanomedicines can affect human health, but by incorporating the above lessons in the early stages of manufacturing, manufacturers can produce efficient products.

CONCLUSION

While ultrasound nanomedicine has dramatically progressed and is continuing to make substantial progress, the field must evolve before human medicine can transform. Nanotheranostics are supplementary to nanomedicine that could be used in medical centers to monitor disease. Nanotheranostics is promising for a deeper understanding of the therapeutic and diagnostic interwoven substances that are necessary to maximize their clinical application potential. Besides, both commercialization and regulatory stages need to be followed by the most promising approaches for bringing ultrasonic nanomedicine from research laboratory studies into clinics.

AUTHOR CONTRIBUTIONS

XL and WG downloaded the references and processed the graphs in the manuscript. XL wrote the first version and WG finalized the manuscript. WG conceived and coordinated the study and critically evaluated the data. All authors read and approved the final manuscript.

FUNDING

The research was supported by Medical and Health Research Project of Zhejiang Province (No. 2019KY303).

REFERENCES

1. Siadatnasab F, Farhadi S, Dusek M, Eigner V, Hoseini A-A, Khataee A. Sonochemical synthesis and structural characterization of an organic-inorganic nanohybrid based on a copper-dithiocarbamate complex and PMo12O403—polyanion as a novel sonocatalyst. *Ultrason Sonochem.* (2020) 64:104727. doi: 10.1016/j.ultsonch.2019.104727
2. Mansoorianfar M, Khataee A, Riahi Z, Shahin K, Asadnia M, Razmjou A, et al. Scalable fabrication of tunable titanium nanotubes *via* sonoelectrochemical process for biomedical applications. *Ultrason Sonochem.* (2020) 64:104783. doi: 10.1016/j.ultsonch.2019.104783
3. Saani SM, Abdolalizadeh J, Heris SZ. Ultrasonic/sonochemical synthesis and evaluation of nanostructured oil in water emulsions for topical delivery of protein drugs. *Ultrason Sonochem.* (2019) 55:86–95. doi: 10.1016/j.ultsonch.2019.03.018
4. Allami HA, Tabasizadeh M, Rohani A, Nayebzadeh H, Farzad A. Effect of ultrasonic irradiation on the properties and performance of biodiesel produced from date seed oil used in the diesel engine. *Ultrason Sonochem.* (2020) 60:104672. doi: 10.1016/j.ultsonch.2019.104672
5. Aber S, Khajeh RT, Khataee A. Application of immobilized ZnO nanoparticles for the photocatalytic regeneration of ultrasound pretreated-granular activated carbon. *Ultrason Sonochem.* (2019) 58:104685. doi: 10.1016/j.ultsonch.2019.104685
6. Azarhoosh MJ, Halladj R, Askari S, Aghaeinejad-Meybodi A. Performance analysis of ultrasound-assisted synthesized nano-hierarchical SAPO-34 catalyst in the methanol-to-lights-olefins process *via* artificial intelligence methods. *Ultrason Sonochem.* (2019) 58:104646. doi: 10.1016/j.ultsonch.2019.104646
7. Sheydaei M, Fattahi M, Ghalamchi L, Vatanpour V. Systematic comparison of sono-synthesized Ce-, La-and Ho-doped ZnO nanoparticles and using the optimum catalyst in a visible light assisted continuous sono-photocatalytic membrane reactor. *Ultrason Sonochem.* (2019) 56:361–71. doi: 10.1016/j.ultsonch.2019.04.031
8. Panahi P, Nouruzi N, Doustkhah E, Mohtasham H, Ahadi A, Ghiasi-Moaser A, et al. Zirconium based porous coordination polymer

(PCP) bearing organocatalytic ligand: A promising dual catalytic center for ultrasonic heterocycle synthesis. *Ultrason Sonochem.* (2019) 58:104653. doi: 10.1016/j.ultsonch.2019.104653
9. Bayrami A, Alioghli S, Rahim Pouran S, Habibi-Yangjeh A, Khataee A, Ramesh S. A facile ultrasonic-aided biosynthesis of ZnO nanoparticles using Vaccinium arctostaphylos L. leaf extract and its antidiabetic, antibacterial, and oxidative activity evaluation. *Ultrason Sonochem.* (2019) 55:57–66. doi: 10.1016/j.ultsonch.2019.03.010
10. Bayrami A, Ghorbani E, Pouran SR, Habibi-Yangjeh A, Khataee A, Bayrami M. Enriched zinc oxide nanoparticles by Nasturtium officinale leaf extract: joint ultrasound-microwave-facilitated synthesis, characterization, and implementation for diabetes control and bacterial inhibition. *Ultrason Sonochem.* (2019) 58:104613. doi: 10.1016/j.ultsonch.2019.104613
11. Soltani RDC, Miraftabi Z, Mahmoudi M, Jorfi S, Boczkaj G, Khataee A. Stone cutting industry waste-supported zinc oxide nanostructures for ultrasonic assisted decomposition of an anti-inflammatory non-steroidal pharmaceutical compound. *Ultrason Sonochem.* (2019) 58:104669. doi: 10.1016/j.ultsonch.2019.104669
12. Daneshvar H, Dorraji MSS, Amani-Ghadim AR, Rasoulifard MH. Enhanced sonocatalytic performance of ZnTi nano-layered double hydroxide by substitution of Cu (II) cations. *Ultrason Sonochem.* (2019) 58:104632. doi: 10.1016/j.ultsonch.2019.104632
13. Soltani RDC, Mashayekhi M, Naderi M, Boczkaj G, Jorfi S, Safari M. Sonocatalytic degradation of tetracycline antibiotic using zinc oxide nanostructures loaded on nano-cellulose from waste straw as nanosonocatalyst. *Ultrason Sonochem.* (2019) 55:117–24. doi: 10.1016/j.ultsonch.2019.03.009
14. Bawa. *Ultrasonic Treatment of Nanoparticles for Pharmaceutical*.
15. Niemann MU, Srinivasan SS, Phani AR, Kumar A, Goswami DY, Stefanakos EK. Nanomaterials for hydrogen storage applications: a review. Joshi R, editor. *J Nanomater.* (2008) 2008:950967. doi: 10.1155/2008/950967
16. Kang J, Al-Sabah S, Théo R. Effect of single-walled carbon nanotubes on strength properties of cement composites. *Mater (Basel, Switzerland).* (2020) 13:1305. doi: 10.3390/ma13061305
17. Zeineldin M, Megahed A, Burton B, Blair B, Aldridge B, Lowe JF. Effect of single dose of antimicrobial administration at birth on fecal microbiota development and prevalence of antimicrobial resistance genes in piglets. *Front Microbiol.* (2019) 10:1414. doi: 10.3389/fmicb.2019.01414
18. Zeineldin MM, Megahed A, Blair B, Burton B, Aldridge B, Lowe J. Negligible impact of perinatal tulathromycin metaphylaxis on the developmental dynamics of fecal microbiota and their accompanying antimicrobial resistome in piglets. *Front Microbiol.* (2019) 10:726. doi: 10.3389/fmicb.2019.00726
19. Lammers T, Ulbrich K, HPMA. copolymers: 30 years of advances. *Adv Drug Deliv Rev.* (2009) 62:119–21. doi: 10.1016/j.addr.2009.12.004
20. Allmeroth M, Moderegger D, Gündel D, Buchholz H-G, Mohr N, Koynov K, et al. PEGylation of HPMA-based block copolymers enhances tumor accumulation *in vivo*: a quantitative study using radiolabeling and positron emission tomography. *J Control release.* (2013) 172:77–85. doi: 10.1016/j.jconrel.2013.07.027
21. Yuan J, Zhang H, Kaur H, Oupicky D, Peng F. Synthesis and characterization of theranostic poly (HPMA)-c (RGDyK)-DOTA-64Cu copolymer targeting tumor angiogenesis: tumor localization visualized by positron emission tomography. *Mol Imaging.* (2013) 12:7290.2012.00038. doi: 10.2310/7290.2012.00038
22. Moghimi SM, Hunter AC. Capture of stealth nanoparticles by the body's defences. *Crit Rev Ther Drug Carrier Syst.* (2001) 18:527–50. doi: 10.1615/CritRevTherDrugCarrierSyst.v18.i6.30
23. Soppimath KS, Aminabhavi TM, Kulkarni AR, Rudzinski WE. Biodegradable polymeric nanoparticles as drug delivery devices. *J Controll Release.* (2001) 70:1–20. doi: 10.1016/S0168-3659(00)00339-4
24. Mok H, Park TG. Hybrid polymeric nanomaterials for siRNA delivery and imaging. *Macromol Biosci.* (2012) 12:40–8. doi: 10.1002/mabi.201100169
25. Svenson S. Theranostics: are we there yet? *Mol Pharm.* (2013) 10:848–56. doi: 10.1021/mp300644n
26. Vijayakumar MR, Muthu MS, Singh S. Copolymers of poly (lactic acid) and D-α-tocopheryl polyethylene glycol 1000 succinate-based nanomedicines: versatile multifunctional platforms for cancer diagnosis and therapy. *Expert Opin Drug Deliv.* (2013) 10:529–43. doi: 10.1517/17425247.2013.758632
27. Gupta AK, Gupta M. Synthesis and surface engineering of iron oxide nanoparticles for biomedical applications. *Biomaterials.* (2005) 26:3995–4021. doi: 10.1016/j.biomaterials.2004.10.012
28. Yoo D, Lee J-H, Shin T-H, Cheon J. Theranostic magnetic nanoparticles. *Acc Chem Res.* (2011) 44:863–74. doi: 10.1021/ar200085c
29. Huang G, Chen H, Dong Y, Luo X, Yu H, Moore Z, et al. Superparamagnetic iron oxide nanoparticles: amplifying ROS stress to improve anticancer drug efficacy. *Theranostics.* (2013) 3:116. doi: 10.7150/thno.5411
30. Li L, Jiang W, Luo K, Song H, Lan F, Wu Y, et al. Superparamagnetic iron oxide nanoparticles as MRI contrast agents for non-invasive stem cell labeling and tracking. *Theranostics.* (2013) 3:595–615. doi: 10.7150/thno.5366
31. Yen SK, Padmanabhan P, Selvan ST. Multifunctional iron oxide nanoparticles for diagnostics, therapy and macromolecule delivery. *Theranostics.* (2013) 3:986. doi: 10.7150/thno.4827
32. Mornet S, Vasseur S, Grasset F, Duguet E. Magnetic nanoparticle design for medical diagnosis and therapy. *J Mater Chem.* (2004) 14:2161–75. doi: 10.1039/b402025a
33. Laurent S, Forge D, Port M, Roch A, Robic C, Vander Elst L, et al. Magnetic iron oxide nanoparticles: synthesis, stabilization, vectorization, physicochemical characterizations, and biological applications. *Chem Rev.* (2008) 108:2064–110. doi: 10.1021/cr068445e
34. Clemente-Casares X, Santamaria P. Nanomedicine in autoimmunity. *Immunol Lett.* (2014) 158:167–74. doi: 10.1016/j.imlet.2013.12.018
35. Zhang X, Dong Y, Zeng X, Liang X, Li X, Tao W, et al. The effect of autophagy inhibitors on drug delivery using biodegradable polymer nanoparticles in cancer treatment. *Biomaterials.* (2014) 35:1932–43. doi: 10.1016/j.biomaterials.2013.10.034
36. Smith BA, Smith BD. Biomarkers and molecular probes for cell death imaging and targeted therapeutics. *Bioconjug Chem.* (2012) 23:1989–2006. doi: 10.1021/bc3003309
37. Pan J, Liu Y, Feng S-S. Multifunctional nanoparticles of biodegradable copolymer blend for cancer diagnosis and treatment. *Nanomedicine.* (2010) 5:347–60. doi: 10.2217/nnm.10.13
38. Medarova Z, Pham W, Farrar C, Petkova V, Moore A. *In vivo* imaging of siRNA delivery and silencing in tumors. *Nat Med.* (2007 M) 13:372–7. doi: 10.1038/nm1486
39. Muthu MS, Singh S. Targeted nanomedicines: effective treatment modalities for cancer, AIDS and brain disorders. (2009) 4:105–18 doi: 10.2217/17435889.4.1.105
40. Müller RH, Rühl D, Runge S, Schulze-Forster K, Mehnert W. Cytotoxicity of solid lipid nanoparticles as a function of the lipid matrix and the surfactant. *Pharm Res.* (1997) 14:458–62. doi: 10.1023/A:1012043315093
41. Mehnert W, Mäder K. Solid lipid nanoparticles: production, characterization and applications. *Adv Drug Deliv Rev.* (2001) 47:165–96. doi: 10.1016/S0169-409X(01)00105-3
42. Wissing SA, Kayser O, Müller RH. Solid lipid nanoparticles for parenteral drug delivery. *Adv Drug Deliv Rev.* (2004) 56:1257–72. doi: 10.1016/j.addr.2003.12.002
43. Müller RH, Mäder K, Gohla S. Solid lipid nanoparticles (SLN) for controlled drug delivery—a review of the state of the art. *Eur J Pharm Biopharm.* (2000) 50:161–77. doi: 10.1016/S0939-6411(00)00087-4
44. Singh I, Swami R, Khan W, Sistla R. Lymphatic system: a prospective area for advanced targeting of particulate drug carriers. *Expert Opin Drug Deliv.* (2014) 11:211–29. doi: 10.1517/17425247.2014.866088
45. Bae KH, Lee JY, Lee SH, Park TG, Nam YS. Optically traceable solid lipid nanoparticles loaded with siRNA and paclitaxel for synergistic chemotherapy with in situ imaging. *Adv Heal Mater.* (2013) 2:576–84. doi: 10.1002/adhm.201200338
46. Fahmy TM, Fong PM, Park J, Constable T, Saltzman WM. Nanosystems for simultaneous imaging and drug delivery to T cells. *AAPS J.* (2007) 9:E171–80. doi: 10.1208/aapsj0902019
47. Fréchet JM. Functional polymers and dendrimers: reactivity, molecular architecture, and interfacial energy. *Science.* (1994) 263:1710–5. doi: 10.1126/science.8134834

48. Bosman AW, Janssen HM, Meijer EW. About dendrimers: structure, physical properties, and applications. *Chem Rev.* (1999) 99:1665–88. doi: 10.1021/cr970069y
49. Jansen JF. de Brabander-van den Berg EM, Meijer EW. Encapsulation of guest molecules into a dendritic box. *Science.* (1994) 266:1226–9. doi: 10.1126/science.266.5188.1226
50. Li Y, Cheng Y, Xu T. Design, synthesis and potent pharmaceutical applications of glycodendrimers: a mini review. *Curr Drug Discov Technol.* (2007) 4:246–54. doi: 10.2174/157016307783220503
51. Taratula O, Schumann C, Duong T, Taylor KL, Taratula O. Dendrimer-encapsulated naphthalocyanine as a single agent-based theranostic nanoplatform for near-infrared fluorescence imaging and combinatorial anticancer phototherapy. *Nanoscale.* (2015) 7:3888–902. doi: 10.1039/C4NR06050D
52. Xue Y, Gao Y, Meng F, Luo L. Recent progress of nanotechnology-based theranostic systems in cancer treatments. *Cancer Biol Med.* (2021) 18:336. doi: 10.20892/j.issn.2095-3941.2020.0510
53. Baril P, Martin-Duque P, Vassaux G. Visualization of gene expression in the live subject using the Na/I symporter as a reporter gene: applications in biotherapy. *Br J Pharmacol.* (2010) 159:761–71. doi: 10.1111/j.1476-5381.2009.00412.x
54. Zhang Y, Wang J. Targeting uptake transporters for cancer imaging and treatment. *Acta Pharm Sin B.* (2020) 10:79–90. doi: 10.1016/j.apsb.2019.12.005
55. Belmar-Lopez C, Mendoza G, Oberg D, Burnet J, Simon C, Cervello I, et al. Tissue-derived mesenchymal stromal cells used as vehicles for anti-tumor therapy exert different *in vivo* effects on migration capacity and tumor growth. *BMC Med.* (2013) 11:139. doi: 10.1186/1741-7015-11-139
56. Chen YW, Su YL, Hu SH, Chen SY. Functionalized graphene nanocomposites for enhancing photothermal therapy in tumor treatment. *Adv Drug Deliv Rev.* (2016) 105:190–204. doi: 10.1016/j.addr.2016.05.022
57. Taratula O, Patel M, Schumann C, Naleway MA, Pang AJ, He H, et al. Phthalocyanine-loaded graphene nanoplatform for imaging-guided combinatorial phototherapy. *Int J Nanomedicine.* (2015) 10:2347–62. doi: 10.2147/IJN.S81097
58. Grünwald GK, Vetter A, Klutz K, Willhauck MJ, Schwenk N, Senekowitsch-Schmidtke R, et al. Systemic image-guided liver cancer radiovirotherapy using dendrimer-coated adenovirus encoding the sodium iodide symporter as theranostic gene. *J Nucl Med.* (2013) 54:1450–7. doi: 10.2967/jnumed.112.115493
59. Taratula O, Schumann C, Naleway MA, Pang AJ, Chon KJ, Taratula O, et al. multifunctional theranostic platform based on phthalocyanine-loaded dendrimer for image-guided drug delivery and photodynamic therapy. *Mol Pharm.* (2013) 10:3946–58. doi: 10.1021/mp400397t
60. Yadollahpour A, Hosseini SAA, Jalilifar M, Rashidi S, Rai BMM. Magnetic nanoparticle-based drug and gene delivery: A review of recent advances and clinical applications. *Int J Pharm Technol.* (2016) 8:11451–66. Available from: https://www.scopus.com/inward/record.uri?eid=2-s2.0-84975275516&partnerID=40&md5=733b63c2cadfcb469915e0c8561f60af
61. Rezaee Z, Yadollahpour A, Bayati V, Dehbashi FN. Gold nanoparticles and electroporation impose both separate and synergistic radiosensitizing effects in HT-29 tumor cells: An *in vitro* study. Int J Nanomedicine. (2017) 12:1431–9. doi: 10.2147/IJN.S128996
62. Ali Y, Zohre R, Mostafa J, Samaneh R. Applications of upconversion nanoparticles in molecular imaging: A review of recent advances and future opportunities. *Biosci Biotechnol Res Asia.* (2015) 12:131–40. doi: 10.13005/bbra/1615
63. Yadollahpour A, Rashidi S. Magnetic nanoparticles: a review of chemical and physical characteristics important in medical applications. *Orient J Chem.* (2015) 31:25–30. Available from: https://www.scopus.com/inward/record.uri?eid=2-s2.0-84983233410&doi=10.13005%2Fojc%2F31.Special-Issue1.03&partnerID=40&md5=5a631cd2f5948d5aa5cdce8f6a6a4c5f
64. Ali Y, Zohre R, Mostafa J, Samaneh R. Dye-doped fluorescent nanoparticles in molecular imaging: a review of recent advances and future opportunities. (2014) doi: 10.13005/msri/110203
65. Yuen AKL, Hutton GA, Masters AF, Maschmeyer T. The interplay of catechol ligands with nanoparticulate iron oxides. *Dalton Transac.* (2012) 41:2545–59. doi: 10.1039/c2dt11864e
66. Kyle S, Saha S. Nanotechnology for the detection and therapy of stroke. *Adv Healthc Mater.* (2014) 3:1703–20. doi: 10.1002/adhm.201400009
67. Proulx J, Joshi C, Vijayaraghavalu S, Saraswathy M, Labhasetwar V, Ghorpade A, et al. Arginine-modified polymers facilitate poly (Lactide-co-glycolide)-based nanoparticle gene delivery to primary human astrocytes. *Int J Nanomedicine.* (2020) 15:3639–47. doi: 10.2147/IJN.S250865
68. Lasic DD. Novel applications of liposomes. *Trends Biotechnol.* (1998) 16:307–21. doi: 10.1016/S0167-7799(98)01220-7
69. Yadollahpour A, Venkateshwarlu G. Applications of gadolinium nanoparticles in magnetic resonance imaging: A review on recent advances in clinical imaging. *Int J Pharm Technol.* (2016) 8:11379–93. Available from: https://www.scopus.com/inward/record.uri?eid=2-s2.0-84992229880&partnerID=40&md5=d4a8f7ea8dd5f49ca2da14613902b215
70. Voinea M, Simionescu M. Designing of "intelligent" liposomes for efficient delivery of drugs. *J Cell Mol Med.* (2002) 6:465–74. doi: 10.1111/j.1582-4934.2002.tb00450.x
71. Torchilin VP. Recent advances with liposomes as pharmaceutical carriers. *Nat Rev Drug Discov.* (2005) 4:145–60. doi: 10.1038/nrd1632
72. Grange C, Geninatti-Crich S, Esposito G, Alberti D, Tei L, Bussolati B, et al. Combined delivery and magnetic resonance imaging of neural cell adhesion molecule-targeted doxorubicin-containing liposomes in experimentally induced Kaposi's sarcoma. *Cancer Res.* (2010) 70:2180–90. doi: 10.1158/0008-5472.CAN-09-2821
73. Papahadjopoulos D, Allen TM, Gabizon A, Mayhew E, Matthay K, Huang SK, et al. Sterically stabilized liposomes: improvements in pharmacokinetics and antitumor therapeutic efficacy. *Proc Natl Acad Sci USA.* (1991) 88:11460–4. doi: 10.1073/pnas.88.24.11460
74. Al-Jamal WT, Al-Jamal KT, Tian B, Lacerda L, Bomans PH, Frederik PM, et al. Lipid-quantum dot bilayer vesicles enhance tumor cell uptake and retention *in vitro* and *in vivo*. *ACS Nano.* (2008) 2:408–18. doi: 10.1021/nn700176a
75. Al-Jamal WT, Kostarelos K. Liposomes: from a clinically established drug delivery system to a nanoparticle platform for theranostic nanomedicine. *Acc Chem Res.* (2011) 44:1094–104. doi: 10.1021/ar200105p
76. Leung SJ, Romanowski M. Light-activated content release from liposomes. *Theranostics.* (2012) 2:1020–36. doi: 10.7150/thno.4847
77. Nie Y, Ji L, Ding H, Xie L, Li L, He B, et al. Cholesterol derivatives based charged liposomes for doxorubicin delivery: preparation, *in vitro* and *in vivo* characterization. *Theranostics.* (2012) 2:1092–103. doi: 10.7150/thno.4949
78. Muthu MS, Feng SS. Nanopharmacology of liposomes developed for cancer therapy. *Nanomedicine (Lond).* (2010) 5:1017–9. doi: 10.2217/nnm.10.75
79. Muthu MS, Kulkarni SA, Xiong J, Feng SS. Vitamin E TPGS coated liposomes enhanced cellular uptake and cytotoxicity of docetaxel in brain cancer cells. *Int J Pharm.* (2011) 421:332–40. doi: 10.1016/j.ijpharm.2011.09.045
80. Muthu MS, Kulkarni SA, Raju A, Feng SS. Theranostic liposomes of TPGS coating for targeted co-delivery of docetaxel and quantum dots. *Biomaterials.* (2012) 33:3494–501. doi: 10.1016/j.biomaterials.2012.01.036
81. Kataoka K, Harada A, Nagasaki Y. Block copolymer micelles for drug delivery: design, characterization and biological significance. *Adv Drug Deliv Rev.* (2001) 47:113–31. doi: 10.1016/S0169-409X(00)00124-1
82. Mahmud A, Xiong XB, Aliabadi HM, Lavasanifar A. Polymeric micelles for drug targeting. *J Drug Target.* (2007) 15:553–84. doi: 10.1080/10611860701538586
83. Sawant RR, Jhaveri AM, Koshkaryev A, Zhu L, Qureshi F, Torchilin VP. Targeted transferrin-modified polymeric micelles: enhanced efficacy *in vitro* and *in vivo* in ovarian carcinoma. *Mol Pharm.* (2014) 11:375–81. doi: 10.1021/mp300633f
84. Bogman K, Erne-Brand F, Alsenz J, Drewe J. The role of surfactants in the reversal of active transport mediated by multidrug resistance proteins. *J Pharm Sci.* (2003) 92:1250–61. doi: 10.1002/jps.10395
85. Zhan C, Li B, Hu L, Wei X, Feng L, Fu W, et al. Micelle-based brain-targeted drug delivery enabled by a nicotine acetylcholine receptor ligand. *Angew Chemie Int Ed.* (2011) 50:5482–5. doi: 10.1002/anie.201100875
86. Ning W, Shang P, Wu J, Shi X, Liu S. Novel amphiphilic, biodegradable, biocompatible, thermo-responsive ABA triblock copolymers based on PCL and PEG analogues *via* a combination of ROP and RAFT: Synthesis, characterization, and sustained drug release from self-assembled micelles. *Polymers (Basel).* (2018) 10:214. doi: 10.3390/polym10020214

87. Jones MC, Leroux JC. Polymeric micelles—a new generation of colloidal drug carriers. *Eur J Pharm Biopharm*. (1999) 48:101–11. doi: 10.1016/S0939-6411(99)00039-9
88. Torchilin VP. Targeted polymeric micelles for delivery of poorly soluble drugs. *Cell Mol Life Sci*. (2004) 61:2549–59. doi: 10.1007/s00018-004-4153-5
89. Vriezema DM, Comellas Aragonès M, Elemans JA, Cornelissen JJ, Rowan AE, Nolte RJ. Self-assembled nanoreactors. *Chem Rev*. (2005) 105:1445–89. doi: 10.1021/cr0300688
90. Torchilin VP, Lukyanov AN, Gao Z, Papahadjopoulos-Sternberg B. immunomicelles: targeted pharmaceutical carriers for poorly soluble drugs. *Proc Natl Acad Sci USA*. (2003) 100:6039–44. doi: 10.1073/pnas.0931428100
91. Mi Y, Liu Y, Feng SS. Formulation of Docetaxel by folic acid-conjugated d-α-tocopheryl polyethylene glycol succinate 2000 (Vitamin E TPGS(2k)) micelles for targeted and synergistic chemotherapy. *Biomaterials*. (2011) 32:4058–66. doi: 10.1016/j.biomaterials.2011.02.022
92. Kumar R, Kulkarni A, Nagesha DK, Sridhar S. *In vitro* evaluation of theranostic polymeric micelles for imaging and drug delivery in cancer. *Theranostics*. (2012) 2:714–22. doi: 10.7150/thno.3927
93. Liu Z, Liang XJ. Nano-carbons as theranostics. *Theranostics*. (2012) 2:235–7. doi: 10.7150/thno.4156
94. Savic R, Luo L, Eisenberg A, Maysinger D. Micellar nanocontainers distribute to defined cytoplasmic organelles. *Science*. (2003) 300:615–8. doi: 10.1126/science.1078192
95. Moghimi SM, Hunter AC, Murray JC, Szewczyk A. Cellular distribution of nonionic micelles. *Science*. (2004) 303:626–8. doi: 10.1126/science.303.5658.626
96. Kim SC, Kim DW, Shim YH, Bang JS, Oh HS, Kim SW, et al. *In vivo* evaluation of polymeric micellar paclitaxel formulation: toxicity and efficacy. (2001) 72:191–202. doi: 10.1016/S0168-3659(01)00275-9
97. Kim DW, Kim SY, Kim HK, Kim SW, Shin SW, Kim JS, et al. Multicenter phase II trial of Genexol-PM, a novel Cremophor-free, polymeric micelle formulation of paclitaxel, with cisplatin in patients with advanced non-small-cell lung cancer. *Ann Oncol*. (2007) 18:2009–14. doi: 10.1093/annonc/mdm374
98. Lee KS, Chung HC, Im SA, Park YH, Kim CS, Kim SB, et al. Multicenter phase II trial of Genexol-PM, a Cremophor-free, polymeric micelle formulation of paclitaxel, in patients with metastatic breast cancer. *Breast Cancer Res Treat*. (2008) 108:241–50. doi: 10.1007/s10549-007-9591-y
99. Lim WT, Tan EH, Toh CK, Hee SW, Leong SS, Ang PCS, et al. Phase I pharmacokinetic study of a weekly liposomal paclitaxel formulation (Genexol-PM) in patients with solid tumors. *Ann Oncol*. (2010) 21:382–8. doi: 10.1093/annonc/mdp315
100. Daniel MC, Astruc D. Gold nanoparticles: assembly, supramolecular chemistry, quantum-size-related properties, and applications toward biology, catalysis, and nanotechnology. *Chem Rev*. (2004) 104:293–346. doi: 10.1021/cr030698+
101. Xiao Y, Hong H, Matson VZ, Javadi A, Xu W, Yang Y, et al. Gold nanorods conjugated with doxorubicin and cRGD for Combined anticancer drug delivery and PET imaging. *Theranostics*. (2012) 2:757–68. doi: 10.7150/thno.4756
102. Chen H, Zhang X, Dai S, Ma Y, Cui S, Achilefu S, et al. Multifunctional gold nanostar conjugates for tumor imaging and combined photothermal and chemo-therapy. *Theranostics*. (2013) 3:633–49. doi: 10.7150/thno.6630
103. Rengan AK, Jagtap M, De A, Banerjee R, Srivastava R. Multifunctional gold coated thermo-sensitive liposomes for multimodal imaging and photo-thermal therapy of breast cancer cells. *Nanoscale*. (2014) 6:916–23. doi: 10.1039/C3NR04448C
104. Connor EE, Mwamuka J, Gole A, Murphy CJ, Wyatt MD. Gold nanoparticles are taken up by human cells but do not cause acute cytotoxicity. *Small*. (2005) 1:325–7. doi: 10.1002/smll.200400093
105. Kumar R, Korideck H, Ngwa W, Berbeco RI, Makrigiorgos GM, Sridhar S. Third generation gold nanoplatform optimized for radiation therapy. *Transl Cancer Res*. (2013) 2:10.3978/j.issn.2218-676X.2013.07.02. doi: 10.3978/j.issn.2218-676X.2013.07.02
106. Han G, Martin CT, Rotello VM. Stability of gold nanoparticle-bound DNA toward biological, physical, and chemical agents. *Chem Biol Drug Des*. (2006) 67:78–82. doi: 10.1111/j.1747-0285.2005.00324.x
107. Lee SM, Kim HJ, Kim SY, Kwon MK, Kim S, Cho A, et al. Drug-loaded gold plasmonic nanoparticles for treatment of multidrug resistance in cancer. *Biomaterials*. (2014) 35:2272–82. doi: 10.1016/j.biomaterials.2013.11.068
108. Heo DN, Yang DH, Moon HJ, Lee JB, Bae MS, Lee SC, et al. Gold nanoparticles surface-functionalized with paclitaxel drug and biotin receptor as theranostic agents for cancer therapy. *Biomaterials*. (2012) 33:856–66. doi: 10.1016/j.biomaterials.2011.09.064
109. Liu L, Yong KT, Roy I, Law WC, Ye L, Liu J, et al. Bioconjugated pluronic triblock-copolymer micelle-encapsulated quantum dots for targeted imaging of cancer: *in vitro* and *in vivo* studies. *Theranostics*. (2012) 2:705–13. doi: 10.7150/thno.3456
110. Baughman RH, Zakhidov AA, De Heer WA. Carbon nanotubes - The route toward applications. *Science*. (2002) 297:787–92. doi: 10.1126/science.1060928
111. McDevitt MR, Chattopadhyay D, Kappel BJ, Jaggi JS, Schiffman SR, Antczak C, et al. Tumor targeting with antibody-functionalized, radiolabeled carbon nanotubes. *J Nucl Med*. (2007) 48:1180–9. doi: 10.2967/jnumed.106.039131
112. Porter AE, Gass M, Muller K, Skepper JN, Midgley PA, Welland M. Direct imaging of single-walled carbon nanotubes in cells. *Nat Nanotechnol*. (2007) 2:713–7. doi: 10.1038/nnano.2007.347
113. Fubini B, Ghiazza M, Fenoglio I. Physico-chemical features of engineered nanoparticles relevant to their toxicity. *Nanotoxicology*. (2010) 4:347–63. doi: 10.3109/17435390.2010.509519
114. Boncel S, Müller KH, Skepper JN, Walczak KZ, Koziol KK. Tunable chemistry and morphology of multi-wall carbon nanotubes as a route to non-toxic, theranostic systems. *Biomaterials*. (2011) 32:7677–86. doi: 10.1016/j.biomaterials.2011.06.055
115. Nerl HC, Cheng C, Goode AE, Bergin SD, Lich B, Gass M, et al. Imaging methods for determining uptake and toxicity of carbon nanotubes *in vitro* and *in vivo*. *Nanomedicine (Lond)*. (2011) 6:849–65. doi: 10.2217/nnm.11.87
116. Chen Z, Ma L, Liu Y, Chen C. Applications of functionalized fullerenes in tumor theranostics. *Theranostics*. (2012) 2:238–50. doi: 10.7150/thno.3509
117. Shen H, Zhang L, Liu M, Zhang Z. Biomedical applications of graphene. *Theranostics*. (2012) 2:283–94. doi: 10.7150/thno.3642
118. Yang K, Feng L, Shi X, Liu Z. Nano-graphene in biomedicine: theranostic applications. *Chem Soc Rev*. (2013) 42:530–47. doi: 10.1039/C2CS35342C
119. Robinson JT, Welsher K, Tabakman SM, Sherlock SP, Wang H, Luong R, et al. High performance *in vivo* near-IR (>1 μm) imaging and photothermal cancer therapy with carbon nanotubes. *Nano Res*. (2010) 3:779–93. doi: 10.1007/s12274-010-0045-1
120. Das M, Datir SR, Singh RP, Jain S. Augmented anticancer activity of a targeted, intracellularly activatable, theranostic nanomedicine based on fluorescent and radiolabeled, methotrexate-folic acid-multiwalled carbon nanotube conjugate. *Mol Pharm*. (2013) 10:2543–57. doi: 10.1021/mp300701e
121. Riehemann K, Schneider SW, Luger TA, Godin B, Ferrari M, Fuchs H. Nanomedicine–challenge and perspectives. *Angew Chem Int Ed Engl*. (2009) 48:872–97. doi: 10.1002/anie.200802585
122. Shi J, Kantoff PW, Wooster R, Farokhzad OC. Cancer nanomedicine: progress, challenges and opportunities. *Nat Rev Cancer*. (2017) 17:20–37. doi: 10.1038/nrc.2016.108
123. Dilnawaz F, Acharya S, Sahoo SK. Recent trends of nanomedicinal approaches in clinics. *Int J Pharm*. (2018) 538:263–78. doi: 10.1016/j.ijpharm.2018.01.016
124. Szebeni J, Storm G. Complement activation as a bioequivalence issue relevant to the development of generic liposomes and other nanoparticulate drugs. *Biochem Biophys Res Commun*. (2015) 468:490–7. doi: 10.1016/j.bbrc.2015.06.177
125. Jackman JA, Mészáros T, Fülöp T, Urbanics R, Szebeni J, Cho NJ. Comparison of complement activation-related pseudoallergy in miniature and domestic pigs: foundation of a validatable immune toxicity model. *Nanomedicine*. (2016) 12:933–43. doi: 10.1016/j.nano.2015.12.377
126. Hua S, de Matos MBC, Metselaar JM, Storm G. Current trends and challenges in the clinical translation of nanoparticulate nanomedicines: pathways for translational development and commercialization. *Front Pharmacol*. (2018) 9:790. doi: 10.3389/fphar.2018.00790

127. Dreifuss T, Betzer O, Shilo M, Popovtzer A, Motiei M, Popovtzer R, et al. challenge for theranostics: is the optimal particle for therapy also optimal for diagnostics? *Nanoscale.* (2015) 7:15175–84. doi: 10.1039/C5NR03119B
128. Gaspar R. Regulatory issues surrounding nanomedicines: setting the scene for the next generation of nanopharmaceuticals. *Nanomedicine (Lond).* (2007) 2:143–7. doi: 10.2217/17435889.2.2.143
129. Tinkle S, Mcneil SE, Mühlebach S, Bawa R, Borchard G, Barenholz YC, et al. Nanomedicines: Addressing the scientific and regulatory gap. *Ann N Y Acad Sci.* (2014) 1313:35–56. doi: 10.1111/nyas.12403
130. Barenholz Y. Doxil®–the first FDA-approved nano-drug: lessons learned. *J Controll Release.* (2012) 160:117–34. doi: 10.1016/j.jconrel.2012.03.020
131. Gabizon A, Shmeeda H, Barenholz Y. Pharmacokinetics of pegylated liposomal doxorubicin: review of animal and human studies. *Clin Pharmacokinet.* (2003) 42:419–36. doi: 10.2165/00003088-200342050-00002
132. Wiesing U, Clausen J. The clinical research of nanomedicine: a new ethical challenge? *Nanoethics.* (2014) 8:19–28. doi: 10.1007/s11569-014-0191-0
133. Resnik DB, Tinkle SS. Ethical issues in clinical trials involving nanomedicine. *Contemp Clin Trials.* (2007 J) 28:433–41. doi: 10.1016/j.cct.2006.11.001
134. Hofmann-Amtenbrink M, Grainger DW, Hofmann H. Nanoparticles in medicine: current challenges facing inorganic nanoparticle toxicity assessments and standardizations. *Nanomed Nanotechnol Biol Med.* (2015) 11:1689–94. doi: 10.1016/j.nano.2015.05.005
135. Hare JI, Lammers T, Ashford MB, Puri S, Storm G, Barry ST. Challenges and strategies in anti-cancer nanomedicine development: An industry perspective. *Adv Drug Deliv Rev.* (2017) 108:25–38. doi: 10.1016/j.addr.2016.04.025
136. Sainz V, Conniot J, Matos AI, Peres C, Zupancic E, Moura L, et al. Regulatory aspects on nanomedicines. *Biochem Biophys Res Commun.* (2015) 468:504–10. doi: 10.1016/j.bbrc.2015.08.023
137. Accomasso L, Cristallini C, Giachino C. Risk assessment and risk minimization in nanomedicine: a need for predictive, alternative, and 3Rs strategies. *Front Pharmacol.* (2018) 9:228. doi: 10.3389/fphar.2018.00228
138. Ragelle H, Danhier F, Préat V, Langer R, Anderson DG. Nanoparticle-based drug delivery systems: a commercial and regulatory outlook as the field matures. *Expert Opin Drug Deliv.* (2017) 14:851–64. doi: 10.1080/17425247.2016.1244187

Conflict of Interest: The authors declare that the research was conducted in the absence of any commercial or financial relationships that could be construed as a potential conflict of interest.

Publisher's Note: All claims expressed in this article are solely those of the authors and do not necessarily represent those of their affiliated organizations, or those of the publisher, the editors and the reviewers. Any product that may be evaluated in this article, or claim that may be made by its manufacturer, is not guaranteed or endorsed by the publisher.

frontiers in Medicine

ORIGINAL RESEARCH
published: 25 February 2022
doi: 10.3389/fmed.2022.843749

Identification of Signature Genes and Characterizations of Tumor Immune Microenvironment and Tumor Purity in Lung Adenocarcinoma Based on Machine Learning

Haiming Feng[1†], *Ye Zhao*[2†], *Weijian Yan*[1], *Xiaoping Wei*[1], *Junping Lin*[1], *Peng Jiang*[1], *Cheng Wang*[1] *and Bin Li*[1*]

[1] Department of Thoracic Surgery, Second Clinical Medical College, Lanzhou University, Lanzhou, China, [2] First Clinical Medical College, Lanzhou University, Lanzhou, China

OPEN ACCESS

Edited by:
Ali Yadollahpour,
The University of Sheffield,
United Kingdom

Reviewed by:
Shengye Wang,
Zhejiang Cancer Hospital, China
Fangzhou Song,
Chongqing Medical University, China

***Correspondence:**
Bin Li
dr.leebin@outlook.com

[†] *These authors have contributed equally to this work*

Specialty section:
This article was submitted to Precision Medicine, a section of the journal Frontiers in Medicine

Received: *26 December 2021*
Accepted: *12 January 2022*
Published: *25 February 2022*

Citation:
Feng H, Zhao Y, Yan W, Wei X, Lin J, Jiang P, Wang C and Li B (2022) Identification of Signature Genes and Characterizations of Tumor Immune Microenvironment and Tumor Purity in Lung Adenocarcinoma Based on Machine Learning. Front. Med. 9:843749. doi: 10.3389/fmed.2022.843749

The implication of the Estimation of Stromal and Immune cells in Malignant tumor tissues using expression data (ESTIMATE) method to determine the tumor microenvironment (TME) and tumor immune score including tumor purity represents an efficient method to identify and assess biomarkers for immunotherapy response in precision medicine. In this study we utilized a machine learning algorithm to analyze the Cancer Genome Atlas (TCGA) and Gene Expression Omnibus database (GEO) lung adenocarcinoma (LUAD) transcriptome data to evaluate the association between TME and tumor purity. Furthermore, we investigated whether fewer TME components or a few dominant genes can infer tumor purity. The results indicated that the 29 immune infiltrating components determined by the ssGSEA method could screen the 5 TME components [chemokine C-C-Motif receptor (CCR), T-helper-cells, Check-point, Treg, and tumor-infiltrating lymphocytes (TIL)] that significantly contributed the most to tumor purity prediction through regression tree and random forest regression methods. The findings revealed that higher activity of these five immune infiltrating components significantly lowered the tumor purity. Moreover, 5 TME components contributed significantly to the improvement of Mean Square Error (MES); therefore, we selected these five sets' genes and analyzed survival data to establish a prognostic model. We screened out 11 prognostic-related genes and constructed a risk model comprising 11 genes with good predictive value for patients' prognosis. Furthermore, we obtained four genes (GIMAP6, CD80, IL16, and CCR2) that had predictive advantages for tumor purity using random forest classification and random forest regression. The comprehensive score of genes for tumor purity prediction (CSGTPP) was obtained by least absolute shrinkage and selection operator (LASSO) regression indicated that four genes could be successfully used to classify high and low CSGTPP samples and that tumor purity was negatively correlated with CSGTPP. Survival analysis revealed that the higher the CSGTPP, the better the

prognosis of patients. The association between a cluster of differentiation 274 (CD274) and CSGTPP revealed a higher expression of CD274 in the high CSGTPP group. Collectively, we speculated that CSGTPP could serve as a predictor of the response to immunotherapy and a promising indicator of immunotherapy effect.

Keywords: lung adenocarcinoma, machine learning, tumor immune microenvironment, tumor purity, gene expression, signature genes

INTRODUCTION

The tumor microenvironment (TME) represents a dynamic cellular milieu consisting of tumor cells, extracellular matrix (ECM), the blood and lymphatic vasculature, stroma, fibroblasts, infiltrating immune cells, and neighboring tumor related non-tumor cells. The immune system plays a critical role in immunosurveillance, as the immune cells of the immune system can recognize and eliminate tumor cells within the TME, thereby contributing to tumor progression. However, to evade the immune surveillance, tumor cells adopt multiple strategies to avoid immune recognition and instigate an immunosuppressive TME. Accumulating evidence indicates that defects in any of these mechanisms might contribute to the failure of the anti-tumor immunity and immune escape (1). Different tumor types adopt different strategies to escape the immune surveillance and killing of tumor cells by the immune system, thereby generating immune tolerance and promoting tumor occurrence and development (2). Immunotherapy, aiming to restore and boost the body's natural defenses to eradicate tumor cells, has emerged as a breakthrough therapeutic strategy for cancer. Several classes have emerged within immunotherapeutic agents, including monoclonal antibody immune checkpoint inhibitors, therapeutic antibodies, cancer vaccines, cell therapy, and small molecule inhibitors (3). In particular, the immune checkpoint inhibitors have shown potent anti-tumor activity across multiple malignancies such as melanoma, non-small cell lung cancer, kidney cancer, and prostate cancer. Several immunotherapy drugs have been approved by the US FDA (Food and Drug Administration, FDA) for clinical application (4). Immunotherapy can produce a more significant sustained response in patients with advanced cancer than conventional chemotherapy (5). However, this response only occurs in a small subset of patients. The efficacy of immunotherapy usually depends on the infiltration of immune cells into the TME. The immune cells of immune systems infiltrate into the TME and contribute to the modulation of tumor progression. TME is highly heterogeneous and consists of tumor cells, stromal cells, ECM, and immune cells that drive tumor cells fate to progression and metastasis. The immune system *in vitro* can recognize tumor antigens and kill tumor cells. Increasing studies have highlighted the complex and dynamic interactions between cells of the immune system and the TME in cancer progression. Moreover, TME plays an essential role in suppressing or enhancing the immune response. Understanding the complexity of interactions between TME and the immune cells will help select patients for immunotherapy and improve the curative effect of patients with immunotherapy. Tumor purity represents the proportion of tumor cells in tumor tissue (6). Studies have shown that tumor purity is significantly associated with the clinical characteristics, genome expression, tumor's biological characteristics, and prognosis of patients with cancer. It is noteworthy that ignoring the impact of tumor purity can lead to systematic bias in tumor genomic analyses, recurrence risk, and efficacy prediction. An accurate assessment of tumor purity is helpful to analyze tumor samples objectively. Therefore, the present study aimed to investigate the relationship between the immune microenvironment and Lung adenocarcinoma (LUAD) tumor purity through machine learning algorithms. And explored if tumor purity can be inferred from the genomic analyses, and investigated the correlation between tumor purity and immunotherapy.

MATERIALS AND METHODS

Data Source and Pre-processing

The RNA-Seq based transcriptome profiles (FPKM; Fragments per Kilobase of transcript per Million mapped reads) and corresponding clinical data of LUAD patients were downloaded from the TCGA portal, the gdc-client software download tool. Additionally, the expression profiles of LUAD patients (GSE68465, sequenced using Affymetrix, HG-U133A plus 2.0 Array, up to November 2020) were also obtained from the GEO database (http://www.ncbi.nlm.nih.gov/geo/). All analyses were performed using R software (R Foundation for Statistical Computing, Vienna, Austria, 3.4.1 Version).

Assessment of the Degree of Tumor Immune Infiltration

Using the most well-recognized and commonly used immune cell marker genes (7), we assessed the infiltration of different types of immune cells by single-sample Gene Set Enrichment Analysis (ssGSEA) with Gene Set Variation Analysis (GSVA) package in R package. Subsequently, based on the ssGSEA value, the samples were divided into high, medium, and low immune activity clusters.

Calculation of the Immune Score of the TME

We obtained stromal score, immune score, estimate score, and tumor purity based on the transformed expression matrix, and tumor purity was calculated through the "Estimate" R package (8).

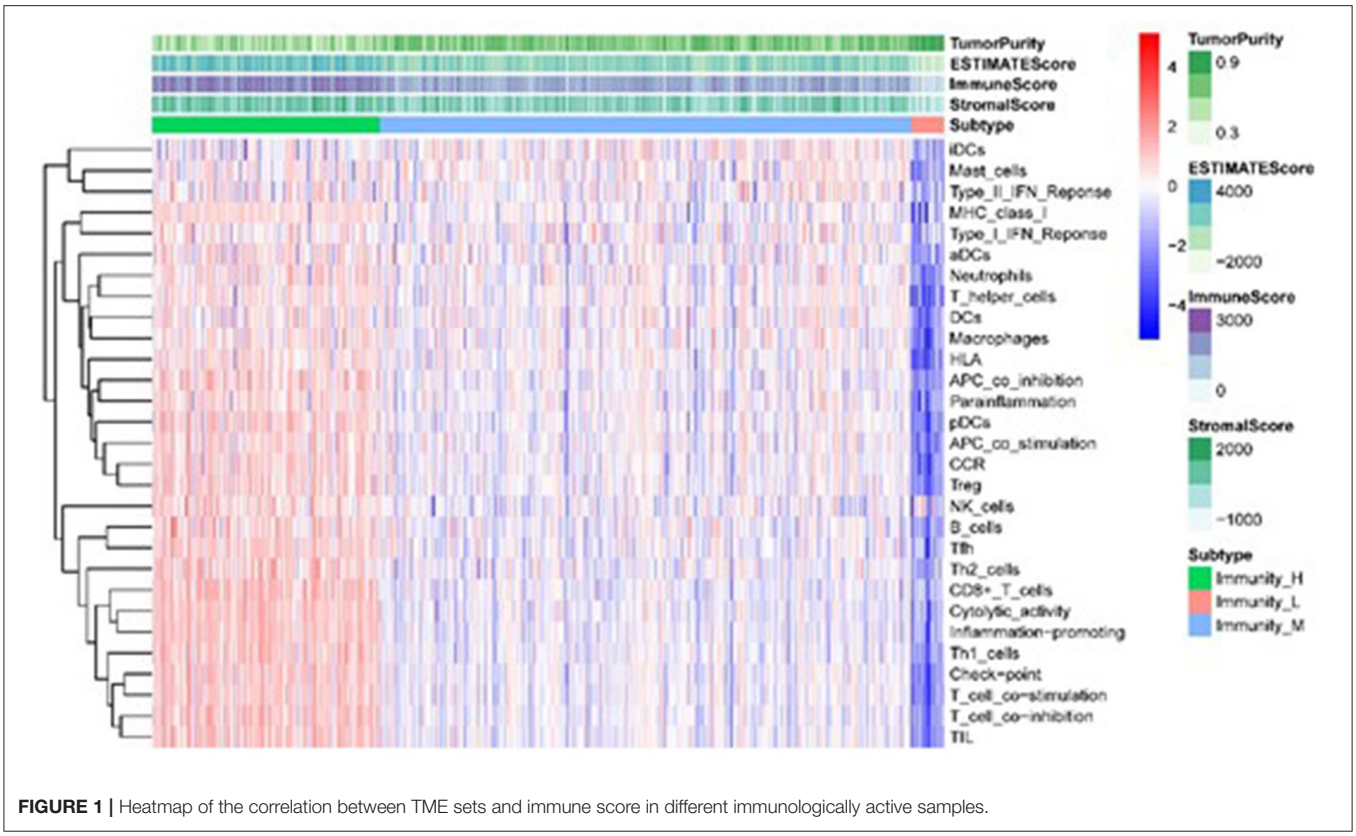

FIGURE 1 | Heatmap of the correlation between TME sets and immune score in different immunologically active samples.

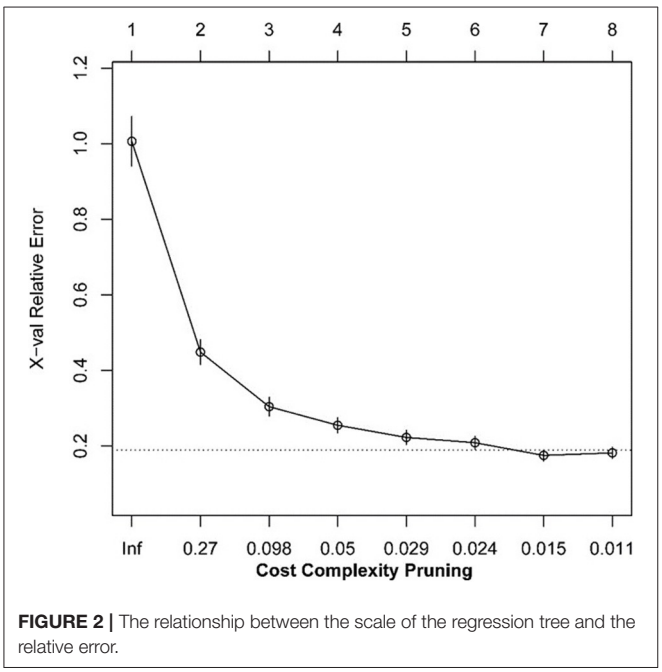

FIGURE 2 | The relationship between the scale of the regression tree and the relative error.

Determination of the Primary Immune Infiltration Gene Sets Using Machine Learning

Using regression trees and random forest regression, we established a regression model and assumed that immune infiltration and immune purity were correlated. Then, based on the ssGSEA sets, we selected the ssGSEA sets that most significantly contributed to the improvement in Mean Square Error (MES) with "partykit" and caret package in R. TCGA data were randomly divided into training set and validation set with the ratio of 7:3, GSE68465 data were used as the test set.

Correlation Between Target ssGSEA Sets and Tumor Purity

The association between the target ssGSEA sets value and tumor purity in high, medium, and low immunocompetent samples was determined using the "ggally" package in R.

Survival Analysis of Target ssGSEA Sets and Tumor Purity

According to the target, ssGSEA sets value and tumor purity; the samples were divided into high and low groups. We further investigated the clinical data and survival outcome (excluding samples with missing clinical data and survival time of fewer than 30 days) to assess the association between each clinical characteristic and prognosis with the "survminer" package in R software.

LASSO Regression Analysis for the Construction of the Prognostic Gene Model

Univariate Cox proportional hazards regression analysis was performed to screen target ssGSEA sets genes significantly

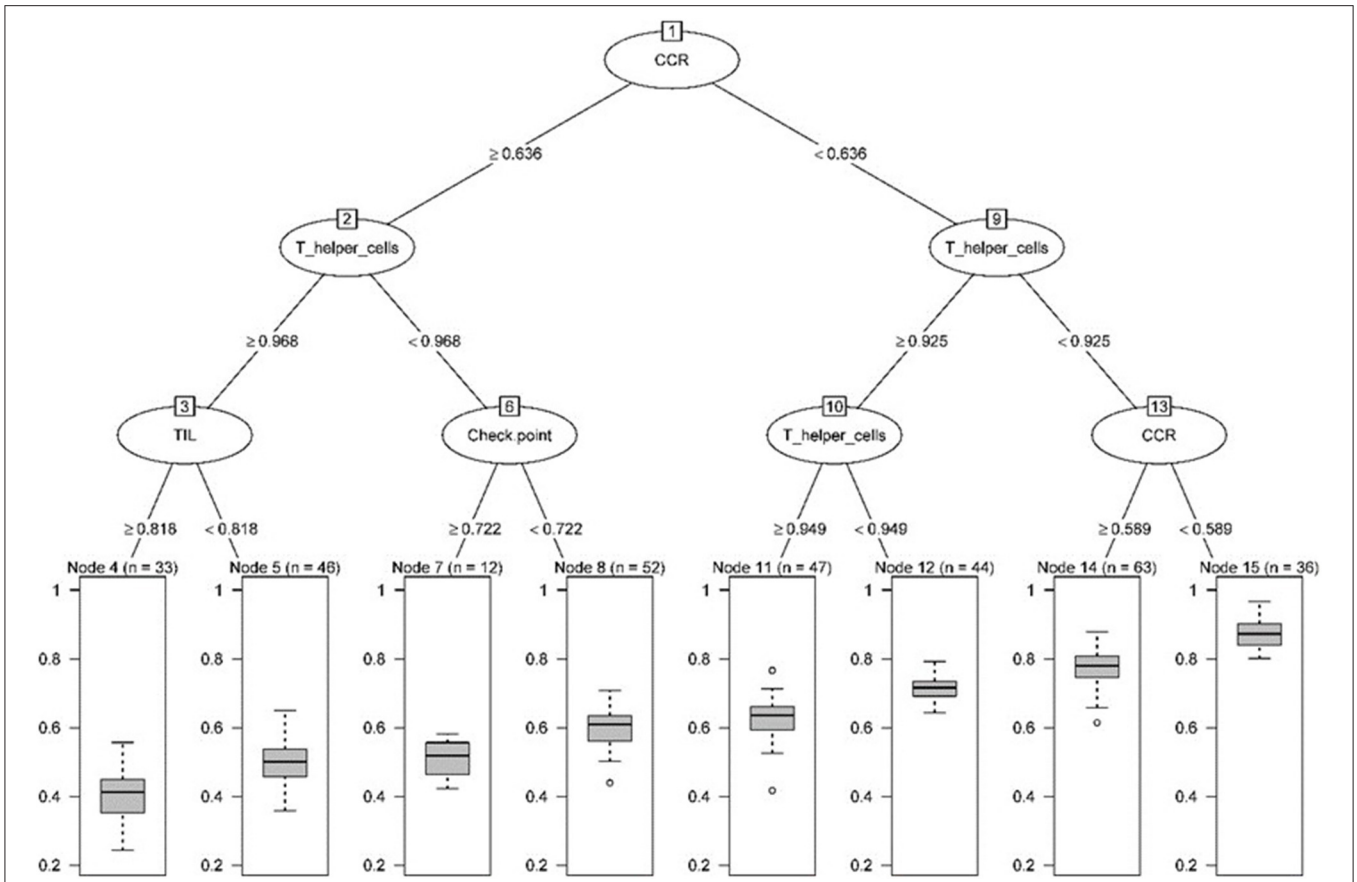

FIGURE 3 | Pruning tree containing the number of splits, nodes, observation TME sets, and prediction results.

associated with overall survival (OS) in the TCGA LUAD dataset. Then, using R-glmnet package, we performed LASSO Cox regression analysis of the identified OS-related genes. Multivariable Cox proportional hazards regression analysis was performed to establish the prognosis model of target ssGSEA sets genes. The LUAD samples were divided into high risk and low risk by the median risk score; the Kaplan–Meier curve was constructed, and the log-rank test was conducted to compare the survival differences between the two groups. The ROC curve was used to evaluate the accuracy of the model. GSE68465 data was utilized as the validation set to further evaluate the model.

The Implication of Target Genes for Tumor Purity Classification

We established the corresponding relationship between the sample gene expression matrix and the tumor purity after screening the target gene using Cox proportional hazards regression analysis. Using the random forest regression method R-random Forest package, we constructed the model to evaluate the linear relationship between the target genes and the tumor purity and screen the most significantly contributed genes to the improvement in MES value. Then, we divided the samples into two groups according to tumor purity. Subsequently, a relationship with gene expression data was analyzed to evaluate

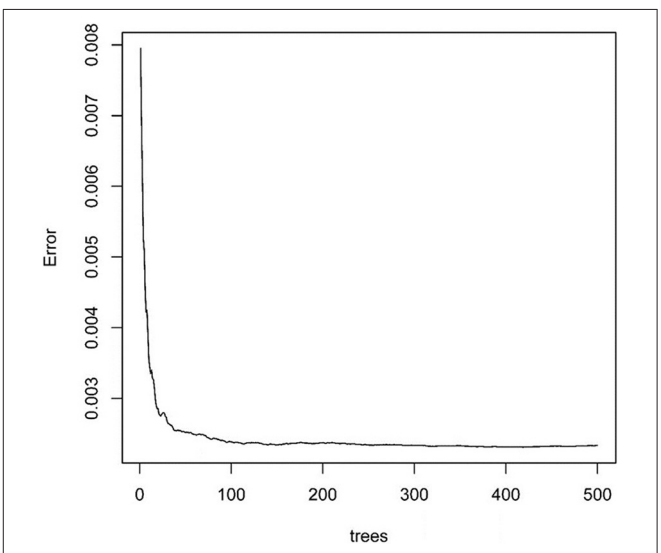

FIGURE 4 | The relationship between split tree count and error.

the effect of the target genes' classification on tumor purity by random forest classification method achieved by R-random Forest package. At the same time, the average reduction of the

Gini index was used to evaluate the contribution of the genes to the classification, and significantly associated genes were selected based on the method of random forest regression. TCGA data were divided into a training set and validation set at a ratio of 7:3; GSE68465 data was used as a test set.

The Implication of Target Genes in the Sample Classification

In order to visualize the effect of the target genes on the sample classification, we used Principal Component Analysis (PCA) to classify the samples corresponding to the target gene by using the R packages "FactoMineR" and "factoextra." In this step, we sorted the samples of TCGA and GEO according to tumor purity. The first 33% of samples presented low purity samples, and the last 33% of samples represented high purity samples.

Lasso Regression Analysis of Target Gene to Predict the Effect of Immunotherapy

We constructed a LASSO regression model from the target genes screened in TCGA LUAD data and the tumor purity of the corresponding sample to calculate the comprehensive score of genes for tumor purity prediction (CSGTPP) = $\sum$ Xα* coef α, where coef α is coefficient, and Xα is gene relative expression, the samples were divided into high CSGTPP and low groups. PCA was applied to analyze the classification effect of the target genes and the survival prognosis of the two groups. And then, we analyzed the differences in target genes and tumor purity between the two groups. Finally, we further explored immunotherapy's effect by comparing the differences in the immune target gene, CD274, in the two groups.

RESULTS

ssGSEA Sets Value and Tumor Purity

We identified 535 TCGA LUAD gene expression matrices and 443 GEO gene expression matrices and analyzed the results of 29 immune infiltration sets in LUAD. Simultaneously, we determined tumor purity scores by the ESTIMATE method. We excluded samples with incomplete survival data and survival time <30 days after sorting out the clinical data. A total of 443 TCGA clinical survival samples and 442

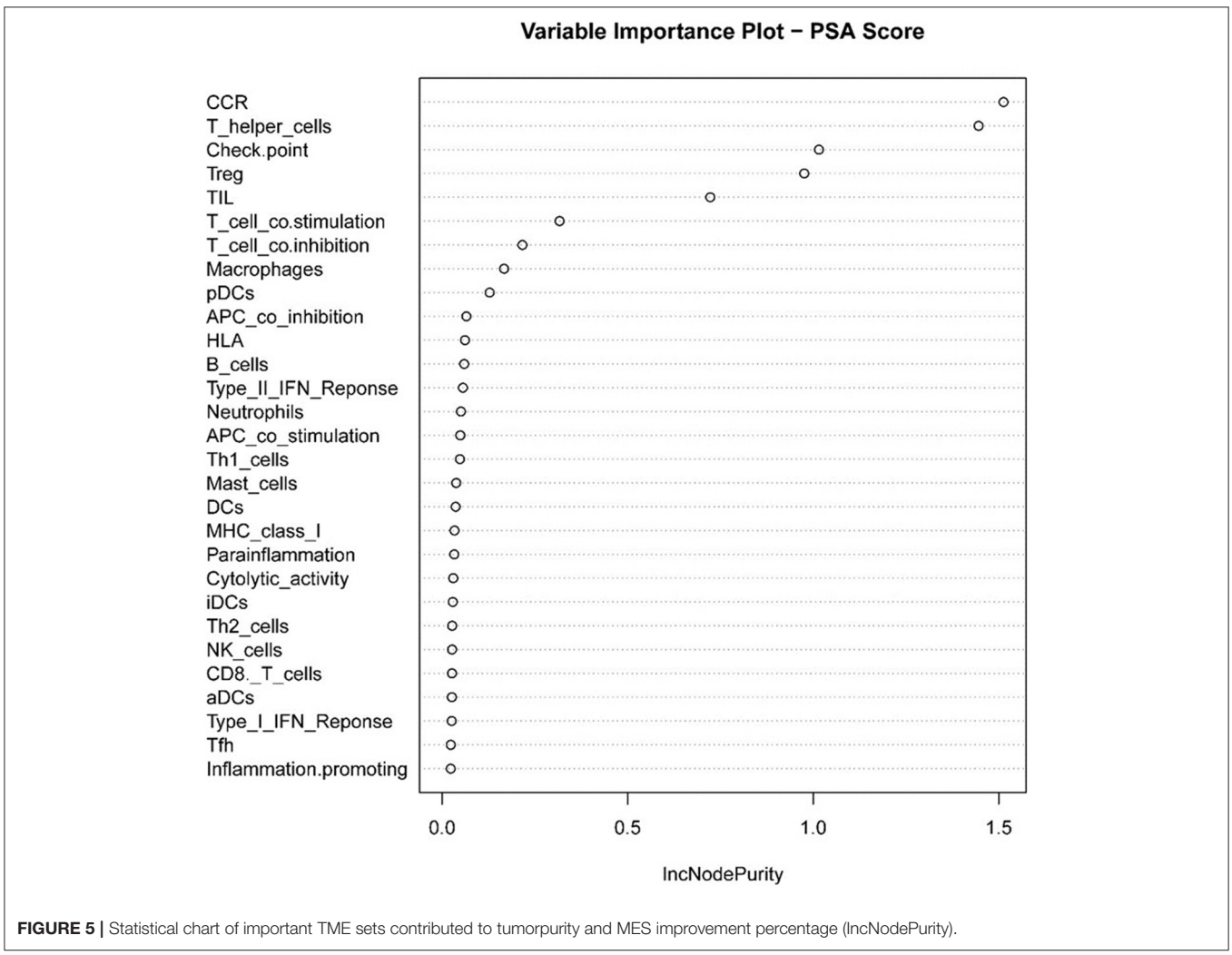

FIGURE 5 | Statistical chart of important TME sets contributed to tumorpurity and MES improvement percentage (IncNodePurity).

GEO clinical samples were included to construct the LASSO regression model. However, we eliminated clinical samples with incomplete TNM data, and finally, 307 TCGA clinical samples and 339 GEO clinical samples were selected for subsequent analysis.

Distribution of Immune Infiltrating Gene Sets and Tumor Purity in Different Immune Active Samples

Using the 29 immune infiltration sets with the "sparcl" package in R, we calculated the immune activity of 535 TCGA and 443 GEO LUAD samples and divided them into three groups of low, medium, and high. Cluster analyses indicated the immune infiltration and immune scores of the three groups of tumor samples, and further analysis of the results revealed that with the increase in immune activity, 29 immune infiltrating gene sets and estimateScore were positively correlated. In contrast, tumor purity decreased with the increase in tumor immune activity (**Figure 1**).

Predominant Immune Infiltration Gene Sets

We transformed 29 immune infiltration sets and tumor purity into corresponding matrices, divided TCGA LUAD data into training set and validation set at a ratio of 7:3, and used regression tree to build the predictive model, GEO LUAD data was used as the test set to verify the model. MES is an excellent indicator of the calibration model. After constructing the model with the "Rpart" function and using 10-fold cross-validation, it was found that when the number of splits was 6, there was the smallest splitting error (xerror = 0.175; **Figure 2**); therefore, we chose the tree size to be 7, and used the "partykit" package to reduce branches, and apparently received 8 prediction results (**Figure 3**). Moreover, we used the "predict" function to envisage the validation set and the calculated MES to be 0.004, indicating that model was stable. Similarly, we used GEO data for testing, and the calculated MES value was 0.083. The model exhibited a good countermeasure effect.

Next, we used the "randomForest" function to perform regression analysis on the aforementioned data. We estimated that the number of specific optimal trees was 419, but from the relationship between the MES and the number of trees in the model, it could be observed that as the number of trees increases to about 100 trees, the error improvement was not evident, therefore, we chose 100 trees as the random forest regression (**Figure 4**). The resulting MES obtained was 0.002, and nearly 89.28% of the variance was explained. To end, we analyzed the

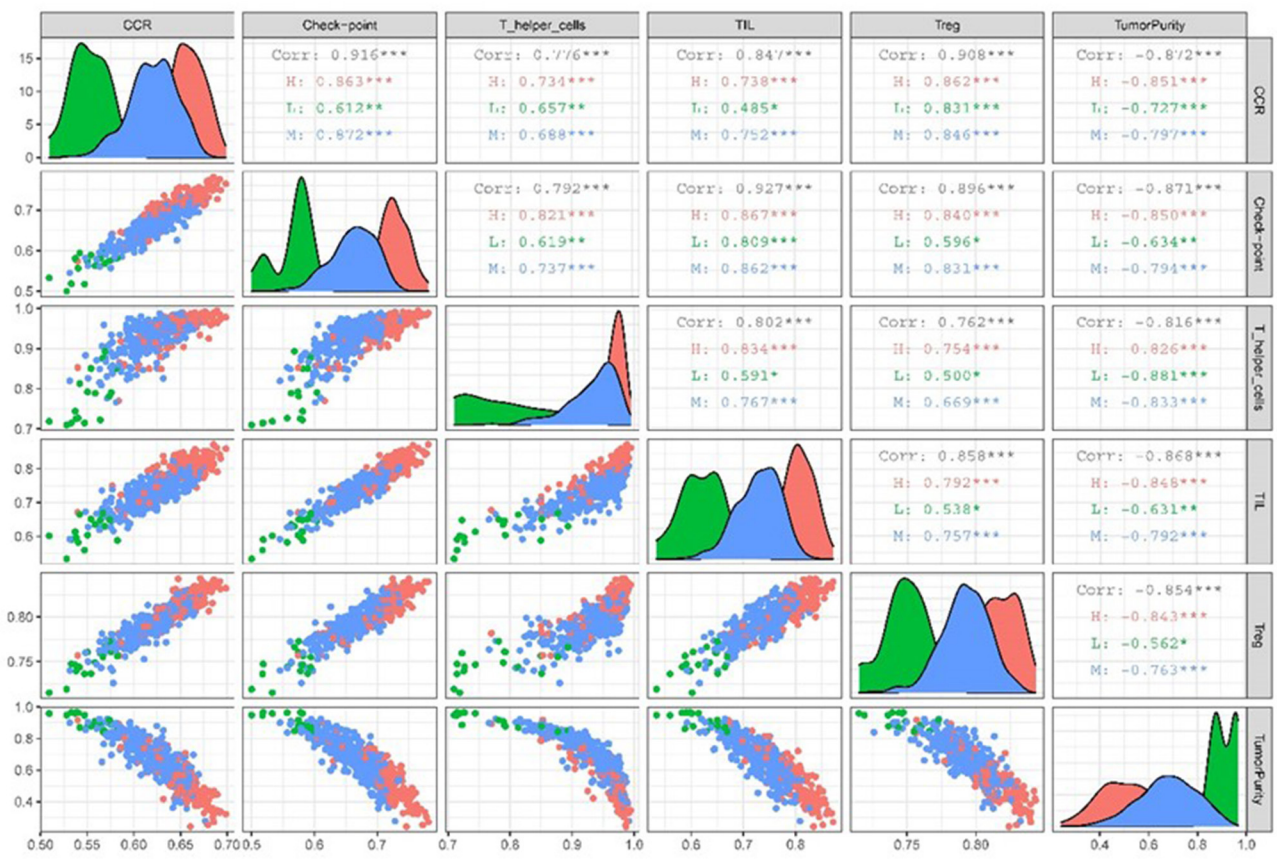

FIGURE 6 | Scatter plot of correlation matrix between target TME sets and tumor purity in different immunocompetent samples.

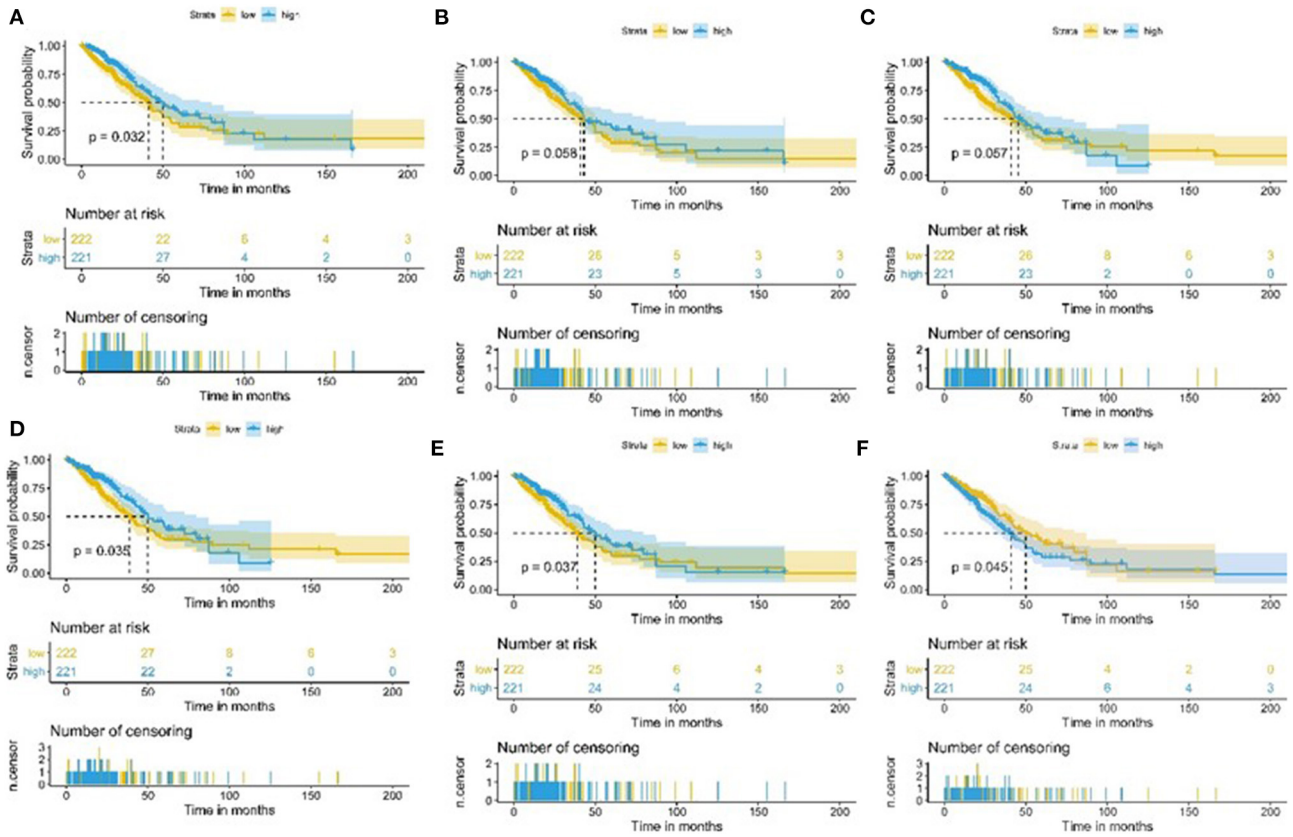

FIGURE 7 | Kaplan-Meier curve of patients with high and low TME sets and tumor purity group. **(A)** Kaplan-Meier curve of patients with high and low CCR2 group; **(B)** Kaplan-Meier curve of patients with high and low T-helper-cells group; **(C)** Kaplan-Meier curve of patients with high and low Check-point group; **(D)** Kaplan-Meier curve of patients with high and low Treg group; **(E)** Kaplan-Meier curve of patients with high and low TIL group; **(F)** Kaplan-Meier curve of patients with high and low Tumorpurity group.

critical scalar that drives the result. As represented in **Figure 5**, CCR, T-helper-cells, Check-point, Treg, and TIL contributed significantly to the improvement of MES. The model presented good MES values with the validation and test sets, which were found to be 0.002 and 0.087, respectively. On comparison of the two methods of regression tree and random forest regression, the results indicated that both models had good predictive value. Therefore, we selected CCR, T-helper-cells, Check-point, Treg, and TIL immune infiltration sets as our target sets.

Association Between Target ssGSEA Sets and Tumor Purity

We used the "Ggally" package in R software to estimate the correlation between target immune infiltration sets and tumor purity among different immunologically active samples from TCGA LUAD data. The results revealed that tumor purity and immune infiltration among different immunologically active samples were significantly negatively correlated (**Figure 6**).

Survival Prognosis Analysis of Target ssGSEA Sets and Tumor Purity

We used 443 TCGA LUAD samples to investigate further the relationship between target immune infiltration sets and tumor purity and survival prognosis; the results suggested that the lower the purity of the tumor, the better the prognosis. Conversely, it was also evident that the higher the degree of immune infiltration, the better the patient's survival (**Figure 7**).

Prognostic Model and Genes Associated With Prognosis

One hundred and three immune infiltrating genes from CCR, T-helper-cells, Check-point, Treg, and TIL sets of TCGA LUAD data were analyzed by Univariate Cox regression. There were 21 genes associated with a prognosis and entered into the LASSO regression analysis (**Figure 8**); a total of 11 genes (IL3RA, MAGEH1, CCR2, ACP5, TGFBI, CHRNA6, KSR1, GIMAP6, CD80, IL16, and CD52) were identified for building model. The coefficients of each gene were presented in **Table 1**.

We assessed the prognostic value of risk scores, which were estimated with the formula risk score = $\sum$ Xβ* coef β, where coef β was coefficient, and Xβ was gene relative expression. For TCGA LUAD data, the risk score in both univariate and multivariate analysis was significantly related to overall survival (OS) (HR = 3.179, 95% CI = 2.111–4.786, $P < 0.001$; HR = 2.069, 95%

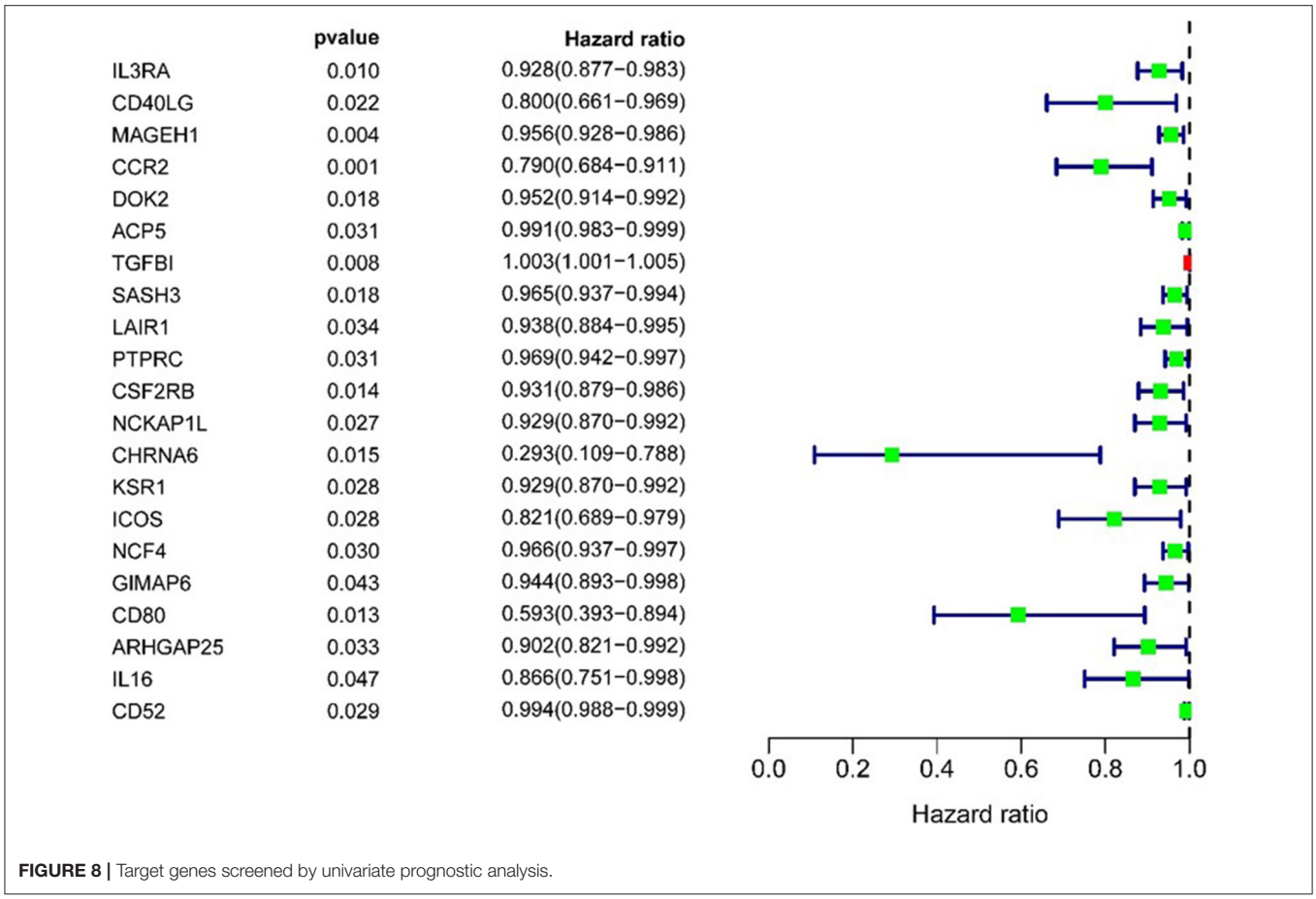

FIGURE 8 | Target genes screened by univariate prognostic analysis.

TABLE 1 | The coefficients of genes for building model.

Genes	Coefficients
IL3RA	−0.0323529240412679
MAGEH1	−0.0313240392509636
CCR2	−0.258547384333454
ACP5	−0.00104506851750573
TGFBI	0.00291649350382021
CHRNA6	−0.473404652074516
KSR1	−0.0660881115987976
GIMAP6	0.020759981275271
CD80	−0.188951143790105
IL16	0.128342508954468
CD52	−0.000223112433304806

CI = 1.363–3.139, $P < 0.001$, respectively.) (**Figures 9A,B**). It was observed that the patients with low-risk scores exhibited significantly better prognosis than those with a high-risk score (**Figures 10A,B**) both in TCGA and GEO LUAD data by the Kaplan–Meier cumulative curve. The AUC of risk score was 0.68, which implied that the Cox model could pretty well-predict the prognosis (**Figure 9C**).

The Implication of Target Genes for Tumor Purity Classification

We established the corresponding relationship between the 11 genes expression matrix and the tumor purity and performed random forest regression to predict the linear relationship between 11 gene expression and tumor purity. As mentioned before, 465 TCGA LUAD data were divided into a training set and validation set at a ratio of 7:3, while 443 GEO LUAD data was used as the test set to verify the model. We selected 100 trees for the random forest regression analysis, the resulting MES was 0.003, and almost 85.45% of the variance was explained. Finally, we obtained four genes (CD80, CCR2, GIMAP6, and IL16) that significantly improved MES. The model exhibited good MES values on the validation and test sets, which were 0.003 and 0.094, respectively (**Figures 11**, **12**).

Next, the above data were classified by random forest, and the classification tree was selected as 47 trees for the model construction; therefore, the error rate obtained was 11.41% with an accuracy rate of 88.59% (accuracy = (146+149)/333). The accuracy of the prediction results on the validation set and test set was 90.91% (accuracy = (61+59)/132) and 97.41% (accuracy = (224+229)/465), respectively. Using the correlation between genes and Gini index, we obtained 4 most contributing genes (GIMAP6, CD80, IL16, and CCR2), which were consistent

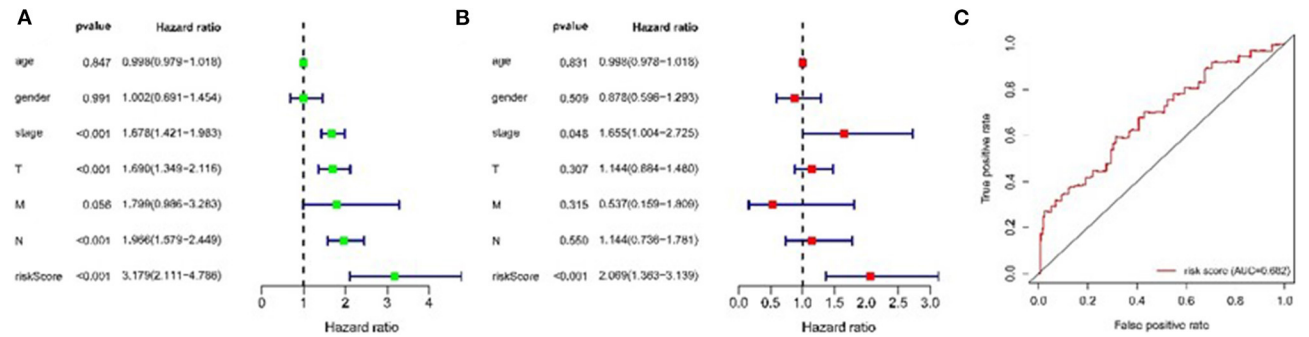

FIGURE 9 | Construction of TME-related genes model for patients with LUAD. **(A)** Prognostic values of TME-related genes by univariate Cox regression analysis. **(B)** Prognostic values of TME-related genes by multivariate Cox regression analysis. **(C)** ROC curve of TME-related genes.

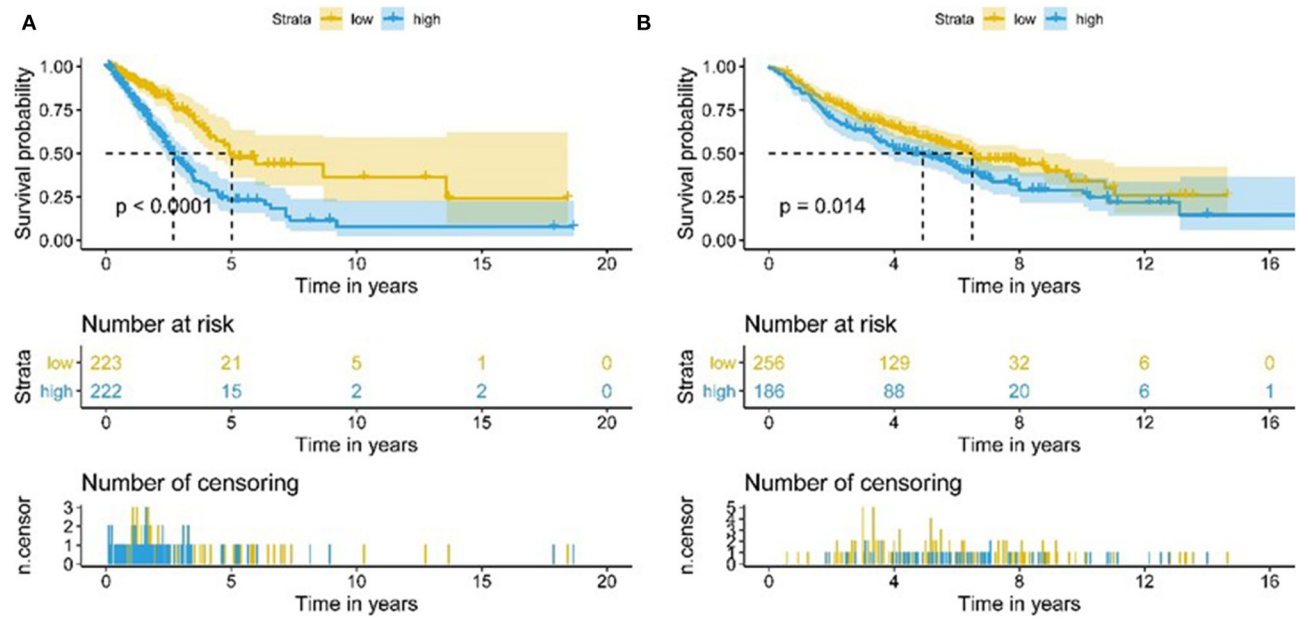

FIGURE 10 | Kaplan-Meier analysis of OS for LUAD patients using TCGA and GEO database. **(A)** Kaplan-Meier survival curves of the relative OS of high- and low-risk groups in TCGA database. **(B)** Kaplan-Meier survival curves of the relative OS of high- and low-risk groups in GEO database.

with the random forest regression for the target genes (**Figures 13**, **14**).

The Implication of Target Genes in the Sample Classification

Four genes labeled tumor samples, and PCA analysis revealed that four genes could be better divided into high and low purity groups. The proportions of the first and second principal components of TCGA data and GEO data were 90.5 and 82.4%, respectively. The results indicated that the sample's tumor purity could be inferred through the expression of the four genes, and the gene expression and tumor purity were associated (**Figure 15**).

LASSO Regression Analysis of Target Gene and Tumor Purity

We divided the 443 TCGA LUAD samples with complete clinical data into high and low groups according to tumor purity, and obtained CSGTPP (0.21*CCR2+ 0.06*GIMAP6+0.64*CD80+ 0.21*IL16) with LASSO regression analysis, and then divided the samples into high and low two groups. The simultaneous analysis revealed that the four genes were highly expressed in the high CSGTPP group ($p < 0.0001$) (**Supplementary Figures 1A–D**), and tumor purity was negatively correlated with CSGTPP (**Supplementary Figure 2A**). Using PCA, we determined the expression of four genes can be used to classify the two groups well with the first principal component and the second principal component

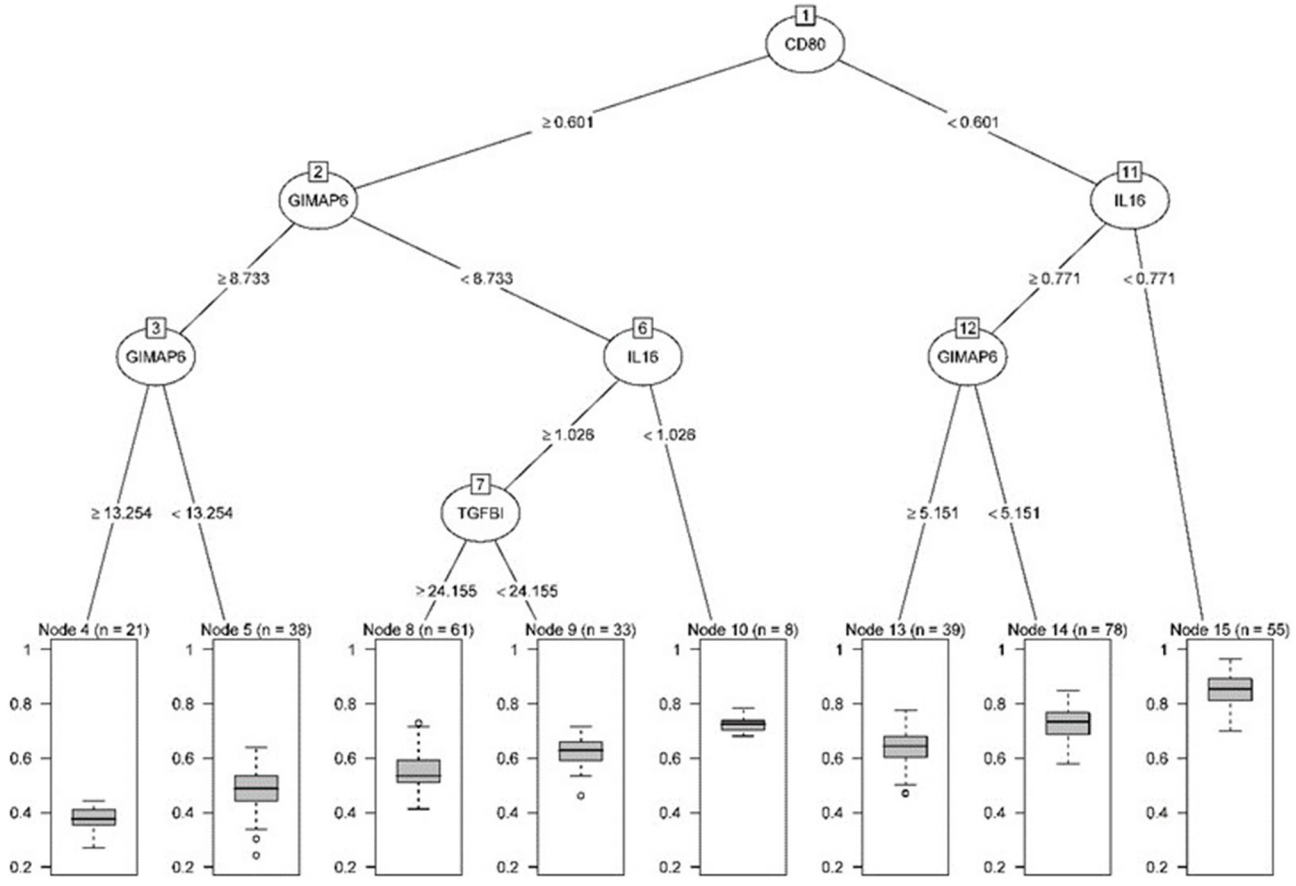

FIGURE 11 | Pruning tree containing the number of splits, nodes, observation genes, and prediction results.

value of 89.1% (**Supplementary Figure 2B**). Survival analysis revealed that patients in the high CSGTPP group exhibited a prognostic benefit ($P < 0.0001$), which echoed the poor prognosis of patients with higher tumor purity, as mentioned above (**Supplementary Figure 2C**). Finally, we explored the difference of CD274 gene expression in the CSGTPP two groups, and the results showed that the higher expression of CD274 in the high CSGTPP group ($p < 0.0001$) (**Supplementary Figure 2D**).

DISCUSSION

Recent advancement of omics technologies has significantly improved our understanding of the complexity and diversity of the immune components of the TME and its important impact on response to immunotherapy (9, 10). Further understanding of the tumor immune microenvironment will help improve the efficacy and response rates to immunotherapy. Therefore, an increasing number of studies have been conducted to study the TME and analyze immune cells' composition in tumor tissues. A large number of immune cells often gathered in and around tumors. There exist an inextricably link between these immune cells and tumor cells. Therefore, analyzing the composition and proportion of immune cells constitutes an integral part of studying the TME (11). Presently, there are two main methods for exploring the immune components of tumors. The first method includes high-precision single-cell-sequencing and single-cell-RNA-sequencing (scRNA-seq); the other method includes the speculation method that enables prediction based on the program using bulk RNA-seq data. However, estimation of tumor purity is considered crucial and warrants further investigation (12–14).

Recently, immunotherapy has emerged as a novel alternative therapeutic strategy for patients without driver genes mutation and has changed the treatment landscape of non-small cell lung cancer (NSCLC) (15, 16). Immunotherapy is an expensive therapy with significant clinical side effects; therefore, it remains critical to identify patients who will benefit from treatment with cancer immunotherapy. Therefore, it becomes increasingly essential to identify immune cells that exist in tumors; besides, deciphering immune cells present within the TME represents a significant area of implication in basic and clinical research.

Machine learning, an artificial intelligence method, utilizes complex algorithms in analyzing large-scale and heterogeneous data sets to extract useful patterns (17, 18). Machine learning

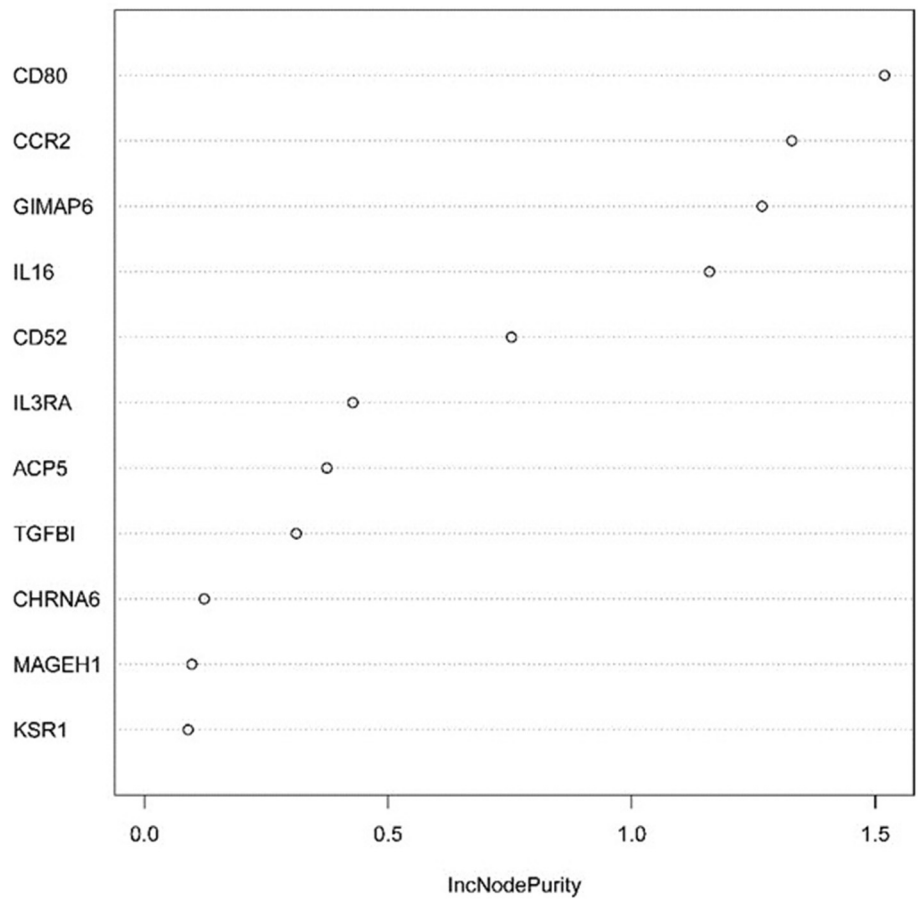

FIGURE 12 | Statistical chart of important TME-related genes contributed to the model and MES improvement percentage (IncNodePurity).

has shown great potential with promising results in biomedicine, human genome project, cancer whole-genome project, international machine learning competition project, and other projects (19). Collection and analyses of large data sets related to medical treatment and patient prognosis can transform medicine into a data-driven and result-oriented discipline, which profoundly impacts disease detection diagnosis, prognosis, and response to therapy (20). We focused on the TCGA and GEO data of lung adenocarcinoma patients with high morbidity and high mortality rates globally to explore and mine the immune microenvironment and tumor purity in lung adenocarcinoma and identified some potential data-level relationships using existing research findings, based on the algorithms of regression trees, random forest regression, and random forest classification.

We used regression trees and random forest regression methods to analyze the predictive value of LUAD immune microenvironment for tumor purity and selected five immune microenvironment components that contributed the most to predicting tumor purity (CCR, T-helper-cells, Check-point, Treg, and TIL), which were negatively associated with tumor purity and tumor T, M and stage but not with N stage. A prognostic model was constructed based on 5 TIM genes, and 11 TIM-related genes were screened, which confirmed that immune risk characteristics were significantly related to the OS of LUAD patients. This relationship was still valid after controlling for clinicopathological characteristics. The risk score constructed based on 11 genes can be used as an independent prognostic factor for LUAD patients. We hypothesized whether tumor purity can be predicted at the gene expression level. Therefore, we investigated the predictive ability of 11 genes for tumor purity using random forest regression and random forest classification. Both TCGA and GEO data showed a good predictive value, and four genes (GIMAP6, CD80, IL16, CCR2) contributed the most to predicting tumor purity. GIMAP6, CD80, IL16, and CCR2 in LUAD were reported to be related to immune tolerance in NSCLC (21–24). CSGTTP was further estimated by LASSO regression and was found to be significantly associated with the patient's prognosis. The four genes' mRNA levels can clearly stratify high and low tumor purity and CSGTTP, confirming our hypothesis that these four genes could predict the tumor purity at the gene

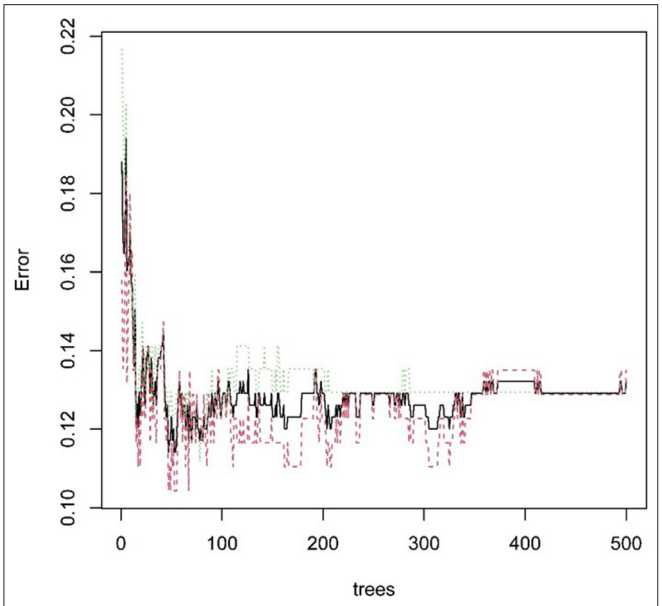

FIGURE 13 | Statistical graph of the relationship between the prediction error and the number of split trees.

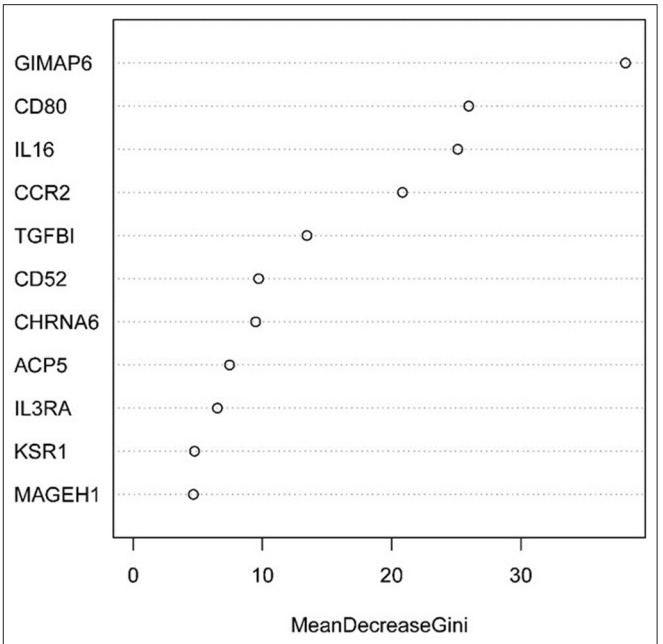

FIGURE 14 | Statistical chart of important TME-related genes contributed to the model and Gini Index.

level. These four genes were derived from CCR, TIL, and checkpoint immune infiltration components; thereby, we further analyzed the association between TIM, gene, and tumor purity. In order to further explore whether tumor purity could be used as a predictive indicator of immunotherapy, we excavated that PD-L1 expression was positively correlated with CSGTTP, while tumor purity was negatively correlated with CSGTTP. PD-L1, as an effective indicator of immunotherapy, has been studied extensively. Although there are difficulties in estimating tumor purity, we can convert the estimation of tumor purity to the estimation of CSGTTP, thereby indirectly establishing the relationship between tumor purity and PD-L1. The higher CSGTTP indicates lower tumor purity, implying that patients may benefit from immunotherapy.

Currently, detection of PD-L1 expression remains the marker for identifying NSCLC patients that are more possibly respond to immunotherapy. Many chemoimmunotherapy trials have demonstrated the benefits of checkpoint inhibitors combined chemotherapy for LUAD (25) for all PD-L1 levels. Notably, patients with low PD-L1 expression exhibit poorer clinical outcomes, emphasizing PD-L1 as a biomarker even with chemotherapy as the first-line treatment. Although PD-L1 expression is important for predicting response, many trials highlighted that checkpoint inhibitor still cannot benefit from these drugs in sub-sets of patients with high PD-L1 expression. Tumor mutational burden (TMB) may be a potentially important biomarker for immunotherapy response, and the correlation between TMB and the response of immunotherapy has been demonstrated in a variety of tumor types (26). While limited by lack of testing platforms standardization and "high" TMB threshold, this indicator can only be applied to subsets of patients. The degree of lymphocyte infiltration observed in tumor tissue may have prognostic value. Previous studies have demonstrated high levels of tumor-infiltrating lymphocytes (TIL) with promising prognosis in NSCLC, which infiltrated more CD8 positive, CD3 positive, and CD4 positive TIL (27). High TIL density is believed to reflect the patient's tumor microenvironment, where T cells are inflamed. Therefore, the predictive value of TIL density as a biomarker of immunotherapy has also been studied. The five immune infiltration components we selected also included TIL. Immune gene expression characteristics represent a novel area of research on predictive indicators of immunotherapy. Studies have shown that it has potential use as a biomarker for anti-PD-1 and PD-L1 therapy, and may have predictive value, and is compatible with several cancer types and related to treatment response (28, 29).

The tumor immune score and matrix score can be obtained based on many algorithms to estimate tumor purity and the relationship between immune microenvironment and immunotherapy. Thus, the investigation of each component as the effect of immunotherapy remains an active area of research. However, thus far, tumor purity has not been thoroughly accessed as immunotherapy-associated markers. Tumor heterogeneity affects tumor immunotherapy, and tumor purity represents the homogeneity of tumors from a particular perspective, and it is easier to establish a relationship with the immune microenvironment, thereby guiding immunotherapeutic decisions. Although it remains challenging to estimate tumor purity accurately, the relationship between immune genes and tumor purity using the value of dominant genes on tumor purity is expected to infer tumor purity at the level of dominant genes and the correlation between tumor purity

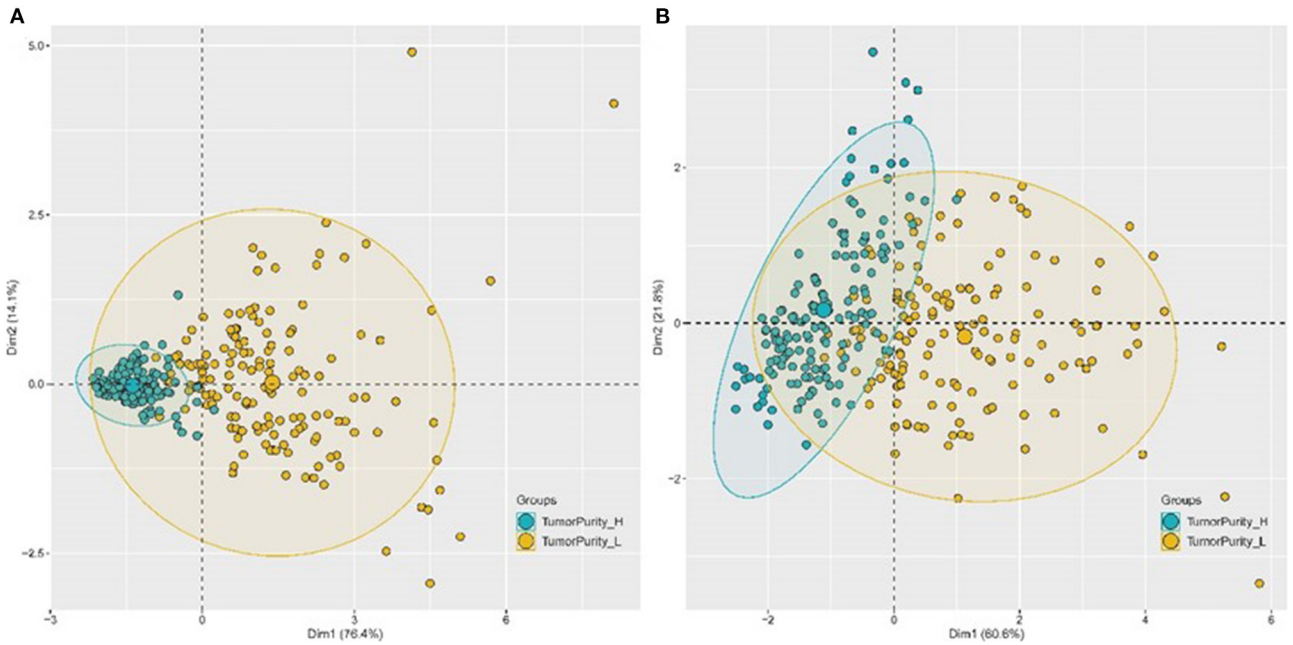

FIGURE 15 | PCA chart of the classification effect of four genes on tumor purity. **(A)** PCA chart of the classification effect of four genes on tumor purity in TCGA database. **(B)** PCA chart of the classification effect of four genes on tumor purity in GEO database.

and immunotherapy. We believe that this study highlights the significance of tumor purity as an immunotherapy-related biomarker; however, further studies are warranted to validate these findings.

CONCLUSION

In conclusion, CCR, T-helper-cells, Checkpoint, Treg, and TIL as the main immune infiltration components could better reflect tumor purity. We speculated that CSGTPP, derived from immune-related genes, could serve as a predictor of the response to immunotherapy and could stratify candidate for immunotherapy.

DATA AVAILABILITY STATEMENT

The datasets presented in this study can be found in online repositories. The names of the repository/repositories and accession number(s) can be found at: The Cancer Genome Atlas; GEO, GSE68465.

AUTHOR CONTRIBUTIONS

BL and HF have designed the research. HF and YZ analyzed data and wrote the paper. WY retrieved and collected data. CW and JL were responsible for drawing. BL revised the manuscript. All authors read and approved the final manuscript.

FUNDING

This project was supported by Natural Science Foundation of Gansu Provincial China (No. 20JR10RA733).

SUPPLEMENTARY MATERIAL

The Supplementary Material for this article can be found online at: https://www.frontiersin.org/articles/10.3389/fmed.2022.843749/full#supplementary-material

Supplementary Figure 1 | Significant difference in screened genes expression in high and low comprehensive score of genes for tumor purity prediction (CSGTPP) group. **(A)** Significant difference of GIMAP6 in high and low CSGTPP groups; **(B)** Significant difference of CD80 in high and low CSGTPP groups; **(C)** Significant difference of CCR2 in high and low CSGTPP groups; **(D)** Significant difference of IL16 in high and low CSGTPP groups.

Supplementary Figure 2 | Significant differences of tumor purity, sample classification, survival prognosis and CD274 expression in the high and low CSGTPP groups. **(A)** Significant difference in tumor purity between high and low CSGTPP groups; **(B)** PCA chart of the classification effect of four genes on tumor low and high CSGTPP in TCGA database; **(C)** Kaplan-Meier survival curves of the relative OS of high- and low-CSGTPP groups in TCGA database; **(D)** Significant difference of CD274 expression in the high and low CSGTPP groups.

REFERENCES

1. Koelwyn GJ, Quail DF, Zhang X, White RM, Jones LW. Exercise-dependent regulation of the tumour microenvironment. *Nat Rev Cancer.* (2017) 17:620–32. doi: 10.1038/nrc.2017.78
2. Smyth MJ, Ngiow SF, Ribas A, Teng MW. Combination cancer immunotherapies tailored to the tumour microenvironment. *Nat Rev Clin Oncol.* (2016) 13:143–58. doi: 10.1038/nrclinonc.2015.209
3. Hirsch FR, Scagliotti GV, Mulshine JL, Kwon R, Curran WJ Jr, Wu YL, et al. Lung cancer: current therapies and new targeted treatments. *Lancet.* (2017) 389:299–311. doi: 10.1016/S0140-6736(16)30958-8
4. Akinleye A, Rasool Z. Immune checkpoint inhibitors of PD-L1 as cancer therapeutics. *J Hematol Oncol.* (2019) 12:1–3. doi: 10.1186/s13045-019-0779-5
5. Fukumura D, Kloepper J, Amoozgar Z, Duda DG, Jain RK. Enhancing cancer immunotherapy using antiangiogenics: opportunities and challenges. *Nat Rev Clin Oncol.* (2018) 15:325–40. doi: 10.1038/nrclinonc.2018.29
6. Yadav VK, De S. An assessment of computational methods for estimating purity and clonality using genomic data derived from heterogeneous tumor tissue samples. *Brief Bioinform.* (2015) 16:232–41. doi: 10.1093/bib/bbu002
7. He Y, Jiang Z, Chen C, Wang X. Classification of triple-negative breast cancers based on immunogenomic profiling. *J Exp Clin Cancer Res.* (2018) 37:1–3. doi: 10.1186/s13046-018-1002-1
8. Yoshihara K, Shahmoradgoli M, Martínez E, Vegesna R, Kim H, Torres-Garcia W, et al. Inferring tumour purity and stromal and immune cell admixture from expression data. *Nat Commun.* (2013) 4:2612. doi: 10.1038/ncomms3612
9. Vitale I, Manic G, Coussens LM, Kroemer G, Galluzzi L. Macrophages and metabolism in the tumor microenvironment. *Cell Metab.* (2019) 30:36–50. doi: 10.1016/j.cmet.2019.06.001
10. Pitt JM, Marabelle A, Eggermont A, Soria JC, Kroemer G, Zitvogel L. Targeting the tumor microenvironment: removing obstruction to anticancer immune responses and immunotherapy. *Ann Oncol.* (2016) 27:1482–92. doi: 10.1093/annonc/mdw168
11. Li X, Wenes M, Romero P, Huang SC, Fendt SM, Ho PC. Navigating metabolic pathways to enhance antitumour immunity and immunotherapy. *Nat Rev Clin Oncol.* (2019) 16:425–41. doi: 10.1038/s41571-019-0203-7
12. Junttila MR, De Sauvage FJ. Influence of tumour microenvironment heterogeneity on therapeutic response. *Nature.* (2013) 501:346–54. doi: 10.1038/nature12626
13. Aran D, Sirota M, Butte AJ. Systematic pan-cancer analysis of tumour purity. *Nat Commun.* (2015) 6:8971. doi: 10.1038/ncomms9971
14. Rhee JK, Jung YC, Kim KR, Yoo J, Kim J, Lee YJ, et al. Impact of tumor purity on immune gene expression and clustering analyses across multiple cancer types. *Cancer Immunol Res.* (2018) 6:87–97. doi: 10.1158/2326-6066.CIR-17-0201
15. Apetoh LL, Ladoire S, Coukos G. Ghiringhelli F. Combining immunotherapy and anticancer agents: the right path to achieve cancer cure? *Ann Oncol.* (2015) 26:1813–23. doi: 10.1093/annonc/mdv209
16. Bodor JN, Kasireddy V, Borghaei H. First-line therapies for metastatic lung adenocarcinoma without a driver mutation. *J Oncol Pract.* (2018) 14:529–35. doi: 10.1200/JOP.18.00250
17. Mullainathan S, Spiess J. Machine learning: an applied econometric approach. *J Econ Perspect.* (2017) 31:87–106. doi: 10.1257/jep.31.2.87
18. Bouton CE, Shaikhouni A, Annetta NV, Bockbrader MA, Friedenberg DA, Nielson DM, et al. Restoring cortical control of functional movement in a human with quadriplegia. *Nature.* (2016) 533:247–50. doi: 10.1038/nature17435
19. Obermeyer Z, Emanuel EJ. Predicting the future—big data, machine learning, and clinical medicine. *N Engl J Med.* (2016) 375:1216. doi: 10.1056/NEJMp1606181
20. Kindle RD, Badawi O, Celi LA, Sturland S. Intensive care unit telemedicine in the era of big data, artificial intelligence, and computer clinical decision support systems. *Crit Care Clin.* (2019) 35:483–95. doi: 10.1016/j.ccc.2019.02.005
21. Shadur B, Asherie N, Kfir-Erenfeld S, Dubnikov T, NaserEddin A, Schejter YD, et al. A human case of GIMAP6 deficiency: a novel primary immune deficiency. *Eur J Hum Genet.* (2021) 29:657–62. doi: 10.1038/s41431-020-00773-x
22. Sugiura D, Maruhashi T, Okazaki IM, Shimizu K, Maeda TK, Takemoto T, et al. Restriction of PD-1 function by cis-PD-L1/CD80 interactions is required for optimal T cell responses. *Science.* (2019) 364:558–66. doi: 10.1126/science.aav7062
23. Winter C, Silvestre-Roig C, Ortega-Gomez A, Lemnitzer P, Poelman H, Schumski A, et al. Chrono-pharmacological targeting of the CCL2-CCR2 axis ameliorates atherosclerosis. *Cell Metab.* (2018) 28:175–82. doi: 10.1016/j.cmet.2018.05.002
24. Li ZW, Sun B, Gong T, Guo S, Zhang J, Wang J, et al. GNAI1 and GNAI3 reduce colitis-associated tumorigenesis in mice by blocking IL6 signaling and down-regulating expression of GNAI2. *Gastroenterology.* (2019) 156:2297–312. doi: 10.1053/j.gastro.2019.02.040
25. Gandhi L, Rodríguez-Abreu D, Gadgeel S, Esteban E, Felip E, De Angelis F, et al. Pembrolizumab plus chemotherapy in metastatic non–small-cell lung cancer. *N Engl J Med.* (2018) 378:2078–92. doi: 10.1056/NEJMoa1801005
26. Yarchoan M, Hopkins A, Jaffee EM. Tumor mutational burden and response rate to PD-1 inhibition. *N Engl J Med.* (2017) 377:2500. doi: 10.1056/NEJMc1713444
27. Brambilla E, Le Teuff G, Marguet S, Lantuejoul S, Dunant A, Graziano S, et al. Prognostic effect of tumor lymphocytic infiltration in resectable non–small-cell lung cancer. *J Clin Oncol.* (2016) 34:1223. doi: 10.1200/JCO.2015.63.0970
28. Ayers M, Lunceford J, Nebozhyn M, Murphy E, Loboda A, Kaufman DR, et al. IFN-γ-related mRNA profile predicts clinical response to PD-1 blockade. *J Clin Invest.* (2017) 127:2930–40. doi: 10.1172/JCI91190
29. Prat A, Navarro A, Paré L, Reguart N, Galván P, Pascual T, et al. Immune-related gene expression profiling after PD-1 blockade in non–small cell lung carcinoma, head and neck squamous cell carcinoma, and melanoma. *Cancer Res.* (2017) 77:3540–50. doi: 10.1158/0008-5472.CAN-16-3556

Conflict of Interest: The authors declare that the research was conducted in the absence of any commercial or financial relationships that could be construed as a potential conflict of interest.

frontiers | Frontiers in Medicine

TYPE Original Research
PUBLISHED 26 September 2022
DOI 10.3389/fmed.2022.906648

OPEN ACCESS

EDITED BY
Ali Yadollahpour,
The University of Sheffield,
United Kingdom

REVIEWED BY
Shengye Wang,
Zhejiang Cancer Hospital, China
Yukun Li,
Hebei Medical University, China

*CORRESPONDENCE
Jixiang Wu
wjxmed@sina.com
Jugao Fang
fangjg19651110@163.com

SPECIALTY SECTION
This article was submitted to Precision Medicine, a section of the journal Frontiers in Medicine

RECEIVED 28 March 2022
ACCEPTED 09 September 2022
PUBLISHED 26 September 2022

CITATION
Han B, Hao S, Wu J, Fang J and Han Z (2022) Predictive features of central lymph node metastasis in papillary thyroid microcarcinoma: Roles of active surveillance in over-treatment. *Front. Med.* 9:906648. doi: 10.3389/fmed.2022.906648

Predictive features of central lymph node metastasis in papillary thyroid microcarcinoma: Roles of active surveillance in over-treatment

Bo Han[1,2,3], Sen Hao[3], Jixiang Wu[1]*, Jugao Fang[2]* and Zhengxue Han[4]

[1]Department of General Surgery, Beijing Tongren Hospital, Capital Medical University, Beijing, China, [2]Department of Otolaryngology Head and Neck Surgery, Beijing Tongren Hospital, Capital Medical University, Beijing, China, [3]Department of Head and Neck Surgery, Baotou Cancer Hospital, Baotou, China, [4]Department of Oral and Maxillofacial-Head and Neck Oncology, Beijing Stomatological Hospital, Capital Medical University, Beijing, China

Background: Low-risk papillary thyroid microcarcinoma (PTMC) without clinically evident lymph nodes, extrathyroidal expansions, and distant metastases may be candidates for active monitoring.

Objective: The purpose of this research is to identify risk factors for papillary thyroid microcarcinoma (PTMC) metastasis to central cervical lymph nodes (CLNM) and to discuss the viability of an active surveillance strategy to minimize unnecessary therapy for patients.

Methods: This single-center retrospective study was conducted on the data and medical records of the patients who were diagnosed with PTMC and underwent surgery at the Baotou Cancer Hospital, China, between January 1, 2018, and December 31, 2019. Both lobectomy and complete thyroid resections were performed, and central lymph node dissections (CLND) were used in all patients. Comparisons and analyses were conducted on the preoperative ultrasound (US) characteristics, the post-operation pathological results, and lymph node metastasis.

Results: We analyzed 172 patients with PTMC with average age 48.32 ± 10.59 years old, with 31 males and 142 females. US testing showed 74 (43.0%) patients had suspicious lymph nodes; 31 (41.9%) had capsular invasion and 52 (30.2%) patients were confirmed to have CLNM. Based on logistic regression analysis, central lymph node metastasis was shown to be more common in individuals with PTMC who were older than 45 years old, male, and had tumors that lacked micro-calcification on US imaging. Postoperative pathology assessments suggested that 58 cases (33.7%) were more suitable candidates for active surveillance cohorts.

Conclusions: While active surveillance might benefit many PTMC patients, treatments for the patients should also encompass occult lymph node metastasis, especially in patients with over 45 years old, male, tumor without micro-calcification in the US imaging. Furthermore, the prediction of lymph nodes in the central cervical *via* the preoperative US and the PTMC risk

stratification accuracy need to be improved. Our findings showed about 30% of the patients with PTMC had no active surveillance high-risk factors but required surgical treatment. Fear of cancer in the PTMC patients, although informed of the details, is still the main reason for choosing surgical treatment over active surveillance.

KEYWORDS

active surveillance, cervical lymph node metastasis, central lymph node dissections, occult lymph node metastasis, papillary thyroid microcarcinoma

Introduction

Thyroid cancer prevalence has increased substantially over the last several decades, but mortality from the disease have stayed essentially stable (1, 2). About half of this increase may be attributable to better detection and diagnosis of slow-growing, non-cancerous tumors called intrathyroidal papillary thyroid microcarcinoma (PTMC) (3). The current definition of PTMC is papillary thyroid cancer (PTC) with an MTD $\leq$ 10 mm. Recent studies have shown that if left untreated, the vast majority of malignant cancers would not be fatal (4, 5). Thus, there is a risk of overdiagnosis if thyroid cancer is diagnosed only on the basis of the presence of these tiny tumors (6, 7). Accurate diagnostics made with modern ultrasound (US) and fine needle aspirate biopsy (FNAB) equipment may be the major explanation for the rise in PTMC detection (8). Traditional therapy for PTMCs has been surgical resection or thyroidectomy; however, active surveillance (AS) has emerged as an alternative strategy in the past three decades, with the goal of identifying the subset of individuals who would develop clinically and hence need rescue operations.

Active surveillance has been found to be a viable first-line therapy strategy for low-risk PTMC in recent trials (4, 5, 9, 10).

For low-risk PTMC, active monitoring was originally evaluated as a therapy option in Japan. Japan introduced active monitoring into standards in 2010, and the United States followed suit 5 years later in 2015. The Japan Association of Endocrine Surgeons (JAES) and the Japanese Society of Thyroid Surgeons (JSTS) issued the first guidelines for differentiated thyroid carcinomas, which included active monitoring as a therapy option for low-risk PTMC (11). Active monitoring as a therapeutic option for low risk PTMC was also included in the recommendations of the American Thyroid Association (ATA) in 2015. However, several clinical and technological aspects determine whether or not active monitoring is useful and feasible for low risk PTMC patients. For individuals with PTMC considered to be at "extremely low risk," active monitoring is suggested as a treatment option according to the ATA's 2015 recommendations (12). Active surveillance can partially reduce unnecessary surgeries for patients diagnosed with PTCM, which is usually indolent and has a good prognosis, so that the possibility of over-treatment could be reduced in some patients.

However, occult lymph node metastasis (LNM) is still a possibility for clinical node-negative (CN0) PTMC. Therefore, the necessity and extent of surgical treatment option for low PTMC patients remain a controversial subject (6). The purpose of this retrospective study is to better understand the benefits and drawbacks of using preoperative ultrasound for the prediction of central lymph node metastasis (CLNM) in the cervical region, as well as to analyze data on occult central lymph node metastasis to determine the optimal mix of surgery, active surveillance, and avoidance of treatment in patients with PTMC. Examining the potential of an active monitoring method to prevent over-treatment in patients is central to the goals of this research, which aims to investigate the predictive aspects of CLNM of PTMC.

Methods

This was a single-center retrospective study conducted on the data and medical records of the patients who were diagnosed with PTMC and underwent surgery at the Baotou Cancer Hospital, China, between January 1, 2018, and December 31, 2019. Data and medical records of the patients with PTMC who underwent monitoring and therapeutic procedures at the otolaryngology (ear, nose, and throat) division of Baotou Cancer Hospital, China between January 1, 2018, and December 31, 2019, were analyzed retrospectively for this research. The patients were all candidates for thyroid surgery, either lobectomy or complete thyroid removal. Prophylactic central lymph node dissection (CLND) was also done on the same side as the lesion, as recommended by the Chinese guidelines for the diagnosis and treatment of thyroid nodule and differentiated thyroid carcinoma. Comparisons and analyses were conducted on the preoperative ultrasound characteristics of PTMC, the pathological results post-operation, and lymph node metastasis.

SPSS (IBM SPSS Inc., Chicago, IL, Windows version 22.0.0) was used to conduct statistical analyses on the study's data, including the *t*-test, Pearson's Chi-square test or Fisher's exact test, and ROC curve and logistic regression. The normality of

TABLE 1 Clinical characteristics and results of US imaging and pathologic assessments of the patients.

Category	*N* (%)	US suspicious CLN
All	172	74 (43.0%)
Sex		
Female	142 (82.0%)	56 (75.7)
Male	31 (18.0%)	18 (24.3)
Age (mean ± SD) (year)	48.32 ± 10.59	47.62 ± 12.06
Age group		
Group 1 age < 45	57 (33.1)	26 (35.1)
Group 2 45 ≥ age > 55	63 (36.6)	28 (37.8)
Group 3 age ≥ 55	52 (30.2)	20 (27.0)
Preoperative US TI-RADS grade		
3	10 (5.8%)	3 (4.1)
4a	42 (24.4%)	18 (24.3)
4b	77 (44.8%)	33 (44.6)
4c	1 (0.6%)	0
5	41 (23.8%)	19 (25.7)
6	1 (0.6%)	1 (1.4)
Tumor site		
Unifocal	121 (70.3%)	49 (66.2)
Double or multifocal	51 (29.7%)	25 (33.8)
The max diameter (mean ± SD)	5.68 ± 2.48 mm	5.95 ± 2.32 mm
US capsular invasion	50 (29.1%)	31 (41.9)
US microcalcification	101 (58.7%)	48 (64.9)
Postoperative pathologic results		
Unifocal	121 (70.3)	49 (66.2)
Double or multifocal	51 (29.7)	25 (33.8)
Capsule invasion	74 (43.0)	31 (41.9)
Nerve invasion	5 (2.9)	4 (5.4)
Fewer than 5 CLNM	164 (95.3)	–
Co-exist thyroid goiter	73 (42.4)	23 (31.1)
Co-exist Hashimoto thyroiditis	55 (32.0)	28 (37.8)
Complications		
Recurrent nerve palsy	0	
Temporary hypoparathyroidism	9 (5.2)	
Permanent hypoparathyroidism	2 (1.2)	

the data that was continuously collected was tested. Normally distributed research data were reported as means standard deviations (SD), whereas skewed variables were shown as medians (Inter Quartile Range). In order to compare and contrast the various groups, we utilized the *t*-test for normally distributed data, the non-parametric test (*Mann-Whitney U*) for data with a skewed distribution, and the Pearson Chi-square test for data based on counts. In the case of normally distributed data, Pearson's correlation coefficient was used to examine the intercorrelations between the variables, whereas in the case of skewed data, *Spearman's* correlation coefficient was used.

TABLE 2 Statistical data of the patients with central cervical lymph nodes metastasis (CLNM).

	Group 1 Age < 45	Group 2 45 ≤ age < 55	Group 3 Age ≥ 55	Total
n (%)	57 (33.1)	63 (36.6)	52 (30.2)	172
CLNM patients (%)	24 (42.1)	14 (26.9)	14 (26.9)	52
CLNM lymph nodes (%)	85 (64.4)	24 (18.2)	23 (17.4)	132
CLN dissected (%)	322 (35.2)	343 (37.4)	251 (27.4)	916

Results

After applying inclusion and exclusion criteria, of 1,586 patients hospitalized for thyroid disease, 172 PTMC patients were included in this study [age: 48.32 ± 10.59 (SD) years old, and male/female ratio 31/142]. Ninety-eight cases of suspected lymph nodes were not detected *via* preoperative US, 20 cases (20.4%) of CLNM were confirmed *via* pathology, and 74 cases (43.2%) were found to have suspicious LN *via* preoperative US (Table 1).

Patients with lymph node metastases were found to be less common in the Group 2 (45 ≤ age < 55 years old), compared to the Group 1 (<45 years old) and the Group 3 (≥55 years old) ($P = 0.018$). No statistically significant differences were found between any of the groups (Table 3). Table 2 displays postoperative pathology results.

Using US imaging to identify CLNM has a sensitivity of 0.62, specificity of 0.35, and an area under the curve (AUC) of 0.63. For PTMC patients, the probability of central lymph node metastasis was highest among those who were male, over the age of 45, and whose tumors lacked micro-calcification on US imaging. The remaining parameters did not show any statistically significant link (Table 3).

According to active surveillance exclusion criteria as per reported by Ito et al. (5) postoperative pathology confirmed 58 cases (33.7%) that showed the following characteristics: no metastasis near the trachea, located at the dorsal side of thyroid gland, no lymph node metastasis in six areas, no capsule invasion, and no high-grade malignancy.

Discussion

The over-treatment of indolent lesions with mostly low malignant potential is not uncommon, but it may be caused by the lack of evidence and comprehensive understanding regarding the disease at that time. The progression of diagnosis technology has caused a rapid increase in PTMC cases. However,

TABLE 3 Statistical data of the logistics regression analysis.

Category	OR (95% CI)	*P*-value
Gender		
Male	1.00	
Female	2.09 (0.18–0.96)	$P = 0.040$
Age (year)		
Age < 45	1.00	
Age ≥ 45	2.09 (1.01–4.30)	$P = 0.046$
US microcalcification		
None	1.00	
Sandy	0.48 (0.23–0.99)	$P = 0.046$

lack of accurate and precise classification and prediction still exists for the disease, which may increase the amount of unnecessary invasive treatments.

AS partially slowed down the PTMC over-treatment trend safely and prudently. Emerging evidences from active surveillance studies have demonstrated that many low-risk PTMC patients can benefit from active surveillance and their morbidity probability is reduced. This is caused by operations and follow-up radioiodine therapies with increased risk stratification *via* confirmed lymph node metastasis, including hypothyroidism, hypocalcemia, recurrent laryngeal nerve palsy, inconvenience and side effects of postoperative TSH treatment, salivary gland reaction, secondary leukemia, and other damage possibilities. High-risk patients were not considered for active surveillance by Ito et al. because of unfavorable lesion characteristics such as proximity to the trachea or dorsal thyroid surface, potential invasion of the recurrent laryngeal nerve, clinically apparent nodal metastasis, or high-grade malignancy on FNAB findings (5). In addition, the American Thyroid Association Guidelines outline a plethora of variables that classify individuals into high- or low-risk profiles, although these are generally pathologic abnormalities discovered only after surgical resection (13). Therefore, applying risk stratification pre-operation in clinical practice is difficult.

It remains unknown whether or not PTMC is associated with occult central lymph node metastasis, or whether or not risk stratification is upgraded. Moreover, It remains uncertain whether or not it is safe and controllable to wait until these hidden lymph nodes can be detected clinically. Likewise, it is unknown whether or not this will increase the local recurrence rate or the probability of secondary operations and side injuries. Lastly, how to accurately select these patients and conduct more detailed risk stratifications remains unknown.

PTC has a relatively high rate of lymph node metastasis so that lymph node metastasis derived from PTC first involves the central compartment (14). A meta-analysis (19 studies comprising 4,014 patients) found that the rate of central cervical lymph node metastases (CLNM) of PTC was 48.0% and the rate of lateral CLNM of PTC was 59.2% (15). Another meta-analysis found that, even without clinically cervical lymph node metastasis (cN0) PTMC, there was still about 33% (95% CI 29–37) of CLNM (16). Our finding was consistent with this study where we found that the CLNM rate of PTMC was 30.2%. A meta-analysis study reported that in PTC patients lymph nodes were involved in 80% of recurrences (17).

However, there is a lack of simple and reliable methods for conducting accurate preoperative judgments of occult lymph node metastasis and the biological characteristics of PTMC. Ultrasound accuracy when diagnosing central lymph nodes remains low. A meta-analysis concluded that for detecting central CLNM with ultrasound the pooled sensitivity was 0.33 [95% confidence interval (95% CI): 0.31–0.35], the specificity was 0.93 (95% CI: 0.92–0.94), the DOR was 5.63 (95% CI: 3.50–9.04), and the area under curve (AUC) was 0.69. In this study, we used pre-operative US imaging for detection of CLNM and the sensitivity was 0.62, the specificity was 0.35, and the area under curve (AUC) was 0.63. If the US imaging does not find a suspicious lymph node, then the lymph node FNAB target cannot be determined. There is not enough evidence to show that such PTMCs with CLNM are indolent and could be safely monitored. Moreover, this must be conducted preoperatively or at the latest intraoperatively to evaluate the central compartment LN status precisely. However, this study found that even if suspected lymph nodes were noted, it is hard identifying the suspicious LN found preoperatively *via* US was precisely consistent with the metastasis LN confirmed by the pathology postoperatively. Patients in this region have a lot of difficulties receiving preoperative molecular or gene detection or PET/CT due to economic limitations and medical insurance clauses. In turn, providing accurate information regarding central lymph nodes pre-operation is very difficult.

Not all patients are comfortable with observational treatment when presented with a cancer diagnosis, and many refuse active surveillance as a treatment option (4). Additionally, follow-up examinations are costly, time-consuming, and inconvenient for both patients and clinicians, which prevents utilizing them widely for detecting LN metastasis (18). In the outpatient department used by the authors, around less than 1/4 of PTMC patients who meet the standard willingly choose AS. However, most of the other patients, although they have been informed of the relevant details, choose surgical treatment for fear of cancer, and they have a strong desire for a radical cure rather than any kind of secondary surgery for recurrence. Therefore, it remains uncertain whether or not active surveillance risk stratification should supply psychological evaluation considerations. In this study, 33.7% of patients may be more suitable to join the active surveillance cohort. This is the first research to

our knowledge to examine PTMC and overtreatment at a single location using preoperative ultrasonography and postoperative histology.

Lymph node metastasis (LNM) is a major recurrence predictor and affects PTMC patients' survival rate, although it does not seem to alter PTMC patients' 10-year disease-free survival rate (7). Updated technology in the future might be relied on to provide more objective and accurate primary lesions and lymph nodes. It can be predicted that technological progress will allow for more and more suspected metastatic lymph nodes to be found pre-operation. Therefore, it remains uncertain as to whether or not active surveillance can still be used for low-risk PTMC patients even if they have lymph node metastasis. Likewise, methods for stratifying the risk of lymph nodes remain unknown. More evidence may be provided by a large amount of data and long-term prognosis observations.

This study had some limitations that should be considered in generalizing the findings into the general population. The study's single-center retrospective design was a weakness, and even after removing potentially relevant data, it remained gaps that may introduce bias. There is not a single accepted method for quantitatively assessing mental health. Long-term surveillance and follow-up of patients in this research is still necessary to determine their prognosis.

Conclusions

Despite a meteoric rise in the number of cases identified, mortality from intrathyroidal papillary microcarcinomas has been about the same. Active monitoring has arisen as an alternative to surgical resection with the purpose of identifying the subset of individuals who will develop clinically and would benefit from rescue operations. These tumors (particularly those between 1 and 2 cm) show no development during follow-up, grow at very slow rates, and can even shrink in size. Since papillary microcarcinomas are so common and observational results are so good, active monitoring may be a viable option for carefully chosen individuals. Active surveillance might benefit many PTMC patients and reduce damages caused by surgical therapies and related treatments, but PTMC treatments should also focus on the existence of occult lymph node metastasis, especially in patients with over 45 years old, male, tumor without micro-calcification in US. While accuracy of preoperative US imaging in the prediction of lymph nodes in the central cervical regions needs improvement, CLNM potential should be kept track of vigilantly in PTMC patients with microcalcification or suspected lymph nodes. Further studies should be conducted to improve the PTMC risk stratification accuracy. In this study, about 30% of the patients with PTMC had no active surveillance high-risk factors but required surgical treatment. Although informed of the details, PTMC patients' fear of cancer is still the main reason for choosing surgical treatment for active surveillance.

Data availability statement

The original contributions presented in the study are included in the article/supplementary material, further inquiries can be directed to the corresponding authors.

Ethics statement

The studies involving human participants were reviewed and approved by the Baotou Cancer Hospital, China. The patients/participants provided their written informed consent to participate in this study.

Author contributions

BH, JW, and JF contributed to conception and design of the study. SH organized the database. ZH performed the statistical analysis. BH wrote the first draft of the manuscript. SH, JW, JF, and ZH wrote sections of the manuscript. All authors contributed to manuscript revision, read, and approved the submitted version.

Conflict of interest

The authors declare that the research was conducted in the absence of any commercial or financial relationships that could be construed as a potential conflict of interest.

Publisher's note

References

1. Lamartina L, Leboulleux S, Borget I, Schlumberger M. Global thyroid estimates in 2020. *Lancet Diabetes Endocrinol.* (2022) 10:235–6. doi: 10.1016/S2213-8587(22)00048-1

2. Lim H, Devesa SS, Sosa JA, Check D, Kitahara CM. Trends in thyroid cancer incidence and mortality in the United States, 1974-2013. *JAMA*. (2017) 317:1338–48. doi: 10.1001/jama.2017.2719

3. Pizzato M, Li M, Vignat J, Laversanne M, Singh D, La Vecchia C, et al. The epidemiological landscape of thyroid cancer worldwide: GLOBOCAN estimates for incidence and mortality rates in 2020. *Lancet Diabetes Endocrinol.* (2022) 10:264–72. doi: 10.1016/S2213-8587(22)00035-3

4. Walgama E, Sacks WL, Ho AS. Papillary thyroid microcarcinoma: optimal management versus overtreatment. *Curr Opin Oncol.* (2020) 32:1–6. doi: 10.1097/CCO.0000000000000595

5. Ito Y, Miyauchi A, Inoue H, Fukushima M, Kihara M, Higashiyama T, et al. An observational trial for papillary thyroid microcarcinoma in Japanese patients. *World J Surg.* (2010) 34:28–35. doi: 10.1007/s00268-009-0303-0

6. McDow AD, Pitt SC. Extent of surgery for low-risk differentiated thyroid cancer. *Surg Clin North Am.* (2019) 99:599–610. doi: 10.1016/j.suc.2019.04.003

7. Xu Y, Xu L, Wang J. Clinical predictors of lymph node metastasis and survival rate in papillary thyroid microcarcinoma: analysis of 3607 patients at a single institution. *J Surg Res.* (2018) 221:128–34. doi: 10.1016/j.jss.2017.08.007

8. Du L, Wang Y, Sun X, Li H, Geng X, Ge M, et al. Thyroid cancer: trends in incidence, mortality and clinical-pathological patterns in Zhejiang Province, Southeast China. *BMC Cancer.* (2018) 18:291. doi: 10.1186/s12885-018-4081-7

9. Tuttle RM, Fagin JA, Minkowitz G, Wong RJ, Roman B, Patel S, et al. Natural history and tumor volume kinetics of papillary thyroid cancers during active surveillance. *JAMA Otolaryngol Head Neck Surg.* (2017) 143:1015–20. doi: 10.1001/jamaoto.2017.1442

10. Molinaro E, Campopiano MC, Pieruzzi L, Matrone A, Agate L, Bottici V, et al. Active surveillance in papillary thyroid microcarcinomas is feasible and safe: experience at a single Italian center. *J Clin Endocrinol Metab*. (2020) 105:e172–80. doi: 10.1210/clinem/dgz113

11. Zhang H, Zheng X, Liu J, Gao M, Qian B. Active surveillance as a management strategy for papillary thyroid microcarcinoma. *Cancer Biol Med.* (2020) 17:543. doi: 10.20892/j.issn.2095-3941.2019.0470

12. Haugen BR, Alexander EK, Bible KC, Doherty GM, Mandel SJ, Nikiforov YE, et al. 2015 American Thyroid Association management guidelines for adult patients with thyroid nodules and differentiated thyroid cancer: the American Thyroid Association guidelines task force on thyroid nodules and differentiated thyroid cancer. *Thyroid*. (2016) 26:1–133. doi: 10.1089/thy.2015.0020

13. Ho AS, Chen I, Melany M, Sacks WL. Evolving management considerations in active surveillance for micropapillary thyroid carcinoma. *Curr Opin Endocrinol Diabetes Obes.* (2018) 25:353–9. doi: 10.1097/MED.0000000000000438

14. Zhao H, Huang T, Li H. Risk factors for skip metastasis and lateral lymph node metastasis of papillary thyroid cancer. *Surgery.* (2019) 166:55–60. doi: 10.1016/j.surg.2019.01.025

15. Zhao H, Li H. Meta-analysis of ultrasound for cervical lymph nodes in papillary thyroid cancer: diagnosis of central and lateral compartment nodal metastases. *Eur J Radiol.* (2019) 112:14–21. doi: 10.1016/j.ejrad.2019.01.006

16. Liu LS, Liang J, Li JH, Liu X, Jiang L, Long JX, et al. The incidence and risk factors for central lymph node metastasis in cN0 papillary thyroid microcarcinoma: a meta-analysis. *Eur Arch Oto Rhino Laryngol.* (2017) 274:1327–38. doi: 10.1007/s00405-016-4302-0

17. Mehanna H, Al-Maqbili T, Carter B, Martin E, Campain N, Watkinson J, et al. Differences in the recurrence and mortality outcomes rates of incidental and nonincidental papillary thyroid microcarcinoma: a systematic review and meta-analysis of 21 329 person-years of follow-up. *J Clin Endocrinol Metab.* (2014) 99:2834–43. doi: 10.1210/jc.2013-2118

18. Liu T, Zhou S, Yu J, Guo Y, Wang Y, Zhou J, et al. Prediction of lymph node metastasis in patients with papillary thyroid carcinoma: a radiomics method based on preoperative ultrasound images. *Technol Cancer Res Treat.* (2019) 18:1533033819831713. doi: 10.1177/1533033819831713

frontiers | Frontiers in Integrative Neuroscience

TYPE Original Research
PUBLISHED 05 October 2022
DOI 10.3389/fnint.2022.842404

OPEN ACCESS

EDITED BY
Ali Yadollahpour,
The University of Sheffield,
United Kingdom

REVIEWED BY
Shengye Wang,
Zhejiang Cancer Hospital, China
Zhenwei Shi,
Guangdong Academy of Medical Sciences, China
Sridhar Goud Nerella,
National Institutes of Health (NIH), United States

*CORRESPONDENCE
Zhaohui Zhong
zhongzhaohuicjh@163.com

RECEIVED 23 December 2021
ACCEPTED 01 September 2022
PUBLISHED 05 October 2022

CITATION
Chen J, Zhong Z, Wang W, Yu G, Zhang T and Wang Z (2022) Quantitative evaluation of diaphragmatic motion during forced breathing in chronic obstructive pulmonary disease patients using dynamic chest radiography. *Front. Integr. Neurosci.* 16:842404. doi: 10.3389/fnint.2022.842404

Quantitative evaluation of diaphragmatic motion during forced breathing in chronic obstructive pulmonary disease patients using dynamic chest radiography

Jianghong Chen[1], Zhaohui Zhong[1]*, Wei Wang[2], Ganggang Yu[2], Tingting Zhang[1] and Zhenchang Wang[1]

[1]Department of Radiology, Beijing Friendship Hospital, Capital Medical University, Beijing, China, [2]Department of Respiration, Beijing Friendship Hospital, Capital Medical University, Beijing, China

Objective: To quantitatively evaluate the bilateral diaphragmatic motion difference during forced breathing between chronic obstructive pulmonary disease (COPD) patients and healthy individuals using dynamic chest radiography technique.

Methods: This prospective study included the COPD patients (n: 96, f/m: 17/79, age: 66 ± 8 years old) and healthy individuals (n: 50, f/m: 42/8, age: 53 ± 5 years old) that underwent dynamic chest radiography with a flat panel X-ray detector system during forced breathing in a standing position. After analyzing the excursions, duration and velocity of diaphragmatic motion were automatically calculated using the postprocessing software. The parameters of diaphragmatic motion including excursion, duration, velocity, inhalation/exhalation times were assessed in all subjects for both diaphragms. The correlation between lung function parameters and diaphragmatic motion excursions were further evaluated.

Results: The excursions of diaphragmatic motion in COPD patients were significantly decreased in COPD patients compared with healthy individuals during forced breathing ($P < 0.05$). The excursion in COPD patients was 35.93 ± 13.07 mm vs. 41.49 ± 12.07 mm in healthy individuals in the left diaphragm, and 32.05 ± 12.29 mm in COPD patients vs. 36.88 ± 10.96 mm in healthy individuals in the right diaphragm. The duration of diaphragmatic motion significantly decreased in COPD patients, compared with the healthy individuals ($P < 0.05$). The inhalation time in COPD patients was 2.03 ± 1.19 s vs. 2.53 ± 0.83 s in healthy individuals in the left diaphragm and 1.94 ± 1.32 s in COPD patients vs. 2.23 ± 1.21 s in healthy individuals in the right diaphragm. The exhalation time was 4.77 ± 1.32 s in COPD patients vs. 6.40 ± 2.73 s in healthy individuals in the left diaphragm and 4.94 ± 3.30 s in COPD patients vs. 6.72 ± 2.58 s in healthy individuals in the right diaphragm. The peak

velocity of diaphragmatic motion showed no significant difference between COPD and healthy groups. The excursions of bilateral diaphragmatic motion showed moderate correlation with FEV1/FVC (r = 0.44, $P < 0.001$). Multi-linear regression analysis showed that the excursions of bilateral diaphragm are significantly associated with COPD occurrence ($P < 0.05$).

Conclusion: The excursions and duration of diaphragmatic motion during forced breathing are significantly decreased in COPD patients, compared with healthy individuals. Our study showed that precise bilateral diaphragmatic motion activity can be evaluated by dynamic chest radiography.

KEYWORDS

chronic obstructive pulmonary disease (COPD), diaphragmatic motion, forced breathing, dynamic chest radiograph, prospective study

Introduction

Chronic obstructive pulmonary disease (COPD) is a chronic, preventable and treatable, respiratory condition, characterized by shortness of breath, cough and recurrent exacerbations (Lozano et al., 2012). In this disorder, anomalies in the small airways of the lungs limit the airflow in and out of the lungs. Different risk factors and processes have been reported as main causes of narrowing airways including destruction of parts of the lung, mucus blocking the airways, and inflammation and swelling of the airway lining (Morgan and Summer, 2008). COPD is the third leading cause of mortalities worldwide, causing 3.23 million deaths in 2019 (Stanaway et al., 2018). In China, COPD is among the four most common chronic diseases. With a prevalence of 13.7% in Chinese populations over 40 years of age and affecting approximately 100 million people, COPD is currently a major public health issue that imposes significant economic burden in China (Wang et al., 2018). This disorder causes persistent and progressive respiratory symptoms, including difficulty in breathing, cough and phlegm production. COPD is a systematic chronic disease that affects both men and women and the whole body is involved in the disorder. COPD-associated symptoms such as inflammatory cytokines, insufficient oxygen supply of tissue, electrolyte disturbance and long-term use of steroid hormone will severely affect the skeleton muscles throughout the body (Barreiro and Gea, 2015; Jaitovich and Barreiro, 2018) including diaphragm, which will further cause diaphragm fatigue and contraction weakness (Charususin et al., 2018). Pulmonary ventilation is highly dependent on diaphragm mobilization, which attributes for nearly 80% of the pulmonary ventilation. Therefore, accurate assessment of diaphragm function helps to evaluate the progression of COPD and can provide guidance for the clinical treatment of COPD.

Precision medicine for therapy and diagnosis of disorders has dramatically progressed during the recent years (Agustí et al., 2017; Sidhaye et al., 2018). Precision medicine for COPD has also witnessed significant development recently. Recent findings from modeling, imaging and molecular studies on the heterogeneous and complicated nature of COPD have identified different clinical and inflammatory phenotypes that highlight the need for shifting the focus of health management strategy from prototypic disease labels toward targeted therapies (Agustí et al., 2017; Wouters et al., 2017; Sidhaye et al., 2018; Franssen et al., 2019; Ulrik et al., 2020).

In brief, precision medicine approach aims to identify and connect the right treatment to the right patient, meanwhile minimizing the risk of adverse effects. Recent studies have identified several treatable features for different types of COPD including pulmonary, extra-pulmonary, psychological, and environmental traits (Hersh, 2019; Dennett et al., 2021). The next step is identifying and quantifying physiological features, molecular pathways and underlying mechanisms of these treatable traits through innovative modeling or detection techniques and then developing noble reliable point-of-care biomarkers to predict and/or differentiate responders from non-responders to targeted therapies or precision medicine (Wouters et al., 2017; Cazzola et al., 2018; Sidhaye et al., 2018).

In this study, we used a flat panel X-ray detector, which can obtain dynamic chest radiography of breathing motion in patient in the standing position. Dynamic radiographs are more conducive to intuitively diaphragmatic motion, compared with the static images of conventional chest radiographs. More importantly, post-processing of the image obtained from this type of detector, further provides quantitative parameters such as the excursions, durations and peak velocity of diaphragm longitudinal motion, which is conducive to precise evaluation of the diaphragmatic motion in patient. Recently, several

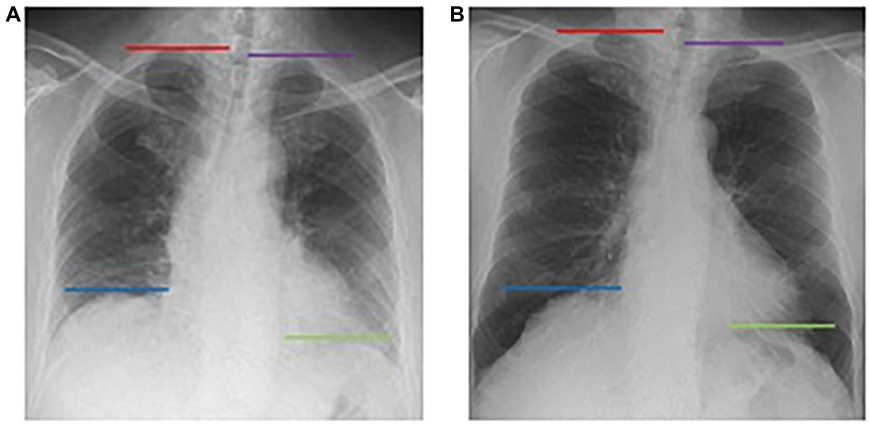

FIGURE 1
The Kinetic Analysis Tool™ automatically recognizes the bilateral pulmonary apexes and diaphragm dome. Dynamic X-ray working station automatically marked the bilateral diaphragm dome (right diaphragm: blue line; left diaphragm: green line) and lung apex (right lung: red line; left lung: purple line) in both end exhalation **(A)** and end inhalation **(B)**, and tracing the position change with breathing.

relevant studies reported the application of this device to evaluate the diaphragmatic motion, which reported significant outcomes, but these studies are limited to single-center and small-sample of COPD patients. To the best knowledge of the authors, this study is the first application of the dynamic chest radiography to quantitative assessment of diaphragmatic motion in COPD patients in China and will further confirmed its diagnostic value of COPD.

Materials and methods

Clinical materials

All experimental procedures of this study were approved by the institutional review board and Ethics Committee of Beijing Friendship Hospital affiliated to Capital Medical University, Beijing, China (Ethics code: 2018-P2-086-01) that were in accordance with the regulations and guidelines of the studies on human subjects set by the Declaration of Helsinki (General Assembly of the World Medical Association, 2014).

Written informed consent forms were obtained from all patients in the study. The subjects were continuously enrolled from June 2018 to June 2019. The inclusion criteria for COPD patients included: 1. Age range of 40–75 years old, 2. Diagnosis of stage I-IV COPD according to the 2017 Global Initiative for Chronic Obstructive Lung Disease (GOLD) guideline, 3. Current smoking or smoking history for the last 20 years, 4. Written consent for participating in the study. Exclusion criteria included: 1. Patients with bronchial asthma, 2. Patients with other diffuse pulmonary disease, 3. Patients with acute pulmonary infection or pulmonary space-occupying lesions, 4. Patients with obvious pleural or chest wall lesion, 5. Patients with lung surgery history. A total of 96 COPD patients were enrolled in the study, including 79 male (82.29%) and 17 female (17.71%), average age 67 ± 7 years old. The inclusion criteria of healthy individuals included 1. Age range 40–75 years of age, 2. Healthy condition before the study and lack of any history of heart and lung disease, 3. Normal lung function (FEV1/FVC > 70%), 4. No smoking history, 5. Written consent form on participating in the study. The individuals including 8 males (16.00%) and 42 females (84.00%), average age of 53 ± 5 years old were enrolled in the study. The height and body weight of all participate were recorded and body mass index BMI (weight/height ^{2}) were calculated.

Device and data analysis

A flat panel dynamic X-ray digital radiography apparatus (Konica Minolta Inc., Tokyo, Japan) was used in this study. Before radiography, the participants were taught to learn forced inhalation to reach maximum inspiratory capacity (IC) and followed by forced exhalation to reach maximum expiratory capacity. Subjects were in a post-anterior standing position, with scanning parameters of 100 kV tube voltage, 50 mA tube current, 388 × 388 μm, 1,024 × 768 matrix and with an emitting pulse at 15 frames/second. The X-ray were set to pulse emission to reduce the radiation dose, exposure time were set to 15 s with a radiation dose of approximately 0.34 mSv for each participant.

The obtained dynamic chest radiographs were transmitted to the assorted workstation and then went under analysis using the Kinetic Analysis Tool assorted to the workstation. This software can automatically recognize and mark the bilateral lung apex and the edges of diaphragm (**Figure 1**). A radiologist with over 15 years of diagnosis chest radiography experience will select the end-expiratory images and correct the highest point

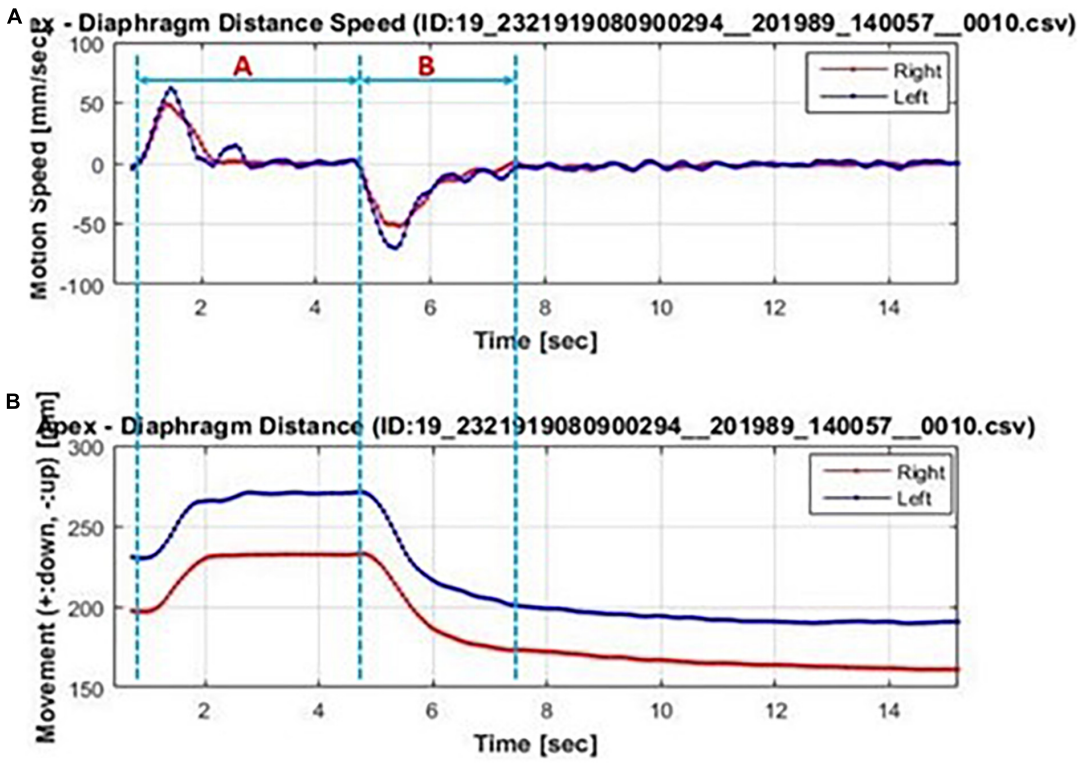

FIGURE 2
Bilateral diaphragmatic motion excursions and velocity vs. time curve automatically generated by the Kinetic Analysis Tool™. Bilateral diaphragm (left diaphragm: blue line; right diaphragm: red line) motion velocity-time curve **(A)** and motion excursions-time curve (B). The forced inhalation stage was marked with blue dotted line A and the forced exhalation stage are marked with blue dotted line B. In **(A)**, the corresponding diaphragm velocity were of positive value in stage A and of negative value in stage B. The wave crest and trough representant the diaphragm maximum motion velocity in inhalation and exhalation, respectively. In **(B)**, the maximum diaphragmatic motion excursions were representant as the difference value between maximum value in stage A and the minimum value in stage B.

of bilateral diaphragm and positions of bilateral lung apexes which will be marked automatically by the software. Then, the motion trail was automatically traced by the software and the time curve of vertical dimension from diaphragm to lung apexes were painted and corresponding diaphragmatic motion velocity vs. time curve (Figure 2). The value of any point on the curves can be displayed, the excursions, durations and peak velocities of bilateral diaphragmatic motion were obtained based on the values were shown on the curves.

Statistical analyses

Statistical analyses were performed using Statistical Package for Social Sciences (SPSS) (IBM SPSS Inc., Chicago IL, Windows version 20). Continuous data were employed with normal distribution test. The variables with normal distribution were presented as means ± standard deviation (s) and variables with skewed distribution were presented in median (Inter Quartile Range, IQR). For comparative analysis of the COPD patients and healthy individuals, *t*-test was used for normal distribution data and non-parametric test (*Mann-Whitney U*) was used for skewed distribution data, and *Pearson* Chi-square test was used for enumeration data. The correlations between pulmonary function parameters and diaphragmatic motion excursions were analyzed using *Pearson* correlation analysis for normal distribution data and *Spearman* correlation analysis for skewed distribution data. For all correlation tests, $r = 0.10 \sim 0.39$ was considered a weak correlation; $r = 0.40 \sim 0.69$ a medium correlation and $r = 0.70 \sim 1.00$ was considered a strong correlation. Multiple linear regression was further used to analyze the correlation between bilateral diaphragmatic motion excursions and the COPD occurrence after correction for the gender, age and BMI. In all statistical analyses the $P < 0.05$ was considered as significant difference.

Results

Basic clinical characteristics of the 96 COPD patients and 50 healthy individuals are presented in Table 1. There

were significant differences in age, gender and height but no significant difference in BMI between the COPD and the healthy groups. Significant difference in IC, which reflects pulmonary capacity, was found between COPD patients and healthy individuals. Pulmonary ventilation parameters such as forced vital capacity (FVC), forced expiratory volume in on second (FEV1), and FEV1/FVC were significantly different between COPD patients and healthy individuals.

The bilateral diaphragmatic motion activity during forced breathing in both groups were recorded and sorted in Table 2. The diaphragmatic motion excursions and durations of inhalation and exhalation during forced breathing are significantly decreased in COPD patients, compared with healthy individuals ($P < 0.05$), but no significant difference of diaphragmatic motion velocity is observed between the two groups. The motion excursions of left diaphragm are significantly higher than the right side in both COPD and healthy groups ($P = 0.025$ in COPD patients and $P = 0.048$ in healthy individuals). In COPD patients, the motion velocity of left diaphragm is significantly higher than the right side in both inhalation stage ($P = 0.005$) and exhalation stage ($P = 0.006$), but there is no significant difference between left and right sides in healthy individuals ($P = 0.083$ in inhalation stage and $P = 0.109$ in exhalation stage).

Then, the correlations between pulmonary function parameters and bilateral diaphragm longitudinal motion excursions were analyzed (Table 3). The FEV1/FVC% predicted values showed the highest correlation with the diaphragmatic motion excursions among all the lung function parameters, which was of moderate correlation (Figure 3).

Finally, multiple linear regression analysis was conducted to analyze the correlations between bilateral diaphragmatic motion excursions and the COPD occurrence after corrected for the gender, age and BMI. The results showed that COPD occurrence ($P = 0.003$) and FEV1% predicted values ($P = 0.001$) are independent influencing factors of left diaphragmatic motion excursions. Moreover, COPD occurrence ($P = 0.010$) and FEV1% predicted values ($P = 0.002$) are independent

TABLE 1 Basic clinical characteristics and pulmonary function assessment of COPD patients and healthy individuals.

	COPD patients ($n = 96$)	Healthy individuals ($n = 50$)	Statistics$t$ or χ^2-value	P-value
Age (year)	66.21 ± 8.31	53.44 ± 5.38	9.84	<0.001
Gender (male/female)	79/17	8/42	60.00	<0.001
Height (cm)	167.50(6.75)	160.00(7.25)	−4.81	<0.001
Weight (kg)	68.94 ± 12.27	66.98 ± 9.24	0.99	0.322
BMI (Kg/m^2)	24.69 ± 3.94	25.65 ± 2.94	−1.52	0.131
Lung function				
FEV1% predicted value (%)	58.18 ± 21.49	110.60 ± 21.44	25.37	<0.001
FEV1/FVC% predicted value (%)	53.56 ± 11.11	79.87 ± 5.32	−19.34	<0.001
FVC% predicted value (%)	83.76 ± 20.00	102.75 ± 14.08	−6.66	<0.001
IC% predicted value (%)	79.92 ± 25.07	105.10 ± 15.18	−7.47	<0.001

TABLE 2 Comparative analysis of bilateral diaphragmatic motion activity during forced breathing in COPD patients and healthy individuals.

		COPD patients ($n = 96$)	Healthy individuals ($n = 50$)	Statistics t- or Z-value	P-value
Diaphragm longitudinal motion excursions (mm)	Left	35.93 ± 13.07	41.49 ± 12.07	−2.501	0.014
	Right	32.05 ± 12.29	36.88 ± 10.96	−2.334	0.021
Diaphragm descending time during inhalation (s)	Left	2.03(1.19)	2.53 ± 0.83	−2.45	0.014
	Right	1.94(1.32)	2.23(1.21)	−2.62	0.009
Diaphragm ascending time during exhalation (s)	Left	4.77(3.25)	6.40 ± 2.73	−2.42	0.016
	Right	4.94(3.30)	6.72 ± 2.58	−2.93	0.003
Peak diaphragmatic motion velocity in inhalation (mm/s)	Left	38.50 ± 14.42	37.94 ± 12.51	0.232	0.817
	Right	32.98 ± 12.70	33.64 ± 12.05	−0.301	0.764
Peak diaphragmatic motion velocity in exhalation (mm/s)	Left	34.46 ± 14.68	37.00(23.88)	−1.38	0.168
	Right	25.50(19.38)	29.25(18.63)	−1.86	0.063

TABLE 3 Correlation analysis of pulmonary function parameters and bilateral total diaphragmatic motion excursions during forced breathing.

Pulmonary function parameter	Diaphragmatic motion excursions	
	r	*P*
FEV1% predicted values	0.364	<0.001**
FEV1/FVC% predicted values	0.440	<0.001**
FVC% predicted values	0.245	0.016*
IC% predicted values	0.325	0.002**

*$P < 0.05$, **$P < 0.01$.

influencing factor of right diaphragmatic motion excursions (Table 4).

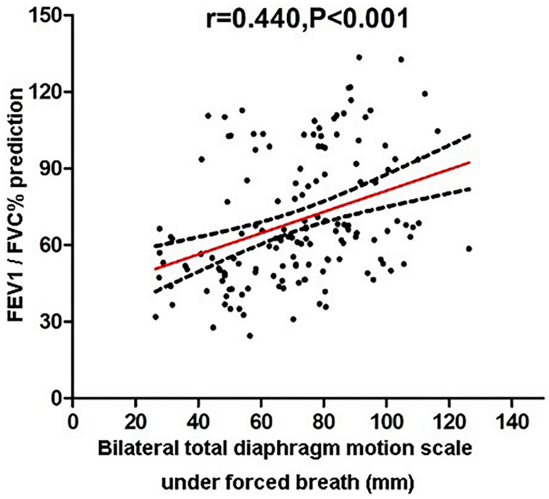

FIGURE 3
Correlation analysis of FEV1/FVC% predicted values and bilateral total diaphragmatic motion excursions during forced breathing.

Discussion

The contraction and dilation of diaphragm are the main driving force of pulmonary ventilation. In healthy people, the bilateral diaphragm is smoothy and dome-shaped with excursions of approximately 2∼3 cm during tidal breathing and 3∼6 cm during deep breathing (Yamada et al., 2017a). In this study, all subjects were in standing position during dynamic chest radiography with a flat panel X-ray detector, which maintains the normal daily position of patients. Therefore, the data acquired by dynamic chest radiography is more accurate than other imaging methods such as computed tomography (CT) and magnetic resonance imaging (MRI), in which subjects are in a supine position. The enroll criteria for the COPD patients followed the 2017 GOLD, that is, the patient has persistent respiratory symptoms, airflow limitation, and FEV1/FVC < 0.7 on pulmonary function tests after giving bronchodilators, which indicates the patient has persistent airflow limitation. The latest 2020 GOLD Guideline still maintains the diagnostic criteria of 2017 GOLD Guideline (Global Initiative for Chronic Obstructive Lung Disease, 2020).

As the airflow limitation and air trapping in COPD patients causes significantly increased respiratory load. It is reported that the respiratory load increased 5∼10 times in COPD patients compared with healthy individuals (MacIntyre and Leatherman, 1989). What's more, excessive expansion of lung tissue causes diaphragmatic depression, which leads to shortened initial contraction length of diaphragm, reduces diaphragm tension and affecting the respiratory movements. The inflammatory cytokines produced by COPD severely affect skeletal muscles throughout the whole body, including the diaphragm. In addition, tissue insufficient oxygen supply, electrolytic disorder further damages the diaphragm (Barreiro and Gea, 2015; Yamada et al., 2017b; Charususin et al., 2018; Jaitovich and Barreiro, 2018; Lee and Kim, 2019) and will finally cause diaphragm fatigue or even respiratory failure, which will severely reduce patient's life quality. Previous studies mainly focused on evaluation of diaphragm morphology or functional imaging (Kharma, 2013; Koo et al., 2018; Do Nascimento and Fleig, 2020). Traditional X-ray imaging is a preliminary test for evaluating diaphragm morphology alteration (Chetta et al., 2005). Further CT test will identify a variety of causes of abnormal morphology and position of diaphragm (Nason et al., 2012), for example, diaphragmatic elevation caused by subphrenic lesions or unilateral diaphragmatic paralysis caused by malignant lesions invading phrenic nerve. Dynamic MRI test can further evaluate diaphragm function, but the MRI is technically complicated and require high operation skills (Kiryu et al., 2006). Ultrasonography is the most common imaging modality to evaluate the morphology and function of diaphragm in clinic. It is simple and free of ionizing radiation and it can be used to measure both the direction and excursions of diaphragmatic motion (Connolly and Mittendorfer, 2016; Corbellini et al., 2018). The dynamic X-ray radiography used in this study has its own unique advantages compared with the abovementioned imaging methods. First, the equipment requires low patient compliance, especially for patients who cannot hold their breath long enough to complete a CT scan or for patients who cannot tolerate long scanning time of MRI, this equipment can also be used to evaluate the diaphragmatic motion in COPD patients. Then, this equipment can be used to monitor the morphological changes, motion excursions and motion consistency of bilateral diaphragms thoroughly. More importantly, it can provide quantitative data such as diaphragmatic motion excursions and velocity, which are conducive to a precise diagnosis.

TABLE 4 Multiple linear regression correction analysis of bilateral diaphragmatic motion excursions and the COPD progress after base line correction.

Variables	Left diaphragm longitudinal motion excursions (mm)			Right diaphragm longitudinal motion excursions (mm)		
	Regression coefficient	*t*	*P*	Regression coefficient	*t*	*P*
COPD occurrence (patient vs. control)	−15.508	−3.073	0.003**	−12.343	−2.615	0.010*
Gender	1.453	0.534	0.594	1.035	0.407	0.685
Age	0.056	0.358	0.721	−0.062	−0.423	0.673
BMI	0.550	1.954	0.053	0.498	1.893	0.060
FEV1% prediction (%)	0.192	3.276	0.001**	0.171	3.105	0.002**

*$P < 0.05$, **$P < 0.01$.

In our preliminary study, we analyzed diaphragmatic motion status of COPD patients during tidal breathing. The results showed that the diaphragmatic longitudinal motion excursions in COPD patients are significantly longer than healthy people, and this finding is consistent with the previous report by Yamada et al. (2017b). On this basis, the present study further analyzed the diaphragmatic motion status of COPD patients during forced breathing. The results showed that the diaphragmatic motion excursions in COPD patients are significantly shorter than healthy individuals, and this finding is consistent with the previous report by Hida et al. (2019). The different results of diaphragmatic motion during different breathing condition reflect that COPD pathological changes affect the diaphragmatic motion activity, which is mentioned above. Forced breathing can better reflects the motion state of diaphragm and pulmonary function, compared with tidal breathing. During forced breathing the diaphragm can no longer maintain its compensatory ability of diaphragm as in tidal breathing. In our study, the bilateral diaphragmatic motion velocity shows no significant difference between COPD patients and healthy individuals in both inhalation and exhalation phase. However, Hida et al., 2019 reported that the left diaphragmatic motion velocity is significantly lower than healthy individuals in inhalation phase, that might be because of the difference of the sample size of the study subjects and patient's overall lung function. Hida et al. (2019) enrolled only 31 COPD patients, so their results need further validation from multi-central studies with a larger sample size. We further compared the difference in bilateral diaphragmatic motion during forced breathing between COPD patients and healthy individuals. Our results showed that the left diaphragmatic motion excursions are significantly bigger than the right side in both groups and the maximum motion velocity of left diaphragm is significantly higher than the right side. This difference could be attributed to the restriction caused by liver over the active contraction and descending of right diaphragm.

Univariate analysis showed that the diaphragmatic motion excursion during forced breathing was of moderate correlation with FEV1/FVC (r = 0.440). Because the enrolled COPD patients were of elderly age group and predominantly male, and we failed to enroll enough age- and gender-matched healthy individuals with matched age and gender. After correction for the gender, age and BMI, multiple linear regression analysis showed that COPD occurrence and FEV1% predicted values is an independent influence factor of bilateral diaphragmatic motion excursions. Hida et al. (2019), using the same dynamic X-ray device as we do reported that in COPD patients the diaphragmatic motion excursions are correlated to VC and FEV1 during forced breathing using the same. Yamada et al. (2017b) reported that COPD occurrence and BMI are independent influence factor of diaphragmatic motion excursions. Therefore, dynamic X-ray device can be used as an auxiliary diagnosis to evaluate the lung function and degree of diaphragm lesions in COPD patients, especially for those with poor pulmonary function or unable to complete the pulmonary function test due to failure to comprehend and cooperate with the instructions. What's more, using the post-processing function of the device we can also obtain the functional images of pulmonary ventilation and pulmonary circulation from the images of dynamic chest films. The clinical applications of this device needed further development and utilization.

This study has some limitations. First, it was a single-center trial. Therefore, studies with larger sample size are needed to validate the results. Second, the dynamic digital radiography system is a newly developed device. The obtained radiographs only contained anteroposterior position information but lacked lateral position information, so further improvement is needed to provide more objective data for clinical study. Third, there were relatively few GOLD grades III or IV patients enrolled in this study, no further grading study has been carried out, so we still need to increase the sample size to further improve the assessment.

Conclusion

In conclusion, the objective and accurate quantitative data of diaphragmatic motion can be obtained using dynamic

chest radiography, which is a valuable examination method to evaluate the condition of COPD patients.

Data availability statement

The original contributions presented in this study are included in the article/supplementary material, further inquiries can be directed to the corresponding author.

Ethics statement

All experimental procedures of this study were approved by the Institutional Review Board and Ethics Committee of Beijing Friendship Hospital affiliated to Capital Medical University, Beijing, China (Ethics code: 2018-P2-086-01) that were in accordance with the regulations and guidelines of the studies on human subjects set by the Declaration of Helsinki. The patients/participants provided their written informed consent to participate in this study.

Author contributions

JC and ZZ conducted the analytical part, wrote the first version of the manuscript, and finalized the manuscript. WW, GY, and TZ collected the data. ZW supervised the study. ZZ conceived and coordinated the study, and critically evaluated the data. All authors read and approved the final manuscript.

Funding

This study was supported by the Beijing Scholar 2015 [No. (2015)160], Beijing Hospitals Authority Clinical Medicine Development of Special Funding Support (No. ZYLX202101), and Beijing Municipal Health Commission.

Conflict of interest

The authors declare that the research was conducted in the absence of any commercial or financial relationships that could be construed as a potential conflict of interest.

Publisher's note

All claims expressed in this article are solely those of the authors and do not necessarily represent those of their affiliated organizations, or those of the publisher, the editors and the reviewers. Any product that may be evaluated in this article, or claim that may be made by its manufacturer, is not guaranteed or endorsed by the publisher.

References

Agustí, A., Celli, B., and Faner, R. (2017). What does endotyping mean for treatment in chronic obstructive pulmonary disease? *Lancet* 390, 980–987. doi: 10.1016/S0140-6736(17)32136-0

Barreiro, E., and Gea, J. (2015). Respiratory and limb muscle dysfunction in COPD. *COPD* 12, 413–426. doi: 10.3109/15412555.2014.974737

Cazzola, M., Rogliani, P., Puxeddu, E., Ora, J., and Matera, M. G. (2018). An overview of the current management of chronic obstructive pulmonary disease: Can we go beyond the GOLD recommendations? *Exp. Rev. Respir. Med.* 12, 43–54. doi: 10.1080/17476348.2018.1398086

Charususin, N., Dacha, S., Gosselink, R., Decramer, M., Von Leupoldt, A., Reijnders, T., et al. (2018). Respiratory muscle function and exercise limitation in patients with chronic obstructive pulmonary disease: A review. *Exp. Rev. Respir. Med.* 12, 67–79. doi: 10.1080/17476348.2018.1398084

Chetta, A., Rehman, A. K., Moxham, J., Carr, D. H., and Polkey, M. I. (2005). Chest radiography cannot predict diaphragm function. *Respir. Med.* 99, 39–44. doi: 10.1016/j.rmed.2004.04.016

Connolly, A. M., and Mittendorfer, B. (2016). Tracking diaphragm movement using ultrasound to assess its strength. *J. Physiol.* 594, 7147. doi: 10.1113/JP273313

Corbellini, C., Boussuges, A., Villafañe, J. H., and Zocchi, L. (2018). Diaphragmatic mobility loss in subjects with moderate to very severe COPD may improve after in-patient pulmonary rehabilitation. *Respir. Care.* 63, 1271–1280. doi: 10.4187/respcare.06101

Dennett, E. J., Janjua, S., Stovold, E., Harrison, S. L., McDonnell, M. J., and Holland, A. E. (2021). Tailored or adapted interventions for adults with chronic obstructive pulmonary disease and at least one other long-term condition: A mixed methods review. *Cochrane Database Syst. Rev.* 7:CD013384. doi: 10.1002/14651858.CD013384.pub2

Do Nascimento, I. B., and Fleig, R. (2020). Mobility impact and methods of diaphragm monitoring in patients with chronic obstructive pulmonary disease: A systematic review. *Clinics* 75:e1428. doi: 10.6061/clinics/2020/e1428

Franssen, F. M. E., Alter, P., Bar, N., Benedikter, B. J., Iurato, S., Maier, D., et al. (2019). Personalized medicine for patients with COPD: Where are we? *Int. J. Chron. Obstruct. Pulmon. Dis.* 14, 1465–1484. doi: 10.2147/COPD.S175706

General Assembly of the World Medical Association (2014). World medical association declaration of Helsinki: Ethical principles for medical research involving human subjects. *J. Am. Coll. Dent.* 81, 14–18.

Global Initiative for Chronic Obstructive Lung Disease (2020). *2020 Gold reports – Evidence-based strategy document for COPD diagnosis, management, and prevention, with citations from the scientific literature*. Bethesda, MD: National Heart, Lung and Blood Institute.

Hersh, C. P. (2019). Pharmacogenomics of chronic obstructive pulmonary disease. *Exp. Rev. Respir. Med.* 13, 459–470. doi: 10.1080/17476348.2019.1601559

Hida, T., Yamada, Y., Ueyama, M., Araki, T., Nishino, M., Kurosaki, A., et al. (2019). Decreased and slower diaphragmatic motion during forced breathing in severe COPD patients: Time-resolved quantitative analysis using dynamic chest radiography with a flat panel detector system. *Eur. J. Radiol.* 112, 28–36. doi: 10.1016/j.ejrad.2018.12.023

Jaitovich, A., and Barreiro, E. (2018). Skeletal muscle dysfunction in chronic obstructive pulmonary disease what we know and can do for our patients. *Am. J. Respir. Crit. Care Med.* 198, 175–186. doi: 10.1164/rccm.201710-2140CI

Kharma, N. (2013). Dysfunction of the diaphragm: Imaging as a diagnostic tool. *Curr. Opin. Pulm. Med.* 19, 394–398. doi: 10.1097/MCP.0b013e3283621b49

Kiryu, S., Loring, S. H., Mori, Y., Rofsky, N. M., Hatabu, H., and Takahashi, M. (2006). Quantitative analysis of the velocity and synchronicity of diaphragmatic motion: Dynamic MRI in different postures. *Magn. Reson. Imaging* 24, 1325–1332. doi: 10.1016/j.mri.2006.08.009

Koo, C. W., Johnson, T. F., Gierada, D. S., White, D. B., Blackmon, S., Matsumoto, J. M., et al. (2018). The breadth of the diaphragm: Updates in embryogenesis and role of imaging. *Br. J. Radiol.* 91:20170600.

Lee, E. N., and Kim, M. J. (2019). Meta-analysis of the effect of a pulmonary rehabilitation program on respiratory muscle strength in patients with chronic obstructive pulmonary disease. *Asian Nurs. Res (Korean Soc. Nurs. Sci).* 13, 1–10. doi: 10.1016/j.anr.2018.11.005

Lozano, R., Naghavi, M., Foreman, K., Lim, S., Shibuya, K., Aboyans, V., et al. (2012). Global and regional mortality from 235 causes of death for 20 age groups in 1990 and 2010: A systematic analysis for the Global Burden of Disease Study 2010. *Lancet* 380, 2095–2128. doi: 10.1016/S0140-6736(12)61728-0

MacIntyre, N. R., and Leatherman, N. E. (1989). Mechanical loads on the ventilatory muscles. A theoretical analysis. *Am. Rev. Respir. Dis.* 139, 968–973. doi: 10.1164/ajrccm/139.4.968

Morgan, R. K., and Summer, R. (2008). "Chronic obstructive pulmonary disease," in *International encyclopedia of public health*, (Amsterdam: Elsevier Inc), 709–717. doi: 10.1016/B978-012373960-5.00213-6

Nason, L. K., Walker, C. M., Mcneeley, M. F., Burivong, W., Fligner, C. L., and David Godwin, J. (2012). Imaging of the diaphragm: Anatomy and function. *Radiographics* 32, E51–E70. doi: 10.1148/rg.322115127

Sidhaye, V. K., Nishida, K., and Martinez, F. J. (2018). Precision medicine in COPD: Where are we and where do we need to go? *Eur. Respir. Rev.* 27:180022. doi: 10.1183/16000617.0022-2018

Stanaway, J. D., Afshin, A., Gakidou, E., Lim, S. S., Abate, D., Abate, K. H., et al. (2018). Global, regional, and national comparative risk assessment of 84 behavioural, environmental and occupational, and metabolic risks or clusters of risks for 195 countries and territories, 1990-2017: A systematic analysis for the Global Burden of Disease Stu. *Lancet* 392, 1923–1994. doi: 10.1016/S0140-6736(18)32225-6

Ulrik, C. S., Vijverberg, S., Hanania, N. A., and Diamant, Z. (2020). Precision medicine and treatable traits in chronic airway diseases - where do we stand? *Curr. Opin. Pulm. Med.* 26, 33–39. doi: 10.1097/MCP.0000000000000639

Wang, C., Xu, J., Yang, L., Xu, Y., Zhang, X., Bai, C., et al. (2018). Prevalence and risk factors of chronic obstructive pulmonary disease in China (the China Pulmonary Health [CPH] study): A national cross-sectional study. *Lancet* 391, 1706–1717. doi: 10.1016/S0140-6736(18)30841-9

Wouters, E. F. M., Wouters, B. B. R. A. F., Augustin, I. M. L., and Franssen, F. M. E. (2017). Personalized medicine and chronic obstructive pulmonary disease. *Curr. Opin. Pulm. Med.* 23, 241–246. doi: 10.1097/MCP.0000000000000377

Yamada, Y., Ueyama, M., Abe, T., Araki, T., Abe, T., Nishino, M., et al. (2017a). Difference in the craniocaudal gradient of the maximum pixel value change rate between chronic obstructive pulmonary disease patients and normal subjects using sub-mGy dynamic chest radiography with a flat panel detector system. *Eur. J. Radiol.* 92, 37–44. doi: 10.1016/j.ejrad.2017.04.016

Yamada, Y., Ueyama, M., Abe, T., Araki, T., Abe, T., Nishino, M., et al. (2017b). Difference in diaphragmatic motion during tidal breathing in a standing position between COPD patients and normal subjects: Time-resolved quantitative evaluation using dynamic chest radiography with flat panel detector system ("dynamic X-ray phrenicograph. *Eur. J. Radiol.* 87, 76–82. doi: 10.1016/j.ejrad.2016.12.014

frontiers | Frontiers in Medicine

TYPE Original Research
PUBLISHED 23 February 2023
DOI 10.3389/fmed.2023.832878

OPEN ACCESS

EDITED BY
Sergio Machado,
Federal University of Santa Maria,
Brazil

REVIEWED BY
Sridhar Goud Nerella,
National Institutes of Health,
United States
Tiina Sairanen,
Hospital District of Helsinki and Uusimaa,
Finland

*CORRESPONDENCE
Rongfeng Wang
✉ wrf1611@163.com
Mingwu Xia
✉ xiamingwu1965@163.com

†These authors have contributed equally to this work

SPECIALTY SECTION
This article was submitted to Precision Medicine, a section of the journal Frontiers in Medicine

RECEIVED 10 December 2021
ACCEPTED 07 February 2023
PUBLISHED 23 February 2023

CITATION
Cao S, Zhai M, He J, Cui P, Ge T, Wang J, Xu W, Wang R and Xia M (2023) Prevalence and associated factors of basilar artery dolichosis in patients with acute cerebral infarction. *Front. Med.* 10:832878. doi: 10.3389/fmed.2023.832878

Prevalence and associated factors of basilar artery dolichosis in patients with acute cerebral infarction

Shugang Cao[1†], Mingfeng Zhai[2†], Jun He[1], Ping Cui[3], Tingting Ge[1], Jian Wang[1], Wen'an Xu[1], Rongfeng Wang[1*] and Mingwu Xia[1*]

[1]Department of Neurology, Hefei Hospital Affiliated to Anhui Medical University, Hefei, China, [2]Department of Neurology, The People's Hospital of Fuyang, Fuyang, China, [3]Department of Radiology, Hefei Hospital Affiliated to Anhui Medical University, Hefei, China

Introduction: Little attention has been given to the factors associated with basilar artery (BA) dolichosis. This study aims to elucidate the prevalence and associated factors of BA dolichosis in patients with acute cerebral infarction (ACI).

Methods: We collected the clinical and laboratory data of 719 patients with ACI admitted to our department. Magnetic resonance angiography was used to evaluate the geometric parameters of the BA and intracranial vertebral arteries (VAs). A BA curve length >29.5 mm or bending length (BL) >10 mm was identified as BA dolichosis. Univariate and multivariate logistic regression were performed to determine the factors associated with BA dolichosis.

Results: Among 719 patients with ACI, 238 (33.1%) demonstrated BA dolichosis, including 226 (31.4%) with simple BA dolichosis and 12 (1.7%) with basilar artery dolichoectasia (BADE). Pearson correlation analyses showed that BA curve length was positively correlated with BL (r=0.605). Multivariate logistic regression analysis demonstrated that current smoking (OR=1.50, 95% CI: 1.02–2.21, p=0.039), diabetes mellitus (OR=1.66, 95% CI: 1.14–2.41, p=0.008), BA diameter (OR=3.04, 95% CI: 2.23–4.13, p<0.001), BA bending (OR=4.24, 95% CI: 2.91–6.17, p<0.001) and BL (OR=1.45, 95% CI: 1.36–1.55, p<0.001) were significantly associated with BA dolichosis.

Conclusion: This study suggests that BA dolichosis was common in patients with ACI, and the morphological parameters of the vertebrobasilar artery and acquired risk factors (including smoking and diabetes) were risk factors for BA dolichosis.

KEYWORDS

stroke, cerebral infarction, basilar artery dolichosis, vertebrobasilar dolichoectasia, diabetes mellitus

1. Introduction

Basilar artery dolichoectasia (BADE), a typical type of vertebrobasilar dolichoectasia (VBD), is characterized by elongation and dilatation of the BA. Some studies have argued that BADE may result from the combination of congenital developmental defects in the BA and the combined action of multiple risk factors for atherosclerosis (1–3) and that it may evolve dynamically (1, 4). Passero et al. (1). performed imaging follow-ups for 156 VBD patients with

an average disease duration of 11.7 years and showed that 43% of patients had morphological developments in the BA, including increases in BA length (BAL), BA diameter, and bending length (BL). A large BA diameter, high bifurcation of the BA, and elongation and dilatation of the anterior cerebral artery were factors correlated with morphological developments in the BA. In addition, the morphological progression of BA may further influence the prognosis of these patients (5–7).

BADE is an uncommon vasculopathy in the Chinese Han population, and many patients with simple BA dolichosis cannot be classified as having BADE. Our previous study found that among 101 patients with acute pontine infarction, 33 patients (32.7%) presented with simple BA dolichosis, and only one patient (1.0%) developed BADE (7). Another investigation showed that in 346 community-dwelling older adults, 11 individuals (3.2%) had BA ectasia, 36 individuals (11.6%) had BA dolichosis, and only 4 individuals (1.2%) had BADE (2). However, little attention has been given to the prevalence of BA dolichosis and its associated risk factors, which is commonly observed in Chinese patients with acute cerebral infarction (ACI). The length of the BA does not remain constant (8), and its morphological remodeling may also be influenced by genetic factors (such as abnormalities in the structure and function of vascular muscle fibers and variations in different vertebrobasilar morphological indices) and acquired environmental factors (1–3). Therefore, based on this hypothesis, this study aimed to elucidate the prevalence and associated factors of BA dolichosis in the Chinese population by analyzing the clinical and imaging data of patients with ACI in our stroke unit.

2. Methods

2.1. Study design and patients

This was a cross-sectional study that purposely selected patients with ACI. All patients consecutively admitted between July 2015 and June 2019 to our department were selected according to the following inclusion criteria: age 18–80 years old, admission within 7 days after onset, and diagnosis of ACI by diffusion-weighted imaging. Patients with infarct foci involving both the anterior and posterior circulation, segmental thickening of the BA or BA aneurysms, evidence of hemodynamically severe BA stenosis (≥70%) or occlusion affecting data measurements, or incomplete clinical or imaging information were excluded. This study was approved by the Institutional Review Board of Hefei Hospital Affiliated to Anhui Medical University. Written informed consent was obtained from all patients or their guardians. All patients were registered in the Anhui Stroke Network Registry.

2.2. Clinical and laboratory data

Detailed clinical data were acquired from the patients, including age, sex, current smoking status, the presence of hypertension, diabetes mellitus, and dyslipidemia, as well as admission systolic and diastolic blood pressure. Hypertension was defined as a resting systolic/diastolic blood pressure of ≥140/≥90 mm Hg on repeated measurements or if the patient was taking anti-hypertension drugs. Diabetes mellitus was diagnosed when the patient had a fasting blood glucose level of ≥7.0 mmol/L, was taking oral hypoglycemic agents, or had been treated with insulin. Dyslipidemia was diagnosed if the patient had a total cholesterol level of ≥5.60 mmol/L, a triglyceride level of ≥1.81 mmol/L, or a low-density lipoprotein level of ≥3.57 mmol/L, or if the patient had taken lipid-lowering medications for these conditions. Laboratory information, including blood glucose, total cholesterol, triglycerides, low-density lipoprotein, C-reactive protein, and homocysteine levels, was systematically recorded.

2.3. Imaging protocol and analysis

Magnetic resonance imaging (MRI) and magnetic resonance angiography (MRA) were performed using a 1.5 Tesla MRI scanner (Siemens Healthineers, Model: Avanto I class, Germany). The geometrical parameters of the BA were analyzed by syngo 3-D VesselView. The scanning parameters and method for evaluating the BA characteristics, including BA diameter, BA curve length, BAL, BL, and BADE, were described in a previously published study (7). Among them, BAL is defined as the linear distance from the confluence point of the bilateral VAs to the initial point of the BA division into the bilateral posterior cerebral arteries, and BL is defined as the vertical distance from the bending point of the BA to the standard line of the BAL (9, 10). A BA curve length > 29.5 mm or BL > 10 mm was diagnosed as BA dolichosis, and BA ectasia was defined as a BA diameter > 4.5 mm at any location along its course. Patients meeting the above two criteria simultaneously were considered to have BADE (11). The severity of the BA bending was classified as moderate ($0 < BL \leq 10$ mm) and prominent (BL > 10 mm). We further evaluated the maximum bend of the BA, which was divided into the proximal, middle, and distal portions of the BA. Image analysis was performed by two experienced neurologists, and the mean values of the above parameters were recorded as the results for further analysis. The line of the BAL was used to determine the location of BA bending (toward the right or left side or straight) (10). When there was any disagreement, a radiologist with 10 years of experience was consulted to resolve the issue. The diameters of the V4 segment of the bilateral vertebral arteries (VAs) were measured. From the vertebrobasilar artery junction, a series of three measurements with 3-mm intervals at each side was taken, and the mean diameter served as the VA diameter (12). VA dominance was defined as a difference in the diameter of both vertebral arteries of at least 0.3 mm or as an existing asymmetry in the merging of both VAs at the vertebrobasilar junction (10, 12). A Bland–Altman plot was used to analyze the agreement between the two readers.

2.4. Statistical analysis

All statistical analyses were performed using SPSS version 22.0 for Windows (SPSS Inc., Chicago, IL). Normally distributed variables are expressed as the mean ± standard deviation (mean ± SD), while nonnormally distributed variables are shown as the median (M) and interquartile range (IQR). Categorical variables are expressed as absolute numbers and percentages (%). Differences in continuous variables between groups were assessed by Student's *t*-test (normally distributed) or the Mann–Whitney *U*-test (nonnormally distributed).

Differences in categorical variable distributions between groups were assessed by the χ^2 test or Fisher's exact test. Univariate and multivariate logistic regression were performed to determine the factors associated with BA dolichosis. Odds ratios (ORs) and 95% confidence intervals (CIs) were subsequently calculated. Potential relationships between variables were assessed by Pearson correlation analysis, and the correlation coefficient was expressed as *r*. All tests used a two-sided *p*-value of 0.05 as a threshold for significance. All plots were drawn using GraphPad Prism software (version 8.0).

3. Results

3.1. Baseline characteristics

A total of 719 patients with ACI were included in the study, of whom 452 had anterior circulation infarction and 267 had posterior circulation infarction. The mean age was 63.7 ± 10.4 years, and 69.5% were male. Among them, 238 patients (33.1%) demonstrated BA dolichosis, including 226 patients (31.4%) with simple BA dolichosis and 12 patients (1.7%) with BADE, while other 481 patients (66.9%) had no BA dolichosis. The proportion of BA dolichosis in patients with anterior and posterior circulation infarction was 32.5% (147/452) and 34.1% (91/267), respectively, with no statistically significant difference between the two groups. Further analysis revealed that in patients aged ≤64 years (median age), the proportion of BA dolichosis in patients with anterior and posterior circulation infarction were 35.9% and 34.1%, respectively, while in patients aged >64 years, the proportion of BA dolichosis were 29.5% and 34.1%, respectively.

A total of 403 patients had BA bending (including 380 patients with moderate bending and 23 patients with prominent bending), and 316 patients did not have BA bending (Figure 1). BA diameter ($p < 0.001$) and BL ($p < 0.001$) were significantly higher in patients with BA dolichosis than in those with non-BA dolichosis (Figures 2A,B). The BA curve length ($p < 0.001$) and BAL ($p < 0.001$) in patients with BA bending were significantly higher than those in patients with non-BA bending (Figures 2C,D). The proportion of BA bending was significantly higher in the BA dolichosis group than in the non-BA dolichosis group (77.7% vs. 45.3%, $p < 0.001$). No patient was diagnosed with simple BA ectasia. In 378 patients (94.7%) with BA bending, the maximum bend of the BA was located at the middle of the BA, with only 9 patients bending in the proximal region of the BA and 16 patients bending in the distal portion of the BA.

3.2. Univariate and multivariate logistic regression analysis of factors associated with BA dolichosis

Male sex ($p < 0.001$), current smoking ($p = 0.001$), diabetes mellitus ($p = 0.019$), diastolic blood pressure ($p = 0.013$), BA diameter ($p < 0.001$), left VA diameter ($p = 0.001$), right VA diameter ($p = 0.002$), and BA bending ($p < 0.001$) were significantly greater in patients with BA dolichosis than in patients without BA dolichosis in univariate analysis (Table 1). After adjusting for variables with a potential association (variables with a *p*-value <0.1 in univariate analysis), current smoking (OR = 1.50, 95% CI: 1.02–2.21, $p = 0.039$), diabetes mellitus (OR = 1.66, 95% CI: 1.14–2.41, $p = 0.008$), BA diameter (OR = 3.04, 95% CI: 2.23–4.13, $p < 0.001$), and BA bending (OR = 4.24, 95% CI: 2.91–6.17, $p < 0.001$) were significantly associated with BA dolichosis (Table 2). When BA bending was replaced by BL, a quantitative indicator indicating the degree of BA bending, in the above logistic regression model, BL (OR = 1.45, 95% CI: 1.36–1.55, $p < 0.001$) was also significantly associated with BA dolichosis (Table 2).

3.3. Correlation analysis between dependent variables

Pearson correlation analyses showed a positive correlation between BA curve length and BL ($r = 0.605$, $p < 0.001$; Figure 3). In addition, BA diameter, left VA diameter, and right VA diameter were

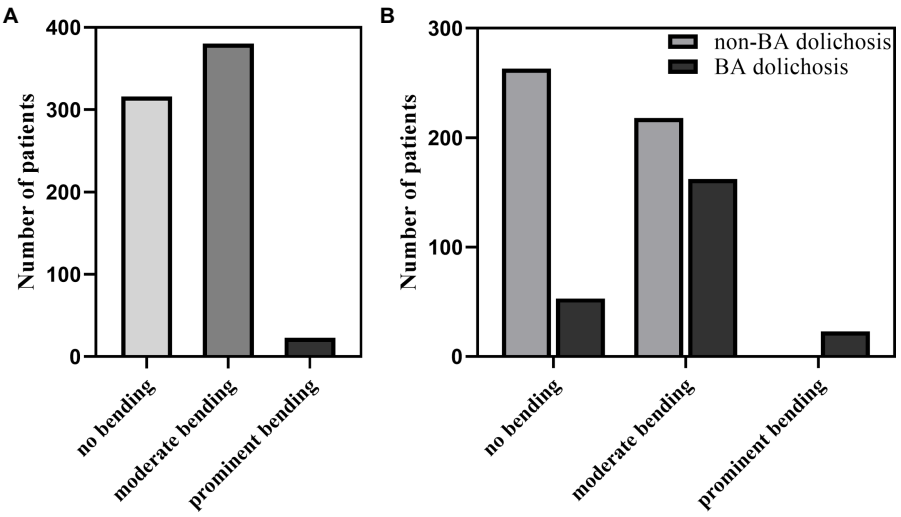

FIGURE 1
BA bending distribution in the entire study population **(A)**; BA bending distribution in patients with BA dolichosis and non-BA dolichosis **(B)**.

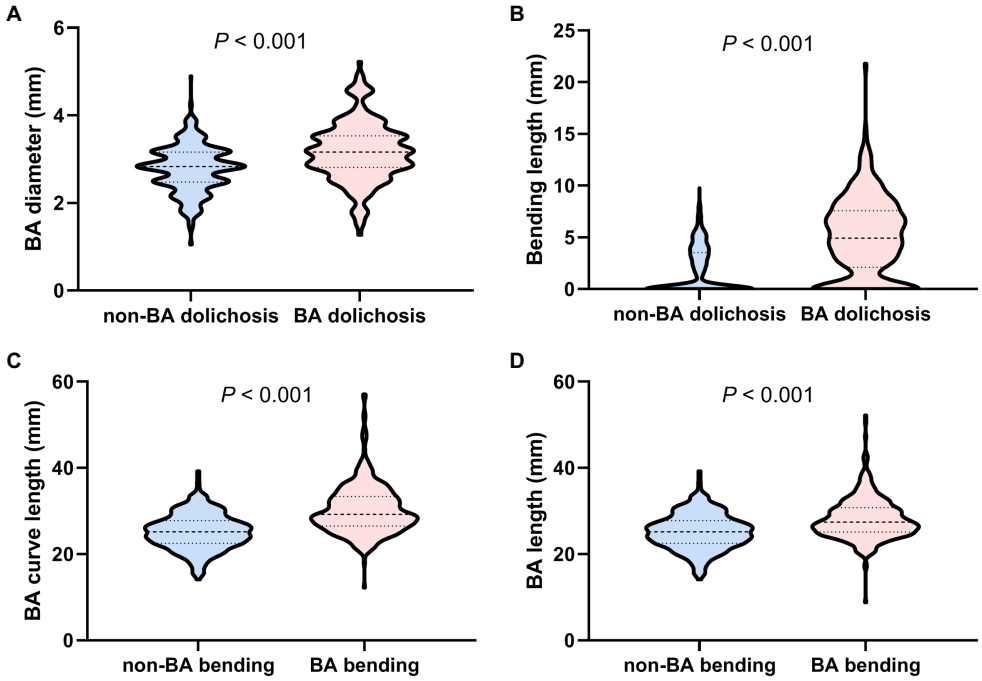

FIGURE 2
Comparison of BA diameter and BL between patients with BA dolichosis and non-BA dolichosis **(A,B)**; Comparison of BA curve length and BAL between patients with BA bending and non-BA bending **(C,D)**.

positively correlated with BA curve length, BAL, and BL, respectively, and the VA diameter difference was also significantly positively correlated with BL (Supplementary Figure).

4. Discussion

In the present study, we hypothesized that the length of the BA may be related to the innate geometric patterns of the vertebrobasilar artery and acquired risk factors. We found that BA dolichosis was highly associated with smoking, diabetes mellitus, BA diameter, and BA bending in patients with ACI. In addition, the BA curve length was also positively correlated with the BL, BA diameter, and VA diameter.

BADE is uncommon in stroke patients, but we found BA dolichosis to be relatively common in patients with ACI, and that there was little difference in the proportion of BA dolichosis between patients with anterior and posterior circulation infarction (32.5% vs. 34.1%). This may be related to the fact that simple BA dolichosis has a less pronounced effect on stroke than BADE, especially in young and middle-aged patients, which does not usually cause a higher proportion of posterior circulation infarction. However, this proportional difference may widen with increasing age, as suggested by the subgroup analysis of this study, which was more pronounced in patients older than 64 years. This also suggests that BA dolichosis may be influenced by congenital factors and develops when the patient reaches adulthood (1), yielding little difference in the proportion of BA dolichosis between younger patients with anterior and posterior circulation infarction, but may lead to an increased risk of posterior circulation infarction with advancing age and increasing atherosclerotic factors (13).

Although we briefly compared the BA geometrical properties between patients with and without BA dolichosis in our previous study (7), we did not evaluate the factors associated with BA dolichosis and the sample size was small. The present study had a sample size more than 7 times larger than the previous one and analyzed the factors associated with BA dolichosis more systematically. Previous studies have concluded that BADE diagnoses in healthy young people and children suggest congenital susceptibility as a potential cause of congenital developmental defects in the BA (14, 15). Pathological studies have confirmed that degeneration of the internal elastic lamina and smooth muscular atrophy are the main features of BADE in adults (16). However, it is challenging to obtain pathological data in a clinical context, but the geometric patterns of the vertebrobasilar artery that are influenced by congenital factors can be directly visualized by vascular imaging. From another perspective, this study revealed that BA curve length was positively related to BA diameter and BL; that is, a greater diameter and curvature of the BA might be related to a longer BA. The vessel radius is the most essential determinant of blood flow; a larger BA diameter leads to more blood flow and greater pulling force, thereby acting as a potential stimulus for morphological changes in the BA (e.g., elongation, ectasia, and/or curvature), especially when BA bending already exists. Multivariate analysis also demonstrated that BA diameter and BA bending were closely related to BA dolichosis, further supporting the above viewpoint. Additionally, we found that BA curve length was positively correlated with BL and that BL, a quantitative indicator representing the degree of BA bending, was another risk factor associated with BA dolichosis. However, the underlying mechanism is not clear. Presumably, in addition to being associated with congenital vascular development, the uneven blood

TABLE 1 Univariate logistic regression analysis of factors associated with BA dolichosis in patients with ACI.

Variable	BA dolichosis group (*n*=238)	Non-BA dolichosis group (*n*=481)	Unadjusted OR (95%CI)	Value of *p*
Demographic data				
Age (years)	63.1 ± 10.3	64.0 ± 10.4	0.99 (0.98–1.01)	0.289
Male sex, *n* (%)	187 (78.6)	313 (65.1)	1.97 (1.37–2.83)	<0.001
Risk factors				
Current smoking, *n* (%)	86 (36.1)	119 (24.7)	1.72 (1.23–2.41)	0.002
Hypertension, *n* (%)	152 (63.9)	293 (60.9)	1.13 (0.82–1.56)	0.443
Diabetes mellitus, *n* (%)	84 (35.3)	129 (26.8)	1.49 (1.07–2.08)	0.020
Dyslipidemia, *n* (%)	72 (30.3)	124 (25.8)	1.25 (0.89–1.76)	0.205
Blood pressure on admission				
Systolic blood pressure (mmHg)	152.3 ± 21.1	150.1 ± 20.0	1.01 (1.00–1.01)	0.168
Diastolic blood pressure (mmHg)	90.6 ± 12.5	88.1 ± 12.1	1.02 (1.00–1.03)	0.013
Laboratory indices				
Blood glucose (mmol/L)	6.26 ± 2.91	6.65 ± 3.03	0.96 (0.90–1.01)	0.111
Total cholesterol (mmol/L)	4.30 ± 0.86	4.34 ± 0.98	0.95 (0.80–1.12)	0.514
Triglycerides (mmol/L)	1.99 ± 1.27	1.96 ± 1.42	1.02 (0.91–1.14)	0.776
Low-density lipoprotein (mmol/L)	2.59 ± 0.74	2.65 ± 0.86	0.91 (0.75–1.10)	0.307
C-reactive protein (mg/L)	6.57 ± 11.10	7.21 ± 13.09	1.00 (0.98–1.01)	0.511
Homocysteine (μmol/L)	16.50 ± 13.94	15.00 ± 11.17	1.01 (1.00–1.02)	0.125
Vertebrobasilar artery features				
BA diameter (mm)	3.17 ± 0.68	2.78 ± 0.53	3.12 (2.32–4.19)	<0.001
Left VA diameter (mm)	2.52 ± 0.94	2.29 ± 0.77	1.41 (1.16–1.72)	0.001
Right VA diameter (mm)	2.28 ± 0.81	2.09 ± 0.77	1.38 (1.13–1.70)	0.002
VA diameter difference (mm)	0.98 ± 0.93	0.85 ± 0.77	1.20 (1.00–1.44)	0.054
BL (mm)	4.97 (2.22, 7.71)	0 (0, 3.53)	1.44 (1.35–1.53)	<0.001
BA bending, *n* (%)	185 (77.7)	218 (45.3)	4.21 (2.96–6.00)	<0.001
VAD, *n* (%)	168 (70.6)	338 (70.3)	1.02 (0.72–1.14)	0.930

BA, basilar artery; VA, vertebral artery; BL, bending length; VAD, vertebral artery dominance.

TABLE 2 Multivariate logistic regression analysis of factors associated with BA dolichosis.

Models	Adjusted OR (95% CI)	Value of *p*
Model 1 (with BA bending)		
Current smoking	1.50 (1.02–2.21)	0.039
Diabetes mellitus	1.66 (1.14–2.41)	0.008
BA diameter	3.04 (2.23–4.13)	<0.001
BA bending	4.24 (2.91–6.17)	<0.001
Model 2 (with BL)		
Smoking	1.73 (1.16–2.59)	0.007
Diabetes mellitus	1.59 (1.06–2.38)	0.026
BA diameter	3.36 (2.40–4.69)	<0.001
BL	1.14 (1.36–1.55)	<0.001

flow within a curved BA, with the greatest blood pressure at the bend, also exacerbates the progression of BA curvature and elongation with increasing age (8).

In addition, the study by Hong et al. showed that the difference in the diameter of the VAs was the only independent predictor of moderate to severe BA dolichosis (12). Unlike their study, we only demonstrated a positive correlation between the VA diameter difference and BL. Even so, it is still generally believed that the BA usually curves in the opposite direction of the larger VA (12). The asymmetrical blood flow from the bilateral VAs might be an important hemodynamic contributor to BA mechanical changes, such as BA curvature and elongation (9, 11).

Risk factors for atherosclerosis may also play an important role in the development of BA dolichosis. The BA and VA morphological variants or structural deformation mentioned above can cause atherosclerosis, which in turn further aggravates BA dolichosis, and they can generate a vicious circle thereby increasing the risk of posterior circulation infarction (7, 13, 17, 18). Known influencing factors of BADE include aging, hypertension, diabetes mellitus, and smoking, among others, which are also targets that merit particular attention and intervention (3, 9). This study found that smoking and diabetes mellitus were also closely associated with BA dolichosis, supporting the hypothesis that atherosclerosis may be involved in the development of BA dolichosis. Previous studies have suggested that

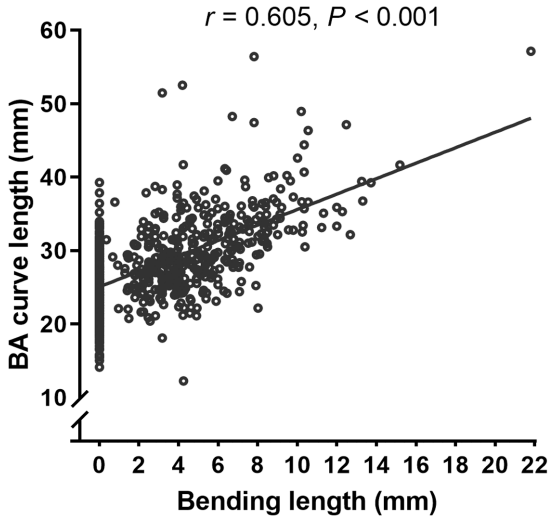

FIGURE 3
Pearson correlation analyses showed a positive correlation between BA curve length and BL (r=0.605, p<0.001).

hypertension is critical in the development of VBD, especially the increase in BA diameter due to the influence of high blood pressure and subsequent hemodynamic changes (4). However, it remains unclear whether blood pressure directly affects BA length. In this study, univariate analysis revealed that the BA dolichosis group had a high proportion of hypertension and significantly elevated diastolic blood pressure, but multivariate analysis did not confirm that they were independent influencing factors of BA dolichosis. The results may need to be further verified with larger sample studies. Additionally, there was a higher proportion of males in the BA dolichosis group. Deng et al. suggested that compared with females, males had a larger BA diameter, which is associated with BA length, while the overall height of males was greater than that of females and therefore could explain the longer BA in male individuals (19).

The present study also has some limitations. First, this study only included patients with ACI. Many patients showed a high prevalence of risk factors for atherosclerosis. Therefore, a separate or comparative analysis of influencing factors of BA dolichosis in healthy people is also warranted. Second, this study did not provide a long-term follow-up of the dynamic evolution of BA curve length. Third, this study did not evaluate the flow dynamics of the vertebrobasilar artery, which may help to elucidate the mechanism of the formation and development of BA dolichosis.

5. Conclusion

In this study, we found that BA dolichosis was common in patients with ACI, and the morphological parameters of the vertebrobasilar artery and acquired risk factors (including smoking and diabetes) were risk factors for BA dolichosis.

Data availability statement

The raw data supporting the conclusions of this article will be made available by the authors, without undue reservation.

Ethics statement

The studies involving human participants were reviewed and approved by the Institutional Review Board of Hefei Hospital Affiliated to Anhui Medical University. The patients/participants provided their written informed consent to participate in this study.

Author contributions

This work was conceptualized by MX, SC, and XW and all approved the protocol. Data collection was done by MZ, JH, PC, TG, SC, and JW. Statistical analysis was undertaken by MZ and SC. SC, MZ, and JH prepared the manuscript. MX and WX were recipients of the obtained funding and were involved in the interpretation of the data and the manuscript revision work was conceptualized by MX, SC, and WX and all approved the protocol. All authors contributed to the article and approved the submitted version.

Funding

This study was supported by grants from Anhui Provincial Key Research and Development Plan (1804h08020233).

Conflict of interest

The authors declare that the research was conducted in the absence of any commercial or financial relationships that could be construed as a potential conflict of interest.

Publisher's note

All claims expressed in this article are solely those of the authors and do not necessarily represent those of their affiliated organizations, or those of the publisher, the editors and the reviewers. Any product that may be evaluated in this article, or claim that may be made by its manufacturer, is not guaranteed or endorsed by the publisher.

Supplementary material

The Supplementary material for this article can be found online at: https://www.frontiersin.org/articless/10.3389/fmed.2023.832878/full#supplementary-material

References

1. Passero, SG, and Rossi, S. Natural history of vertebrobasilar dolichoectasia. *Neurology*. (2008) 70:66–72. doi: 10.1212/01.wnl.0000286947.89193.f3

2. Del Brutto, OH, Mera, RM, Del Brutto, VJ, Costa, AF, Zambrano, M, and Brorson, J. Basilar artery Dolichoectasia: prevalence and correlates with markers of cerebral small

vessel disease in community-dwelling older adults. *J Stroke Cerebrovasc Dis*. (2017) 26:2909–14. doi: 10.1016/j.jstrokecerebrovasdis.2017.07.014

3. Ikeda, K, Nakamura, Y, Hirayama, T, Sekine, T, Nagata, R, Kano, O, et al. Cardiovascular risk and neuroradiological profiles in asymptomatic vertebrobasilar dolichoectasia. *Cerebrovasc Dis*. (2010) 30:23–8. doi: 10.1159/000313440

4. Gutierrez, J, Sacco, RL, and Wright, CB. Dolichoectasia-an evolving arterial disease. *Nat Rev Neurol*. (2011) 7:41–50. doi: 10.1038/nrneurol.2010.181

5. Pico, F, Labreuche, J, Gourfinkel-An, I, and Amarenco, PGENIC Investigators. Basilar artery diameter and 5-year mortality in patients with stroke. *Stroke*. (2006) 37:2342–7. doi: 10.1161/01.STR.0000236058.57880.03

6. Mangrum, WI, Huston, J 3rd, Link, MJ, Wiebers, DO, McClelland, RL, Christianson, TJ, et al. Enlarging vertebrobasilar nonsaccular intracranial aneurysms: frequency, predictors, and clinical outcome of growth. *J Neurosurg*. (2005) 102:72–9. doi: 10.3171/jns.2005.102.1.0072

7. Cao, SG, Ni, X, Wu, Q, He, J, Cui, P, Ge, T, et al. Basilar artery dolichosis is associated with a poor 90-day outcome in acute isolated pontine infarction. *Sci Rep*. (2020) 10:6557. doi: 10.1038/s41598-020-62873-4

8. Ngo, MT, Kwak, HS, and Chung, GH. Change in basilar artery length and bending according to aging and vertebral artery dominance: a longitudinal study. *Sci Rep*. (2020) 10:8904. doi: 10.1038/s41598-020-65682-x

9. Nishikata, M, Hirashima, Y, Tomita, T, Futatsuya, R, Horie, Y, and Endo, S. Measurement of basilar artery bending and elongation by magnetic resonance cerebral angiography: relationship to age, sex and vertebral artery dominance. *Arch Gerontol Geriatr*. (2004) 38:251–9. doi: 10.1016/j.archger.2003.10.006

10. Zhang, DP, Zhang, SL, Zhang, JW, Zhang, HT, Fu, SQ, Yu, M, et al. Basilar artery bending length, vascular risk factors, and pontine infarction. *J Neurol Sci*. (2014) 338:142–7. doi: 10.1016/j.jns.2013.12.037

11. Ubogu, EE, and Zaidat, OO. Vertebrobasilar dolichoectasia diagnosed by magnetic resonance angiography and risk of stroke and death: a cohort study. *J Neurol Neurosurg Psychiatry*. (2004) 75:22–6. PMID: 14707300

12. Hong, JM, Chung, CS, Bang, OY, Yong, SW, Joo, IS, and Huh, K. Vertebral artery dominance contributes to basilar artery curvature and peri-vertebrobasilar junctional infarcts. *J Neurol Neurosurg Psychiatry*. (2009) 80:1087–92. doi: 10.1136/jnnp.2008.169805

13. Cao, S, Zhu, X, Wu, Q, Ni, X, He, J, Cui, P, et al. Basilar artery dolichosis increases the risk of long-term recurrence in patients with pontine infarction: a prospective cohort study. *Front Neurol*. (2021) 12:788145. doi: 10.3389/fneur.2021.788145

14. Su, PH, Chen, JY, Chen, SJ, Yang, MS, and Liu, YL. Basilar artery dolichoectasia in a boy with a combination of partial monosomy 18p and partial trisomy 20q. *Clin Dysmorphol*. (2006) 15:225–8. doi: 10.1097/01.mcd.0000228422.66789.a2

15. Forrest, KM, Siddiqui, A, Lim, M, and Wraige, E. Basilar artery dolichoectasia in childhood: evidence of vascular compromise. *Childs Nerv Syst*. (2011) 27:193–6. doi: 10.1007/s00381-010-1267-y

16. Lou, M, and Caplan, LR. Vertebrobasilar dilatative arteriopathy (dolichoectasia). *Ann N Y Acad Sci*. (2010) 1184:121–33. doi: 10.1111/j.1749-6632.2009.05114.x

17. Zheng, J, Sun, B, Lin, R, Teng, Y, Zhao, X, and Xue, Y. Association between the vertebrobasilar artery geometry and basilar artery plaques determined by high-resolution magnetic resonance imaging. *BMC Neurosci*. (2021) 22:20. doi: 10.1186/s12868-021-00624-5

18. Yu, J, Zhang, S, Li, ML, Ma, Y, Dong, YR, Lou, M, et al. Relationship between the geometry patterns of vertebrobasilar artery and atherosclerosis. *BMC Neurol*. (2018) 18:83. doi: 10.1186/s12883-018-1084-6

19. Deng, D, Cheng, FB, Zhang, Y, Zhou, HW, Feng, Y, and Feng, JC. Morphological analysis of the vertebral and basilar arteries in the Chinese population provides greater diagnostic accuracy of vertebrobasilar dolichoectasia and reveals gender differences. *Surg Radiol Anat*. (2012) 34:645–50. doi: 10.1007/s00276-012-0960-9

Frontiers in Medicine

Translating medical research and innovation into improved patient care

A multidisciplinary journal which advances our medical knowledge. It supports the translation of scientific advances into new therapies and diagnostic tools that will improve patient care.

Discover the latest Research Topics

See more →

Frontiers

Avenue du Tribunal-Fédéral 34
1005 Lausanne, Switzerland
frontiersin.org

Contact us

+41 (0)21 510 17 00
frontiersin.org/about/contact